School of Science and Engineering
Department of Applied Geology

The Cycling of Redox Sensitive Elements at Subduction Zones: Insights from Subducted Mantle Lithosphere

Rosalind Joanne Crossley

This thesis is presented for the Degree of
Doctor of Philosophy
of
Curtin University

November 2016

DECLARATION

To the best of my knowledge and belief this thesis contains no material previously published by any other person except where due acknowledgement has been made.

This thesis contains no material which has been accepted for the award of any other degree or diploma in any university.

Rosalind J. Crossley

11/11/2016

ACKNOWLEDGEMENTS

Firstly, thanks very much to my supervisor Associate Prof. Katy Evans for making this exciting PhD possible. Thank you for your support, patience and all your advice. My analytical, academic writing and presentation skills have improved greatly with your supervision these past few years. Many thanks to my associate supervisors, Prof. Steve Reddy for discussions and advice on Alpine geology, and Dr. Prok Vasilyev and my former associate supervisor Dr. Greg Lester for all your help and advice.

I'm very grateful to all the other Applied Geology staff, for discussions and advice over the past few years. Thanks to Mrs Annette Labrooy for her administrative assistance and Mr Andy Wieczorek for inductions for the rock saws and for health and safety advice.

I thank Dr. Heejin Jeon and Associate Prof. Matt Kilburn for their help with SIMS and NanoSIMS, and Dr. Malcolm Roberts for his assistance with the JEOL Hyperprobe at the Centre of Microscopy and Microanalysis, University of Western Australia. Thanks to Associate Prof. Noreen Evans and Mr Brad McDonald for help with LA-ICP-MS. I'd also like to thank Noreen for teaching me how to use Iolite for LA-ICP-MS data reduction and for feedback which helped to improve the HSE manuscript. Ms Elaine Miller and Ms Kelly Merigot are thanked for their assistance with the Tescan Mira, Tescan Integrated Mineral Analyser (TIMA), and Neon SEMs. I thank Dr Alessandro Bragagni and Ms Iris Speelmanns from Bonn University, Germany, for the Bonn standard for HSE, and for invaluable discussions on HSE analytical methods.

I acknowledge the facilities, and the scientific and technical assistance of the Australian Microscopy and Microanalysis Research Facility at the Centre for Microscopy, Characterisation and Analysis, The University of Western Australia, a facility funded by the University, State and Commonwealth Governments. I acknowledge the facilities of the GeoHistory and Microscopy and Microanalysis facilities at the John de Laeter Centre, Curtin University. I acknowledge support from the Australian Research Council (ARC) Future Fellowship grant awarded to Associate Prof. Katy Evans (FF12000579) and from Curtin University who

provided support with a Curtin International Postgraduate Research Scholarship (CIPRS). Thanks to Geoconferences WA and Curtin for travel grants that allowed me to attend Goldschmidt in 2015 and 2016 to present my research.

To all my friends, near and far, thank you all so much for your support. To Steph Walker and Rehemat Bhatia in the UK, thanks for all the chats, sharing the PhD journey with you has been a great support. Thanks to Courtney Henry for introducing me to meditation, it helped to keep me calm in the final months of my thesis! I'm thankful to all the Applied Geology PhD students, old and new, thanks for all the chats over cups of tea and coffee and for making my PhD journey so much easier. I'd like to thank Sarah Hayes for being my field partner in Corsica and for discussions about Corsica. Also thanks to Sarah and Luke Daly for a couple of samples, they turned out to be very exciting! Thanks to Fiona Mothersole for discussions about serpentinites. Thank you to my office neighbours, Jen Porter and Shirley Hu for weekend/late night office company, and also to Jen for office popcorn and chocolate supplies!

To my family, thank you so much for all your incredible support in everything over the years. This PhD would not have been possible without you. Mum and Dad, thanks so much for everything you have done for me and for always being there for me, even when you're so far away. Thanks very much to my sister, Caroline, for all your encouragement while living with me these past two years.

ABSTRACT

Subduction zones are sites of major, minor and trace element exchange between the exterior and interior of the Earth. Redox sensitive elements are elements which exist in multiple valence states such as iron, sulfur and highly siderophile elements (HSE). These elements have the ability to oxidise or reduce exterior components of the Earth; the oceans and atmosphere, and the interior; the mantle. The mantle above the subducting plate and beneath volcanic arcs, the sub-arc mantle, is the site of formation of economic metal deposits such as copper, gold and silver. Current genetic models for these deposits require an oxidised sub-arc mantle. However, the oxidation state of the sub-arc mantle remains controversial due to the confounding effects of late stage processes in arc lavas such as fractional crystallisation and degassing.

Serpentinites are hydrated mantle rocks that are important hosts to redox sensitive elements. Upon subduction and devolatilisation, serpentinites have the potential to transfer redox sensitive elements to oxidise or reduce the sub-arc mantle and other lithologies. 'Hybrid' rocks represent 'mixed' lithologies from sedimentary, ultramafic or mafic pre-cursors, and the high-pressure counterparts are considered to form at the slab-mantle interface. In this study, high-pressure serpentinites at various proximities to and from other lithologies, and hybrid ultramafic/mafic rocks from the Western Alps and Alpine Corsica are investigated.

This work explores the changes to the distribution of iron, sulfur and HSE within subducted serpentinites and hybrid rocks on a sample and mineral scale. Whole rock major and trace element geochemistry, including HSE, in combination with detailed textural analyses of silicate, oxide and sulfides, and mineral major, minor and trace element data are used to assess the changes in iron, sulfur and HSE from seafloor alteration, through to subduction and exhumation. Mineral parageneses place constraints on the timing of the growth of mineral hosts to sulfur, iron and HSE, which in turn can be used to assess the changes to sulfur and oxygen activities.

Subduction-related spinels show substantial evidence for alteration both in texture and in trace element geochemistry, likely resulting from the reaction

between antigorite and primary spinel in the presence of local oxidising and/or Fe^{3+} bearing fluids, whereas an increase in the mode of magnetite at the onset of exhumation in hybrid ultramafic/mafic rocks likely records fluid infiltration at this stage. Additionally, one sample from Pfulwe in the Western Alps is enriched in titanium, providing the tantalising possibility of the mobilisation of seemingly 'immobile' elements, including Fe^{3+}. Quantitative major and minor element mapping of selected grains of oxides and sulfides reveal additional insights into the intrinsic (internal) or extrinsic (external) processes responsible for modification of these minerals either during seafloor alteration, subduction or exhumation.

To the author's best knowledge, this study presents the first *in-situ* HSE analyses of sulfides and oxides within high-pressure serpentinites and hybrid ultramafic/mafic rocks. In addition, there are currently no published articles on isotopic analyses of sulfides in high-pressure serpentinites and hybrid rocks. Net changes in HSE concentrations compared to pre-subduction analogues were not observed for serpentinites, with the exception of moderate Au enrichment in one sample. However, HSE concentrations in sulfides are shown to be depleted with some exceptions. The redistribution of HSE from sulfides to alloys are proposed to explain the depletion as a result of more reducing conditions or mobilisation on a micron to millimetre scale. Based on current knowledge, the enrichment of Ru in sulfides, and depletion of Os and Ir, indicates the exsolution of Os and Ir under reducing conditions. However, this contrasts with heavy sulfur isotope signatures measured in the same samples, which indicate oxidised sulfur. Alternatively, the mechanisms and conditions could differ for the solubility and precipitation of different HSE, or the isotopic signatures could record a different stage of alteration.

Sulfur isotope compositions in most samples are most simply explained by fixation on the seafloor and retention throughout subduction, with heterogeneous compositions reflecting local mobilisation and redox exchange. Therefore, the isotopic signatures could be set at an earlier stage than the redistribution of HSE occurred. However, a shift towards heavy signatures recorded in one sample is texturally associated with advanced stages of exhumation. Heterogeneous and heavy signatures of up to 15.5‰ in this sample are attributed to a mixed fluid source from mafic/ultramafic fluids.

Further work is required to develop an improved understanding of titanium solubility and the solubility and precipitation of HSE-bearing alloys to constrain the conditions of formation. The assessment of the sensitivity of HSE distribution to sulfidation and/oxidation could benefit from stable isotope and electron energy loss spectroscopy (EELS). In addition, suggestions are made for further research to distinguish between mass independent fractionation factors ($\Delta^{33}S$) caused by bacterial or hydrothermal sulfate reduction on the seafloor, or that caused by the S^{3-} ion at high-pressures, in particular more precise $\Delta^{33}S$ measurements and the determination of fractionation factors for S^{3-} ions.

TABLE OF CONTENTS

CHAPTER 5

LIST OF FIGURES

LIST OF TABLES

CHAPTER 1

INTRODUCTION

1.1 Aims and objectives of this study

The aim of this study is to constrain the release or retention of the redox sensitive elements from high-pressure rocks, with a focus on Fe, S and highly siderophile elements (HSE), and to determine the implications of the transfer of redox sensitive elements between subduction zone components, specifically for the oxidation state of the sub-arc mantle. This will be addressed through four objectives, as follows:

1) To determine the changes in iron and sulphur bearing phases throughout the subduction cycle by investigating the changes to mineral hosts of these elements and proportions of these elements during metamorphic fluid infiltration.

2) To trace the distribution of HSE through the metamorphic evolution of serpentinites and hybrid ultramafic/mafic rocks in subduction zones by investigating the changes to the bulk HSE concentration and mineral scale distribution of HSE during subduction and exhumation.

3) To assess the processes which affect the distribution of iron on a mineral scale through the analysis of textures and trace element chemistry of spinel grains from the seafloor, through subduction and exhumation.

4) To determine the source and redox state of sulphur and iron retained in and fluxed from and to ultramafic rocks during subduction related metamorphism and exhumation.

1.2 Thesis structure

Chapters 3, 4 and 6 are intended to be published as separate manuscripts, and therefore due to the nature of the thesis some repetition of the geological settings, background information and methods is necessary.

Chapter two outlines the geological settings of the Zermatt-Saas Zone and Alpine Corsica, field observations and descriptions of samples proximal to serpentinites analysed in chapters 3 to 6.

Chapter three has been accepted for publication in 'Geochemistry, Geophysics and Geosystems'. This chapter addresses the oxidation state and redistribution of iron and titanium throughout the metamorphic evolution of serpentinites from the Zermatt-Saas Zone, Western Alps. This is achieved through detailed textural analysis of oxide minerals in the samples, compositional data of oxide minerals and whole rock geochemistry. Mineral parageneses, incorporating information from silicate, oxide and sulphide textures, mineral compositions and whole rock geochemistry forms the basis of this work. This chapter contributes to objectives 1 and 4.

Chapter four is under review in the Journal of Petrology and focuses on tracing HSE hosted in serpentinites and hybrid rocks from Alpine Corsica through the subduction cycle and assesses the potential consequences of interaction of ultramafic rocks with metasediments and mafic rocks on the sulphur and oxygen activities, and HSE distribution. Bulk HSE concentrations and comparison to HSE concentrations of primitive mantle, slow-spreading margin, ocean-continent transition peridotite, mafic and hybrid rocks provides an insight into sample scale HSE transfer. Mineral parageneses places constraints on the timing of sulphide growth (the major host of HSE), oxides and metal alloys and the activities of oxygen and sulphur (aO_2–aS_2) from pre-subduction to exhumation. Mineral scale insights into the distribution of HSE in high-pressure serpentinites and hybrid rocks is achieved through LA-ICP-MS determination of HSE concentrations in sulphides and oxides, and the detection of small (~2–25 μm^2) platinum group minerals using high resolution SEM mapping techniques. This chapter addresses objectives 1 and 2.

Chapter five focuses on the mineral textures and trace element geochemistry of several generations of spinels to assess the role of fluids, pressure and temperature on the mineral-scale redistribution of iron. Trace element geochemistry is focused on chalcophile and lithophile element concentrations derived from LA-ICP-MS analyses. This chapter addresses objective 1 and 3.

Chapter six is under review in 'Chemical Geology' and investigates sulphur redox state, the likelihood of sulphur transfer to the sub-arc mantle from serpentinite or hybrid rock dehydration, and the distribution of sulphur within subducted

serpentinites through a combination of petrographic analysis, in-situ sulphur isotope and trace element analyses of sulphides hosted in serpentinites and hybrid rocks from Alpine Corsica. This chapter addresses objectives 1 and 4.

Chapter seven summarises, interprets and synthesises the results to address the objectives outlined above and the implications for changes to the oxidation state of hydrated mantle lithosphere during subduction and exhumation, and potential consequences for the oxidation state of other subduction zones components, specifically the sub-arc mantle. In addition, suggestions for further work are made.

1.3 Background

1.3.1 The oxidation state of the sub-arc mantle

Subduction zones connect the interior of the Earth (the mantle) to the exterior (the crust, atmosphere and oceans), where the cycling of major, minor and trace elements occur and thus subduction zones control the fate of these elements. The cycling of elements with variable oxidation state (redox sensitive elements) e.g. Fe, S and C, have the ability to oxidise or reduce the atmosphere, oceans and mantle throughout geological time (e.g. Evans, 2012). The oxidation state of the sub-arc mantle is controversial but important to understand because current genetic models for arc-related ore deposits require the sub-arc mantle to be oxidised (e.g. Mungall, 2002; Richards, 2009; 2011). Therefore, an increased knowledge of the controls on the oxidation state of the sub-arc mantle would allow better targeting of the world's largest metal deposits such as Cu, Mo, Au and Ag deposits.

On the basis of high oxygen fugacities (fO_2) calculated from olivine-orthopyroxene-spinel thermobarometry (Ballhaus et al., 1991; Nell and Wood, 1991; Parkinson and Arculus, 1999), and elevated Fe^{3+}/total Fe in arc primitive basaltic glasses and melt inclusions compared to those from a mid ocean ridge setting (Kelley & Cottrell, 2009), it has been proposed that the oxidation state of the sub-arc mantle is elevated compared to oceanic and continental mantle. On the other hand, V/Sc analyses of basalts (Lee et al., 2005; Mallman and O'Neill, 2009), and measurements of Zn/Fe_{tot} (where $Fe_{tot} = Fe^{2+} + Fe^{3+}$) ratios (Lee et al., 2010) have shown that primitive arc magmas and MORB have similar V/Sc ratios, Zn/Fe_{tot} ratios. Oxidised Fe (Fe^{3+}) and V (V^{5+}) are more compatible in a melt phase

than more reduced Fe (Fe^{2+}), V (V^{2+}, V^{3+} or V^{4+}), Zn (Zn^{+} or Zn^{2+}) and Sc (mostly as Sc^{3+}), suggesting that primary melts in both settings have the same oxidation state (Lee et al., 2010). Therefore, it has been proposed that high oxygen fugacities and increased ferric iron contents in arc lavas are associated with processes such as degassing, fractional crystallisation of reduced minerals and assimilation of oxidised minerals (Lee et al., 2010; Mallman and O'Neill, 2009). In addition, primitive arc melts have lighter Fe isotope signatures than mid-ocean ridge mantle sources (Dauphas et al., 2009; Nebel et al., 2013), suggesting a Fe^{3+}-depleted or Fe^{2+} enriched source that could be interpreted as an indication of a more reduced source. However, the isotopic signature was proposed to be consistent with melt depletion in the protolith, regardless of oxidation state (Nebel et al., 2015).

In an attempt to minimise the effects of late stage processes and reconcile these conflicting views, Evans et al. (2012) used oxygen fugacity data from primitive olivine and spinel crystals (olivine-spinel oxybarometry) in primary arc, mid ocean ridge and ocean island basalts (OIB). The results indicated that arc basalts at depth are more oxidised than MORB or OIB and implied that the sub-arc mantle is 1-4 log units more oxidised than the oceanic or continental mantle. However, there is still a lack of consensus because a range of methods have been used to estimate oxygen fugacity (e.g. Richards, 2015).

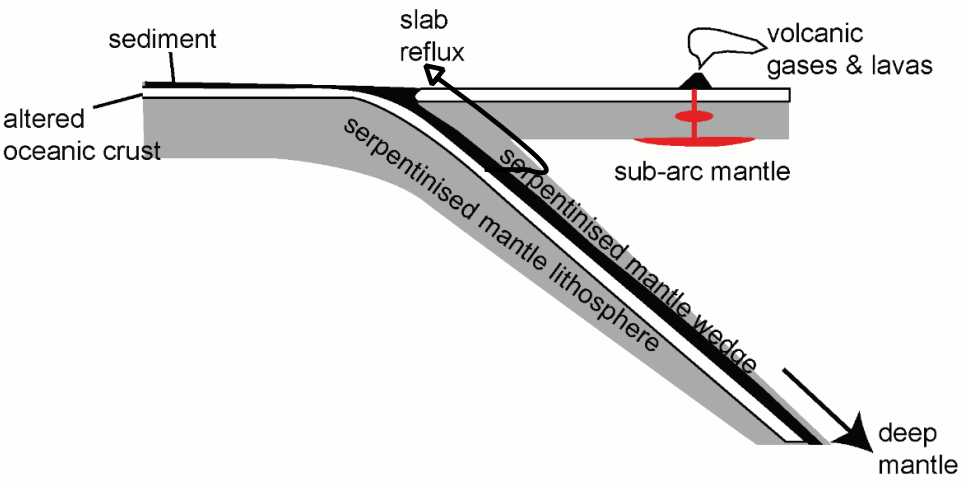

Figure 1.1: Schematic diagram of a subduction zone, redrawn from Evans, 2012.

1.3.2 The concept of redox budget

In order to make quantitative estimates of redox fluxes from the slab to the sub-arc mantle, extensive variables to describe redox fluxes are required. Redox budget is suitable for this purpose (Evans, 2006). The use of redox budget allows the determination of oxidising capacity transferred to the mantle, and quantification of the inputs and outputs of redox sensitive elements into and out of subduction zones. fO_2 cannot be used for quantification of fluxes as it is an intensive variable and therefore is not sensitive to the quantity of redox sensitive elements moving within the system e.g. from the subducting slab to the sub-arc mantle. In contrast, redox budget is an extensive variable and therefore is sensitive to the quantity of material in the system and can effectively measure a sample's ability to oxidise or reduce. Redox reactions involve the movement of electrons so redox budget calculations include the number of electrons in the sample being considered relative to a reference state:

$$RB = \sum_i n_i v_i$$

where RB = redox budget, i = redox state considered, n_i = no. moles of redox state i in sample of interest, v_i = no electrons to take 1 mole of redox state i to the reference redox state.

As shown in the equation, redox budget is completely dependent on the reference state chosen, thus it is possible to measure the oxidising capacity of the subducted material in relation to the environment that it is being introduced to and vice versa. An increase in redox budget implies that the quantity of oxidising capacity has increased relative to the oxidising capacity of the same amount of material prior to the introduction of new material.

Despite large uncertainties, redox budget calculations of the inputs and outputs of Fe, S and C to subduction zones demonstrate that subduction increases the redox budget of the mantle where Fe, C and S that is added to the mantle is more oxidised than Fe, C and S in the mantle (Evans, 2012). Two of the key uncertainties highlighted in Evans (2012) that will be investigated in this thesis include the

proportion and redox state of Fe and S in subducted mantle lithosphere and the composition of metamorphic fluids released during subduction.

1.3.3 Mechanisms of oxidising the sub-arc mantle

Fluids or melts released from devolatilisation of mafic, ultramafic, sediments and subduction mélange from the subducting slab with the ability to carry oxidised elements e.g. sulphate and ferric iron, are considered to be the predominant mechanism for oxidising the sub-arc mantle (e.g. Kelly and Cottrell 2009; Evans, 2012; Tomkins and Evans, 2015). Subduction mélange material is composed of hybrid mafic/ultramafic rocks/sediments between the slab and the sub-arc mantle (e.g. Spandler and Pirard, 2013). Mechanisms of fluid or melt transport of slab components through the mantle wedge include porous flow, where systems have low fluid:rock interactions and are rock dominated, and channelised flow with high fluid:rock interaction ratios and systems are fluid dominated (Manning, 2004, Fig. 1.2a and b). Porous flow takes ~ 100 times longer than channelised flow (Manning, 2004). In another model, fluid transport via conduits has been proposed to occur over kilometre-scale distances, pulsating through slabs over a time scale of hundreds of years (John et al., 2012). There is no general consensus on the dominant end member of fluid flow in subduction zones at present, and it could be that a continuum of these flow mechanisms exist (Manning, 2004; Spandler and Pirard, 2013). In addition, the length and time scales of fluid flow are poorly constrained. Other potential mechanisms for fluid transfer are via diapirs and plumes where hybrid rocks of upwelling mélange diapirs undergo partial melting as a result of heating in the mantle wedge and interaction with slab-derived fluids to allow effective transport of melts to the mantle wedge (Hack and Thompson, 2010; Marschall and Schumacher, 2012; Spandler and Pirard, 2013, Fig. 1.2c). For example, direct transport of HSE elements to the sub-arc mantle could be possible via this mechanism. (Penniston-Dorland et al., 2014).

There are large uncertainties regarding the quantity of subducted oxidised material, the depth the oxidised material is subducted to, the composition of melts and/or fluids, and the mode of transport via fluids in subduction zones. The positive correlation between trace elements that remain unaffected by magmatic differentiation processes, e.g. Ba/La ratios with Fe^{3+}/Fe_{tot} in back-arc basin basalts,

where Ba/La ratios positively correlate with H_2O, suggest that oxidation is a function of H_2O addition from the slab to mantle (Kelly and Cottrell, 2009). Experimental data suggests that H_2O may act to increase Fe^{3+}/Fe_{tot} in the hydrous melts in the mantle (e.g. Kushiro, 1972), although this would require disassociation of H_2 from O^{2-}, and subsequent removal of H_2 from the high pressure region, for which there is conflicting evidence (Brandon and Draper, 1996; Frost and Ballhaus, 1998). Ferric iron in silicate melts could provide a more efficient means to increase the oxidation state of the sub-arc mantle (Frost and Ballhaus, 1998), or, alternatively, a hydrous silica-rich melt or water-rich fluid (Brandon and Draper, 1996), or complete miscibility between the two end members (Draper and Green, 1997; Shen and Keppler, 1997). Silicate melts are capable of transferring 400 times more ferric iron than aqueous fluids, where this value is further increased to 10,000 times due to the lower mass of aqueous fluids released than silicate melts (Mungall, 2002). However, aqueous fluids are considered to be important carriers of sulphate to the sub-arc mantle (e.g. Mungall, 2002; Tomkins and Evans, 2015). On the other hand, the addition of water to the sub-arc mantle could alter the partitioning of ferric and ferrous iron between the melt and residue (Evans et al., 2012), due to the influence of water on the eutectic position in silicate melts (e.g. Inoue, 1994). The addition of water causes depolymerisation of silicate melts (Zotov et al., 1996; Zotov and Keppler, 1998), and Fe^{2+}/Fe^{3+} is a function of the degree of polymerisation (Mysen et al., 1985) so that elevated Fe^{3+}/Fe^{2+} ratios in a wet melt are elevated compared to those of a dry melt (Evans et al., 2012). Therefore higher Fe^{3+}/Fe^{2+} in a wet melt may not necessarily reflect an increase in oxygen fugacity.

Constraining the composition and nature of slab derived fluids is vital to the understanding of element transfer to the sub-arc mantle. For example, Fe^{3+} is not considered to be efficiently transported in aqueous fluids (Schneider and Eggler, 1986). On the other hand, fluids with increased salinity, miscible fluids or silicate melts may effectively transport Fe^{3+} although the relevant conditions are difficult to access experimentally so these suggestions are a matter of conjecture rather than fact (Kelly and Cottrell, 2009). Sulphur, a fluid mobile element, does not require highly saline fluids or silicate melts for effective transport, and the 8 electron difference between sulphate (S^{6+}) and sulphide (S^{2-}) and the moderate solubility of

sulphate suggests that sulphur transfer to the sub-arc mantle could effectively oxidise the sub-arc mantle (Kelly and Cottrell, 2009).

Another factor that could be important for oxidation of the sub-arc mantle is focused oxidised fluid pathways to the sub-arc mantle enhanced by weaknesses in the slab, such as those associated with precursors to transform faults, and changes to pressure and temperature during subduction (Evans and Tomkins, 2011). Such structures could enhance the transfer of oxidised fluids to the sub-arc mantle, and therefore increase the redox budget and oxidation state of the mantle.

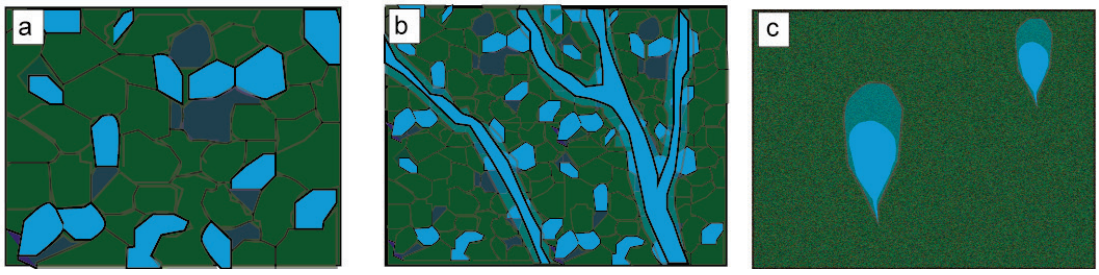

Figure 1.2: Schematic diagram illustrating the mechanisms of fluid flow in the sub-arc mantle (a) porous flow (Manning, 2004) (b) channelised flow (Manning, 2004) and (c) diapiric flow (Marschall and Schumacher, 2012). Dark blue represents the formation of hydrous minerals e.g. phlogipite in the mantle. Similar mechansims of fluid flow may occur during slab reflux up the slab-mantle interface. Adapted from Spandler and Pirard (2013).

1.3.4 The role of serpentinites in the transfer of redox budget

Mantle peridotite is exposed on the ocean floor at slow spreading margins and ocean-continent transition zones, or a continuum of the two end members (e.g. e.g. Manatschal and Muntener, 2009). Serpentinisation on the seafloor involves the reaction of water with olivine and pyroxene to produce magnetite, brucite and serpentine, H_2 and CH_4. Seafloor serpentinites are highly hydrated, containing up to 15 wt% water (Alt and Shanks, 1998; 2003; Alt et al., 2012a). Seafloor serpentinisation also results in the addition of elements to the peridotite including redox sensitive elements such as Fe, C and S. For example the production of magnetite and Fe^{3+} bearing serpentine increases the ferric iron content (e.g. Andreani et al., 2013; Lecuyer and Ricard, 1999; Debret et al., 2014) and as a result, the redox budget of mantle peridotite increases. Previous studies have used the redox state of Fe in high-pressure ultramafic rocks to infer the redox state of subduction zone fluids to provide an insight into the cycling of iron and other redox sensitive elements (e.g. Debret et al., 2015; Debret et al., 2016).

Furthermore, oceanic serpentinites contain up to 1.1 wt% sulphur and 1.6% carbon (Alt and Shanks, 1998; 2003; Delacour et al., 2008), where the concentrations of these elements are significantly elevated compared to their precursor peridotites which are estimated to contain 0.01–0.025 wt% sulphur (Evans, 2012). Fluids derived from low to moderate temperature seafloor serpentinisation can be highly alkaline and enriched in methane and hydrogen, and can mix with seawater to precipitate carbonates in the ultramafics (e.g. Schwarzenbach et al., 2013). Ultramafic rocks contribute an estimated 0.6 to 3.0 x 10^{12} mol C per year to subduction zones (Alt et al., 2012b; Evans et al., 2012; Galvez et al., 2013). The carbonation of ultramafic rocks acts as a seal to fluid flow (Schwarzenbach, 2016), so the subduction of ultramafic rocks could have major consequences for the deep cycling of carbon.

Seafloor serpentinisation also results in the addition of sulphur to ultramafic rocks exposed on the seafloor, where up to 0.4–6 x10^{12} g of S is added per year, and in the alteration of primary mantle sulphur isotope signatures to heavier values (Alt and Shanks, 2003). The high sulphur concentration and isotopic signature ($\delta^{34}S$) of serpentinites relative to peridotite may be retained during subduction, lost during devolatilisation and/or modified during retrogression (Evans and Tomkins, 2011). Sulphur bearing phases in high-pressure veins and fluid inclusions demonstrate sulphur mobility during subduction (Ferrando et al., 2005; Philippot and Selverstone, 1991).

Seafloor serpentinisation is considered to be the dominant source of hydrated mantle lithosphere and hence the enrichment of redox sensitive elements prior to subduction in the ultramafic rocks studied here. Alternatively, hydration of peridotites from the overlying mantle wedge can occur from fluids devolatilised from the dehydrating slab (e.g. Guillot et al., 2000), which could be dragged down into subduction zones via corner flow and melting processes (e.g. Bouilhol et al., 2015). Additionally, serpentinisation can result from seawater infiltration along normal faults as the plate bends to enter the trench (e.g. Kerrick, 2002), where serpentinisation of 10–20% of protolith phases occurs, producing a layer several kilometres thick (Ranero & Sallares, 2004). In summary, serpentinites are important carriers of water (up to 15 wt%, e.g. Ulmer and Trommsdorff, 1999) and redox budget to depth, and potentially contribute a greater quantity of redox budget than

mafic and sedimentary rocks to subduction zones (Evans, 2012), and therefore could have major implications for the oxidation state of the sub-arc mantle and deep mantle.

1.3.5 The effect of other lithologies on the evolution of the redox budget of serpentinites during subduction

The lower part of the subducting slab consists of serpentinites, while the upper layer is comprised of metamafic rocks, with metasediments forming the top layer (Fig. 1.3). Aqueous fluids released from serpentinites are thought to infiltrate the overlying mafic layer (Zack and John, 2007), while metasediments at the top of the slab could interact with fluids devolatilised from serpentinites and mafic rocks (Zack and John, 2007). However, processes at ocean-continent transition zones and the associated faulting may juxtapose metasediments with serpentinites resulting in a more complex oceanic lithosphere model (e.g. Zack and John, 2007), and hence fluid flow regime. Additionally, at pressures associated with eclogite facies, mafic rocks, metasediments and serpentinites have different rheological properties, resulting in the relatively low permeability of mafic rocks which typically convert to gneiss, compared to serpentinites and metasediments where minerals such as chlorite, serpentine and white mica create schistosity that is preserved to depth (Spandler and Pirard, 2013 and references therein). The contrasting properties of the different lithologies results in the diversion of strain and fluid-flow into the serpentinites and metasediments (Ague, 2007; Spandler and Pirard, 2013).

Several authors have studied the interaction of different types of lithologies in the subduction channel. Carbon isotopic analyses and Raman spectroscopy on graphite within metasediment in contact with serpentinite at Malaspina, Alpine Corsica, revealed the transfer of carbon from carbonates to graphite as a result of reduction (Malvoisin et al., 2012; Galvez et al., 2013). A progressive increase in Pb, Ba, Cs, Rb and U, heavier $\delta^{18}O$, and lighter $\delta^{37}Cl$ in metasediment was observed towards a serpentinite contact at Punta Rossa in the Western Alps (Barnes et al., 2014). Interaction with fluids derived from serpentinite or other external fluids is apparent in the Monviso ophiolite in the Western Alps, where Cr-rich and Ni-rich zones in high-pressure veins cut eclogite facies metagabbro (Spandler et al., 2011). Sediment-serpentinite interaction is evident in the Queyras Schistes Lustrés complex, Western Alps (Lafay et al., 2013) and in Cuban and Dominican Republic

serpentinites (Deschamps et al., 2011), where sediment derived fluid mobile elements (FME) were incorporated into serpentinites at the onset of subduction (Deschamps et al., 2011; Lafay et al., 2013), but not at the highest pressures. In contrast, metasomatic high-pressure sediment-serpentinite interaction is proposed to have affected peridotite from in Cima di Gagnone, Central Alps with positive fluid mobile element anomalies (B, Li, As and Sb) recorded in all peak eclogite-facies metamorphism, as well as at the onset of subduction (Scambelluri et al., 2014; Cannaò et al., 2015).

In addition, as a consequence of the differences in rheological properties between lithologies at eclogite facies depths, metasomatism and shearing results in the formation of a mélange zones, alteration of the fluid and rock composition, resulting in the formation of hybrid rocks (Spandler et al., 2008; Spandler and Pirard, 2013). Some studies have noted the hybridisation of mafic and ultramafic rocks in the subduction channel (Spandler et al., 2008; Penniston-Dorland et al., 2012; 2014; Bebout and Penniston-Dorland, 2016). Hybrid lithologies have been shown to be important carriers of volatile elements e.g. H_2O and CO_2 to the sub-arc mantle and to greater depths within subduction zones (Spandler et al., 2008). Hybrid rocks may also be important carriers of sulphur in subduction zones (see chapter 6). In addition, mechanical or metasomatic mixing of mafic and ultramafic rocks could be important for transfer of HSE within the subduction channel (Penniston-Dorland et al., 2012; 2014). Hybridisation of rocks occurs in between the slab and the sub-arc mantle. Therefore, the distance required for the transport of elements in fluids devolatilised from minerals in hybrid rocks i.e. talc, chlorite and serpentin is much less than from other lithologies within the slab (Spandler and Pirard, 2013, Fig. 1.3). The transfer of fluids and therefore elements from the subducting slab to the sub-arc mantle have been suggested to be dominantly derived from serpentinite dehydration in the slab at depths of 150 to 200 km where fluid flow to the slab-mantle interface may be enhanced via faults, or alternatively, fluids are

devolatilised from serpentinites and hybrid lithologies within the mélange zone (Spandler and Pirard, 2013 and references therein, Fig. 1.3).

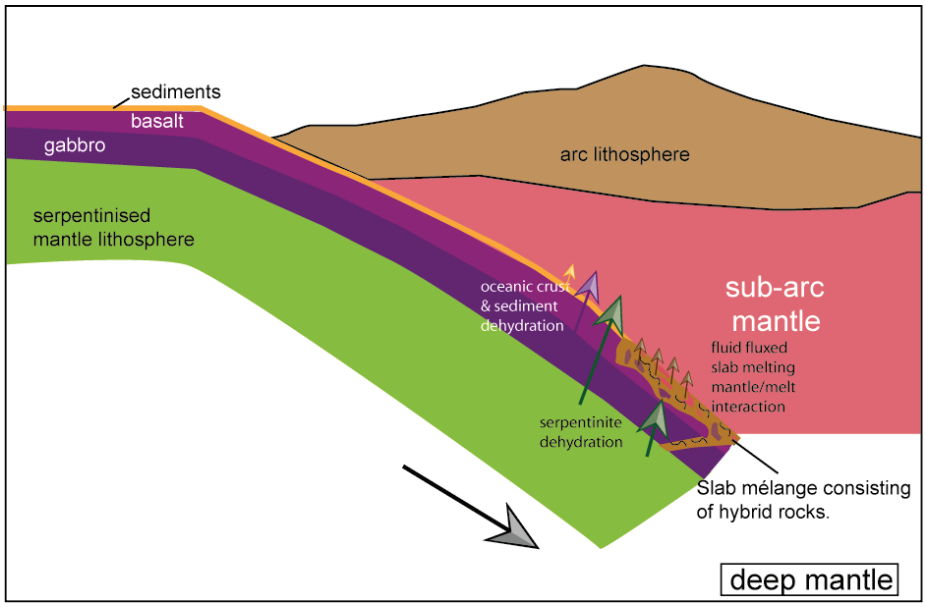

Figure 1.3: Schematic diagram of fluxes to the sub-arc mantle from the oceanic crust, sediments and serpentinites in the slab during subduction. The dehydration of serpentinite could also induce slab melting and interaction with the mantle at depth, and the resulting transfer of melts to the sub-arc mantle. Adapted from Spandler and Pirard (2013) and Dale et al. (2009).

1.4 Geochemistry

1.4.1 Major elements

Serpentinisation results in the addition of water to peridotites exposed on the seafloor, where serpentine phases contain up to 15wt%. The loss on ignition (LOI) wt% reflects the water content of the sample, and when carefully combined with textural observations from the phases present in serpentinite samples, can be a useful proxy for the degree of serpentinisation (Deschamps et al., 2013). Brucite formation results in higher water contents and is reflected in higher LOI wt% of up to 20 wt% (Deschamps et al., 2013). Subducted serpentinites have lower water contents (10–12wt%, typically) as a result of dehydration at higher pressure and the resultant growth of antigorite over the lower pressure serpentine polymorphs lizardite and chrysotile.

Seawater alteration has a slight effect on the Mg/Si ratios (Niu, 2004; Snow and Dick, 2004), however insights from a global serpentinite dataset suggest that protolith major element compositions are preserved during seafloor alteration, with the preservation of SiO_2/(sum of oxides) ratios, where the sum of oxides includes

MgO, Fe_2O_3 (total), Al_2O_3, TiO_2, CaO, Cr_2O_3, MnO, NiO, Na_2O, K_2O and P_2O_5 (Deschamps et al., 2013).

Several authors have noted the depletion of CaO associated with serpentinisation (Deschamps et al., 2013 and references therein). The low Al_2O_3 content of seafloor serpentinites is proposed to have been retained from their refractory mantle origin (Deschamps et al., 2013). Hattori and Guillot (2007) suggest that the geological setting of serpentinites can be assessed on the basis of MgO/SiO_2 plotted against Al_2O_3/SiO_2 content. However, it has been proposed that subducted serpentinites record a decrease in MgO and an increase in Al_2O_3, associated with the possible incorporation of Al_2O_3 into antigorite (Padrón-Navarta et al., 2008, see chapter 3), and the inability of antigorite to host as much MgO in its structure (Deschamps et al., 2013).

The major element composition of mineral hosts to the redox sensitive elements sulphur and iron within rocks that have been cycled from the seafloor through subduction zones and subsequent exhumation are important to constrain in order to characterise changes in the distribution of these redox sensitive elements through the subduction cycle. In addition, Fe and S major element concentrations of sulphides and spinels are required for internal standardisation for the reduction of laser-ablation-inductively-coupled-plasma-mass-spectrometry (LA-ICP-MS) derived trace element data.

1.4.2 Highly siderophile elements

The highly siderophile elements (HSE) consist of the six platinum group elements (PGE), which include Os, Ir, Ru (the Iridium-group or IPGE), Rh, and Pt and Pd (the platinum-group or PPGE), Au and Re. IPGE and PPGE display different behaviour during mantle melting. PPGE, Re and Au are moderately compatible to moderately incompatible during melting and fractional crystallisation with melting temperatures of <2000ºC, whereas IPGE are highly compatible, with melting temperatures >2000 ºC (Woodland et al., 2002; Gannoun et al., 2016 and references therein). Abyssal peridotites are considered to be the residue of mantle melting at mid ocean ridges and thus are expected to have low PPGE/IPGE ratios, as Re, Au and PPGE are preferentially removed durin partial melting (Gannoun et al., 2016 and references therein) and IPGE are retained (e.g. Brandon et al., 2000). Seafloor

serpentinisation of abyssal peridotite, whether in a slow-spreading ridge setting or ocean-continent transition zone, results in some mobility of Pd, thus Pd can be more or less enriched in seafloor serpentinites than its mantle residue precursor (e.g. Alard et al., 2005). Pt is also considered more mobile than other PGE in seafloor and mantle environments (e.g. Rehkämper et al., 1997; McInnes et al., 1999).

HSE are strongly siderophile and highly chalcophile, and hence strongly partition into spinels, sulphides and metals. Mantle sulphides, although low in abundance (Luguet et al., 2003), are the dominant host of HSE in the mantle (e.g. Mitchell and Keys, 1981). Chapter 4 investigates the HSE distribution between these phases. Re also partitions into other mantle phases such as garnet, clinopyroxene, orthopyroxene and spinel (e.g. Mallman and O'Neill, 2007). In addition, IPGE are highly compatible and PPGE are moderately compatible in Cr-spinel (Hart and Ravizza, 1996; Puchtel and Humayun, 2001), but HSE compatibility in spinels differ with increasing oxygen fugacity (only Ru, Rh and Ir remain highly compatible) and with increasing Fe^{3+} content in spinel, where only Ir and Rh are slightly compatible in spinels enriched in Fe^{3+} after replacement of Cr^{3+} (Brenan et al., 2012).

1.4.3 Sulphur isotopes

Sulphur is the 14th most common element in the Earth's crust and given that sulphides are important hosts to sulphur, the origin of sulphur and processes that have occurred subsequently can be assessed through the use of sulphur stable isotopes (Seal, 2006). Isotopes are atoms of the same element with the same number of protons and electrons but have different number of neutrons. In the case of sulphur, it has 16 protons and either 16, 17, 18, 19 or 20 neutrons so that the atomic mass is 32, 33, 34, 35 or 36 amu, respectively (e.g. Seal, 2006). The four stable sulphur isotopes include ^{32}S, ^{33}S, ^{34}S, and ^{36}S, with abundancies of 95.02, 0.75, 4.21 and 0.02%, respectively (MacNamara and Thode, 1950; Seal, 2006), while ^{35}S is unstable. Stable isotopes maintain constant concentrations over time, unlike radiogenic isotopes which continue to decay over time until they become stable.

Isotopic ratios are given, conventionally, with the minor isotope as the numerator and the major isotope of element as the denominator, e.g. $^{34}S/^{32}S$. These ratios are small so the convention is to express the isotopic composition with the

delta (δ) notation relative to a reference material, which in the case of sulphur is most often the Vienna Canyon Diablo Troilite (VCDT):

$$\delta^{34}\mathrm{S}\ (‰) = \left\{\left[\left({}^{34}\mathrm{S}/{}^{32}\mathrm{S}\right)_{sample} - \left({}^{34}\mathrm{S}/{}^{32}\mathrm{S}\right)_{VCDT}\right] * \left[\left({}^{34}\mathrm{S}/{}^{32}\mathrm{S}\right)_{VCDT}\right]^{-1}\right\} * 1000$$

where the units are per mil (‰) or parts per thousand. Vienna Canyon Diablo Troilite (VDCT) has a δ^{34}S value of 0.0‰, and ^{34}S/^{32}S ratio of 4.50045 x 10^{-3} (Ault and Jensen, 1963, Seal, 2006).

Fractionation is the partitioning of isotopes among sulphur-bearing phases, in the case of S isotopes. There are several controls on the fractionation of stable isotopes; equilibrium fractionations, which decrease with an increase in temperature, mass where larger fractionations are associated with light elements and isotopes with different relative masses, bond strength, where heavy isotopes preferentially associate with stiff bonds, and kinetic isotope fractionations. An increased bond strength, and hence the incorporation of heavy isotopes is often associated with higher values of the valence e (e.g. Schauble et al., 2004 and references therein) so redox reactions can cause significant sulphur isotope fractionations between two sulphur species in geological systems (e.g. Seal, 2006). Given that ^{34}S is the most abundant sulphur isotope and that variations are greater for ^{34}S/^{32}S than ^{33}S/^{32}S because fractionation is proportional to mass, ^{34}S/^{32}S (δ^{34}S) measurements, are the most commonly measured isotopes. Oxidation results in species enriched in ^{34}S and therefore heavy δ^{34}S, whereas reduction is associated with a depletion in ^{34}S and hence light δ^{34}S. Therefore sulphur isotopes δ^{34}S can be used to constrain the source and redox state of sulphur, and processes such as fluid interaction that have occurred since sulphide crystallisation. Different sulphur sources can have very different sulphur isotope values. For example, mantle sulphide has a δ^{34}S of ~0‰ (Ohmoto and Rye, 1979), whereas seawater sulphate has heavy δ^{34}S of ~20‰ (e.g. Alt and Shanks, 2003).

The cap delta (Δ) notation is used to describe the extent of mass independent fractionation (MIF), which is a variation in isotope abundance that is not dependent on mass and deviates from the terrestrial fractionation line, a geochemical plot of one isotope ratio against another for the Earth-Moon system, for example between

$\delta^{34}S$ and $\delta^{33}S$, where the slope of the fractionation line is 0.515, as described below (Seal, 2006).

$$\Delta^{33}S = \delta^{33}S - 1000\left[\left(1 - \frac{\delta^{34}S}{1000}\right)^{0.515} - 1\right]$$

1.5 Summary

In summary, serpentinites are hydrated mantle rocks that are important hosts to a wide range of elements, including those that are redox sensitive such as iron, sulphur and highly siderophile elements. Therefore upon subduction and devolatilisation, serpentinites may have a significant role in the release of fluids and redox sensitive elements to the sub-arc mantle. Interaction with other lithologies either within the slab or within subduction mélange zones may also play a significant role in the transfer of elements and oxidation of the sub-arc mantle or the deep mantle. The transfer of redox sensitive elements from the slab will be assessed through the use of whole rock geochemistry, petrographic analysis augmented by scanning electron microscopy techniques, mineral compositions, *in-situ* trace element geochemistry including highly siderophile elements, and *in-situ* sulphur isotopes.

1.6 References

Ague, J. J. (2007), 'Models of permeability contrasts in subduction zone mélange: implications for gradients in fluid fluxes, Syros and Tinos Islands, Greece', *Chemical Geology* **239**(3), 217–227.

Alard, O.; Luguet, A.; Pearson, N. J.; Griffin, W. L.; Lorand, J.-P.; Gannoun, A.; Burton, K. W. & O'Reilly, S. Y. (2005), 'In situ Os isotopes in abyssal peridotites bridge the isotopic gap between MORBs and their source mantle', *Nature* **436**(7053), 1005–1008.

Allen, D. E. & Seyfried, W. (2003), 'Compositional controls on vent fluids from ultramafic-hosted hydrothermal systems at mid-ocean ridges: An experimental study at 400 C, 500 bars', *Geochimica et Cosmochimica Acta* **67**(8), 1531–1542.

Alt, J. C.; Garrido, C. J.; Shanks, W.; Turchyn, A.; Padrón-Navarta, J. A.; Sánchez-Vizcaino, V. L.; Pugnaire, M. T. G. & Marchesi, C. (2012b), 'Recycling of water, carbon, and sulphur during subduction of serpentinites: A stable isotope study of Cerro del Almirez, Spain', *Earth and Planetary Science Letters* **327**, 50–60.

Alt, J. C.; Shanks, W.; Crispini, L.; Gaggero, L.; Schwarzenbach, E. M.; Früh-Green, G. L. & Bernasconi, S. M. (2012a), 'Uptake of carbon and sulphur during seafloor serpentinization and the effects of subduction metamorphism in Ligurian peridotites', *Chemical Geology* **322**, 268–277.

Alt, J. C. & Shanks, W. C. (2003), 'Serpentinization of abyssal peridotites from the MARK area, Mid-Atlantic Ridge: sulphur geochemistry and reaction modeling', *Geochimica et Cosmochimica Acta* **67**(4), 641–653.

Alt, J. C. & Shanks, W. C. (2003), 'Serpentinization of abyssal peridotites from the MARK area, Mid-Atlantic Ridge: sulphur geochemistry and reaction modeling', *Geochimica et Cosmochimica Acta* **67**(4), 641–653.

Alt, J. C. & Shanks, W. C. (1998), 'Sulphur in serpentinized oceanic peridotites: Serpentinization processes and microbial sulphate reduction', *Journal of Geophysical Research: Solid Earth* **103**(B5), 9917–9929.

Andreani, M.; Mével, C.; Boullier, A.-M. & Escartin, J. (2007), 'Dynamic control on serpentine crystallization in veins: Constraints on hydration processes in oceanic peridotites', *Geochemistry, Geophysics, Geosystems* **8**(2).

Andreani, M.; Munoz, M.; Marcaillou, C. & Delacour, A. (2013), '$$XANES study of iron redox state in serpentine during oceanic serpentinization', *Lithos* **178**, 70–83.

Ballhaus, C.; Berry, R. & Green, D. (1991), 'High pressure experimental calibration of the olivine-orthopyroxene-spinel oxygen geobarometer: implications for the oxidation state of the upper mantle', *Contributions to Mineralogy and Petrology* **107**(1), 27–40.

Barnes, J. D.; Beltrando, M.; Lee, C.-T. A.; Cisneros, M.; Loewy, S. & Chin, E. (2014), 'Geochemistry of Alpine serpentinites from rifting to subduction: A view across paleogeographic domains and metamorphic grade', *Chemical Geology* **389**, 29–47.

Bouilhol, P.; Magni, V.; van Hunen, J. & Kaislaniemi, L. (2015), 'A numerical approach to melting in warm subduction zones', *Earth and Planetary Science Letters* **411**, 37–44.

Brandon, A. D. & Draper, D. S. (1996), 'Constraints on the origin of the oxidation state of mantle overlying subduction zones: an example from Simcoe, Washington, USA', *Geochimica et Cosmochimica Acta* **60**(10), 1739–1749.

Brandon, A. D.; Snow, J. E.; Walker, R. J.; Morgan, J. W. & Mock, T. D. (2000), '190 Pt–186 Os and 187 Re–187 Os systematics of abyssal peridotites', *Earth and Planetary Science Letters* **177**(3), 319–335.

Brenan, J. M.; Finnigan, C. F.; McDonough, W. F. & Homolova, V. (2012), 'Experimental constraints on the partitioning of Ru, Rh, Ir, Pt and Pd between chromite and silicate melt: the importance of ferric iron', *Chemical Geology* **302**,

16–32.

Bromiley, G. D. & Pawley, A. R. (2003), 'The stability of antigorite in the systems MgO-SiO2-H2O (MSH) and MgO-Al2O3-SiO2-H2O (MASH): The effects of Al3+ substitution on high-pressure stability', *American Mineralogist* **88**(1), 99–108.

Cannaт, E.; Agostini, S.; Scambelluri, M.; Tonarini, S. & Godard, M. (2015), 'B, Sr and Pb isotope geochemistry of high-pressure Alpine metaperidotites monitors fluid-mediated element recycling during serpentinite dehydration in subduction mélange (Cima di Gagnone, Swiss Central Alps)', *Geochimica et Cosmochimica Acta* **163**, 80–100.

Dauphas, N.; Craddock, P. R.; Asimow, P. D.; Bennett, V. C.; Nutman, A. P. & Ohnenstetter, D. (2009), 'Iron isotopes may reveal the redox conditions of mantle melting from Archean to Present', *Earth and Planetary Science Letters* **288**(1), 255–267.

Debret, B.; Andreani, M.; Mucoz, M.; Bolfan-Casanova, N.; Carlut, J.; Nicollet, C.; Schwartz, S. & Trcera, N. (2014), 'Evolution of Fe redox state in serpentine during subduction', *Earth and Planetary Science Letters* **400**, 206–218.

Debret, B.; Bolfan-Casanova, N.; Padrón-Navarta, J. A.; Martin-Hernandez, F.; Andreani, M.; Garrido, C. J.; Sánchez-Vizcaino, V. L.; Gómez-Pugnaire, M. T.; Mucoz, M. & Trcera, N. (2015), 'Redox state of iron during high-pressure serpentinite dehydration', *Contributions to Mineralogy and Petrology* **169**(4), 1–18.

Debret, B.; Millet, M.-A.; Pons, M.-L.; Bouilhol, P.; Inglis, E. & Williams, H. (2016), 'Isotopic evidence for iron mobility during subduction', *Geology* **44**(3), 215–218.

Delacour, A.; Früh-Green, G. L.; Bernasconi, S. M. & Kelley, D. S. (2008), 'Sulphur in peridotites and gabbros at Lost City (30 N, MAR): Implications for hydrothermal alteration and microbial activity during serpentinization', *Geochimica et Cosmochimica Acta* **72**(20), 5090–5110.

Deschamps, F.; Godard, M.; Guillot, S. & Hattori, K. (2013), 'Geochemistry of subduction zone serpentinites: A review', *Lithos* **178**, 96–127.

Deschamps, F.; Guillot, S.; Godard, M.; Andreani, M. & Hattori, K. (2011), 'Serpentinites act as sponges for fluid-mobile elements in abyssal and subduction zone environments', *Terra Nova* **23**(3), 171–178.

Deschamps, F.; Guillot, S.; Godard, M.; Andreani, M. & Hattori, K. (2011), 'Serpentinites act as sponges for fluid-mobile elements in abyssal and subduction zone environments', *Terra Nova* **23**(3), 171–178.

Draper, D. S. & Green, T. H. (1997), 'P–T phase relations of silicic, alkaline, aluminous mantle-xenolith glasses under anhydrous and C–O–H fluid-saturated conditions', *Journal of Petrology* **38**(9), 1187–1224.

Evans, B. W. (2008), 'Control of the products of serpentinization by the Fe2+ Mg-1 exchange potential of olivine and orthopyroxene', *Journal of Petrology* **49**(10), 1873–1887.

Evans, K. (2012), 'The redox budget of subduction zones', *Earth-Science Reviews* **113**(1), 11–32.

Evans, K. (2006), 'Redox decoupling and redox budgets: Conceptual tools for the study of earth systems', *Geology* **34**(6), 489–492.

Evans, K.; Elburg, M. & Kamenetsky, V. (2012), 'Oxidation state of subarc mantle', *Geology* **40**(9), 783–786.

Evans, K.; Reddy, S.; Tomkins, A. & Crossley, R. (in revision), 'Effects of geodynamic setting on the redox state of fluids released by subducted mantle lithosphere', *Lithos*.

Evans, K.; Tomkins, A.; Cliff, J. & Fiorentini, M. (2014), 'Insights into subduction zone sulphur recycling from isotopic analysis of eclogite-hosted sulphides', *Chemical Geology* **365**, 1–19.

Ferrando, S.; Frezzotti, M.; Dallai, L. & Compagnoni, R. (2005), 'Multiphase solid inclusions in UHP rocks (Su-Lu, China): remnants of supercritical silicate-rich aqueous fluids released during continental subduction', *Chemical Geology* **223**(1), 68–81.

Ferrando, S.; Frezzotti, M. L.; Orione, P.; Conte, R. C. & Compagnoni, R. (2010), 'Late-Alpine rodingitization in the Bellecombe meta-ophiolites (Aosta Valley, Italian Western Alps): evidence from mineral assemblages and serpentinization-derived H2-bearing brine', *International Geology Review* **52**(10-12), 1220–1243.

Frost, B. R. & Ballhaus, C. (1998), 'Comment on" Constraints on the origin of the oxidation state of mantle overlying subduction zones: an example from Simcoe, Washington, USA" by AD Brandon and DS Draper', *Geochimica et Cosmochimica Acta* **62**, 329–332.

Galvez, M. E.; Martinez, I.; Beyssac, O.; Benzerara, K.; Agrinier, P. & Assayag, N. (2013), 'Metasomatism and graphite formation at a lithological interface in Malaspina (Alpine Corsica, France)', *Contributions to Mineralogy and Petrology* **166**(6), 1687–1708.

Gannoun, A.; Burton, K. W.; Day, J. M.; Harvey, J.; Schiano, P. & Parkinson, I. (2016), 'Highly siderophile element and Os isotope systematics of volcanic rocks at divergent and convergent plate boundaries and in intraplate settings', *Reviews in Mineralogy and Geochemistry* **81**(1), 651–724.

Groppo, C. & Compagnoni, R. (2007), 'Metamorphic veins from the serpentinites of the Piemonte Zone, western Alps, Italy: a review', *Periodico di Mineralogia* **76**, 127–153.

Guillot, S.; Hattori, K. H. & de Sigoyer, J. (2000), 'Mantle wedge serpentinization and exhumation of eclogites: insights from eastern Ladakh, northwest Himalaya', *Geology* **28**(3), 199–202.

Hack, A. C. & Thompson, A. B. (2010), 'Density and viscosity of hydrous magmas and related fluids and their role in subduction zone processes', *Journal of Petrology*, egq048.

Hart, S. R. & Ravizza, G. E. (1996), 'Os partitioning between phases in lherzolite and basalt', *Earth Processes: Reading the Isotopic Code*, 123–134.

Hattori, K. H. & Guillot, S. (2007), 'Geochemical character of serpentinites associated with high-to ultrahigh-pressure metamorphic rocks in the Alps, Cuba, and the Himalayas: Recycling of elements in subduction zones', *Geochemistry, Geophysics, Geosystems* **8**(9).

John, T.; Gussone, N.; Podladchikov, Y. Y.; Bebout, G. E.; Dohmen, R.; Halama, R.; Klemd, R.; Magna, T. & Seitz, H.-M. (2012), 'Volcanic arcs fed by rapid pulsed fluid flow through subducting slabs', *Nature Geoscience* **5**(7), 489–492.

Kelley, K. A. & Cottrell, E. (2009), 'Water and the oxidation state of subduction zone magmas', *Science* **325**(5940), 605–607.

Kerrick, D. (2002), 'Serpentinite seduction', *Science* **298**(5597), 1344–1345.

Kushiro, I. (1972), 'Effect of water on the composition of magmas formed at high pressures', *Journal of Petrology* **13**(2), 311–334.

Lécuyer, C. & Ricard, Y. (1999), 'Long-term fluxes and budget of ferric iron: implication for the redox states of the Earth's mantle and atmosphere', *Earth and Planetary Science Letters* **165**(2), 197–211.

Lafay, R.; Deschamps, F.; Schwartz, S.; Guillot, S.; Godard, M.; Debret, B. & Nicollet, C. (2013), 'High-pressure serpentinites, a trap-and-release system controlled by metamorphic conditions: Example from the Piedmont zone of the western Alps', *Chemical Geology* **343**, 38–54.

Lee, C.-t. A.; Leeman, W. P.; Canil, D. & Li, Z.-X. A. (2005), 'Similar V/Sc systematics in MORB and arc basalts: implications for the oxygen fugacities of their mantle source regions', *Journal of Petrology* **46**(11), 2313–2336.

Lee, C.-T. A.; Luffi, P.; Le Roux, V.; Dasgupta, R.; Albaréde, F. & Leeman, W. P. (2010), 'The redox state of arc mantle using Zn/Fe systematics', *Nature* **468**(7324), 681–685.

Li, X.-P.; Rahn, M. & Bucher, K. (2004), 'Serpentinites of the Zermatt-Saas ophiolite complex and their texture evolution', *Journal of Metamorphic Geology* **22**(3), 159–177.

Luguet, A.; Lorand, J.-P.; Alard, O. & Cottin, J.-Y. (2004), 'A multi-technique study

of platinum group element systematic in some Ligurian ophiolitic peridotites, Italy', *Chemical Geology* **208**(1), 175–194.

Mével, C. (2003), 'Serpentinization of abyssal peridotites at mid-ocean ridges', *Comptes Rendus Geoscience* **335**(10), 825–852.

MacNamara, J. & Thode, H. (1950), 'Comparison of the isotopic constitution of terrestrial and meteoritic sulphur', *Physical Review* **78**(3), 307.

Mallmann, G. & O'Neill, H. S. C. (2009), 'The crystal/melt partitioning of V during mantle melting as a function of oxygen fugacity compared with some other elements (Al, P, Ca, Sc, Ti, Cr, Fe, Ga, Y, Zr and Nb)', *Journal of Petrology* **50**(9), 1765–1794.

Mallmann, G. & O'Neill, H. S. C. (2007), 'The effect of oxygen fugacity on the partitioning of Re between crystals and silicate melt during mantle melting', *Geochimica et Cosmochimica Acta* **71**(11), 2837–2857.

Malvoisin, B.; Chopin, C.; Brunet, F. & Galvez, M. E. (2012), 'Low-temperature wollastonite formed by carbonate reduction: a marker of serpentinite redox conditions', *Journal of Petrology* **53**(1), 159–176.

Manning, C. E. (2004), 'The chemistry of subduction-zone fluids', *Earth and Planetary Science Letters* **223**(1), 1–16.

Marschall, H. R. & Schumacher, J. C. (2012), 'Arc magmas sourced from mélange diapirs in subduction zones', *Nature Geoscience* **5**(12), 862–867.

McCollom, T. M. & Bach, W. (2009), 'Thermodynamic constraints on hydrogen generation during serpentinization of ultramafic rocks', *Geochimica et Cosmochimica Acta* **73**(3), 856–875.

McInnes, B. I.; McBride, J. S.; Evans, N. J.; Lambert, D. D. & Andrew, A. S. (1999), 'Osmium isotope constraints on ore metal recycling in subduction zones', *Science* **286**(5439), 512–516.

Mitchell, R. H. & Keays, R. R. (1981), 'Abundance and distribution of gold, palladium and iridium in some spinel and garnet lherzolites: implications for the nature and origin of precious metal-rich intergranular components in the upper mantle', *Geochimica et Cosmochimica Acta* **45**(12), 2425–2442.

Mungall, J. E. (2002), 'Roasting the mantle: Slab melting and the genesis of major Au and Au-rich Cu deposits', *Geology* **30**(10), 915–918.

Mysen, B. O.; Virgo, D.; Neumann, E.-R. & Seifert, F. A. (1985), 'Redox equilibria and the structural states of ferric and ferrous iron in melts in the system CaO-MgO-Al 2 O 3-SiO 2-Fe-O; relationships between redox equilibria, melt structure and liquidus phase equilibria', *American Mineralogist* **70**(3-4), 317–331.

Nebel, O.; Arculus, R.; Sossi, P.; Jenner, F. & Whan, T. (2013), 'Iron isotopic

evidence for convective resurfacing of recycled arc-front mantle beneath back-arc basins', *Geophysical Research Letters* **40**(22), 5849–5853.

Nebel, O.; Sossi, P.; Bénard, A.; Wille, M.; Vroon, P. & Arculus, R. (2015), 'Redox-variability and controls in subduction zones from an iron-isotope perspective', *Earth and Planetary Science Letters* **432**, 142–151.

Niu, Y. (2004), 'Bulk-rock major and trace element compositions of abyssal peridotites: implications for mantle melting, melt extraction and post-melting processes beneath mid-ocean ridges', *Journal of Petrology* **45**(12), 2423–2458.

lx Nnr-r, J. & Wooo, B. J. (1991), 'High-temperature electrical measurements and thermodynamic properties of FerOo-FeCrrOo-MgCrrOo-FeAlrOa spinels', *American Mineralogist* **76**, 405–426.

Ohmoto, H. & Rye, R. (1979), 'Isotopes of sulphur and carbon. Geochemistry of Hydrothermal Ore Deposits (Barnes, HL, ed.), 509-567', John Wiley & Sons Inc., New York.

Padrón-Navarta, J.; Sánchez-Vizcaino, V. L.; Garrido, C.; Gómez-Pugnaire, M.; Jabaloy, A.; Capitani, G. & Mellini, M. (2008), 'Highly ordered antigorite from Cerro del Almirez HP–HT serpentinites, SE Spain', *Contributions to Mineralogy and Petrology* **156**(5), 679–688.

Parkinson, I. J. & Arculus, R. J. (1999), 'The redox state of subduction zones: insights from arc-peridotites', *Chemical Geology* **160**(4), 409–423.

Penniston-Dorland, S. C.; Gorman, J. K.; Bebout, G. E.; Piccoli, P. M. & Walker, R. J. (2014), 'Reaction rind formation in the Catalina Schist: Deciphering a history of mechanical mixing and metasomatic alteration', *Chemical Geology* **384**, 47–61.

Penniston-Dorland, S. C.; Walker, R. J.; Pitcher, L. & Sorensen, S. S. (2012), 'Mantle–crust interactions in a paleosubduction zone: Evidence from highly siderophile element systematics of eclogite and related rocks', *Earth and Planetary Science Letters* **319**, 295–306.

Philippot, P. & Selverstone, J. (1991), 'Trace-element-rich brines in eclogitic veins: implications for fluid composition and transport during subduction', *Contributions to Mineralogy and Petrology* **106**(4), 417–430.

Plümper, O.; Beinlich, A.; Bach, W.; Janots, E. & Austrheim, H. (2014), 'Garnets within geode-like serpentinite veins: Implications for element transport, hydrogen production and life-supporting environment formation', *Geochimica et Cosmochimica Acta* **141**, 454–471.

Puchtel, I. S. & Humayun, M. (2001), 'Platinum group element fractionation in a komatiitic basalt lava lake', *Geochimica et Cosmochimica Acta* **65**(17), 2979–2993.

Rahn, M. & Bucher, K. (1998), 'Titanian clinohumite formation in the Zermatt-Saas ophiolites, central Alps', *Mineralogy and Petrology* **64**(1-4), 1–13.

Ranero, C. & Sallares, V. (2004), 'Geophysical evidence for hydration of the crust and mantle of the Nazca plate during bending at the north Chile trench', *Geology* **32**(7), 549–552.

Rehkaemper, M.; Halliday, A.; Fitton, J.; Lee, D.-C.; Wieneke, M. & Arndt, N. (1999), 'Ir, Ru, Pt, and Pd in basalts and komatiites: new constraints for the geochemical behavior of the platinum-group elements in the mantle', *Geochimica et Cosmochimica Acta* **63**(22), 3915–3934.

Richards, J. P. (2015), 'The oxidation state, and sulphur and Cu contents of arc magmas: implications for metallogeny', *Lithos* **233**, 27–45.

Richards, J. P. (2011), 'Magmatic to hydrothermal metal fluxes in convergent and collided margins', *Ore Geology Reviews* **40**(1), 1–26.

Scambelluri, M.; Pettke, T.; Rampone, E.; Godard, M. & Reusser, E. (2014), 'Petrology and trace element budgets of high-pressure peridotites indicate subduction dehydration of serpentinized mantle (Cima di Gagnone, Central Alps, Switzerland)', *Journal of Petrology*, egt068.

Scambelluri, M. & Rampone, E. (1999), 'Mg-metasomatism of oceanic gabbros and its control on Ti-clinohumite formation during eclogitization', *Contributions to Mineralogy and Petrology* **135**(1), 1–17.

Schauble, E. A. (2004), 'Applying stable isotope fractionation theory to new systems', *Reviews in Mineralogy and Geochemistry* **55**(1), 65–111.

Schneider, M. E. & Eggler, D. H. (1986), 'Fluids in equilibrium with peridotite minerals: implications for mantle metasomatism', *Geochimica et Cosmochimica Acta* **50**(5), 711–724.

Schwarzenbach, E. M.; Früh-Green, G. L.; Bernasconi, S. M.; Alt, J. C. & Plas, A. (2013), 'Serpentinization and carbon sequestration: A study of two ancient peridotite-hosted hydrothermal systems', *Chemical Geology* **351**, 115–133.

Schwarzenbach, E. M.; Gill, B. C.; Gazel, E. & Madrigal, P. (2016), 'Sulphur and carbon geochemistry of the Santa Elena peridotites: Comparing oceanic and continental processes during peridotite alteration', *Lithos* **252**, 92–108.

Seal, R. R. (2006), 'Sulphur isotope geochemistry of sulphide minerals', *Reviews in mineralogy and geochemistry* **61**(1), 633–677.

Shen, A. H.; Keppler, H. & others (1997), 'Direct observation of complete miscibility the albite-H2O system', *Nature* **385**(6618), 710–712.

Snow, J. E. & Dick, H. J. (1995), 'Pervasive magnesium loss by marine weathering of peridotite', *Geochimica et Cosmochimica Acta* **59**(20), 4219–4235.

Spandler, C.; Hermann, J.; Faure, K.; Mavrogenes, J. A. & Arculus, R. J. (2008),

'The importance of talc and chlorite "hybrid" rocks for volatile recycling through subduction zones; evidence from the high-pressure subduction mélange of New Caledonia', *Contributions to Mineralogy and Petrology* **155**(2), 181–198.

Spandler, C.; Pettke, T. & Rubatto, D. (2011), 'Internal and external fluid sources for eclogite-facies veins in the Monviso meta-ophiolite, Western Alps: implications for fluid flow in subduction zones', *Journal of Petrology* **52**(6), 1207–1236.

Spandler, C. & Pirard, C. (2013), 'Element recycling from subducting slabs to arc crust: A review', *Lithos* **170**, 208–223.

Tomkins, A. G. & Evans, K. A. (2015), 'Separate zones of sulphate and sulphide release from subducted mafic oceanic crust', *Earth and Planetary Science Letters* **428**, 73–83.

Trommsdorff, V. & Evans, B. W. (1980), 'Titanian hydroxyl-clinohumite: formation and breakdown in antigorite rocks (Malenco, Italy)', *Contributions to Mineralogy and Petrology* **72**(3), 229–242.

Ulmer, P.; Trommsdorff, V. & others (1999), 'Phase relations of hydrous mantle subducting to 300 km', *Mantle petrology: field observations and high pressure experimentation: a tribute to Francis R.(Joe) Boyd* **6**, 259–281.

Woodland, S.; Pearson, D. & Thirlwall, M. (2002), 'A platinum group element and Re–Os isotope investigation of siderophile element recycling in subduction zones: comparison of Grenada, Lesser Antilles Arc, and the Izu–Bonin Arc', *Journal of Petrology* **43**(1), 171–198.

Zack, T. & John, T. (2007), 'An evaluation of reactive fluid flow and trace element mobility in subducting slabs', *Chemical Geology* **239**(3), 199–216.

Zotov, N. & Keppler, H. (1998), 'The influence of water on the structure of hydrous sodium tetrasilicate glasses', *American Mineralogist* **83**(7-8), 823–834.

Zotov, N.; Keppler, H.; Hannon, A. & Soper, A. (1996), 'The effect of water on the structure of silicate glasses—A neutron diffraction study', *Journal of Non-Crystalline Solids* **202**(1), 153–163.

CHAPTER 2

GEOLOGICAL SETTING AND FIELDWORK

2.1 Zermatt-Saas Zone

The convergence of the Adriatic and Eurasian tectonic plates led to the closure of the Tethyan oceanic basin during the Late Cretaceous to Early Tertiary period, resulting in subsequent Eocene–Oligocene continental collision (Dewey et al., 1973; Coward and Dietrich, 1989; Beltrando et al., 2010). The Western Alps is subdivided into the Southern Alps, the Axial Belt and the External Zone (Barnes et al., 2014 and references therein). The Southern Alps consists of continental basement and the External Zone lies structurally above the European plate. The Axial Belt is comprised of several tectono-metamorphic units derived from the Adriatic and European extended continental margin and from the Western Tethys Ocean.

The Axial Belt is divided into the Penninic (e.g. Rosenbaum and Lister, 2005; Dal Piaz, 2010; Beltrando et al., 2010) and Austroalpine domains (Pognante et al., 1989; Beltrando et al., 2014). The Zermatt-Saas Zone and the above Combin Zone outcrop between the crystalline basement rocks of the Penninic domain (consisting of Monte Rosa, Gran Paradiso and Dora Maira massifs and basement nappes (e.g. Stampfli, 2001), and the Austroalpine domains, the Sesia Zone (Compagnoni et al., 1977), and Dent Blanche Klippe (Ballèvre et al., 1986; Reddy et al., 1999; Reddy et al., 2003, Fig 2.1). Slivers of metasediments, including manganese-rich sediments, separate the Zermatt-Saas Zone from the structurally lower crystalline basement rocks and the Combin Zone above (Bearth and Schwandler, 1981).

The Zermatt-Saas Zone and the Combin Zone together comprise the Piemonte ophiolite (Reddy et al., 2003 and references therein). The Piemonte ophiolite is also comprised of metabasalts (eclogites and blueschists), metagabbros and calcareous and siliceous metasediments (Reinecke, 1998). There are two proposed models for the origin of the ophiolite; oceanic crust formation associated with mid-ocean rifting, or alternatively oceanic crust associated with an ocean-

continent transition zone. The ophiolite is traditionally considered to represent Tethyan oceanic lithosphere which formed during the Middle-Late Jurassic rifting of the Piemonte-Ligurian ocean, fragmented by regional E-W transform faults (e.g. Sturani, 1975; Trumpy, 1980; Beccaluva et al., 1984; Lemoine, 1985, Angiboust et al., 2009). Multiple reactivation of such faults was proposed to account for the juxtaposition of ultramafic rocks and slivers of continental basement within oceanic units (Ballèvre and Merle, 1993; Reddy et al., 2003; Forster et al., 2004). However, there is increasing evidence for a pre-Alpine juxtaposition of the ultramafic rocks and continental crust in the Western Alps, thus more representative of an ocean-continent transition zone. For example, the preservation of continental slices that are overlain by syn and post-rift sediments and the pre-Alpine ages of cross cutting dykes on an orthogneiss-serpentine contact (Beltrando et al., 2010; 2014).

Estimates of peak metamorphic conditions for eclogite facies metamorphism of the Zermatt-Saas Zone are 1–3 GPa and 550–630ºC (Ernst and Dal Piaz, 1978; Oberhaensli; 1980; Barnicoat and Fry, 1986; Reinecke, 1991; 1998; Bucher et al., 2005; Angiboust et al., 2009). Some workers consider the Zermatt-Saas Zone to represent a continuous slice of lithosphere with P-T estimates of 2.3 ± 0.1 GPa and 540 ± 40ºC across the block (e.g. Angiboust et al., 2009; Angiboust and Agard, 2010). However, in other work, estimates of peak metamorphic conditions differ. For example, coesite-bearing metasediments at Lago di Cignana infers ultra-high-pressure conditions of 2.7–2.9 GPa and 600–630ºC (Reinecke, 1998), whereas southern part of the Zermatt-Saas Zone records lower P-T conditions are proposed of 2.1±0.3 GPa and 550 ± 60ºC (Martin et al., 2008).

Previous estimates of the timing of peak metamorphism were Early–Middle Cretaceous (Baird and Dewey, 1986; Escher and Beaumont, 1997). However, on the basis of geochronology using U-Pb, Sm-Nd and Lu-Hf isotopes, the timing has been constrained to 44 to 40 Ma (Barnicoat et al., 1993; Botwell et al., 1994; Rubatto et al., 1998; Mayer et al., 1999; Dal Piaz et al., 1999; Herwartz et al., 2009). For example, Lu-Hf dating of garnets from the Balma ophiolite (Herwartz et al., 2009), and U-Pb zircon dating in ultra-high-pressure (UHP) eclogites and metasediments at Lago di Cignana (Rubatto et al., 1998) constrained the timing to ~45.5–42 Ma.

The timing of exhumation from high-pressure (~60km) to mid-crustal levels (~30km) is constrained by Rb-Sr dating of foliated and recystallised white mica in combination with structural data to ~44–36 Ma (Cartwright and Barnicoat, 2002; Reddy et al., 1999; 2003).

Samples were collected by Professor Steve Reddy in 2009, and Associate Professor Katy Evans in 2011 from the eclogite facies Zermatt-Saas Zone (Fig. 2.1, 2.2). Ultramafic rocks are found within the eclogite facies Zermatt-Saas Zone and the overlying greenschist facies Combin Zone. The study of detailed geological maps and cross sections of the area (e.g. Forster et al., 2004; Pleuger et al., 2007, Compagnoni et al., 2000; Reddy et al., 2003) confirmed the samples selected were from the high-pressure Zermatt-Saas Zone.

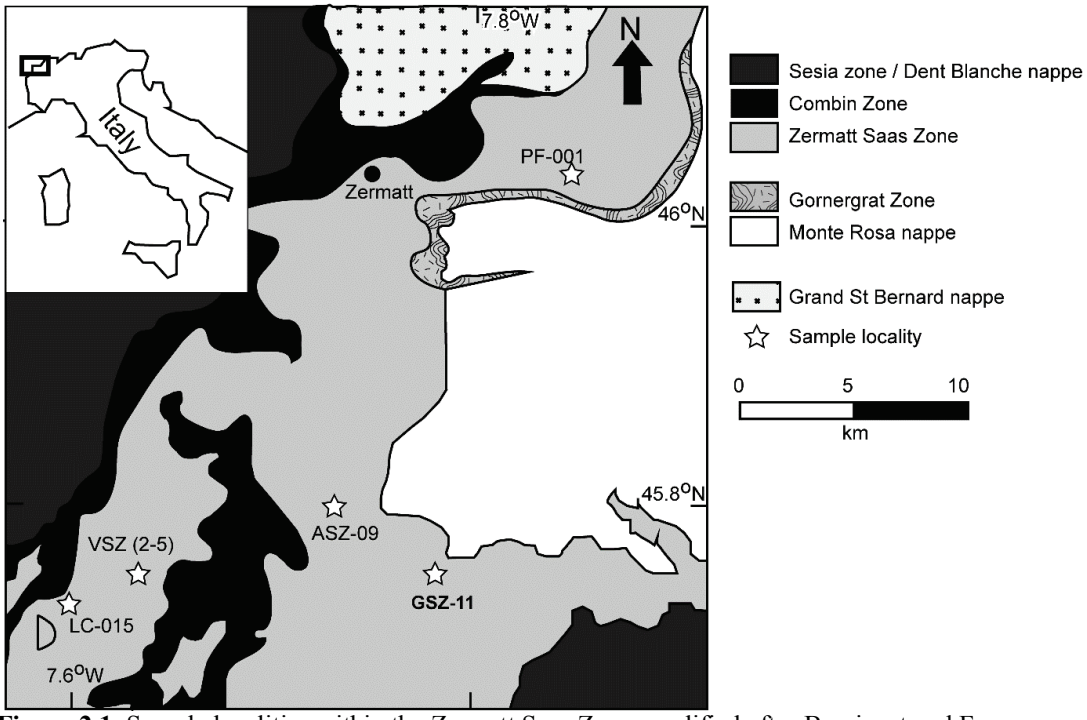

Figure 2.1: Sample localities within the Zermatt Saas Zone, modified after Barnicoat and Fry (1986) and Evans et al. (2014).

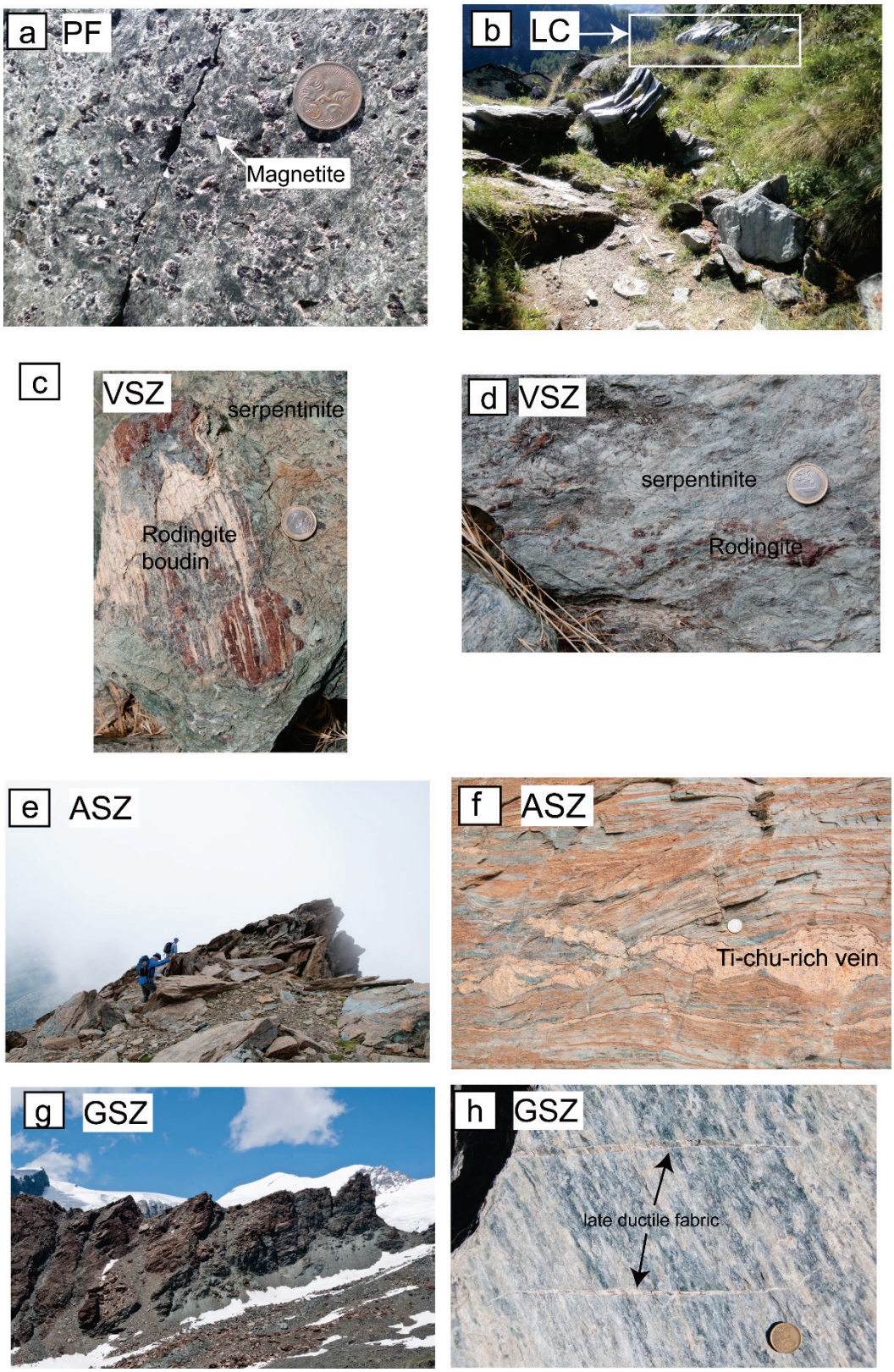

Figure 2.2 (a) Pfulwe outcrop showing large magnetite grains (5 cent coin for scale) (b) Lago di Cignana outcrop overview (c) rodingite boudin-serpentinite contact (1 Euro coin for scale), (d) serpentinite with rodingite layers (1 Euro coin for scale). (e) Outcrop at the top of Monte Rosso. (f) Serpentinite with Ti-clinohumite rich vein (1 Euro coin for scale), and banding demonstrating

compositional heterogeneity. (g) Overview of Gressoney outcrop (~1km across) (h) Gressoney outcrop, showing late cross cutting fabrics (5 cent coin for scale),

2.1.1 Pfulwe

Pfulwe is approximately 10 km to the east of Zermatt (Fig. 2.1). Peak metamorphism occurred under conditions of >2GPa and 550–600 °C (Barnicoat and Fry, 1986). The sample PF-001 is from a homogeneous outcrop with well-defined foliation (Fig. 2.2a) within 20 m of an Allalin gabbro outcrop, where Allalin metagabbros and eclogitic metabasalts are the dominant rock type in this area (Barnicoat and Fry, 1986; Evans et al., 2014).

2.1.2 Lago di Cignana

Lago di Cignana is ~20km to the south-west of Zermatt within the Valtournenche region, the southernmost part of the Zermatt-Saas (Fig. 2.1; 2.2b). Ultra-high pressure peak metamorphism is recorded by the presence of coesite within metasediments and metabasalts to pressures and temperatures of 3.2 GPa and 550ºC (Reinecke, 1998; Groppo et al., 2009) at Lago di Cignana. Further evidence for ultra-high pressure metamorphism is the presence of microdiamonds (Frezzotti et al., 2011). Ultramafic rocks are found proximal to coesite-bearing metasediments (Reinecke, 1991).

2.1.3 Upper Valtournanche

Less than 2km East of Lago di Cignana, in the upper Valtournanche region, foliated serpentinites surround metarodingites (Fig. 2c and d) and eclogites (metabasalts and metagabbros), where mafic rocks have undergone partial retrogression to greenschist facies (Rebay et al., 2012). However, eclogite facies textures are well-preserved and include glaucophane-rich eclogites and rodingites. (Zanoni et al., 2011; Rebay et al., 2012). At this locality, Ti-clinohumite, clinopyroxene and prograde olivine record peak metamorphic conditions (Rebay et al., 2012). Pseudosections P-T modelling constrained metamorphic conditions at >2.5 GPa ±0.3 GPa and >600ºC, approximating the conditions of the ultra-high-pressure sediments at Lago di Cignana (Rebay et al., 2012).

2.1.4 Monte Rosso

ASZ-09 is from the summit of Monte Rosso in the Val d'Ayas, to the northeast of the village of St Jacques. At this locality large blocks of serpentinites and dykes of rodingite outcrop (Fig. 2 e and f).

2.1.5 Gressoney Shear Zone

The Gressoney Shear Zone (GSZ) separates the Zermatt-Saas Zone and Combin Zone and has excellent exposure of high pressure serpentinites (Fig. 2g and h). The GSZ is associated with crustal extension attributed to exhumation (Reddy et al., 1999). Rb-Sr dating of foliated and recystallised white mica in combination with structural data documents the timing of exhumation from high-pressure (~60km) to mid-crustal levels (~30km) to ~44–36 Ma (Reddy et al., 1999; 2003). Thrusting and extension occurred synchronously at upper crustal levels, implying that the more buoyant Monte Rosa continental rocks beneath the Zermatt-Saas Zone (comprised mainly of denser eclogites) could have provided a driving force for extension (Wheeler et al., 2001).

Sample	GPS (WGS 84)	mE	mN	Location Description	Rock type
PF-001	32T	0410417	5096587	Pfulwe, ~20 metres from a metagabbro.	Chlorite schist with large magnetites
LC-015	32T	0415310	5064106	Lago di Cignana	Serpentinite
VSZ-02	32T	0391061	5080719	Upper Valtournanche	Diopside-chlorite-garnet schist
VSZ-03	32T	0391061	5080719	Upper Valtournanche	Serpentinite
VSZ-05	32T	0391061	5080719	Upper Valtournanche	Serpentinite
GSZ-11	32T	0391061	5080719	Gressoney shear zone	Serpentinite
AZS09a	32T	0404124	5081747	Monte Rosso	Serpentinite with large Ti-clinohumites
AZS09b	32T	0404124	5081747	Monte Rosso	Serpentinite with large Ti-clinohumites

Table 2.1: Zermatt-Saas samples selected for this study.

2.2 Alpine Corsica

Alpine Corsica, the north-eastern part of Corsica, consists of stacks of continental and ophiolite lithologies that record high-pressure low-temperatures (HP-LT) metamorphism (e.g. Vitale Brovarone et al., 2011; 2013). Alpine Corsica is considered to have been detached from the main Alpine orogenic block during extension of the Mediterranean during the Oligocene-Miocene period (e.g. Jolivet et al., 1990; Molli and Malavielle, 2010). However, the timing of high-pressure metamorphism is controversial and ranges from the Late Cretaceous to the Late Eocene. The Late Cretaceous timing would be consistent with Alpine Corsica as a

remnant of the Alpine block, i.e. an east dipping subduction zone and is the most widely accepted model at this point in time (c.f. Molli, 2008 and references therein; Argnani, 2009; Molli and Malavielle, 2010; Ravna et al., 2010). Alternatively, on the basis of recent Lu-Hf ages of lawsonite-blueschist and lawsonite-eclogite garnets in metabasalts and metagabbros, the timing of prograde to peak metamorphism was constrained to Late Eocene ages of ~37–34Ma (Vitale Brovarone and Herwartz, 2013). If these ages are accurate, high-pressure metamorphism is not associated with Alpine or east dipping subduction (as recorded in the Zermatt-Saas Zone) but with Apennine or west dipping subduction, although Vitale Brovarone and Herwartz (2013) note that more data is required before any definitive conclusions can be made. It is also possible that Late Cretaceous to Early Tertiary Alpine or east dipping subduction was replaced by the Apennine west-dipping subduction in the Middle Eocene (Jolivet et al., 1998; Lacombe and Jolivet, 2005; Molli and Malavieille, 2010; Agard and Vitale-Brovarone, 2013; Magott et al., 2016). The Alpine or Apennine subduction models are beyond the scope of this thesis to resolve, and in either case the pre-subduction geodynamic setting would have been the same, and from this point on will be referred to as Alpine, the more widely accepted interpretation in the literature.

Alpine Corsica has three dominant domains; the External Continental Units, the Schistes Lustrés complex and the Nappes Supérieures or uppermost units (Vitale Brovarone et al., 2011; 2013). The External Continental Units mainly consist of deformed crystalline basement rocks variably overlain by greenschist to blueschist facies metasediments in the east (Molli et al., 2006; Tribuzio and Giacomini, 2002; Vitale Brovarone et al., 2011). In the west, the crystalline rocks preserve features attributed to the Variscan orogeny, and Carboniferous to Permian magmatic events (e.g. Meresse et al., 2012). Several tectonometamorphic units comprise the Schistes Lustrés complex, which contains metaophiolites, metasediments and slivers of internal continental slices (Vitale Brovarone et al., 2013). The Schistes Lustrés complex is proposed to represent the remnants of the ultra-slow to slow-spreading Middle to Late Jurassic Piemonte-Liguria oceanic basin and its cover sediments, which were subsequently metamorphosed to blueschist to eclogite facies (Vitale Brovarone and Herwartz, 2013; Vitale Brovarone et al., 2013; Magott et al., 2016). The internal continental slices consist

of the Centuri, Serra di Pigno, Farinole, San Petrone and Campitello units. These units are considered to represent pre-subduction continental extensional allochthons, attributed to an ocean-continent transition zone, which were subsequently subducted to blueschist–eclogite metamorphic conditions (e.g. Lahondère, 1996; Vitale Brovarone et al., 2011; Meresse et al., 2012). The Balagne, Nebbio and Macinaggio nappe sheets define the uppermost units, which consist of deformed ophiolites and continental units (Vitale Brovarone et al., 2011; Meresse et al., 2012 and references therein).

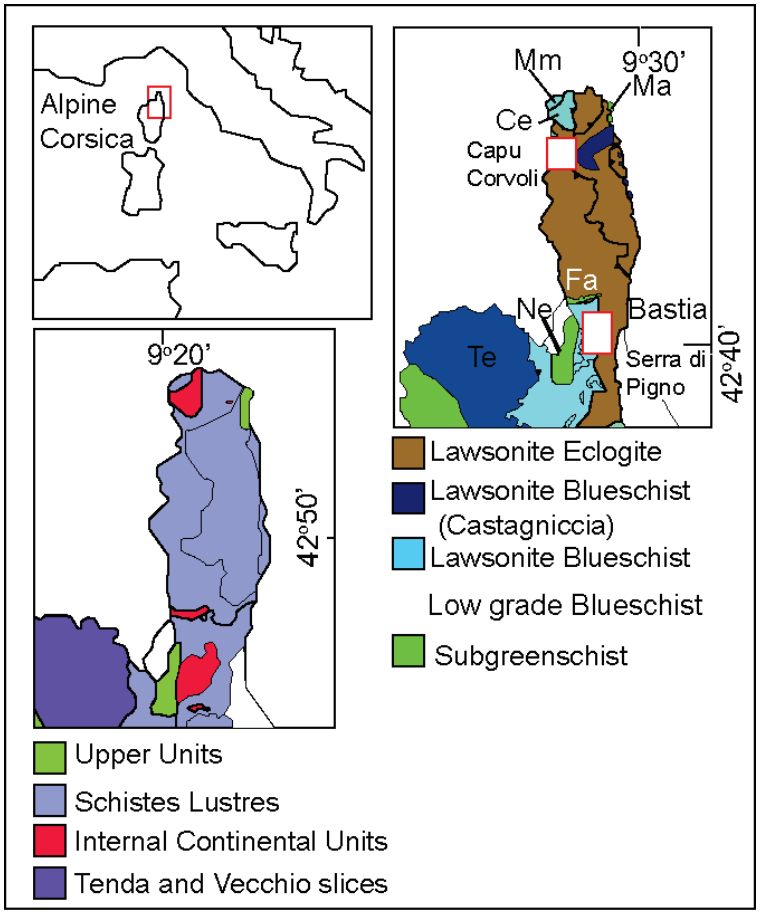

Figure 2.3: map of the location of Alpine Corsica, showing the major domains; the external contintental slices (Tenda and Vecchio), the internal continental units, the Schistes Lustres, and the uppermost units. Also shown is the locations of the main field areas, Capu Corvoli and Serra di Pigno and the metamorphic grade. Maps are redrawn after Vitale Brovarone et al., (2011) and (2013).

Samples were collected from the Schistes Lustrés complex (Table 2.1). Sampling was focussed in the Serra di Pigno region where ultramafic, metagabbros, metabasalts and metasediments were collected in 2013. Hybrid mafic/ultramafic samples were collected by Sarah Hayes and Luke Daly in 2014 from Capu Corvoli. Sample descriptions and bulk compositions are provided in Appendix A.

Sample	GPS (WGS 84)	mE	mN	Location Description	Rock type
CO13-20	32T	0533228	4728387	Serra di Pigno : south of serpentinite ridge.	Psammite
CO13-21	32T	0533373	4729575	Serra di Pigno: proximal to metaquarzite.	Serpentinite
CO13-22	32T	0533373	4729575	Serra di Pigno: proximal to metagabbro	Blueschist (no quartz veins)
CO13-27	32T	0533407	4730454	Serra di Pigno: proximal to metasediments	Serpentinite
CO13-28	32T	0533129	4729974	Serra di Pigno : proximal to serpentinite	Calc schist with organic rich layers
CO13-29	32T	0533099	4730005	Serra di Pigno: distal to serpentinite	Metaquartzite with fine carbonate rich layers
CO13-30	32T	0533099	4730005	Serra di Pigno: within large serpentinite body (low magnetic susceptibility)	Serpentinite breccia
CO13-31	32T	0533430	4729806	Serra di Pigno: distal to other lithologies.	Serpentinite
CO13-32	32T	0533483	4729540	Serra di Pigno: distal to serpentinite.	Metagabbro (no quartz veins)
CO13-33	32T	0533514	4729532	Serra di Pigno: proximal to metagabbro	Serpentinite
CO13-34	32T	0533514	4729532	Serra di Pigno: proximal to serpentinite CO13-33.	Metagabbro with quartz veins.
CO13-35a	32T	0533354	4729442	Serra di Pigno	Metagabbro
CO13-35b	32T	0533354	4729442	Serra di Pigno	Metagabbro
CO13-36	32T	0533354	4729442	Serra di Pigno	Calc schist
CO13-40	32T	0533209	4727971	Serra di Pigno: along serpentinite ridge, distal to other lithologies	Serpentinite with visible Cr-spinel.
CO13-41	32T	0533325	4729413	Serra di Pigno:	Calc schist
CO13-42	32T	0533325	4729413	Serra di Pigno:	Metaquartzite
CO13-49	32T	0533322	4729667	Serra di Pigno: low magnetic susceptibility, enclosed in serpentinite.	Serpentinite breccia
CO13-50	32T	0533222	4729859	Serra di Pigno: from fold nose.	Metagabbro
CO13-55	32T	0533398	4729368	Serra di Pigno: proximal to breccia, calc schist and metagabbro.	Serpentinite
CO13-56a	32T	0533398	4729368	Serra di Pigno: adjacent to serpentinite, close proximity to metagabbro and calc schist	Serpentinite breccia with veins through a large cpx.
CO13-56b	32T	0533398	4729368	Serra di Pigno: adjacent to serpentinite, close proximity to metagabbro and calc schist.	Serpentinite breccia with large cpx clasts.
CO13-57	32T	0533092	4729996	Serra di Pigno: proximal to calc schist.	Metagabbro
CO13-58	32T	0533092	4729996	Serra di Pigno: proximal to metagabbro	Calc schist
CO13-59	32T	0533092	4729996	Serra di Pigno: Proximal to mafic blueschist	Calc schist/blueschist contact
CO13-60a	32T	0533092	4729996	Serra di Pigno: Proximal to calc schist	Mafic blueschist
CO13-60b-1	32T	0533092	4729996	Serra di Pigno: structurally below metagabbro	Mafic blueschist
CO13-60b-2	32T	0533092	4729996	Serra di Pigno: structurally below metagabbro	Mafic blueschist
CO13-61	32T	0533092	4729996	Serra di Pigno: structurally above mafic blueschist	Metagabbro
CO14-03	32T	0529140	4753069	Capu Corvoli: proximal to metagabbro	Chlorite schist
CO13-04	32T	0529107	4753071	Capu Corvoli: proximal to metagabbro	Talc schist
CO13-05	32T	0529154	4753091	Capu Corvoli: proximal to talc and chlorite schist	Metagabbro

Table 2.2: samples collected in Alpine Corsica, GPS co-ordinates and a brief description.

2.2.1 Serra di Pigno Region

The Serra di Pigno region is situated between the villages of Patrimonio in the west and Ville di Pietrabugno in the east (Meresse et al., 2012), ~10km west of Bastia. The lithologies in the region are part of the Pietro di Tenda formation or Sisco unit of the HPLT Schistes Lustrés complex (Caron and Delcey, 1979; Lahondère, 1983; Lahondère et al., 1992; 1994; Meresse et al., 2012). Mapping of a ~2km^2 area ~1.5 km north of the Serra di Pigno continental slice was carried out in September 2013 (Fig. 2.6; 2.7; 2.8). Serra di Pigno was chosen as an area to complete a detailed study because metasediments, metagabbros and metabasalts occur in close proximity to serpentinites, and serpentinites also occur distal to other lithologies, allowing the assessment of lithological controls on the distribution of redox sensitive elements.

Two main foliation orientations are apparent, one with a dip towards the NW, which is attributed to the larger-scale NW limb of a NW-SE trending open antiform, as interpreted previously (Faure and Malavieille, 1981), and minor folds trending to the south-southwest, consistent with Serra di Pigno regional folds (Fig. 2.9, Meresse et al., 2012). Foliation orientated to the SW is consistent with HP-LT foliation, although other foliations dipping to NE and E were recorded (Fig. 2.9).

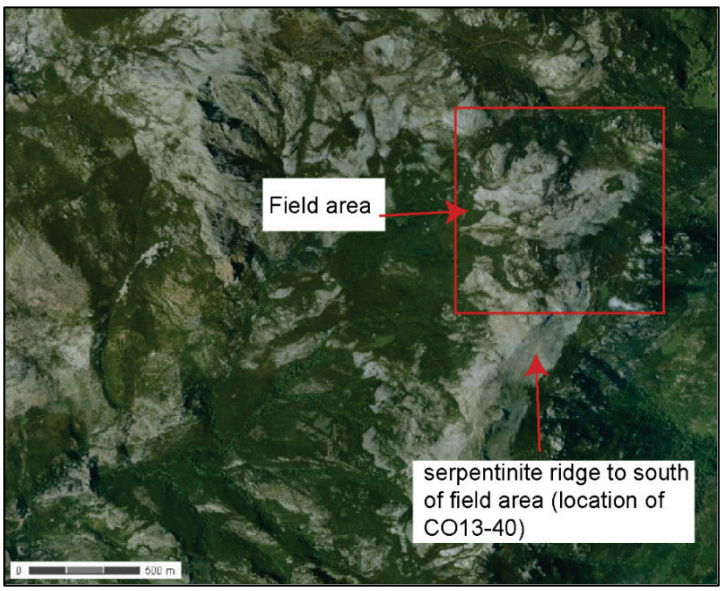

Figure 2.4: Aerial view of the field area.

Figure 2.5: Photo of the field area showing the juxtaposition of lithologies at Serra di Pigno, Cap Corse.

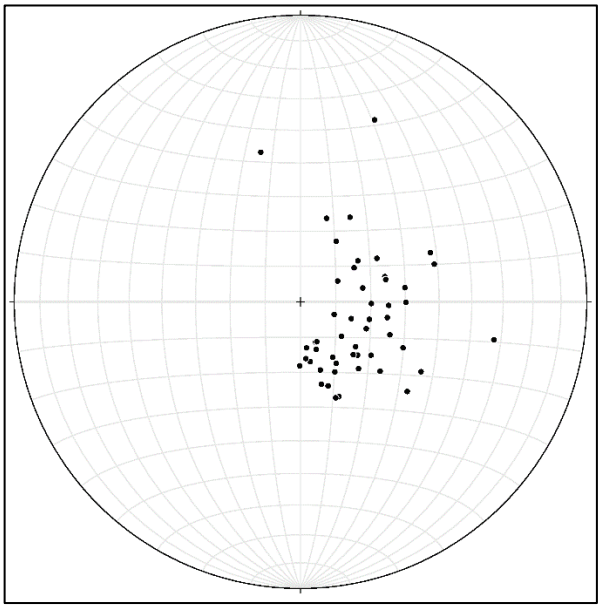

Figure 2.6: A lower hemisphere and equal angle stereographic projection showing poles to foliation for the Serra di Pigno field area.

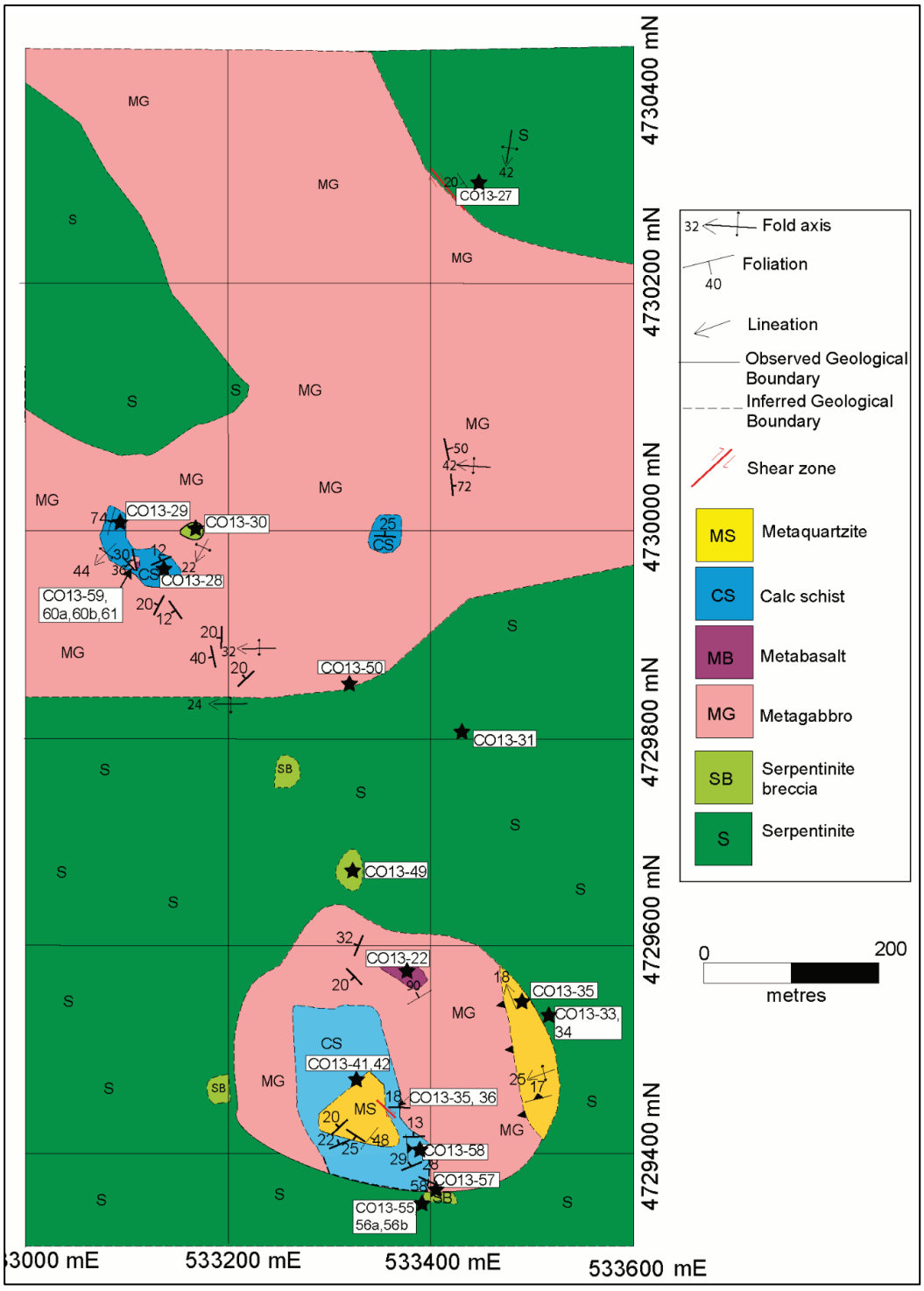

Figure 2.7: Map of Serra di Pigno field area, showing locations of samples collected.

2.2.1.1 Field observations

Contacts of serpentinite contacts with other lithologies were not exposed, with the exception of a contact between a serpentinite breccia and serpentinite (Fig. 2.10). The serpentinite breccia has low magnetic susceptibility at ~$0.2x10^{-3}$k compared to the serpentinite (~$40x10^{-3}$k) and on closer inspection, magnetite pseudomorphs replaced by calcium-rich minerals were observed in the sample.

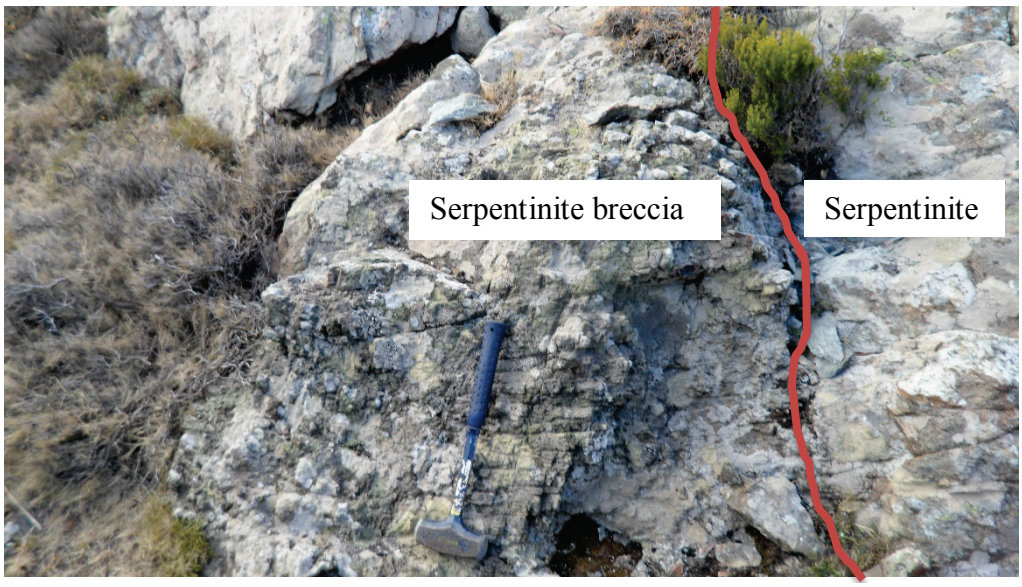

Figure 2.8: contact between serpentinite and serpentinite breccia

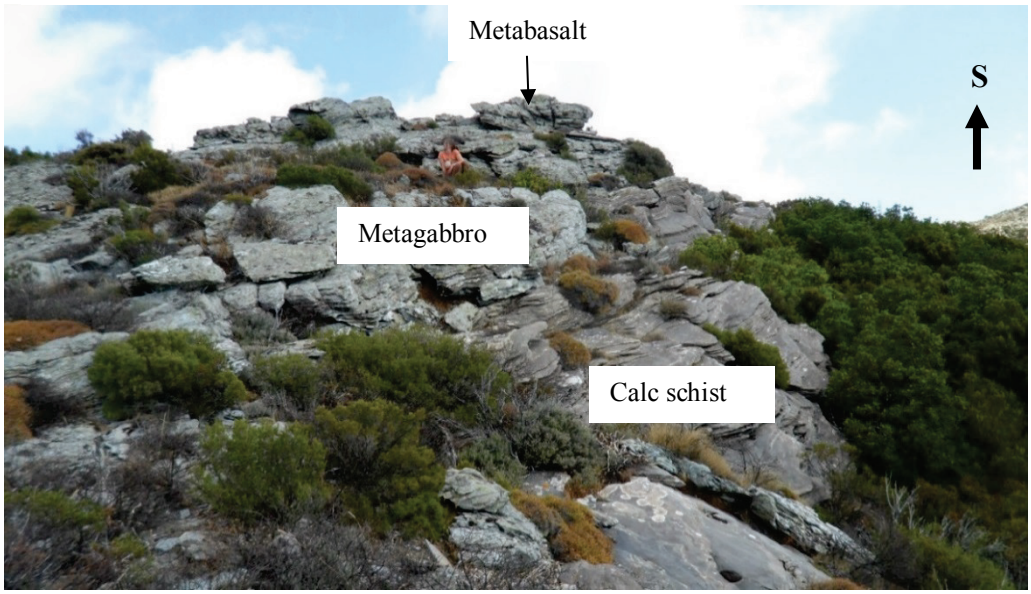

Figure 2.9: Outcrop of calcareous schist, metabasalt and metagabbro where grid mapping was carried out (WGS 32T 053092 4729996).

Grid mapping of an outcrop where contacts between sediments and mafic rocks are exposed provides insights into the relationships between these lithologies on an outcrop scale (Fig. 2.11; 2.12). Veins consisting of brecciated quartz and dolomite clasts, displace the foliated carbonaceous and mica-rich layers in the calc schist. The brecciated nature of these veins in implies these are associated with a deformation event, which postdates deformation defined by the dominant foliation. Large quartz clasts (at least 10cm in size) are observed at lithological boundaries between the calc schist and metagabbro. In addition, large dolomite clasts are observed at contacts between mica-rich and carbonaceous layers. In the metabasalt at the top of the outcrop, quartz veins are smaller in diameter than in metagabbros, but appear to follow foliation, where foliation dips to the SW as for the calc schist, consistent with regional HP foliation (Meresse et al., 2012). These quartz veins are associated with the high P low T mineral glaucophane. Veins likely reflect the paths of fluid flow (e.g. Cartwright and Buick, 2000). The outcrop-scale observations therefore imply that fluid-flow is not pervasive through the metagabbro, occurring along contacts with other lithologies. However, elsewhere within 20 metres to a serpentinite contact, metagabbro is intensely folded and quartz veins are associated with these folds. The foliation trends NW and is therefore not attributed to HP foliation but a later deformation event so later deformation events could enhance fluid flow. In addition, large quartz clasts were found at the base. Veins cut the high-pressure foliation in the calc schist, and locally follow outcrop scale 'horst and graben' structures associated with normal faulting, which suggests that the veins are synchronous with extension postdating high-pressure deformation.

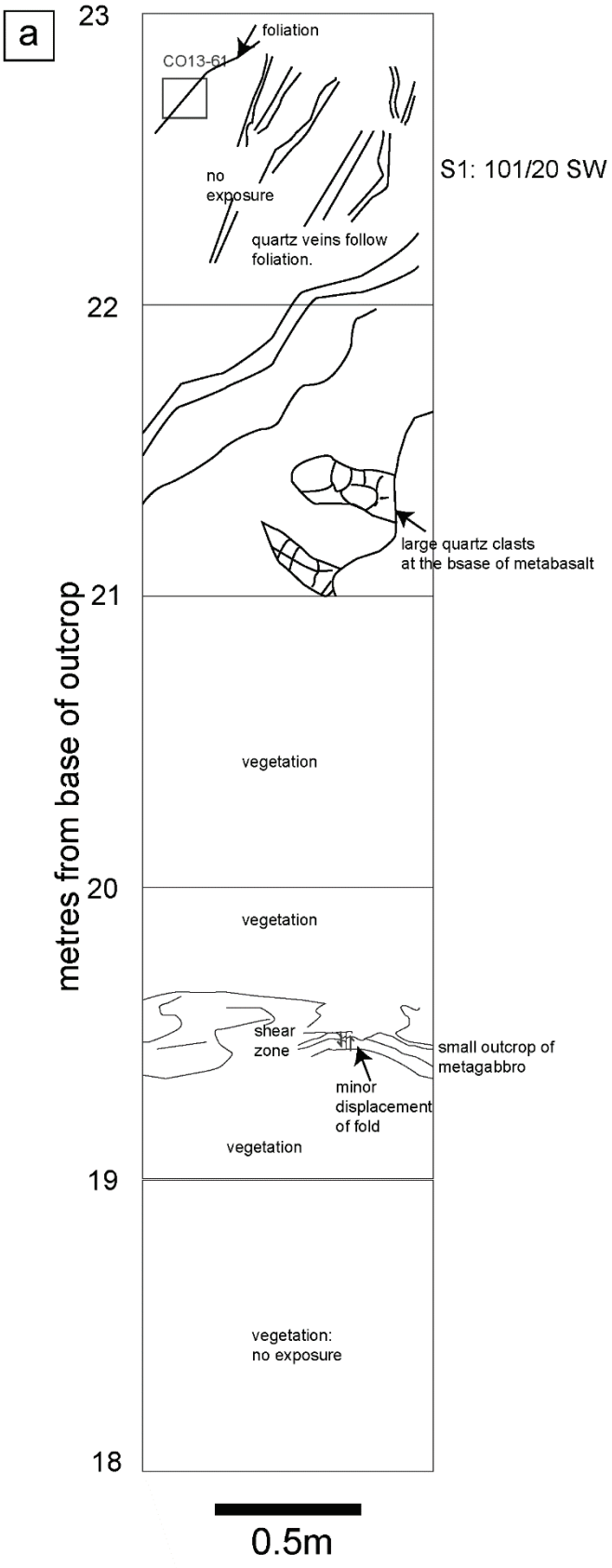
a
23
22
21
20
19
18
metres from base of outcrop
foliation
CO13-61
no exposure
S1: 101/20 SW
quartz veins follow foliation.
large quartz clasts at the bsase of metabasalt
vegetation
vegetation
shear zone
small outcrop of metagabbro
minor displacement of fold
vegetation
vegetation: no exposure
0.5m

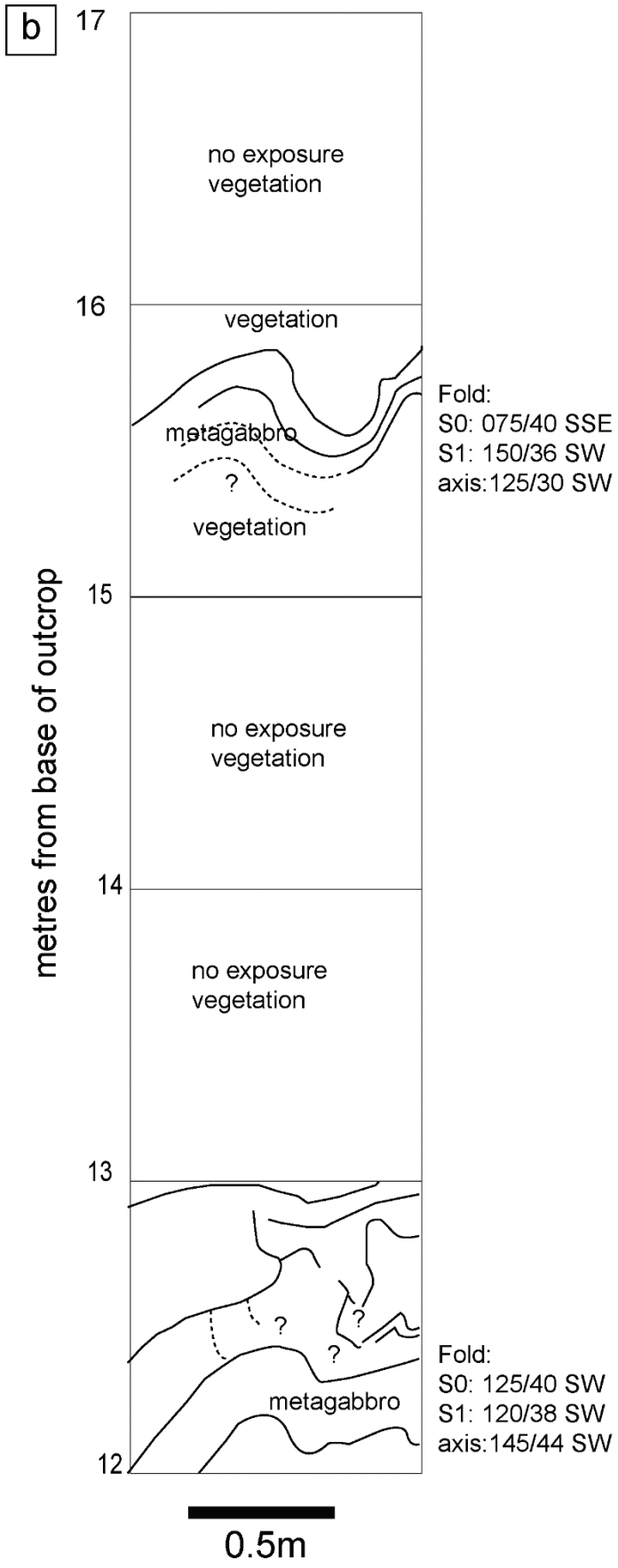
b
17
16
15
14
13
12
metres from base of outcrop
no exposure
vegetation
vegetation
metagabbro
?
vegetation
Fold:
S0: 075/40 SSE
S1: 150/36 SW
axis:125/30 SW
no exposure
vegetation
no exposure
vegetation
?
?
?
metagabbro
Fold:
S0: 125/40 SW
S1: 120/38 SW
axis:145/44 SW
0.5m

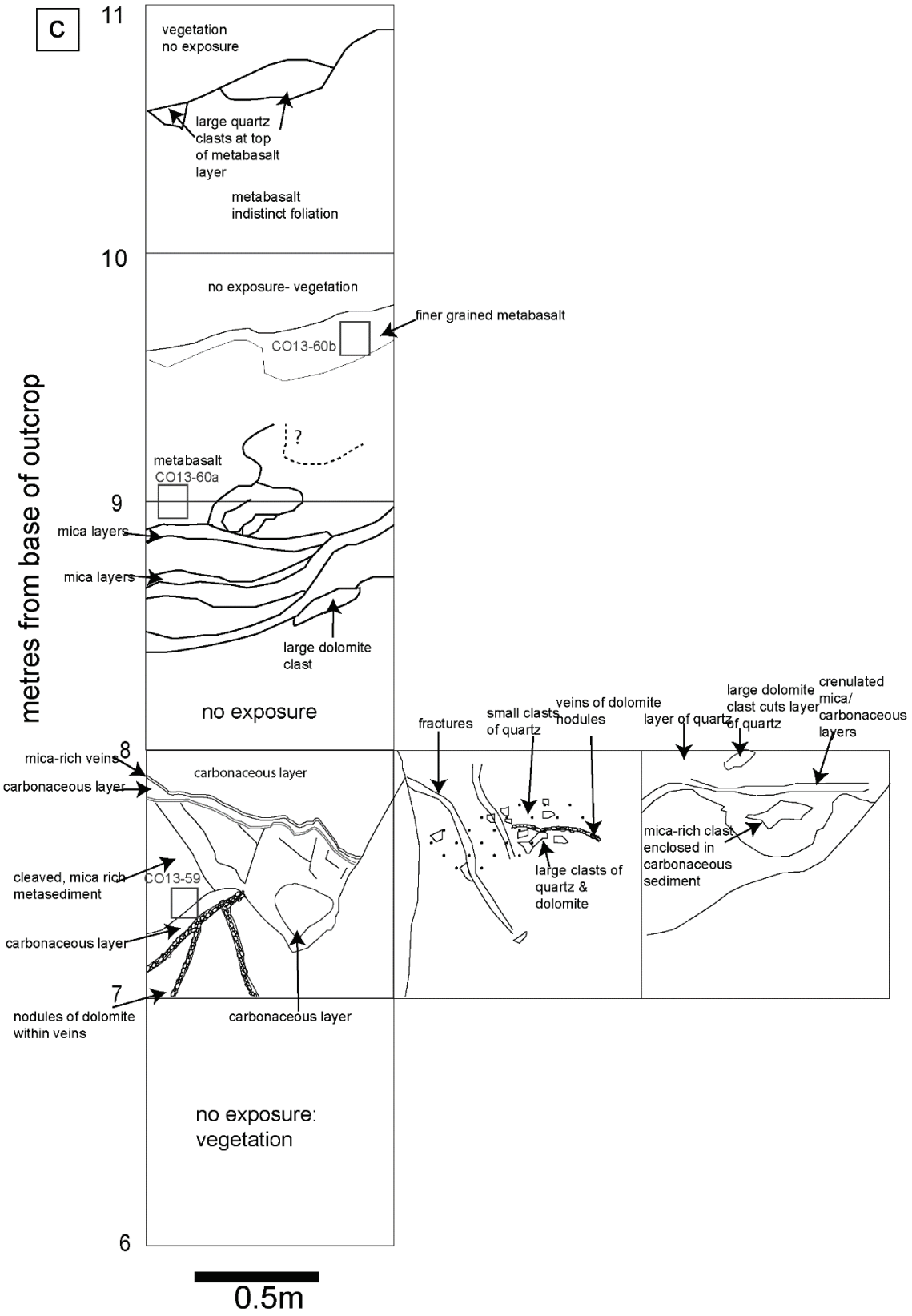
C
11
vegetation
no exposure
large quartz clasts at top of metabasalt layer
metabasalt indistinct foliation
10
no exposure- vegetation
finer grained metabasalt
CO13-60b
?
metabasalt
CO13-60a
9
mica layers
mica layers
large dolomite clast
no exposure
metres from base of outcrop
fractures
small clasts of quartz
veins of dolomite nodules
large dolomite clast cuts layer of quartz
layer of quartz
crenulated mica/ carbonaceous layers
8
mica-rich veins
carbonaceous layer
carbonaceous layer
cleaved, mica rich metasediment
CO13-59
carbonaceous layer
large clasts of quartz & dolomite
mica-rich clast enclosed in carbonaceous sediment
7
nodules of dolomite within veins
carbonaceous layer
no exposure: vegetation
6
0.5m

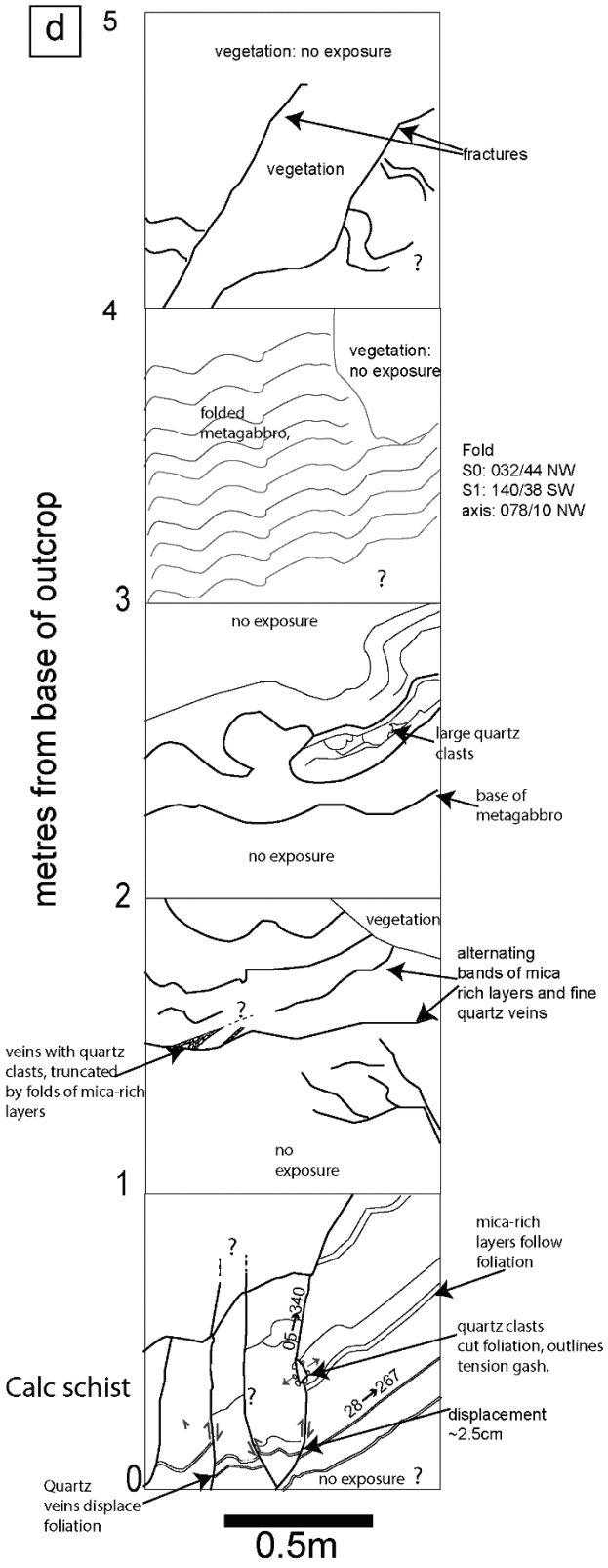

Figure 2.10: Grid map from calcareous schist at the base to metabasalts and metagabbro at the top for the outcrop shown in Fig. 2.9 (WGS 32T 053092 4729996). (a) 18 to 23 metres, (b) 12 to 22 metres (c) 6 to 11 metres (d) 0 to 5 metres from base of the outcrop.

2.2.2 Capu Corvoli Region

The Capu Corvoli region is ~5km north of the village of Pino, Cap Corse. Samples were collected from a shear zone in close proximity to a series of thrust faults with fault planes dipping shallowly to the west-north-west to north-west (Fig. 2.13). Previous interpretations suggest that these thrust faults define the boundary between the tectonometamorphic terranes of the lawsonite-blueschist Upper Castagniccia metasediments and the lawsonite-eclogite ophiolites (Lahondère, 1992). The shear zone is parallel to the thrust faults and records top-to-the-west to north-west shearing. The sense of shear is consistent with coaxial deformation associated with high-pressure metamorphism, as defined by previous workers (Mattauer et al., 1977; 1981; Faure and Malavieille, 1981; Harris, 1985, Warburton, 1986; Magott et al., 2016). Within this shear zone, hybrid talc and chlorite schists in contact with metagabbro can be found (Fig. 2.14). The shearing is consistent with the thrusting of the hybrid rocks and metagabbro over the Upper Castagniccia metasediments. More recent pressure-temperature estimates suggest that the Upper Castagniccia metasediments instead record eclogite conditions (Vitale Brovarone et al., 2013). Given this interpretation, the Capu Corvoli samples could record greater pressures than the Serra di Pigno samples, at a maximum of ~490–550ºC and 1.9–2.6 GPa (Ravna et al., 2010; Vitale Brovarone et al., 2013).

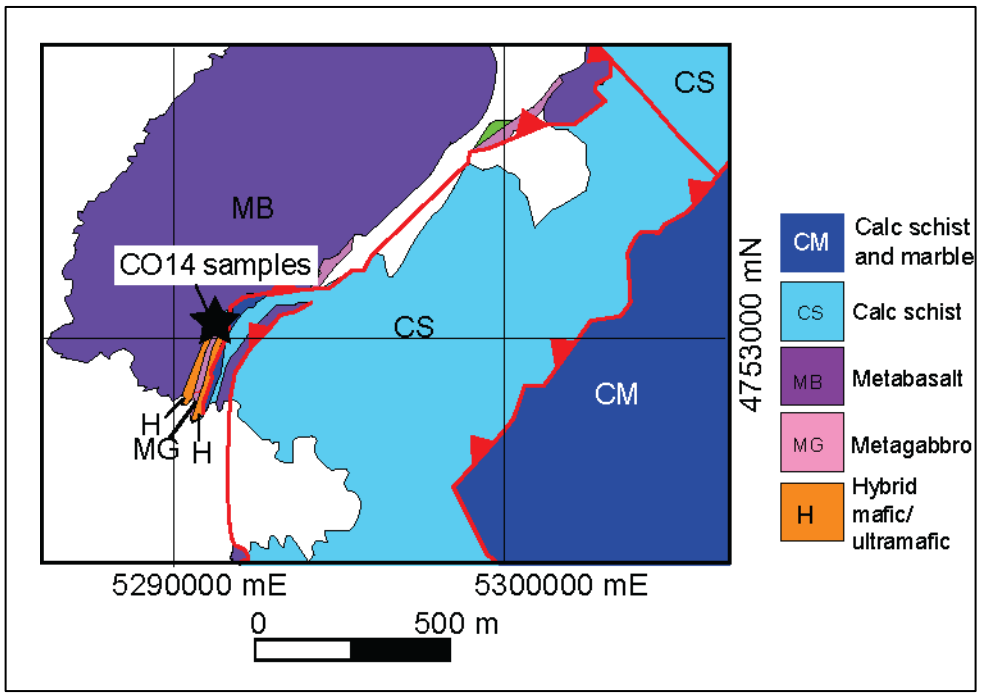

Figure 2.11: map of the Capu Corvoli sample localities (adapted from Lahondère, 1992)

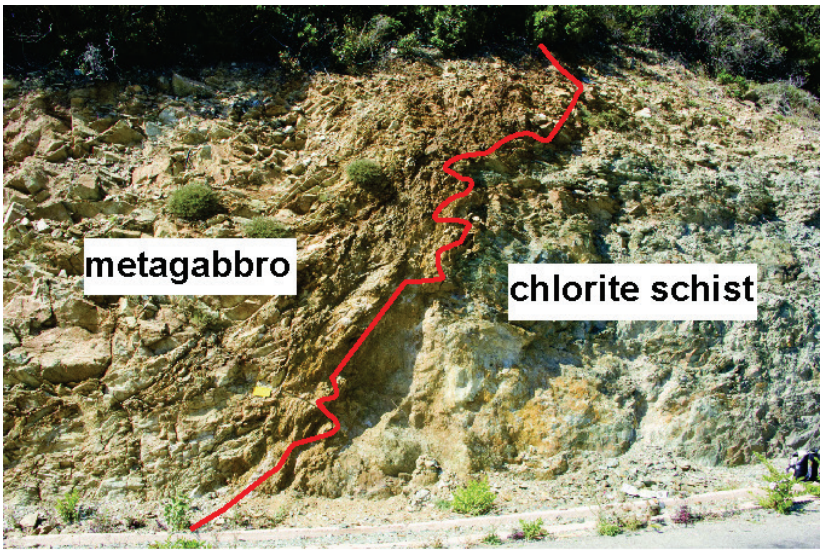

Figure 2.12: contact between metagabbro and chlorite schist (hybrid) at Capu Corvoli.

2.3 P-T paths

P-T paths for the Zermatt-Saas Zone (Reinecke, 1998; Bucher et al., 2005; Angiboust et al., 2009) and Alpine Corsica (Agard and Vitale-Brovarone, 2013) are displayed in Figure 2.15. Throughout this thesis, existing P-T conditions for silicate minerals, detailed sample petrography and mineral chemistry will be used to distinguish between early (primary or seafloor), prograde, peak and retrograde minerals Fe, Ti, S and HSE bearing minerals (i.e. sulphides and oxides). Retrogressive minerals provide insight into the composition of fluids released from the slab. In the P-T paths it is observed that peak pressure (the strict definition of peak metamorphism) occurs prior to peak temperature. Peak temperatures are achieved during the onset of exhumation, which is defined as a decrease in pressure.

During this stage, it is possible that both prograde and exhumation-related fluids infiltrate the rock at the same time under peak temperature conditions.

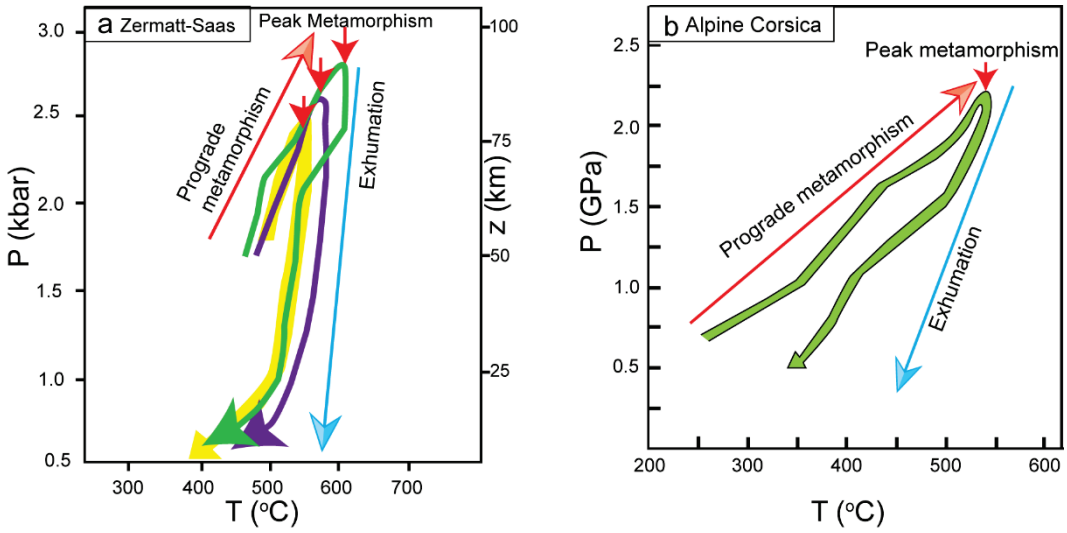

Figure 2.13: P-T paths of (a) Zermatt-Saas Zone; the yellow path is from Angiboust et al. (2009), the purple path from Bucher et al. (2005) and the green from Reinecke (1998), and (b) Alpine Corsica (Agard and Vitale-Brovarone, 2013).

2.4 Mineralogical evolution of serpentinites from seafloor alteration through subduction and exhumation

Seafloor serpentinisation is characterised by the serpentine minerals lizardite and chrysotile at temperatures of <200 to 300 ºC (Bach et al., 2004), whereas antigorite is the dominant serpentine minerals at temperatures of ~250 to 650 ºC (Wunder et al., 2001; Bach et al., 2004; Frost and Beard 2007 and Deschamps et al., 2010), although chrysotile is also metastable with antigorite (Bach et al., 2004). Antigorite and minor chrysotile are therefore the dominant serpentine minerals in subducted hydrated ultramafic rocks, which generally experience peak temperatures of at least 400 ºC (e.g. Hattori and Guillot, 2007; Rebay et al., 2012; Andreani et al., 2013). At temperatures greater than ~650ºC, and hence at greater depths in subduction zones, the dehydration of antigorite to chlorite, orthopyroxene, prograde olivine and garnet occurs (e.g. Evans and Powell, 2015). During antigorite dehydration, a large volume of fluid is released. The release of fluids at the antigorite-chlorite transition has the greatest potential for the release and transfer of redox sensitive elements, volatiles and elements of economic importance. However, the stability of serpentine minerals depends on their mineralogical composition, and most importantly their aluminium content with

higher concentrations of Al associated with the increased stability of antigorite at higher pressures and temperatures (Bromiley and Pawley, 2003; Padron-Navarta et al., 2013) and lizardite (Caruso & Chernosky, 1979). In addition the incorporation of Fe^{3+} into antigorite is proposed to increase antigorite stability at high pressure (Bromiley and Pawley, 2003). Mineral stability is also dependent on whether the system is open or closed and whether the geotherm is hot or cold (Evans and Powell, 2015). It is therefore useful to review the current state-of-the-art knowledge of serpentinite mineralogy from seafloor alteration through to subduction and exhumation.

2.4.1.1 Seafloor alteration

Harzburgites are the most common protoliths of seafloor serpentinites (also known as abyssal serpentinites), but other protoliths include pyroxenites, dunite, lherzolite and wehrlite. The formation of serpentinites on the seafloor occurs when seawater infiltrates peridotites, and primary olivine, orthopyroxene and clinopyroxene (depending on the bulk composition) are replaced by serpentine, magnetite, brucite, talc and tremolite (e.g. Mével et al., 2003). For example, the reaction of olivine with seawater results in the formation of brucite, magnetite, serpentine and hydrogen (Evans, 2008). Mesh textures are produced by serpentine replacement of olivine, and bastite textures result from the replacement of primary orthopyroxene by serpentine. The alteration of orthopyroxene also results in the production of talc. Tremolite may be a product of the reaction of clinopyroxene and orthopyroxene with seawater (e.g. Andreani et al., 2007). Remobilisation of primary sulphur and the addition of sulphur has been proposed to occur during seafloor alteration (Alt and Shanks, 2003). Seawater is enriched in sulphate (SO_4) and as a result sulphate-derived sulphur may be added to peridotites during this stage (Delacour et al., 2008). In addition, recent work has attributed the assemblage andradite + polyhedral chrysolite/lizardite + brucite + magnetite + awaruite in a Norwegian Alpine peridotite to low temperature conditions (<230ºC) and therefore is attributed to seafloor alteration (Plümper et al., 2014). The co-existence of andradite ($(Ca_2Fe_2^{3+}SiO_4)_3$) and awaruite (Ni_2Fe or Ni_3Fe) is associated with the production of H_2 and low SiO_2 (aq) concentrations in seafloor environments (Allen and Seyfried, 2003; McCollom and Bach, 2009; Plümper et al., 2014).

2.4.1.2 Changes in ultramafic mineralogy during subduction to peak metamorphism

Major phase changes in serpentinites during subduction are estimated from mineral texture analyses and thermodynamic modelling (Kerrich and Connolly, 1998; Yang and Powell, 2006; Rebay et al., 2012; Padron-Navarta et al., 2013; Evans and Powell, 2015) and petrographic studies of exhumed high-pressure rocks. During subduction, lizardite becomes unstable and the polymorph antigorite is formed (e.g. Evans, 2004). Antigorite (the high temperature serpentine mineral) forms an equigranular, interlocking texture consisting of fine grains (e.g. Li et al., 2004), and forms a mylonitic texture in rocks where this form of antigorite dominates. Other changes in mineralogy associated with progressive subduction include the reaction of antigorite and brucite to olivine, the introduction of talc and/or orthopyroxene (at higher temperatures than the antigorite + brucite to olivine reaction), and the dehydration of antigorite to chlorite and, at greater pressures and temperatures associated with peak metamorphism, the destabilisation of chlorite and the formation of garnet. Clinopyroxene, compositionally consistent with diopside (e.g. Groppo and Compagnoni, 2007), is also interpreted to grow at high pressure but at a range of temperatures (Evans and Powell, 2015). Other minerals noted at high-pressures, associated with peak metamorphism include Ti-clinohumite (e.g. Rebay et al., 2012), although Ti-clinohumite may also be stable at lower pressures (e.g. Rahn and Bucher, 1998).

Sulphide mineralogy changes from pyrrhotite at lower pressures to pyrite at higher pressure associated with prograde metamorphism (Evans and Powell, 2015). The proportion of sulphides could decrease with prograde metamorphism (Evans et al., submitted), consistent with the low modes of sulphides in subducted samples (e.g. Alt et al., 2012; Debret et al., 2014; Evans and Powell, 2015), although relatively little is known about sulphur mobilisation in subduction zones. Additionally, a decrease in magnetite mode has been observed with increasing metamorphic grade in high-pressure serpentinites (Debret et al., 2014).

2.4.1.3 Mineralogy associated with exhumation

Minerals that overprint known peak minerals are attributed to the onset of exhumation. Texturally, early exhumation has been linked to the formation of mylonites within minor folds (Li et al., 2004). Minerals noted to be associated with

the onset of exhumation in serpentinites include antigorite, ilmenite and magnetite (Groppo and Compagnoni, 2007), which are also breakdown products of high-pressure Ti-clinohumite (Trommsdorff and Evans, 1980). Other minerals noted at the onset of exhumation include carlosturanite ($(Mg, Fe, Ti)_{21}$ $(Si, Al)_{12}$ O_{28} $(OH)_{34}$ $\cdot H_2O$), although this mineral is most likely stable at a wide range of P-T conditions (Groppo and Compagnoni, 2007). Advanced stages of exhumation are associated with recrystallised antigorite grains in the form of an interlocking texture consisting of coarser laths and plates, where magnetite forms clusters associated with this stage (e.g. Li et al., 2004). This stage is also characterised by fibrous antigorite veins, and in later stages of exhumation, chrysotile veins and brucite (e.g. Groppo and Compagnoni, 2007). Ti-clinohumite veins could also be associated with advanced stages of exhumation (Rahn and Bucher, 1998), although also is stable to high-pressures (Scambelluri and Rampone, 1999; Groppo and Compagnoni, 2007; Ferrando et al., 2010; Rebay et al., 2012). Talc rims on high-pressure or early exhumation minerals such as magnetite record decompression as talc stability is restricted to a maximum of 1.5 GPa (Evans and Powell, 2015; Chapter 3).

2.5 References

Allen, D. E. & Seyfried, W. (2003), 'Compositional controls on vent fluids from ultramafic-hosted hydrothermal systems at mid-ocean ridges: An experimental study at 400 C, 500 bars', *Geochimica et Cosmochimica Acta* **67**(8), 1531–1542.

Alt, J. C. & Shanks, W. C. (2003), 'Serpentinization of abyssal peridotites from the MARK area, Mid-Atlantic Ridge: sulphur geochemistry and reaction modeling', *Geochimica et Cosmochimica Acta* **67**(4), 641–653.

Andreani, M.; Mével, C.; Boullier, A.-M. & Escartin, J. (2007), 'Dynamic control on serpentine crystallization in veins: Constraints on hydration processes in oceanic peridotites', *Geochemistry, Geophysics, Geosystems* **8**(2).

Andreani, M.; Munoz, M.; Marcaillou, C. & Delacour, A. (2013), 'XANES study of iron redox state in serpentine during oceanic serpentinization', *Lithos* **178**, 70–83.

Agard, P. & Vitale-Brovarone, A. (2013), 'Thermal regime of continental subduction: the record from exhumed HP–LT terranes (New Caledonia, Oman, Corsica)', *Tectonophysics* **601**, 206–215.

Angiboust, S.; Agard, P.; Jolivet, L. & Beyssac, O. (2009), 'The Zermatt-Saas ophiolite: the largest (60-km wide) and deepest (c. 70–80 km) continuous slice of oceanic lithosphere detached from a subduction zone?', *Terra Nova* **21**(3), 171–180.

Bach, W.; Garrido, C. J.; Paulick, H.; Harvey, J. & Rosner, M. (2004), 'Seawater-peridotite interactions: First insights from ODP Leg 209, MAR 15 N', *Geochemistry, Geophysics, Geosystems* **5**(9).

Ballèvre, M.; Kienast, J.-R. & Vuichard, J.-P. (1986), 'La nappe de la Dent-Blanche (Alpes occidentales): deux unités austroAlpines indépendantes', *Eclogae Geologicae Helvetiae* **79**(1), 57–74.

Barnicoat, A. & Fry, N. (1986), 'High-pressure metamorphism of the Zermatt-Saas ophiolite zone, Switzerland', *Journal of the Geological Society* **143**(4), 607–618.

Beltrando, M.; Manatschal, G.; Mohn, G.; Dal Piaz, G. V.; Brovarone, A. V. & Masini, E. (2014), 'Recognizing remnants of magma-poor rifted margins in high-pressure orogenic belts: The Alpine case study', *Earth-Science Reviews* **131**, 88–115.

Beltrando, M.; Rubatto, D. & Manatschal, G. (2010), 'From passive margins to orogens: The link between ocean-continent transition zones and (ultra) high-pressure metamorphism', *Geology* **38**(6), 559–562.

Bromiley, G. D. & Pawley, A. R. (2003), 'The stability of antigorite in the systems MgO-SiO2-H2O (MSH) and MgO-Al2O3-SiO2-H2O (MASH): The effects of Al3+ substitution on high-pressure stability', *American Mineralogist* **88**(1), 99–108.

Bucher, K., Fazis, Y., De Capitani, C. & Grapes, R., (2005), 'Blueschists, eclogites, and decompression assemblages of the Zermatt-Saas ophiolite: High-pressure metamorphism of subducted Tethys lithosphere, American Mineralogist, **90**(5–6), 821–835.

Caron, J. & Delcey, R. (1979), 'Lithostratigraphie des schistes lustrés corses: diversité des series post-ophiolitiques', *Compte Rendu Académies des Sci, Paris* **208**, 1525–1528.

Cartwright, I. & Buick, I. (2000), 'Fluid generation, vein formation and the degree of fluid–rock interaction during decompression of high-pressure terranes: the Schistes Lustrés, Alpine Corsica, France', *Journal of Metamorphic Geology* **18**(6), 607–624.

Caruso, L. J., & Chernosky, J. V. (1979). The stability of lizardite. *The Canadian Mineralogist*, *17*(4), 757-769.

Compagnoni, R.; Dal Piaz, G.; Hunziker, J.; Gosso, G.; Lombardo, B. & Williams, P. (1977), 'The Sesia-Lanzo Zone, a slice of continental crust with Alpine high pressure-low temperature assemblages in the Western Italian Alps', *Rend. Soc. Ital. Mineral. Petrol* **33**(1), 281–334.

Compagnoni, R., R. F. &. T. E. (2000), 'UHP Terranes in the Western Alps"31st International Geological Congress, Rio de Janeiro, Brazil, 6–17 August, 4 p. (Extended Abstract), CD geobr2000, ISBN 85-901482-5-4.'.

Dal Piaz, G. (1999), 'The Austroalpine-Piedmont nappe stack and the puzzle of Alpine Tethys', *Memorie di Scienze Geologiche* **51**(1), 155–176.

Debret, B.; Andreani, M.; Mucoz, M.; Bolfan-Casanova, N.; Carlut, J.; Nicollet, C.; Schwartz, S. & Trcera, N. (2014), 'Evolution of Fe redox state in serpentine during subduction', *Earth and Planetary Science Letters* **400**, 206–218.

Delacour, A.; Früh-Green, G. L.; Bernasconi, S. M. & Kelley, D. S. (2008), 'Sulphur in peridotites and gabbros at Lost City (30 N, MAR): Implications for hydrothermal alteration and microbial activity during serpentinization', *Geochimica et Cosmochimica Acta* **72**(20), 5090–5110.

Evans, B. W. (2004), 'The serpentinite multisystem revisited: chrysotile is metastable', *International Geology Review* **46**(6), 479–506.

Evans, B. W. (2008), 'Control of the products of serpentinization by the Fe2+ Mg-1 exchange potential of olivine and orthopyroxene', *Journal of Petrology* **49**(10), 1873–1887.

Evans, K.; Tomkins, A.; Cliff, J. & Fiorentini, M. (2014), 'Insights into subduction zone sulphur recycling from isotopic analysis of eclogite-hosted sulphides', *Chemical Geology* **365**, 1–19.

Evans, K. & Powell, R. (2015), 'The effect of subduction on the sulphur, carbon and redox budget of lithospheric mantle', *Journal of Metamorphic Geology* **33**(6), 649–670.

Faure, M. & Malavieille, J. (1981), 'Etude structurale d'un cisallement ductile: le charriage ophiolitique Corse dans la région de Bastia.', *Bulletin de la Societe Geologique de France, 23*.

Ferrando, S.; Frezzotti, M. L.; Orione, P.; Conte, R. C. & Compagnoni, R. (2010), 'Late-Alpine rodingitization in the Bellecombe meta-ophiolites (Aosta Valley, Italian Western Alps): evidence from mineral assemblages and serpentinization-derived H2-bearing brine', *International Geology Review* **52**(10-12), 1220–1243.

Forster, M.; Lister, G.; Compagnoni, R.; Giles, D.; Hills, Q.; Betts, P.; Beltrando, M. & Tamagno, E. (2004), 'Mapping of oceanic crust with HP to UHP metamorphism: the Lago di Cignana Unit (Western Alps)', *Mapping geology in Italy*, 279–286.

Frezzotti, M.; Selverstone, J.; Sharp, Z. & Compagnoni, R. (2011), 'Carbonate dissolution during subduction revealed by diamond-bearing rocks from the Alps', *Nature Geoscience* **4**(10), 703–706.

Frost, B. R. & Ballhaus, C. (1998), 'Comment on" Constraints on the origin of the oxidation state of mantle overlying subduction zones: an example from Simcoe, Washington, USA" by AD Brandon and DS Draper', *Geochimica et Cosmochimica Acta* **62**, 329–332.

Groppo, C. & Compagnoni, R. (2007), 'Metamorphic veins from the serpentinites of the Piemonte Zone, western Alps, Italy: a review', *Periodico di Mineralogia* **76**, 127–153.

Hattori, K. H. & Guillot, S. (2007), 'Geochemical character of serpentinites associated with high-to ultrahigh-pressure metamorphic rocks in the Alps, Cuba, and the Himalayas: Recycling of elements in subduction zones', *Geochemistry, Geophysics, Geosystems* **8**(9).

Herwartz, D.; Münker, C.; Scherer, E. E.; Nagel, T. J.; Pleuger, J. & Froitzheim, N. (2008), Lu-Hf garnet geochronology of eclogites from the Balma Unit (Pennine Alps): implications for Alpine paleotectonic reconstructions'Orogenic Processes in the Alpine Collision Zone', Springer, 173–189.

Jolivet, L.; Dubois, R.; Fournier, M.; Goffé, B.; Michard, A. & Jourdan, C. (1990), 'Ductile extension in alpine Corsica', *Geology* **18**(10), 1007–1010.

Jolivet, L.; Faccenna, C.; Goffé, B.; Mattei, M.; Rossetti, F.; Brunet, C.; Storti, F.; Funiciello, R.; Cadet, J. P.; d'Agostino, N. & others (1998), 'Midcrustal shear zones in postorogenic extension: example from the northern Tyrrhenian Sea', *Journal of Geophysical Research: Solid Earth* **103**(B6), 12123–12160.

Kerrick, D. & Connolly, J. (1998), 'Subduction of ophicarbonates and recycling of

CO2 and H2O', *Geology* **26**(4), 375–378.

Lacombe, O. & Jolivet, L. (2005), 'Structural and kinematic relationships between Corsica and the Pyrenees-Provence domain at the time of the Pyrenean orogeny', *Tectonics* **24**(1).

Lahondère, D. (1996, p. 294), 'Les schistes bleus et les éclogites a lawsonite des unités continentales et océaniques de la Corse alpine: nouvelles données pétrologiques et structurales', Documents du BRGM 240, Orléans.

Lahondère, J.; Conchon, O.; Lahondère, D.; Dominici, R. & Vautrelle, C. (1983), 'Carte géol', *France (1/50000), feuille Bastia (1104). Orléans: BRGM*.

Lahondère, J.; Lahondère, D.; Lluch, D.; Ohnenstetter, M.; Dominici, R. & Vautralle, C. (1992), 'Carte géologique de la France a 1/50000', *Luri, BRGM*.

Lahondère, J.; Conchon, O.; Lahondère, D.; Dominici, R. & Vautrelle, C. (1994, 67 pp.), 'Carte géol.France (1/50000), feuille Vescovato (1107).',*Orléans: BRGM.*.

Li, X.-P.; Rahn, M. & Bucher, K. (2004), 'Serpentinites of the Zermatt-Saas ophiolite complex and their texture evolution', *Journal of Metamorphic Geology* **22**(3), 159–177.

Magott, R.; Fabbri, O. & Fournier, M. (2016), 'Subduction zone intermediate-depth seismicity: Insights from the structural analysis of Alpine high-pressure ophiolite-hosted pseudotachylyte (Corsica, France)', *Journal of Structural Geology* **87**, 95–114.

Mattauer, M.; Faure, M. & Malavieille, J. (1981), 'Transverse lineation and large-scale structures related to Alpine obduction in Corsica', *Journal of Structural Geology* **3**(4), 401–409.

Mattauer, M.; Proust, F. & Etchecopar, A. (1977), 'Lineation "a" et mecanisme de cisaillement simple lie au chevauchement de la nappe des schistes lustres en Corse', *Bulletin de la Société Géologique de France* **7**(4), 841–847.

McCollom, T. M. & Bach, W. (2009), 'Thermodynamic constraints on hydrogen generation during serpentinization of ultramafic rocks', *Geochimica et Cosmochimica Acta* **73**(3), 856–875.

Meresse, F.; Lagabrielle, Y.; Malavieille, J. & Ildefonse, B. (2012), 'A fossil Ocean–Continent Transition of the Mesozoic Tethys preserved in the Schistes Lustrés nappe of northern Corsica', *Tectonophysics* **579**, 4–16.

Mével, C. (2003), 'Serpentinization of abyssal peridotites at mid-ocean ridges', *Comptes Rendus Geoscience* **335**(10), 825–852.

Molli, G. (2008), 'Northern Apennine–Corsica orogenic system: an updated overview', *Geological Society, London, Special Publications* **298**(1), 413–442.

Molli, G. & Malavieille, J. (2011), 'Orogenic processes and the Corsica/Apennines geodynamic evolution: insights from Taiwan', *International Journal of Earth Sciences* **100**(5), 1207–1224.

Padrón-Navarta, J. A., Sánchez-Vizcaíno, V. L., Hermann, J., Connolly, J. A., Garrido, C. J., Gómez-Pugnaire, M. T., & Marchesi, C. (2013). Tschermak's substitution in antigorite and consequences for phase relations and water liberation in high-grade serpentinites. *Lithos*, **178**, 186-196.

Pleuger, J.; Roller, S.; Walter, J. M.; Jansen, E. & Froitzheim, N. (2007), 'Structural evolution of the contact between two Penninic nappes (Zermatt-Saas zone and Combin zone, Western Alps) and implications for the exhumation mechanism and palaeogeography', *International Journal of Earth Sciences* **96**(2), 229–252.

Plümper, O.; Beinlich, A.; Bach, W.; Janots, E. & Austrheim, H. (2014), 'Garnets within geode-like serpentinite veins: Implications for element transport, hydrogen production and life-supporting environment formation', *Geochimica et Cosmochimica Acta* **141**, 454–471.

Rahn, M. & Rahn, K. (1998), 'Titanian clinohumite formation in the Zermatt-Saas ophiolites, central Alps', *Mineralogy and Petrology* **64**(1-4), 1–13.

Ravna, E.; Andersen, T. B.; Jolivet, L. & De Capitani, C. (2010), 'Cold subduction and the formation of lawsonite eclogite–constraints from prograde evolution of eclogitized pillow lava from Corsica', *Journal of Metamorphic Geology* **28**(4), 381–395.

Rebay, G.; Spalla, M. & Zanoni, D. (2012), 'Interaction of deformation and metamorphism during subduction and exhumation of hydrated oceanic mantle: Insights from the Western Alps', *Journal of Metamorphic Geology* **30**(7), 687–702.

Reddy, S.; Wheeler, J.; Butler, R.; Cliff, R.; Freeman, S.; Inger, S.; Pickles, C. & Kelley, S. (2003), 'Kinematic reworking and exhumation within the convergent Alpine Orogen', *Tectonophysics* **365**(1), 77–102.

Reddy, S.; Wheeler, J. & Cliff, R. (1999), 'The geometry and timing of orogenic extension: an example from the Western Italian Alps', *Journal of Metamorphic Geology* **17**, 573–590.

Reinecke, T. (1998), 'Prograde high-to ultrahigh-pressure metamorphism and exhumation of oceanic sediments at Lago di Cignana, Zermatt-Saas Zone, western Alps', *Lithos* **42**(3), 147–189.

Scambelluri, M. & Rampone, E. (1999), 'Mg-metasomatism of oceanic gabbros and its control on Ti-clinohumite formation during eclogitization', *Contributions to Mineralogy and Petrology* **135**(1), 1–17.

Stampfli, G. M. & Borel, G. (2001), *Geology of the Western Swiss Alps: A Guide-book*, Section des Sciences de la terre de l'université.

Trommsdorff, V. & Evans, B. W. (1980), 'Titanian hydroxyl-clinohumite: formation and breakdown in antigorite rocks (Malenco, Italy)', *Contributions to Mineralogy and Petrology* **72**(3), 229–242.

Vitale Brovarone, A.; Beltrando, M.; Malavieille, J.; Giuntoli, F.; Tondella, E.; Groppo, C.; Beyssac, O. & Compagnoni, R. (2011), 'Inherited ocean–continent transition zones in deeply subducted terranes: insights from Alpine Corsica', *Lithos* **124**(3), 273–290.

Vitale Brovarone, A.; Beyssac, O.; Malavieille, J.; Molli, G.; Beltrando, M. & Compagnoni, R. (2013), 'Stacking and metamorphism of continuous segments of subducted lithosphere in a high-pressure wedge: the example of Alpine Corsica (France)', *Earth-Science Reviews* **116**, 35–56.

Vitale Brovarone, A. & Herwartz, D. (2013), 'Timing of HP metamorphism in the Schistes Lustrés of Alpine Corsica: New Lu–Hf garnet and lawsonite ages', *Lithos* **172**, 175–191.

Wheeler, J.; Reddy, S. & Cliff, R. (2001), 'Kinematic linkage between internal zone extension and shortening in more external units in the NW Alps', *Journal of the Geological Society* **158**(3), 439–443.

Wunder, B.; Wirth, R. & Gottschalk, M. (2001), 'Antigorite: Pressure and temperature dependence of polysomatism and water content', *European Journal of Mineralogy* **13**(3), 485–495.

Yang, J.-J. & Powell, R. (2006), 'Calculated phase relations in the system Na2O–CaO–K2O–FeO–MgO–Al2O3–SiO2–H2O with applications to UHP eclogites and whiteschists', *Journal of Petrology* **47**(10), 2047–2071.

CHAPTER 3

REDISTRIBUTION OF IRON AND TITANIUM IN HIGH PRESSURE ULTRAMAFIC ROCKS

Rosalind J. Crossley, Katy A. Evans, Steven M. Reddy and Gregory W. Lester.

This chapter has been accepted for publication in *Geochemistry, Geosystems and Geophysics*

Contributions by co-authors

Rosalind Crossley prepared the samples for bulk composition analysis and characterised the samples using optical microscopy, scanning electron microscopy and electron-probe microanalysis. Steve Reddy collected ASZ, VSZ and GSZ samples in 2009 and 2011, and Katy Evans collected the PF and LC samples in 2011 and prepared the samples for thin section production. Rosalind Crossley is the primary author of this manuscript with valuable discussions, advice and guidance from all co-authors.

Abstract

The redox state of iron in high-pressure serpentinites, which host a significant proportion of Fe^{3+} in subduction zones, can be used to provide an insight into iron cycling and constrain the composition of subduction zone fluids. In this study, we use oxide and silicate mineral textures, interpretation of mineral parageneses, mineral composition data, and whole rock geochemistry of high-pressure retrogressed ultramafic rocks from the Zermatt-Saas Zone to constrain the distribution of iron and titanium, and iron oxidation state. These data provide an insight on the oxidation state and composition of fluids at depth in subduction zones. Oxide minerals host the bulk of iron, particularly Fe^{3+}. The increase in mode of magnetite and observation of

magnetite within antigorite veins in the investigated ultramafic samples during initial retrogression is most consistent with oxidation of existing iron within the samples during the infiltration of an oxidizing fluid since it is difficult to reconcile addition of Fe^{3+} with the known limited solubility of this species. However, high Ti contents are not typical of serpentinites and also cannot be accounted for by simple mixing of a depleted mantle protolith with the nearby Allalin gabbro. Titanium-rich phases coincide with prograde metamorphism and initial exhumation, implying the early seafloor and/or prograde addition and late mobilization of Ti. If Ti addition has occurred, then the introduction of Fe^{3+}, also generally considered to be immobile, cannot be disregarded. We explore possible transport vectors for Ti and Fe through mineral texture analysis.

3.1 Introduction

Subduction of iron has the potential to transfer redox budget to the sub-arc mantle, deep mantle, and metamorphic fluids released from the subducting slab (Evans, 2012). Redox budget is an extensive variable defined as the number of moles of electrons that are required to be added to a sample to reach a reference state (Evans, 2006). Understanding the oxidation state of these subduction zone components, and metamorphic changes in oxidation state, is essential to constrain the oxidizing or reducing capacity introduced to subduction zones throughout geological time. The oxidation state of the sub-arc mantle is of particular significance because current genetic models for arc-related ore deposits require the sub-arc mantle to be oxidized (e.g., Mungall, 2002). The redox state, quantity and composition of subduction zone fluids influence the transport and precipitation of a range of elements that include redox-sensitive elements and elements of economic importance such as Cu, Au and Ag.

The proportion of subducted Fe^{3+} that is transferred to the deep mantle, to the sub-arc mantle or carried by metamorphic fluids up the slab interface is unknown. An estimated 11.4 x 10^{12} mol of Fe^{3+} and 40 x 10^{12} mol of Fe^{2+} is input into subduction zones every year and approximately 4.2 x 10^{12} mol of Fe^{3+} and 6.2 x 10^{12} mol of Fe^{2+} is released in arc lavas each year (Evans, 2012; Lecuyer and Ricard, 1999). The total input of iron is therefore ~ 5 times higher than the output. The input of Fe^{3+} is ~2.7 times higher than that released from arcs, which could imply a net addition of oxidized iron to subduction zones, or, alternatively, Fe reduction during the oxidation of other elements such as sulphur.

Subducted iron is hosted in ocean floor sediments, hydrated mantle and oceanic crust, which are subsequently subducted. The redox state of Fe in high-pressure ultramafic rocks has been previously used to infer the redox state of subduction zone fluids and to provide an insight into Fe cycling (Debret et al., 2014). Hydrated mantle lithosphere hosts a significant proportion of Fe^{3+} in magnetite and Fe^{3+}-bearing serpentine, and therefore has the potential to introduce substantial redox budget into subduction zones (Andreani et al., 2013; Lecuyer and Ricard, 1999; Debret et al., 2014). Careful textural analysis of oxide phases in high-

pressure serpentinites therefore provides a valuable insight on the stability of Fe^{3+}-bearing oxides and the transfer of redox budget during subduction and exhumation.

A significant effort has been devoted to the interpretation of metamorphic conditions using silicate textures in high-pressure ultramafic rocks (Li et al., 2004; Rebay et al., 2012; Scambelluri et al., 2014; Rahn & Bucher, 1998; Scambelluri & Rampone, 1999; Groppo & Compagnoni, 2007; Ferrando et al., 2010), but less work has been carried out on oxide mineral textures. Exceptions include studies of oxide mineral textures in Val Malenco (Peretti et al., 1992; Burkhard, 1993) and Cerro del Almirez (e.g., Lopéz Sanchéz-Vizcaíno et al., 2005; 2009). Oxide mineral textures in Val Malenco serpentinites record reducing conditions during upper-amphibolite facies metamorphism (Peretti et al., 1992), and Cr spinel textures indicate homogenization of spinel phase compositions with increasing metamorphic grade (Burkhard, 1993). In addition, submicroscopic oxide grains within prograde olivine in eclogite facies ultramafic rocks from Cerro del Almirez have provided an insight into the transfer of high field strength element (HFSE) at depths associated the dehydration of antigorite, where oxide minerals (Lopéz Sanchéz-Vizcaíno et al., 2005) are demonstrated to be important hosts of HFSE, including Ti.

Titanium has traditionally been considered to be immobile in aqueous fluids, though studies have shown mobility via complexing (e.g., Manning, 2004; Manning et al., 2008; Tropper and Manning, 2005; Gao et al., 2007; Rapp et al., 2010; Hayden and Manning, 2011; Huang et al., 2015; Tanis et al., 2015; Tanis et al., 2016). However, studies addressing the source of titanium in mineral hosts are rare, with notable exceptions. Ti-rich phases such as Ti-clinohumite in veins in high-pressure serpentinites have been described previously but the origin of such veins are controversial (e.g., Rebay et al., 2012). Some authors attribute Ti-clinohumite veins to high-pressure-low-temperature (HP-LT) metamorphism as a product of fluid mediated Ti remobilization on a sample scale associated with H_2O release during serpentine dehydration (Groppo and Compagnoni, 2007; Scambelluri & Rampone, 1999; Ferrando et al., 2010, Marchesi et al., 2013). The length scale of Ti mobilization is considered to be on a sample scale, although Lopéz Sanchéz-Vizcaíno et al. (2009) attributed different generations of Ti-clinohumite veins to mobility of Ti on different length scales from centimetre to metre scale. Other

workers have proposed that Ti-clinohumite grew during seafloor alteration and remained stable during subduction, and the growth of Ti-clinohumite veins have been suggested to record advanced exhumation (Rahn and Bucher, 1998). Other Ti-rich minerals assessed for evidence of Ti-mobility include the presence of Ti-andradite in ultramafic rocks from Val Malenco, where the mechanism for such mobility was proposed to be transport via aqueous fluids under upper amphibolite conditions (Müntener and Hermann, 1994).

In this study, Ti and Fe redistribution are investigated via detailed textural analysis of mineral hosts to these elements in retrogressed ultramafic samples from the Zermatt-Saas Zone. Textural relations between oxide and silicate minerals are used to constrain the evolution of iron and titanium-bearing phase stability, including oxides, with progressive metamorphism and exhumation. Oxide compositions and whole rock geochemistry are used to quantify the oxidation state of iron and changes to its distribution during subduction-metamorphism, retrogression and exhumation. The results provide insights into the distribution and oxidation state of Fe in high-pressure serpentinites and implications for the transfer of Fe and hence redox budget at depth. In addition, evidence for Ti redistribution and potential mechanisms of Ti mobility are explored.

3.2 Geological setting

3.2.1 Zermatt-Saas Zone

The convergence of the Adriatic and Eurasian tectonic plates led to the closure of the Tethyan oceanic basin during the Late Cretaceous to Early Tertiary period, resulting in subsequent Eocene–Oligocene continental collision (e.g., Beltrando et al., 2010). Ultramafic rocks form parts of the eclogite facies Zermatt-Saas Zone and the overlying greenschist facies Combin Zone, which together comprise the Piemonte ophiolite (Reddy et al., 2003). The Piemonte ophiolite separates the Penninic domain, which consists of the Monte Rosa, Gran Paradiso and Dora Maira massifs (e.g., Stampfli, 2001), and basement nappes, from the Austroalpine domains including the Sesia Zone (Compagnoni et al., 1977) and Dent Blanche Klippe (Ballèvre et al., 1986; Reddy et al., 1999; 2003; Fig. 3.1). The ophiolite consists of metabasalts (eclogites and blueschists), peridotites and metagabbros.

The ophiolite is traditionally considered to represent Tethyan oceanic lithosphere which formed during the Middle-Late Jurassic rifting of the Piemonte-Ligurian ocean (e.g., Angiboust et al., 2009 and references therein). Multiple reactivation of transform faults during the Alpine orogeny was proposed to account for the juxtaposition of ultramafic rocks with slivers of continental basement within oceanic units (Ballèvre and Merle, 1993; Reddy et al., 2003; Forster et al., 2004). However, there is increasing evidence for a pre-Alpine juxtaposition of the ultramafic rocks and continental crust in the Western Alps, which implies that the oceanic setting of the ophiolites reflected an ocean-continent transition zone (Beltrando et al., 2010).

The Zermatt-Saas Zone was metamorphosed to eclogite facies, with earlier estimates of peak metamorphic conditions at 1–3 GPa and 550–630 ºC (Ernst and Dal Piaz, 1978; Oberhänsli; 1980; Barnicoat and Fry, 1986; Reinecke, 1991; 1998; Bucher et al., 2005; Angiboust et al., 2009). Some workers consider the Zermatt-Saas Zone to represent a continuous slice of lithosphere with *P-T* estimates of 2.3 ± 0.1 GPa and 540 ± 40 ºC across the block (e.g., Angiboust et al., 2009; Angiboust and Agard, 2010). However, in other work, estimates of peak metamorphic conditions differ. For example, at Saas-Fee peak metamorphic conditions of 2.5–3 GPa and 600–625 ºC are recorded (Bucher et al., 2005), whereas the southern part of the Zermatt-Saas Zone records lower peak pressures and temperatures of ~2.1 GPa and 550 ºC (Martin et al., 2008).

On the basis of U-Pb dating of zircons in UHP eclogites and metasediments at Lago di Cignana (Rubatto et al., 1998) and Lu-Hf ages of garnets from the Balma ophiolite (Herwartz et al., 2009), the timing of peak metamorphism is constrained to ~45.5–42 Ma. Structural data combined with Rb-Sr dates from fabric-forming recrystallized white mica within the Gressoney Shear Zone documents exhumation of the Zermatt Saas unit from high pressure to mid-crustal levels at ~ 44–36 Ma (Reddy et al., 1999; 2003).

3.2.2 Sample localities

Twenty-four ultramafic samples were collected from Pfulwe Pass (grid reference: WGS 84, zone 32T, 0410417mE and 5096587mN), Gressoney (grid reference: WGS 84, zone 32T, 0415310mE 5064106mN), Upper Valtournenche

(grid reference: WGS 84, zone 32T, 0392710mE 5081150mN; 03910613mE and 5080719mN) and Monte Rosso (grid reference: WGS 84, zone 32T, 0404124mE 5081747mN), where there is a good exposure of high-pressure serpentinites. The details of the localities have been described in detail in previous work; Pfulwe is described by Barnicoat and Fry (1986), Fry and Barnicoat (1987) and Dale et al. (2009), Gressoney by Reddy et al. (1999) and Gasco et al. (2013), Upper Valtournenche by Groppo et al. (2009) and Rebay et al. (2012), and Monte Rosso by Dal Piaz (2010), respectively. Peak temperatures and pressures at the localities are well-established, and the metamorphic conditions recorded by silicate mineral assemblages in Zermatt-Saas ultramafic rocks are well-constrained (Rebay et al., 2012; Li et al., 2004).

Specific sample outcrop descriptions are as follows. The sample LC-015 was obtained from a 4 x 2 m foliated, homogeneous green serpentinite outcrop in Upper Valtournenche. This outcrop occurs in a relatively low-lying and well vegetated area, therefore it is inferred that serpentinite is the dominant rock type in the immediate vicinity, defined as within a few tens of meters. However, mafic eclogites outcrop within 100 meters. GSZ-11 is part of the Zermatt-Saas Zone and was collected from an outcrop below and to the east of Punta Bettolina, Upper Val Gressoney. The sample PF-001 was taken from a 12 x 3 m well foliated, homogeneous, green serpentinite outcrop. In this outcrop, well formed bipyramidal magnetites, of length up to 1 cm on the longest axis, could be clearly seen. This outcrop is within 20 m of Allalin gabbro outcrops. VSZ-02, VSZ-03 and VSZ-05 were collected from a single outcrop consisting of foliated serpentinites surrounding metarodingites and eclogites (metabasalts and metagabbros) above Barmasse in Valtournenche. ASZ-09 is from the summit of Monte Rosso in the

Val d'Ayas, to the northeast of the village of St Jacques. At this locality large blocks of serpentinites and dykes of rodingite outcrop (Fig. 2.2).

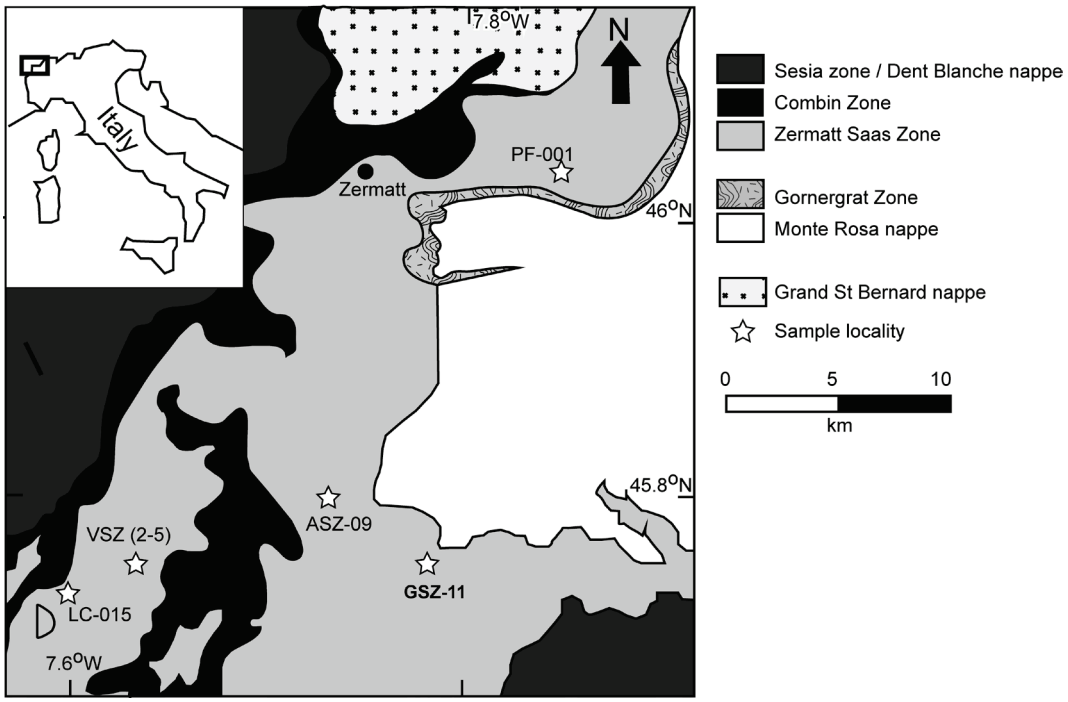

Figure 3. 1*:* (a) a map showing the location of the Zermatt Saas zone and the localities of Lago di Cignana and Pfulwe, modified after Martin *et al.* (2008) and Evans *et al.* (2014). (b) a map of the Lago di Cignana region showing the location of sample LC-015, modified after Groppo *et al.* (2009). (c) a map of the Pfulwe area, with the location of sample PF-001, modified after Angiboust and Agard (2010).

3.3 Methods

3.3.1 Analytical Methods

Sample preparation for bulk composition analysis involved crushing approximately 30g of each sample to a fine powder using a TEMA mill. Whole rock major, minor, selected trace elements and C, S and FeO were obtained. The selection of trace elements for analysis focused on elements that are redox sensitive. Major elements and trace elements were analysed by lithium borate fusion followed by dissolution and inductively coupled plasma optical emission spectrometry (ICP-OES) for major element analysis and Cr, Sc and V, and inductively coupled mass spectrometry (ICP-MS) for Ba, Cs, Ga, Rb, Sn and Sr analysis. The FeO content was determined via titration with ceric sulphate. C and S contents were measured using a CS analyser. Whole rock analysis was carried out by Intertek Genalysis laboratories, Perth, Australia.

The whole rock FeO concentration was determined via titration with ceric sulphate, and the total Fe oxide concentration ($Fe_2O_{3\ tot}$) was analysed using ICP-OES. The whole rock Fe_2O_3 calculated using the following formula (e.g. Gill, 2010):

$$Fe_2O_3 = Fe_2O_{3\ tot} - (FeO*1.11)$$

Thin section billets were cut from the hand samples perpendicular to foliation. Petrographic analysis of the samples was carried out by transmitted and reflected light microscopy. Optical microscopy was augmented by scanning electron microscopy (SEM) and qualitative analysis of minerals by energy dispersive spectroscopy (EDS) at the Microscopy and Microanalysis Facility (MMF), Curtin University. SEM was carried out on the Zeiss Neon 40EsB field emission scanning electron microscope. Major and minor elements in iron and titanium bearing and associated minerals were quantitatively analysed using the wavelength dispersive spectroscopy (WDS) and energy dispersive spectrometry (EDS).

WDS analysis was performed using the JEOL 8530F Hyperprobe at the Centre for Microscopy, Characterisation and Analysis at the University of Western Australia. The accelerating voltage was 15 kV, the beam current was 20 nA and the

beam was defocussed to 4 μm for the analysis of hydrous minerals. The standards used for calibration were wollastonite (Si, Ca), spessartine (Al, Mn; Fe in silicates), jadeite (Na), pyrope (Mg), rutile (Ti), sanidine (K), magnetite (Fe in oxides), willemite (for Zn and to correct for Mn interference on Fe), Cr_2O_3, Ni and V. Off-peak background corrections were used throughout with an on-peak counting time of 20 seconds per element. Data reduction was performed using the Probe for EPMA software package.

Quantitative EDS analysis was achieved using the TESCAN Mira VP-FESEM at the Microscopy and Microanalysis Facility, Curtin University. The operating conditions were as follows; an accelerating voltage of 20KeV, a beam intensity of 14 and a 15mm working distance. Prior to analysis, calibration on a cobalt standard on the sample stage ensured the same working distance and analytical conditions were achieved in both the standard and sample while setting the beam current prior to analysis. 500,000 counts were obtained for each analysis. The Oxford Instruments software allowed the determination of quantitative oxide and element concentrations (wt%) using factory calibration. The calibration was tested on chlorite, pyrite, magnetite, olivine and diopside from the Astimex standard block, which produced consistent results with the known values. To test reproducibility and accuracy, selected minerals that were analysed by WDS were re-analysed with EDS. The results produced were within error of WDS results, and any deviations from these were attributed to natural heterogeneity in mineral compositions.

3.3.2 Mineral formulae calculations

Formulae of minerals were calculated using charge balance and stoichiometric constraints. Conventionally, mineral formulae are reported for a fixed number of oxygen atoms. This strategy is utilized because the number of cations varies due to charge-balanced exchanges between elements with different oxidation states, e.g. $Na^{+} + Al^{3+} = Si^{4+}$. However, this strategy becomes difficult to apply when elements, such as Fe, occur in more than one oxidation state, because the number of oxygens is not well constrained in such cases. Fortunately, in the minerals investigated, likely cation exchanges in the spinel and serpentine mineral groups of interest occur without change in the total number of cations. Therefore, in this work, formulae were calculated to a total number of cations rather than a

fixed number of oxygens. Spinel (magnetite, Cr-magnetite, and Ti-magnetite) formulae were calculated on the basis of 3 cations. Iron speciation is not determined by the microprobe, so the Fe^{3+} content for Fe-only magnetite was calculated assuming the ratio of Fe^{3+}:Fe^{2+} was 2:1, given the stoichiometric constraints. The exchange vector formula for magnetite to Ti-magnetite is $2Fe^{3+} = Fe^{2+} + Ti^{4+}$. In order to calculate Ti-magnetite formulae, where one mole of Ti^{4+} substitutes for one mole of Fe^{3+} on the octahedral site, the number of moles of Fe^{3+} was set to $2(1 - n_{Ti})$ and the remaining iron $(1 + n_{Ti})$, was assumed to be ferrous, where n_{Ti} is the number of moles of Ti in a three cation ulvöspinel. In the case of Cr-bearing magnetite, formulae were calculated assuming one mole of Cr^{3+} was replaced by one mole of Fe^{3+} on the octahedral site via $Cr^{3+} = Fe^{3+}$; the number of moles of Fe^{3+} was then $2 - n_{Cr}$ and the number of moles of Fe^{2+} remained 1.

For other minerals, formulae were calculated on the basis of *n* cations, as follows: for ilmenite *n* = 2, serpentine and chlorite *n* = 20, amphibole *n* = 15, talc *n* = 14, Ti-clinohumite *n* = 13, diopside *n* = 4, olivine *n* = 3, titanite = 3 and garnet *n* =8. Amphibole can undergo substitution involving vacancies, e.g. $Si^{4+} = Al^{3+} + Na^{+}$, which would make the cation sum approach problematic, but there was little evidence for these substitutions in the rocks examined because the Na content of all samples is negligible. Garnet formulae ($X_3Y_2Si_3O_4$) were calculated based on the assumption that Fe^{2+} occupies the X site and partially substitutes for Si, and that Fe^{3+} occupies the Y site. In most cases it was assumed Ti occupies the Y site, however because Fe^{3+} has a greater preference than Ti for the Y site (Huggins et al., 1977), where the sum was equal to or more than 2 cations for the Y site, Ti was also assumed to partially substitute for Si. Sulphide formulae were calculated on the basis of charge balance and stoichiometric constraints.

Serpentine and chlorite appeared in more than one textural setting in the Pfulwe sample. The existence of statistically valid differences between the compositions of these minerals in the different textural settings was tested via Student's t-tests on critical compositional parameters (e.g. $Mg/(Mg+Fe^{2+})$, and Al^{3+} content). Probability values (P) of <0.05 indicated a statistically significant difference in composition between the mineral populations.

3.4 Results

3.4.1 Petrographic analysis

3.4.1.1 Antigorite serpentinites (LC-015 and GSZ-11)

The antigorite serpentinite samples LC-015 and GSZ-11 have been described in detail by Evans et al. (2017). Briefly, the two samples differ in mineral assemblages, where GSZ-11 is olivine (~10%) and chlorite-bearing (~5%), while LC-015 is talc-bearing (~3%). Ilmenite is only present in LC-015. Both samples contain serpentine (>80%), diopside (trace to 3%), magnetite (5–10%), chromite (2-3%) and sulphides (trace to 2%). Two fabric elements are present. S1 is a sheared fabric associated with fine grained antigorite needles which comprise most of the matrix (>50%, atg1) and S2 is comprised of coarse grained antigorite and veins (atg2, Fig. 3.2 a and c). The oxide phases consist of 5–10% magnetite, ~2-3% chromite, and in LC-015, ~2% ilmenite. Some magnetite grains are aligned parallel to the S1 fabric (Fig. 3.2b). Spinel grains consist of Cr-rich cores and Fe-rich rims. Fe-rich rims are overprinted by coarse laths (200–400 μm) of serpentine (atg2) (Fig. 3.2e, f). Matrix grains with lower concentrations of Cr (<10 wt. %), are observed in both GSZ-11 and LC-015 (3g). In GSZ-11, Cr-free magnetite is aligned with atg2 veins. Ilmenite is replaced at the rim by atg2 laths in LC-015 (Fig. 3.2g). Sulphide phases include heazlewoodite and millerite in GSZ-11 and trace pyrite within atg1 associated with diopside in LC-015 (Fig. 3.2d). In GSZ-11 heazlewoodite (Hz1) occurs as grains <60 μm within a sheared antigorite matrix, contains inclusions of or is replaced by antigorite and is included within and/or overprinted by magnetite. Millerite is either included in or replaces magnetite at the rim. Antigorite veins

cross-cut the matrix and olivine, and contain smaller heazlewoodite grains (hz2; 20–50 µm, Fig. 3.2h). Metal phases include trace Cu-Zn.

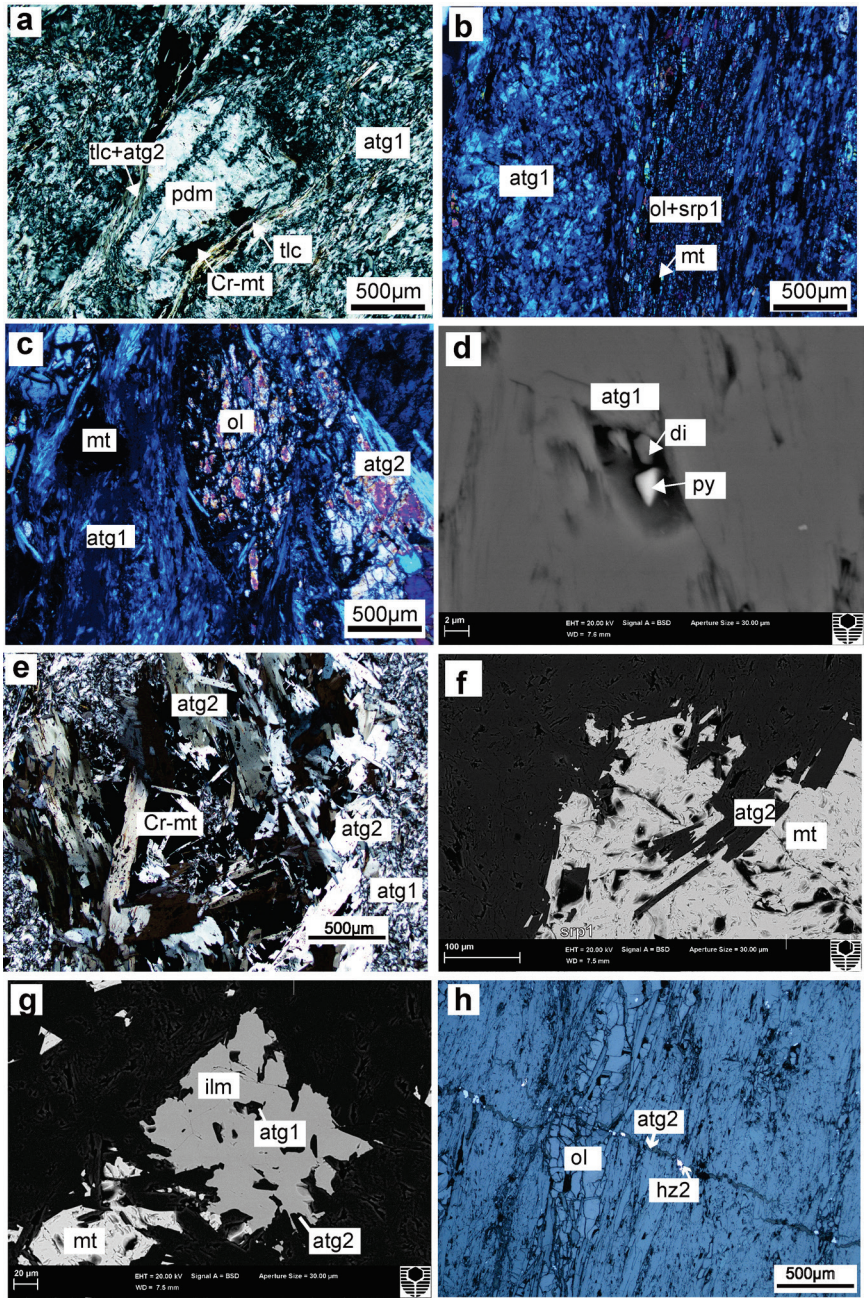

Figure 3.2: Photomicrographs of mineral textures in antigorite serpentinites. a (xpl) an undeformed pseudomorph with mt2 rims which is replaced by tlc and atg2 veins b (xpl) sheared olivine and atg1 aligned with mt2 in GSZ-11. c (xpl) mt2 and olivine replaced by atg2 veins in GSZ-11. d (bse) small di and py grains within atg1. e (xpl) coarse laths of atg2 overprint Cr-mt and the matrix that consists of atg1. f (bse) atg2 laths replace Cr-mt rims on Cr cores. g (bse) ilm grain with inclusions of atg1 and replaced at the rim by atg2. Cr-mt in the matrix is also replaced by atg2. h (rfl) atg2 veins containing hz2 grains cross-cut the foliation. ilm = ilmenite, atg1 = matrix antigorite, Cr-mt = Cr-magnetite, tlc = talc, py = pyrite, pdm = pseudomorph, srp1 = matrix fine antigorite, atg2 = coarse antigorite laths, di = diopside, . xpl = crossed polarised light, bse = back scattered electron, rfl = reflected light.

3.4.1.2 Chlorite-rich ultramafic rock (PF-001)

The details of the Pfulwe sample, PF-001, are described in Evans et al. (2017) but the relevant details are summarized here. The sample is comprised of 40% chlorite, 25% serpentine, 12% magnetite, 10% talc, 8% tremolite, 4% ilmenite, 1% apatite, 1% Ti-magnetite and trace pyrite, chalcopyrite and zircon. S1 is associated with matrix chlorite (Fig. 3.3a). Tremolite is mantled by chlorite associated with S1 and veins of serpentine associated with S2 (Fig. 3.3a, b, c). Chlorite is characterized by brown-blue-green pleochroism and brown anomalous birefringence (Fig. 3.3a). S1 is cross-cut by veins of undulating antigorite (S2) and contains small pyrite and chalcopyrite grains (both <5 μm). S2 is overprinted by large magnetite grains (Fig. 3.3d, e), where magnetite has undergone later brittle deformation and dynamic recrystallization (as evident from its bipyramidal form), and has talc rims (Fig. 3.3e). Serpentine is distinguished from chlorite by its blue anomalous birefringence, in comparison to dark brown-green pleochroism in the chlorite.

Small subhedral ilmenite grains (~10–15 μm in diameter) contain Ti-magnetite cores (1%, Fig. 3.3f). Lamellae of ilmenite in Ti-magnetite are evident in larger grains (Fig. 3.3f). Ilmenite occurs as grains that are aligned with S2 and contain small (2–5 μm) inclusions (identified using SEM) of chlorite and antigorite (Fig. 3.3f). Ilmenite grains are replaced by talc on the rim. Small pyrite and chalcopyrite grains (<5μm) are found in pits in large magnetite grains and within serpentine in the matrix (Fig. 3.3b).

3.4.1.3 Chlorite-garnet-clinopyroxene schist (VSZ-02)

The sample from Upper Valtournenche, VSZ-02, contains ~40% chlorite, 30% garnet, 25% diopside, 5% calcite, 4% titanite, 1% ilmenite and trace apatite. VSZ-02 is proximal to the Ti-clinohumite-bearing serpentinites VSZ-03 and VSZ-05 (section 4.1.4). Fine chlorite comprises the majority of the matrix, defining a planar fabric (S1, Fig. 3.3g). Chlorite also occurs as 30-200 μm inclusions in garnet aggregates and as late veins (<50 μm across), which cut the earlier chlorite fabric (S2, Fig. 3.3h). Diopside consists of porphyroclasts (>1 cm), which are replaced by chlorite along cleavage (di1, Fig. 3.3h). Diopside1 is surrounded by garnet (Fig. 3.3h) where SEM imaging revealed zoning within the garnet, consisting of Fe-poor

cores and Fe-rich rims (Fig 3.3i). A later generation of diopside (di2) also exists in association with coarse chlorite, consisting of grains up to ~1cm which replace or are associated with garnet rims (di2, Fig. 3.3j). Calcite forms patches >500 µm across, and is replaced by garnet rims. Titanite grains (<200 µm) occur within late veins of chlorite through garnet and within diopside porphyroclasts along cleavage (Fig. 3.3g, k, l). Opaque phases include ilmenite (<5 to ~50 µm) as cores to titanite within diopside porphyroclasts (Fig. 3.3k, l).

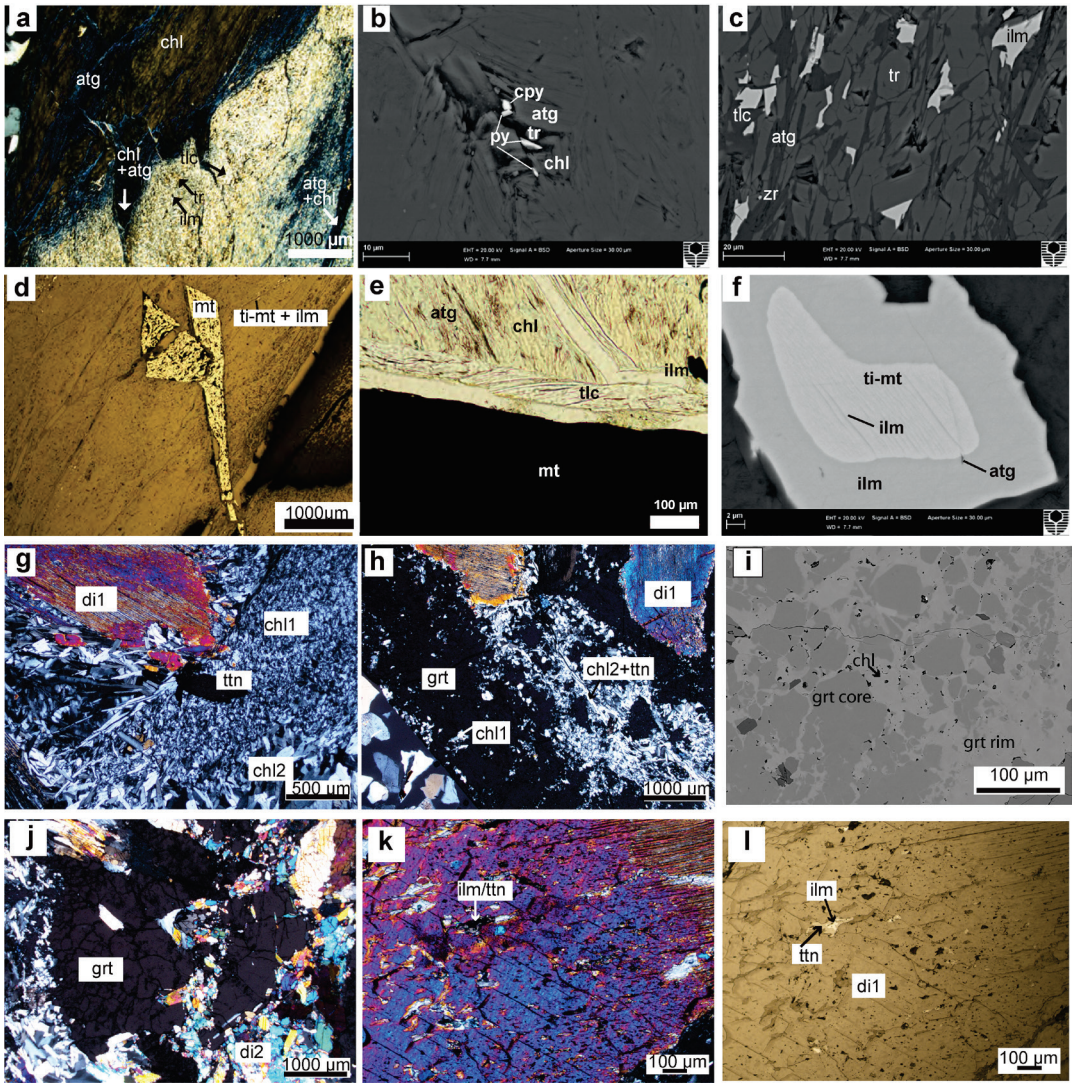

Figure 3.3: Photomicrographs of textures in PF-001 and VSZ-02. PF-001 a (xpl) atg veins overprint chl, where chl defines a planar fabric. Chl replaces tr at the rim, whereas atg replaces tr via small invasive veins. b (rfl) small py, cpy and tr grains included in atg.. c (bse) atg veins replace tr. Ilm grains are orientated along atg veins, where atg and ilm are overprinted by tlc veins. d (rfl) large late mt cut the chl-defined planar fabric and atg veins. Small ilm grains are preferentially aligned along the foliation defined by atg. e (ppl) tlc rims on large mt and tlc cross-cutting chl and atg. f (bse) ilm with a Ti-mt core. Ti-mt contains lamellae of ilmenite. The ilm rim contains inclusions of antigorite. VSZ-02 g (xpl) di1 grains with exosolution lamellae and a sheared chl1 matrix overprited by chl2 laths. h (xpl) Grt with chl1 inclusions, cross-cutting chl2 veins containing ttn. i (bse) dark Fe-poor grt cores with light Fe-rich rims, included in the rims is chl1. j (xpl) grt replaced by di2. k (xpl) ilm/ttn inclusions in di1. l (rfl) ilm cores with ttn rims included in di1. tr = tremolite, atg = antigorite,

chl = chlorite, tlc = talc, Ti-mt = titanomagnetite, ilm = ilmenite, py = pyrite, cpy = chalcopyrite, ap = apatite zr = zircon, di = diopside, ttn = titanite, grt = garnet. xpl = crossed polarised light, rfl = reflected light, bse = back scattered electron.

3.4.1.4 Ti-clinohumite-bearing serpentinites

Upper Valtournenche (VSZ-03 and VSZ-05)

The serpentinite samples from Upper Valtournenche, VSZ-03 and VSZ-05 contain ~75–80% antigorite, 7–10% diopside, 5–8% Ti-clinohumite, 3–5% olivine, 2–3% magnetite, and 1–2% sulphide (heazlewoodite and pentlandite).

Antigorite exists as coarse grained pseudomorphs after diopside and as fine interlocking grains in the matrix (atg1, Fig. 3.4a), as fine laths which replace atg1 and olivine2 (atg2, Fig. 3.4a), and as sheared veins which cut the matrix (atg2, Fig. 3.4b). Diopside is present as large grains with exsolution lamellae (di1; ~100 μm to >1 cm). Diopside1 is associated with olivine (ol1), both of which are replaced by Ti-clinohumite (Ti-chu1, Fig. 3.4b). Ti-chu1 consists of subhedral to euhedral grains typically <100 μm that are replaced by mt1 along cleavage (Fig. 3.4b, c) and atg2 (Fig. 3.4d). Small magnetite grains (mt1) are present along di1 cleavage and on Ti-chu1 rims (Fig 3.4b). Diopside is replaced by fine matrix antigorite (Fig. 3.4c). Ti-clinohumite grains up to 50 μm in diameter are within sheared veins of antigorite which replace antigorite laths (Ti-chu4, Fig. 3.4b). Olivine2 occurs as large grains that are aligned with the atg1 matrix, and are replaced by atg2 and Ti-chu4.

Magnetite (typically <10 μm to 50 μm in diameter) replaces diopside along cleavage and overprints olivine and Ti-chu1 (mt1, Fig. 3.4b, c). Magnetite also occurs as elongated grains along atg2 veins (mt3, Fig. 3.4d), and as larger grains (up to 0.5 cm) which overprint sheared atg2 veins and Ti-chu4 (mt4, Fig. 3.4d).

Sulphide phases include euhedral to subhedral heazlewoodite and pentlandite. Heazlewoodite grains occur as sheared grains with fine antigorite and diopside inclusions, replaced by atg2 (hz1). Other heazlewoodite grains replace coarse antigorite laths and are included in magnetite within sheared antigorite veins (Fig 3.4e, f, hz2). Pentlandite occurs as grains up to 200 μm that occur either as sheared grains within sheared antigorite veins (pn1) or as grains that overprint coarse antigorite laths (pn2). Trace millerite also occurs within antigorite veins.

Monte Rosso (ASZ-09)

ASZ-09 from Monte Rosso, Val d'Aosta, has larger Ti-clinohumite and magnetite grains than the Upper Valtournenche samples. The samples contain 30–40% Ti-clinohumite, 20–30% chlorite, 10–15% antigorite, 8–15% magnetite, 2–10% diopside, 2–3% titanite, 1–2% pentlandite and trace perovskite and ilmenite.

Chlorite surrounds magnetite and large grains of Ti-clinohumite (Fig. 3.4g, h). A fine grained antigorite matrix is present, which is replaced by chlorite (Fig. 3.4g). Two forms of Ti-clinohumite exist, Ti-clinohumite porphyroblasts (Ti-chu2) are associated with or replaced by a patchy chlorite matrix, where Ti-clinohumite contains inclusions of fine antigorite, olivine, euhedral magnetite (~10 μm) and pentlandite (~5 μm, Fig. 3.4i, j, k). Another form of Ti-clinohumite is comprised of sheared augens, associated with pentlandite and diopside (Ti-chu3). These sheared zones wrap around Ti-clinohumite porphyroblasts (Fig. 3.4l). Both chlorite and Ti-chu3 are cut by antigorite needles and/or veins (Fig. 3.4m). Titanite occurs as rims to ilmenite and replaces both types of Ti-clinohumite. Titanite grains contain inclusions of ilmenite up to ~50 μm and are replaced by pentlandite and magnetite (Fig. 3.4n). Large magnetite grains replace Ti-chu2 and antigorite veins cut Ti-chu2 (Fig. 3.4o).

Magnetite occurs in several textural settings. Magnetite2 (mt2) occurs as relatively small euhedral to subhedral grains typically ~30–100 μm which are associated with or replace antigorite, with rare grains up to 1cm that occur as inclusions in Ti-chu2, the larger of which are associated with or replaced by antigorite veins within fractures and has a porous texture (Fig. 3.4i, j). Magnetite also occurs as megacrysts (>0.5 cm) which, in addition to small magnetite matrix grains, are cut by or are associated with chlorite and Ti-chu3 (mt2. Fig. 3.4h). Other magnetite grains are observed as rims on Ti-chu2, overprinting fine interlocking antigorite and synchronous with antigorite veins (mt3, Fig. 3.4o).

Pentlandite occurs as grains within Ti-chu2 porphyroblasts (pn1, Fig. 3.4j, k), sheared grains (up to 1 cm), associated with diopside and Ti-chu3 (pn2), and as rims on titanite (30–50 µm, (Fig. 3.4n, pn3).

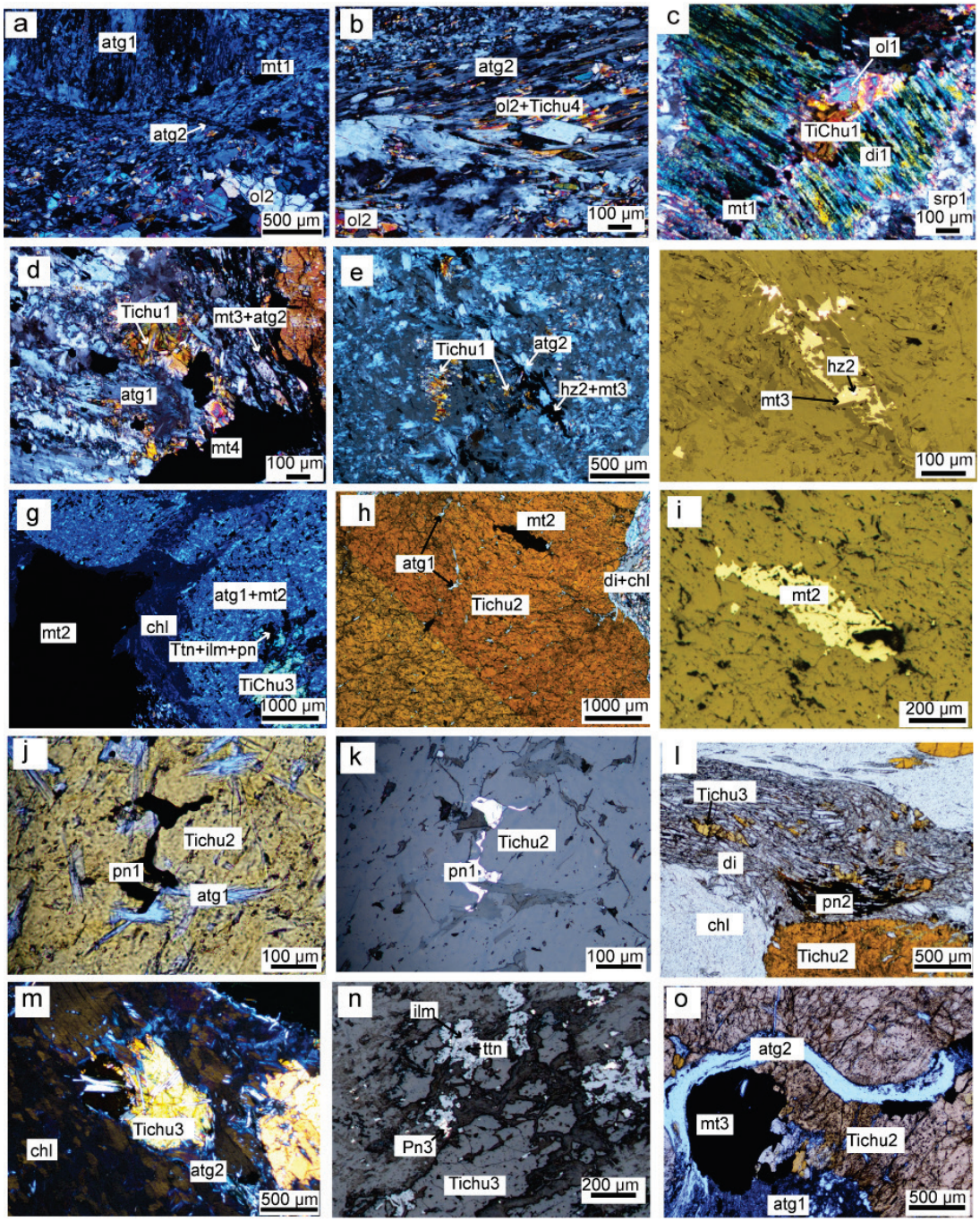

Figure 3.4: Photomicrographs of textural relationships in the Ti-clinohumite bearing samples. VSZ-03 and VSZ-05 a (xpl) atg1 and mt1 replace a pre-existing cpx phase. Ol1 is replaced by atg2 b (xpl) sheared Ti-chu4, overprinting ol2, within atg2 veins. c (xpl) ol1 and Ti-chu1 replace cpx with exsolution lamellae, both are replaced by tiny mt1 grains d (xpl) Ti-chu1 is replaced by atg2, mt3 and Ti-chu4, cross-cut the S1 fabric, and are in turn replaced by large mt4 grains. e (xpl) hz2 replacing coarse antigorite laths. f (rfl) hz2 included in mt3 within sheared antigorite veins. ASZ-09 g (xpl) chl replaces atg1 matrix and mt2. h (xpl) mt2 and atg1 inclusions within Ti-chu2. Di+chl replaces Ti-chu2 at the rim. i (rfl) mt2 with a porous texture within Ti-chu2. j (xpl) pn1 and atg1 within Ti-chu2. k (rfl) pn1 and atg1 within Ti-chu1. l (ppl) sheared pn2, di and Ti-chu3 surrounding Ti-chu1. m (xpl) Ti-chu3 replaced by atg2. n (rfl) ilm cores within ttn replacing Ti-chu3 on the rim, pn3 on ttn rims. o (xpl) mt3 and atg2 replacing atg1, Ti-chu2. ilm = ilmenite, atg = antigorite, mt =

magnetite, Ti-chu = titanoclinohumite, chl = chlorite, ttn = titanite, ol = olivine, pn = pentlandite, atg = antigorite, di = diopside, . xpl = crossed polarised light, bse = back scattered electron.

3.4.2 Whole Rock analysis

Major and trace element data for all samples are reported in Table 3.1. The loss on ignition (LOI) values reflect the degree of serpentinization; pure serpentine contains ~13 wt. % H_2O (Deer, Howie and Zussman, 1962). The LOI values are similar for all ultramafic samples at ~9–11 wt %, consistent with analyses of subducted serpentinites (Deschamps et al., 2013), which yield an average of 11.2 wt % LOI, except an anomalously low LOI value of 7.4wt % for GSZ-11.

There are two distinct groups with respect to Al content and Mg number. Most samples have an Al_2O_3 content of 1.26–3.64 wt %, however PF-001 and VSZ-02 contain 7.23 wt % and 13.3 wt % Al_2O_3 respectively. Likewise, the whole rock Mg# of PF-001 and VSZ-02 are distinct from the rest of the samples; 0.84 and 0.74, respectively compared to the Mg numbers of 0.85–0.90 for all other samples. The TiO_2 content of most samples is low at 0.01–0.09 wt % compared to 0.89 and 0.45 wt % in PF-001 and VSZ-02, respectively; with the Ti-clinohumite-bearing sample ASZ-09 as the exception with a TiO_2 concentration of 0.63 wt %. LC-015 is the most depleted in CaO, with 0.04 wt % compared to 0.67–25.1 wt % CaO in all other samples. Additionally, with the exception of PF-001 and VSZ-02, Cr and Ni contents are typical of a depleted mantle protolith with between 1978–2876 ppm Cr and 1449–2093 ppm Ni compared to 118 ppm and 155 ppm Cr, and 152 ppm and 1449 ppm Ni in PF-001 and VSZ-02, respectively.

Carbon contents of the samples range from 0.03–0.05 wt % with the exception of ASZ-09 which has no detectable carbon. Sulphur is below the detection limit in PF-001, ASZ-09, VSZ-02 and GSZ-11, whereas LC-015 has 0.04 wt % S and VSZ-03 and VSZ-05 have between 0.01 and 0.02 wt % S. Carbon and sulphur contents are consistent with the small proportions of sulphide and carbonate phases observed in thin section (see section 4.1). The total iron content, reported as ΣFe_2O_3, is higher in PF-001 and LC-015 at 11.2–11.5 wt %, compared to 6.5–9.1 wt % in all other samples, with lower contents of total iron in ASZ-09 and VSZ-02. There is a significant difference in $Fe^{3+}/\sum Fe$ ratios between the samples. PF-001 and VSZ-02 have low $Fe^{3+}/\sum Fe$ contents with $Fe^{3+}/\sum Fe$ at 0.39 and 0.43,

respectively, compared to ratios of 0.46 and 0.65 in all other samples, with the highest $Fe^{3+}/\sum Fe$ ratios recorded in LC-015 and ASZ-09.

	PF-001	LC-015	GSZ-11	VSZ-03	VSZ-05	ASZ-09	VSZ-02
wt%	UM	UM	UM	UM	UM	UM	M
SiO_2	37.4	37.7	40.8	40.6	40.4	38.8	42.3
Al_2O_3	7.23	2.03	1.26	2.14	1.29	3.64	13.3
FeO	6.19	3.62	4.05	3.91	3.38	2.52	3.33
Fe_2O_{3tot}	11.2	11.5	8.39	9.12	8.53	7.86	6.47
MgO	33.5	36.4	40.9	35.5	39.3	37.4	10.5
CaO	0.67	0.04	1.10	2.33	0.36	1.17	25.1
Na_2O	0.07	0.09	0.05	0.05	0.01	0.05	0.07
K_2O	0.00	0.01	0.00	0.00	0.00	0.00	0.00
TiO_2	0.89	0.09	0.01	0.06	0.08	0.63	0.45
MnO	0.11	0.14	0.16	0.09	0.12	0.21	0.23
P_2O5	0.02	0.00	0.00	0.00	0.01	0.08	0.02
LOI	10.3	10.7	7.36	9.78	9.16	9.56	2.15
C	0.05	0.04	0.05	0.04	0.03	0.00	0.05
S	0.00	0.04	0.00	0.01	0.02	0.00	0.00
Total	101.5	98.8	100.6	100.4	99.9	99.9	100.7
ppm							
Ba	0.9	1.9	0	1	6.7	12.4	5.7
Co	97	111	118.6	85.4	114	81.6	40
Cr	118	2734	1978	2747	2876	2079	155
Cs	0.3	0.1	0	0.2	0.2	0	0.6
Ni	1449	1929	1990	1747	2093	1498	152
V	136	63	21	74	34	53	213
Sc	13	13	0	14	0	12	48
Zn	53	55	45	49	56	91	16
Rb	0.3	0.7	0.3	0.6	0.4	0.4	0.8
Sr	2.5	2.3	1	1.9	2.1	2.6	34.1

Table 3.1: Whole rock major element (wt%) and trace element (ppm) data for all samples.

3.4.3 Microprobe data

3.4.3.1 Garnet

Garnet in VSZ-02 is zoned with Fe-poor cores (<5 wt % FeO total) and Fe-rich rims (>5 wt % FeO total). The cores and rims are comprised of ~87.5–100 mol % and 75–95 mol % ugrandite (the collective term for Ca-rich end members uvarovite, andradite, and grossular, respectively). Both the cores and the rims are poor in chromium, so ugrandite consists of grossular and andradite only. The

composition of the core and rim, respectively, is $Alm_{1.2–5.4}$ $And_{2.5–7.8}$ $Grs_{88.1–97.0}$ $Pyr_{0–1.5}$ $Sps_{0–0.4}$, and $Alm_{3.4–11.1}$ $And_{7.8–28.1}$ $Grs_{47.2–86.7}$ $Pyr_{0–19.9}$ $Sps_{0–1.48}$. The difference in TiO_2 content between the core and rim is significant at the 5% confidence level (P=0.02), with higher concentrations of TiO_2 in the core (0.5–2.0 wt %) than the rim (0.4–1.3 wt %, Appendix B2).

3.4.3.2 Ti-clinohumite

Ti-clinohumite is present in samples VSZ-03, VSZ-05 and ASZ-09. X_{Mg} (Mg/Mg+Fe) is more heterogeneous in the VSZ samples (0.88–0.93), and significantly lower than the ASZ-09 samples ($P = 6.9x10^{-11}$, students' t-test), where X_{Mg} is 0.93–0.94, reflecting higher FeO contents in the ASZ-09 samples at 5.0–7.1 wt% compared to 6.2–10.7 wt% in VSZ-03 and VSZ-05, while the MgO content is similar in both samples. In addition, the VSZ samples have significantly lower Ti ($P=2.24x10^{-6}$) at 1.9–4.3 wt% TiO_2, compared to 2.0–6.4 wt% in ASZ-09. (Fig. 3.5c; Appendix B3)

3.4.3.3 Titanite

Titanite grains in VSZ-02 are stoichiometric with a slight replacement of Ti by Al (up to 0.14 cations; Appendix B4).

3.4.3.4 Magnetite

LC-015, GSZ-11, VSZ-03 and VSZ-05 have relatively heterogeneous Fe^{2+} and Fe^{3+} contents, whereas ASZ-09 varies in Fe^{2+} content while the Fe^{3+} is homogeneous, and in PF-001 large magnetite grains are homogeneous in composition, with only minor cations other than Fe (Fig. 3.5d Appendix B5). Cr_2O_3 varies within magnetite grains from 0.5–7.7 wt % in LC-015, 0–6.5 wt % in GSZ-11 and 0.2–11.1 wt % in VSZ-03 and VSZ-05 (Fig. 3.5d, Appendix B5), with the exception of one core in LC-015 which has a much higher Cr_2O_3 content of 31.9 ± 1.3 wt % and most grains show a considerable decrease in Cr_2O_3 from core to rim. Cr_2O_3 is low in ASZ-09 grains with up to 0.5 wt %. TiO_2 decreases from core to rim in LC-015 with up to 0.8 wt % TiO_2 in the core compared to a maximum of 0.1 wt % in the rim, and TiO_2 and Cr_2O_3 are similarly low in matrix grains. Magnetite grains in GSZ-11 contain negligible Ti. In the Ti-clinohumite bearing samples, VSZ-03, VSZ-05, and ASZ-09, TiO_2 contents are 0.2–0.7 wt % in all grains (Fig. 3.5e).

Magnetite grains in LC-015 have relatively high MgO and MnO contents compared to those in GSZ-11 and PF-001 (Fig. 3.5d, Appendix B5). In addition, magnetite megacrysts and smaller grains within Ti-clinohumite in ASZ-09, and magnetite replacing diopside cleavage in VSZ-03 and VSZ-05, have higher MgO contents and MnO contents, compared to matrix magnetite in these samples (Fig. 3.5d). PF-001 has low MnO contents in all magnetite grains. Mg and Cr are somewhat correlated in LC-015 and the VSZ samples ($R^2 = 0.6$, Fig. 3.6a), though not in a statistically valid way ($P = 0.17$). In LC-015 the ratio of $Fe^{2+}/(Mg+Fe^{2+})$ of magnetite grains varies from 0.81 to 0.96, compared to 0.9 to 0.96 in VSZ samples.

Ti-magnetite grains occur as cores in ilmenite grains in sample PF-001. The Fe content is 13.8–37.3 wt % Fe_2O_3 and the Ti content is 40.5–14.4 wt % TiO_2, with TiO_2 increasing with decreasing Fe_2O_3. Some of this variation in composition may reflect the presence or absence of sub-microscopic ilmenite lamellae in the analysis volume (Fig. 3.3f). The MnO content of Ti-magnetite ranges from 0.3 to 1.1 wt %, increasing with TiO_2 but decreasing with FeO and MgO. The Cr_2O_3, Al_2O_3, NiO, Na_2O and K_2O content of Ti-magnetites in PF-001 are negligible so analyses of Ti-magnetite plot with those for magnetite on the $Fe^{3+}/(Cr^{3+}+Al^{3+}+Fe^{3+})$ vs. $Fe^{2+}/(Mg+Fe^{2+})$ diagram (Fig. 3.5d, Appendix B5).

3.4.3.5 Ilmenite

Ilmenite is present in LC-015, PF-001, VSZ-02 and ASZ-09, however the small size of grains precluded analysis of most grains in ASZ-09 and VSZ-02, with the exception of two grains reported for ASZ-09. Ilmenite compositions vary significantly between the LC-015 and PF-001 but not between LC-015 and ASZ-09 (Fig. 3.5f; Appendix B5). The Ti content of ilmenite is lower in PF-001 than LC-015 and ASZ-09 with 49.8–51.8 wt % TiO_2 in PF-001, compared to 53.3–55.4 wt % TiO_2 in LC-015 and ASZ-09 (Fig. 3.5f–g). PF-001 ilmenites have considerably higher FeO at 45.4–47.9 wt % (Fig. 3.5f) with minor MnO (1.12–2.51 wt %) and MgO (0.25–1.02 wt %) suggestive of only minor Mn^{2+} and Mg^{2+} replacement (Fig. 3.5g). In contrast, the lower FeO content of LC-015 and ASZ-09 ilmenites at 20.4–27.6 wt % (Fig. 3.5f) reflects replacement of Fe^{2+} by Mg^{2+} at 4.2–7.5 wt % MgO and, more significantly, Mn^{2+} at 13.6–20.4 wt % MnO (Fig. 3.5f). The Al_2O_3 content of the ilmenites is below detection limit in most analyses. There

is a small but detectable amount of V in PF-001 and LC-015, with up to ~0.4±0.02 wt % V_2O_3 in ilmenites in LC-015 (Appendix B6).

3.4.3.6 Sulphides

Sulphides include heazlewoodite in VSZ-03 and GSZ-11, pentlandite in VSZ-05 and ASZ-09, millerite in VSZ-05 and GSZ-11, and small pyrites in LC-015 and PF-001. The formula of heazlewoodite is $Ni_{2.8–3.0}Fe_{0.04–0.16}S_{1.9–2.1}$ in GSZ-11, $Ni_{2.8–2.9}Fe_{0–0.16}S_{2–2.1}$ in VSZ-03 and $Ni_{2.8–2.9}Fe_{0–0.03}S_{2–2.1}$ in VSZ-05, with a small amount of iron (0.02–0.16 cations per formula unit) substituting for Ni. The formula of pentlandite is $Fe_{3.9–4.1}Ni_{4.5–4.7}Co_{0.2–0.3}S_{8.0–8.2}$ in ASZ-09 and $Fe_{3.9–4.1}Ni_{3.9–4.1}Co_{0.7–0.9}S_{8.1–8.2}$ in VSZ-05, with notably higher Co and lower Ni in VSZ-05 compared to ASZ-09. Millerite formulae are $Ni_{0.97–1.03}Fe_{0.02–0.04}S_{0.94–1.00}$ in GSZ-11 and $Ni_{0.93–0.97}Fe_{0.01}S_{1.02–1.06}$ in VSZ-05. Pyrite grains were too small for EPMA analysis (Fig. 3.5h, S5, S11).

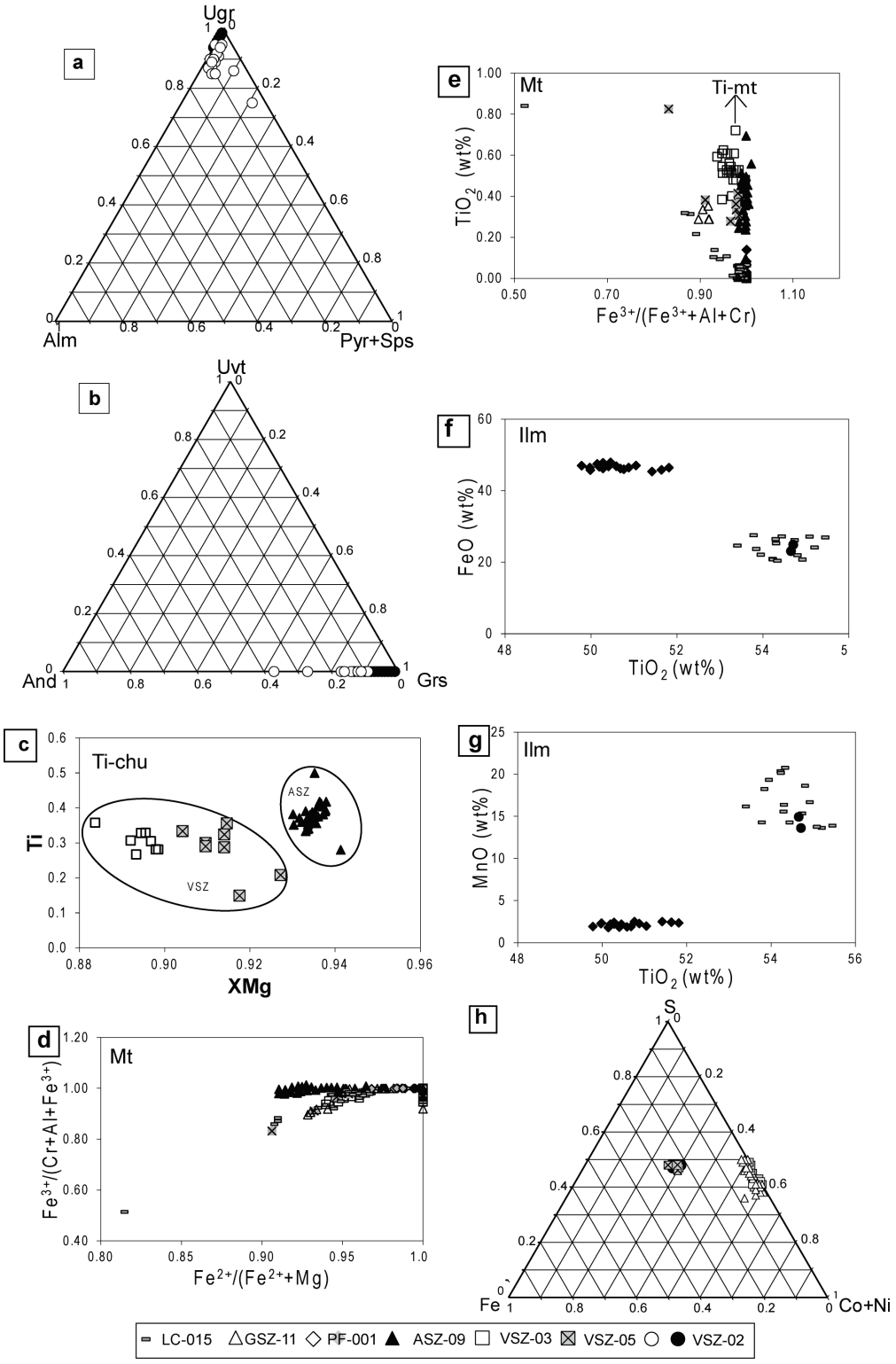

Figure 3.5: Mineral plots. Symbols represent different samples (see legend). (a) Ternary diagram for garnet (almandine, ugrandite, pyrope+spessartine). (b) Ternary diagram with ugrandite end members (grossular, uvarovite and andradite). (c) XMg vs Ti in Ti-chu grains. (d) $Fe^{2+}/Fe+Mg$ vs. $Fe^{3+}/(Cr+Al+Fe^{3+})$ for spinel-group minerals. (e) $Fe^{3+}/(Cr+Al+Fe^{3+})$ vs. TiO_2 (Ti-magnetite not shown) for spinel-group minerals. (f) FeO vs TiO_2 and (g) MnO vs. TiO_2 for ilmenites in LC015, PF001 and ASZ-09. (h) Ternary diagram with sulphide compositions.

3.5 Discussion

3.5.1 Mineral parageneses

The interpreted mineral parageneses are shown in Fig. 3.6. Silicate mineral textures within the samples have been linked to geodynamic events on the basis of well-constrained P-T conditions for silicate minerals from previous studies within the Zermatt-Saas region. The relation of silicate minerals to opaque mineral phases within the samples has been used to constrain the stages of metamorphism at which the opaque minerals grew and hence the distribution of Fe and Ti at each stage of metamorphism (Fig. 3.7). Minerals attributed to early exhumation grew under blueschist to eclogite facies conditions and record high-pressure fluid infiltration, whereas late exhumation refers to assemblages that record decompression.

3.5.1.1 Antigorite serpentinites (LC-015 and GSZ-11)

Chromite cores observed within large spinel grains in LC-015, isolated from the matrix, preserve the earliest textural records. The chromite cores were most likely derived from primary mantle chromite, which were subsequently altered to Cr-poor compositions during initial serpentinization, as has been observed previously in Zermatt-Saas serpentinites (Li et al., 2004).

Seafloor alteration is likely recorded by the presence of Cu-Zn alloys included within atg1 matrix, attributed to desulphurization of primary sulphides under reducing conditions during ocean-floor serpentinization (e.g., Schwarzenbach et al., 2014), although lizardite and chrysotile that are normally associated with this metamorphic stage are not present, suggesting that these phases were recrystallized to antigorite (atg1) during dehydration reactions related to prograde metamorphism.

Atg1 is texturally similar to the interlocking antigorite described by Li et al., (2004) in other Zermatt-Saas serpentinites and contains inclusions of diopside. The lack of exsolution lamellae and small, euhedral grain size of diopside grains in addition to their low Cr and Al contents in both LC-015 and GSZ-11 are characteristic of diopside reported to be related to subduction metamorphism (Li et al., 2004) so this origin is preferred. Thus, atg1 is also interpreted to have maintained stability throughout subduction. Olivine, diopside and magnetite grains

are aligned with the S1 fabric in GSZ-11, suggesting these minerals grew synchronously during prograde metamorphism. Additionally, ilmenite is replaced by coarse laths of antigorite but contains inclusions of fine antigorite, implying stability prior to or at the onset of exhumation.

On the basis of thermodynamic modelling of ultramafic rocks, talc stability is pressure restricted (Evans and Powell, 2015); therefore, magnetite with talc rims in LC-015 grew under high-pressure conditions. Talc is not present in GSZ-11, reflecting lower Si/Fe+Mg ratios than LC-015. Atg2 grains in both LC-015 and GSZ-11 define the S2 foliation, where its texture is similar to the later interpenetrating texture associated with recrystallization described in Li et al., (2004). Atg2 grains replace or are associated with magnetite; hence, atg2 growth occurred at the same time as magnetite under high pressure conditions, prior to the advanced stages of exhumation.

3.5.1.2 Chlorite-rich ultramafic rock (PF-001)

Ti-magnetite growth pre-dates ilmenite because it is preserved as cores within ilmenite, isolated from the matrix. Antigorite inclusions are observed close to the Ti-magnetite core within the ilmenite rim; therefore Ti-magnetite growth is inferred to have occurred within the antigorite stability field. Ti-magnetite is aligned with the planar fabric defined by chlorite associated with S1 foliation. Chlorite is less hydrous than antigorite, and thus the replacement of antigorite by chlorite during dehydration of antigorite is attributed to an increase in temperature (e.g., Padrón-Navarta et al., 2013; Scambelluri et al., 2014; Evans and Powell, 2015). Ti-magnetite therefore existed in both the antigorite and chlorite stability fields and hence may record the transition of antigorite to chlorite as a result of dehydration of antigorite during prograde to peak metamorphism. Olivine is also expected as a prograde product of antigorite dehydration, Ilmenite in PF-001 is suggested to have formed by local alteration and breakdown of the Ti-magnetite during or shortly after peak metamorphism, as the presence of exsolution lamellae records a transition to lower temperature.

Antigorite veins cross-cut the chlorite-defined S1 foliation and are inferred to reflect a transition towards lower pressure and rehydration of the sample. It is also possible that antigorite and chlorite co-existed for some time, as evident from

the elevated Al_2O_3 content of serpentine (Appendix B8) and the intermediate compositions between penninite and antigorite (Appendix B9). The growth of magnetite after chlorite and antigorite is attributed to initial retrogression in PF-001. Talc occurs as rims on large magnetites (Fig. 3.3e) and ilmenite grains in PF-001. Talc rims are consistent with the growth of talc during decompression below ~1.5 GPa (Evans and Powell, 2015). Hence talc is attributed to exhumation and constrains magnetite and ilmenite to pressures greater than ~1 GPa.

3.5.1.3 Chlorite-clinopyroxene-garnet schist (VSZ-02)

The mineralogy and bulk composition (enrichment in SiO_2 and CaO) of VSZ-02 is consistent with those previously described as 'rodingites' in the Zermatt-Saas Zone (e.g., Panseri et al., 2008; Li et al., 2008), consistent with the proximity of VSZ-02 to serpentinite samples VSZ-03 and VSZ-05. Rodingitization of mafic rocks in contact with peridotite was considered to have occurred during seafloor alteration, and the extent of modification during high-pressure metamorphism is debated (Panseri et al., 2008; Li et al., 2008).

Large porphyroclasts of diopside are considered to be remnants of mantle clinopyroxene, with high Al contents and an exsolution texture. Previous studies have attributed hydrogrossular garnet to seafloor alteration in rodingites (e.g., Panseri et al., 2008). The aggregate and Fe-poor nature of garnet cores (with a lesser andradite component) surrounding diopside could be consistent with this stage (Fig. 3.3f). However, garnet cores of a similar texture and composition have also been attributed to conditions up to eclogite facies (Herwartz et al., 2011), therefore garnet cores are constrained to growth prior to peak HP-LT metamorphism.

Fine-grained chlorite is attributed to prograde to peak metamorphism because chlorite defines a high-pressure S1 planar fabric (Fig. 3.3g). A transition to a more andradite-rich composition is recorded in garnet rims, within which are chlorite grains so the Fe-rich composition of the garnet likely records the transition to peak metamorphic conditions. Ilmenite grains within clinopyroxene are associated with fine chlorite and grow along cleavage, and therefore are attributed to the same stage. Large laths and late veins of chlorite, titanite and di2 together define the S2 fabric, which overprint or are synchronous with Fe-rich garnet rims

and therefore mark retrogression. This observation further constrains the Fe-rich garnet to peak conditions.

3.5.1.4 Ti-clinohumite-bearing serpentinite

Upper Valtournenche (VSZ-03 and VSZ-05)

Large diopside grains are partially or completely replaced by antigorite, therefore diopside records early growth prior to prograde metamorphism, consistent with high Al contents, exsolution lamellae and the relatively large grain size. Mt1 replacement of diopside along cleavage, in addition to olivine (e.g., Bach et al., 2004), and associated Ti-clinohumite (Ti-chu1), is either attributed to seafloor alteration as a product of initial serpentinization, or early subduction. Prograde to peak phases include atg1, ol2 and hz1. Olivine2 is associated with atg1 and replaced by laths of late antigorite (atg2) (Fig. 3.4a and b). Hz1 grains are sheared and contain inclusions of atg1, but replaced by atg2, and therefore grew prior to exhumation. Phases related to early exhumation include atg2, mt3 hz2, pn2 and Ti-chu4. Hz2 and pn2 are attributed to this stage because they replace coarse antigorite laths. Ti-chu4 is comprised of augens that overprint ol2 within sheared atg2 veins through the atg1 matrix (Fig. 3.4b). Hz2, mt3 and pn2 are observed within atg2 veins. Mt4 cross cuts the sheared veins and is therefore assigned to more advanced stages of retrogression.

Monte Rosso (ASZ-09)

Primary mantle phases or those that grew during seafloor alteration have not been preserved in ASZ-09. Prograde phases include antigorite, Ti-chu2, pn1 and magnetite2. The inclusion of high-pressure antigorite within Ti-chu2 porphyroblasts suggests that Ti-chu1 grew within the antigorite stability field. The replacement of Ti-chu2 by fine chlorite (where chlorite records peak conditions) and retrogressive late laths and/or needles of antigorite, further constrains the growth of Ti-chu1 to prograde to peak conditions, in contrast to similar textures of Ti-clinohumite that have been previously ascribed to mantle crystallization (Fontana et al., 2008; Rebay et al., 2012). Additionally, because mt2 is preserved within Ti-chu2, found as small grains within the fine antigorite matrix, and associated with or replaces atg1 within Ti-chu2, this generation of magnetite is constrained to high-pressure. The porous nature of the magnetite is indicative of interaction with fluid, possibly from local dehydration of antigorite during prograde

metamorphism. Large magnetite megacrysts are attributed to the same stage of growth as Ti-chu2 or earlier as chlorite occurs as rims to mt2.

The sheared Ti-clinohumite associated with pn2, chlorite and diopside (Ti-chu3) is assigned to high-pressure conditions towards the transition to peak metamorphism because these phases are cut by late antigorite veins. The diopside is Cr and Al-poor and lacks exsolution lamellae, and is therefore inconsistent with diopside stable in the mantle and/or on the seafloor. Titanite, pn3 and ilmenite rims on Ti-chu3 and atg2 are associated with early retrogression. Ilmenite and pn3 replace titanite. The replacement of atg1, Ti-Chu2 by magnetite3 and veins of atg2, infers magnetite growth post-dated peak metamorphism.

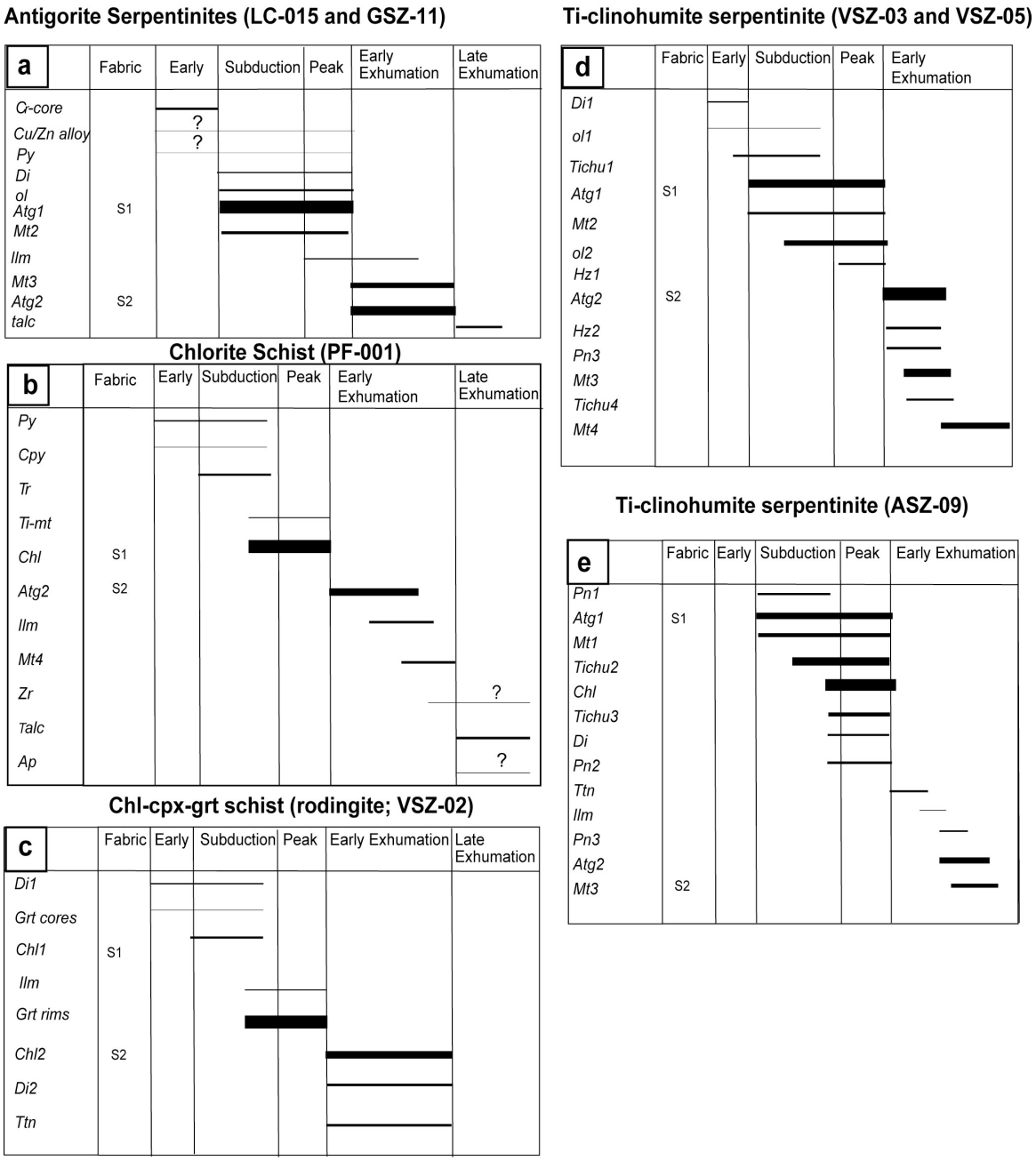

Figure 3.6: Mineral paragenesis diagrams for all samples. The thickness of the lines represents modal abundance.

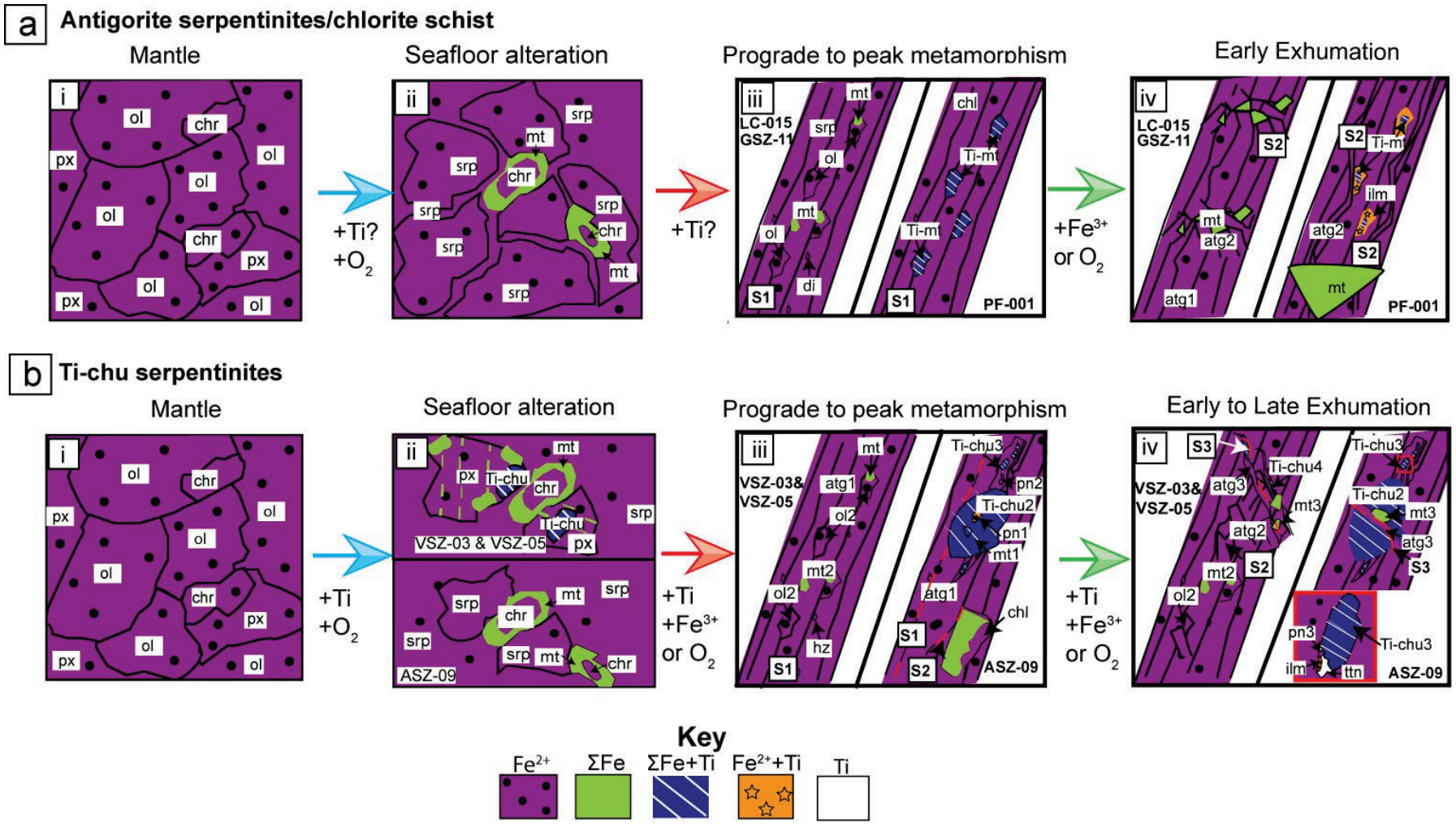
a
Antigorite serpentinites/chlorite schist
Mantle
Seafloor alteration
Prograde to peak metamorphism
Early Exhumation
i
ol
chr
px
ii
srp
mt
chr
+Ti?
+O2
iii
LC-015
GSZ-11
S1
di
Ti-mt
chl
PF-001
+Fe3+
or O2
iv
S2
ilm
atg2
atg1
b
Ti-chu serpentinites
Early to Late Exhumation
VSZ-03 & VSZ-05
ASZ-09
VSZ-03&
VSZ-05
Ti-chu
Ti-chu2
Ti-chu3
Ti-chu4
pn1
pn2
pn3
mt1
mt2
mt3
ol2
atg3
hz
ttn
S3
+Ti
+Fe3+
or O2
Key
Fe2+
ΣFe
ΣFe+Ti
Fe2++Ti
Ti

Figure 3.7: Summary schematic diagram illustrating the distribution of Fe and Ti in the studied ultramafic rocks. (a) Antigorite serpentinites & chlorite schist (LC-015, GSZ-11 and PF-001). (i) Fe^{2+} is the dominant phase assumed in mantle precursors, comprised of the major phases olivine, pyroxene and chromite. (ii) An increase in the modal abundance of magnetite results from oxidation of pre-existing Fe^{2+} during serpentinization on the seafloor. The addition of Ti possibly occurred during this stage in PF-001. (iii) During prograde to peak metamorphism a decrease in $Fe^{3+}/\sum Fe$ results in lower magnetite modes than seafloor precursors (atg serpentinites). Ti addition prior to peak metamorphism results in the growth of Ti-magnetite (PF-001). (iv) The onset of exhumation is associated with an increase in the modal abundance of magnetite and an increase in Ti-rich phases with the addition of Fe^{3+} or oxidation of Fe^{2+} and Ti addition. (b) Ti-clinohumite serpentinites (VSZ-03, VSZ-05 and ASZ-09). (i) Description as for (a). (ii) Oxidation of pre-existing Fe^{2+} and the addition of Ti during serpentinization results in the growth of magnetite1 and Ti-clinohumite1, respectively. (iii) Prograde to peak phases Ti-chu2, Ti-chu3, and magnetite2 are attributed to an increase in Fe^{3+} and Ti or oxidation of pre-cursor Fe^{2+}. (iv) Exhumation is marked by the mobilization/addition of Fe^{3+} in VSZ-02 and VSZ-05, and/or oxidation of Fe^{2+} and an increase in Ti-rich phases; Tichu4 is associated with atg3 veins, Tichu3 is replaced by Ti-rich phases (ilmenite and titanite) and mt3 overprints or is synchronous with atg2. Here, $\sum Fe = Fe^{2+}+Fe^{3+}$.

3.5.2 Comparison of bulk compositions to mantle protoliths

It has been proposed that the northern part of the Western Alps was once an ocean-continent transition (OCT) setting, where ultramafic rocks of the SCLM were juxtaposed with continental rocks during Jurassic rifting (e.g., Beltrando et al., 2010; Beltrando et al., 2014). In this case, ultramafic rocks may have undergone alteration in the SCLM prior to subduction. This hypothesis is tested by comparing the compositions of all ultramafic samples with other proposed OCT mantle samples.

In the Eastern Central Alps, the Lower and Upper Platta samples are proposed to have a distal and proximal OCT origin, and the Malenco peridotite is thought to represent pre-rift SCLM (Müntener et al., 2010). The Platta and Malenco samples are both characterized by trace element enrichment, including Ti (Müntener et al., 2010), consistent with relatively fertile mantle protolith compositions (Deschamps et al., 2013). Samples LC-015, GSZ-11, VSZ-03, VSZ-05 and ASZ09 are similar in composition to the Malenco peridotite with Mg-numbers of 0.87–0.9 and 1.26–3.64 wt % Al_2O_3, compared to 0.9–0.91 and 1.09–3.14 wt % Al_2O_3, in the Malenco peridotite (Fig. 3.8a, b), although these samples have lower Mg numbers relative to the Malenco peridotite. Thus it is proposed that the mantle protolith of these samples could reflect SCLM; however PF-001 is compositionally distinct, and ASZ-09 has a higher Ti content than SCLM.

VSZ-02 is enriched in CaO, Al_2O_3 and TiO_2 relative to anymantle-derived protolith with contents of 25.1, 13.3 and 0.45 wt %, respectively. The major element composition of VSZ-02 is similar to that reported for rodingites in the Zermatt-Saas

Zone (e.g., Li et al., 2008), so this process provides a plausible explanation for the formation of the protolith to VSZ-02.

PF-001 contains Ti and Al at 0.9 wt % and 7.2 wt % respectively, and ASZ-09 contains 0.6 wt % TiO_2. These samples are enriched in Ti, and PF-001 is enriched in Al, relative to typical depleted mantle which contains ~0.08 wt % TiO_2 and ~4.3 wt % Al_2O_3 (Salters and Stracke, 2004), to fertile primitive mantle, for which a maximum of ~0.2 wt % TiO_2 and ~4.4 wt % Al_2O_3 has been estimated (McDonough and Sun, 1995), and relative to Alpine SCLM (Fig. 3.8a). Further, PF-001 has a lower Mg number (0.84) than primitive mantle (Mg number ~0.9, Pearson et al., 2004) and depleted mantle (Mg number ~0.89, Salters and Stracke, 2004, Fig. 3.8b).

The atypical nature of these samples could result from an anomalous protolith composition, infiltration of a silicate melt or assimilation of elements from the neighboring Allalin gabbros (e.g., Bucher and Grapes, 2009).

3.5.3 The origin of Ti enrichment

The low MgO and high Ti and Al contents in PF-001 could be related to the proximity of the Allalin gabbro (e.g., Bucher and Grapes, 2009) or the infiltration of silicate melts prior to mantle exhumation on the seafloor. Müntener et al. (2010) attributed the high Al_2O_3 content in the Lower Platta peridotite to refertilization by a basaltic melt at shallow levels prior to exhumation on the seafloor on the basis of light rare earth element/heavy rare earth element (LREE/HREE) ratios, Sr, Eu and Nd anomalies, and systematic positive U anomalies, compared to Th. However, PF-001 has higher Al_2O_3 and TiO_2 contents, and ASZ-09 has higher TiO_2 than the Lower Platta samples, so a silicate melt infiltration origin for the major element trends is dismissed.

Alternatively, the Allalin gabbro could have affected adjacent mantle lithosphere via physical or chemical mixing processes. In the case of physical mixing, all elements would lie in similar positions on mixing lines between the two end-members, whereas chemical mixing would produce preferential transfer of some elements between lithologies and result in inconsistent apparent proportions of end-members. Scambelluri and Rampone (1999) proposed that mixing between Voltri Massif ultramafic rocks and gabbros enriched in Fe and Ti in the presence of fluids derived from serpentinites could account for the Ti-clinohumite veins hosted

in the serpentinites. Mixing of ultramafic and gabbro rocks was proposed to have occurred prior to subduction, with limited element mobility during high-pressure metamorphism.

In order to investigate if PF-001 is the product of mixing between the mantle protolith and Allalin gabbro, a mixing line between the Allalin gabbro and Zermatt-Saas serpentinites was calculated (Fig. 3.8c, d). The rodingite sample VSZ-02 and Voltri Massif serpentinites from the Voltri Massif (proximal to rodingites, Scambelluri and Rampone, 1999) are also included in the mixing model for comparison. The Allalin gabbro has a variable Al content (15.4–20.2 wt % Al_2O_3) and Ti content (0.13–2.15 wt % TiO_2) (Bucher and Grapes, 2009). The Al content of VSZ-02 is similar to the Allalin gabbro, consistent with the alteration of a gabbro pre-cursor. The Al content of PF-001 lies on a mixing line between the Allalin gabbro and depleted mantle end members ($R^2 = 0.91$, Fig. 3.8c), and is higher than the Voltri Massif serpentinite wall-rock samples on rodingites (Scambelluri & Rampone, 1999). Therefore, the elevated Al content of the sample could be explained by physical mixing of the protolith to PF-001 with the gabbro.

In contrast to the results for Al, the Ti content of PF-001 does not lie in the area of plausible mixing compositions between gabbro and depleted mantle and/or other Zermatt-Saas samples (Li et al., 2004) (Fig. 3.8d). The Ti content of PF-001 is elevated above the expected values by a minimum of 0.5 wt % or a factor of 2, and a maximum of 0.7 wt % TiO_2 or a factor of 4.5, as estimated from the maximum and minimum Ti content of the gabbro, respectively, which suggests that physical mixing alone cannot explain the Ti and Al enrichments simultaneously. Other altered rocks, such as the serpentinized rodingites of Scambelluri and Rampone (2009), and sample VSZ-02, do lie within this region, so, clearly, exceptional levels of alteration, or some other process, is required to explain the data.

If the assumptions that Ti was not added by melt infiltration, and that the stability of Ti-magnetite, is associated with prograde metamorphism in the antigorite and chlorite stability fields are correct, then addition of Ti must have occurred during seafloor or subduction processes.

A possible mechanism for hybridization and Ti enrichment is fluid facilitated mixing, as discussed in section 5.4.

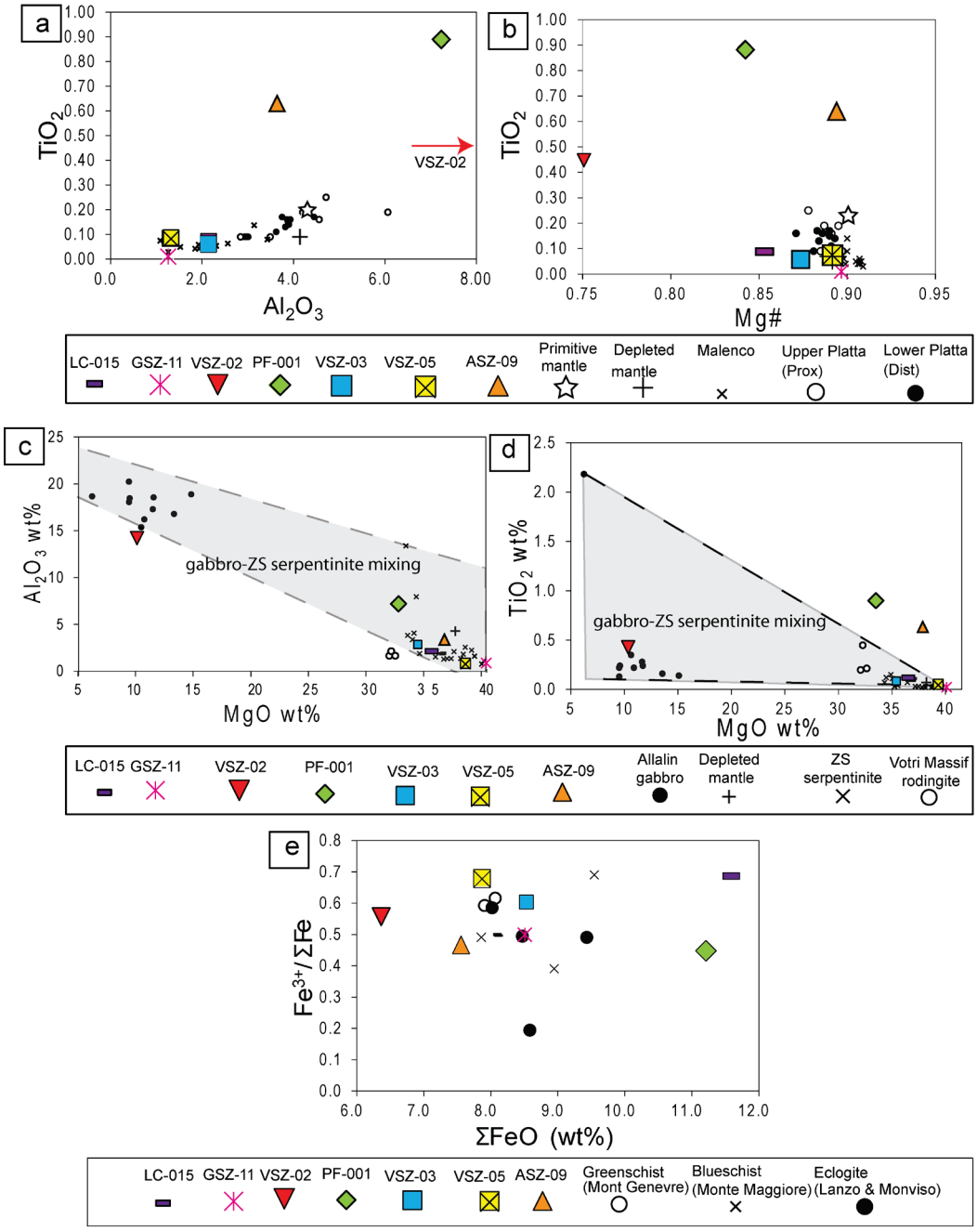

Figure 3.8: Bulk TiO_2 vs. Al_2O_3, (b) TiO_2 vs. Mg#, of the studied samples, Lower Platta and Upper Platta (Müntener et al., 2009) which reflect a distal and proximal OCT setting, respectively, Malenco peridotite samples (Müntener et al., 2009), primitive mantle (McDonough and Sun, 1995; Pearson et al., 2004), and depleted mantle (Salters and Stracke, 2004), (c) Al_2O_3 vs. TiO_2 (d) MgO vs. Al_2O_3 of depleted mantle, Zermatt-Saas serpentinites (Li et al., 2004), Allalin gabbro samples (Bucher and Grapes, 2009), Voltri massif rodingite (Scambelluri and Rampone, 1999), and the studied samples. The shaded area indicates hypothetical compositions that could result from gabbro-depleted mantle/serpentinite mixing, (e) Bulk composition ∑FeO vs $Fe^{3+}/\sum Fe$ data from this study plotted with Western Alps serpentinite data from Debret et al. (2014).

3.5.4 Ti redistribution on a mineral scale by fluid facilitated mixing

Sources of Ti in ultramafic rocks include the breakdown of Ti-bearing primary minerals such as Ti-augite (e.g., Trommsdorff and Evans, 1980), and/or

fluid facilitated transport of Ti either during seafloor alteration or prograde metamorphism. Fluid facilitated addition of Ti could provide sufficient Ti for the formation of Ti-clinohumite within veins as observed in this study and others (Rebay et al., 2012; Groppo and Compagnoni, 2007; Scambelluri & Rampone, 1999; Ferrando et al., 2010). Previous authors attributed such textures to ocean-floor metamorphism or, alternatively, high-pressure, low-temperature conditions. In addition, the presence of Ti-andradite in ultramafic rocks from Val Malenco has been suggested to reflect substantial Ti mobility at upper amphibolite conditions (Müntener and Hermann, 1994). The origin of fluids that could have infiltrated the rock during prograde metamorphism is not known, although fluids are likely to be locally derived (e.g., Scambelluri and Phillippot, 2001), and possibly produced during the dehydration of antigorite to chlorite. It is also possible that large volumes of fluids could be channeled along conduits over a scale of several kilometers over short time periods in 'pulses' (John et al., 2012).

In this study, Ti-bearing minerals are considered to postdate mantle phases (Fig. 3.7ai, bi), and are present at all stages of the subduction cycle (Fig. 3.7). In the antigorite serpentinite/chlorite schist samples this includes titanomagnetite growth before peak metamorphism (Fig. 3.7aiii) and the growth of ilmenite during peak metamorphism to early exhumation. Ti-clinohumite-bearing samples host Ti in early to prograde Ti-clinohumite that replace primary diopside (Fig. 3.7bii), large Ti-clinohumite porphyroblasts that grew during prograde metamorphism, (Fig. 3.7biii), sheared Ti-clinohumite4 within antigorite veins, and ilmenite and titanite rims on Ti-clinohumite3 associated with the onset of exhumation (Fig. 3.7biv). In the rodingite sample, the late growth of titanite along chlorite veins is associated with late exhumation.

Large Ti-clinohumite porphyroclasts without evidence of precursor Ti-rich minerals (Fig. 3.7biii) could provide evidence for Ti addition during subduction within the antigorite stability field. Additionally, the presence of Ti-rich minerals i.e. ilmenite and titanite, that replace minerals with a lower Ti content e.g., Ti-magnetite and Ti-clinohumite (Fig. 3.7aiv, 7biv), could be consistent with Ti addition during the growth of these minerals at least on a local (mm to cm) scale during initial retrogression.

Ti is not normally considered to be mobile in aqueous fluids. For example, on the basis of three measurements of Zermatt-Saas serpentinite samples, a recent study using stable Ti isotopes found that δ^{49}Ti signatures in the serpentinites were similar to MORB, despite extensive dehydration, so it was concluded that Ti was not mobilized (Millet et al., 2016). However, the isotope fractionation effects are not known and complexing of Ti with ligands such as F^-, Cl^-, PO_4^{3-}, CO_3^{2-} and OH^- (Müntener and Hermann, 1994) or aluminosilicate complexes (Tropper and Manning, 2005) can facilitate Ti mobility, as can increased pressure (Müntener and Hermann, 1994). Evidence for such complexing in the samples includes the presence of apatite in PF-001, which raises the possibility of Ti transport facilitated by PO_4^{3-} bearing fluids. However, such a mechanism is not consistent with Ti addition prior to peak metamorphism because apatite grew relatively late and contains magnetite inclusions. Aluminosilicate complexing of Ti, as suggested by Tropper and Manning (2005), could be a more plausible transport vector as evident from the high Al content of PF-001. Another possibility is that H_2S, HS^- and S^{2-} could act as transport vectors for titanium (Agapova, et al., 1989; Gieré, 1993). In ASZ-09, the presence of pentlandite on the rim of a titanite grain with ilmenite cores, where titanite has replaced ilmenite rims on Ti-clinohumite, suggests sulphides could be associated with the addition of Ti (and Fe, see section 5.5) at least on a mm-scale.

3.5.5 Fe redistribution

Iron is usually perceived to be immobile in subduction zone environments because fluids are considered to be of low salinity (Manning, 2004; El Korh et al., 2017). However, if Ti, also usually considered to have limited mobility, is in fact mobile, as discussed above, then transport of other 'immobile' elements such as Fe^{3+} may also be possible. Bulk rock Fe varies considerably within the sample set. Bulk $\sum Fe_2O_3$ values are high in PF-001 and LC-015 with 11.2 and 11.5 wt % $\sum Fe_2O_3$, respectively compared to $\sum Fe_2O_3$ determined from other Western Alps localities (this study; Debret et al., 2014; Fig. 3.8e). Silicate-rich aqueous fluids may have the ability to transport Fe^{3+} under prograde conditions (Ferrando et al., 2005). However, recent experimental work suggests this is not the case (Spandler et al., 2014). Furthermore, Debret et al. (2014) interpreted the lack of trends in $\sum Fe_2O_3$ to indicate that Fe mobility is limited during subduction and subsequent

exhumation, in agreement with the conclusions of Frost et al. (2013). The balance of evidence, therefore, suggests limited evidence for large scale Fe mobility.

Changes in $Fe^{3+}/\sum Fe$ with increasing metamorphic grade are more widely reported. A decrease in $Fe^{3+}/\sum Fe$ with increasing metamorphic grade has been associated with a decrease in the mode of magnetite in a suite of Alpine samples (Debret et al., 2014). These observations are consistent with mineral textures in other Zermatt-Saas samples (Li et al., 2004) and the low mode of magnetite associated with prograde metamorphism in the studied samples presented here.

A number of lines of evidence point to changes in the distribution of ferric iron within the samples during subduction zone metamorphism. Post peak magnetite growth was observed in all ultramafic samples, which may be associated with oxidation of pre-existing Fe^{2+} (Fig. 3.6a, b, d and e; Fig. 3.7aiv and biv). The decreased FeO content of tremolite grains in PF-001 in the vicinity of late magnetite provides support for the notion of localized transfer and oxidation of Fe^{2+} during the onset of exhumation (section 5.1.2). The growth of late magnetite along atg2 veins imply Fe^{3+} redistribution during initial exhumation (Fig 3.7biv). Additionally, the increase in Fe^{3+} from garnet cores to rims in the rodingite sample VSZ-02 during prograde to peak metamorphism records oxidation of Fe^{2+} (Fig 3.5b). A possible electron acceptor exists within the rocks. Lizardite has been shown to have higher $Fe^{3+}/\sum Fe$ ratios than antigorite (Evans et al., 2012). Thus, the electron acceptor needed to aid the transition from Fe^{2+} in silicates to the Fe^{3+} required for magnetite growth may become available when lizardite converts to antigorite. However, preliminary mass balance calculations suggest that the ferric iron budget of lizardite is insufficient to cause the observed changes (Appendix B14).

In this study, the two samples with elevated $\sum Fe_2O_3$ exhibit vastly different $Fe^{3+}/\sum Fe$ ratios of 0.69 for LC-015 and 0.45 for PF-001 (Fig 7.8e). PF-001, with a higher modal abundance of pure magnetite, might be expected to contain a higher proportion of total Fe^{3+} than LC-015. However, the mode of antigorite in LC-015 is greater than in PF-001, and this phase may host a significant proportion of Fe^{3+} (e.g., Evans and Powell, 2015). Interaction with other lithologies may alter the redox state and/or concentration of iron. For instance, VSZ-02, a rodingite, has elevated iron relative to those of a protolith gabbro (e.g., Bucher and Grapes, 2009), and has a Fe^{3+} concentration similar to that of adjacent serpentinites. Given these

factors it is clear that $Fe^{3+}/\sum Fe$ changes with metamorphic grade are complex, and factors such as protolith and interactions with surrounding lithologies must be taken into account if redox transfer processes are to be understood and predicted.

If the electron acceptor provided by the lizardite/antigorite transition is insufficient, as our calculations suggest, then externally derived fluids may have provided a suitable electron acceptor. Fluids responsible for retrogression at high pressure may have been derived from reactions associated with antigorite dehydration during prograde metamorphism deeper in the subducted stack or from other lithologies. For example, the increase in Fe^{3+} from cores to rims of garnets in the rodingite sample VSZ-02 during prograde to peak metamorphism records the transfer and oxidation of Fe^{2+}, which could suggest some influence from the adjacent serpentinite. The production of oxidized fluids from antigorite dehydration is consistent with the decreasing redox budget (the capacity of a rock to oxidize; Evans 2006) of ultramafic rocks with increasing depth in the subduction zone, as observed by Debret et al. (2014), with implications for the redox budget of the deep mantle.

Fluids infiltrating rocks in subduction zones could oxidize iron by provision of electron-accepting species such as SO_2, $SO4^{2-}$, H_2O or CO_2. This process would increase the mode of Fe^{3+}-bearing phases during the earliest stages of exhumation. The possibility that SO_2 or $SO4^{2-}$-bearing fluids are present in subduction zones and that such fluids could increase the redox budget of the sub-arc mantle has been discussed by other workers (Tomkins and Evans, 2015; Mungall, 2002; Evans et al., 2017; Canil and Fellows, 2017). For example, the presence of heazlewoodite inclusions in magnetite within sheared veins in the Ti-clinohumite bearing samples, which record the earliest stages of exhumation, could record SO_2-bearing fluids. Reduction of SO_2 to form sulphides requires electrons, potentially donated by ferrous iron in minerals such as tremolite.

Given these considerations, in-situ oxidation of Fe^{2+} to Fe^{3+} by electron accepting species within an externally derived fluid is the preferred explanation for the increase in Fe^{3+} and redox budget recorded by magnetite growth. However, the fact that all samples display an increase in the proportion of both Ti and Fe^{3+}-rich phases, and/or Ti and Fe^{3+} bearing phases hosted in atg2 veins during the onset of exhumation (Fig. 3.7aiv and biv), a stage which allows greater access to high-

pressure fluids (e.g., Evans et al., 2014), suggests that transportation of these elements could be possible in such fluids.

3.6 Acknowledgements

Elaine Miller is thanked for help with the Zeiss Neon 40EsB FEG SEM, and Kelly Merigot is for assistance with quantitative EDS analysis on the TESCAN Mira VP-FESEM. Malcolm Roberts is thanked for assistance with the JEOL 8530 WDS microprobe. Dan Harlov is thanked for discussions on mineral textures. Anonymous reviewers and Alicia Cruz-Uribe are thanked for comments that have helped to improve this chapter. This research was supported by an ARC Future Fellowship FF12000579 to K.E. and a Curtin International Postgraduate Research Scholarship (CIPRS) to R.J.C. S.M.R. acknowledges support from the ARC Core to Crust Fluid Systems COE. The authors acknowledge the Microscopy and Microanalysis Facility (MMF) facility, John de Laeter Centre, Curtin University. The authors acknowledge the facilities, and the scientific and technical assistance of the Australian Microscopy & Microanalysis Research Facility at the Centre for Microscopy, Characterisation & Analysis, the University of Western Australia, a facility funded by the University, State and Commonwealth Governments.

3.7 References

Andreani, M.; Munoz, M.; Marcaillou, C. & Delacour, A. (2013), 'XANES study of iron redox state in serpentine during oceanic serpentinization', *Lithos* **178**, 70–83.

Angiboust, S. & Agard, P. (2010), 'Initial water budget: The key to detaching large volumes of eclogitized oceanic crust along the subduction channel?', *Lithos* **120**(3), 453–474.

Angiboust, S.; Agard, P.; Jolivet, L. & Beyssac, O. (2009), 'The Zermatt-Saas ophiolite: the largest (60-km wide) and deepest (c. 70–80 km) continuous slice of oceanic lithosphere detached from a subduction zone?', *Terra Nova* **21**(3), 171–180.

Ballèvre, M.; Kienast, J.-R. & Vuichard, J.-P. (1986), 'La nappe de la Dent-Blanche(Alpes occidentales): deux unités austroAlpines indépendantes', *Eclogae Geologicae Helvetiae* **79**(1), 57–74.

Barnicoat, A. & Fry, N. (1986), 'High-pressure metamorphism of the Zermatt-Saas ophiolite zone, Switzerland', *Journal of the Geological Society* **143**(4), 607–618.

Beltrando, M.; Manatschal, G.; Mohn, G.; Dal Piaz, G. V.; Brovarone, A. V. & Masini, E. (2014), 'Recognizing remnants of magma-poor rifted margins in high-pressure orogenic belts: The Alpine case study', *Earth-Science Reviews* **131**, 88–115.

Beltrando, M.; Rubatto, D. & Manatschal, G. (2010), 'From passive margins to orogens: The link between ocean-continent transition zones and (ultra) high-pressure metamorphism', *Geology* **38**(6), 559–562.

Bucher, K. & Grapes, R. (2009), 'The eclogite-facies Allalin Gabbro of the Zermatt–Saas ophiolite, Western Alps: a record of subduction zone hydration', *Journal of Petrology*, egp035.

Bucher, K.; Fazis, Y.; Capitani, C. D. & Grapes, R. (2005), 'Blueschists, eclogites, and decompression assemblages of the Zermatt-Saas ophiolite: High-pressure metamorphism of subducted Tethys lithosphere', *American Mineralogist* **90**(5-6), 821 -835.

Burkhard, D. J. (1993), 'Accessory chromium spinels: their coexistence and alteration in serpentinites', *Geochimica et Cosmochimica Acta* **57**(6), 1297–1306.

Compagnoni, R. (1977). 'The Sesia-Lanzo Zone, a slice of continental crust with Alpine high-pressure-low temperature assemblages in the western Italian Alps'. Rendiconti Societa Italian di Mineralogia e Petrologia, 33, 281-334.

Cressey, G.; Cressey, B. & Wicks, F. (2008), 'The significance of the aluminium content of a lizardite at the nanoscale: the role of clinochlore as an aluminium sink',

Mineralogical Magazine **72**(3), 817–825.

Dal Piaz, G.V. (2004) From the European continental margin to the Mesozoic Thetyan Ocean: A geological map of the upper Ayas Valley (Western Alps). In: Pasquaré, G., Venturini C., (Eds), Groppelli G., (Ass.t Ed.), Mapping Geology in Italy. APAT - Agenzia per la Protenzione dell'Ambiente e per i Servizi Tecnici, Dipartimento Difesa del Suolo - Servizio Geologico d'Italia, S.EL.CA., Firenze, 267-272

Dale, C.; Burton, K.; Pearson, D.; Gannoun, A.; Alard, O.; Argles, T. & Parkinson, I. (2009), 'Highly siderophile element behaviour accompanying subduction of oceanic crust: whole rock and mineral-scale insights from a high-pressure terrain', *Geochimica et Cosmochimica Acta* **73**(5), 1394 -1416.

Debret, B.; Andreani, M.; Munoz, M.; Bolfan-Casanova, N.; Carlut, J.; Nicollet, C.; Schwartz, S. & Trcera, N. (2014), 'Evolution of Fe redox state in serpentine during subduction', *Earth and Planetary Science Letters* **400**, 206–218.

Deer, W.A., Howie, R., & Zussman, J. (1962), *Rock Forming Minerals: sheet silicates, vol.3.*, Longmans. London.

Deschamps, F.; Godard, M.; Guillot, S. & Hattori, K. (2013), 'Geochemistry of subduction zone serpentinites: A review', *Lithos* **178**, 96–127.

Evans, B. W.; Darby Dyar, M. & Kuehner, S. M. (2012), 'Implications of ferrous and ferric iron in antigorite', *American Mineralogist* **97**(1), 184–196.

Evans, K. (2012), 'The redox budget of subduction zones', *Earth-Science Reviews* **113**(1), 11–32.

Evans, K.; Tomkins, A.; Cliff, J. & Fiorentini, M. (2014), 'Insights into subduction zone sulphur recycling from isotopic analysis of eclogite-hosted sulphides', *Chemical Geology* **365**, 1–19.

Evans, K. & Powell, R. (2015), 'The effect of subduction on sulphur, carbon, and redox budget contents of lithospheric mantle.', *Journal of Metamorphic Geology*.

Ferrando, S.; Frezzotti, M.; Dallai, L. & Compagnoni, R. (2005), 'Multiphase solid inclusions in UHP rocks (Su-Lu, China): remnants of supercritical silicate-rich aqueous fluids released during continental subduction', *Chemical Geology* **223**(1), 68–81.

Ferrando, S.; Frezzotti, M. L.; Orione, P.; Conte, R. C. & Compagnoni, R. (2010), 'Late-Alpine rodingitization in the Bellecombe meta-ophiolites (Aosta Valley, Italian Western Alps): evidence from mineral assemblages and serpentinization-derived H2-bearing brine', *International Geology Review* **52**(10-12), 1220–1243.

Fontana, E., Panseri, M., & Tartarotti, P. (2008). Oceanic relict textures in the Mount Avic serpentinites, Western Alps. Ofioliti, 33(2), 105-118.

Forster, M.; Lister, G.; Compagnoni, R.; Giles, D.; Hills, Q.; Betts, P.; Beltrando, M. & Tamagno, E. (2004), 'Mapping of oceanic crust with HP to UHP metamorphism: the Lago di Cignana Unit (Western Alps)', *Mapping geology in Italy*, 279–286.

Frost, B. R.; Evans, K. A.; Swapp, S. M.; Beard, J. S. & Mothersole, F. E. (2013), 'The process of serpentinization in dunite from New Caledonia', *Lithos* **178**, 24–39.

Gao, J., John, T., Klemd, R., & Xiong, X. (2007). Mobilization of Ti–Nb–Ta during subduction: Evidence from rutile-bearing dehydration segregations and veins hosted in eclogite, Tianshan, NW China. *Geochimica et Cosmochimica Acta*, 71(20), 4974–4996.

Gasco, I., Gattiglio, M., & Borghi, A. (2013). Review of metamorphic and kinematic data from Internal Crystalline Massifs (Western Alps): PTt paths and exhumation history. Journal of Geodynamics, 63, 1-19.

Gieré, R. (1993). Transport and deposition of REE in H2S-rich fluids: Evidence from accessory mineral assemblages. Chemical Geology, 717, 110(1–3), 251–268.

Gill, R. (2010), *Igneous rocks and processes: a practical guide*, John Wiley & Sons.

Groppo, C.; Beltrando, M. & Compagnoni, R. (2009), 'The P–T path of the ultra-high pressure Lago Di Cignana and adjoining high-pressure meta-ophiolitic units: insights into the evolution of the subducting Tethyan slab', *Journal of Metamorphic Geology* **27**(3), 207–231.

Groppo, C. & Compagnoni, R. (2007), 'Metamorphic veins from the serpentinites of the Piemonte Zone, western Alps, Italy: a review', *Periodico di Mineralogia* **76**, 127–153.

Herwartz, D., Münker, C., Scherer, E. E., Nagel, T. J., Pleuger, J., & Froitzheim, N. (2008). Lu-Hf garnet geochronology of eclogites from the Balma Unit (Pennine Alps): implications for Alpine paleotectonic reconstructions. *Swiss Journal of Geosciences*, 101(1), 173-189.

Lécuyer, C. & Ricard, Y. (1999), 'Long-term fluxes and budget of ferric iron: implication for the redox states of the Earth's mantle and atmosphere', *Earth and Planetary Science Letters* **165**(2), 197–211.

López Sánchez-Vizcaino, V.; Gómez-Pugnaire, M. T.; Garrido, C. J.; Padrón-Navarta, J. A. & Mellini, M. (2009), 'Breakdown mechanisms of titanclinohumite in antigorite serpentinite (Cerro del Almirez massif, S. Spain): a petrological and TEM study', *Lithos* **107**(3), 216–226.

López Sánchez-Vizcaino, V.; Trommsdorff, V.; Gómez-Pugnaire, M.; Garrido, C.; Müntener, O. & Connolly, J. (2005), 'Petrology of titanian clinohumite and olivine at the high-pressure breakdown of antigorite serpentinite to chlorite harzburgite (Almirez Massif, S. Spain)', *Contributions to Mineralogy and Petrology* **149**(6), 627–646.

Lapen, T. J.; Johnson, C. M.; Baumgartner, L. P.; Mahlen, N. J.; Beard, B. L. & Amato, J. M. (2003), 'Burial rates during prograde metamorphism of an ultra-high-pressure terrane: an example from Lago di Cignana, western Alps, Italy', *Earth and Planetary Science Letters* **215**(1), 57–72.

Li, X.-P.; Rahn, M. & Bucher, K. (2004), 'Serpentinites of the Zermatt-Saas ophiolite complex and their texture evolution', *Journal of Metamorphic Geology* **22**(3), 159–177.

Martin, S.; Rebay, G.; Kienast, J.-R. & Mével, C. (2008), 'An eclogitised oceanic palaeo-hydrothermal field from the St. Marcel Valley (Italian Western Alps)', *Ofioliti* **33**(1), 49–63.

McDonough, W. F., & Sun, S. S. (1995). The composition of the Earth. *Chemical Geology*, 120(3-4), 223-253.

Müntener, O. & Hermann, J. (1994), 'Titanian andradite in a metapyroxenite layer from the Malenco ultramafics (Italy): implications for Ti-mobility and low oxygen fugacity', *Contributions to Mineralogy and Petrology* **116**(1-2), 156–168.

Müntener, O.; Manatschal, G.; Desmurs, L. & Pettke, T. (2009), 'Plagioclase peridotites in ocean–continent transitions: refertilized mantle domains generated by melt stagnation in the shallow mantle lithosphere', *Journal of Petrology*, egp087.

Mungall, J. E. (2002), 'Roasting the mantle: slab melting and the genesis of major Au and Au-rich Cu deposits', *Geology* **30**(10), 915–918.

Peretti, A.; Dubessy, J.; Mullis, J.; Frost, B. R. & Trommsdorff, V. (1992), 'Highly reducing conditions during Alpine metamorphism of the Malenco peridotite (Sondrio, northern Italy) indicated by mineral paragenesis and H2 in fluid inclusions', *Contributions to Mineralogy and Petrology* **112**(2-3), 329–340.

Rahn, M. & Rahn, K. (1998), 'Titanian clinohumite formation in the Zermatt-Saas ophiolites, central Alps', *Mineralogy and Petrology* **64**(1-4), 1–13.

Rebay, G.; Spalla, M. & Zanoni, D. (2012), 'Interaction of deformation and metamorphism during subduction and exhumation of hydrated oceanic mantle: Insights from the Western Alps', *Journal of Metamorphic Geology* **30**(7), 687–702.

Reddy, S.; Wheeler, J.; Butler, R.; Cliff, R.; Freeman, S.; Inger, S.; Pickles, C. & Kelley, S. (2003), 'Kinematic reworking and exhumation within the convergent Alpine Orogen', *Tectonophysics* **365**(1), 77–102.

Reddy, S.; Wheeler, J. & Cliff, R. (1999), 'The geometry and timing of orogenic extension: an example from the Western Italian Alps', *Journal of Metamorphic Geology* **17**, 573–590.

Reinecke, T. (1998), 'Prograde high-to ultrahigh-pressure metamorphism and exhumation of oceanic sediments at Lago di Cignana, Zermatt-Saas Zone, western Alps', *Lithos* **42**(3), 147–189.

Rubatto, D.; Gebauer, D. & Fanning, M. (1998), 'Jurassic formation and Eocene subduction of the Zermatt–Saas-Fee ophiolites: implications for the geodynamic evolution of the Central and Western Alps', *Contributions to Mineralogy and Petrology* **132**(3), 269–287.

Salters, V. J. & Stracke, A. (2004), 'Composition of the depleted mantle', *Geochemistry, Geophysics, Geosystems* **5**(5).

Scambelluri, M., & Philippot, P. (2001). Deep fluids in subduction zones. *Lithos*, 55(1), 213-227.

Scambelluri, M.; Pettke, T.; Rampone, E.; Godard, M. & Reusser, E. (2014), 'Petrology and trace element budgets of high-pressure peridotites indicate subduction dehydration of serpentinized mantle (Cima di Gagnone, Central Alps, Switzerland)', *Journal of Petrology*, egt068.

Scambelluri, M. & Rampone, E. (1999), 'Mg-metasomatism of oceanic gabbros and

its control on Ti-clinohumite formation during eclogitization', *Contributions to Mineralogy and Petrology* **135**(1), 1–17.

Schwarzenbach, E. M.; Gazel, E. & Caddick, M. J. (2014), 'Hydrothermal processes in partially serpentinized peridotites from Costa Rica: evidence from native copper and complex sulphide assemblages', *Contributions to Mineralogy and Petrology* **168**(5), 1–21.

Spandler, C.; Hermann, J.; Faure, K.; Mavrogenes, J. A. & Arculus, R. J. (2008), 'The importance of talc and chlorite "hybrid" rocks for volatile recycling through subduction zones; evidence from the high-pressure subduction mélange of New Caledonia', *Contributions to Mineralogy and Petrology* **155**(2), 181–198.

Spandler, C.; Pettke, T. & Hermann, J. (2014), 'Experimental study of trace element release during ultrahigh-pressure serpentinite dehydration', *Earth and Planetary Science Letters* **391**, 296–306.

Spandler, C. & Pirard, C. (2013), 'Element recycling from subducting slabs to arc crust: A review', *Lithos* **170**, 208–223.

Stampfli, G. M. & Borel, G. (2001), *Geology of the Western Swiss Alps: A Guide-book*, Section des Sciences de la terre de l'université.

Tomkins, A. G. & Evans, K. A. (2015), 'Separate zones of sulphate and sulphide release from subducted mafic oceanic crust', *Earth and Planetary Science Letters* **428**, 73–83.

Trommsdorff, V. & Evans, B. W. (1980), 'Titanian hydroxyl-clinohumite: formation and breakdown in antigorite rocks (Malenco, Italy)', *Contributions to Mineralogy and Petrology* **72**(3), 229–242.

Tropper, P. & Manning, C. E. (2005), 'Letter: Very low solubility of rutile in H2O at high pressure and temperature, and its implications for Ti mobility in subduction zones', *American Mineralogist* **90**(2-3), 502–505

CHAPTER 4

TRACING HIGHLY SIDEROPHILE ELEMENTS THROUGH SUBDUCTION: INSIGHTS FROM HIGH-PRESSURE SERPENTINITES AND 'HYBRID' ROCKS FROM ALPINE CORSICA

This chapter is under review for publication in the *Journal of Petrology*

Crossley R.J., Evans, K.A., Evans, N.J., Bragagni, A., McDonald, B.J., Reddy, S.M. & Speelmanns, I.M., "Tracing Highly siderophile elements through subduction: insights from high-pressure serpentinites and 'hybrid' rocks from Alpine Corsica", *Journal of Petrology*, under review.

Contributions by co-authors

Rosalind Crossley collected the samples and carried out sample preparation for whole rock and LA-ICP-MS analysis, characterised the samples (optical microscopy, scanning electron microscopy and electron-probe-microanalysis) and chose areas for LA-ICP-MS analysis. LA-ICP-MS analyses were carried out with assistance from Noreen Evans and Brad McDonald. Noreen Evans also provided training for data reduction using Iolite. Alessandro Bragagni determined the concentrations of the HSE in the Bonn SulphVI standard, and Iris Speelmanns synthesised the Bonn SulphVI standard. Rosalind Crossley is the primary author of this manuscript with advice, discussions and guidance from all co-authors, listed in order of the most contributing author first.

Abstract

Highly siderophile elements (HSE; Os, Ir, Ru, Rh, Pt, Pd, Au and Re) include redox sensitive and economically critical elements (PGE and Au) and therefore are important tracers of redox conditions within subducted samples. Fractionation of these elements from their mantle concentrations may have implications for Re-Os isotopic signatures in the mantle and the formation of arc-related ore deposits. Here

a multi-technique study is presented to trace HSE in serpentinites and hybrid ultramafic/mafic rocks from Alpine Corsica through the subduction cycle on a sample and mineral (>200 μm to <2 μm) scale.

Comparison of bulk HSE concentrations to those of the primitive upper mantle (PUM), pre-subduction analogues of peridotite from the Kane Fracture Zone and the Internal Ligurides, and to gabbro and gabbro eclogites and hybrid mafic/ultramafic rocks provide an insight into sample scale HSE transfer. Mineral parageneses place temporal constraints on the growth of HSE hosts (sulphides, oxides and metal alloys), and elucidates changes to the activities of oxygen and sulphur (aO_2–aS_2) from pre-subduction to exhumation. LA-ICP-MS determination of HSE concentrations in sulphides and oxides, and the detection of small (~2–25 μm^2) platinum group minerals using high resolution SEM mapping techniques, provides a mineral scale insight into the distribution of HSE in high-pressure serpentinites and hybrid mafic/ultramafic rocks.

Serpentinite whole rock data do not significantly deviate from PUM concentrations, on a hand specimen scale. However, HSE the HSE concentration of hybrid rocks (talc schist and chlorite schist) deviate from protolith concentrations on a hand sample scale. Talc schist has higher concentrations of Re and chlorite schist has lower Ir and Ru concentrations compared to PUM and mafic protoliths. Therefore, with the exception of hybrid samples, HSE are not mobile on the scale of the whole rock or greater. On a mineral scale, the studied prograde and retrogressive sulphides are depleted in HSE compared to sulphides from pre-subduction oceanic settings. Dilution by an increase in sulphide mode is a feasible explanation for HSE depletion in samples with relatively high modes of early exhumation-related sulphides and hence sulphur concentrations, and therefore, we tentatively infer sulphur addition during the onset of exhumation for these sulphides. However, low sulphur concentrations in some serpentinites are not consistent with this explanation and therefore we propose that millimetre to centimetre scale mobilisation of HSE from sulphides to alloys occurred in these samples during prograde metamorphism and the onset of exhumation. Mineral scale HSE measurements in combination with textural analysis provides a powerful tool to assess the evolution of HSE hosts (sulphide, metal alloy and spinels), the extent of HSE fractionation and changes in aS_2 and aO_2, and hence redox conditions throughout the subduction cycle.

4.1 Introduction

Subduction of oxidised redox sensitive elements can influence the oxidation state of the sub-arc mantle, deep mantle and metamorphic fluids released from the subducting slab (Evans, 2012). The oxidation state of the sub-arc mantle is of particular significance because, currently, genetic models for arc-related Cu and Au ore deposits require an oxidised sub-arc mantle (e.g. Mungall, 2002). Major hosts of highly siderophile elements (HSE; platinum group elements (PGE), Re and Au) also contain redox sensitive elements. Such hosts include sulphides, spinels and PGE-rich alloys (e.g. Mitchell and Keays, 1981; Hart and Ravizza, 1996; Puchtel and Humayun, 2001; Page et al., 2012; 2016; Brenan and Andrews, 2001). *In-situ* analysis of HSE hosts in rocks that have undergone subduction and subsequent exhumation can therefore provide a wealth of information on the cycling of HSE, fluid composition and redox conditions. Careful textural analysis of mineral hosts to HSE, combined with trace element chemistry can be used to assess their stability during subduction metamorphism and exhumation, the release or retention of redox sensitive elements (Fe, S and PGE) and, therefore, the transfer of redox budget to the sub-arc mantle. Furthermore, PGE and Au are economically critical elements, and thus understanding the behaviour of these elements during subduction is vital to the discovery of new arc-related ore deposits (e.g. Richards et al., 2009). In spite of these incentives, *in-situ* studies of HSE hosts in subducted rocks are scarce, with notable exceptions (e.g. Dale et al., 2009; Aulbach et al., 2012; Evans et al. 2014).

Processes that affect the HSE-hosting lithologies during subduction (hydrated mantle lithosphere, altered oceanic crust, seafloor sediments and continental units from extended continental margins) are difficult to distinguish because the hosts are affected by many stages of alteration (e.g. on the seafloor, and during subduction and exhumation). Determination of HSE concentrations in sulphides, spinels, alloy phases and platinum group minerals (the major hosts of HSE), in combination with mineral textural analysis, have the potential to record redox conditions because the distribution of HSE is sensitive to the concentration of sulphur (e.g. Fleet et al., 1999), oxygen activity (aO_2) and sulphur activity (aS_2) (Mungall and Brenan, 2014).

The hydrated mantle lithosphere component of the slab is of particular interest because upon dehydration of this lithology at depth within the subduction channel has the potential to release large volumes of fluids to the sub-arc mantle upon dehydration of antigorite (e.g., Deschamps et al., 2013; Debret et al., 2014; Scambelluri and Tonarini, 2012; Scambelluri et al., 2014; Debret and Sverjensky, 2017). In addition, the nature of fluids released from serpentinites has important consequences for element cycling. For example, elevated $^{187}Os/^{188}Os$ ratios in sub-arc mantle xenoliths from the Cascardes, USA, and Japan, suggests ^{187}Os transport in slab-derived oxidised and Cl-rich fluids (Brandon et al., 1996). Previous studies of HSE transfer from subducted lithologies, particularly on the mantle lithosphere component of the slab, are limited with the exception of whole rock determination of HSE concentrations in serpentinites from La Corea mélange in Cuba (Blanco-Quintero et al., 2011), where HSE were concluded to have behaved conservatively during metamorphism.

Mixing of sediments/oceanic crust and mantle lithosphere along the slab/sub-arc mantle interface at high pressures produces 'hybrid' rocks, which have mixed chemical and isotopic signatures (e.g., Spandler et al., 2008; Spandler and Pirard, 2013). Recently, hybrid rocks have been recognised as important carriers of volatile elements including sulphur, to greater depths than that of serpentinised mantle (Spandler et al., 2008; Spandler and Pirard, 2013), thus could be vital in the transport of fluids and elements to the sub-arc mantle. Tentatively, the similarity of HSE concentrations between rinds of eclogite facies blocks within subduction mélange, and the surrounding peridotite were inferred to imply centimetre scale mobility of all HSE, although physical mixing is more likely (Penniston-Dorland et al., 2012), thus the role of interaction between lithologies in HSE distribution during subduction should be assessed. Moreover, studies of HSE transfer on a mineral scale in subducted rocks are rare, with notable exceptions. For example, on the basis of *in-situ* analyses of PGE in sulphides in combination with whole rock analyses of gabbros unaffected by metamorphism, gabbroic eclogites and basaltic eclogites from the Zermatt-Saas zone, Western Alps, Dale et al. (2009) inferred the mobility of Pt and Re in basalts and Pd in gabbros on a sample scale or greater during metamorphism). In addition, *in-situ* analyses of HSE within sulphides in eclogitic

diamonds from the Diavik mine, central Slave craton suggested the mobilisation of Au by serpentinite derived reducing and Cl-poor fluids (Aulbach et al., 2012).

This study presents the first *in-situ* trace element analysis of sulphides in subducted serpentinites and hybrid mafic/ultramafic rocks. Insights into subduction-modified HSE concentrations on a scale larger than a fist-sized sample and on the centimetre to millimetre scale are obtained by comparison of whole rock and sulphide HSE concentrations to whole rock and sulphide data in pre-subduction protoliths from the Kane Fracture Zone (KFZ), which is a slow-spreading centre (Luguet et al., 2003; Alard et al., 2005) and from the Internal Ligurides (IL), which forms part of an inferred ocean-continent transition (OCT) zone (Luguet et al., 2004). In addition, lithological controls on HSE redistribution are established by comparison to unmetamorphosed mafic rocks (Dale et al., 2009) and hybrid ultramafic/mafic rinds (Penniston-Dorland et al., 2012; 2014). Mineral composition data and textural analyses are used to construct mineral parageneses, with a focus on sulphides and oxides. These are combined with sulphide HSE concentrations to provide insights into changes to redox conditions on a mineral scale.

4.2 Geological Setting

4.2.1 Alpine Corsica

Alpine Corsica consists of three main domains; the External Continental units, the Schistes Lustrés complex, and the uppermost units or the Nappes Supérieures (Vitale Brovarone et al., 2011; 2013). The External Continental units consist of deformed crystalline rock including continental basement rocks e.g. the Tenda massif, and are inconsistently overlain by low metamorphic grade greenschist to blueschist facies sediments (Molli et al., 2006; Tribuzio and Giacomini, 2002; Vitale Brovarone et al., 2011). The Schistes Lustrés complex is considered to be comprised of several tectonometamorphic units, consisting of metaophiolites (including serpentinites, metagabbros and metabasalts), metasediments and slivers of internal continental slices (Vitale Brovarone et al., 2013). The uppermost units include the Balagne, Nebbio and Macinaggio nappe sheets (Vitale Brovarone et al., 2011; Meresse et al., 2012 and references therein).

The ophiolites and metasediments of the Schistes Lustrés complex, from which the samples in this study were collected, are considered to represent fragments of the ultra slow to slow-spreading Middle to Late Jurassic Piemonte-Liguria oceanic basin and its cover sediments, which were subsequently subducted to high pressure-low temperature blueschist to lawsonite-eclogite facies from 55 Ma until 34 Ma (Vitale Brovarone and Herwartz, 2013; Vitale Brovarone et al., 2013; Magott et al., 2016). Retrograde metamorphism to greenschist facies occurred from the late Oligocene to early Miocene (Jolivet et al., 1990; 1991; 1998; Fournier et al., 1991, Magott et al., 2016).

The juxtaposition of the ophiolites and internal continental slices within the Schistes Lustrés complex is controversial. On the basis of small scale structural work, deformation analysis and shear fabrics, some workers considered the units to have been juxtaposed as a result of tectonic thrusting of ophiolites onto continental basement during the Late Cretaceous as part of the Alpine Orogeny (e.g. Mattauer et al., 1981; Fournier et al., 1991). However, the juxtaposition could have occurred during pre-Alpine Jurassic Tethyan extension in an ocean-continent transition (OCT) zone (Vitale Brovarone et al., 2011; 2013; Meresse et al., 2012), as proposed for other localities in the Western Alps (e.g. Beltrando et al., 2010). The evidence for an OCT setting is well-preserved in Alpine Corsica. For example, the pre-Alpine contact, inferred to be a detachment fault, between ultramafic rocks and continental slices at Monte San Petrone, which pre-dates high-pressure ductile fabrics, and the Jurassic-Cretaceous metasediments overlying the ultramafic rocks and continental slices which do not show evidence of cataclastic deformation (Vitale Brovarone et al., 2011). Other evidence for an OCT setting is found within the Serra di Pigno region, where ultramafic clasts are found within carbonate metasediments, ophicalcites, and significantly variable metasedimentary successions interlayered with mafic and ultramafic lithologies and breccias are consistent with this interpretation (Meresse et al., 2012).

4.2.2 The Serra di Pigno Region

Serra di Pigno is located ~10 km west of Bastia, on Cap Corse, Alpine Corsica, between Patrimonio in the west to Ville di Pietrabugno in the east (Meresse et al., 2012, Fig 1.1a). In this study, the selected samples CO13-31, CO13-40,

CO13-21, CO13-33 and CO13-55 (WGS 84, zone 32T, 0533430 mE 4729806 mN, 0533122 mE 4728302 mN, 0533228 mE 4728387 mN, 0533514 mE 4729532 mN and 0533398 mE 4729368 mN, respectively, Fig. 4.1b) are from the Patrimonio unit, which structurally overlies the Serra di Pigno gneiss and is below the Cima de Gratera metagabbro (Meresse et al., 2012). The Serra di Pigno region lies within the lawsonite-blueschist zone based on P-T estimates of 1.3 GPa and 455 ± 35 °C (Lahondère and Guerrot, 1997). However, on the basis of Raman spectroscopy of carbonaceous material (RSCM), the eastern part of the region is inferred to record eclogite facies peak conditions (Vitale Brovarone et al., 2013). According to the reclassified tectono-metamorphic units in Vitale Brovarone et al. (2013), our samples lie on or close to the boundary between the blueschist and eclogite terrains. This interpretation corresponds to maximum peak metamorphism temperatures of 414–471 °C and pressures of 1.3–2.6 GPa (Lahondère and Guerrot, 1997; Vitale Brovarone et al., 2013).

4.2.3 The Capu Corvoli Region

The chlorite schist and talc schist hybrid samples, CO14-03 and CO14-04 (WGS 84, zone 32T, 0529140 mE 4753069 mN and 0529107 mE 4753071 mN, respectively), and metagabbro sample CO14-05 (WGS 84, zone 32T, 0529154 mE 4753091 mN) were collected from Capu Corvoli (~5 km north of the village of Pino), Cap Corse (Fig. 4.1a). The samples are from a shear zone that lies parallel to a series of nearby thrust faults with WNW to NW-orientated fault planes (Fig. 4.1c), which have previously been interpreted to separate the lawsonite-blueschist Upper Castagniccia metasediments and lawsonite-eclogite ophiolites (Lahondère, 1992). These structures dip shallowly to the WNW to NW and the shear zone records top-to-the-west to NW shearing, consistent with thrusting of the hybrid samples and metagabbro over calc schist of the Upper Castagniccia unit. The top to the west to northwest sense of shear is broadly consistent with non coaxial deformation associated with prograde metamorphism (Mattauer et al., 1977; 1981; Faure and Malavielle, 1981; Harris, 1985; Warburton, 1986; Magott et al., 2016).

On the basis of RSCM, recent P-T estimates suggest the Upper Castagniccia metasediments at Capu Corvoli record eclogite conditions (e.g. Vitale Brovarone et al., 2013 and references therein, Fig. 4.1a). This interpretation suggests that the

Capu Corvoli samples studied here record higher pressures than the Serra di Pigno samples and maximum peak P-T estimates of the lawsonite-eclogite ophiolites are ~490–550 °C and 1.9–2.6 GPa (Ravna et al., 2010; Vitale Brovarone et al., 2013).

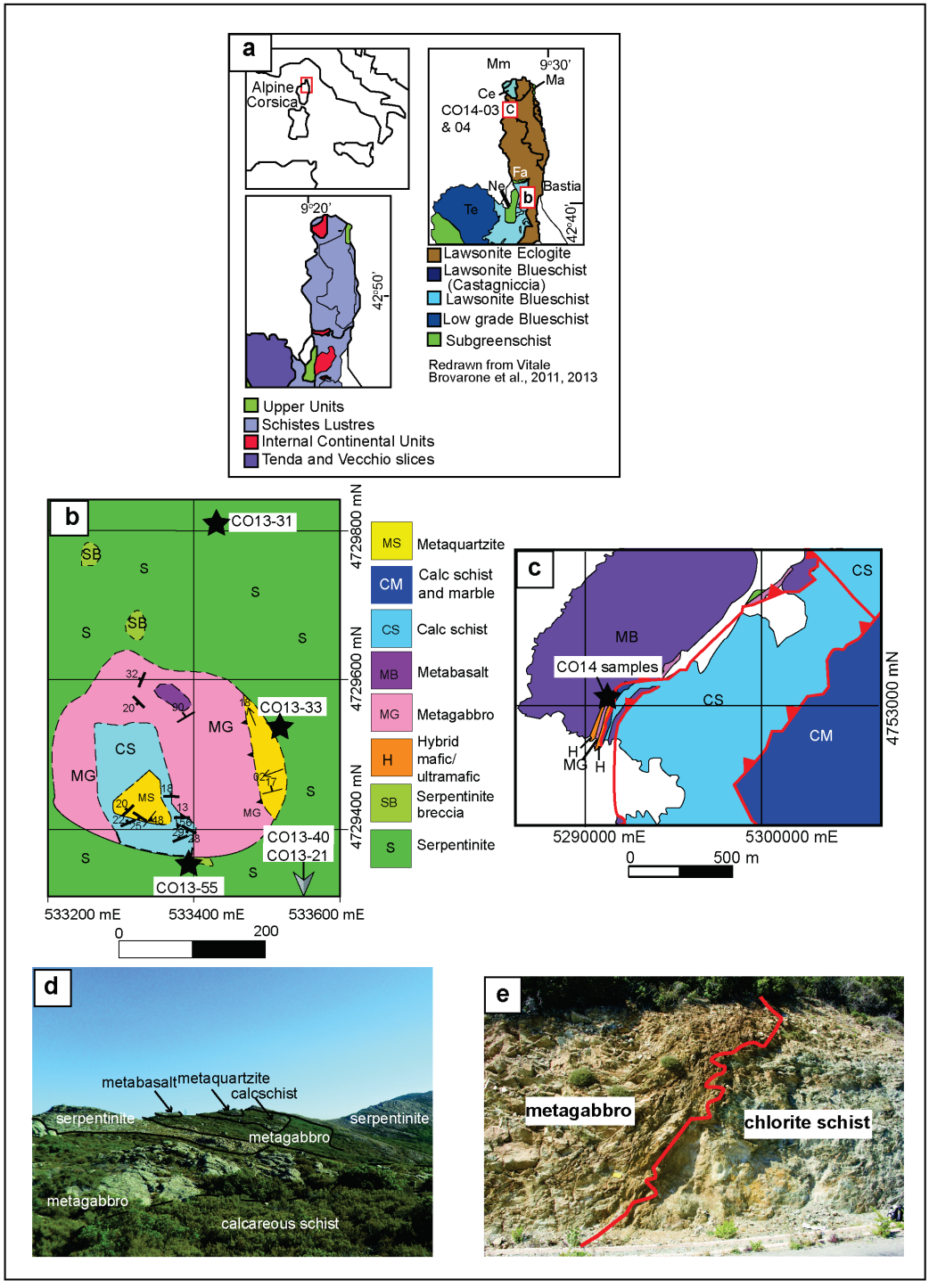

Figure 4.1 (a) map showing the locations and P-T conditions of the field areas Serra di Pigno and Capu Corvoli on Cap Corse, Corsica (redrawn from Brovarone et al., 2011, 2013). **(b)** map of Serra di Pigno sample localities. **(c)** map of Capu Corvoli sample localities (adapted from Lahondère,

1992). **(d)** Field photo showing the juxtaposition of lithologies at Serra di Pigno. **(e)** Field photo of the contact between metagabbro and serpentinite at Capu Corvoli.

4.3 Methods

4.3.1 Sample collection

Thirty samples of serpentinites, metaquartzites, calc schists, metagabbros, metabasalts and hybrid talc schists and chlorite schists were collected from Serra di Pigno and Capu Corvoli. The sample suite from Serra di Pigno includes serpentinites adjacent to metasediments, metagabbros and metabasalts, and distal to these lithologies (Fig. 4.1b, d). The hybrid mafic/ultramafic samples from Capu Corvoli are in the form of slivers next to metagabbro, in close proximity to calcareous schist (Fig. 4.1c, e).

4.3.2 Analytical Methods

4.3.2.1 Bulk composition Analysis

For each sample, approximately 55g of representative, unweathered rock was crushed using a TEMA Tungsten Carbide mill. Blank samples consisting of a quartz crush were used as controls, sample duplicates were made for accuracy, and in order to test precision, samples were split into two containers in preparation for analysis. Samples were analysed for major, minor and selected trace elements (including HSE), C, S, FeO and total iron (as Fe_2O_3 in Table 4.1), at Intertek Genalysis, Maddington, Western Australia. Lithium borate fusion followed by dissolution and inductively coupled plasma optical emission spectrometry (ICP-OES) was used for analysis of major elements and Cr, Sc and V. Four acid (HF, HCl, HNO_3 and HClO) digestion inductively coupled plasma mass spectrometry (ICP-MS) was required for As, Bi, Cd, Cu, In, Pb, Re, Sb, Se, Te and Tl analyses. Loss on ignition (LOI) was measured using Thermo Gravimetric Analysis at 1000ºC. The FeO content was determined via titration with ceric sulphate.

Whole rock PGE (Pt, Pd, Rh, Ru, Ir and Os) and Au were analysed with nickel sulphide fire-assay (NiS-FA) pre-concentration followed by ICP-MS. The method is described in Gervilla et al., (2005) and is based on the method of Chan and Finch (2001). 25g of the sample was fused with a flux of borax, soda ash, silica,

nickel oxide and sulphur at 1200ºC. The reaction with sulphur reduced NiO to NiS, and formed an NiS matte and an immicible slag, where NiS sequestered PGE and Au. The NiS matte was separated from the slag, weighed, pulverised and dissolved in boiling HCl. Several reagents were added to the HCl, and PGE and Au were recovered as insoluble residues on a cellulose nitrate membrane filter. PGE and Au were sealed in borosilicate test tubes and dissolved in aqua regia. The addition of a proprietary reagent enhanced the recovery of Os, which would have otherwise volatilised. The solutions were diluted with 10% nitric acid. Concentrations were determined using a Perkin Elmer Elan 9000 quadropole ICP-MS and corrected for Cu and Ni argide interferences, and for drift and plasma fluctuations.

The detection limits for HSE are 1 ppb for PGE and 2 ppb for Au and Re. Two procedural blanks were measured as controls, where concentrations of HSE are below detection limits, with the exception of Pd (1ppb) and Re (2 ppb) in one measurement. Whole rock HSE uncertainties are reported in Appendix C1. Recently, the efficiency of NiS-FA to collect all PGE has been questioned with workers preferring the isotope dilution (ID) high-pressure Asher or the Carius tube digestion techniques, which are considered better for PGE recovery and have low level blanks (e.g. Puchtel et al., 2004; Becker et al., 2006; Lorand et al., 2008). However, the results obtained for the reference material AMIS0278 are within 5% of certified concentrations for AMIS0278, therefore PGE recovery for our samples was optimal using the NiS-FA technique, and further, the two control blanks did not have detectable PGE, with the exception of Pd in one blank (Appendix C1). In addition, the NiS-FA technique allows the analysis of larger sample masses, with 25g of each sample analysed in this study, in contrast to <5g in isotope dilution techniques. Thus the nugget effect is minimised using the NiS-FA method, which is particularly advantageous given the presence of platinum group minerals in our samples. Futhermore, using the NiS-FA technique it is possible to synchronously analyse Rh and Au (Savard et al., 2010).

4.3.2.2 Scanning Electron Microscopy

Thin section billets were cut perpendicular to foliation and parallel to lineation, and thin sections were made for optical microscopy, scanning electron microscopy (SEM) and energy dispersive spectroscopy (EDS) work. Samples for

in-situ trace element analysis were selected after petrographic analysis using transmitted and reflected light microscopy and subsequent SEM and EDS characterisation. SEM and EDS work was undertaken at the Microscopy and Microanalysis Facility (MMF), in the John de Laeter Centre (JdLC), Curtin University using a Zeiss Neon 40EsB field emission SEM. All samples were coated with ~25 nm carbon prior to SEM and EDS work. The accelerating voltage for EDS was 20 kV. Small, opaque phases (1–5 μm) were detected and analysed using the Oxford Instruments Feature Mapping facility on the JdLC Tescan Mira 3 SEM. Copper was used for optimisation of the detector. Thresholds were set to grain brightness in BSE. The lower threshold was set to a brightness just above that of magnetite. The analysis running time was ~5 to 12 hours per sample, dependent on the number of metal alloys and small sulphide phases identified.

The results of feature mapping using the Tescan Mira 3 were complemented using the new Tescan Integrated Mineral Analyser (TIMA) at the JdLC MMF, Curtin University. The technique utilised a bright field search, set to a BSE signal brightness of greater than 90%. A 1 μm step size was used to allow optimum detection of grain sizes with a minimum size of 1 μm. The counts per pixel were set to 3000. Analysis of multiple thin sections at once were possible using the TIMA, and the analysis time was ~5 hours in total for 9 thin sectons. Data processing was carried out using the TIMA 1.4.4.1 software.

4.3.2.3 Electron Probe Microanalysis (EPMA)

Major and minor elements of carbon coated sulphides, oxides and silicates were quantitatively analysed on the JEOL 8530F Hyperprobe at the Centre for Microscopy, Characterisation and Analysis (CMCA), the University of Western Australia. Mean atomic number (MAN) background corrections were used throughout with an on-peak counting time of 20 seconds per element. The accelerating voltage was set at 15 kV, the beam current at 20 nA. Multiple analyses were carried out per grain to identify any sample heterogeneity. The standards used for calibration of sulphides were Ni, Co, Pyrite (S), Crocoite (Pb), ZnO, Cu, Bi_2Se_3, GaAs (As), and Sb. Data reduction was performed using the Probe for EPMA v.10.8.1 software package (Donovan et al, 2012). The compositions of the matrix silicate phases were necessary to correct LA-ICP-MS data for silicate

contamination in sulphide grains <50 µm. The same conditions were used for analyses of silicates and oxides, however the standards were as follows; wollastonite (Si), rutile (Ti), Kakanui pyrope (Mg, Al), V, Cr_2O_3, magnetite (Fe for oxides), San Carlos olivine (Fe for silicates), Ni, Mn, Durango apatite (Ca), Jadeite (Na), orthoclase (K).

4.3.2.4 LA-ICP-MS

Trace element contents of sulphide and spinel grains were obtained *in-situ* by Laser Ablation Inductively Coupled Mass Spectroscopy (LA-ICP-MS) at the GeoHistory Facility, JdLC, Curtin University, using a Resonetics RESOlution M-50 with a Compex 102 Excimer laser, coupled to an Agilent 7700s quadropole ICP-MS. Prior to LA-ICP-MS, thin section billets were polished to 1 µm. Background signal was collected for 20s, followed by ablation of the sample grains for 40 s, at a repetition rate of 7 Hz for large grains and 10 Hz for smaller grains in order to obtain sufficient counts above limits of detection. Ablation was performed in an atmosphere of ultra-high purity He and N_2 with a laser energy density at the sample surface of 2 J/cm^2. The spot size was set to 70 µm for grains >70 µm in diameter and to 50 µm for smaller grains. The HSE laser ablation time resolved spectrum were carefully studied in order to identify spikes in counts that indicated intersection of discrete HSE-bearing phases within the sulphide or spinel grains.

Data reduction was carried out using the IGOR Pro 6.36 platform and the Trace Elements data reduction scheme in Iolite v. 2.5 (Paton et al., 2011). HSE analyses included ^{101}Ru, ^{103}Rh, ^{105}Pd, ^{186}Re, ^{189}Os, ^{193}Ir, ^{195}Pt and ^{197}Au. Integration of HSE in sulphides and spinels utilised Laflamme Po726 as the primary standard for PGE and ^{197}Au, and BonnSulphVI (a synthesised sulphide doped with HSE; Bragagni et al., 2015) as the secondary standard for PGE and as the primary standard for Re. ^{57}Fe was used as the internal isotope standard for pentlandite, pyrite and spinel grains, due to the high concentration of Fe in these minerals and because ^{57}Fe is not subject to the ^{40}Ar ^{16}O interference on ^{56}Fe (Danyushevsky et al., 2011). However, for heazlewoodite, which is Fe-poor, ^{34}S was used as the internal isotope standard.

To check the analytical accuracy BonnSulphVI was treated as an unknown and calibrated against Laflamme Po726. HSE were determined with an accuracy of ≤11%, with the exception of Pt where the percent deviation from accepted values was 25% (Appendix C2). The poorer accuracy on Pt could reflect heterogeneity in the standards at the 50 μm scale.

For sample grain analysis, other interferences of possible significance include $^{63}Cu\ ^{40}Ar$ on ^{103}Rh and $^{65}Cu\ ^{40}Ar$ on ^{105}Pd, where ^{63}Cu is 69% of total Cu, but Cu is of relatively low concentrations in the sulphides (up to 2170 ppm) and spinels (up to 650 ppm) analysed. The higher than expected concentrations Cu in spinel reflect minute Cu-rich sulphide and alloy phases (<5 μm). In the case of discrete Cu-rich phases within sulphide grains, the time resolved spectrum for each analysis was checked for correlations between ^{65}Cu and ^{103}Rh and ^{105}Pd peaks. The typical profiles for sulphides are shown in Appendix C3. A correlation between ^{65}Cu and ^{103}Rh and ^{105}Pd was observed in one grain, however other grains did not show a significant correlation, and ^{103}Rh was typically homogeneous throughout the ablation period, despite the heterogeneous Cu distribution.

In addition, $^{61}Ni\ ^{40}Ar$ interferences on ^{101}Ru, may produce higher concentrations of ^{101}Ru, however this effect is considered minimal because ^{61}Ni is a low abundance isotope (1%), there is no significant correlation between ^{101}Ru and ^{60}Ni (R^2=0.2) in the most Ni-rich sulphides (550000 ppm Ni), and the concentrations of ^{101}Ru derived on Bonn SulphVI run as an unknown against Laflamme Po726 (where Bonn SulphVI contains 45600 ppm Ni) are in good agreement with the reference values. To further clarify that $^{61}Ni\ ^{40}Ar$ interferences on ^{101}Ru are minimal, apparent Ru concentrations in antigorite were measured. The concentration of Ru in antigorite is considered negligible, and therefore the apparent Ru concentrations provide the $^{61}Ni\ ^{40}Ar$ production rate. A maximum of 0.06 ppm Ru is present in analyses with 5000 ppm Ni. On the basis of 0.06 ppm Ru in antigorite with 5000 ppm Ni, assuming that total Ni has 1.1 % of the interference isotope ^{61}Ni, then 550000 ppm Ni (the maximum concentration of Ni in pentlandite) contributes 0.07 ppm Ru. The $^{61}Ni\ ^{40}Ar$ production rate would therefore be 1.82% for grains that have Ru concentrations of 4 ppm, which would be lost in the uncertainty.

For small pentlandite grains (50 μm or less in diameter) in serpentinites CO13-33 and CO13-55, some proportion of matrix antigorite was incorporated in the ablation analysis volume and thus analyses of HSE in antigorite grains were necessary to correct the trace element data. Transient ablation across sulphide grains would have been an appropriate tool for ablation of small grains in theory, but the shallower depth of ablation would have resulted in lower counts, and concentrations below detection for most HSE. ^{28}Si was used as the internal standard for the reduction of matrix data because of its relative abundance in the Nist 612 standard and because EPMA analyses indicated that Si concentrations in the matrix are homogeneous (Appendix C4). S, Au, Re, Pd and Pt concentrations were negligible in matrix silicate minerals (Appendix C4, C5) and S concentrations within the analysed sulphide minerals are relatively homogeneous (Table 4.2, Appendix C6). Therefore, the correction for matrix ablation was performed using the S content in the sulphides as a guide to calculating a 'dilution factor' for each ablation, which was then used to correct the content of PGE, Au and Re in these small grains (Appendix C6).

The Cr and Fe zonation of spinel grains was on a finer scale than the spot size, producing mixed Cr and Fe peaks in the time resolved spectra. Using EPMA determined maximum and minimum Fe concentrations for each grain (Appendix C7 and C8), maximum and minimum HSE concentrations were obtained for each grain, where ^{57}Fe was used as internal standard (Appendix C9).

4.4 Results

4.4.1 Oxide and sulphide petrography

The prominent features of the oxide and sulphide petrography are described below. The complete petrographic descriptions can be found in Appendix C10. Percentages provided in the text are volume % of any given mineral determined from petrographic analysis.

4.4.1.1 Spinels

Serpentinites: Serra di Pigno. All of the Serra di Pigno serpentinites contain spinels typically with Cr-rich cores (~2–6%) and Fe-rich porous spinel and/or

magnetite rims, although veins of magnetite are observed cross-cutting the Cr-spinel core, and concentrically zoned alternating Cr and Fe-rich bands are both observed in some large spinel grains (1–2.5 mm) in CO13-40. 'Porous' Cr-spinel cores, where fine grained antigorite grains occupy pore space, (Fig. 4.2a). In addition, in CO13-33 some grains have magnetite-Cr-spinel lamellae cores. Magnetite rims on the Cr-spinel grains are overprinted by chlorite at the rim, and/or fine grained matrix antigorite. Later generations of magnetite (~3–8%) replace lizardite (where present) and fine grained matrix antigorite and are included in or are synchronous with later generations of cross-cutting coarse atg2 and 1–2 μm fine balangeroite (Mg-Ni-rich silicate) veins (see chapter 5).

Hybrid rocks: Capu Corvoli. Similar to the Serra di Pigno serpentinites, spinels with Cr-rich cores (~2%) and Fe-rich magnetite rims (~3%) are observed in the talc schist sample, CO14-04 (~40–100 μm, Fig. 4.2b). The chlorite schist sample, CO14-03 contains large 1–5mm euhedral magnetite grains (15%) which cut the matrix comprised of orientated chlorite laths and fine antigorite intergrowths. Magnetite grains have undergone brittle deformation (Fig. 4.2c). Titanite occurs as ~2–5 μm inclusions in magnetite and as grains up to ~50 μm throughout the matrix (Fig. 4.2c).

4.4.1.2 Sulphides

Serpentinites: Serra di Pigno. CO13-31 contains heazlewoodite which co-exists with or contains inclusions of early euhedral magnetite (Fig. 4.2d) and millerite (Fig. 4.2e). Heazlewoodite is ~50–100 μm in diameter and is associated with or cross-cut by a later generation of antigorite (Fig. 4.2d), and, in places, balangeroite veins. Pentlandite occurs on the edges of heazlewoodite grains, overprints late antigorite and contains inclusions of both early fine-grained antigorite and a late generation of magnetite. Feature mapping revealed the presence of trace Co-rich pentlandite (>10wt% Co) within antigorite veins.

CO13-40 contains trace chalcopyrite grains in 'porous' Cr-spinel cores and pentlandite as the dominant sulphide phase (up to ~50 μm) which contain inclusions of fine grained antigorite and overprinted by coarse laths of antigorite at the rim

(Fig. 4.2f). Some pentlandite grains show alteration to more Co and As rich compositions towards the rim, appearing darker in reflected light (Fig. 4.2e).

CO13-21 contains two generations of pentlandite, pn1 and pn2. Pn1 is fine grained (1–5μm) and included in fine antigorite and pn2 is coarser (~10–50 μm, Fig. 4.2g) and is overprinted by or contains inclusions of coarse antigorite, late magnetite and rare millerite (<5 μm).

CO13-33 contains trace chalcopyrite (<1 μm) within Cr-rich cores to spinel. Trace heazlewoodite (1–2 μm in diameter) are found with balangeroite veins. Three generations of pentlandite are found within CO13-33. Pn1 (1%) are elongate grains (~5–20 μm across, Fig. 4.2h), associated with coarse antigorite. Pn2 (2%) are ~30-50 μm in size, and are associated with fine antigorite veins (<0.5 μm across) which cross cut two earlier generations of fine and coarse antigorite. Pn2 replaces the zoned Cr to Fe-rich spinels and chlorite (Fig. 4.2i). Pn3 grains are comprised of are euhedral grains in the matrix, ~35 μm in size (Fig. 4.2j).

CO13-55 includes pentlandite (pn1–4), pyrite and chalcopyrite. Pn1 (<1%) consist of euhedral grains ~5 μm in diameter which are included in mt1 on rims of Cr-rich spinel. Pyrite grains (<5 μm, <1%) occur as rims on, and are in textural equilibrium with, early magnetite grains (Fig. 4.2a) and are also included in coarse antigorite and diopside with chalcopyrite. Pn2 is comprised of larger grains 10–30 μm in diameter, contain small Cr-rich spinel grains (2–3 μm, too small to determine the precise composition) and overprints or is in equilibrium with mt1 but is itself cut by coarse veins of antigorite. Pn3 is associated with or overprinted by late magnetite, antigorite and diopside 'veins' through fine matrix antigorite (1%, 10–30 μm, Fig. 4.2k). Pn4 occurs as euhedral grains ~50 μm in diameter which replaces or is synchronous with late antigorite veins (1%, Fig. 4.2l).

Hybrid rocks: Capu Corvoli. Pyrite is the dominant sulphide in both hybrid samples. In the talc schist sample, CO14-04 there are two texturally distinct forms of pyrite (py1 and py2). Py1 grains (5%) are ~100 μm in size, contain inclusions of Cr-rich spinel (~5 μm) pyrrhotite (po1, ~1-2 μm, Fig. 4.2b). Py1 grains have an iron hydroxide rim with ~5–10 μm inclusions of pyrrhotite (po2, Fig. 4.2b). Py2 (10%) occurs as large euhedral grains, (50–300 μm) which cuts the chlorite-talc1 matrix and appear to have undergone brittle deformation. Py2 has a talc rim (Fig. 4.2l) and

contains inclusions of talc that are up to 50 μm in diameter, though these are connected to the matrix. In CO14-03, pyrite exists as euhedral aggregates (~50–100 μm) on the rims of large magnetite grains (~3%, Fig. 4.2c) and within magnetite (<1%), although these are associated with fractures in magnetite. Matrix pyrites (30– 1000 μm, ~2%) are relatively euhedral and either occur as single grains or as aggregates.

4.4.1.3 Alloys

Serpentinites. Scanning electron microsocopy mapping techniques revealed trace 2–5 μm Pt-rich metal alloys on the rim of two heazlewoodite grains in CO13-31 (Fig. 4.2n), and SEM work revealed 1–5 μm Cu-rich alloys as inclusions within 'porous' Cr-spinel grains in CO13-40 and 5 μm kamacite grains (the Fe-rich end member of Fe-Ni alloys) along 1–2 μm veins of balangeroite (Mg-Ni-rich silicate veins) in CO13-33.

Hybrid rocks: Capu Corvoli. A ~10 μm^2 Pt-grain was detected towards the rim of py1 grain in CO14-04 (Fig. 4.2o).

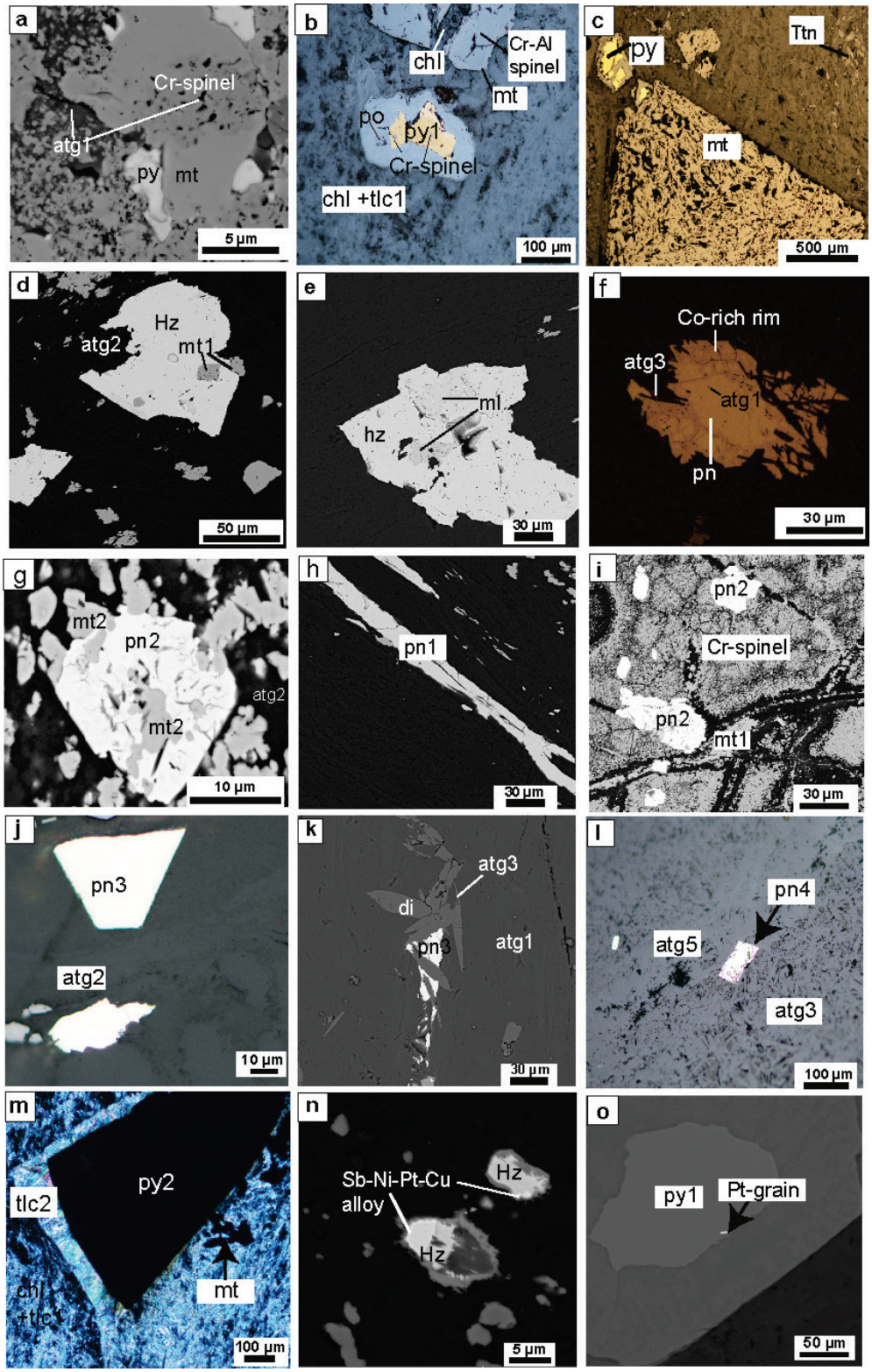

Figure 4.2. Images illustrating textural features in the samples. bse = backscattered electron image, rfl = reflected light image, xpl = cross polarised light image, py = pyrite, tlc = talc, hz = heazlewoodite, atg = antigorite, mt = magnetite, po = pyrrhotite, ttn = titanite. (**a)** porous Cr-spinel with antigorite inclusions and an Fe-rich spinel and pyrite rim in CO13-55 (bse) **(b)** py1 grains in CO14-04 with inclusions of chromite and an iron hydroxide rim, which contains inclusions of po (rfl). **(c)** pyrite rims on large magnetite grains in CO14-03 (rfl). **(d)** heazlewoodite grain with inclusions of mt1, overprinted by a later phase of antigorite (atg2) in CO13-31 (bse) **(e)** heazlewoodite grain with inclusions of millerite in CO13-31 (bse) **(f)** pentlandite grain in CO13-40 overprinted by atg3 on the rim (rfl) **(g)** pentlandite grain in CO13-21 with inclusions of magnetite (mt2) (bse) **(h)** elongate grains of pn1 in CO13-33 (bse) **(i)** pn2 overprinting earlier Cr-spinels and mt1 in CO13-33 (bse). **(j)** euhedral pn3 grains in association with antigorite veins in CO13-33 (rfl). **(k)** pn3 cut by larger laths of diopside and associated with diopside and magnetite 'veins' in CO13-55 (bse). **(l)** euhedral grains of pn4 overprinting atg3 and atg5 in CO13-55 (rfl). **(m)** py2 grains with a talc2 rim in C O1 4-04 (xpl). **(n)** Pt-rich metal a lloy on the rim of two heazlewoodite grains in CO13-31 (bse). **(o)** Pt-rich metal

4.4.2 Major element data

4.4.2.1 Whole Rock

Serpentinites - Serra di Pigno. Major and trace element data for the Serra di Pigno serpentinite samples (CO13-31, CO13-40, CO13-21, CO13-33 and CO13-55) are reported in Table 4.1. LOI gives a proxy for the extent of serpentinisation in the minerals where serpentine is the dominant hydrous phase, because pure serpentine contains ~13 wt% H_2O (Deer, Howie and Zussman, 1963). The LOI values of 10.7–12.1 wt% for the Serra di Pigno serpentinites suggest a high degree of serpentinisation, consistent with the high mode of antigorite in these samples and with analyses of subducted serpentinites which produce an average of 11.2 wt% LOI (Deschamps et al., 2013). The Serra di Pigno samples are all relatively depleted in terms of melt extraction (Al_2O_3 contents range from 1.19–2.01 wt%), and are almost completely depleted in CaO, (0.03–0.16 wt% CaO), with the exception of CO13-55 which contains 2.04 wt% CaO. The depletion of CaO is likely to reflect primary melt depletion, in addition to depletion associated with serpentinisation (e.g. Deschamps et al., 2013). Ni and Cr concentrations are consistent with the observed Al_2O_3 depletion and range from 2028–2287 ppm and 1812–2750 ppm, respectively. Carbon contents are low and similar in all serpentinites with 200–300 ppm C.

Sulphur contents are generally low and variable with concentrations ranging from 200–1100 ppm, where the highest concentrations are recorded in CO13-21 and CO13-33. The total iron content, reported as $Fe_2O_{3\ tot}$, varies from 6.42–9.09wt%. The concentration of Fe_2O_3 was calculated from FeO and $Fe_2O_{3tot,}$ and varies from 2.80–5.76 wt%, with the lowest concentration in CO13-55 and the highest in CO13-33.

Hybrid rocks: Capu Corvoli. The Capu Corvoli hybrid rocks CO14-03 and CO14-04 have lower LOI values than Serra di Pigno (7.24 wt% and 5.45 wt%, respectively). These values are consistent with the low proportion of serpentine in these samples and the high proportion of anhydrous minerals in CO14-03, particularly magnetite, and with the lower proportion of H_2O in talc in CO14-04 (~4.6 wt%).

On a whole rock scale, the Capu Corvoli samples differ in composition. In comparison to the Serra di Pigno serpentinites, the chlorite schist sample, CO14-03, has a higher concentrations of ΣFe_2O_3 (20.4 wt%) and Al_2O_3 (10.9 wt%), and a lower SiO_2 content (34.4 wt%). The high Fe content is consistent with the high mode of magnetite, and the high Al_2O_3 content is consistent with high modes of chlorite. In comparison, CO14-04 has similar Al_2O_3 and ΣFe_2O_3 concentrations to the Serra di Pigno samples with 1.82 wt% Al_2O_3 and 8.5 wt% ΣFe_2O_3, but is highly altered from mantle compositions with 24.8 wt% MgO and 58.7 wt% SiO_2, where such Mg and Si contents, in addition to the low LOI value is consistent with the high mode of talc. The CaO content of CO14-03 is similar to the Serra di Pigno serpentinites, whereas CO14-03 has a high CaO content (4.97 wt%).

In comparison to both primitive and depleted mantle values, CO14-03 has much lower Cr and Ni concentrations, with 621 ppm Cr and 613 ppm Ni, consistent with a mafic component (e.g. Spandler et al., 2008) while CO14-04 has similar Cr and Ni concentrations to the Serra di Pigno serpentinites with 2061 ppm Cr and 1579 ppm Ni, reflecting mantle concentrations of these elements.

The metagabbro proximal to the serpentinites was characterised for bulk composition (CO14-05, Table 4.1) and contains 7.45 wt% MgO, 12.3 wt% Fe_2O_{3tot}, 2.78 wt% TiO_2, 46.5 wt% SiO_2 and 13.7 wt% Al_2O_3.

Higher concentrations of sulphur are found in the Capu Corvoli hybrid rocks than the Serra di Pigno serpentinites at 540 ppm S in CO14-03 and 960 ppm S in CO14-04. The higher concentration of S in the Capu Corvoli hybrid samples is consistent with a higher mode of sulphides in these samples and with the presence of sulphur-rich pyrite as the dominant sulphide instead of the relatively S-poor pentlandite and heazlewoodite. The metagabbro proximal to the hybrid rocks contains 670 ppm of sulphur, which approximates the average of the CO14-03 and CO14-04 sulphur concentrations (Table 4.1).

	CO13-31	CO13-40	CO13-21	CO13-33	CO13-55	CO14-03	CO14-04	CO14-05
wt%	***Serpentinites***					***Hybrid***	***Rocks***	***Gabbro***
SiO_2	40.5	42.2	38.5	39.2	42.6	31.4	58.7	46.5
Al_2O_3	1.19	1.52	2.01	1.88	1.69	10.8	1.82	13.7
FeO	2.56	4.15	2.03	2.90	3.26	12.3	5.65	7.94
Fe_2O_3tot	6.54	9.09	7.07	8.98	6.42	20.4	8.48	12.3
MgO	39.0	36.4	38.7	38.4	37.7	17.9	24.8	7.45
CaO	0.03	0.16	0.06	0.04	2.04	4.97	0.03	9.94
Na_2O	0.13	0.11	0.13	0.09	0.14	0.10	0.03	1.76
K_2O	0.01	<0.01	0.01	<0.01	<0.01	<0.01	0.01	0.01
TiO_2	0.03	0.04	0.03	0.05	0.02	5.24	0.04	2.78
MnO	0.13	0.10	0.11	0.09	0.11	0.18	0.06	0.19
P_2O_5	<0.01	<0.01	<0.01	<0.01	0.02	0.09	0.01	0.11
LOI	11.7	11.2	12.1	11.6	10.7	7.24	5.45	5.13
Total	99.2	100.8	98.7	100.3	101.3	98.39	99.44	99.91
ppm								
C	200	200	200	300	200	200	300	570
S	300	300	700	1100	200	430	940	670
Cr	2245	2750	2470	2411	1812	621	2061	186
Co	103	113	130	114	99.2	123.1	85.2	45.5
Ni	2028	2287	2165	2254	2047	613	1579	89.6
Cu	3.10	n.a.	n.a.	8.40	4.30	24.3	18.5	105.4
Zn	39.0	63.0	37.0	40.0	32.0	92.0	56.0	67
Ga	1.80	2.60	2.90	2.10	2.70	19.90	3.70	17.4
As	<0.5	n.a.	n.a.	1.50	2.70	1.10	3.00	1.4
Se	<0.5	n.a.	n.a.	<0.5	<0.5	1.20	2.50	1.3
Mo	<0.1	<0.1	<0.1	<0.1	<0.1	0.10	<0.1	<0.1
Ag	<0.05	n.a.	n.a.	<0.05	<0.05	<0.05	<0.05	0.06
Cd	<0.02	n.a.	n.a.	<0.02	<0.02	0.03	<0.02	0.1
In	<0.01	n.a.	n.a.	0.01	<0.01	<0.01	<0.01	0.06
Sn	<1	<1	<1	<1	<1	2.0	<1	3
Sb	0.15	n.a.	n.a.	0.24	0.13	0.59	0.22	0.38
Te	<0.05	n.a.	n.a.	0.05	0.06	0.05	0.07	<0.1
Tl	<0.02	n.a.	n.a.	<0.02	<0.02	<0.02	<0.02	<0.02
Pb	1.10	n.a.	n.a.	1.10	0.70	0.80	0.60	<0.5
Bi	0.02	n.a.	n.a.	0.02	0.02	0.02	0.02	0.01
ppb								
Os	4	n.a.	n.a.	3	2	5	3	n.a.
Ir	4	n.a.	n.a.	3	3	<1	4	n.a.
Ru	6	n.a.	n.a.	5	6	2	5	n.a.
Rh	1	n.a.	n.a.	1	1	<1	2	n.a.
Pt	9	n.a.	n.a.	7	7	3	8	n.a.
Pd	11	n.a.	n.a.	6	6	8	8	n.a.
Re	<2	n.a.	n.a.	<2	<2	2	6	<2
Au	4	n.a.	n.a.	2	2	5	4	n.a.

Table 4.1 whole rock data, n.a. = not analysed, n.d. = not detected, < symbol followed by a number, represents concentrations less than the detection limit.

4.4.2.2 Sulphides

Electron probe-derived major element concentrations for sulphides analysed by LA-ICP-MS are provided in Table 4.2. Feature mapping revealed some compositional variation in small sulphides (<5 μm), that were excluded from LA-ICP-MS analysis. The sulphides detected in feature mapping are shown with small symbols in Fig. 4.3. In addition, Fig. 4.3 includes pyrrhotite, millerite and chalcopyrite compositions which were not analysed by LA-ICP-MS due to their small size. Formulae of sulphide minerals were calculated using charge balance and stoichiometric constraints. All sulphides are stoichiometric, including the minor sulphide phases of millerite (NiS) in CO13-21 and CO13-31, pyrite (FeS_2) and chalcopyrite ($CuFeS_2$) in CO13-55, and pyrrhotite ($Fe_{7.1}S_{8.0}$) in CO14-04. The average formulae of pentlandite grains is $Fe_{3.6}Ni_{4.9}Co_{0.3}S_{8.1}$ in CO13-33 (n=37) and $Fe_{3.7}Ni_5Co_{0.3}S_{8.1}$ in CO13-55 (n=33). Small amounts of Fe substitute for Ni in heazlewoodite grains in CO13-31 (up to 0.01 Fe per formula unit of Ni_3S_2). Minor Co and Ni replace Fe in pyrite (up to 0.01 cations per formula unit) in CO14-03 and CO14-04.

sample	**CO13-31**	**CO13-33**	**CO13-55**	**CO14-03**	**CO14-04**
phase	hz (n=24)	pn (n=36)	pn (n=30)	py (n=22)	py (n=61)
wt%					
Si	0.04(3)	0.03(2)	0.06(8)	<0.02	<0.02
Mg	0.09(4)	0.08(7)	0.07(4)	<0.02	<0.02
Ni	73.2(5)	37.1(5)	37(1)	<0.02	0.2(2)
Fe	0.2(2)	25.7(5)	26(1)	45.6(5)	46.8(4)
Co	<0.02	2.35(7)	2.3(2)	0.96(46)	0.2(4)
S	27.0(1)	33.2(4)	33.3(3)	53.8(2)	53.9(3)
Cu	0.058(3)	0.00(11)	<0.02	<0.02	<0.02
Se	0.30(2)	0.14(2)	0.15(2)	n.d.	n.d.
Bi	0.12(1)	0.13(1)	0.13(1)	n.d.	n.d.
As	0.33(2)	0.23(2)	0.26(3)	<0.02	0.02(5)
Sb	<0.02	<0.02	<0.02	<0.02	0.02(1)
Total	101.5(5)	99.2(9)	98.9(7)	100.4(3)	101.1(3)
mole %					
Ni	59.152(2)	29.0(3)	29(1)	-	-
Fe	0.188(1)	21.1(4)	21(1)	33.6(2)	33.2(1)
Co	-	1.82(5)	1.7(2)	0.7(3)	0.1(3)
S	39.973(1)	47.5(3)	47.7(3)	66.8(2)	66.6(2)
S/Fe+Ni+Co	0.67353(4)	0.92(1)	0.92(1)	1.99(1)	1.99(1)

Table 4.2 EPMA derived sulphide compositions (in wt%) with standard deviation (2σ) in brackets. The number after < indicates the detection limit. n.d. = not determined

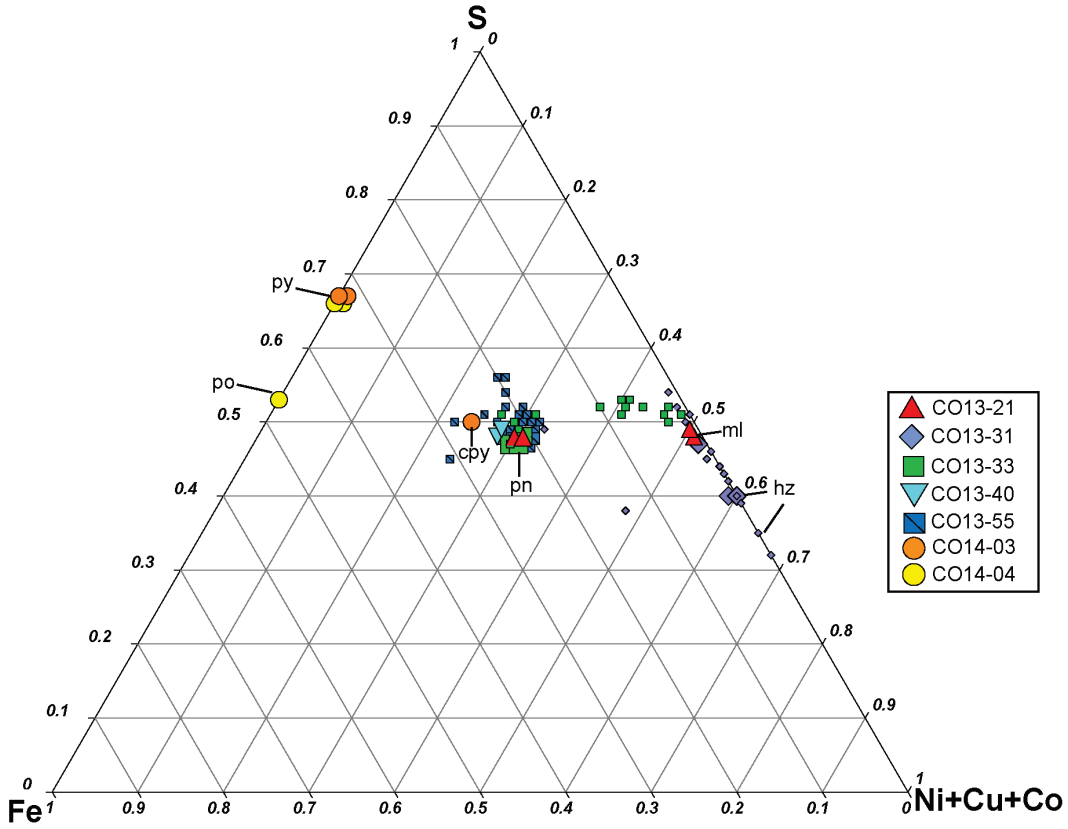

Figure 4.3: Major element compositions of sulphides in all samples plotted on the ternary diagram Fe+S+Ni+Cu+Co (mol %). Small symbols represent feature mapping data. Large symbols represent EPMA data (Table 4.2).

4.4.3 Highly siderophile elements (platinum group elements, Au & Re)

4.4.3.1 Whole Rock

Whole rock HSE data (Table 4.1) are normalised to primitive upper mantle (PUM; Becker et al., 2006; Fischer-Gödde et al., 2011; Fig 4.4a), and compared to subducted serpentinites from La Corea, Cuba (Blanco-Quintero et al., 2011), the pre-subduction analogues of serpentinised peridotite from the IL, which represents Tethyan lithosphere in an OCT or slow-spreading centre setting (Luguet et al., 2004) and the KFZ (a slow-spreading centre) peridotite (Luguet et al., 2003; Alard et al., 2005) (Fig. 4.4a). Comparison of hybrid whole rock samples to their protolith additionally required the use of data from the Zermatt-Saas gabbros and gabbro eclogites (Dale et al., 2009) and hybrid mafic/ultramafic rinds (Penniston-Dorland et al., 2012). All samples show relatively flat to minor fractionation patterns with

somewhat enriched Pd-group PGE (Rh, Pt, Pd; PPGE) over Ir-group PGE (Os, Ir and Ru; IPGE).

IPGE (Os, Ir and Ru). Osmium varies from 2 ppb in CO13-55 to 4 ppb in CO13-31. Iridium is of similar concentrations in all whole rock samples (3–4 ppb), with the exception of CO14-03 which contains <1 ppb Ir. The Ru concentration (2 ppb) of the Capu Corvoli hybrid rock, CO14-03, is comparable to concentrations in hybrid rinds from the Catalina schist (Penniston-Dorland et al., 2012) but the concentration of Ru in all other samples is comparable to PUM (5–6 ppb).

PPGE (Rh, Pt and Pd). Rhodium is similarly depleted relative to PUM in all samples at 1ppb, the detection limit, with only CO14-04 containing Rh significantly above the detection limit (2 ppb). Platinum is similar to PUM and KFZ peridotite values in all samples (6–9 ppb) with the exception of CO14-03 where the Pt content is comparable to that of hybrid mafic/ultramafic rocks (Penniston-Dorland et al., 2012; 2014) and peridotite from the IL (Luguet et al., 2004). Palladium concentrations in the Serra di Pigno (6–11 ppb) and Capu Corvoli (8 ppb) samples are consistent with Pd in serpentinites from the IL, where concentrations of up to 12 ppb are reported (Luguet et al., 2004), and KFZ peridotites which contain up to ~8 ppb Pd (Alard et al., 2005).

Re & Au. Only CO14-04 has a Re concentration significantly above the blank concentration (6 ppb). CO14-03 has the same concentration as the blank at 2 ppb, whereas all other samples have concentrations significantly lower (Fig. 4.4a). Au is above the detection limit in CO13-31, CO14-03 and CO14-04 at 4–5 ppb.

4.4.3.2 Sulphides

In-situ LA-ICP-MS-derived HSE data for sulphides are reported in Table 4.3. Sulphides that were large enough for LA-ICP-MS analysis include heazlewoodite in CO13-31, pn2 in CO13-33, pn4 in CO13-55, pyrite in CO14-03 and py2 in CO14-04.

There is significant heterogeneity in HSE concentrations in pentlandite and heazlewoodite, both within the same serpentinite sample and between different samples (Fig. 4.4b and c). Highly siderophile element concentrations in pyrite are

substantially lower than heazlewoodite and pentlandite, but the highest Re concentrations are found in pyrite.

IPGE (Os, Ir & Ru). Iridium-group PGE concentrations in heazlewoodite and pentlandite in the Serra di Pigno serpentinites, CO13-31, CO13-33 and CO13-55 are Ir ≤ Os < Ru. Ruthenium concentrations are similar to those recorded in sulphides from the KFZ (Luguet et al., 2003; Alard et al., 2005), with generally higher concentrations in heazlewoodite than pentlandite, with the exception of grain s4-3 in CO13-55.In comparison, Os and Ir concentrations are more variable; with comparable Os and Ir concentrations to the KFZ sulphides for two grains (CO13-31 s1 and CO13-55 s4-3) whereas most heazlewoodite grains contain similar Os and Ir to hydrothermal sulphides from the IL (Luguet et al., 2004) and pentlandite has lower Os and Ir concentrations, similar to those recorded in gabbroic sulphides (Dale et al., 2009). The pyrites in the Capu Corvoli hybrid rocks, CO14-03 and CO14-04, are depleted in IPGE relative to heazlewoodite and pentlandite, with concentrations of Os and Ir at or below the detection limit and Ru concentrations below the detection limit for pyrite grains in CO14-03 to up to 0.03 ppm in CO14-04. These concentrations are consistent with those reported for gabbroic eclogite pyrites (Dale et al., 2009).

PPGE (Rh, Pt & Pd). Platinum-group PGE concentrations are variable in pentlandite and heazlewoodite in the Serra di Pigno serpentinites, with Pt < Pd ≤ Rh. Pentlandite grains in CO13-33 have Rh and Pd concentrations up to 100 times higher than heazlewoodite and pentlandite grains in CO13-55.Pyrites in the Capu Corvoli hybrid rocks display similar trends to the Serra di Pigno serpentinites with Pt < Pd ≤ Rh, but have lower PPGE concentrations by up to an order of magnitude. Palladium is slightly lower in concentration than Rh, and Pt approximates or is less than detection limit.

Re and Au. Pyrite in the Capu Corvoli hybrid samples has higher concentrations of Re compared to the Serra di Pigno Ni-rich sulphides, where pyrites in CO14-04 have Re concentrations of up to 1000 times the Serra di Pigno sulphides, comparable to Re concentrations reported in KFZ sulphides (Luguet et al., 2003; Alard et al., 2005). There are higher concentrations of Re in the rim of pyrite grains, compared to the core in CO14-04. In comparison, CO14-03 has

variable concentrations of Re from below detection to 2 orders of magnitude lower than CO14-04 pyrites. Au concentrations are low or below the detection limit in most sulphide grains with the exception of two heazlewoodite grains in CO13-31 with 0.044 and 0.049 ppm Au, a pentlandite grain in CO13-55 with 0.191 ppm Au and all CO14-03 grains (0.003–0.086 ppm Au).

4.4.3.3 Spinels

IPGE (Os, Ir and Ru). Most spinel grains have concentrations of IPGE below detection limits, with detectable concentrations of Os and Ir only in one grain in CO13-31 (0.723 ppm maximum, mt1-2), where Ir<Os<Ru. Ruthenium is detectable in another two grains in CO13-31 (with a maximum concentration of 1.19 ppm), and six grains in CO13-33 (with maximum concentrations from 0.0049–0.476 ppm). IPGE were not detected in CO14-03 magnetites.

PPGE (Rh, Pt and Pd). Rhodium, Pt and Pd are detectable.in one grain, mt1-2 (with maximum concentrations of 0.140, 0.062 and 0.249 ppm, respectively) in CO13-31. In CO13-33, Rh is detectable.in three grains (with maximum concentrations of 0.009–0.049 ppm in grains m1-1, m1-4 and m1-9), Pt is below detection in all grains, and Pd is only detectable in grain CO13-33m1-1 (to a maximum of 0.025 ppm). 4 and m1-9), Platinum is below detection in all grains, and Pd is only detectable in grain CO13-33m1-1 (to a maximum of 0.025 ppm).

Table 4.3:HSE data for all sulphides (ppm). Standards include Po726 for PGE and Au, and Bon-NBS-6b for Re. <value reflects the detection limit.

	CO13-31									*CO13-33*					
ppm	s1 hz	s2-2 hz	s3-2 hz	s4-4 hz	s5-5 hz	s5-6 hz	s6-4 hz	s7-4 hz	s7-6 hz	s1-2 pn	s2-13 pn	s2-18 pn	s2-23 pn	s3-2 pn	s4-3 pn
Os	2.19	<0.003	<0.012	<0.017	<0.009	<0.004	<0.025	<0.038	<0.004	<0.032	<0.024	<0.013	<0.037	<0.036	<0.016
Ir	0.427	<0.002	<0.009	<0.005	<0.004	<0.003	<0.003	0.035	<0.003	<0.008	<0.006	<0.004	<0.007	<0.004	<0.009
Ru	3.84	3.55	4.09	4.02	4.08	3.91	3.37	3.84	3.63	2.28	2.22	1.90	2.10	2.41	2.04
Rh	<0.015	0.003	0.01	<0.004	<0.004	<0.004	<0.005	0.037	<0.004	0.043	0.043	0.077	0.141	0.028	0.156
Pt	<0.004	<0.005	<0.014	0.008	<0.009	<0.005	<0.014	0.086	<0.005	<0.017	<0.017	0.177	<0.025	<0.009	<0.018
Pd	0.028	0.016	0.026	0.025	0.019	0.021	0.023	0.158	0.018	0.184	0.458	0.138	0.227	0.051	0.310
Au	0.004	0.002	<0.013	0.006	0.009	<0.004	0.044	0.049	0.008	<0.013	<0.017	<0.009	<0.028	<0.017	<0.008
Re	0.031	<0.007	<0.007	<0.007	<0.010	<0.004	<0.008	0.032	0.009	<0.027	0.017	<0.009	<0.026	<0.018	<0.026

	CO13-55						*CO14-03*								
ppm	s4-8 pn	s3-3 pn	s2-3 pn	s1-3 pn	s4-2 pn	s4-3 pn	s1-1 py	s1-2 py	s1-3 py	s1-4 py	s1-5 py	s1-6 py	s2-1 py	s2-2 py	s2-3 py
Os	<0.058	<0.011	<0.041	<0.007	0.310	1.558	<0.004	<0.004	<0.004	<0.003	<0.008	<0.008	<0.003	<0.004	<0.004
Ir	<0.004	<0.005	<0.018	<0.004	<0.007	0.443	<0.001	<0.001	<0.001	<0.001	<0.001	<0.001	<0.001	<0.001	<0.001
Ru	2.44	2.51	2.39	2.38	1.71	7.62	<0.003	<0.001	<0.003	<0.003	<0.003	<0.002	<0.002	<0.003	<0.005
Rh	0.106	<0.003	0.031	<0.005	<0.015	0.047	<0.001	<0.001	<0.001	<0.001	<0.001	<0.001	0.015	<0.002	<0.002
Pt	<0.020	<0.012	<0.007	<0.003	<0.028	0.026	<0.002	<0.002	<0.002	<0.002	<0.002	<0.002	<0.003	<0.001	<0.004
Pd	0.217	0.033	0.055	0.007	<0.028	0.037	<0.002	<0.003	<0.003	<0.002	<0.002	<0.001	0.031	<0.002	<0.003
Au	<0.024	<0.005	<0.014	<0.006	<0.007	0.191	0.003	0.003	0.004	0.061	0.003	0.006	0.018	0.047	0.004
Re	<0.052	<0.008	<0.01	<0.007	<0.007	<0.004	<0.002	<0.001	<0.003	<0.001	0.005	0.0157	0.003	<0.004	0.008

ppm	s2-4 py	s2-5 py	s2-6 py	s2-7 py	s3-1 py	s3-2 py	s3-3 py	s3-4 py	s3-5 py	s1-1 py	s1-2 py	s1-3 py	s2-1 py	s2-2 py	s2-3 py
Os	<0.004	<0.004	<0.004	<0.003	<0.010	<0.013	<0.008	<0.004	<0.004	<0.003	<0.006	<0.006	<0.003	<0.007	<0.003
Ir	<0.001	<0.001	<0.001	<0.001	<0.001	<0.001	<0.002	<0.001	<0.001	<0.002	<0.002	<0.001	<0.001	<0.002	<0.002
Ru	<0.004	<0.003	<0.003	<0.006	<0.004	<0.003	<0.004	<0.003	<0.003	<0.003	0.012	0.003	0.014	0.006	0.009
Rh	<0.002	<0.001	<0.001	<0.002	<0.001	<0.001	<0.001	<0.001	<0.001	<0.002	<0.001	<0.0006	<0.001	<0.002	<0.001
Pt	<0.001	<0.002	<0.004	<0.003	<0.002	<0.004	<0.003	<0.001	<0.002	<0.004	<0.003	<0.002	<0.004	<0.004	<0.003
Pd	<0.002	<0.002	<0.001	<0.002	<0.003	<0.002	<0.002	<0.002	<0.002	<0.005	<0.005	<0.003	<0.002	<0.004	<0.005
Au	0.006	0.014	0.024	0.003	0.003	<0.007	0.006	0.086	0.025	<0.002	0.003	<0.003	<0.004	0.003	<0.003
Re	0.0105	<0.004	0.0105	0.005	0.004	<0.002	<0.003	0.0045	<0.003	0.489	0.463	0.491	0.445	0.466	0.374

ppm	s3-1-1 py	s3-1-2 py	s3-1-3 py	s4-1 py	s4-2 py
Os	<0.012	<0.005	<0.006	<0.012	<0.01
Ir	<0.012	<0.002	<0.003	<0.009	<0.008
Ru	0.002	0.029	0.026	0.015	0.014
Rh	<0.004	<0.003	<0.001	<0.003	<0.003
Pt	<0.004	<0.006	<0.004	<0.008	<0.011
Pd	<0.01	0.010	0.023	<0.005	<0.005
Au	0.003	<0.007	<0.007	<0.01	<0.009
Re	0.326	0.431	0.503	0.321	0.43

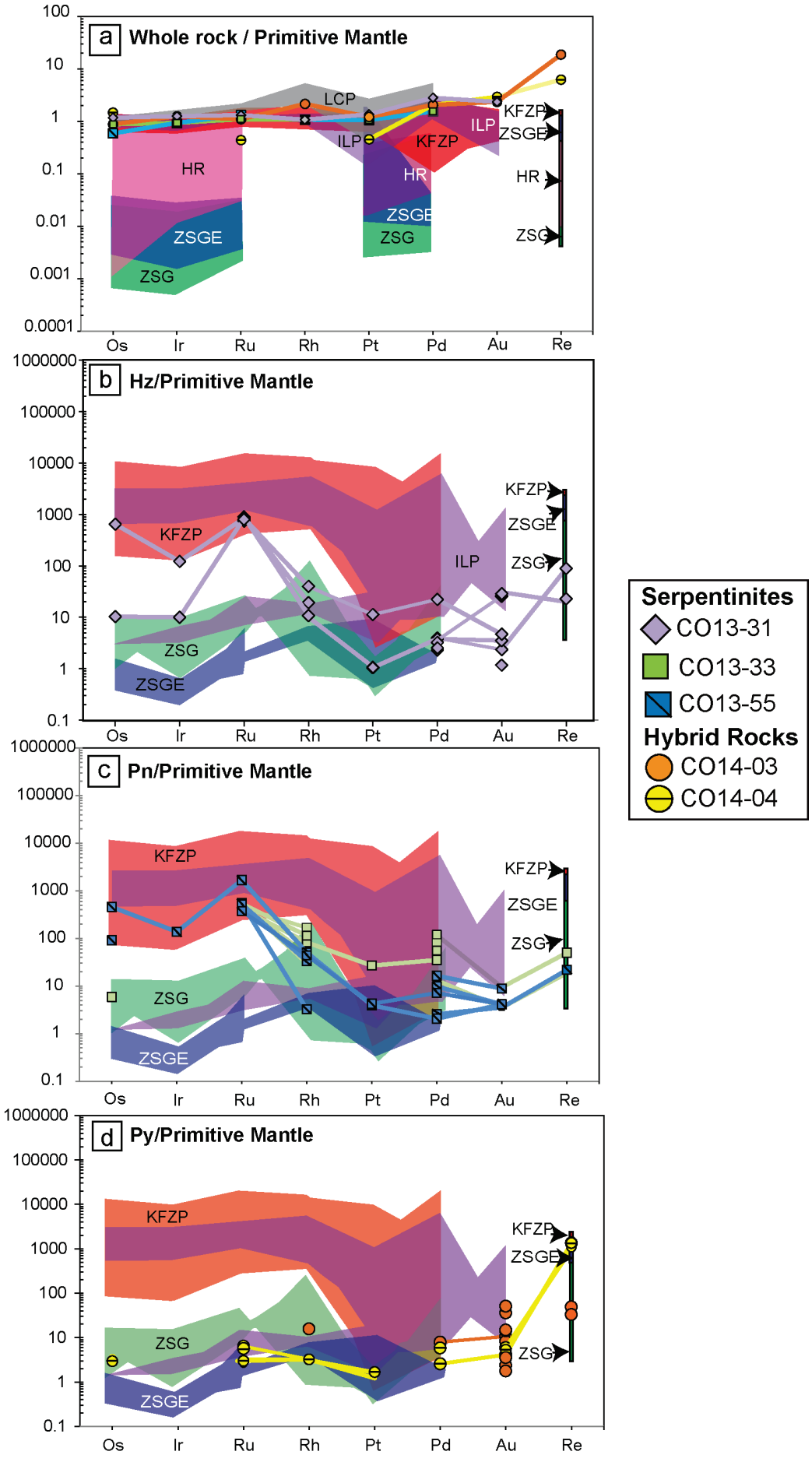
a Whole rock / Primitive Mantle
b Hz/Primitive Mantle
c Pn/Primitive Mantle
d Py/Primitive Mantle
Os Ir Ru Rh Pt Pd Au Re
LCP
ILP
KFZP
HR
ZSGE
ZSG
Serpentinites
CO13-31
CO13-33
CO13-55
Hybrid Rocks
CO14-03
CO14-04

Figure 4.4 Primitive upper mantle (PUM) normalised concentrations of HSE in **(a)** whole rock **(b)** heazlewoodite in CO13-31 **(c)** pentlandite in CO13-33 and CO13-55, and **(d)** pyrite in CO14-03 and CO14-04. For comparison to pre-subduction protoliths in (a), whole rock HSE data is plotted for slow-spreading centre peridotite from the Kane Fracture Zone (red; KFZP, Luguet et al., 2003; Alard et al., 2005), subducted serpentinite from La Corea, Cuba (purple; LCP; Blanco-Quintero et al., 2011), serpentinised peridotite from the Internal Ligurides, Ligurian Alps (dark grey; ILP; Luguet et al., 2004), and to assess lithological controls on HSE distribution, HSE concentrations of Zermatt-Saas gabbro (green; ZSG; Dale et al., 2009) and Zermatt-Saas gabbro eclogite (blue; ZSGE; Dale et al., 2009) and hybrid rinds from Penniston-Dorland et al. (pink; HR; 2012; 2014) are shown. For comparison of sulphide data, of (b) heazlewoodite (Hz), (c) pentlandie (Pn) and (d) pyrite (Py), pyrrhotite and pentlandite data from the Kane Fracture Zone (red; KFZP; Alard et al., 2005), pentlandite and pyrrhotite data from the Internal Ligurides, Ligurian Alps (purple; ILP; Luguet et al., 2004), and pyrrhotite/pyrite data from Zermatt-Saas gabbro (green; ZSG; Dale et al., 2009) and Zermatt-Saas gabbro eclogite pyrite data from the Zermatt-Saas (blue; Dale et al., 2009) are shown. Data is normalised to the primitive upper mantle HSE concentrations of Becker et al. (2006) and Fischer-Gödde et al. (2010).

4.5 Discussion

4.5.1 Bulk composition: protoliths

With the exception of one sample (CO13-55), the bulk compositions of the Serra di Pigno samples, have lower CaO contents than the depleted mantle (Salters and Stracke, 2004), with ratios of CaO/Al_2O_3 ranging from 0.03–0.10, compared to the depleted mantle CaO/Al_2O_3 ratio of 0.82. The low CaO is consistent with peridotites that have undergone lithospheric mantle serpentinisation in an oceanic setting (e.g. Deschamps et al., 2013 and references therein). In contrast, the mineralogy, bulk composition, textural and field relations of the Capu Corvoli samples, CO14-03 and CO14-04, are comparable to the ultramafic/mafic rocks previously described as 'hybrid' rocks in mélange zones (e.g. Spandler et al., 2008; Miller et al., 2009; Barnes et al., 2014). In detail, the mineralogy and bulk composition of CO14-03 and CO14-04 are consistent with chlorite and talc schist, respectively, similar to the high-pressure rocks from New Caledonia described by Spandler et al. (2008). The chlorite schist is defined by low SiO_2, high MgO, FeO and Al_2O_3, whereas the talc schist is defined by high SiO_2, and low LOI (Table 4.1). The hybrid nature of the Capu Corvoli samples originated either via hydrothermal fluid metasomatism, or mechanical mixing on the seafloor or during subduction prior to peak metamorphism (Fitzherbert et al., 2004; Spandler et al., 2008). In order

to trace HSEs in serpentinites through the subduction cycle, it is necessary to compare bulk HSE concentrations in the subducted samples with HSE concentrations in the inferred possible protoliths from OCT zones and slow-spreading centre settings for the Serra di Pigno samples and to hybrid and mafic rocks for the Capu Corvoli samples.

4.5.2 Comparison of bulk HSE concentrations to protoliths: whole rock scale mobilisation of HSE

4.5.2.1 Comparison to bulk HSE concentrations in mantle, slow-spreading centre and OCT ultramafic protoliths: Serra di Pigno

Bulk rock HSE concentrations of the Serra di Pigno samples are similar to those estimated for PUM, except for the slightly higher concentrations of Pd in serpentinite CO13-31. This is unexpected given that the samples are depleted in terms of melt extraction (with low Al_2O_3 content and likely low pre-serpentinisation CaO content), consistent with a residual mantle protolith. Residual mantle is progressively depleted in Re, Au, Pd, Pt and Rh (in order of elements removed first), compared to the PUM (Pearson et al., 2004; Becker et al., 2006; Fischer-Gödde et al., 2011), therefore lower concentrations of PPGE, Au and Re would be expected than those measured here but IPGE should be similar to PUM. Similar IPGE concentrations to PUM could suggest that IPGE mobilisation was limited on a scale greater than that of the fist-sized rock sample or greater scale. However, the concentrations of Au in CO13-31, and Pt and Pd in all Serra di Pigno samples exceed their expected depleted mantle protolith concentrations. The KFZ (a slow-spreading centre) and IL (an ultra-slow spreading centre to an OCT setting) are analogues of the possible pre-subduction setting of the samples studied here. Pd and Pt concentrations in the Serra di Pigno samples are similar to their seafloor analogues, for which Pd and Pt enrichment relative to mantle protoliths was considered to result from melt percolation in the mantle and low to moderate degrees of partial melting (Luguet et al., 2003; 2004; Alard et al., 2005). In such ultra-slow to slow spreading margin settings, the low degree of melting would likely not be sufficient to extract the sulphide melt completely from the mantle residue, and hence Pt and Pd would not be extensively depleted (e.g. Barnes et al., 2015). As the degree of melting increases, the residual melt becomes progressively

depleted in HSE hosts such as sulphides (e.g. Fischer-Gödde et al., 2011). Conversely, the Serra di Pigno samples have lower CaO concentrations (0.03–2.04 wt%), compared to the IL (0.80–2.09wt%) suggesting that the bulk composition underwent alteration during serpentinisation, thus possible Pd and Pt mobility during serpentinisation cannot be dismissed. Nonetheless, given the similar Pt and Pd concentrations in the samples studied here compared to periodites from the pre-subduction settings, there was probably little modification of the whole rock concentrations of these elements during subduction to blueschist-eclogite facies metamorphism.

4.5.2.2 Comparison to bulk HSE concentrations in mantle, hybrid mafic/ultramafic samples, gabbro and gabbro eclogite: Capu Corvoli hybrid rocks

With the exception of Ir and Ru in CO14-03, the Capu Corvoli samples have higher HSE concentrations than hybrid and mafic samples from other studies (Dale et al., 2009; Penniston-Dorland et al., 2014), and are similar to those of the KFZ (Luguet et al., 2003; Alard et al., 2005) and IL (Luguet et al., 2004). With the exception of Ir and Ru, the similarity of the HSE concentrations to pre-subduction ultramafic protoliths implies that the HSE budget has been retained from the ultramafic protolith during the hybridisation process. The hybrid rock, CO14-04, is has a higher Re concentration relative to PUM and slow-spreading centre serpentinites. Rhenium loss during prograde metamorphism of mafic rocks has been proposed previously (Becker, 2000; Dale et al., 2007, 2009; Penniston-Dorland et al., 2012). Re behaves incompatibly in the mantle (Brenan 2008; Fonseca et al., 2007; Mallmann and O'Neill, 2007), concentrating in crustal rocks such as gabbros and metabasalts, and therefore the transfer of Re to the ultramafic sample via fluids sourced from the dehydration of nearby mafic rocks may have occurred (e.g. Dale et al., 2009). Higher concentrations of Re could, therefore, be a function of physical or fluid-mediated mixing of gabbro/ultramafic rocks in the subduction channel, consistent with the hybrid nature of CO14-04. The shearing of the metagabbro and serpentinite most likely facilitated pervasive fluid flow and mixing between the lithologies, thus fluid transportation of Re is the preferred mechanism. Addition of Re during subduction is consistent with HSE data from Penniston-Dorland et al.

(2012), who report enriched Re concentrations in hybrid rinds relative to mafic cores in high-pressure mélange units from the Catalina Schist, Franciscan Complex and the Samana Metamorphic Complex.

The depletion of Ir and Ru in CO14-03 compared to the pre-subduction peridotite protoliths is also consistent with hybrid rind compositions (Penniston-Doland et al., 2012; 2014), and hence the depletion of these elements was probably inherited from the mafic component of the sample, where IPGE are retained in the residual mantle. However, the concentration of Os in CO14-03 is similar to protolith concentrations requires a mechanism for the decoupling of Ir and Ru from Os. The lack of Os depletion could be accounted for by Os retention in silicate minerals, which in CO14-03 could include actinolite, talc and chlorite, or discrete alloys derived from the ultramafic component of the sample (e.g. Dale et al., 2009), while Ru and Ir are lost. Thus, selective mobilisation of Ru and Ir over Os could have occured but the limited data presented here is not sufficient to determine the precise mechanism. Regardless, hybridisation could result in significant fractionation of IPGE at least on a whole rock scale.

4.5.3 Centimetre to millimetre scale redistribution of HSEs

Constraints on the timing of the growth of major hosts to HSE, and constraints on the timing of sulphide growth and determination of HSE concentrations in mineral hosts can be used to trace centimetre to millimetre scale HSE redistribution in serpentinites through the subduction cycle. Sulphide and oxide parageneses, which are used to constrain both the aO_2 and aS_2, and the distribution of HSE through the metamorphic evolution of the samples, are summarised in Fig. 4.5. The complete mineral parageneses are provided in Appendix C11.

4.5.3.1 Serra di Pigno mineral parageneses

Serpentinites distal to other lithologies (CO13-31 and CO13-40)

Both CO13-31 and CO13-40 serpentinite samples contain Cr-Al spinel and magnetite (mt1). Cr-Al spinel cores are attributed to mantle growth prior to serpentinisation, although are considered to have undergone alteration during serpentinisation and prograde metamorphism (see chapter 5). Mt1 in both samples

occurs as rims on seafloor bastite and contains inclusions of prograde atg1 and therefore postdates early serpentine phases. Chlorite growth occured during prograde-peak metamorphism from antigorite dehydration, overprinting atg1 and cross-cutting atg2 veins. Chlorite rims on mt1 therefore further constrains mt1 to growth during or prior to prograde metamorphism. Orientated and foliated atg1 in both samples has a fine and interlocking texture consistent with prograde growth (e.g. Li et al., 2004), and defines the dominant foliation.

Sulphide phases in CO13-31 include millerite, pentlandite and heazlewoodite. Millerite contains inclusions of prograde antigorite (atg1) and is included in later-grown phases such as heazlewoodite. It is uncertain as to whether the antigorite inclusions recrystallized from earlier serpentine phases such as lizardite. and therefore millerite and mt1 growth could have occurred during seafloor serpentinisation. However, millerite maintained stability during subduction. Heazlewoodite and Co-rich pentlandite (trace) are assigned to prograde to peak metamorphism based on their aassociation with the prograde to peak phases; chlorite, balengeroite and antigorite. Balangeroite growth has been ascribed to prograde metamorphism within the antigorite stability field in both the Piemonte zone in the Alps (Groppo and Compagnoni, 2007), and Sasaguri, Japan (Evans and Kuehner, 2011). Heazlewoodite contains inclusions of prograde atg1 and mt1, and is also associated with or overprinted by balangeroite and atg2 veins. Therefore, heazlewoodite grew prior to initial exhumation, and given its association with balangeroite, heazlewoodite growth occurred during subduction. Sulphide phases in CO13-40 include early chalcopyrite associated with Cu-alloys within porous Cr-spinel, and pentlandite. Pentlandite overprints the foliation defined by fine grained antigorite, and therefore growth is attributed to prograde to peak metamorphism. A late generation of antigorite cuts pentlandite and mt1, and further constrains pentlandite to growth prior to retrogression (Fig. 4.5a, Appendix C10, C11).

Serpentinites proximal to metasediments and metagabbro (CO13-21, CO13-33 and CO13-55)

In all samples proximal to other lithologies, Cr-rich spinel is interpreted to have been present prior to subduction, and modified during serpentinisation and/or prograde metamorphism (see chapter 5). Chalcopyrite, Pn1 and atg1, and

heazlewoodite, kamacite and balangeroite in CO13-33 record similar textures to CO13-31, and are therefore are inferred to have grown during prograde metamorphism. Chlorite is associated with peak metamorphism. Pn2 growth in the proximal samples is attributed to peak metamorphism through to early exhumation because pn2 replaces chlorite and/or coarse antigorite (atg3), and contains inclusions of fine prograde antigorite and, in CO13-21, is synchrounous with mt2. In CO13-21, further supporting evidence for pn2 recystallisation during this stage includes the network and brecciated texture of mt2, which is consistent with fluid infiltration under brittle conditions such as those expected during retrogression

Late pentlandite, pn3, is observed in CO13-33 and CO13-55, and occurs as euhedral grains in the matrix, overprinting retrogressive atg4 veins, consistent with an exhumation origin. In CO13-55, late retrogressive atg5 veins and diopside overprint pn3. Diopside growth is constrained to retrogression because it overprints prograde antigorite (atg1) and peak chlorite and occurs as randomly orientated idioblastic prisms, consistent with retrogressive diopside previously described (Groppo and Compagnoni, 2007). Pn4 , hosted in sample CO13-55, is attributed to a later stage of retrogression associated with exhumation due to its association with antigorite veins and lack of deformation (Fig. 4.5a, Appendix C10, C11).

4.5.3.2 Capu Corvoli mineral parageneses

Chlorite schist (lower contact with metagabbro): CO14-03

There is no evidence for the preservation of primary or seafloor phases in CO14-03. Chlorite and antigorite are the texturally earliest phases and grew during prograde to peak metamorphism, and possibly during the early stages of exhumation. Magnetite growth is constrained to growth during the onset of exhumation because magnetite cuts the foliated chl1 and antigorite matrix, and therefore postdates these phases and the main foliation. Furthermore, magnetite has undergone brittle deformation and a later retrogressive generation of chlorite (chl2) cuts magnetite grains. Pyrite grew during a later stage of exhumation after magnetite, as evidenced by its occurrence as rims on, or in fractures within large euhedral magnetite grains (Fig. 4.5b, Appendix C10, C11).

Talc schist (upper contact with metagabbro): CO14-04

The earliest assemblage consists of Cr-Al spinel, a Pt-rich grain and pyrrhotite (po1), which are either primary or attributed to seafloor alteration. Pyrrhotite1, the Pt-rich grain and Cr-Al spinel are included in pyrite (py1) and are therefore synchronous. Talc1, py1, magnetite and po2 growth is constrained to prograde metamorphism or peak metamorphism. Talc1 is attributed to metasomatism during prograde metamorphism (e.g. Spandler et al., 2008). Pyrrhotite2 is included in iron hydroxide rims on py1 and is therefore texturally later than py1. Inclusions of primary or seafloor phases in py1, and the fact that py1 and po2 cut the talc1 matrix, suggests that py1 and po2 grew late during, or after, prograde metamorphism. Magnetite is proposed to be synchronous with py1 because both py1 and magnetite texturally postdate Cr-spinel. Chlorite is associated with peak metamorphism and cuts Cr-spinels and magnetite, providing further constraints on the prograde growth of py1 and magnetite. Pyrite2 growth is constrained to an early stage of exhumation, because py2 cuts the prograde talc1 matrix, and chlorite associated with peak metamorphism. Pyrite2 growth is further constrained to initial retrogression prior to decompression by coarse talc rims on py2. Coarse talc (talc2) cuts the talc1 and chlorite matrix, and therefore is texturally late (Fig. 4.2o). Talc2 rims are likely to be recording decompression associated with exhumation, as proposed for high pressure serpentinites (Evans & Powell, 2015) (Fig. 4.5b, with exhumation, as proposed for high pressure serpentinites (Evans & Powell, 2015) (Fig. 4.5b, Appendix C10, C11).

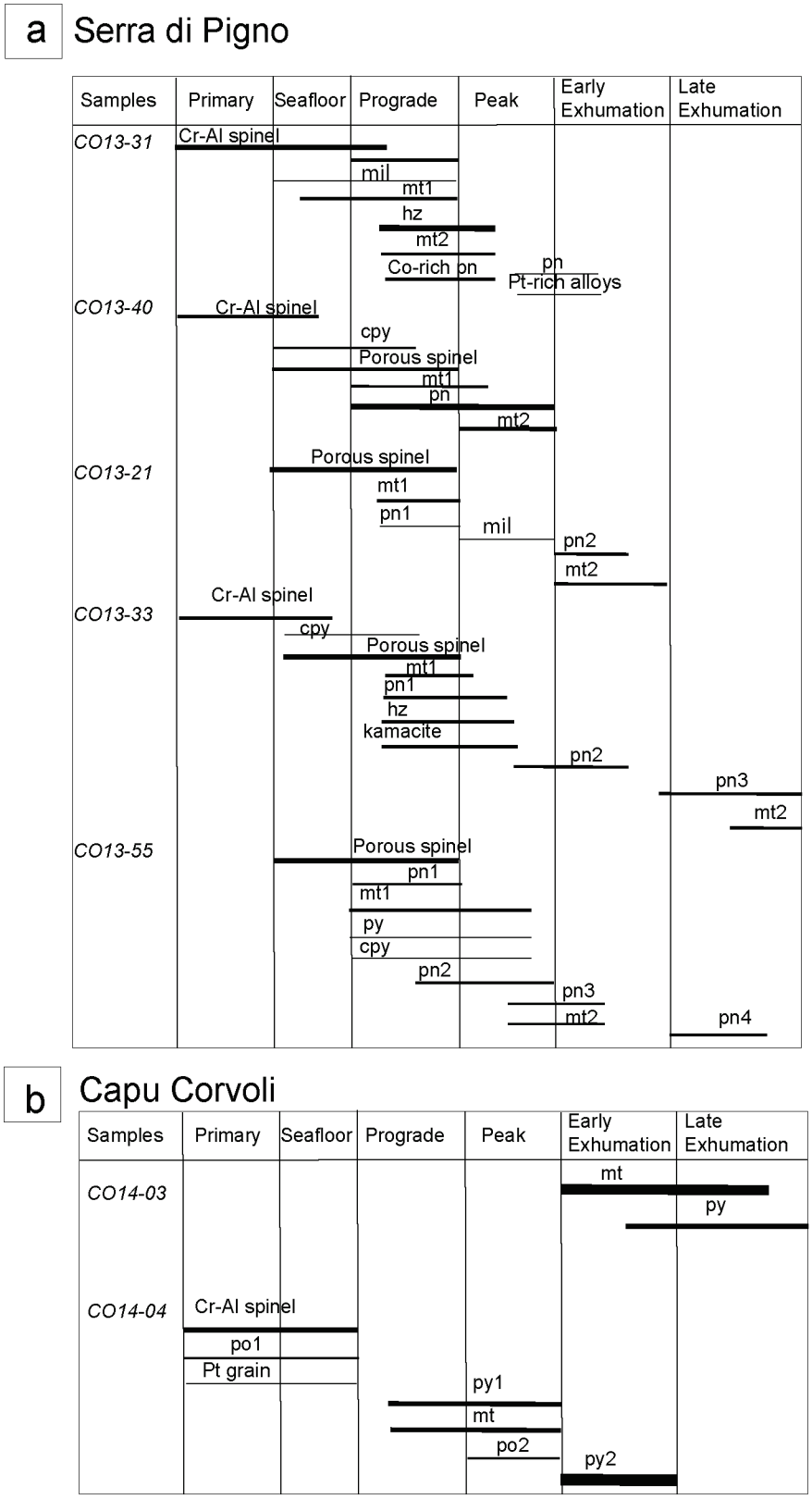

Figure 4.5 Summary sulfide and oxide parageneses for (a) Serra di Pigno samples and (b) Capu Corvoli samples. Full mineral parageneses can be found in Appendix C11.

4.5.3.3 Redox evolution: evidence from sulphide parageneses

Evans et al. (2017) present activity-activity diagrams of oxide and sulphide stability as a function of aO_2 and aS_2 at high pressure (2 GPa, 555 ºC). The buffered assemblages are oxide and sulphide assemblages; awaruite-heazlewoodite-magnetite-pentlandite-pyrite-pyrrhotite-magnetite, and hematite-pyrite-magnetite. Fields of sulphide ± magnetite assemblages in the Serra di Pigno and Capu Covoli samples that were encountered during their metamorphic evolution were plotted on the activity-activity diagram (Fig. 4.6). It is noted that lower temperatures and pressures may be recorded at Serra di Pigno (blueschist–eclogite facies; 414–471°C and 1.3–2.6 GPa; Vitale Brovarone, 2013) than Capu Corvoli (eclogite facies; estimated 435–507 ºC and 1.9–2.6 GPa; Ravna et al., 2010; Vitale Brovarone et al., 2011; 2013). However, with the exception of the millerite-vaesite reaction position, the relative positions of the buffering assemblages are unaffected by a pressure increase from 0.5 to 2 GPa (Evans et al., 2017). Consequently, trends of aO_2 and aS_2 for specific sulphide assemblages are not influenced by any differences in metamorphic conditions recorded at the two localities. In addition, kamacite is not included in the phase diagram, but it is proposed that metal alloys such as kamacite record similar aS_2, with slightly lower aO_2 than awaruite + magnetite (Frost, 1985; Schwazenbach et al., 2012; Foustoukos et al., 2015).

The trends in $aO_2 - aS_2$ are inconsistent for the Serra di Pigno serpentinites as a function of the stage of metamorphism the mineral assemblages are recording, or sample position relative to other lithologies (Fig. 4.6a and b). Serpentinite samples record increases and decreases in $aO_2 - aS_2$ during progressive metamorphism, without any systematic link to either stage of metamorphism or the nature of adjacent lithologies. Mineral assemblages are low variance with two or three phases in most cases, suggesting that the environment is rock-buffered, so the composition of the fluids infiltrating the rocks are in equilibrium with the mineral phases (e.g. Goodge and Holdaway, 1995). Therefore, the mineralogical evolution of the Serra di Pigno serpentinites was controlled by rock-buffered fluid-rock interaction.

In contrast, hybrid ultramafic/mafic samples from Capu Corvoli, plot at higher aS_2 than the Serra di Pigno serpentinites (Fig. 4.6c). Mafic rocks prior to subduction generally contain more sulphur than serpentinites (e.g. Delacour et al., 2008) so the proximity of the hybrid samples to metagabbro could explain the increased aS_2. On the other hand, measurement of the sulphur content in the metagabbro sandwiched between CO14-03 and CO14-04 approximates the mean of the two samples (685 ppm S) with a sulphur content of 670 ppm S (Table 4.1). It is therefore possible that sulphur loss from the metagabbro occurred during metamorphism. Thus, metasomatic or mechanical mixing of mafic and ultramafic rocks during subduction could have increased the sulphur concentration (and hence aS_2). The high variance of the mineral assemblage in CO14-03, with one oxide or sulphide phase at any given stage (i.e. magnetite or pyrite) suggests that the system is fluid buffered. On the other hand, CO14-04 may record a change from rock-buffered with two or three phases to a fluid-buffered assemblage with one phase (py2) during the transition from prograde to early retrograde metamorphism, consistent with fluid infiltration during exhumation.

Hybrid rocks are considered as important carriers of volatile elements in subduction zones, given their stability to greater depths than serpentinites (Spandler et al., 2008) consistent with elevated aS_2 and possibly aO_2 in the Capu Corvoli hybrid samples. The loss of hydrogen-bearing fluids from the hybrid samples during prograde metamorphism would also increase the aO_2 and aS_2 in the residual rock, but the assemblages related to prograde through to exhumation in CO14-04 record an increase in aO_2 and aS_2, suggesting the infiltration of oxidised fluids during exhumation. The dehydration of mafic and metasedimentary rocks at the blueschist-eclogite transition, consistent with the P-T conditions recorded by the samples presented here, has been proposed to be the major source of fluids for metasomatism, and hence hybrid rock production (Spandler et al., 2008).

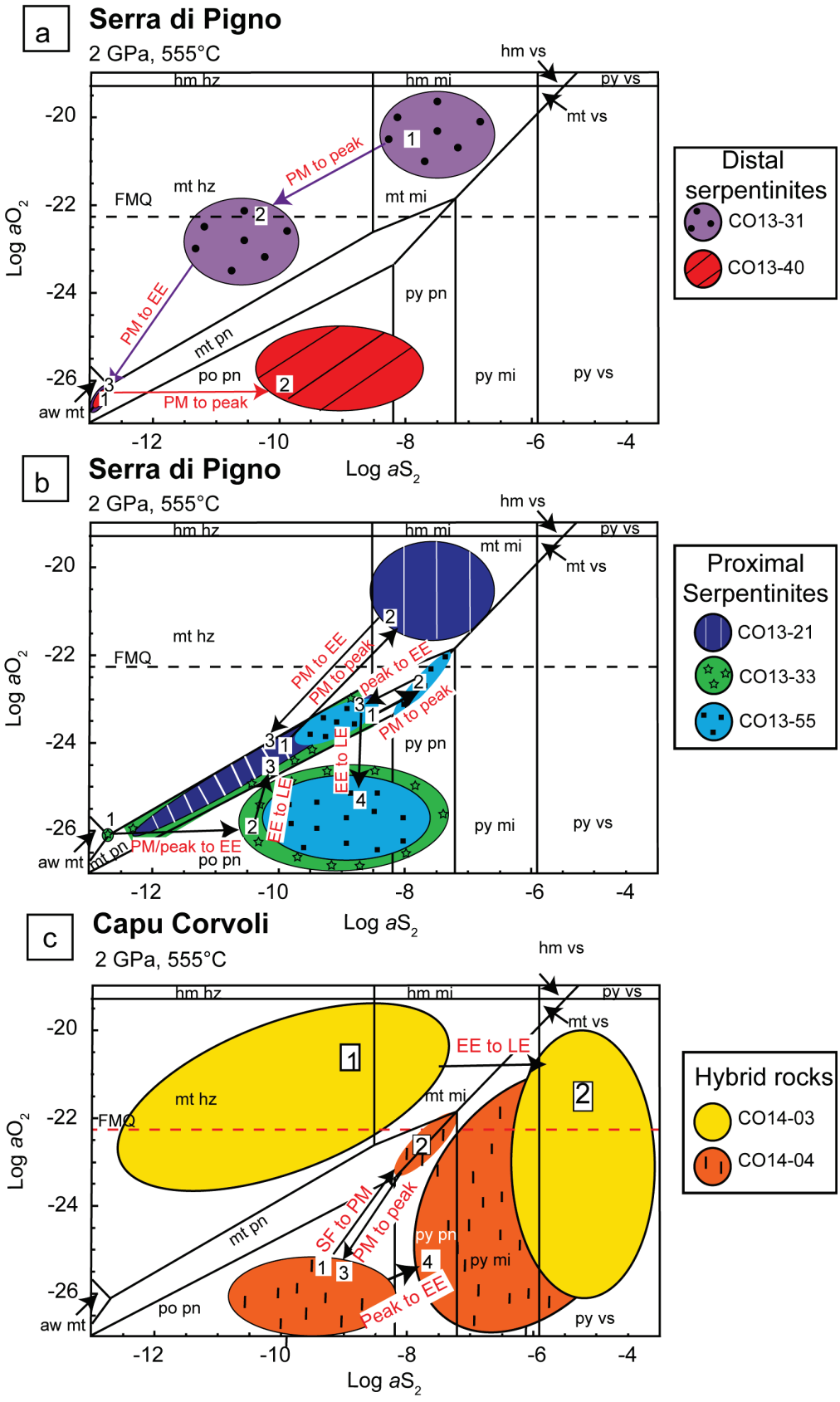

Figure 4.6 Activity-activity aO_2–aS_2 diagram at 2 GPa after Evans et al. (2017) for (a) Serra di Pigno serpentinites distal to other lithologies, (b) Serra di Pigno serpentinites proximal to other lithologies and (c) Capu Corvoli hybrid rocks. The numbers and arrows indicate the order of stability of the mineral assemblages from early (1) to late (e.g. 3). PM, peak, EE and LE are abbreviations for the stage of metamorphism. PM = prograde metamorphism, Peak = peak metamorphism, EE = early exhumation and LE = late exhumation. FMQ= Fayalite-magnetite-quartz buffer.

4.5.3.4 Mineral scale HSE distribution

The sulphides analysed from samples from both Serra di Pigno and Capu Corvoli are depleted in HSE relative to sulphides from the KFZ (Alard et al., 2005) and the IL (OCT setting; Luguet et al., 2004), with the exception of Ru and to a lesser extent, Pd and Pt in the Ni-sulphide grains, Re in Capu Corvoli pyrites and Au in CO14-03 pyrites. However three hydrothermal sulphide grains sampled from the IL (Luguet et al., 2004), also record depleted PGE contents relative to unaltered IL and slow-spreading centre sulphides. The IL hydrothermal sulphides have similar Os and Ir concentrations to the Ni-rich sulphides from Serra di Pigno but do not show a significant Ru enrichment. In addition the IL hydrothermal sulphides are more enriched in PPGE than all sulphides except pentlandite related to peak to early exhumation from CO13-33, which record similar PGE concentrations.

Consistent with Re enrichment on a whole rock scale (Fig. 4.4a), pyrites in the Capu Corvoli samples (particularly CO14-04), are enriched in Re relative to the Ni-rich sulphides from Serra di Pigno and slow-spreading centre sulphides. In this section, mechanisms of variable HSE depletion, and elevated Ru and Pd concentrations in the sulphides are discussed.

HSE depletion in sulphides: sulphur addition

One possible explanation for HSE depletion in high-pressure sulphides is an increase in the mode of sulphides. The addition of sulphur would increase the mode of sulphides and thus HSE concentrations in the sulphides would be diluted. This is a plausible explanation for samples with a high bulk sulphur concentration such as CO13-33 (1100 ppm S) and the Capu Corvoli samples, where CO14-03 and CO14-04 have S concentrations of 430 ppm and 940 ppm, respectively. However, this explanation does not apply in all cases because CO13-31 and CO13-55 have lower bulk S contents of 300 ppm and 200 ppm, respectively. Furthermore, comparison of the sulphur contents with those from other slow-spreading centre or OCT serpentinites from the Ligurian and Voltri Massif (Alt et al., 2012), demonstrates that it is difficult to constrain changes in sulphur content during subduction, because pre-subduction sulphur contents are extremely variable, and the variation is most likely retained during subduction (Alt et al., 2012). The northern Appenine serpentinites have highly variable sulphur concentrations that

range from ~200–1400 ppm, where these serpentinites are considered to have been part of slow to ultra-slow spreading centre or OCT mantle lithosphere, like the Alpine Corsican samples, except they were not significantly affected by high pressure metamorphism (Alt et al., 2012). A similar variation in sulphur concentrations is observed for subducted serpentinites from the Voltri Massif, with sulphur contents of ~130–2400 ppm (Alt et al., 2012). The variable sulphur contents are consistent with the lack of systematic trends between sulphur and PGE contents observed in samples from the same locality (Luguet et al., 2004).

HSE depletion in sulphides: alloy formation and redox implications

An alternative explanation for sulphide HSE depletion is the presence of other minerals in which HSE are more compatible. Although debated in the literature, IPGE (Os, Ir and Ru) can be highly compatible and Pd and Pt moderately compatible in primary Cr-rich spinel phases (Hart and Ravizza 1996; Puchtel and Humayun 2001) and thus their growth before sulphides, could account for HSE depletion in sulphides. Yet, with the exception of one grain in the sample distal to contacts, spinels are depleted in HSE (Appendix C9). The porous texture of some spinel grains and magnetite rims on Cr-rich spinel suggests that primary spinel has been strongly altered to more Fe^{3+}-rich compositions. The observed low HSE concentrations in the spinels presented here are consistent with experimental data, where derived partition coefficients for Ru, Ir, Rh are lower for Fe^{3+}-rich spinels, and Pt and Pd are highly incompatible (Brenan et al., 2012). Thus, it is likely that HSE were redistributed from primary spinel grains to other phases during serpentinisation and implies that the ferric iron content and Cr content of the whole rock, and hence mode of magnetite relative to Cr-spinel serves as a useful indicator for the distribution of HSE prior to *in-situ* analysis. Metal alloy grains are a potential candidate as hosts for HSE because Pt-bearing alloys were observed on the rim of two heazlewoodite grains in CO13-31, and near the rim of a py1 grain in CO14-04, and kamacite was observed in balangeroite veins in CO13-33. Platinum-bearing grains therefore may account for variable depletion in Pt in the Ni sulphides and depletion in pyrite in Capu Corvoli samples. Alloy formation may also explain depletion of Au in the Ni-rich sulphides where Au probably occurs as native grains

(Luguet et al., 2004), or as Pt-Au alloys (Lorand et al., 2010), which were not observed in the samples.

Highly siderophile element distribution is sensitive to redox (e.g., Mungall et al., 2006). In agreement with the activity-activity diagrams (Fig. 4.6), Pt alloys are considered to be stable under low fO_2 (Mungall and Brenan, 2014), and Pt exsolves from sulphide under low fS_2 (Peregoedova et al., 2004) therefore the observed Pt-bearing alloys on the edge of sulphides likely reflects more low fO_2 and fS_2 and hence increasingly reducing conditions. Overall, PGE depletion in the sulphides compared to seafloor pre-cursors could a shift to lower fO_2 and fS_2 during subduction, as alloys host the majority of PGE.

Elevated Ru in the Ni-rich sulphides of the Serra di Pigno samples

Bulk Ru is similar to the PUM concentrations in the Serra di Pigno serpentinites, whereas sulphides are enriched in Ru relative to PUM. Therefore, Ru mobility occurred on a scale no greater than a centimetre. Higher Ru contents in the studie serpentinites compared to gabbro and gabbro eclogite sulphides (Dale et al., 2009, Fig. 4.4b and c) could be accounted for by the compatibility of Ru during mantle melting (Penniston-Dorland et al., 2012). Yet, the relative depletion of the other IPGE, Os and Ir, which should behave similarly to Ru and concentrate in the mantle rather than the crust, requires an alternative explanation. Likewise, the destabilisation of primary spinel, a phase in which IPGE are compatible in, would release Os, Ir and Ru, consistent with the low concentrations of IPGE the altered spinels in the samples (Appendix C9) but Os and Ir in addition to Ru, would also be expected to be incorporated into the Ni-rich sulphides, and therefore Ru enrichment in Ni-rich sulphides requires an alternative explanation.

Metal alloy formation or destabilisation could control the distribution of Ru. The exsolution of Os, Ir and Pt-rich metal alloys under reducing conditions (Foustoukos et al., 2015) and/or low aS_2 (Fonseca et al., 2009, 2012; Gonzaléz Jimenéz et al., 2012), could leave residual Ru-rich sulphides during subduction and/or early exhumation suggesting mobility on less than a millimetre scale. Increased Ru in heazlewoodite compared to pentlandite, where heazlewoodite reflects lower aS_2 than pentlandite (Fig. 4.6), is consistent with this explanation.

Pd enrichment in the Serra di Pigno sulphides

Texturally late sulphides inferred to be associated with exhumation in the Serra di Pigno samples are relatively enriched in Pd compared to earlier sulphides. Palladium is particularly enriched in pentlandites in the sample in contact with metaquartzite and metagabbro (CO13-33) but not in pentlandites in the sample proximal to calcschist and metagabbro (CO13-55). Compared to seafloor sulphides, moderate enrichment is also evident in heazlewoodite grains in the sample distal to lithological contacts. The noticeable difference in Pd concentration between pentlandites in CO13-33 compared to pentlandites in CO13-55 suggests that Pd content is not solely a function of the sulphide composition (i.e. Ni, S or Fe content), and thus differences may instead reflect Pd mobilisation. The whole rock Pd is similar in both CO13-33 and CO13-55, so Pd mobilisation would be on a centimetre scale or less. Instead, the timing of pentlandite growth could be a dominant control on Pd distribution between the sulphides. In the case of CO13-55, pn4 is texturally late, and therefore, Pd may have been retained in earlier phases of pentlandite, and as a result, late pentlandite hosts negligible Pd. In contrast, pn2 in CO13-33 is attributed to peak metamorphism to early exhumation, which could explain its relative Pd enrichment. Unfortunately, the small grain size of the earlier sulphide phases in CO13-55 precluded the ablation of early grains to fully test this hypothesis. However, the heterogeneous but relatively high Pd concentrations in CO13-33 implies equilibration on limited length scales, consistent with low fluid-rock ratios, and thus restricted mobilisation of Pd, even at the centimetre scale. In addition, given the similar Pd concentration of CO13-33 sulphides to IL (Luguet et al., 2004) hydrothermally altered sulphides, any mobilisation would have occurred prior to subduction.

However, Pd/Ru =~1 in the whole rock, whereas Pd/Ru =~0.001–0.002 in the sulphides, which suggests that sulphides only host ~0.5-1% of the Pd budget in the rocks. Therefore, a phase with high Pd/Ru must be present. Pd can be hosted in native Pd grains in solid solution with native Pt, such as those observed in Monte Maggiore, in the north of Cap Corse (Ohnenstetter et al., 1992) and within chalcopyrite (e.g. Luguet et al., 2004; Dale et al., 2009). Unfortunately, ^{105}Pd is subject to interference by ^{63}Cu, so it is difficult to assess whether their apparent correlation in laser ablation time resolved profiles are discrete phases within the

sulphide grains or a result of interference. However, Pd only correlates with Cu in one heazlewoodite grain in CO13-31 (Appendix C3), whereas in other pentlandite and heazlewoodite grains this correlation is not significant suggesting that Pd could exist as discrete native phases (up to ~5 μm as determined from the ablation of 1μm per second). The Pd spikes were not observed in most profiles, so the relative enrichment of Pd in CO13-33 pentlandites compared to CO13-55 pentlandites is also likely a function of timing of growth as described above. The inclusion of Pd-rich phases in sulphides associated with peak metamorphism would imply that these discrete phases grew at a relatively early stage, thus their retention and the high concentration of Pd in the sample containing prograde to peak sulphide phases only (CO13-31, Table 4.1, Fig. 4.4a), suggests that Pd was retained during subduction in the Serra di Pigno serpentinites.

4.5.3.5 The role of alloys as hosts of HSE: mass balance calculations

The formation and stability of alloy grains could explain the observed distribution of HSE in the Serra di Pigno samples and a small number of alloy grains were observed in the samples. Two Pt-bearing alloy grains were observed in CO13-31 and kamacite is present in balangeroite veins in CO13-33 but none were observed in CO13-55, in spite of utilising high resolution feature mapping techniques and assessing laser ablation time resolved profiles for peaks of these elements within the sulphide grains. It is therefore possible that alloys are present but in such low modes that they are not always observed. To test this hypothesis, mass balance calculations were carried out to determine the volume % of the alloy in the rock, and the probability of observing them in a single thin section. Note that these calculations may overestimate the probability of alloy observation, because small sulphide phases which were not analysed by LA-ICP-MS may contain some of the HSE budget.

Based on the few observed alloys in thin section, the area of individual Pt-bearing alloys is 25 μm^2 or less, with the smallest observed Pt-bearing alloy on the rim of heazlewoodite ~2 μm^2 in size. The size of the thin section is ~1.24 x 10^9 μm^2. If the area of the alloy grains is taken as 25 μm^2, the mode of one alloy grain is 2 x 10^{-6} vol%. The average density of alloys is taken as 12 g/cm^3, though this value could be between 8 and 20 g/cm^3, depending on the composition of the alloy. Most

of the thin section is comprised of serpentine in the case of the Serra di Pigno samples, or talc and chlorite in the case of the Capu Corvoli samples, where all three phases have an average specific gravity of ~2.75 g/cm^3, so the average density of alloys would be ~4 times that of serpentine. By weight, the mass of the alloy in a thin section containing a 25 μm^2 alloy grain would therefore be 8.73 x 10^{-6} wt%. Using the example of CO13-31, which has a total concentration of 38 ppb or 3.8 x 10^{-6} wt% HSE, the bulk HSE content provides only ~40% of the mass required to give a 25 μm^2 in each section, and, on average, one grain would be observed if two or more thin sections were examined. If the alloy grains were smaller, at least one grain would expected to be present in each thin section, although such small grains might be difficult to detect. For example, the smallest alloy grain detected is 2 μm^2 giving a mode of 1.61 x 10^{-7}vol%, and mass of 7.03 x 10^{-7} wt%, where the total HSE budget is ~540% of the mass of the alloy, so ~5 grains would be expected to be observed in each thin section. Alloys with a higher density, e.g. pure Os-Ir alloys would have a higher density of ~20 g/cm^3 (e.g. Walker et al., 2005) so the likelihood of observing such an alloy would be lower. For example, taking the alloy area of ~25 μm^2, with a mass of 1.45 x 10^{-5} wt%, the total HSE concentration would account for ~26% of the mass of the alloy, thus one grain would be seen approximately every four thin sections.

To summarise, the detection of alloys depends on the composition, size, and density of the alloy, where alloys of lower density would be of higher mode compared and would be easier to detect. On the other hand, high density alloys would require analysis of multiple thin sections via automated mapping techniques, which is beyond the scope of this study.

4.5.4 Implications for cycling of HSE in subduction zones

HSE have not been mobilised on a more than a cm-scale in the serpentinites but Re enrichment in the talc schist sample , and Ru and Ir depletion in the chlorite schist sample suggest that mobilisation of these elements could be possible. The enrichment of Re in the hybrid Capu Corvoli samples could suggest the possible transfer of these elements via fluids from metagabbro proximal to the samples, although Re mobility has only been proposed from metabasalts previously (Dale et al., 2009). However, shearing of the metagabbro would have provided a mechanism

for more pervasive fluid flow, and thus Re transport. Mixing between mafic and ultramafic lithologies could have occurred either on the seafloor via melt infiltration processes or in mélange zones between the mantle wedge and subducting slab either by metasomatic, or mechanical processes (e.g. Spandler and Pirard, 2013). Given that the sample with elevated Re (CO14-04) is from a shear zone associated with thrusting, where the shear zone most likely acted as a fluid conduit during convergence, we propose that Re was mobilised during fluid-mediated mixing of mafic and ultramafic lithologies during subduction. Hybrid rocks are recognised as significant contributors to volatile element cycling in subduction zones, with the ability to retain volatiles to greater depths than serpentinites (Spandler et al., 2008; Spandler and Pirard, 2013). The hybrid samples are considered to have recorded higher temperatures and pressures than the serpentinite samples (section 4.2). The elevated concentration of sulphur, and hence mode of sulphides, and the higher aS_2 recorded in the hybrid samples is consistent with retention of sulphur, a volatile element, to greater depths in these rocks. Hybrid rocks are generally positioned between the sub-arc mantle and the slab, and thus, transport of these elements would occur over short distances (Spandler and Pirard, 2013), or mélange material may be directly transported to the sub-arc mantle (Marschall and Schumacher, 2012). Regardless, of the precise mechanism, high Re concentrations, and the fractionation of IPGE in the hybrid rocks could be inherited by the sub-arc mantle, and subsequently arc magmas (e.g. Dale et al., 2009; Marschall & Schumacher, 2012; Penniston-Dorland et al., 2014). Rhenium transfer to the sub-arc mantle and/or deep mantle and fractionation of Os from other IPGE could have consequences for the feasibility of the Re-Os isotope system as tracers of recycled crustal material in these reservoirs (e.g. Dale et al., 2009).

4.6 Conclusions

Sulphide parageneses of high-pressure serpentinites have the potential to provide a wealth of information regarding changes in aO_2, aS_2, and HSE distribution during metamorphism. Detailed observations of samples from Alpine Corsica reveals a range of trajectories in $aO_2 - aS_2$ space, with $aO_2 - aS_2$ both increasing and decreasing with progression of metamorphism. This variety cannot be linked systematically to proximity of specific lithologies in the blueschist-eclogite facies terrain, suggesting that sulphide assemblages are most likely

controlled by internal rock buffering processes. In contrast, hybrid samples, associated with blueschist-eclogite to eclogite terrains record higher $aO_2 - aS_2$ than the Serra di Pigno and this is interpreted to record the infiltration of fluids devolatilised from metagabbros.

HSE behaved conservatively during subduction and exhumation in the serpentinites, with limited mobility on a whole rock scale. In contrast, the Capu Corvoli hybrid mafic/ultramafic samples show evidence for Re, Ru and Ir fractionation during cycling to the sub-arc mantle and deep mantle in 'mélange zones'. The cause of whole-rock HSE fractionation in the Capu Corvoli samples is attributed to either mechanical or fluid-mediated transfer from the proximal metagabbro. Lower HSE concentrations in the Capu Corvoli sulphides related to advanced stages of exhumation could be attributed to HSE dilution by sulphur introduction during the onset of exhumation. However, a different explanation is required for Serra di Pigno sulphide HSE depletion, where with the exception of one sample, samples have a low bulk sulphur concentration. In addition, the sample with the highest sulphur concentration records highest HSE.

Alloys may provide an important host for HSE. For example, the Ru-rich nature of the Ni-rich sulphides is proposed to be a result of exsolution of Os and Ir alloys, although the conditions of HSE alloy formation (e.g. Os-Ir and Pt alloys) are not fully understood and alloys are difficult to detect. This is particularly true for pure and therefore high density HSE alloys, where detection may require the analysis of several thin sections. Further work is required to fully constrain the controls on the solubility or precipitation of HSE (e.g. Foustoukos et al., 2015), particularly at high pressure. An enhanced understanding of alloy formation would also improve constraints on evolving redox conditions during subduction and exhumation.

4.7 Acknowledgements

Luke Daly and Sarah Hayes are thanked for samples CO14-03 to 05 and for discussions on field observations of these samples. Malcolm Roberts is thanked for his assistance with the JEOL 8530 WDS microprobe at the Centre for Microscopy, Characterisation and Analysis, the University of Western Australia. Elaine Miller is thanked for her help with feature mapping on the Tescan Mira 3 and Kelly Merigot is thanked for assistance with the TIMA at the JdLC Microscopy and

Microanalysis Facility (MMF), Curtin University. Richard Holdsworth at Intertek Genalysis is thanked for information on certified reference materials and further details on NiS-FA for whole rock PGE analysis. Chris Ballhaus is thanked for proposing the collaboration between the Geohistory Facility (JdLC, Curtin University) and Bonn University. SMR acknowledges the ARC Core to Crust Centre of Excellence (COE) grant (CE1101017). The TIMA instrument was funded by a grant from the Australian Research Council (LE140100150) and is operated by the John de Laeter Centre at Curtin University with the support of the Geological Survey of Western Australia, University of Western Australia and Murdoch University. This work was supported by an Australian Research Council (ARC) Future Fellowship (FF12000579 to K.E.) and a Curtin International Postgraduate Research Scholarship (CIPRS) to R.J.C.

4.8 References

Alard, O.; Luguet, A.; Pearson, N. J.; Griffin, W. L.; Lorand, J.-P.; Gannoun, A.; Burton, K. W. & O'Reilly, S. Y. (2005), 'In situ Os isotopes in abyssal peridotites bridge the isotopic gap between MORBs and their source mantle', *Nature* **436**(7053), 1005–1008.

Alt, J. C.; Shanks, W.; Crispini, L.; Gaggero, L.; Schwarzenbach, E. M.; Früh-Green, G. L. & Bernasconi, S. M. (2012), 'Uptake of carbon and sulfur during seafloor serpentinization and the effects of subduction metamorphism in Ligurian peridotites', *Chemical Geology* **322**, 268–277.

Aulbach, S.; Stachel, T.; Seitz, H.-M. & Brey, G. P. (2012), 'Chalcophile and siderophile elements in sulphide inclusions in eclogitic diamonds and metal cycling in a Paleoproterozoic subduction zone', *Geochimica et Cosmochimica Acta* **93**, 278–299.

Barnes, J. D.; Beltrando, M.; Lee, C.-T. A.; Cisneros, M.; Loewy, S. & Chin, E. (2014), 'Geochemistry of Alpine serpentinites from rifting to subduction: A view across paleogeographic domains and metamorphic grade', *Chemical Geology* **389**, 29–47.

Barnes, S. J.; Mungall, J. E. & Maier, W. D. (2015), 'Platinum group elements in mantle melts and mantle samples', *Lithos* **232**, 395–417.

Becker, H. (2000), 'Re–Os fractionation in eclogites and blueschists and the implications for recycling of oceanic crust into the mantle', *Earth and Planetary Science Letters* **177**(3), 287–300.

Becker, H.; Horan, M.; Walker, R.; Gao, S.; Lorand, J.-P. & Rudnick, R. (2006), 'Highly siderophile element composition of the Earth's primitive upper mantle: constraints from new data on peridotite massifs and xenoliths', *Geochimica et Cosmochimica Acta* **70**(17), 4528–4550.

Beltrando, M.; Compagnoni, R. & Lombardo, B. (2010), '(Ultra-) High-pressure metamorphism and orogenesis: An Alpine perspective', *Gondwana Research* **18**(1), 147–166.

Blanco-Quintero, I.; Fernández, J. A. P.; Casco, A. G.; Tauler, E. & others (2011), 'Serpentinites and serpentinites within a fossil subduction channel: La Corea mélange, eastern Cuba', *Geologica Acta* **9**(3).

Bragagni, A.; Fonseca, R.; van Acken, D.; Speelmanns, I.; Heuser, A. & A., L. (2015), 'Highly Siderophile Elements and 187Os/188Os in Individual Sulfides by Isotope Dilution', *Goldschmidt Abstracts* 374.

Brandon, A. D.; Creaser, R. A.; Shirey, S. B. & Carlson, R. W. (1996), 'Osmium recycling in subduction zones', *Science* **272**(5263), 861–863.

Brenan, J. M. & Andrews, D. (2001), 'High-temperature stability of laurite and Ru–Os–Ir alloy and their role in PGE fractionation in mafic magmas', *The Canadian Mineralogist* **39**(2), 341–360.

Brenan, J. M.; Finnigan, C. F.; McDonough, W. F. & Homolova, V. (2012), 'Experimental constraints on the partitioning of Ru, Rh, Ir, Pt and Pd between chromite and silicate melt: the importance of ferric iron', *Chemical Geology* **302**, 16–32.

Chan, T. & Finch, I. (2001), Determination of platinum-group elements and gold by inductively coupled plasma mass spectrometry, in 'Australian Platinum Conference, Perth, Western Australia', pp. 1–9.

Chopin, C.; Beyssac, O.; Bernard, S. & Malavieille, J. (2008), 'Aragonite–grossular intergrowths in eclogite-facies marble, Alpine Corsica', *European Journal of Mineralogy* **20**(5), 857–865.

Compagnoni, R.; Giovanni, F. & Flora, L. (1983), 'Balangeroite, a new fibrous silicate related to gageite from Balangero, Italy', *Am. Mineral,* 214–19.

Dale, C.; Burton, K.; Pearson, D.; Gannoun, A.; Alard, O.; Argles, T. & Parkinson, I. (2009), 'Highly siderophile element behaviour accompanying subduction of oceanic crust: whole rock and mineral-scale insights from a high-pressure terrain', *Geochimica et Cosmochimica Acta* **73**(5), 1394–1416.

Dale, C.; Gannoun, A.; Burton, K.; Argles, T. & Parkinson, I. (2007), 'Rhenium–osmium isotope and elemental behaviour during subduction of oceanic crust and the implications for mantle recycling', *Earth and Planetary Science Letters* **253**(1), 211–225.

Dale, C. W.; Macpherson, C. G.; Pearson, D. G.; Hammond, S. J. & Arculus, R. J. (2012), 'Inter-element fractionation of highly siderophile elements in the Tonga Arc due to flux melting of a depleted source', *Geochimica et Cosmochimica Acta* **89**, 202–225.

Danyushevsky, L.; Robinson, P.; Gilbert, S.; Norman, M.; Large, R.; McGoldrick, P. & Shelley, M. (2011), 'Routine quantitative multi-element analysis of sulphide minerals by laser ablation ICP-MS: Standard development and consideration of matrix effects', *Geochemistry: Exploration, Environment, Analysis* **11**(1), 51–60.

Debret, B.; Bolfan-Casanova, N.; Padrón-Navarta, J. A.; Martin-Hernandez, F.; Andreani, M.; Garrido, C. J.; Sánchez-Vizcaino, V. L.; Gómez-Pugnaire, M. T.; Mucoz, M. & Trcera, N. (2015), 'Redox state of iron during high-pressure serpentinite dehydration', *Contributions to Mineralogy and Petrology* **169**(4), 1–18.

Debret, B.; Koga, K. T.; Nicollet, C.; Andreani, M. & Schwartz, S. (2014), 'F, Cl and S input via serpentinite in subduction zones: implications for the nature of the fluid released at depth', *Terra Nova* **26**(2), 96–101.

Debret, B.; Millet, M.-A.; Pons, M.-L.; Bouilhol, P.; Inglis, E. & Williams, H. (2016), 'Isotopic evidence for iron mobility during subduction', *Geology* **44**(3), 215–218.

Debret, B. & Sverjensky, D. (2017), 'Highly oxidising fluids generated during serpentinite breakdown in subduction zones', *Scientific Reports* 7, 10351, doi:10.1038/s41598-017-09626-y.

Deer, W.; Howie, R. & Zussman, J. (1963), 'Rock forming minerals, Sheet Silicates, v. 3', London, Longman Green and Co., 270p.

Delacour, A.; Früh-Green, G. L. & Bernasconi, S. M. (2008), 'Sulfur mineralogy and geochemistry of serpentinites and gabbros of the Atlantis Massif (IODP Site U1309)', *Geochimica et Cosmochimica Acta* **72**(20), 5111–5127.

Deschamps, F.; Godard, M.; Guillot, S. & Hattori, K. (2013), 'Geochemistry of subduction zone serpentinites: A review', *Lithos* **178**, 96–127.

Donovan, J.; Kremser, D. & Fournelle, J. (2012), 'Probe for EPMA: acquisition, automation and analysis', Probe Software, Inc., Eugene, Oregon.

Evans, B. W. & Kuehner, S. M. (2011), 'A nickel-iron analogue of balangeroite and gageite (Sasaguri, Kyushu, Japan)', *European Journal of Mineralogy* **23**(5), 717–720.

Evans, K. (2012), 'The redox budget of subduction zones', *Earth-Science Reviews* **113**(1), 11–32.

Evans, K. (2006), 'Redox decoupling and redox budgets: Conceptual tools for the study of earth systems', *Geology* **34**(6), 489–492.

Evans, K. & Powell, R. (2015), 'The effect of subduction on the sulphur, carbon and redox budget of lithospheric mantle', *Journal of Metamorphic Geology* **33**(6), 649–670.

Evans, K.; Reddy, S.; Tomkins, A.; Crossley, R. & Frost, B. (2017), 'Effects of geodynamic setting on the redox state of fluids released by subducted mantle lithosphere', *Lithos* **278**, 26–42.

Evans, K.; Tomkins, A.; Cliff, J. & Fiorentini, M. (2014), 'Insights into subduction zone sulfur recycling from isotopic analysis of eclogite-hosted sulfides', *Chemical Geology* **365**, 1–19.

Faure, M. & Malavieille, J. (1981), 'Etude structurale d'un cisallement ductile: le charriage ophiolitique Corse dans la région de Bastia.', *Bulletin de la Societe Geologique de France*, 23.

Fischer- Gödde0, M.; Becker, H. & Wombacher, F. (2010), 'Rhodium, gold and other highly siderophile element abundances in chondritic meteorites', *Geochimica et Cosmochimica Acta* **74**(1), 356–379.

Fitzherbert, J.; Clarke, G.; Marmo, B. & Powell, R. (2004), 'The origin and P–T evolution of peridotites and serpentinites of NE New Caledonia: prograde interaction between continental margin and the mantle wedge', *Journal of Metamorphic Geology* **22**(4), 327–344.

Fleet, M.; Crocket, J.; Liu, M. & Stone, W. (1999), 'Laboratory partitioning of platinum-group elements (PGE) and gold with application to magmatic sulfide–PGE deposits', *Lithos* **47**(1), 127–142.

Fonseca, R. O.; Campbell, I. H.; O'Neill, H. S. C. & Allen, C. M. (2009), 'Solubility of Pt in sulphide mattes: implications for the genesis of PGE-rich horizons in layered intrusions', *Geochimica et Cosmochimica Acta* **73**(19), 5764–5777.

Fonseca, R. O.; Laurenz, V.; Mallmann, G.; Luguet, A.; Hoehne, N. & Jochum, K. P. (2012), 'New constraints on the genesis and long-term stability of Os-rich alloys in the Earth's mantle', *Geochimica et Cosmochimica Acta* **87**, 227–242.

Fonseca, R. O.; Mallmann, G.; O'Neill, H. S. C. & Campbell, I. H. (2007), 'How chalcophile is rhenium? An experimental study of the solubility of Re in sulphide mattes', *Earth and Planetary Science Letters* **260**(3), 537–548.

Fournier, M.; Jolivet, L.; Goffé, B. & Dubois, R. (1991), 'Alpine Corsica metamorphic core complex', *Tectonics* **10**(6), 1173–1186.

Foustoukos, D. I.; Bizimis, M.; Frisby, C. & Shirey, S. B. (2015), 'Redox controls on Ni–Fe–PGE mineralization and Re/Os fractionation during serpentinization of abyssal peridotite', *Geochimica et Cosmochimica Acta* **150**, 11–25.

Frost, B. R. (1985), 'On the stability of sulfides, oxides, and native metals in serpentinite', *Journal of Petrology* **26**(1), 31–63.

Galvez, M. E.; Martinez, I.; Beyssac, O.; Benzerara, K.; Agrinier, P. & Assayag, N. (2013), 'Metasomatism and graphite formation at a lithological interface in Malaspina (Alpine Corsica, France)', *Contributions to Mineralogy and Petrology* **166**(6), 1687–1708.

Gervilla, F.; Proenza, J.; Frei, R.; González-Jiménez, J.; Garrido, C.; Melgarejo, J.; Meibom, A.; Diaz-Martinez, R. & Lavaut, W. (2005), 'Distribution of platinum-group elements and Os isotopes in chromite ores from Mayari-Baracoa Ophiolitic Belt (eastern Cuba)', Contributions to Mineralogy and Petrology 150(6), 589–607.

González-Jiménez, J. M.; Griffin, W. L.; Gervilla, F.; Kerestedjian, T. N.; O'Reilly, S. Y.; Proenza, J. A.; Pearson, N. J. & Sergeeva, I. (2012), 'Metamorphism disturbs the Re-Os signatures of platinum-group minerals in ophiolite chromitites', *Geology* **40**(7), 659–662.

Goodge, J. W. & Holdaway, M. J. (1995), 'Rock-buffered fluid evolution of metapelites and quartzites in the Picuris Range, northern New Mexico', *Journal of Petrology* **36**(5), 1229–1250.

Groppo, C. & Compagnoni, R. (2007), 'Metamorphic veins from the serpentinites of the Piemonte Zone, western Alps, Italy: a review', *Periodico di Mineralogia* **76**, 127–153.

Guillot, S.; Hattori, K. H. & de Sigoyer, J. (2000), 'Mantle wedge serpentinization and exhumation of eclogites: insights from eastern Ladakh, northwest Himalaya', *Geology* **28**(3), 199–202.

Hanley, J. J.; Pettke, T.; Mungall, J. E. & Spooner, E. T. (2005), 'The solubility of platinum and gold in NaCl brines at 1.5 kbar, 600 to 800 C: a laser ablation ICP-MS pilot study of synthetic fluid inclusions', *Geochimica et Cosmochimica Acta* **69**(10), 2593–2611.

Harris, L. (1985), 'Progressive and polyphase deformation of the schistes lustrés in Cap Corse, Alpine Corsica', *Journal of Structural Geology* **7**(6), 637–650.

Hart, S. R. & Ravizza, G. E. (1996), 'Os partitioning between phases in lherzolite and basalt', *Earth Processes: Reading the Isotopic Code*, 123–134.

Jolivet, L.; Daniel, J.-M. & Fournier, M. (1991), 'Geometry and kinematics of extension in Alpine Corsica', *Earth and Planetary Science Letters* **104**(2), 278–291.

Jolivet, L.; Dubois, R.; Fournier, M.; Goffé, B.; Michard, A. & Jourdan, C. (1990), 'Ductile extension in alpine Corsica', *Geology* **18**(10), 1007–1010.

Jolivet, L.; Faccenna, C.; Goffé, B.; Mattei, M.; Rossetti, F.; Brunet, C.; Storti, F.; Funiciello, R.; Cadet, J. P.; d'Agostino, N. & others (1998), 'Midcrustal shear zones in postorogenic extension: example from the northern Tyrrhenian Sea', *Journal of Geophysical Research: Solid Earth* **103**(B6), 12123–12160.

Lahondère, J.; Lahondıre, D.; Lluch, D.; Ohnenstetter, M.; Dominici, R. & Vautralle, C. (1992), 'Carte géologique de la France a 1/50000', Luri, BRGM.

Lahondère, D. & Guerrot, C. (1997), 'Datation Nd-Sm du métamorphisme éclogitique en Corse alpine: un argument pour l'existence, au Crétacé supérieur, d'une zone de subduction active localisée le long du block corse-sarde', *Géologie de la France* **3**, 3-11.

Lorand, J.-P.; Alard, O. & Luguet, A. (2010), 'Platinum-group element micronuggets and refertilization process in Lherz orogenic peridotite (northeastern Pyrenees, France)', *Earth and Planetary Science Letters* **289**(1), 298–310.

Lorand, J.-P.; Luguet, A.; Alard, O.; Bezos, A. & Meisel, T. (2008), 'Abundance and distribution of platinum-group elements in orogenic lherzolites; a case study in a Fontete Rouge lherzolite (French Pyrénées)', *Chemical Geology* **248**(3), 174–194.

Loucks, R. R. & Mavrogenes, J. A. (1999), 'Gold solubility in supercritical hydrothermal brines measured in synthetic fluid inclusions', *Science* **284**(5423), 2159–2163.

Luguet, A.; Lorand, J.-P.; Alard, O. & Cottin, J.-Y. (2004), 'A multi-technique study of platinum group element systematic in some Ligurian ophiolitic peridotites, Italy', *Chemical Geology* **208**(1), 175–194.

Luguet, A.; Lorand, J.-P. & Seyler, M. (2003), 'Sulfide petrology and highly siderophile element geochemistry of abyssal peridotites: A coupled study of samples from the Kane Fracture Zone (45 W 23 20N, MARK area, Atlantic Ocean)', *Geochimica et Cosmochimica Acta* **67**(8), 1553–1570.

Magott, R.; Fabbri, O. & Fournier, M. (2016), 'Subduction zone intermediate-depth seismicity: Insights from the structural analysis of Alpine high-pressure ophiolite-hosted pseudotachylyte (Corsica, France)', *Journal of Structural Geology* **87**, 95–114.

Mallmann, G. & O'Neill, H. S. C. (2007), 'The effect of oxygen fugacity on the partitioning of Re between crystals and silicate melt during mantle melting', *Geochimica et Cosmochimica Acta* **71**(11), 2837–2857.

Malvoisin, B.; Chopin, C.; Brunet, F. & Galvez, M. E. (2012), 'Low-temperature wollastonite formed by carbonate reduction: a marker of serpentinite redox conditions', *Journal of Petrology* **53**(1), 159–176.

Manatschal, G. & Müntener, O. (2009), 'A type sequence across an ancient magma-poor ocean–continent transition: the example of the western Alpine Tethys ophiolites', *Tectonophysics* **473**(1), 4–19.

Marschall, H. R. & Schumacher, J. C. (2012), 'Arc magmas sourced from mélange diapirs in subduction zones', *Nature Geoscience* **5**(12), 862–867.

Mattauer, M.; Faure, M. & Malavieille, J. (1981), 'Transverse lineation and large-scale structures related to Alpine obduction in Corsica', *Journal of Structural Geology* **3**(4), 401–409.

Mattauer, M.; Proust, F. & Etchecopar, A. (1977), 'Lineation" a" et mecanisme de cisaillement simple lie au chevauchement de la nappe des schistes lustres en Corse', *Bulletin de la Société Géologique de France* **7**(4), 841–847.

Meresse, F.; Lagabrielle, Y.; Malavieille, J. & Ildefonse, B. (2012), 'A fossil Ocean–Continent Transition of the Mesozoic Tethys preserved in the Schistes Lustrés nappe of northern Corsica', *Tectonophysics* **579**, 4–16.

Miller, D. P.; Marschall, H. R. & Schumacher, J. C. (2009), 'Metasomatic formation and petrology of blueschist-facies hybrid rocks from Syros (Greece): implications for reactions at the slab–mantle interface', *Lithos* **107**(1), 53–67.

Mitchell, R. H. & Keays, R. R. (1981), 'Abundance and distribution of gold, palladium and iridium in some spinel and garnet lherzolites: implications for the nature and origin of precious metal-rich intergranular components in the upper mantle', *Geochimica et Cosmochimica Acta* **45**(12), 2425–2442.

Molli, G.; Tribuzio, R. & Marquer, D. (2006), 'Deformation and metamorphism at the eastern border of the Tenda Massif (NE Corsica): a record of subduction and exhumation of continental crust', *Journal of Structural Geology* **28**(10), 1748–1766.

Mungall, J. E. (2002), 'Roasting the mantle: slab melting and the genesis of major Au and Au-rich Cu deposits', *Geology* **30**(10), 915–918.

Mungall, J. E. & Brenan, J. M. (2014), 'Partitioning of platinum-group elements and Au between sulfide liquid and basalt and the origins of mantle-crust fractionation of the chalcophile elements', *Geochimica et Cosmochimica Acta* **125**, 265–289.

Ohnenstetter, M. (1992), 'Platinum group element enrichment in the upper mantle peridotites of the Monte Maggiore ophiolitic massif (Corsica, France): mineralogical evidence for ore-fluid metasomatism', *Mineralogy and Petrology* **46**(1), 85–107.

Pagé, P. & Barnes, S.-J. (2016), 'The influence of chromite on osmium, iridium, ruthenium and rhodium distribution during early magmatic processes', *Chemical Geology* **420**, 51–68.

Pagé, P.; Barnes, S.-J.; Bédard, J. H. & Zientek, M. L. (2012), 'In situ determination of Os, Ir, and Ru in chromites formed from komatiite, tholeiite and boninite magmas: implications for chromite control of Os, Ir and Ru during partial melting and crystal fractionation', *Chemical Geology* **302**, 3–15.

Paton, C.; Hellstrom, J.; Paul, B.; Woodhead, J. & Hergt, J. (2011), 'Iolite: Freeware for the visualisation and processing of mass spectrometric data', *Journal of Analytical Atomic Spectrometry* **26**(12), 2508–2518.

Pearson, D.; Irvine, G.; Ionov, D.; Boyd, F. & Dreibus, G. (2004), 'Re–Os isotope systematics and platinum group element fractionation during mantle melt extraction: a study of massif and xenolith peridotite suites', *Chemical Geology* **208**(1), 29–59.

Penniston-Dorland, S. C.; Gorman, J. K.; Bebout, G. E.; Piccoli, P. M. & Walker, R. J. (2014), 'Reaction rind formation in the Catalina Schist: Deciphering a history of mechanical mixing and metasomatic alteration', *Chemical Geology* **384**, 47–61.

Penniston-Dorland, S. C.; Walker, R. J.; Pitcher, L. & Sorensen, S. S. (2012), 'Mantle–crust interactions in a paleosubduction zone: Evidence from highly siderophile element systematics of eclogite and related rocks', *Earth and Planetary Science Letters* **319**, 295–306.

Peregoedova, A.; Barnes, S.-J. & Baker, D. R. (2004), 'The formation of Pt–Ir alloys and Cu–Pd-rich sulfide melts by partial desulfurization of Fe–Ni–Cu sulfides: results of experiments and implications for natural systems', *Chemical Geology* **208**(1), 247–264.

Peretti, A.; Dubessy, J.; Mullis, J.; Frost, B. R. & Trommsdorff, V. (1992), 'Highly reducing conditions during Alpine metamorphism of the Malenco peridotite (Sondrio, northern Italy) indicated by mineral paragenesis and H2 in fluid inclusions', *Contributions to Mineralogy and Petrology* **112**(2-3), 329–340.

Puchtel, I. S. & Humayun, M. (2001), 'Platinum group element fractionation in a komatiitic basalt lava lake', *Geochimica et Cosmochimica Acta* **65**(17), 2979–2993.

Puchtel, I. S.; Humayun, M.; Campbell, A. J.; Sproule, R. A. & Lesher, C. M. (2004), 'Platinum group element geochemistry of komatiites from the Alexo and Pyke Hill areas, Ontario, Canada', *Geochimica et Cosmochimica Acta* **68**(6), 1361–1383.

Ravna, E.; Andersen, T. B.; Jolivet, L. & De Capitani, C. (2010), 'Cold subduction and the formation of lawsonite eclogite–constraints from prograde evolution of eclogitized pillow lava from Corsica', *Journal of Metamorphic Geology* **28**(4), 381–395.

Rehkämper, M.; Halliday, A.; Fitton, J.; Lee, D.-C.; Wieneke, M. & Arndt, N. (1999), 'Ir, Ru, Pt, and Pd in basalts and komatiites: new constraints for the geochemical behavior of the platinum-group elements in the mantle', *Geochimica et Cosmochimica Acta* **63**(22), 3915–3934.

Richards, J. P. (2009), 'Postsubduction porphyry Cu-Au and epithermal Au deposits: Products of remelting of subduction-modified lithosphere', *Geology* **37**(3), 247–250.

Savard, D.; Barnes, S.-J. & Meisel, T. (2010), 'Comparison between Nickel-Sulfur Fire Assay Te Co-precipitation and Isotope Dilution with High-Pressure Asher Acid Digestion for the Determination of Platinum-Group Elements, Rhenium and Gold', *Geostandards and Geoanalytical Research* **34**(3), 281–291.

Scambelluri, M.; Pettke, T.; Rampone, E.; Godard, M. & Reusser, E. (2014), 'Petrology and trace element budgets of high-pressure peridotites indicate subduction dehydration of serpentinized mantle (Cima di Gagnone, Central Alps, Switzerland)', *Journal of Petrology* **55**(3), 459–498.

Scambelluri, M. & Tonarini, S. (2012), 'Boron isotope evidence for shallow fluid transfer across subduction zones by serpentinized mantle', *Geology* **40**(10), 907–910.

Schwarzenbach, E. M.; Früh-Green, G. L.; Bernasconi, S. M.; Alt, J. C.; Shanks III, W. C.; Gaggero, L. & Crispini, L. (2012), 'Sulfur geochemistry of peridotite-hosted hydrothermal systems: comparing the Ligurian ophiolites with oceanic serpentinites', *Geochimica et Cosmochimica Acta* **91**, 283–305.

Spandler, C.; Hermann, J.; Faure, K.; Mavrogenes, J. A. & Arculus, R. J. (2008), 'The importance of talc and chlorite "hybrid" rocks for volatile recycling through subduction zones; evidence from the high-pressure subduction mélange of New Caledonia', *Contributions to Mineralogy and Petrology* **155**(2), 181–198.

Spandler, C. & Pirard, C. (2013), 'Element recycling from subducting slabs to arc crust: A review', *Lithos* **170**, 208–223.

Tribuzio, R. & Giacomini, F. (2002), 'Blueschist facies metamorphism of peralkaline rhyolites from the Tenda crystalline massif (northern Corsica): evidence for involvement in the Alpine subduction event?', *Journal of Metamorphic Geology* **20**(5), 513–526.

Vitale Brovarone, A.; Beltrando, M.; Malavieille, J.; Giuntoli, F.; Tondella, E.; Groppo, C.; Beyssac, O. & Compagnoni, R. (2011), 'Inherited ocean–continent transition zones in deeply subducted terranes: insights from Alpine Corsica', *Lithos* **124**(3), 273–290.

Vitale Brovarone, A.; Beyssac, O.; Malavieille, J.; Molli, G.; Beltrando, M. & Compagnoni, R. (2013), 'Stacking and metamorphism of continuous segments of subducted lithosphere in a high-pressure wedge: the example of Alpine Corsica (France)', *Earth-Science Reviews* **116**, 35–56.

Vitale Brovarone, A. & Herwartz, D. (2013), 'Timing of HP metamorphism in the Schistes Lustrés of Alpine Corsica: New Lu–Hf garnet and lawsonite ages', *Lithos* **172**, 175–191.

Walker, R.; Brandon, A.; Bird, J.; Piccoli, P.; McDonough, W. & Ash, R. (2005), '187 Os–186 Os systematics of Os–Ir–Ru alloy grains from southwestern Oregon', *Earth and Planetary Science Letters* **230**(1), 211–226.

Warburton, J. (1986), 'The ophiolite-bearing Schistes Lustrés nappe in Alpine Corsica: a model for the emplacement of ophiolites that have suffered HP/LT metamorphism', *Geological Society of America Memoirs* **164**, 313–332.

Xiong, Y. & Wood, S. (2000), 'Experimental quantification of hydrothermal solubility of platinum-group elements with special reference to porphyry copper environments', *Mineralogy and Petrology* **68**(1-3), 1–28.

Xiong, Y. & Wood, S. A. (2002), 'Experimental determination of the hydrothermal solubility of ReS_2 and the Re-ReO_2 buffer assemblage and transport of rhenium under supercritical conditions', *Geochem. Trans* **3**(1), 1–10

CHAPTER 5

PROCESSES RECORDED BY SUBDUCTED SPINELS

Abstract

In this chapter, major element geochemistry, minor and trace element geochemistry of spinel grains are used to assess the processes that affect the stability of spinel throughout the subduction cycle. The results indicate substantial disturbance to the geochemistry of spinels during seafloor alteration and prograde evolution of Alpine Corsican serpentinites and hybrid ultramafic/mafic rocks. The primary mechanism for such alteration is proposed to be reaction of matrix phases with primary spinel cores, producing porous rims progressively enriched in Fe^{3+} and/or magnetite rims in the presence of a fluid phase. Detailed quantitative mapping of a spinel grain in a high-pressure serpentinite emphasises that the proportion of ferric iron in the spinel structure is not a simple function of pressure related to metamorphic conditions but likely results from dissolution-precipitation reactions on a mineral scale.

5.1 Introduction

Spinel, represented by the compositional range $FeAl_2O4$–$MgAl_2O_4$–$FeCr_2O_4$–$MgCr_2O_4$, is regarded as a mineral resistant to alteration and therefore has been used for constraining petrogenetic processes (Irvine, 1965; 1967; Dick and Bullen, 1984; Arai, 1992; Barnes and Roeder, 2001) and the geodynamic setting of ultramafic rocks (e.g. Kamenetsky et al., 2001). However, a number of studies have suggested that the chemical composition and structure of spinel can be modified during metamorphism (Barnes, 2000; Barnes and Roeder, 2001; Gervilla et al., 2012; Prabhakar and Bhattacharya 2013; Singh and Singh, 2013; Gargiulo et al., 2013; Mukherjee et al., 2010; 2015; Colás et al., 2014; 2016). Typically, hydrothermal or metamorphic modification of primary spinel is associated with the depletion of MgO and Al_2O_3 and an enrichment in FeO and Cr_2O_3, with higher concentrations of ferric iron towards the rim of the grain, which may form magnetite (Evans and Frost, 1975; Bliss and MacLean, 1975; Wylie et al., 1987; Kimbell,

1990; Frost, 1991; Barnes, 2000; Mellini et al., 2005; Merlini et al., 2009; Mukherjee et al., 2010; Grieco and Merlini, 2012; Gervilla et al., 2012).

The timing of spinel alteration is controversial, with some authors suggesting spinel alteration during seafloor alteration (Mellini et al., 2005; Barra et al., 2014), while others propose alteration during prograde metamorphism (Evans and Frost, 1975; Bliss and MacLean, 1975; Barnes, 2000), or during retrograde metamorphism (Gervilla et al., 2012; Colás et al., 2014). For example, the reaction of matrix silicates such as chlorite with primary cores to produce ferrian chromite are considered to occur prior to exhumation (e.g. Evans and Frost, 1975; Bliss and MacLean, 1975; Barnes, 2000). Alteration of primary spinel during retrograde metamorphism is proposed to result from a two stage reaction (Gervilla et al., 2012; Colás et al., 2014). The initial reaction of olivine with reducing fluids is proposed to produce porous chromite associated with chlorite, followed by circulation of oxidising fluids though pores in porous chromite that converts chromite to ferrian chromite via the addition of Fe^{3+} (Gervilla et al., 2012; Colás et al., 2014).

It is essential to constrain changes to spinel stability during subduction-related metamorphism because spinels are important hosts to iron, therefore changes in the ferric and ferrous iron content of spinels during alteration provide constraints on the transport and/or oxidation of iron within subduction zones, with implications for the oxidation state of the sub-arc mantle and/or deep mantle (e.g. Evans, 2012; Evans et al., 2012a; Debret et al., 2016).

The abundance of trace elements in spinels compared to major elements usually correlates with the major element composition. For example, Zn, Mn, Ni, Co and Cu substitute in the place of Mg and Fe^{2+}, whereas V and Ti substitute for Fe^{3+}, Al and Cr, thus an increase in Zn and Co should correlate with a decrease in either Mg or Fe^{2+}. An excess or depletion of these trace elements within spinels relative to expected trends could reflect an external source of trace elements such as an infiltrating fluid, or disturbance by metamorphism. Colás et al. (2014) demonstrated that additional constraints on the processes responsible for alteration of primary spinel can be revealed with *in-situ* analyses of trace elements that are able to substitute into the spinel structure.

Previous textural, major element and trace element studies have focused on the effect of metamorphism on spinels within chromitites (e.g. Gervilla et al., 2012; Colás et al., 2014; Colás et al., 2016) rather than isolated spinel grains within peridotites. Colás et al. (2014) suggested that the relatively silica rich and spinel poor peridotite bodies could record more intense changes in their minor and trace element signatures due to higher silicate/chromite ratios that would effectively increase the fluid:spinel ratio and thus the extent of reaction between the infiltrating fluids and spinel. To test this hypothesis, this study presents trace element variation in spinels in high-pressure serpentinites and a chlorite schist from Alpine Corsica. The results are discussed in the context of metamorphic and/or hydrothermal alteration processes. The timing of spinel growth, including magnetite, is constrained through careful examination of mineral textures. The concentrations of trace elements measured in the different generations of spinels are related to their major element geochemistry to assess the effects of metamorphism and/or fluid infiltration on the spinel composition.

5.2 Geological setting and sampling

Samples were collected from Serra di Pigno and Capu Corvoli, Cap Corse, Alpine Corsica, the details of which are described in chapter 4. Sampling focused on the Schistes Lustrés complex, which consists of metasediments, serpentinites, metagabbros and metabasalts, and internal continental slices. The pre-subduction setting is considered as an ocean-continent transition zone, or a magma- poor rifted margin resulting from slow to ultra-slow seafloor spreading rates (e.g. Brovarone et al., 2011; 2013). The Serra di Pigno samples studied here underwent blueschist to eclogite facies metamorphism (~1.3–2.6 GPa and ~414–471ºC; Lahondère and Guerrot, 1997; Vitale Brovarone et al., 2013), whereas Capu Corvoli is considered to record higher pressures approximating eclogite facies metamorphism (1.9–2.6 GPa and ~490–550 °C; Ravna et al., 2010; Vitale Brovarone et al., 2013). The timing of peak metamorphism is estimated at 37 Ma (Vitale Brovarone and Herwartz, 2013). The samples from Serra di Pigno were collected at various proximities to metasediments and mafic rocks (see chapter 4). The samples from Capu Corvoli are from a shear zone, proximal to metagabbro and near to thrust

faults that divide Upper Castagniccia metasediments from metaophiolites (Lahondère, 1992).

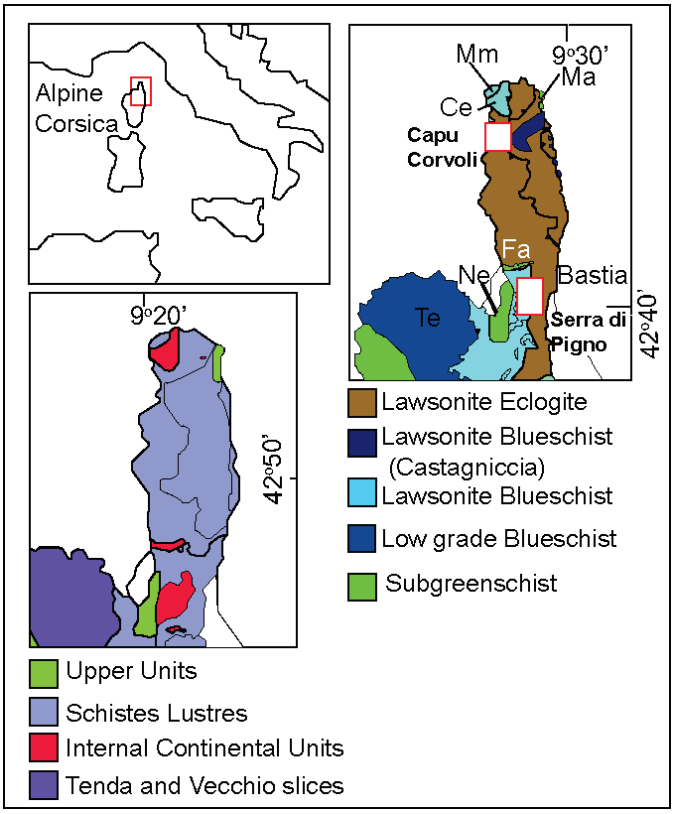

Figure 5.1: Location map of the sample localities at Serra di Pigno and Capu Corvoli, Alpine Corsica.

5.3 Methods

5.3.1 Electron probe microanalysis (EPMA)

Major and minor elements of oxides and silicates were quantitatively analysed by wavelength dispersive spectrometry on the JEOL 8530F Hyperprobe at the Centre for Microscopy, Characterisation and Analysis (CMCA), the University of Western Australia. Multiple analyses were carried out per grain to identify any sample heterogeneity, and for Cr-Al spinels and porous chromite, traverses across spinel grains from core to rim were made to assess major element compositional zonation.

The on-peak counting time was 20 seconds for each element, with an accelerating voltage of 15kV, and beam current of 20 nA. Mean atomic number (MAN) background corrections were used throughout. The compositions of the matrix silicate phases were required to correct the compositions of spinel grains that contain silicate inclusions. The standards used were wollastonite (Si), rutile (Ti),

Kakanui pyrope (Mg, Al), V, Cr_2O_3, magnetite (Fe for oxides), San Carlos olivine (Fe for silicates), Ni, Mn, Durango apatite (Ca), Jadeite (Na), orthoclase (K). Data reduction was performed using the Probe for EPMA v.10.8.1 software package (Donovan et al, 2012).

5.3.2 LA-ICP-MS

Trace element concentrations of spinel grains were obtained *in-situ* by Laser Ablation Inductively Coupled Mass Spectroscopy (LA-ICP-MS) at the John de Laeter Centre, Curtin University, using a Resonetics RESOlution M-50 with a Compex 102 Excimer laser, coupled to an Agilent 7700s quadropole ICP-MS. Samples were polished with 1 µm paste for analysis. Prior to ablation, background signal was collected for 20 seconds. Samples were ablated in an atmosphere of ultra-high purity He and N_2 for 40 seconds, at a repetition rate of 10 Hz. The laser energy density at the sample surface was 2 J/cm^2. The spot size was set to 70 µm for large grains (>70 µm), and 50 µm for smaller grains or where there was zoning on the scale of <70 µm.

Data reduction was carried out using the IGOR Pro 6.36 platform and Iolite v. 2.5 (Paton et al., 2011). Each element isotope peak per analysed spot was integrated in order to obtain element isotope concentrations. Trace elements analysed include ^{24}Mg, ^{27}Al, ^{28}Si, ^{45}Sc, ^{47}Ti, ^{50}V, ^{52}Cr, ^{55}Mn, ^{59}Co, ^{60}Ni, ^{65}Cu, ^{66}Zn, ^{69}Ga and ^{118}Sn. GSD-1g was used as the standard for analysis, which is a synthetic basalt. ^{57}Fe was used as the internal isotope, because Fe is of moderate to high concentrations across the entire compositional range of the spinels analysed here, and because ^{57}Fe is not subject to interference from elements such as ^{40}Ar or ^{16}O (Danyushevsky et al., 2011).

To check the accuracy of the analyses, GSD-1g was treated as an unknown and calibrated against glass standards NIST 610, and NIST 612, where the NIST standards have been previously reported to provide reliable trace element results for magnetite without the need for a matrix matched external standard (Dare et al., 2012; Nadoll and Koenig, 2011; Savard et al., 2010; Nadoll et al., 2014). All elements were within 10% of the reference values for GSD-1g (Appendix D1). The accuracy checks were carried out using ^{28}Si, because it is of common abundance in both the GSD-1g and NIST 610 and 612 standards.

Analyses of the matrix antigorite were necessary to trace and quantify antigorite contamination in the magnetite analyses and to identify contamination by inclusions in porous spinel in samples CO13-31 and CO13-33. ^{28}Si was used as the internal standard for the reduction of LA-ICP-MS matrix trace element data because of its relative abundance in the matrix and the GSD-1g standard and because EPMA analyses of Si indicate that Si is homogeneously distributed in serpentine. The Fe concentration in the matrix antigorite was determined for spots in close proximity to spinel grains.

Mixing calculations were performed to quantify the proportion of matrix in the spinel LA-ICP-MS analyses. The following steps were carried out for the calculations. (1) The Fe concentrations of the spinel grains were determined by EPMA and input to Iolite as the internal standard for data reduction using the standard GSD-1gA. (2) Data output from step (1) which showed significant matrix contamination (>0.5 wt% Si) were noted and underwent further correction via step (3) onwards. (3) A mixing line between spinel and antigorite was calculated using the proportions of 10% to 100% magnetite. Using the Si concentration output from the initial Iolite data reduction it was possible to produce a preliminary estimate of the proportion of the spinel (i.e. the proportion of Fe actually analysed). (4) The corrected proportion of Fe was input to Iolite to obtain new trace element values and a new proportion of Si. (5) The initial and corrected Si output from Iolite (step 4) were plotted against the initial and corrected Fe concentrations and the proportion of spinel analysed was determined where the line of best fit for the initial and corrected Fe and Si data crossed the mixing line between the end members. (6) The trace element concentrations were then corrected by this proportion minus the concentration of the trace element in the matrix (Appendix D2), provided that matrix values were above the detection limit.

Elements which could not be corrected due to high matrix concentrations are presented as maximum concentrations and are indicated with * in Appendix D3. Mg and Al abundances were particularly affected by matrix contamination, so EPMA analyses were used for these elements instead. A further correction was required for spinel data where the spot size was greater than the scale of zonation in Fe concentrations. A traverse was taken across these grains to obtain maximum

and minimum Fe concentrations using EPMA (Appendix C7), which subsequently provided maximum and minimum values for trace elements (Appendix D3).

5.4 Results

5.4.1 Petrographic analysis

Here, the different generations of spinels observed in the samples are reported. The complete petrography is described in detail in Appendix C10. The z below are in reflected light, but the zonation is also distinguishable in backscattered light.

5.4.1.1 Cores of spinels

Dark grey cores (in reflected light) exhibit a brecciated texture in CO13-31. Some spinel cores form a sharp contact with lighter grey rims (in reflected light) in the Serra di Pigno samples distal to other lithologies (CO13-31 and CO13-40), and in the talc schist from Capu Corvoli, CO14-04 (Fig. 5.2a). In the talc schist, cores of spinel grains are cut by patchy matrix chlorite (Fig. 5.2b), whereas in CO13-31 spinel grains occur within a matrix of early fine grained antigorite and are sheared (Fig. 5.2c).

5.4.1.2 Porous spinel

In CO13-31 and CO13-40, 'porous' lighter grey (in reflected light) spinel rims, are observed, where fine antigorite is contained within pore space (Fig. 5.2d). In samples CO13-21, CO13-33 and CO13-55, porous spinels are surrounded by magnetite rims (Fig. 5.2d-e), and rarely exhibit primary (non-porous) cores. In CO13-33, spinel grains form boudins and antigorite veins locally wrap around the grains (Fig. 5.2e, f). This type of spinel is zoned with darker grey porous cores and lighter grey porous rims in backscattered electron images (Fig. 5.2e). Veins of magnetite locally cut porous spinel or forms lamellae with porous spinel. In porous grey spinel in CO13-33 and CO13-40, trace chalcopyrite is observed as <1 to 5 μm grains.

5.4.1.3 Magnetite rims

Some cores to spinel are directly in contact with magnetite rims such as in CO14-04 (Fig. 5.2a), while in other samples porous spinel form sharp contacts with outer magnetite rims (Fig. 5d and e). Magnetite rims on porous spinel are

overprinted by patchy chlorite (Fig. 5.2f), pentlandite (Fig. 5.2e), and in two samples, CO13-21 and CO13-55, Ti-andradite garnet, comprising 50–300 μm grains, which also grows within the pore space (Fig. 5.2g).

5.4.1.4 Matrix magnetite

Matrix magnetite is observed as orientated clasts associated with or as inclusions to fine antigorite. This magnetite also is observed with inclusions of fine antigorite, or as grains overprinted by veins or coarse laths of antigorite (Fig. 5.2h–i). Matrix magnetite grains are typically variable in size (1 to >75 μm in size). Matrix magnetite in CO13-31 is associated with or occurs as inclusions in fine antigorite and balangeroite $(Mg,Fe^{2+},Fe^{3+}, Mn)_{42}Si_{15}(O,OH)_{90}$) veins. In CO13-33, matrix magnetite replaces pentlandite grains and matrix magnetite is associated with or replaced by antigorite veins (Fig. 5.2h–i).

5.4.1.5 Large magnetites cross-cutting foliation

Magnetite in the chlorite schist from Capu Corvoli occurs as large 1–5 mm euhedral grains that cut the chlorite defined matrix foliation (Fig. 5.2j–l). Additionally, late chlorite veins cut magnetite grains (Fig. 5.2j) and coarse talc wraps around magnetite rims (Fig. 5.2k).

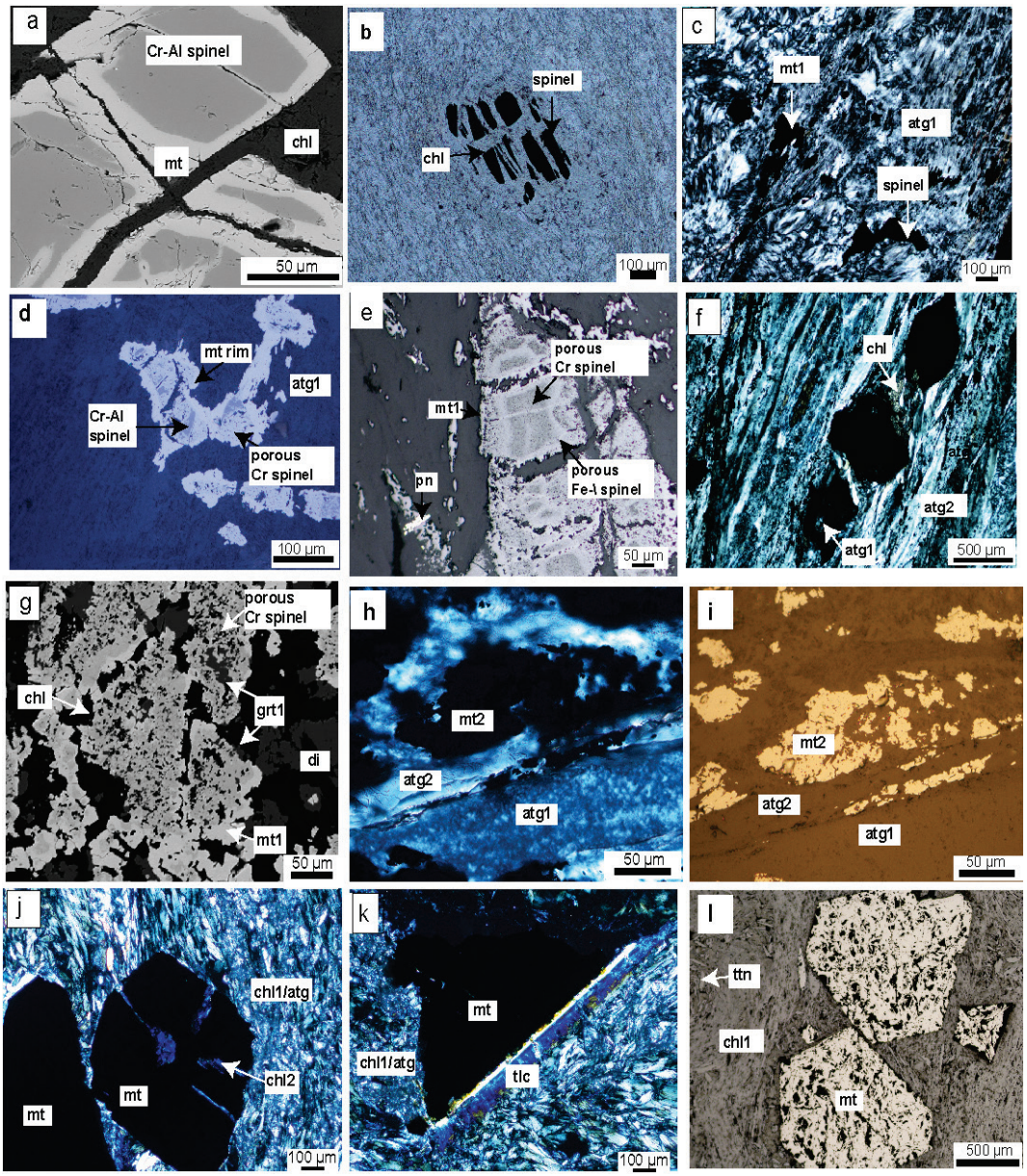

Figure 5.2: microphotographs showing textural features, bse = backscatter electron, rl = reflected light and xpl = cross-polarised light. Mt = magnetite, chl = chlorite, atg = antigorite, pn = pentlandite, grt = garnet, tlc = talc and ttn = titanite. (a) bse: Cr-Al cores with sharp contacts with magnetite rims in CO14-04, (b) xpl: chlorite cross-cutting a spinel grain in CO14-04, (c) xpl: spinel and magnetite in antigorite matrix in CO13-3, (d) rl: Cr-Al spinel cores rimmed by porous Cr-spinel and magnetite in CO13-31, (e) bse: porous Cr-rich spinel cores enclosed in Fe-rich spinel followed by magnetite rims in CO13-33, (f) xpl: spinel boudins in CO13-33 with patchy chlorite rims, (g) bse: porous Cr-rich spinel in CO13-55 with magnetite rims, chlorite and andradite infilling pore space, (h) xpl: matrix magnetite cut by antigorite veins in CO13-31, (i) rl: matrix magnetite cut by antigorite veins in CO13-31, (j) xpl: magnetite cut by chlorite in CO14-03, (k) xpl: magnetite with talc rims in CO14-03 and (l) rl: magnetite in CO14-03.

5.4.2 EPMA major and minor elements

Formulae of spinel minerals were calculated to three cations, assuming ratios obeyed stoichiometric constraints and charge balance. In the calculations it was assumed that two cations occupied the octahedral site, either Al^{3+}, Fe^{3+} or Cr^{3+}, and

one cation of Mg^{2+} and/or Fe^{2+} occupied the tetrahedral site per formula unit (Table 5.1 and 5.2).

Here the term 'spinel' is used to refer to the spinel group (consisting of Al, Fe^{3+} and Cr series) and not in the strict sense referring to either spinel ($MgAl_2O_4$) or the spinel series (where the dominant trivalent ion is Al). The general formula of spinel is AB_2O_4 (Bragg, 1915; Fleet, 1981), where site A is the tetrahedral site, and B is the octahedral site. The divalent cations Zn^{2+}, Mn^{2+}, Ni^{2+}, Co^{2+} and Cu^{2+} can substitute in the place of Mg^{2+} and Fe^{2+} at the tetrahedral site, whereas the trivalent cations V^{3+}, Sc^{3+} and Ga^{3+}, and Ti^{4+} can substitute for Fe^{3+}, Al^{3+} and Cr^{3+} at the octahedral site (e.g. Wechsler et al., 1984).

The dark grey cores to porous spinel and/or magnetite rims in section 5.4.1 are identified as Cr-Al spinel, that is, compositions that lie in the solid solution between the chromite (Cr) series and spinel (Al) series. Porous spinel is of a composition between the magnetite (Fe^{3+}) and chromite end members with a minor Al^{3+} component in the more Cr-rich end member. Porous Cr-rich spinel refers to a phase where Cr is more abundant than Fe. This phase was identified as darker grey porous spinel in section 5.4.1, either surrounding Cr-Al cores or as cores to lighter grey porous spinel, which is here identified as Fe-rich spinel, where Fe is more abundant than Cr. However, Cr and Fe-rich spinel each still have significant Fe and Cr components, respectively. Magnetite refers to the end member with the trivalent ion dominated by Fe^{3+}.

5.4.2.1 Cr-Al spinels and porous rims

Cr/(Cr+Al) ratios are ~0.4 in all Cr-Al cores, increasing to 0.8 to 1.0 in all porous grains, with a slight deviation to 0.7–0.8 in three Cr-rich porous grains in CO13-31 (Fig. 5.3a). The increase in Cr/(Cr+Al) ratios reflects the decrease from core to rim of Al_2O_3 from a maximum of 32.0wt% in the core to a minimum of 0.06 wt% in the Cr-rich porous rim in CO13-31, CO13-33 and CO13-40. Cr_2O_3 contents remain relatively constant between the Cr-Al core and Cr-rich porous rim in the case of CO13-33 (average 23.8wt% to 21.1wt% in the core and rim, respectively), or decrease from core to rim as for CO13-31 and CO13-40 (average 38.9 to 25.4wt% and 37.7 to 19.5wt% from core to rim in CO13-33 and CO13-40, respectively).

$Fe^{2+}/(Mg+Fe^{2+})$ ratios are variable in Cr-Al cores and there are no apparent trends from cores to porous rims with ratios of 0.4 to 0.9 in the cores and 0.3 to 0.8 for Cr-rich porous end members in CO13-31, CO13-33 and CO13-40. Towards the edge of porous rims there is a slight increase in Fe^{2+} with $Fe^{2+}/(Mg+Fe^{2+})$ ratios of 0.5 to 0.8 (Fig. 5.3a and b).

An increase in Fe^{3+} between Cr-Al cores and porous rims is recorded with ratios of $Fe^{3+}/(Fe^{3+}+Al^{3+}+Cr^{3+})$ from 0 to 0.5 for the cores and 0.35 to 0.65 for the porous rims in samples CO13-31, CO13-33 and CO13-40. $Fe^{3+}/(Fe^{3+}+Al^{3+}+Cr^{3+})$ ratios increases to 0.7–0.9 towards the edge of porous spinel in the same samples (Fig. 5.2 and 5.3).

Titanium oxide varies between 0.2 and 0.4wt% in CO13-31 and CO13-33 and between 0.6–0.9 wt% in CO14-04 (Fig. 5.3c). There is a significant positive correlation between TiO_2 (wt%) and $Fe^{3+}/(Cr+Al+Fe^{3+})$ ratios from 0.1 to 0.4 (R^2=0.76) with TiO_2 (wt%) increasing from a maximum of 0.4wt% in Cr-Al cores to a maximum of 0.9wt% in porous Cr-rich spinel. However, at $Fe^{3+}/(Fe^{3+}+Al^{3+}+Cr^{3+})$ ratios from 0.4 to 0.6 there is a negative correlation with TiO_2 (R^2= 0.61–0.78, Fig. 3a).

5.4.2.2 Magnetite

Magnetite rims have variable $Fe^{3+}/(Fe^{3+}+Al^{3+}+Cr^{3+})$ ratios between 0.88 and 1. In comparison, matrix magnetite grains have $Fe^{3+}/(Fe^{3+}+Al^{3+}+Cr^{3+})$ ratios approaching the pure magnetite end member, 0.97–1 c.p.f.u. In addition, Fe/Fe+Mg ratios are more variable for magnetite rims, with values of 0.91–0.99, compared to 0.97–0.99 for matrix magnetite. This is likely to be related to small inclusions in magnetite rims because such analyses also show proportional Si enrichments to Mg.

Magnetite grains in CO13-31 and CO13-33 have a component of Cr^{3+} with averages of 1.37 wt% (n=24) and 1.50 wt% Cr_2O_3 (n=18). A small proportion of CO13-31 grains (<1%) are enriched in Ti, with a maximum of 6.13 wt% TiO_2 (avg. 2.13 wt%, n = 6, Fig. 5.3c) with decreasing Ti towards the rim of the grains, whereas all other magnetites are relatively Ti-poor (avg 0.21 wt%, n =18). In Ti-rich grains, MnO contents are up to 1.97wt%. In addition, magnetite grains in CO13-31 are relatively Ni-rich with up to 1.62 wt % Ni (avg 0.61 wt%). In comparison, CO13-33 grains are relatively Ti and Ni-poor (avg 0.10 wt% TiO_2 and 0.26 wt% NiO).

The composition of CO13-55 magnetite is similar to that of CO13-31 and CO13-33, but with lower NiO (avg 0.14 wt%), Cr (avg 0.81 wt%) and similar Ti concentrations to CO13-33 magnetite (avg 0.11 wt% TiO_2).

In contrast, CO14-03 spinels are pure magnetite grains with a variable and minor substitution of Ti within the magnetite structure (below detection limit to 0.24wt %).

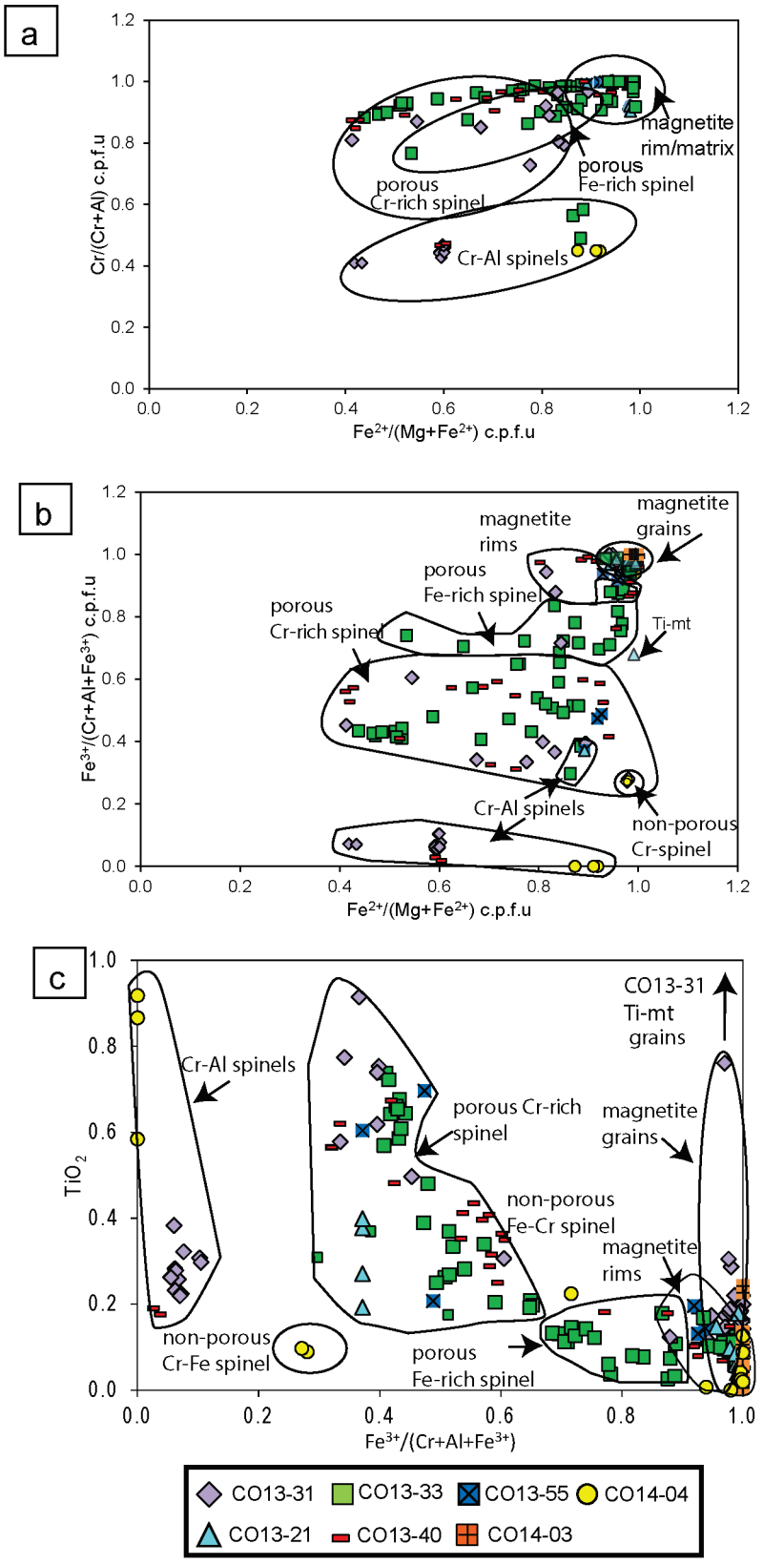

Figure 5.3: Plots of major element spinel compositions (a) plot of $Fe^{2+}/(Mg+Fe^{2+})$ vs Cr/(Cr+Al) (b) $Fe^{2+}/Mg+Fe^{2+}$ vs $Fe^{3+}/Cr+Al+Fe^{3+}$ (c) $Fe^{3+}/Cr+Al+Fe^{3+}$ vs TiO_2 (wt%)

	Cr-Al spinel cores				Porous Cr-rich spinel					Non porous Cr-rich spinel	Porous Fe-rich spinel	Magnetite rim			
Sample	CO13-31	CO13-33	CO13-40	CO14-04	CO13-21	CO13-31	CO13-33	CO13-40	CO13-55	CO14-04	CO13-33	CO13-31	CO13-40	CO13-55	CO14-04
wt%	n=13	n=3	n=3	n=3	n=4	n=8	n=26	n=14	n=3	n=3	n=18	n=6	n=16	n=3	n=7
SiO_2	0.1(4)	b.d.l	b.d.l	b.d.l	4(3)	2(3)	4(3)	4(4)	1(1)	b.d.l	1(1)	0.4(6)	0.4(7)	0.07(7)	b.d.l
TiO_2	0.28(4)	0.3(1)	0.18(1)	0.8(2)	0.3(1)	0.7(2)	0.5(2)	0.4(1)	0.5(3)	0.09(1)	0.10(4)	0.2(1)	0.12(4)	0.16(3)	0.04(5)
Al_2O_3	29(2)	13(1)	28.6(3)	19.8(3)	0.8(6)	2(2)	0.9(7)	1.0(9)	0.07(6)	2.2(2)	0.3(4)	0.1(2)	b.d.l	b.d.l	b.d.l
Cr_2O_3	34.3(9)	24(6)	37.7(3)	38.9(1)	20(8)	25(5)	21(6)	20(7)	23(4)	20(8)	6(2)	1(1)	1.2(8)	1.6(2)	0.3(5)
V_2O_3	0.24(2)	0.12(3)	0.235(5)	0.3(1)	0.03(2)	0.13(4)	0.06(1)	0.04(2)	0.10(2)	0.080(2)	0.03(1)	b.d.l	b.d.l	b.d.l	0.09(5)
Fe_2O_3	3(1)	27(8)	0.9(3)	-	37(9)	33(6)	37(10)	39(9)	38(8)	26.6(6)	57(3)	63(2)	61(1)	61.8(2)	63.2(6)
FeO	21.3(7)	27(1)	18.4(6)	37(1)	26(4)	27(4)	28(5)	30(5)	33.7(8)	36.2(1)	35(2)	35.3(4)	36.1(8)	36.5(2)	37.2(2)
MnO	0.5(4)	3.3(9)	0.18(3)	1.6(3)	3.8(2)	4(1)	2.8(8)	1.4(5)	2.4(4)	1.31(2)	0.02(1)	0.29(2)	0.08(6)	0.16(8)	b.d.l
MgO	11.9(9)	2.2(2)	13.3(3)	2.6(7)	5(3)	3(3)	5(3)	5(4)	0.7(3)	0.20(2)	0.06(7)	0.7(5)	0.4(4)	0.3(1)	b.d.l
ZnO	0.4(1)	n.d.	0.195(2)	n.d.	0.9(4)	0.7(2)	0.7(2)	0.5(3)	0.5(1)	n.d.	0.1(1)	b.d.l	b.d.l	n.d.	n.d.
NiO	0.16(3)	0.10(6)	0.06(2)	0.09(3)	0.12(4)	0.4(1)	0.2(4)	0.07(7)	0.15(5)	0.13(4)	0.23(4)	0.51(2)	0.2(7)	0.11(3)	b.d.l
CaO	b.d.l	b.d.l	b.d.l	b.d.l	b.d.l	b.d.l	b.d.l	b.d.l	b.d.l	b.d.l	b.d.l	0.01(1)	b.d.l	b.d.l	b.d.l
Total	101(1)	97(1)	99.7(1)	101(1)	99(1)	99.4(8)	99(2)	100(1)	101(2)	101.5(2)	100(1)	100.3(2)	100(1)	100.9(2)	100.9
							Cations per 3 cations								
Si	0.00(0)	-	-	-	0.3(2)	0.2(2)	0.3(2)	0.3(2)	0.1(1)	-	0.1(1)	0.03(5)	0.03(6)	0.006(5)	-
Ti	0.005(1)	0.01(2)	0.0035(2)	0.0041(3)	0.007(2)	0.014(4)	0.010(3)	0.009(3)	0.01(1)	0.0022(1)	0.0023(1)	0.004(1)	0.0028(9)	0.0038(8)	0.001(1)
Al	1.03(5)	0.54(6)	1.02(1)	1.10(1)	0.03(2)	0.10(9)	0.04(3)	0.04(3)	0.003(3)	0.09(1)	0.01(2)	0.00(1)	-	-	-
Cr	0.82(3)	0.7(2)	0.9(1)	0.896(5)	0.6(2)	0.7(2)	0.6(1)	0.5(2)	0.7(1)	1.02(1)	0.2(1)	0.02(3)	0.04(3)	0.049(7)	0.01(1)
V	0.0057(5)	0.003(1)	0.0055(1)	0.0070(2)	0.0009(6)	0.004(1)	0.0015(2)	0.0011(5)	0.0030(6)	0.00226(7)	0.0010(3)	-	-	-	0.002(2)
Fe^{3+}	0.08(3)	1.6(2)	0.03(1)	-	1.0(3)	0.9(2)	1.0(3)	1.1(3)	1.1(3)	26.6(6)	1.7(1)	1.84(8)	1.83(5)	1.829(4)	1.88(1)
Fe^{2+}	0.45(2)	0.8(2)	0.39(1)	0.84(2)	1.7(4)	0.7(1)	0.7(2)	0.7(2)	0.88(2)	36.2(1)	0.92(7)	0.94(3)	0.97(3)	0.974(6)	0.996(1)
Mn	0.01(1)	0.10(3)	0.0026(4)	0.04(1)	0.11(5)	0.13(4)	0.08(2)	0.04(2)	0.08(1)	0.041(1)	0.02(1)	0.009(6)	0.003(2)	0.005(3)	-
Mg	0.5(3)	0.11(1)	0.6(1)	0.11(3)	0.3(1)	0.2(2)	0.2(2)	0.2(2)	0.04(1)	0.011(1)	0.06(7)	0.04(3)	0.02(2)	0.017(7)	-
Zn	0.02(1)	n.d.	0.00897(1)	n.d.	0.03(1)	0.02(1)	0.02(1)	0.02(1)	0.018(2)	n.d.	0.004(4)	-	-	n.d.	n.d.
Ni	0.01(1)	0.003(2)	0.0014(5)	0.0021(7)	0.0010(5)	0.11(3)	0.005(1)	0.0011(8)	0.005(1)	0.00(0)	0.006(1)	0.015(1)	0.01(2)	0.0032(8)	-
Ca	-	-	-	-	-	-	-	-	-	-	-	-	-		-

Table 5.1: Average compositions of zoned spinel grains with standard uncertainty in brackets normalised to 3 cations. b.d.l. = below detection limit (0.03 to 0.05 wt%) for minor elements. n.d. = not determined. The results for individual analyses are provided in Appendix C7.

	Matrix magnetite					Large magnetite
Sample	CO13-21	CO13-31	CO13-33	CO13-40	CO13-55	CO14-03
wt%	n=12	n=21	n=18	n=5	n=12	n=20
SiO_2	0(1)	0.1(1)	0.2(3)	0.4(9)	0.06(5)	0.06(5)
TiO_2	0.08(5)	1(1)	0.10(3)	0.09(4)	0.11(2)	0.07(7)
Al_2O_3	b.d.l	b.d.l	0.1(2)	b.d.l	b.d.l	0(0)
Cr_2O_3	0.9(8)	1(1)	1(1)	1(1)	0.8(8)	0.01(1)
V_2O_3	b.d.l	b.d.l	0.03(1)	b.d.l	0.03(1)	0.20(6)
Fe_2O_3	66(1)	66(2)	66(1)	66(1)	66.9(9)	67.8(3)
FeO	32(3)	32(1)	32.4(7)	32(2)	33.0(3)	33.8(2)
MnO	0.26(6)	0.4(4)	0.2(1)	0.10(5)	0.16(3)	0(0)
MgO	1(2)	0.4(1)	0.4(4)	0.5(9)	0.28(4)	0(0)
ZnO	n.d.	n.d.	n.d.	n.d.	n.d.	n.d.
NiO	0.09(2)	0.6(3)	0.26(6)	b.d.l	0.14(7)	b.d.l
CaO	b.d.l	b.d.l	b.d.l	b.d.l	b.d.l	b.d.l
Total	100.9(7)	100.2(8)	99.9(9)	100.5(6)	100.9(7)	101.9(4)
			Cations per 3 cations			
Si	0.02(4)	0.003(3)	-	0.02(3)	0.002(2)	-
Ti	0.002(1)	0.02(3)	0(0)	0.002(1)	0.0025(5)	0(0)
Al	-	-	0(1)	-	-	0(0)
Cr	0.9(8)	0.04(3)	0.04(3)	0.04(3)	0.02(2)	0(0)
V	-	0.0009(4)	0(0)	-	0.0007(4)	0.005(2)
Fe^{3+}	1.97(2)	1.94(5)	1.95(4)	1.96(3)	1.97(2)	67.8(3)
Fe^{2+}	0.9(1)	0.95(2)	0.96(2)	0.95(7)	0.974(5)	33.8(2)
Mn	0.008(2)	0.02(1)	0.01(0)	0.003(1)	0.0048(8)	0(0)
Mg	0.04(8)	1.0(1)	0.02(2)	0.03(4)	0.015(2)	0(0)
Zn	n.d.	n.d.	n.d.	n.d.	n.d.	
Ni	0.0026(4)	0.02(1)	0.007(2)	-	0.004(2)	0(0)
Ca	-		-	-	-	-

Table 5.2: Average compositions of matrix magnetite grains with standard uncertainty in brackets normalised to 3 cations. b.d.l. = below detection limit (0.03 to 0.05 wt%) for minor elements. n.d. = not determined. The results for individual analyses are provided in Appendix C8.

5.4.3 EPMA mapping

Electron probe microanalysis maps are presented for Fe, Cr, Mg, Si, Al and Ti for a single spinel grain in sample CO13-40 with an cyclically zoned core and a rim consisting of magnetite 'veins' cutting through a porous Cr-Fe rim (Fig. 5.4). These maps show unusual zonation patterns in the core, with a Fe-rich core and oscillatory zoning alternating between Fe-rich and Fe-poor zones. Furthermore, this grain has a zone that is relatively Si rich (up to 5 wt%), corresponding with an enrichment in Mg and Al (up to 5wt%) and a slight enrichment in Ti (up to 0.5 wt%, compared to 0.2–0.3 in the Fe-rich zones).

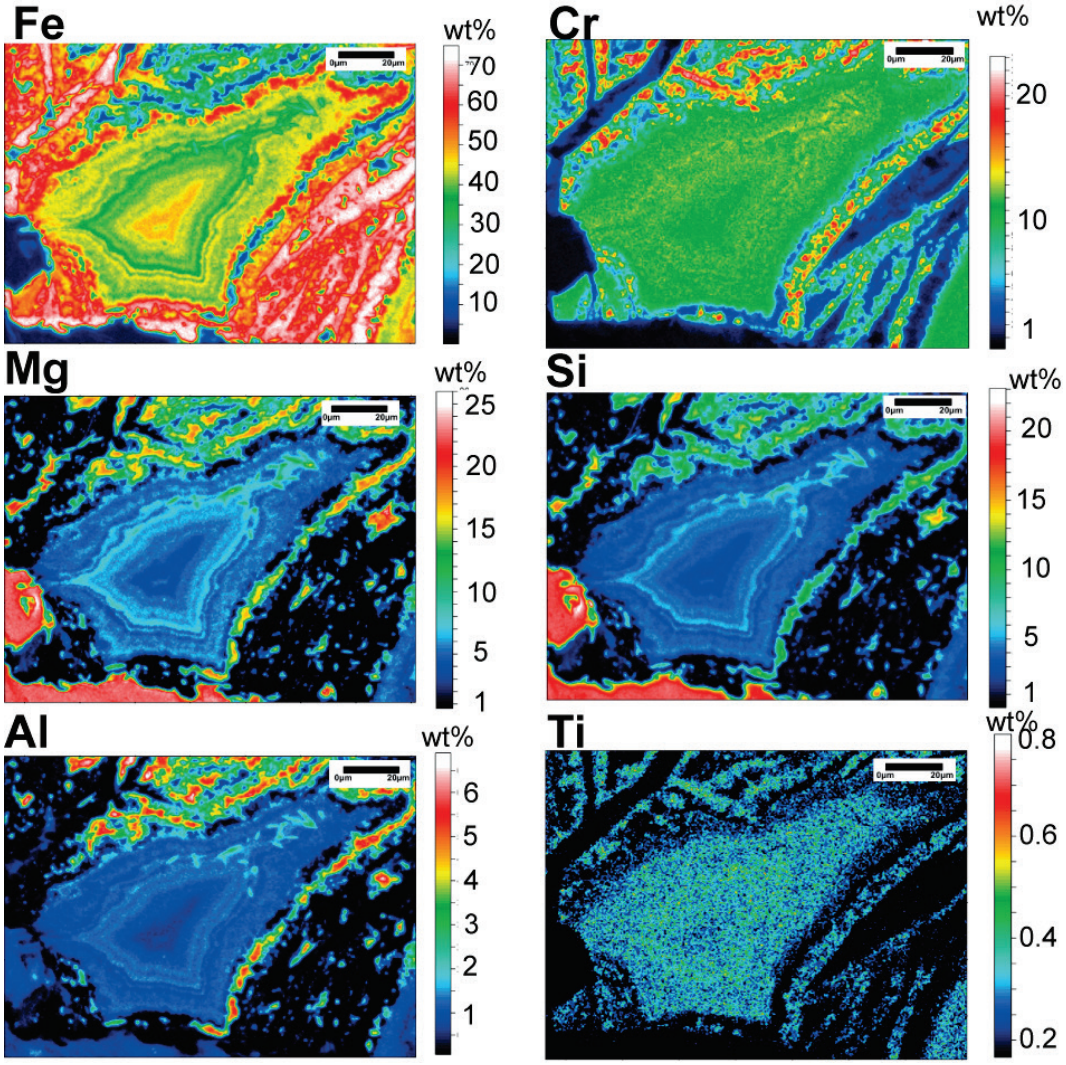

Figure 5.4 Quantitative WDS element maps of a spinel grain from the serpentinite sample CO13-40. The elements include Fe, Cr, Mg, Si, Al and Ti. The map displays a cyclically zoned core, with a Cr-rich porous rim cut by magnetite veins, as evident in the Fe, Cr and Ti maps.

5.4.4 Trace element data

In order to compare spinel grains to unaltered or primary grains, minor and trace element data results are normalised to a homogeneous chromite from a mid-ocean ridge basalt from the East Pacific Rise (Pagé and Barnes, 2009). Spinel from a magma poor rifted margin i.e. a slow or ultra-slow spreading margin, the proposed pre-subduction setting of the samples, would have been preferred, but to the author's best knowledge no such minor and trace element data exists at present.

The length scale of chemical heterogeneity is smaller than the spot size of the LA-ICP-MS analyses of Cr-Al cores in CO13-31 and the Cr-rich spinel cores in CO13-33, therefore these analyses have included a proportion of the porous rims, therefore minimum and maximum trace element values are reported corresponding to minimum and maximum Fe concentrations, respectively, the range of which are shown with error bars in Figure 4a and b. Additionally inclusions of antigorite in the porous rims and matrix grains were corrected for using the method outlined in section 5.4.2. However, comparison of grains from CO13-31 and CO13-33 allows a direct comparison between spinel grains that still preserve Cr-Al rich cores (CO13-31), and grains where primary cores have been completely altered to porous grains (CO13-33).

Cr-Al spinels in CO13-31 are heterogeneous relative to the magnetite and porous rims of C013-33. In comparison to 'unaltered' spinel, CO13-31 spinel cores are variably enriched by an order of magnitude in Zn, up to ten times more enriched in Co, up to two orders of magnitude more enriched in Mn, and have variable Sc contents. Porous CO13-33 Cr-rich grains show a similar trace element pattern to Cr-Al cores in CO13-31 and rare Cr-Al cores in the same sample, but are more homogeneous in composition and are relatively depleted in Co and Ga and enriched in V. For two grains in CO13-33, it was possible to directly compare Cr-Al cores with porous Cr-rich rims where Ti, Zn and V are enriched in porous Cr-rich rims compared to the cores. The cores in CO13-33 have ten times the enrichment in Ni. Fe-rich porous rims are up to an order of magnitude depleted in Zn, Ti and Sc, and slightly depleted in Mn and V, and up to ten times more enriched in Ga compared to Cr-Fe porous spinel. Magnetite rims were frequently too thin to analyse via laser ablation but on the basis of two analyses, they are depleted in Zn and V by two orders of magnitude compared to porous spinel and Cr-Al spinel. Trace element

signatures of magnetite rims are not distinguishable from matrix magnetite in CO13-31.

In comparison to matrix magnetite and magnetite rims in CO13-31, analyses of magnetite in the hybrid rock CO14-03 show variable trace element enrichment. Analyses close to rims of magnetite or of smaller grains enclosed in chlorite (n=3) are enriched in Ti and V over almost two orders of magnitude compared to magnetite cores in CO14-03 and relative to that of CO13-31 matrix magnetites. In addition, compared to magnetite in CO13-31, Ni is approximately ten times depleted and Co is half the concentration of CO13-31 magnetites.

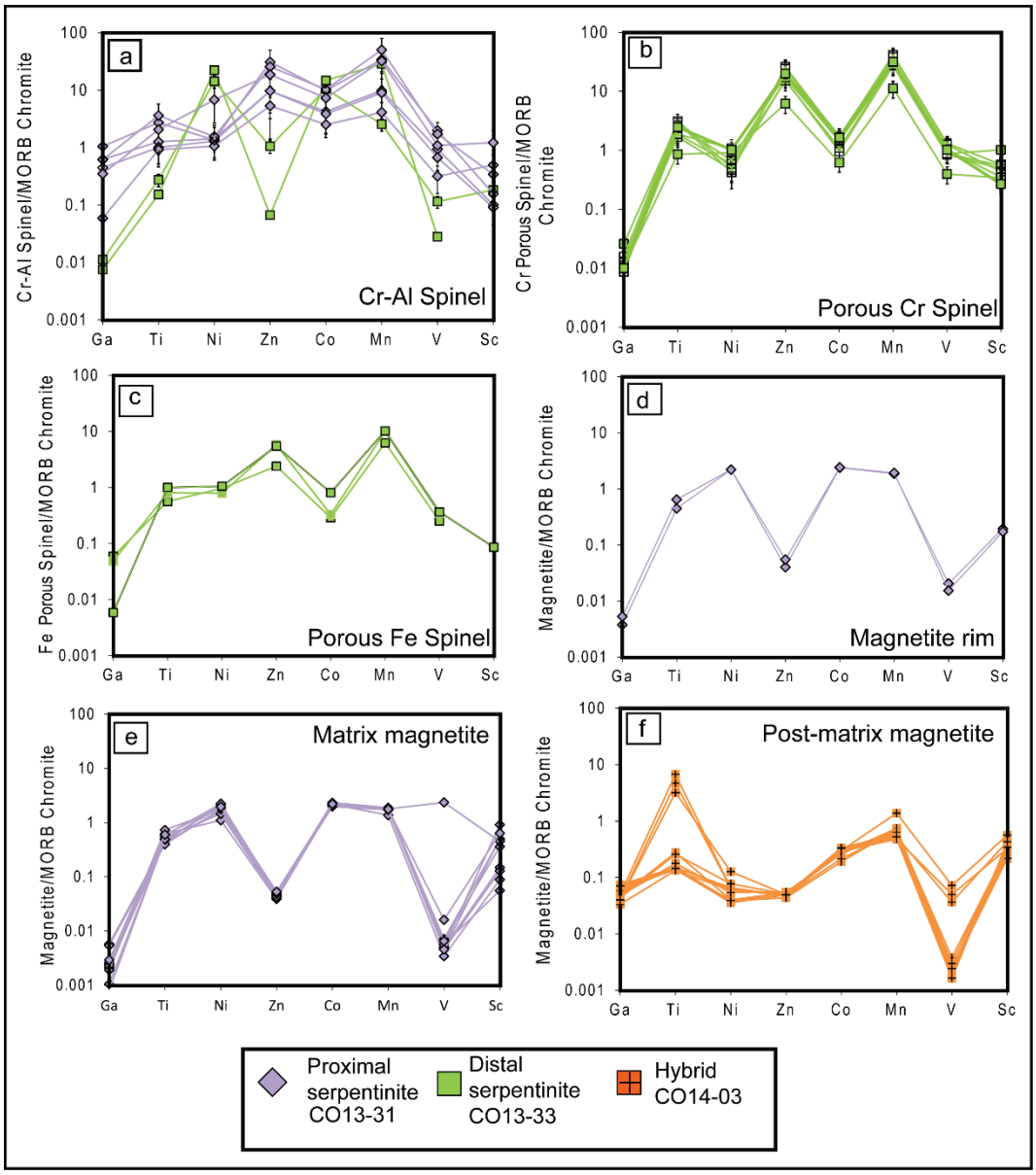

Figure 5.5: Spidergrams showing the distribution of minor and trace elements in spinel grains in (a) Cr-Al spinels (b) porous Cr-rich spinels (c) porous Fe-rich spinel (d) magnetite rim on porous spinel

(e) matrix magnetite and (f) large euhedral magnetite grains which cross-cut matrix. The analyses are normalised to MORB chromite from the East Pacific Rise (Pagé and Barnes, 2009).

5.5 Discussion

5.5.1 Timing of spinel alteration

5.5.1.1 Primary

Cr-Al spinels are proposed to be primary on the basis of their Al-rich composition, although the cores could have undergone alteration during seafloor alteration from more Mg-rich primary compositions. These grains are interpreted to have undergone subsequent alteration to form porous spinels and magnetite rims during either seafloor alteration and/or metamorphism. The origin of 'Fe^{3+}-rich chromite porous or non-porous rims are widely debated in the literature. The redox state of fluids, modal abundance of silicates versus chromite and fluid:rock ratios contribute to the formation and evolution of chromites. Constraints on the timing of the spinel alteration are discussed below.

5.5.1.2 Seafloor alteration

Further insights on the timing of spinel alteration are provided by comparison to pre-subduction sample analogues. The pre-subduction setting of the samples is proposed to have been a slow spreading to ultra-slow spreading centre (e.g. Vitale Brovarone et al., 2011; 2013; Meresse et al., 2012). To provide constraints on the timing of primary spinel alteration to porous and magnetite rims, the Serra di Pigno and Capu Corvoli spinel textures are compared to those of spinels from Internal Liguride serpentinites (Mellini et al., 2005), which provide an analogue for the pre-subduction oceanic setting of the Corsican samples. Mellini et al. (2005) report pristine anhedral Al-spinels surrounded by porous Al-spinel, an outer zone of Fe^{3+}-rich chromite +chlorite/lizardite rims, and magnetites that are interpreted to have formed synchronously with serpentinisation. In the Internal Liguride serpentinites, chlorite and lizardite incorporate Al and Mg from the altered spinel core (Mellini et al., 2005). Similarly, Barra et al. (2014), report Cr-Al rich cores, surrounded by porous Fe^{3+}-rich chromite' from the La Cabaña peridotite, south-central Chile, where the chromite is similar in composition to those outlined in this study. However, in these studies, magnetite rims on porous chromite, which are consistently observed in the samples studied here, were not always present,

suggesting that the origin of the spinels studied here underwent further alteration during the subduction cycle.

5.5.1.3 Prograde metamorphism

Additional spinel alteration could have occurred during prograde alteration. In a previous study, the outer rim of magnetite was inferred as a product of serpentinisation which reacts with the core during prograde metamorphism to produce Fe^{3+}-rich chromite (Bliss and MacLean, 1975). In addition, chlorite is not always observed surrounding the spinels, chlorite replaces antigorite and is more often observed aligned with a planar foliation (Fig. 5.2f), away from spinel, therefore at least some chlorite is metamorphic in origin. Furthermore, all porous spinel is within the compositional range of the Cr-rich core and magnetite rim end members, consistent with formation from the reaction of these end members (c.f. Khalil and El-Makky, 2009).

Prograde fine grained antigorite inclusions are observed in porous spinel grains, connected through pore space to the matrix. This texture implies the growth of porous spinel synchronously with or after fine grained antigorite, which likely grew at the expense of chrysotile and lizardite. Other authors have reported chlorite rather than antigorite in pore spaces of spinel under eclogite facies conditions (e.g. Gervilla et al., 2012). The presence of chlorite rather than antigorite may be a result of higher bulk Al contents in the chromitites studied by Gervilla et al. (2012) from the Golyamo Kamenyane metamorphosed ultramafic massif in southern Bulgaria and northern Greece than the samples presented in this study, or because of the higher pressures and temperatures associated with eclogite facies than the blueschist to eclogite facies samples presented here. Gervilla et al. (2012) and Colás et al. (2014) consider porous spinel to be an alteration product of Cr-Al spinel. These workers propose a two stage process for the formation of chlorite and porous spinel during retrograde metamorphism. Chlorite and porous rims of spinel enriched in FeO and Cr_2O_3, are proposed to be a product of the reaction between Al-rich spinel and olivine during fluid infiltration while $Fe^{3+}/(Cr+Fe^{3+}+Al)$ ratios remain unchanged in the reaction:

Mg-rich chromite + forsterite + water → clinochlore + Fe-rich chromite + brucite.

The second stage involves the circulation of oxidising fluids though pores in porous chromite that converts chromite to ferrian chromite via the addition of Fe^{3+} (Gervilla et al., 2012; Colás et al., 2014).

In the case of the samples studied here, detailed petrographic analysis, augmented by SEM analysis, did not reveal the presence of prograde olivine. It is possible that olivine was serpentinised during fluid infiltration associated with retrogression. Additionally there is no increase in the concentration of Cr_2O_3 between cores and porous Cr-rich spinel rims but a significant Fe_2O_3 increase and loss of Al_2O_3 is evident. However, chlorite is observed overprinting magnetite rims (and hence porous spinel and antigorite), in CO13-33. Chlorite stability may have been facilitated by the Al addition sourced from primary Cr-Al spinel either during seafloor alteration or retrogression associated under peak conditions. Andradite garnet, observed filling the pore space in two samples (CO13-21 and CO13-55) has previously been attributed to both seafloor (Plümper et al., 2014) and peak metamorphism (Muntener and Hermann, 1994). Andradite in our samples is associated with or overprinted by chlorite, (Fig. 5.2g). Chlorite also overprints or is synchronous with magnetite rims, thus magnetite growth is synchronous with andradite growth. Magnetite in association with andradite has previously been attributed to formation under metasomatic conditions such as those associated with skarn deposits (e.g. Deer, Howie and Zussman, 1992). The textural evidence alone is insufficient to distinguish between seafloor growth or metasomatic during high-pressure fluid infiltration.

An alternative explanation for the formation of relatively Fe^{3+}-rich porous rims is reaction between primary spinel and antigorite in the presence of a fluid to produce porous rims of Fe^{3+}-rich chromite and Cr-rich chlorite. Such a reaction was inferred in mélange hosted Kalkan chromitite in the Southern Urals, Russia (Merlini et al., 2009):

chromite + antigorite + water + oxygen → Fe-chromite + Cr-chlorite

Analyses of chlorite surrounding rims on porous spinel and magnetite in the samples analysed here record elevated Cr_2O_3 concentrations of 0.94–3.88wt% (n=4) in CO13-33 and 1.54–1.81wt% (n=3) in CO13-55, which suggests that the reaction of primary spinel and antigorite is applicable to the samples studied here

(Appendix D4). This reaction would require oxidised fluids or fluids with the ability to carry Fe^{3+} or the presence of electron acceptors such as SO_4^{2-} or SO_2. The source of such fluids could be the dehydration of other lithologies or precursor serpentine phases during prograde metamorphism at greater depths in the subduction channel. Lizardite has been proposed to host significant proportions of Fe^{3+}, with higher Fe^{3+}/Fe_{tot} ratios than antigorite (Evans, et al., 2012b). It is also noted that in serpentinites proximal to other lithologies (CO13-33 and CO13-55), primary Cr-Al cores are rare, with altered spinels consisting of porous Cr-rich porous cores are surrounded by porous Fe-rich rims and/or magnetite. This could imply higher fluid:spinel ratios compared to the distal serpentinite samples, CO13-31 and CO13-40, where primary cores are more abundant. However, on the thin section scale, low variance mineral assemblages imply that the system was rock buffered (Chapter 4).

In the distal serpentinite samples (CO13-31 and CO13-40), matrix magnetite is associated with or occurs as inclusions in fine antigorite and balangeroite veins, where such veins have previously been attributed to prograde metamorphism (e.g. Groppo and Compagnoni 2007; Evans and Kuehner, 2011), therefore matrix magnetite is also attributed to this stage.

5.5.1.4 Retrograde

The late generation of matrix magnetite in the samples CO13-21, CO13-33 and CO13-55 replaces pentlandite grains attributed to the onset of exhumation (Chapter 4). This magnetite therefore postdates magnetite rims on porous spinel, and is synchronous with, or replaced by, retrogressive antigorite veins (Fig. 5.2h–i).

Magnetite in the chlorite schist from Capu Corvoli (CO14-03) comprises large 1–5mm euhedral grains that cut the chlorite/antigorite defined matrix foliation (Fig. 5.2j–l). The fine chlorite/antigorite matrix is attributed to prograde to peak metamorphism, magnetite is attributed to a stage that postdates peak metamorphism. Additionally, late chlorite veins cut magnetite grains (Fig. 5.2j) and coarse talc wraps around magnetite (Fig. 5.2k). Talc is attributed to lower pressures associated with late stages of exhumation (e.g. Evans and Powell, 2015), thus magnetite is constrained to the onset of exhumation.

5.5.2 A trace element record of modification to spinel during metamorphism

The divalent cations Zn^{2+}, Mn^{2+}, Ni^{2+}, Co^{2+} and Cu^{2+} substitute for Mg^{2+} and Fe^{2+} at the tetrahedral site, whereas the trivalent cations V^{3+}, Sc^{3+} and Ga^{3+}, and Ti^{4+} can substitute for Fe^{3+}, Al^{3+} and Cr^{3+} at the octahedral site (e.g. Wechsler et al., 1984). In general, cation substitution is considered to take place at low oxygen fugacity (or activity), due to the increased ionic radius of oxidised cations e.g. V^{5+} compared to V^{3+} (Buddington and Lindsley, 1964; Frost, 1991; Lindsley, 1991). Other factors that could affect the partitioning of trace elements into the spinel structure include temperature, fluid composition (and therefore element availability), silica and sulphur activity and fluid:rock ratios (e.g. Nadoll et al., 2014 and references therein).

In order to provide additional insights into the processes and/or conditions that modified primary spinel compositions, the minor and trace element signatures of primary to altered Cr-rich porous spinels were compared to those of unaltered spinel from Pagés and Barnes (2009), and between the different generations of spinel recorded in the samples from relatively unaltered cores, to porous rims and magnetite.

5.5.2.1 Changes to trace element geochemistry from core to porous rims

Modification to the trace element signatures of primary spinels is recorded in CO13-31 Cr-Al spinel with heterogeneous enrichment in Ni, Zn, Co and Mn, a slight enrichment in Ti and a variable depletion in Ga, V and Sc compared to the unaltered spinel of Pagés and Barnes (2009). This trace element signature requires modification via metamorphism and/or hydrothermal alteration. In the samples studied, low variance mineral assemblages suggest that significant fluid: rock interaction did not occur (see chapter 4), therefore controls from external fluids during metamorphism are likely to be minor. Initial serpentinisation on the seafloor could result in the observed signatures in the Cr-Al spinel cores. The alteration of primary olivine and mobilisation of Ni, Mn, Zn and Co may have caused enrichment of these elements (Gahlan and Arai, 2007), and the seafloor alteration signature may have been retained during metamorphism at low fluid:rock ratios. An increase in Zn, Co and Mn concentrations during metamorphism at amphibolite facies metamorphism has previously been reported (Colás et al., 2014). Additionally, Ni enrichment under greenschist facies conditions has been suggested

(e.g. Barnes, 2000). Enrichment in Ni, Zn, Co and Mn is therefore attributed to seafloor to early prograde metamorphism.

The transition from Cr-Al cores to porous rims is recorded by a decrease in Co, Ni and Ga and an increase in V and Sc. The increase in V from the cores to Cr-rich porous cores could reflect moderate oxygen activities (V^{3+}), because V at higher oxidation states (V^{5+}) is incompatible in the spinel structure. Ga has similar site preferences to Al (e.g. Colás et al., 2014) and therefore the decrease of Ga from core to rim is consistent with the loss of Al^{3+}. EPMA analyses, with a smaller spot size than laser ablation, reveal an initial increase in Ti between the core and the porous rims with the lowest Fe^{3+} concentrations (Fig. 5.3c), which was likely homogenised in laser ablation analysis spots. Ti^{4+} requires coupled substitution with Fe^{2+} to replace Fe^{3+} at the octahedral site. Colás et al. (2014) also observed heterogeneous Ti in the porous spinel and suggested that Ti incorporation could be facilitated by the infiltration of fluids that promoted the re-ordering of octahedral sites in porous chromite.

The decoupled behaviour of Co and Zn is surprising because these elements have a similar ionic radius and both show preference for the tetrahedral site in spinel (McClure, 1957; Fanlo et al., 2015), and Zn has behaved similarly to Mn, which has a larger ionic radius. Site preference energies for Mn and Zn could account for the similar behaviour of these elements (Fanlo et al., 2015). In addition, co-enrichments of Co and Zn have previously been proposed to result from the diffusion of these elements (Fanlo et al., 2015). Therefore the decoupled behaviour of these elements here suggests that diffusion was not a major control on the distribution of Co and Zn and could reflect modification via processes such as metamorphism or dissolution-precipitation reactions (e.g. Putnis and Austrheim, 2010). On the basis of textural evidence (section 5.5.1), it is suggested that interaction with antigorite in the presence of fluids released from the dehydration to antigorite could explain such signatures.

The Fe-rich porous rims are depleted in Zn, Ti, V compared to Cr-rich porous spinel. The depletion in Ti and V is attributed to increased Fe^{3+} at the octahedral site, whilst the Zn depletion is attributed to increased Fe^{2+}.

5.5.2.2 Magnetite

The trace element patterns of magnetite in the distal serpentinite sample, CO13-31 do not appear to show substantial differences between rims and matrix prograde magnetite. Both show a relative depletion in Zn, Mn and V compared to porous Fe-rich porous spinel rims.

Late magnetite grains associated with exhumation in the hybrid sample CO14-03 are enriched in Ti, and slightly depleted in Ni and Co compared to the serpentinite magnetite grains in CO13-31. Three ablation sites in close proximity to chlorite record V and Ti enrichment of up to two orders of magnitude, compared to other magnetite grain cores in CO14-03. Titanite, a phase also attributed to exhumation (see Appendix C10), was observed along fractures in magnetite and therefore could be the source for Ti, and possibly, to a lesser extent, V. Compared to matrix magnetite in the serpentinite sample CO13-31, the lower Ni contents overall are due to the bulk composition, because CO14-03 has significantly lower bulk Ni contents compared to CO13-31 (see chapter 4) reflective of its departure from ultramafic compositions. In general, Co depletion is likely to result from incorporation into pyrite grains, which shows complex zonation patterns (see Chapter 6), likely controlled via fluids given the late exhumation stage of growth.

5.5.3 EPMA mapping insights into spinel alteration

The cyclic zoning of Fe, Cr, Mg, Al, Si and Ti in the core of the mapped spinel grain from distal serpentinite sample CO13-40 and the veins or 'banded' magnetite/Cr-Fe spinel rim in the same grain could reflect extrinsic (external) factors e.g. fluid infiltration and/or change of fluid composition, pressure, temperature, pH and/or oxidation state. Alternatively intrinsic (local) factors such as rates of diffusion could be of more importance (e.g. Shore and Fowler, 1998).

The core to this grain has also incorporated a significant amount of silica. Si^{4+} can substitute for Fe^{3+} at the tetrahedral site (e.g. Shimazaki, 1998), which is consistent with a zone of the lowest concentration of Fe (~30 wt%) but highest Si (~5wt%) and vice versa. The Fe-rich core is unusual, the inverse to that usually reported from either prograde metamorphism (e.g. Barnes, 2000) and the textures reported in section 5.5.2, or retrograde metamorphism (e.g. Gervilla et al., 2012; Colás et al., 2014), where primary Cr-Al-rich cores are surrounded by rims

relatively enriched in Fe. It has been suggested that the uptake of Si into the spinel structure could reflect changes to pressure and more reducing conditions (Ringwood, 1968). However, the effects of pressure and oxidation state were suggested to be minimal in magnetite grains from the Sambagwa high-pressure samples from Japan (Shimazaki, 1998). Shimizaki (1998) noted that Si rich spinels are almost found exclusively in hydrothermal settings, and therefore dissolution-precipitation mechanisms could enhance the incorporation of Si. Precipitation of ferric hydroxide could promote the adsorption of silicic acid under weakly alkaline conditions to form Si-rich magnetite at higher temperatures, although it is not certain if iron is oxidised at the site of precipitation or carried as ferric iron in solution (Shimazaki, 1998).

The cyclic zonation in the CO13-40 grain therefore likely results from dissolution-precipitation reactions (e.g. Putnis and Austrheim, 2010), in agreement with the disturbance of trace element patterns from primary spinel to porous and magnetite rims, and matrix magnetite grains.

5.6 Conclusions

Major and trace element chemistry of spinel grains indicate substantial modification during the evolution of Alpine Corsican serpentinites and hybrid ultramafic/mafic rocks. The primary mechanism for alteration of Cr-Al-rich spinel cores is proposed to be initial serpentinisation, where magnetite occurs as rims to Cr-rich cores. Magnetite rims that grew during this stage may react with Cr-rich cores to produce Fe^{3+}-rich chromite compositions between these two end members. Additional alteration stages occur during seafloor alteration to early prograde metamorphism. Antigorite reacts with primary spinel cores to produce porous rims in the presence of a fluid phase. The detailed quantitative mapping of a spinel grain in a high-pressure serpentinite emphasises that the proportion of ferric iron in the spinel structure likely results from dissolution-precipitation reactions on a mineral scale.

5.7 References

Arai, S. (1992), 'Chemistry of chromian spinel in volcanic rocks as a potential guide to magma chemistry', *Mineralogical Magazine* **56**(383), 173–184.

Barnes, S. J. (2000), 'Chromite in komatiites, II. Modification during greenschist to mid-amphibolite facies metamorphism', *Journal of Petrology* **41**(3), 387–409.

Barnes, S. J. & Roeder, P. L. (2001), 'The range of spinel compositions in terrestrial mafic and ultramafic rocks', *Journal of Petrology* **42**(12), 2279–2302.

Barra F, Gervilla F, Hernández E, Reich M, Padrón-Navarta JA (2014) 'Altered chromian spinels from La Cabaña peridotite, south central Chile: considerations on the formation of ferritchromite.', *Miner Petrol.* **10**, 819–836.

Bliss, N. & MacLean, W. (1975), 'The paragenesis of zoned chromite from central Manitoba', *Geochimica et Cosmochimica Acta* **39**(6), 973–990.

Bragg, W. H. (1915), 'XXX. The structure of the spinel group of crystals', *The London, Edinburgh, and Dublin Philosophical Magazine and Journal of Science* **30**(176), 305–315.

Buddington, A. & Lindsley, D. (1964), 'Iron-titanium oxide minerals and synthetic equivalents', *Journal of petrology* **5**(2), 310–357.

Colás, V.; González-Jiménez, J. M.; Griffin, W. L.; Fanlo, I.; Gervilla, F.; O'Reilly, S. Y.; Pearson, N. J.; Kerestedjian, T. & Proenza, J. A. (2014), 'Fingerprints of metamorphism in chromite: New insights from minor and trace elements', *Chemical Geology* **389**, 137–152.

Colás, V.; Padrón-Navarta, J. A.; González-Jiménez, J. M.; Griffin, W. L.; Fanlo, I.; O'reilly, S. Y.; Gervilla, F.; Proenza, J. A.; Pearson, N. J. & Escayola, M. P. (2016), 'Compositional effects on the solubility of minor and trace elements in oxide spinel minerals: Insights from crystal-crystal partition coefficients in chromite exsolution', *American Mineralogist* **101**(6), 1360–1372.

Danyushevsky, L.; Robinson, P.; Gilbert, S.; Norman, M.; Large, R.; McGoldrick, P. & Shelley, M. (2011), 'Routine quantitative multi-element analysis of sulphide minerals by laser ablation ICP-MS: Standard development and consideration of matrix effects', *Geochemistry: Exploration, Environment, Analysis* **11**(1), 51–60.

Dare, S. A.; Barnes, S.-J. & Beaudoin, G. (2012), 'Variation in trace element content of magnetite crystallized from a fractionating sulphide liquid, Sudbury, Canada: implications for provenance discrimination', *Geochimica et Cosmochimica Acta* **88**, 27–50.

Debret, B.; Millet, M.-A.; Pons, M.-L.; Bouilhol, P.; Inglis, E. & Williams, H. (2016), 'Isotopic evidence for iron mobility during subduction', *Geology* **44**(3), 215–218.

Deer, W. A.; Howie, R. A.; Zussman, J. & others (1992), *An introduction to the rock-forming minerals*, Vol. 696, Longman London.

Dick, H. J. & Bullen, T. (1984), 'Chromian spinel as a petrogenetic indicator in abyssal and alpine-type peridotites and spatially associated lavas', *Contributions to mineralogy and petrology* **86**(1), 54–76.

Evans, B. W.; Darby Dyar, M. & Kuehner, S. M. (2012), 'Implications of ferrous and ferric iron in antigorite', *American Mineralogist* **97**(1), 184–196.

Evans, B. W. & Frost, B. R. (1975), 'Chrome-spinel in progressive metamorphism—a preliminary analysis', *Geochimica et Cosmochimica Acta* **39**(6-7), 959–972.

Evans, B. W. & Kuehner, S. M. (2011), 'A nickel-iron analogue of balangeroite and gageite (Sasaguri, Kyushu, Japan)', *European Journal of Mineralogy* **23**(5), 717–720.

Evans, K. (2012), 'The redox budget of subduction zones', *Earth-Science Reviews* **113**(1), 11–32.

Evans, K.; Elburg, M. & Kamenetsky, V. (2012a), 'Oxidation state of subarc mantle', *Geology* **40**(9), 783–786.

Fanlo, I.; Gervilla, F.; Colás, V. & Subias, I. (2015), 'Zn-, Mn-and Co-rich chromian spinels from the Bou-Azzer mining district (Morocco): Constraints on their relationship with the mineralizing process', *Ore Geology Reviews* **71**, 82–98.

Fleet, M. (1981), 'The structure of magnetite', *Acta Crystallographica Section B: Structural Crystallography and Crystal Chemistry* **37**(4), 917–920.

Frost, B. R. (1991), 'Stability of oxide minerals in metamorphic rocks', *Reviews in Mineralogy and Geochemistry* **25**(1), 469–488.

Gahlan, H. A. & Arai, S. (2007), 'Genesis of peculiarly zoned Co, Zn and Mn-rich chromian spinel in serpentinite of Bou-Azzer ophiolite, Anti-Atlas, Morocco', *Journal of Mineralogical and Petrological Sciences* **102**(2), 69–85.

Gargiulo, M.; Bjerg, E. & Mogessie, A. (2013), 'Spinel group minerals in metamorphosed ultramafic rocks from Rio de Las Tunas belt, Central Andes, Argentina', *Geologica Acta* **11**(2), 133–148.

Gervilla, F.; Padrón-Navarta, J.; Kerestedjian, T.; Sergeeva, I.; González-Jiménez, J. & Fanlo, I. (2012), 'Formation of ferrian chromite in podiform chromitites from the Golyamo Kamenyane serpentinite, Eastern Rhodopes, SE Bulgaria: a two-stage process', *Contributions to Mineralogy and Petrology* **164**(4), 643–657.

Grieco, G. & Merlini, A. (2012), 'Chromite alteration processes within Vourinos ophiolite', *International Journal of Earth Sciences* **101**(6), 1523–1533.

Groppo, C. & Compagnoni, R. (2007), 'Metamorphic veins from the serpentinites of the Piemonte Zone, western Alps, Italy: a review', *Periodico di Mineralogia* **76**, 127–153.

Irvine, T. (1965), 'Chromian spinel as a petrogenetic indicator: Part 1. Theory', *Canadian Journal of Earth Sciences* **2**(6), 648–672.

Irvine, T. (1967), 'Chromian spinel as a petrogenetic indicator: Part 2. Petrologic applications', *Canadian Journal of Earth Sciences* **4**(1), 71–103.

Kamenetsky, V. S.; Crawford, A. J. & Meffre, S. (2001), 'Factors controlling chemistry of magmatic spinel: an empirical study of associated olivine, Cr-spinel and melt inclusions from primitive rocks', *Journal of Petrology* **42**(4), 655–671.

Khalil, K.I. & El-Makky, A.M., (2009), Alteration mechanisms of chromian-spinel during serpentinization at Wadi Sifein area, Eastern Desert, Egypt, *Resource Geology,* **59**(2), 194–211.

Kimball, K. L. (1990), 'Effects of hydrothermal alteration on the compositions of chromian spinels', *Contributions to Mineralogy and Petrology* **105**(3), 337–346.

Lahondère, J.; Lahondure, D.; Lluch, D.; Ohnenstetter, M.; Dominici, R. & Vautralle, C. (1992), 'Carte géologique de la France a 1/50000', *Luri, BRGM*.

Lahondère, D. & Guerrot, C. (1997), 'Datation Nd-Sm du métamorphisme éclogitique en Corse alpine: un argument pour l'existence, au Crétacé supérieur, d'une zone de subduction active localisée le long du block corse-sarde.', *Géologie de la France* **3**, 3-11.

Lindsley, D. H. & Banerjee, S. (1991), 'Oxide minerals: petrologic and magnetic significance', .

McClure, D. S. (1957), 'The distribution of transition metal cations in spinels', *Journal of Physics and Chemistry of Solids* **3**(3-4), 311–317.

Mellini, M.; Rumori, C. & Viti, C. (2005), 'Hydrothermally reset magmatic spinels in retrograde serpentinites: formation of "ferritchromit" rims and chlorite aureoles', *Contributions to Mineralogy and Petrology* **149**(3), 266–275.

Meresse, F.; Lagabrielle, Y.; Malavieille, J. & Ildefonse, B. (2012), 'A fossil Ocean–Continent Transition of the Mesozoic Tethys preserved in the Schistes Lustrés nappe of northern Corsica', *Tectonophysics* **579**, 4–16.

Merlini, A.; Grieco, G. & Diella, V. (2009), 'Ferritchromite and chromian-chlorite formation in mélange-hosted Kalkan chromitite (Southern Urals, Russia)', *American Mineralogist* **94**(10), 1459–1467.

Mukherjee, R.; Mondal, S. K.; Rosing, M. T. & Frei, R. (2010), 'Compositional variations in the Mesoarchean chromites of the Nuggihalli schist belt, Western Dharwar Craton (India): potential parental melts and implications for tectonic

setting', *Contributions to Mineralogy and Petrology* **160**(6), 865–885.

Mukherjee, R., Mondal, S. K., González-Jiménez, J. M., Griffin, W. L., Pearson, N. J., & O'Reilly, S. Y. (2015). Trace-element fingerprints of chromite, magnetite and sulphides from the 3.1 Ga ultramafic–mafic rocks of the Nuggihalli greenstone belt, Western Dharwar craton (India). *Contributions to Mineralogy and Petrology*, **169**(6), 1–23.

Müntener, O. & Hermann, J. (1994), 'Titanian andradite in a metapyroxenite layer from the Malenco ultramafics (Italy): implications for Ti-mobility and low oxygen fugacity', *Contributions to Mineralogy and Petrology* **116**(1-2), 156–168.

Nadoll, P.; Angerer, T.; Mauk, J. L.; French, D. & Walshe, J. (2014), 'The chemistry of hydrothermal magnetite: a review', *Ore Geology Reviews* **61**, 1–32.

Nadoll, P. & Koenig, A. E. (2011), 'LA-ICP-MS of magnetite: methods and reference materials', *Journal of Analytical Atomic Spectrometry* **26**(9), 1872–1877.

Pagé, P. & Barnes, S.-J. (2009), 'Using trace elements in chromites to constrain the origin of podiform chromitites in the Thetford Mines ophiolite, Québec, Canada', *Economic Geology* **104**(7), 997–1018.

Paton, C.; Hellstrom, J.; Paul, B.; Woodhead, J. & Hergt, J. (2011), 'Iolite: Freeware for the visualisation and processing of mass spectrometric data', *Journal of Analytical Atomic Spectrometry* **26**(12), 2508–2518.

Plümper, O.; Beinlich, A.; Bach, W.; Janots, E. & Austrheim, H. (2014), 'Garnets within geode-like serpentinite veins: Implications for element transport, hydrogen production and life-supporting environment formation', *Geochimica et Cosmochimica Acta* **141**, 454–471.

Prabhakar, N. & Bhattacharya, A. (2013), 'Origin of zoned spinel by coupled dissolution–precipitation and inter-crystalline diffusion: evidence from serpentinized wehrlite, Bangriposi, Eastern India', *Contributions to Mineralogy and Petrology* **166**(4), 1047–1066.

Putnis, A. & Austrheim, H. (2010), 'Fluid-induced processes: metasomatism and metamorphism', *Geofluids* **10**(1-2), 254–269.

Ravna, E.; Andersen, T. B.; Jolivet, L. & De Capitani, C. (2010), 'Cold subduction and the formation of lawsonite eclogite–constraints from prograde evolution of eclogitized pillow lava from Corsica', *Journal of Metamorphic Geology* **28**(4), 381–395.

Ringwood, A. (1958), 'The constitution of the mantle—I: Thermodynamics of the olivine-spinel transition', *Geochimica et Cosmochimica Acta* **13**(4), 303–321.

Savard, D.; Barnes, S. & Raju, P. S. (2010), Accurate LA-ICP-MS calibration for magnetite analysis using multiple reference materials, *in* 'Goldschmidt Conference Abstracts A'.

Shimazaki, H. (1998), 'On the occurrence of silician magnetites', *Resource Geology* **48**(1), 23–29.

Singh, A. K. & Singh, R. B. (2013), 'Genetic implications of Zn-and Mn-rich Cr-spinels in serpentinites of the Tidding Suture Zone, eastern Himalaya, NE India', *Geological Journal* **48**(1), 22–38.

Vitale Brovarone, A.; Beltrando, M.; Malavieille, J.; Giuntoli, F.; Tondella, E.; Groppo, C.; Beyssac, O. & Compagnoni, R. (2011), 'Inherited ocean–continent transition zones in deeply subducted terranes: insights from Alpine Corsica', *Lithos* **124**(3), 273–290.

Vitale Brovarone, A.; Beyssac, O.; Malavieille, J.; Molli, G.; Beltrando, M. & Compagnoni, R. (2013), 'Stacking and metamorphism of continuous segments of subducted lithosphere in a high-pressure wedge: the example of Alpine Corsica (France)', *Earth-Science Reviews* **116**, 35–56.

Vitale Brovarone, A. & Herwartz, D. (2013), 'Timing of HP metamorphism in the Schistes Lustrés of Alpine Corsica: New Lu–Hf garnet and lawsonite ages', *Lithos* **172**, 175–191.

Wechsler, B. A.; Lindsley, D. H. & Prewitt, C. T. (1984), 'Crystal structure and cation distribution in titanomagnetites (Fe (sub 3-x) Ti x O 4)', *American Mineralogist* **69**(7-8), 754–770.

Wylie, A. G.; Candela, P. A. & Burke, T. M. (1987), 'Compositional zoning in unusual Zn-rich chromite from the Sykesville District of Maryland and its bearing on the origin of" ferritchromit"', *American Mineralogist* **72**(3-4), 413–422.

Yokoyama, T.; Nakazato, T. & Tarutani, T. (1980), 'Polymerization of silicic acid adsorbed on iron (III) hydroxide', *Bulletin of the Chemical Society of Japan* **53**(4), 850–853.

CHAPTER 6

INSIGHTS INTO SULPHUR CYCLING AT SUBDUCTION ZONES FROM *IN-SITU* ISOTOPIC ANALYSIS OF SULPHIDES IN HIGH-PRESSURE SERPENTINITES AND 'HYBRID' SAMPLES FROM ALPINE CORSICA

Rosalind J. Crossley, Katy A. Evans, Heejin Jeon & Matt Kilburn

This chapter is a manuscript under review in *Chemical Geology*.

Contributions by co-authors

Rosalind Crossley collected the Serra di Pigno samples, was responsible for sample preparation including cutting thin section billets, crushing for bulk sample analysis and drilling areas of interest from thin section billets following careful petrographic analysis augmented by scanning electron microscopy, the collection of EPMA analyses with the assistance of Malcolm Roberts at the CMCA, University of Western Australia, and all data reduction/synthesis of EPMA. SIMS and NanoSIMS data collection and reduction was carried out with the assistance of Heejin Jeon and Matt Kilburn at CMCA. Rosalind Crossley wrote this manuscript with helpful feedback, guidance and discussions with Katy Evans, and discussions on technical aspects of SIMS and NanoSIMS with Heejin Jeon and Matt Kilburn.

Abstract

$\delta^{34}S$ values of sulphides provide information on sulphur sources and processes subsequent to sulphide crystallisation, such as fluid infiltration or loss, and are sensitive to the redox state of sulphur in the host mineral. Therefore it may be possible to use $\delta^{34}S$ to constrain the redox state and fluxes of sulphur. Further, the proximity of serpentinites to ocean crust and metasediments may influence their isotopic signatures during subduction. For example, seafloor serpentinites associated with mafic intrusions have heavier $\delta^{34}S$ values.

In this study the redox state, the likelihood of sulphur addition to the sub-arc mantle from serpentinite dehydration, and the distribution of sulphur within subducted serpentinites from Alpine Corsica is investigated by a combination of petrographic analysis, in situ sulphur isotopic analysis and trace element analyses of sulphides hosted in these rocks.

Sulphur-derived from the mantle ($\delta^{34}S$ values ~ 0.1‰) was not the sole sulphur source in these samples with $\delta^{34}S$ values of 1.9–15.5‰ for all sulphides, with the heaviest values recorded in pyrites of a hybrid mafic/ultramafic sample. Heavy $\delta^{34}S$ is preserved in sulphides attributed to prograde metamorphism, and is most consistent with the retention of isotopic signatures from hydrothermal sulphate reduction on the seafloor. However, a shift towards heavier $\delta^{34}S$ from prograde sulphides to sulphides associated with the advanced stages of exhumation suggests that late stage exhumation enhanced access to slab-derived fluids which carry oxidised sulphur (sulphate or SO_2).

6.1 Introduction

Sulphur is subducted in variable oxidation states from sulphate (+6) to sulphide (-2) within altered ocean crust, hydrated mantle lithosphere and ocean floor sediments, to contribute a significant flux of redox budget to subduction zones. In addition, the S input into subduction zones is an order of magnitude higher than the flux of S released (Evans, 2012; Evans et al., 2014). While it is well established that sulphur is input to subduction zones in significant quantities, changes to the oxidation state of sulphur, the processes that sulphur undergoes during subduction and the quantity of sulphur transferred to the sub-arc mantle and deep mantle are poorly constrained. The redox state and the concentration sulphur of the sub-arc mantle are of particular importance because genetic models for arc-related ore deposits currently require an oxidised sub-arc mantle.

The *in-situ* measurement of sulphur isotopes (i.e. $\delta^{34}S$) in sulphur-bearing mineral phases within rocks that have undergone subduction and, at a later stage, exhumation can be used to constrain the source, redox state and processes that sulphur has undergone throughout the subduction cycle. Heavy sulphur (^{34}S) partitions preferentially into oxidised species e.g. present day seawater sulphate is ~20-21‰ (Rees, 1978; Ueda & Sakai, 1984; Woodhead et al., 1987; Marini et al., 2011) whereas mantle sulphide is ~0‰ (0.1±0.5‰; Sakai et al., 1984; Shanks et al., 1995; Alt et al., 1998). The observation that porphyry arc-related ore deposits have heavier $\delta^{34}S$ values up to ~13‰ than the mantle (Alt et al., 1993; Ishihara & Sasaki, 1989), requires a source of heavy sulphur, which is proposed to have originated via sulphate transfer from the slab (Richards, 2015). Pre-subduction fixation of sulphate in serpentinised mantle lithosphere, oceanic crust and sediments has been proposed to account for sulphate enrichment in the slab (Ishihara and Sasaki, 1979; Shanks et al., 1981; Wallace & Edmonds, 2011; Alt et al., 2012a; Debret et al., 2014; Evans et al., 2014). However, sulphur release and retention within the slab during subduction, and how these processes occur are not well understood.

Attempts have been made to constrain subduction-related fluxes of S from the mafic component of the crust (Evans *et al.,* 2014; Marschall & Shimizu, 2012; Aulbach *et al.,* 2012), but fluxes from the hydrated mantle lithosphere during

subduction are rarely investigated, with some exceptions (e.g. Alt et al., 2012; Shimizu et al., 2013). The hydrated mantle lithosphere component of the slab is of particular interest because its dehydration at depth within the subduction channel has the potential to release a significant volume of fluids to the sub-arc mantle. Such fluids are thought to be responsible for transferring up to 40wt% of the initial bulk sulphur in the slab to the mantle wedge (Jégo & Dasgupta, 2013). In addition, seafloor serpentinites are sulphur enriched (and ^{34}S-enriched) compared to mantle with $\delta^{34}S$ ~20‰ (Alt & Shanks, 2003; Alt et al., 2012a, Tostevin et al., 2014), due to a contribution from seawater-derived sulphate. Thus upon subduction serpentinites have the potential to carry oxidised sulphur to the sub-arc mantle or deep mantle.

Few studies have attempted to address the contribution of serpentinites to sulphur cycling, and therefore the magnitude of sulphur fluxed from serpentinites to different components of subduction zones is poorly constrained with estimates of S fluxed from serpentinites varying by an order of magnitude. For example, Alt *et al.* (2012b) proposed that the loss of oxidised sulphur during the transition of antigorite-serpentinites to chlorite harzburgite contributes a flux of up to 0.49×10^{11} mol S per year to the sub-arc mantle; lower than the concentration of sulphur fluxed from ocean crust or sediments. However, the retention of up to 1.6×10^{11} mol S per year in post-dehydration ultramafic rocks may contribute significantly to the recycling of S to the deep mantle (Alt et al., 2013). In another study, redox budget calculations implied that serpentinites may contribute the largest redox budget to subduction zones, with estimates of input sulphur fluxes of $0.7 \pm 0.8 \times 10^{12}$ mol S per year (Evans, 2012).

$\delta^{34}S$ may reflect the original sulphur source, in addition to processes subsequent to sulphide crystallisation such as fluid infiltration or loss (Evans et al., 2014). Therefore, measurements of $\delta^{34}S$ can be used to constrain the redox state and fluxes of sulphur. In addition, the proximity of serpentinites to ocean crust and metasediments in the subduction channel may influence their sulphur isotope signatures. For example, seafloor serpentinites associated with gabbroic intrusions have been shown to have heavier $\delta^{34}S$ values than serpentinites elsewhere (Alt et al., 2012a). Whole rock $\delta^{34}S$ data is available for subducted ultramafic rocks (Alt et al., 2012a; b) but subducted ultramafic rocks undergo several stages of alteration

starting at the seafloor, then through subduction and exhumation. These stages are recorded by partial preservation of sulphide mineral assemblages related to each metamorphic stage, so whole rock sulphur isotope analysis provides a mixed signature. *In-situ* $\delta^{34}S$ measurements of sulphides provide an opportunity to sample the evolution of fluids through the metamorphic evolution of the samples, provided the sulphide parageneses are well constrained.

$\Delta^{33}S$ is used to describe the extent of mass independent fractionation (MIF), i.e. the degree to which variations in isotope abundance are not dependent on mass. MIF isotopic signatures for sulphur deviates from the terrestrial line defined by the slope of a fractionation line between $\delta^{34}S$ and $\delta^{33}S$ for the Earth-Moon system, where the slope is 0.515 (Seal, 2006 and references therein). Seawater sulphate has a $\Delta^{33}S$ value of 0.050±0.0003‰ (Ono et al., 2012), whereas mid ocean ridge basalts (MORB) from the East Pacific Rise are within error of the Vienna Canyon Diablo Troilite (VCDT) with $\Delta^{33}S$ values of ~0.001±0.017‰ (Ono et al., 2012). A study of samples from the Iberian Margin basement has revealed that serpentinised peridotites have higher $\Delta^{33}S$ values than basaltic samples with values ranging from –0.01 to 0.16‰ compared to -0.06 to 0.09‰ in the basalts (Ono et al., 2012). $\Delta^{33}S$ has been shown to provide additional information compared to the measurement of only $\delta^{34}S$ values (Ono et al., 2012), and allows the assessment of the distinction between open and closed system sulphate reduction, and between bacterial sulphate reduction and hydrothermal sulphate reduction.

Hybrid rocks (a product of chemical, isotopic or physical mixing between lithological end members) may have the potential to carry volatile elements (including sulphur) to depths beyond the blueschist-eclogite transition, to greater depths than serpentinites (e.g. Spandler et al. 2008) and thus here hybrid samples will also be investigated. In this study, the redox state, the likelihood of sulphur transfer to the sub-arc mantle from serpentinite dehydration, and the distribution of sulphur within subducted serpentinites and hybrid mafic/ultramafic rocks are investigated through a combination of petrographic analysis, *in-situ* sulphur isotope and trace element analyses of sulphides hosted in these rocks. To the authors' best knowledge the only other published *in-situ* sulphur isotope values for subducted ultramafic rocks are reported in two conference abstracts, Santiago-Ramos et al.

(2012) and Shimizu et al. (2013) who report $\delta^{34}S$ values from Erro Tobbio serpentinites.

6.2 Geological Background

The geological setting is described in detail in chapter 4. Briefly, thirty samples were collected from the Schistes Lustrés complex at the two localities Serra di Pigno and Capu Corvoli, Cap Corse (Fig. 6.1). The Schistes Lustrés complex is comprised of internal continental slices, metasediments and metaophiolites (which include serpentinites, metagabbros and metabasalts). The pre-subduction setting of these lithologies is consistent with either ultra-slow spreading centre or an ocean-continent transition zone (e.g. Vitale Brovarone et al., 2013). These localities were chosen because they allow the assessment of lithological controls on the isotopic composition of sulphur, and record slightly different P-T conditions, Capu Corvoli records a higher metamorphic grade compared to Sierra di Pigno.

Serra di Pigno lies approximately 10 km west of Bastia, on Cap Corse. The sample collection includes metagabbros, metasediments and serpentinites Serpentinites were collected proximal to and distal to metagabbros and metasediments. Hybrid samples were collected from Capu Corvoli. The samples from the Serra di Pigno region record blueschist to eclogite facies metamorphism and underwent peak metamorphism at ~37 Ma (Vitale Brovarone and Herwartz, 2013). The pressure-temperature conditions recorded during subduction are estimated to be a minimum of ~1.3–2.6 GPa (Lahondère and Guerrot, 1997; Vitale Brovarone et al., 2013), and a peak metamorphic temperature of ~414–471ºC, on the basis of Raman spectroscopy of carbonaceous material (Vitale Brovarone et al., 2013).

The chlorite schist and talc schist hybrid mafic/ultramafic samples were collected at Capu Corvoli, Cap Corse. The samples are from a shear zone with a top-to-the-west to northwest sense of shear, parallel to a series of proximal WNW to NW shallowly dipping thrust faults, which were previously interpreted to divide the lawsonite-blueschist Upper Castagniccia metasediments and lawsonite-eclogite ophiolites (Lahondère, 1992). The sense of shear is uniform with deformation associated with prograde metamorphism (Mattauer et al., 1977; 1981; Faure and Malavielle, 1981; Harris, 1985; Warburton, 1986; Magott et al., 2016). Within the

shear zone, slivers of the hybrid lithologies are juxtaposed with metagabbro. Recent P-T estimates suggest that the Upper Castagniccia metasediments record eclogite facies metamorphism (Vitale Brovarone et al., 2013 & references therein). Thus, the Capu Corvoli samples record similar or higher P-T conditions than the Serra di Pigno samples at ~490–550 °C and 1.9–2.6 GPa (Ravna et al., 2010; Vitale Brovarone et al., 2013).

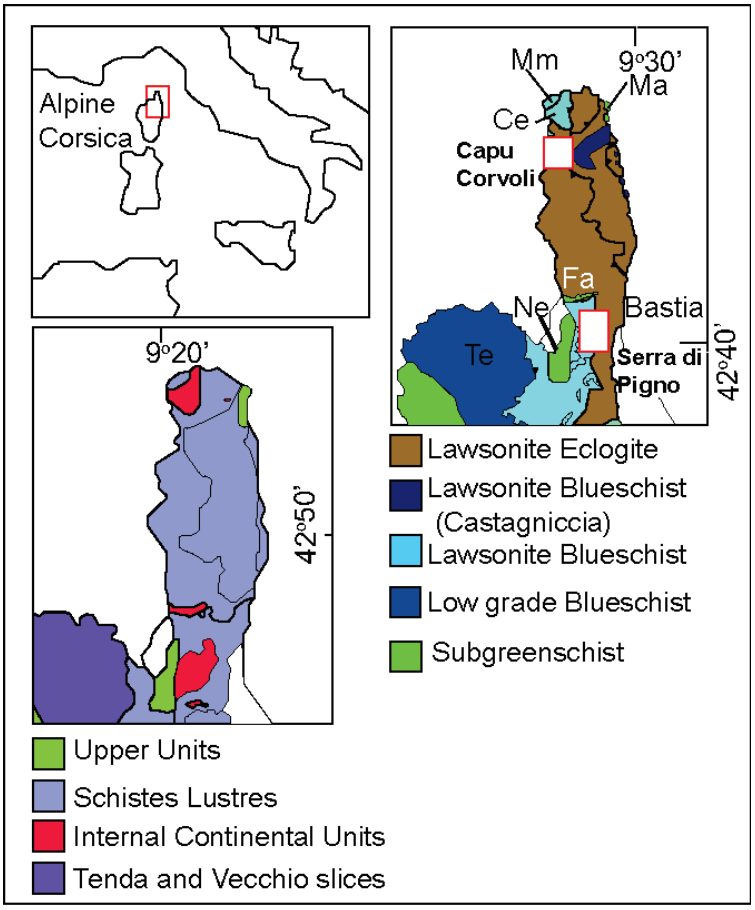

Figure 6.1: Geological map of the sample localities at Serra di Pigno and Capu Corvoli, Alpine Corsica.

6.3 Petrography

6.3.1 Serra di Pigno

6.3.1.1 Serpentinite CO13-40

CO13-40 is a serpentinite sample distal to other lithologies (WGS 84, zone 32T, 0533122 mE 4728302 mN). Phases stable prior to subduction and consistent with primary growth or seafloor growth and/or alteration include lower pressure chrysotile (200–500 µm wide laths, 5%), lizardite pseudomorphs of primary orthopyroxene (bastite, 10%), andradite garnet which occurs as rims on bastite, and

Cu-Al spinel (see chapter 5). Fine grained antigorite (60%) is attributed to prograde metamorphism and defines the dominant foliation. Prograde to peak metamorphic phases which overprint the foliation defined by fine grained antigorite include pentlandite (up to ~50 μm in diameter) and magnetite (mt1). A late generation of antigorite cuts pentlandite and mt1 (Fig. 6.2a, b), and further constrains pentlandite to growth prior to retrogression associated with exhumation. A later stage of retrogression is recorded by late tremolite veins in CO13-40, which cross cut antigorite, lizardite and chrysotile, and ilmenite (~3%).

6.3.1.2 Serpentinite CO13-33

CO13-33 is a serpentinite sample proximal to metagabbro and metaquartzite (WGS 84, zone 32T 0533514 mE 4729532 mN). Primary or seafloor minerals include Cr-Al spinel. Phases associated with prograde metamorphism include an early generation of pentlandite (pn1; Fig. 6.2c), heazlewoodite, kamacite (~5 μm), fine matrix antigorite (~20%) and fine balangeroite veins (<5 μm across). Additionally porous spinel with antigorite inclusions, is inferred to have been stable during prograde metamorphism (see chapter 5). Peak metamorphic phases include chlorite, which is partially replaced by pentlandite (pn2; Fig 3d) and therefore pn2 is attributed to peak metamorphism or the onset of exhumation, and is overprinted by a later generation of magnetite at the rim. A late phase of pentlandite, pn3, occurs as euhedral to subhedral grains that overprint a late generation of antigorite, and is synchronous with or includes late magnetite (Fig. 6.3e), thus is related to the onset of exhumation.

6.3.1.3 Serpentinite CO13-55

CO13-55 is a serpentinite sample proximal to metagabbros and calcareous schist (WGS 84, zone 32T, 0533398 mE 4729368 mN). No primary phases are apparent, with all spinel altered to 'porous spinel', as outlined in chapter 5. Phases that were stable during prograde metamorphism include the fine-grained antigorite matrix (<1 to 5 μm) and pentlandite1 (pn1), where inclusions of antigorite and pn1 occur in altered Fe-rich spinel rims implies the synchronous growth of antigorite and pn1. Prograde to peak phases include andradite garnet (grt1), chlorite, pyrite, chalcopyrite, pentlandite (pn2) and early magnetite (mt1). The growth of pn2 and mt1 are synchronous and contain inclusions of primary or seafloor Cr-rich spinel,

and are cut by retrogressive antigorite (Fig. 5.2f). Phases associated with the onset of exhumation include pn3 and mt2. Pn3 and mt2 are associated with diopside which overprints the prograde phases chlorite and early antigorite. Pn4 is synchronous with or occurs as rims on and therefore postdates late antigorite cross-cutting veins (Fig. 5.2h), where antigorite veins cut prograde to peak phases (pyrite, chalcopyrite, pn2 and mt1) and phases associated with the onset of exhumation (pn3 and mt2).

6.3.2 Capu Corvoli

6.3.2.1 Chlorite schist CO14-03

CO14-03 is a chlorite schist in contact with a metagabbro that lies structurally above the sample (WGS 84, zone 32T, 0529140 mE 4753069 mN). There is little evidence for the retention of primary or seafloor phases. The earliest phases associated with prograde to peak metamorphism are fine, orientated laths of foliated chlorite and antigorite, which together comprise the matrix. Magnetite is constrained to the onset of exhumation because it cuts the prograde to peak antigorite-chlorite defined foliation, has undergone brittle deformation and is cut by second generation of chlorite (chl2) veins, and overprinted by titanite, thus growth is constrained to the earliest stages of exhumation. Pyrite is associated with growth during later stages of exhumation and occurs as euhedral aggregates isolated in the matrix, as rims on magnetite or within fractures in magnetite. Pyrite is enclosed by titanite at the rim and some grains contain inclusions of titanite towards the rim. Titanite replaces magnetite and therefore postdates early exhumation. Pyrite is therefore attributed to an advanced stage of exhumation.

6.3.2.2 Talc schist CO14-04

CO14-04 is a talc schist sample in contact with the same metagabbro associated with CO14-03 but in this case the metagabbro lies structurally below the sample (WGS 84, zone 32T, 0529107 mE 4753071 mN). Primary or seafloor phases consist of an early generation of pyrrhotite (po1, <5 μm), Cr-rich spinel cores to magnetite, and a Pt-rich alloy grain (rare, ~2 μm). Prograde phases include py1, an early generation of talc (talc1), magnetite, a later generation of pyrrhotite (po2) and chlorite. Talc1 growth is attributed to metasomatism during subduction (e.g. Spandler et al., 2008). Py1 contains inclusions of primary phases or those associated

with seafloor alteration; po1, Cr-rich spinel and the Pt-rich alloy. Given the inclusion of Cr-spinel in py1, and magnetite rims on Cr-rich spinel, py1 and magnetite growth are inferred to be synchronous. Chlorite, which is attributed to peak metamorphism, cross-cuts magnetite, thus the growth of magnetite and py1 predate peak metamorphism. Po2 is texturally later than py1, given its inclusion in rims on py1, though possible incorporation from the matrix cannot be excluded. A second generation of pyrite, py2, is constrained to growth during the onset of exhumation. Py2 cuts the prograde talc1 matrix and peak metamorphic chlorite, and has coarse talc2 rims, where this generation of talc is attributed to decompression associated with exhumation (Evans & Powell, 2015).

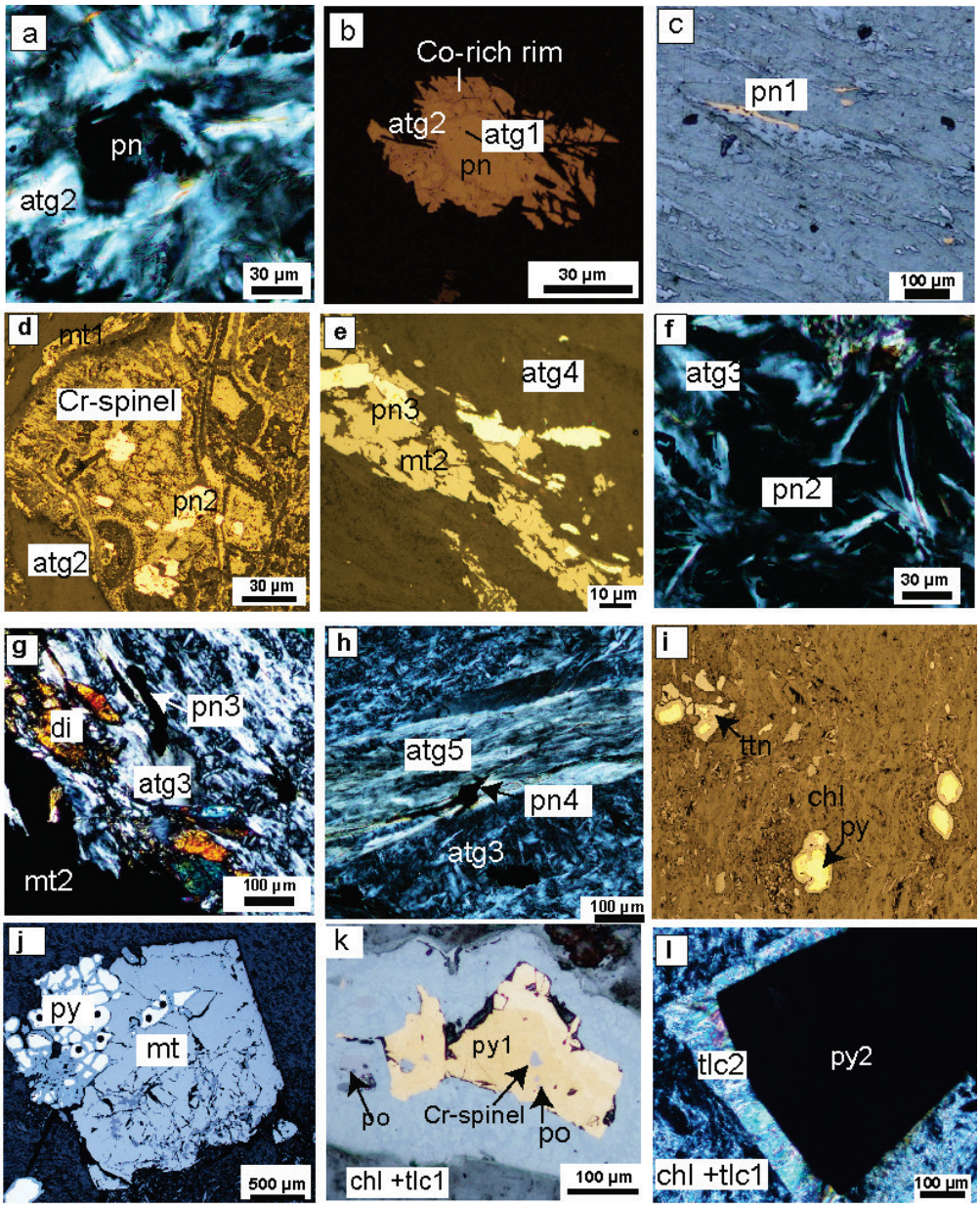

Figure 6.2: microphotographs illustrating key textures, bse = backscattered electron, rfl = reflected light and xpl = cross-polarised light image. (a) xpl: pentlandite (pn) in CO13-40 overprinted by late generation antigorite (atg2). (b) rfl: pentlandite with a Co-rich rim in CO13-40, early antigorite inclusions (atg1) and overprinted by atg2. (c) rfl: early pentlandite (pn1) in CO13-33 aligned with atg1 foliation. (d) bse: pn2 overprints early Cr- rich spinel grains in CO13-33. (e) rfl: pn3 grains in CO13-33 cross-cut late antigorite and associated with magnetite (mt2) (f) xpl: pn2 cross-cut by atg3 in CO13-55 (g) xpl: pn3 associated with atg3 in CO13-55 (h) xpl: euhedral grain of pn4 overprinting late atg3 and atg5 in antigorite, (i) rfl: pyrite grains within matrix in CO14-03. (j) pyrite rims on magnetite in CO14-03. (k) rfl: py1 grains in CO14-04 with inclusions of chromite and an iron hydroxide rim, which contains inclusions of po. (l) xpl: py2 grains with a talc2 rim in CO14-04 (xpl).

6.4 Methods

The samples selected for this study contain sulphides of suitable size for secondary ion mass spectrometry (SIMS) analysis. Thin section billets were cut perpendicular to sample foliation. Prior to *in-situ* analysis, detailed petrographic

analysis was undertaken using transmitted and reflected light microscopy, and scanning electron microscopy (SEM) and energy dispersive spectrometry (EDS). Electron probe microanalysis (EPMA) was carried out prior to secondary ion mass spectrometry (SIMS) to determine compositions of sulphides. In addition, EPMA and NanoSIMS mapping were employed to seek for any discrete zoning in sulphide mineral chemistry. Detailed methods of SIMS, EPMA and NanoSIMS are described in this section.

6.4.1 Secondary Ion Mass Spectrometry

Prior to SIMS and NanoSIMS analysis, representative areas were selected from thin section billets and drilled from each sample using a hollow cylindrical diamond coated drill bit that produces 7 mm pucks. The pucks were mounted in epoxy, polished and coated with ~30 nm of Au to provide electrical conductivity at high voltage and thus prevent sample charging (see Appendix E1 for more details on the mount preparation and polishing techniques). The mounts were trimmed by approximately one third to allow a reusable standard piece that contains Sierra pyrite and VMSO pentlandite to be mounted alongside the unknown samples in the ion probe. Sierra pyrite (where other fragments from the same pyrite block have been previously reported as Sonora-3) is from a 9 kg cube of pyrite from a Cretaceous porphyry copper mine in Sonora, Mexico, described in Wacey et al. (2011), Farquhar et al. (2013) and Evans et al. (2014). VMSO pentlandite is sourced from a massive sulphide lens from the Ni-Cu-PGE Long-Victor mine, Kambalda, Western Australia (Barnes et al., 2013, and references therein) metamorphosed to amphibolite facies. VMSO pentlandite is interlayered on a centimetre-scale with pyrrhotite and pyrite. All $\delta^{34}S$ values in this study are relative to Vienna Canyon Diablo Troilite (VCDT), the value of which is assumed to be 0.0450045 (Ault and Jensen, 1963).

The bulk $\delta^{34}S$ for Sierra pyrite and VMSO pentlandite were measured by laser fluorination at McGill University, where the absolute $\delta^{34}S$ values of 2.17 ± 0.04‰ and 3.22 ± 0.05 ‰, respectively, and absolute $\delta^{33}S$ values of 1.09 ± 0.02‰ and 1.66 ± 0.02 ‰ were determined (LaFlamme et al., 2016). $\delta^{33}S$ and $\delta^{34}S$ heterogeneity in Sierra pyrite was assessed by preliminary SIMS analysis and is on the scale of less than a centimetre. $\Delta^{33}S$ yielded average values of -0.02 ±0.01‰

with a 0.08‰ reproducibility for Sierra pyrite, and 0.00 ± 0.02‰ with a reproducibility of 0.12‰ for VMSO (La Flamme et al., 2016). These standards have shown high precision over the course of three years, for example, the external precision for $\delta^{34}S$ of Sierra is < 0.1 ‰ for over 1000 analyses (LaFlamme et al., 2016), and both Sierra and VMSO are of similar major element (Fe, Ni, Co and S) compositions to the pyrites and pentlandites studied here (section 6.5.1, Appendix E2).

Ion microprobe analysis was carried out on the Cameca IMS 1280 at the CMCA, University of Western Australia. In situ analysis of sulphides was carried out as follows for pyrite grains, a 2.35 nA focused ion beam was used to presputter the analysis area with 15 x 15 µm rasters for 30 s prior to automatic secondary centring and the acquisition of 20 x 4 analysis cycles. For the smaller grains of pentlandite, the presputter time was reduced to 10 s and the rasters to 10 x 10 µm to avoid overlap of analyses. The presputter time for standards was 30 s for all analyses. The Faraday cup collected ^{32}S, ^{33}S and ^{34}S. Nuclear magnetic resonance (NMR) and an electron gun were used for all analyses.

Standard measurements per four to five analyses allowed the assessment of instrumental drift. The method for data reduction was as follows. Raw standard data (Sierra and VMSO) for $^{34}S/^{32}S$ were used to check for drift. If a drift correction was required, the following equation was used,

$$\mathrm{R_{drift}} = \mathrm{RD} - \mathrm{c} * \mathrm{n}, \mathrm{RD}$$

where $\mathrm{R_{drift}}$ is the drift correction ratio, RD is the Raw Data for $^{34}S/^{32}S$, c = intercept, n = time. The internal error $\sigma_{abs(DC)}$, was then calculated using the formula,

$$\sigma_{abs(DC)} = \sqrt{\left(\frac{\sigma int}{100xRD}\right)^2 (n + err\ on\ c)^2, \frac{\sigma_{int}}{100} * RD},$$

where err = error on intercept and σ_{int} in relative percent. Dividing the drift corrected value by laser fluorination values (Farquhar et al., 2013) allowed the instrumental mass fractionation (α) to be calculated for the Sierra or VMSO (depending if the run was for pyrite or pentlandite, respectively),

$$\sigma_{abs(\alpha)} = \sqrt{\left(\sigma_{\frac{abs(DC)}{LF}}\right)^2 + \left(\left(\frac{DC}{LF}\right)^2 \sigma_{LF^2}\right)},$$

where $\sigma_{abs(DC)}$ is the drift corrected value and LF is the laser fluorination value.

SIMS corrected ratios were then calculated by dividing the drift corrected values by the mean IMF (α) for Sierra or VMSO,

$$\sigma_{abs(SIMS)} = \sqrt{\left(\frac{1}{\alpha_{std} * \sigma_{abs(DC)}}\right)^2 + \left(\left(\frac{DC}{\alpha^2 * \sigma_{abs(\alpha)}}\right)^2\right)},$$

where α_{std} is the mean instrumental mass fractionation (α) calculated for the standard (std). $\delta^{34}S$ values were then calculated using the SIMS corrected ratios relative to VCDT ^{34}S, using the following formula:

$$\delta^{34}S\ (‰) = \left\{\left[\left({}^{34}S/{}^{32}S\right)_{sample} - \left({}^{34}S/{}^{32}S\right)_{VCDT}\right] * \left[\left({}^{34}S/{}^{32}S\right)_{VCDT}\right]^{-1}\right\} * 1000$$

The standard deviation (2σ) of $\delta^{34}S$ values were calculated using the equation,

$$2\sigma_{abs} = 2 * \sqrt{\left(\frac{1000}{\alpha * VCDT\ {}^{34}S}\right)^2 * \left(\sigma_{abs(DC)}{}^2\right) + \left(DC^{34}S * \frac{\sigma_{abs\alpha}}{{}^{34}S\alpha}\right)^2 + \left(\frac{\left(DC^{34}S * VCDT0\right)}{{}^{34}S/{}^{32}S_{VCDT}{}^2}\right)^2}$$

Data was discarded for samples with field aperture x and y values of more than 60, where such values indicate that the beam is not central. In addition, some analysis sites were near the edge of the grain. Analyses from these sites were treated as suspect and ignored. Incorporation of minute antigorite inclusions in the analysis volume (<2 μm) may affect S ratios via the changes to matrix fractionation effects, although the inclusions would not contain sufficient sulphur to alter $\delta^{34}S$ values. However, sulphide grains were checked carefully for such inclusions using SEM and nominally inclusion-free sulphides were analysed. Additionally, the ^{32}S intensity of the standards and samples were compared to check the ^{32}S measurements were consistent, where analyses with significant differences in intensity were discarded.

6.4.2 EPMA Mapping

Trace element mapping was carried out on sulphide grains selected for SIMS analysis using the JEOL 8530F Hyperprobe at the Centre for Microscopy, Characterisation and Analysis (CMCA) at the University of Western Australia. The carbon coating was 25 nm in thickness. Operating conditions included a 20 kV accelerating voltage, a 20 nA beam current, and a 40s dwell time. Mean atomic number (MAN) background corrections were used with a total on-peak counting time of 20 s per element. The standards used for calibration include Ni, Co, Pyrite (S) and Ap200 (arsenopyrite; As). Detectors used included PETJ for S kα, TAP for As lα, and LiF for Fe kα. Two detectors were used for optimum detection of Co kα and Ni kα; LiFH and LiF. Data reduction was performed using the Probe for EPMA software (Donovan et al., 2012), and maps were generated using Surfer 10.2. Point analyses were carried out under the same operating conditions but additional standards were used for calibration including wollastonite (Si), San Carlos Olivine (Mg), Crocoite (Pb), ZnO, Cu, Mn, Cr_2O_3, Bi_2Se_3, Ag, GaAs (As), and Sb, and the LiF detector was used for detection of Ni kα and Co kα, and additional elements were detected on the TAP detector (Si kα, Mg kα and Se lα), PETJ (Pb mα), LiFH (Zn kα, Cu kα, Mn kα, Cr kα), PETJ (Ag lα and Bi mα) and LiF (Sb lα).

6.4.3 NanoSIMS

Mapping of small pentlandite grains in sample CO13-40 was performed on the Cameca NanoSIMS 50 at the CMCA, the University of Western Australia. Secondary ion images were acquired using a focused Cs^+ primary ion beam, with a nominal beam diameter of ~100 nm. The electron multipliers were positioned to detect the secondary ions FeS^-, CoS^-, NiS^-, CuS^-, AsS^-, Te^- and Au^- on masses 88, 91, 92, 97, 107, 130 and 197, respectively. Not all ion species were acquired simultaneously. The mass spectrometer was tuned using a 30 μm entrance slit, and peak positions were calibrated using sulphide minerals and metallic Au. Areas of 60 × 60 μm and 30 x 30 μm were imaged at a pixel resolution of 512 × 512, with a primary beam current of approximately 2.8 pA, and a dwell time of 25 ms/pixel. Smaller areas of 15 × 15 μm were imaged at a pixel resolution of 256 × 256, with a primary beam current of approximately 1.2 pA and a dwell time of 45 ms/pixel. All areas were pre-sputtered to 10^{17} Cs ions/cm^2 prior to imaging. All images were

corrected for 44 ns detector deadtime and processed using the NRIMS plugin for ImageJ (http://nrims.harvard.edu/software).

6.5 Results

6.5.1 Compositions of sulphide methods

Average major element concentrations for sulphides are given in Table 6.1. Formulae of sulphide minerals were calculated using charge balance and stoichiometric constraints. Different generations of sulphides were indistinguishable on the basis of mineral formulae. The mineral formulae for pentlandite in CO13-33 and CO13-55 is $Fe_{3.5–3.9}Ni_{4.8–5.2}Co_{0.3}S_8$ (n = 37 and 33, respectively). Pentlandite in CO13-40 is more enriched in Fe and contains lower concentrations of Ni and slightly lower Co concentrations with the formula $Fe_{4–4.2}Ni_{4.6–4.8}Co_{0.2–0.3}S_8$. Pyrites in CO14-03 and CO14-04 are stoichiometric (FeS_2) with minor (up to 0.01 cations) Co and Ni replacing Fe per formula unit in each sample.

sample	CO13-40	CO13-33	CO13-55	CO14-03	CO14-04
phase	pn (n=10)	pn (n=36)	pn (n=30)	py (n=22)	py (n=61)
wt%					
Si	n.d.	0.03(2)	0.06(8)	b.d.l	b.d.l
Mg	n.d.	0.08(7)	0.07(4)	b.d.l	b.d.l
Ni	35.0(3)	37.1(5)	37(1)	b.d.l	0.2(2)
Fe	28.6(5)	25.7(5)	26(1)	45.6(5)	46.8(4)
Co	1.62(4)	2.35(7)	2.3(2)	0.96(46)	0.2(4)
S	33.8(4)	33.2(4)	33.3(3)	53.8(2)	53.9(3)
Cu	n.d.	0.00(11)	b.d.l	b.d.l	b.d.l
Se	n.d.	0.14(2)	0.15(2)	n.d.	n.d.
Bi	n.d.	0.13(1)	0.13(1)	n.d.	n.d.
As	b.d.l	0.23(2)	0.26(3)	b.d.l	0.02(5)
Sb	n.d.	b.d.l	b.d.l	b.d.l	0.02(1)
Total	99.0(7)	99.2(9)	98.9(7)	100.4(3)	101.1(3)
mole %					
Ni	27.2(1)	29.0(3)	29(1)	-	-
Fe	23.4(4)	21.1(4)	21(1)	33.6(2)	33.2(1)
Co	1.26(3)	1.82(5)	1.7(2)	0.7(3)	0.1(3)
S	48.1(5)	47.5(3)	47.7(3)	66.8(2)	66.6(2)
S/Fe+Ni+Co	0.93(1)	0.92(1)	0.92(1)	1.99(1)	1.99(1)

Table 6.1: EPMA data for sulphides. Number in brackets is two standard deviations. b.d.l indicates the concentration is below detection. The full analytical results are reported in Appendix C6.

Grain	Sulphide	Average $\delta^{34}S_{VCDT}$ (‰)	1σ (‰)	# Analyses	Av 2σ on single analysis (‰)
CO13-40					
CO13-40-a1-s1	Pn	7.23	1.22	3	0.98
CO13-40-a1-s2	Pn	9.33	2.33	2	1.03
CO13-40-a1-s3	Pn	8.80	n.a.	1	0.93
CO13-40-a1-s4	Pn	4.27	n.a.	1	1.10
CO13-40-a2-s1	Pn	7.57	n.a.	1	0.31
CO13-40-a2-s2	Pn	5.39	n.a.	1	0.37
CO13-40-a2-s3	Pn	6.32	0.35	2	0.46
CO13-40-a3-s1	Pn	6.72	1.04	3	0.36
CO13-40-a3-s2	Pn	5.93	0.99	2	0.46
CO13-40-a3-s3	Pn	8.85	n.a.	1	0.32
CO13-40-a3-s4	Pn	10.43	n.a.	1	0.90
CO13-40-a3-s5	Pn	6.77	n.a.	1	1.14
CO13-40-a3-s6	Pn	6.21	n.a.	1	1.09
CO13-40-a3-s8	Pn	8.73	2.15	3	0.96
CO13-40-a3-s9	Pn	8.81	0.04	2	0.81
CO13-40-a3-s10	Pn	9.36	n.a.	1	0.86
CO13-40-a3-13	Pn	8.83	n.a.	1	0.78
CO13-40-a3-14	Pn	5.03	n.a.	1	0.79
CO13-40-a3-15	Pn	4.39	n.a.	1	0.94
CO13-40-a3-16	Pn	8.03	n.a.	1	0.82
CO13-33					
CO13-33-a2-s2	Pn2	5.50	n.a.	1	0.76
CO13-33-a2-s3	Pn2	7.88	n.a.	1	0.74
CO13-33-a2-s4	Pn2	9.19	0.81	2	0.81
CO13-33-a2-s5	Pn3	3.89	n.a.	1	0.90
CO13-33-a2-s6	Pn3	7.27	n.a.	1	0.75
CO13-33-a2-s7	Pn3	8.42	n.a.	1	0.72
CO13-33-a2-s8	Pn3	8.20	n.a.	1	0.82
CO13-33-a2-s9	Pn2	7.91	n.a.	1	0.76
CO13-33-a3-s1	Pn1	5.47	n.a.	1	0.78
CO13-33-a3-s2	Pn1	8.82	n.a.	1	0.79
CO13-33-a3-s4	Pn2	6.54	n.a.	1	0.73
CO13-33-a3-s6	Pn2	7.54	n.a.	1	0.83
CO13-33-a3-s7	Pn2	7.56	n.a.	1	0.74
CO13-33-a3-s10	Pn3	1.75	n.a.	1	0.74
CO13-33-a3-s13	Pn1	6.53	n.a.	1	0.74
CO13-33-a3-s14	Pn1	8.40	n.a.	1	0.75
CO13-33-a3-s15	Pn2	7.78	n.a.	1	0.76
CO13-55					
CO13-55-a1-s1	pn4	6.02	0.75	2	0.35
CO13-55-a1-s2	pn2	5.18	1.66	2	0.36
CO13-55-a1-s3	pn4	5.91	n.a.	1	0.42
CO13-55-a2-s1	pn2	4.97	0.83	4	0.41
CO13-55-a2-s2	pn3	3.25	0.20	2	0.38
CO13-55-a2-s3	pn3	5.90	0.82	2	0.39
CO13-55-a3-s1	pn4	7.44	0.36	2	0.36
CO13-55-a3-s2	pn2	3.13	0.22	3	0.41
CO13-55-a3-s2b	pn2	2.95	n.a.	1	0.50
CO14-03					
CO14-03-a1-1-8	Py	6.85	0.58	9	0.21
CO14-03-a2-1-4	Py	12.70	1.99	4	0.21
CO14-03-a2-5	Py	15.08	n.a.	1	0.21
CO14-03-a2-7-8	Py	10.30	3.93	2	0.21
CO14-03-a2-9-13	Py	8.13	1.75	5	0.21
CO14-03-a3-1-2	Py	7.79	0.29	2	0.21
CO14-03-a3-3-4	Py	11.16	3.14	2	0.21
CO14-03-a3-5-6	Py	10.54	4.20	2	0.21
CO14-03-a3-7-8	Py	7.32	0.37	2	0.21
CO14-03-a3-9-11	Py	10.17	3.26	3	0.22
CO14-04					
CO14-04-a1-s1	Py2	3.96	0.20	17	0.15
CO14-04-a2-s1, 1-9, 22-32	Py2	4.48	0.22	20	0.11
CO14-04-a2-s2, 11-14, 21-23	Py1	4.31	0.16	7	0.11
CO14-04-a2-s3	Py1	5.06	0.10	1	0.10
CO14-04-a3-s1	Py1	5.06	0.40	3	0.10
CO14-04-a3-s2	Py1	5.02	n.a.	1	0.10

Table 6.2: $\delta^{34}S$ sulphur isotope analyses of pentlandite (pn) and pyrite (py) grains.

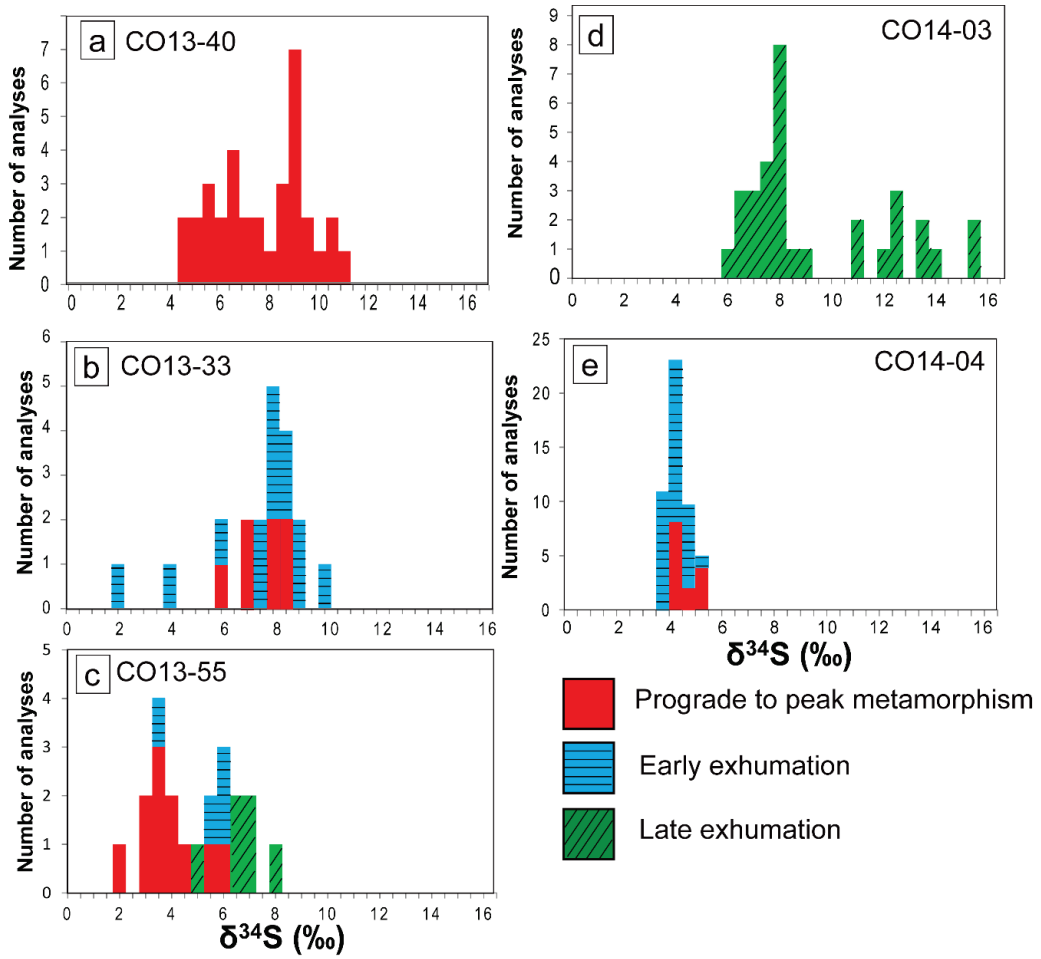

Figure 6.3: Histograms of $\delta^{34}S$ values in sulphides for (a) CO13-40, (b) CO13-33, (c) CO13-55, (d) CO14-03 and (e) CO14-04. Red/no lines= sulphide grains related to prograde and peak metamorphism. Blue/horizontal lines = sulphide grains related to early exhumation. Green/diagonal lines = sulphide grains related to late exhumation.

Grain	Sulphide	$\Delta^{33}S_{VCDT}$ (‰)	2σ abs (‰)
CO13-40			
CO13-40 a3 s1-2	pn	0.52	0.30
CO13-40 a3 s3	pn	0.38	0.24
CO13-40 a3 s12-3	pn	0.67	0.50
CO13-55			
CO13-55 a2 s1-1	pn2	0.33	0.23
CO13-55 a2 s3-1	pn3	0.37	0.28
CO13-55 a3 s2-1	pn2	0.38	0.23
CO13-55 a3 s2-4	pn2	0.49	0.31
CO14-04			
CO14-04 s1 area 1	py1	0.11	0.10
CO14-04 s1 (9) area 2	py2	-0.16	0.12
CO14-04 s1 area 3	py1	-0.17	0.15

Table 6.3: non zero $\Delta^{33}S$ sulphur isotope analyses in pentlandite (pn) and pyrite (py) grains.

6.5.2 Sulphur isotope compositions and trace element mapping

Here the results are reported for $\delta^{34}S$, non-zero $\Delta^{33}S$ values, and EPMA trace element mapping. The complete sulphur isotope analyses including the $\delta^{33}S$ values and measured standard sulphur isotope compositions are provided in Appendix E4.

6.5.2.1 Serra di Pigno

Distal Serpentinite CO13-40.

$\delta^{34}S$ values in CO13-40 pentlandite range from 4.3 to 10.4‰ (n=30) (Table 6.2, Fig. 6.3a, Fig. 6.4a–e, Appendix E4). Three analyses have non-zero $\Delta^{33}S$ values of 0.52±0.30‰ (area3_s12-3), 0.67±0.50‰ (area3_s1-2) and 0.38±0.24‰ (area3_s3) (Table 6.3), where errors are 2σ. Trace element NanoSIMS maps reveal zonation in Cu, Co, As and Ni. Co, As and Ni zoning is decoupled from the Cu zoning (Fig. 6.4f). High Co and Cu counts at the margins of the grain most likely record the presence of cobaltite and chalcopyrite veins at grain boundaries. Due to the small size of the grains (up to 50 μm), it was not possible to determine the relationship of the zonation to the $\delta^{34}S$ ratios, therefore homogeneous areas were chosen for analysis.

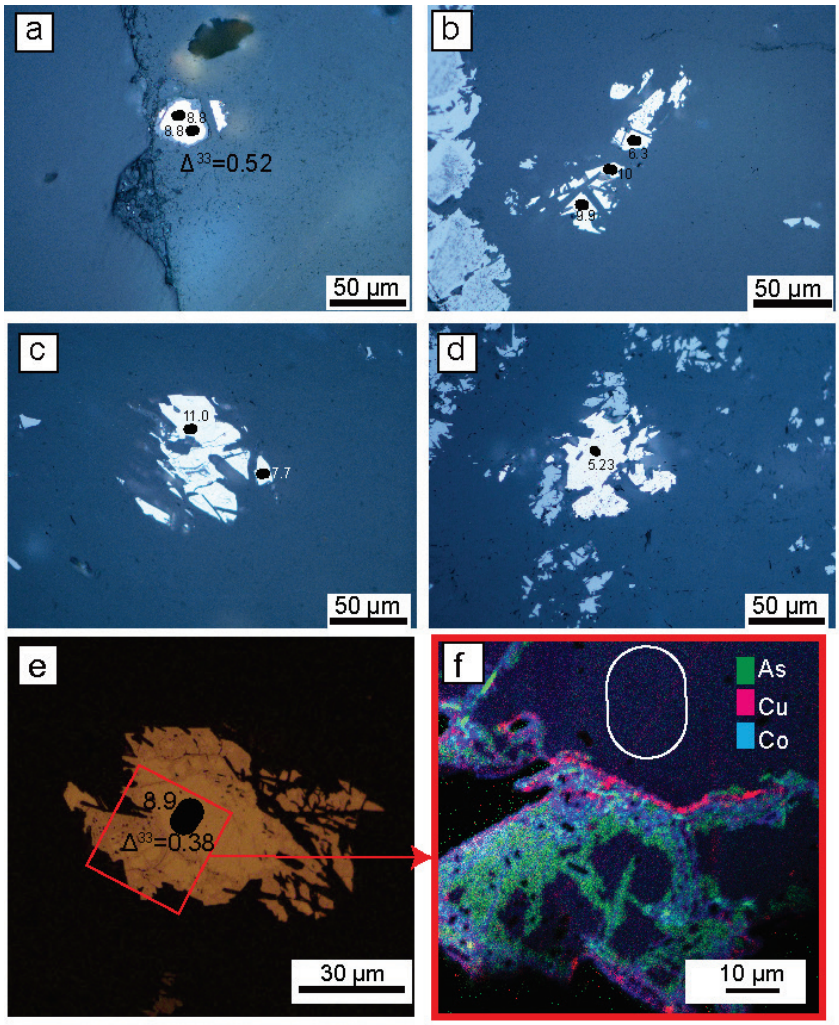

Figure 6.4: CO13-40. Reflected light images of pentlandite grains (a) s1 in area 3, (b) s8 in area 3, (c) s2 in area 1, (d) s9 in area 3 and (e) s3 in area 3. (f) NanoSIMS map of grain s3 in area 3, circle indicates point of SIMS analysis. All values are $\delta^{34}S$ unless otherwise indicated.

Serpentinite proximal to metaquartzite and metagabbro CO13-33

$\delta^{34}S$ values in pentlandite in CO13-33 range from 1.8 to 8.8 ‰ (n = 18) (Table 6.2; Fig. 6.3b; Fig. 6.5a–e). The sulphides analysed include pn1 (n=4; Fig. 6.5a), pn2 (n=9; Fig. 6.5b, c) and pn3 (n=5; Fig. 6.5d–e). The histograms display a unimodal distribution (Fig 6.3b) and the Mann-Whitney U tests (Appendix E3) reveal no significant variation in $\delta^{34}S$ between the different generations of pentlandite from early to late grains. Pn1 grains have similar $\delta^{34}S$ signatures to pn2 grains with values of 6.5 to 8.8‰ in pn1 grains, compared to 5.5 to 8.3‰ in pn2 grains (p value = 0.79), where the p value indicates the probability that the analyses are from the same distribution. $\delta^{34}S$ values of pn3 grains vary from 1.8–8.4‰, and are not significantly different from pn1 and pn2 ($p\ value = 0.79$).

EPMA mapping reveals homogenous Co concentrations in the interior of pn2, but higher Co concentrations towards pn2 rims, (Fig. 6.5f).

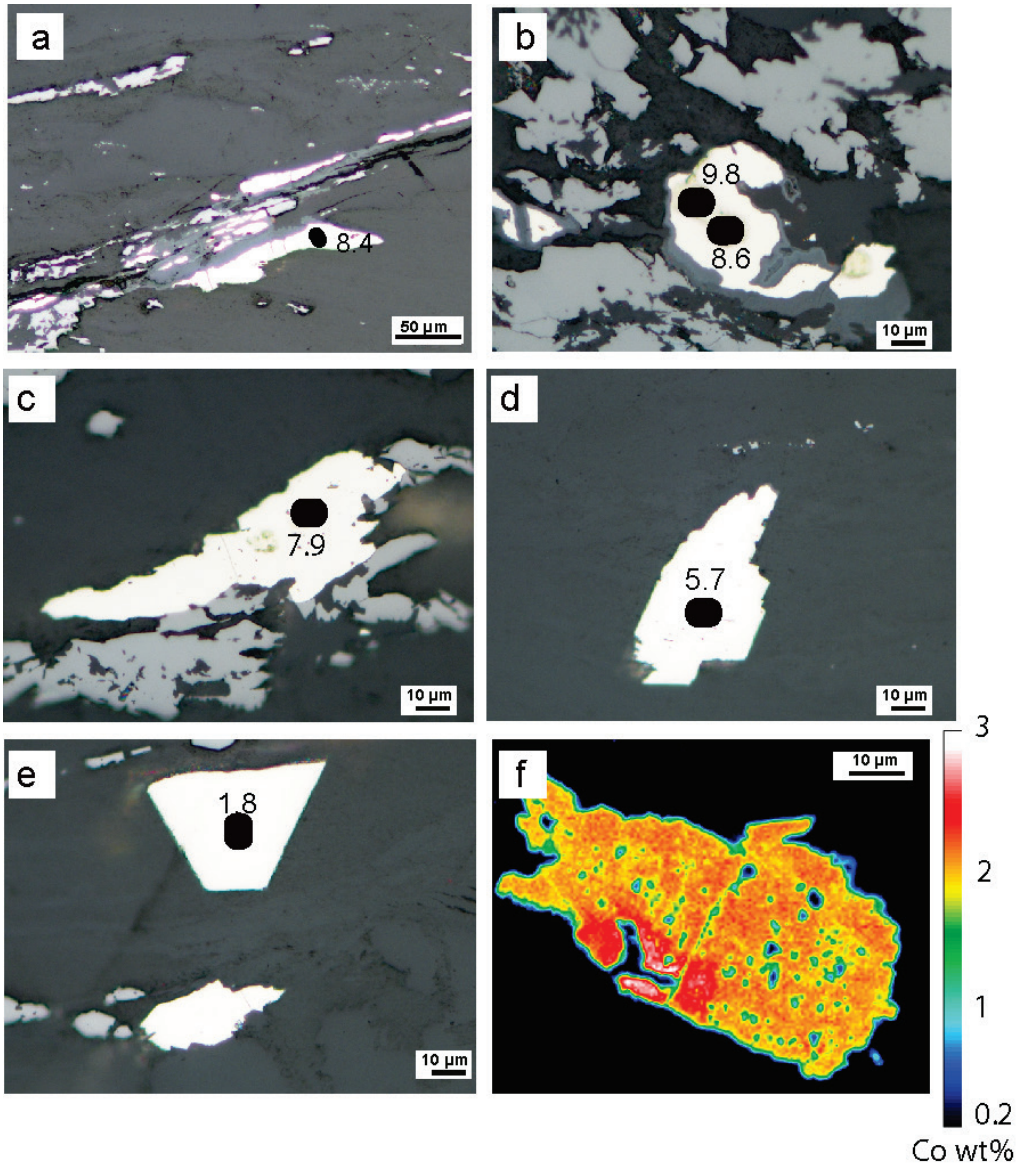

Figure 6.5: CO13-33. Reflected light images of pentlandite grains. (a) s14 in area 3, (b) s4 in area 2, (c) s3 in area 2, (d) s10 in area 2 and (e) s10 in area 3. (f) Co map (wt%) of a pn2 grain. All values are $\delta^{34}S$.

Serpentinite proximal to calcareous-schist, metagabbro and zoisite-actinolite schist CO13-55

$\delta^{34}S$ values in pentlandite within CO13-55 range from 1.9 to 8.0‰ (n=19; Table 6.2, Fig. 6.3c); pn2 from 1.9 to 5.7‰ (n=10; Fig. 6.6a–c), pn3 $\delta^{34}S$ from 3.1–6.5‰ (n=5; Fig. 6.6d–e) and pn4 from 5.5–8.0‰ (n=5; Fig. 6.6f). The Mann Whitney U test revealed a significant difference between pn2 and pn4 at a level of significance of 1% (p value = 0.0078), but not between pn3 and pn4 (p value = 0.05). Four analyses have significant $\Delta^{33}S$ values of 0.33±0.23‰ (area2_s1-1, pn2),

0.37±0.28‰ (area2_s3-1; pn3), 0.38±0.23‰ (area3_s2-1, pn2) and 0.49±0.31‰ (Table 6.3, pn2). Zonation in Co is not evident in CO13-55 pentlandites (Fig. 6.3b).

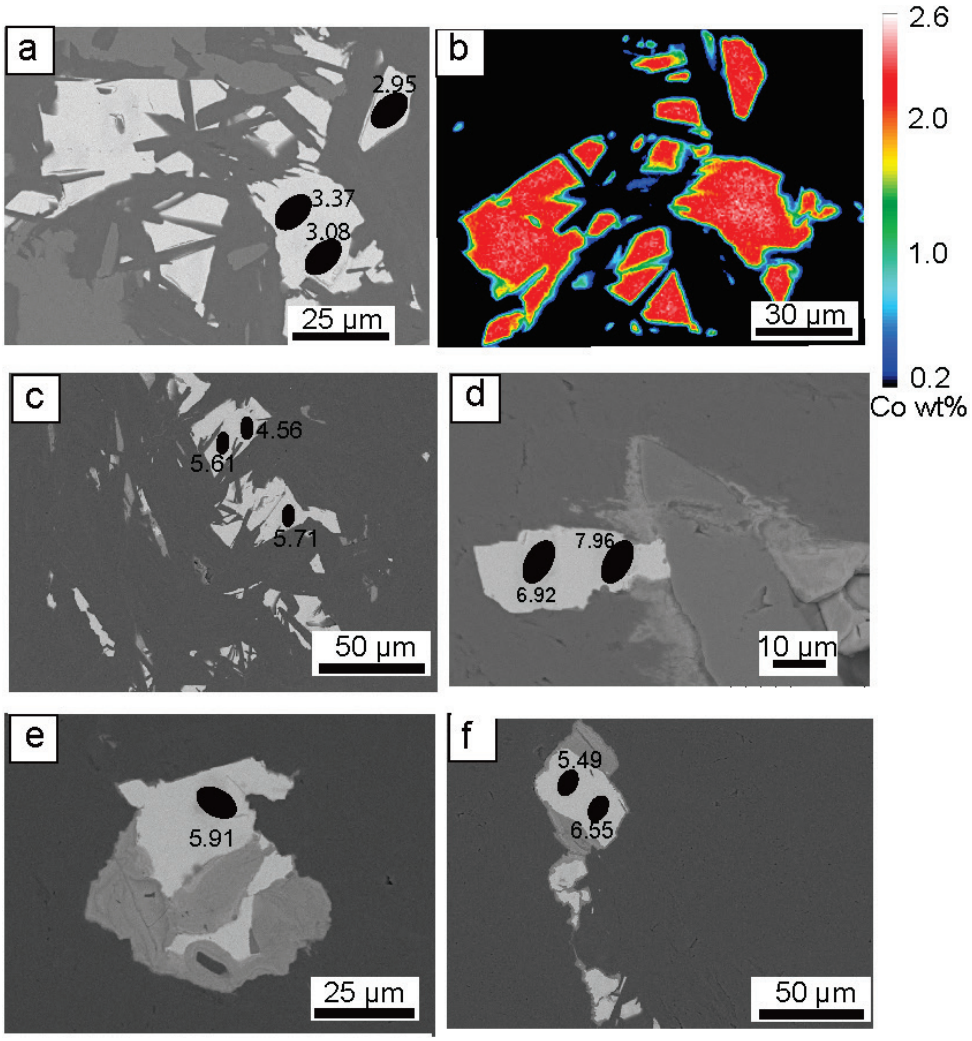

Figure 6.6: CO13-55 pentlandite. (a) bse image s1 in area 3. (b) Co map (wt%) of grain s1 in area 3. (c) bse image of grain s1 in area 2. (d) bse image of grain s2 in area 3. (e) bse image of grain 3 in area 1. (f) bse image of s1 in area 1. All values are $\delta^{34}S$.

6.5.2.2 Capu Corvoli

Chlorite Schist CO14-03

CO14-03 pyrite $\delta^{34}S$ values are very heterogeneous with values ranging from 5.9 to 15.5‰ (n=32; Table 6.2, Fig. 6.3d). The majority of grains have $\delta^{34}S$ values from 6–9‰ (n = 21), with heavier $\delta^{34}S$ from 10.8–15.5‰ (n = 11). Although no differences in relative timing are inferred from textural analysis, pyrites that did not form clusters (Fig. 6.7 a–c, n=17) were compared to pyrites that did, one group of which was on a magnetite rim (Fig. 6.7d–e, n=15), with a low probability that these two groups of pyrite have the same $\delta^{34}S$ values (p=0.0057). EMPA mapping reveals

fine scaled zonation of Co from 0.1 to 1.2 wt%, and of Ni from 0.1 to 0.4 wt% (Fig. 6.8a–c). The Co and Ni zonation does not show a significant correlation with $\delta^{34}S$ (R^2 = 0.3 and 0.23, respectively, Fig. 6.8d).

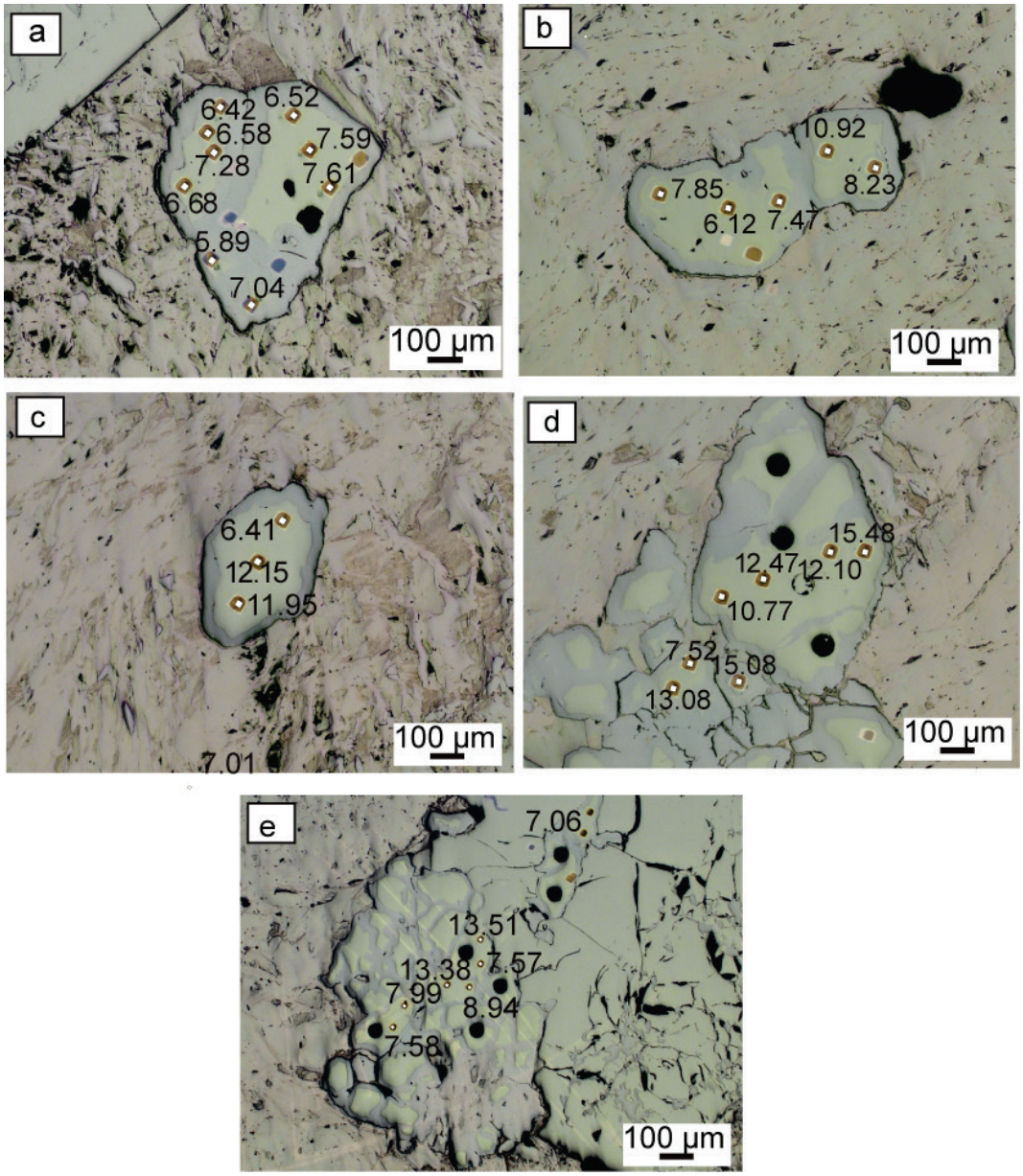

Figure 6.7: CO14-03. Reflected light images of gold coated (a) matrix grain within 1mm of magnetite, area 1 analyses 1-8. (b) matrix grain area 2 analyses 9-13 (c) matrix grain area 3 within 1mm of magnetite analyses 9–11. (d) large cluster of pyrite aggregates in matrix area 2 1–8. (e) large cluster of pyrite grains on rim of large magnetite, area 3 analyses 1–8. All values are $\delta^{34}S$.

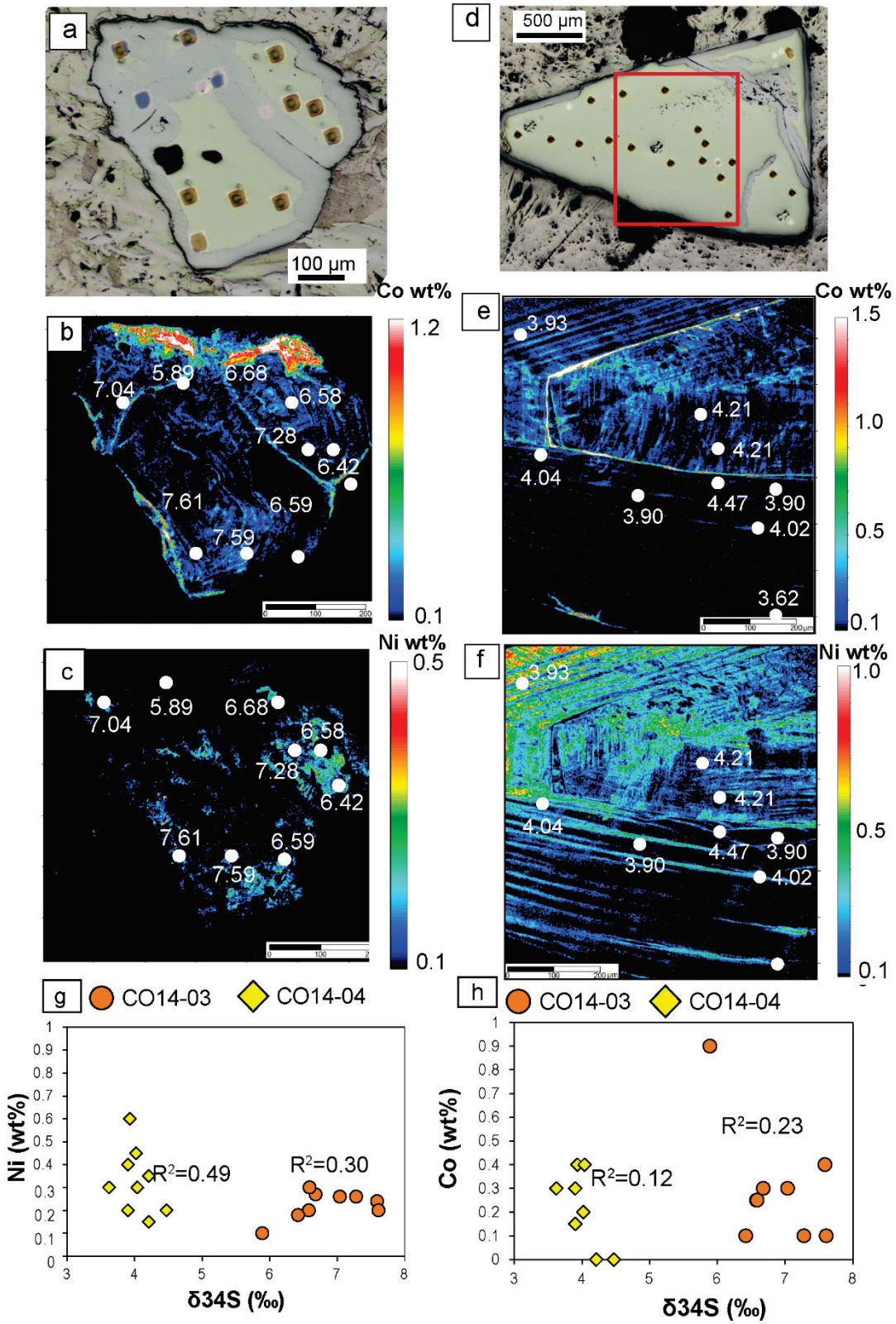

Figure 6.8: (a) reflected light image of matrix pyrite grain in CO14-03, area 1 analyses 1-8, the same grain is shown in images b-c (b) EPMA derived trace element map of Co in pyrite grain (c) EPMA derived trace element map of Ni (d) reflected light image of s1 in area 1 in CO14-04; the same grain is shown in images e–f. (g) Co (wt%) plotted against $\delta^{34}S$ in CO14-03 and CO14-04. (h) Ni (wt%) plotted against $\delta^{34}S$ in CO14-04. CO14-03 = orange circle) and CO14-04 = yellow diamond).

Talc Schist CO14-04

CO14-04 pyrites appear to be relatively homogeneous with $\delta^{34}S$ values of 3.6–5.4‰ (n=49). Py1 has slightly heavier values (4.1–5.4‰, n=12; Fig. 6.9a–d), compared to py2 which has a larger range from 3.1–5.0‰ (n=37; Fig. 6.9e–f), where there is a low probability of both pyrite generations being of the same isotopic composition (p=0.0065). Additionally, three significant $\Delta^{33}S$ values were found, s1 in area 1 (0.11±0.10), s1 analysis 9 in area 2 (-0.16±0.12) and S1 in area 3 (-0.17±0.15). Sulphur did not drop in counts compared to the standards and the beam was central for these analyses so the non-zero MIF values are interpreted as real.

EPMA maps show Co and Ni zonation at a finer scale than the interaction volume of SIMS analysis (Fig. 6.8d–f). Calculations revealed that the correlation between Co and $\delta^{34}S$ is significant at a 5% level of significance (P=0.048, R^2=0.49; Fig. 6.8g) but Ni is decoupled from $\delta^{34}S$ (R^2=0.12, Fig. 6.8h).

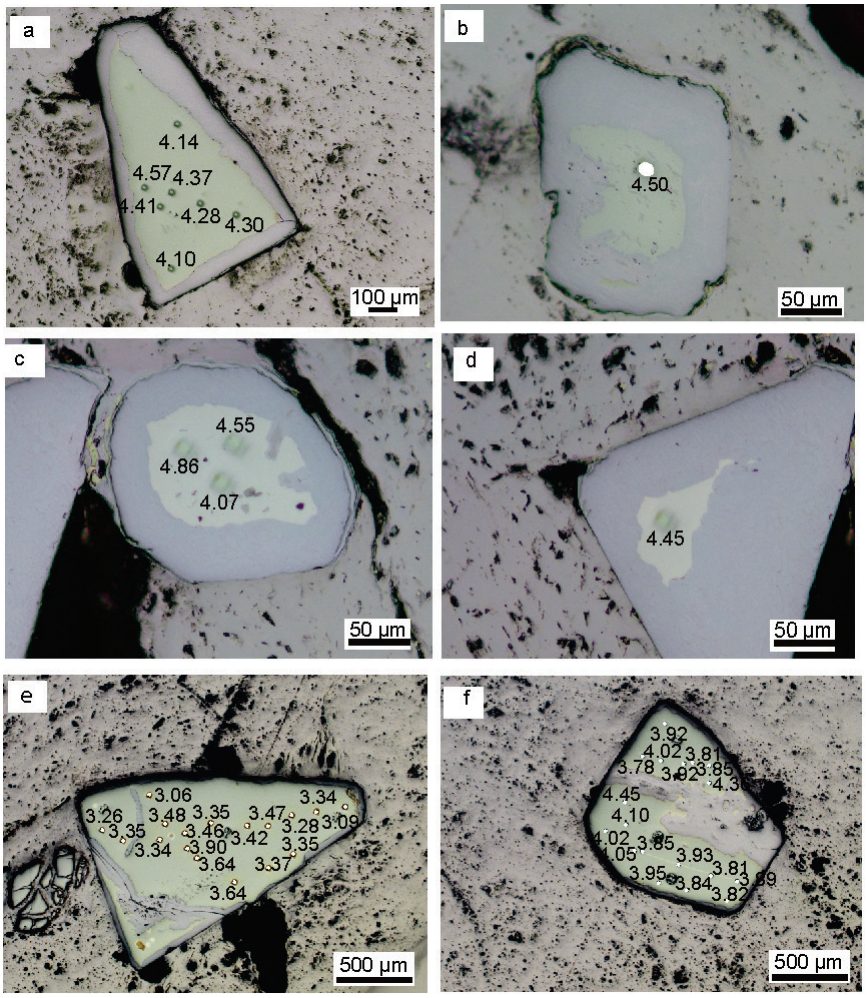

Figure 6.9: CO14-04. Reflected light images of gold coated py1 grains (a) s2 in area 2, (b) s3 in area 2, (c) s1 in area 3, (d) s2 in area 3 and py2 grains in (e) s1 in area 1 and (f) s1 in area 2.

6.6 Discussion

Summary of Observations

Primary, seafloor and prograde phases of sulphides provide an insight on the inputs of sulphur to subduction zones, while sulphides associated with the onset of exhumation, provide a record of fluid composition released from the slab. Primary sulphide grains occur as polyhedral blebs with concave inward boundaries (Seyler et al., 2007; Schwarzenbach et al., 2012) and mantle derived sulphur has $\delta^{34}S$ value near to zero (e.g. Alt et al., 1998; Sakai et al., 1984; Shanks et al., 1995). The samples from Serra di Pigno and Capu Corvoli record a wide range of sulphur isotopic concentrations from 1.7–15.5 ‰. Therefore, textures and isotope values typical of primary sulphides are not observed so it is concluded that primary sulphides are not preserved in the studied samples.

The Serra di Pigno samples proximal to metasediments and metagabbros show different trends in $\delta^{34}S$ values. Sulphur in the late grains is shown to be isotopically heavier in late grains in CO13-55 (section 4.2.3) with $\delta^{34}S$ values from 5.5–8.0‰ in comparison to earlier sulphides with 1.9 to 6.5‰. However, there is no significant difference between early and late grains in CO13-33 which displays an apparent unimodal distribution. $\delta^{34}S$ values in CO13-40, the sample distal to the metagabbro and metasediments are not significantly different from those in CO13-33 (p=0.65), but the difference between the sample proximal to metagabbro, metasediments and schists, CO13-55, and the distal sample, CO13-40, is significant ($p=1.81\times10^{-5}$), with values of 1.9–8.0‰ and heavier values of 4.3 to 10.4‰, respectively.

The chlorite schist and talc schist samples from Capu Corvoli, proximal to metagabbro and only metres apart from each other, show very different S isotope values, CO14-03 has very heterogeneous sulphur isotope values from 5.9 to 15.5‰, whereas CO14-04 has lighter and more homogeneous S isotopic values from 3.6 to 5.4‰.

The isotopic compositions of the sulphides are assessed in the context of sulphur speciation in the fluid, rock buffering versus fluid buffering of the samples,

trace element composition, the effects of metamorphism (i.e. temperature and pressure), and pH.

6.6.1 Sulphur speciation and fractionation

Temperature influences isotopic re-equilibration, fractionation factors and rates of diffusion during metamorphism (e.g. Seal, 2006). The effect of temperature on $\delta^{34}S$ depends on the speciation of sulphur; the effect of temperature on $\delta^{34}S$ fractionation between fluid and sulphide minerals is greater for oxidised sulphur (SO_2 and SO_4^{2-}) than reduced sulphur (H_2S and HS^-). The speciation of aqueous sulphur in ultramafic rocks at high-pressure conditions is poorly constrained, though H_2S (e.g. Peretti et al., 1992), SO_2 or SO_4^{2-} (e.g. Debret et al., 2016) are the most likely species. More recently, the S^{3-} ion has been proposed to be present in high-pressure fluids such as those attributed to subduction zones (Pokrovski and Dubessy, 2015). The effects of fractionation between these species during metamorphism are assessed in this section.

6.6.1.1 The effect of rock buffering on sulphur isotope fractionation

The oxide and sulphide assemblages in the Serra di Pigno serpentinites and the early assemblage of CO14-04 from Capu Corvoli are inferred to be low variance and rock buffered on the basis of plots of the assemblages on an activity-activity diagrams of oxide and sulphide stability as a function of aO_2 and aS_2 at high pressure (2 GPa, 555ºC, Chapter 4) presented in Evans et al. (in revision). The prograde mineral assemblage in the serpentinites analysed is serpentine + pentlandite + magnetite ± pyrite ± heazlewoodite, and in the hybrid sample, CO14-04, is talc + chlorite + magnetite + pyrite + pyrrhotite. The oxide and sulphide assemblages plot at relatively low aO_2 and aS_2, therefore reduced species such as H_2S or HS^- are inferred to be in solution.

Calculations were undertaken to assess the possible effect of isotope fractionation between sulphur hosted in the minerals and sulphur hosted in the fluids as an effect of prograde metamorphism. A minimum temperature of 250ºC was chosen to maximise the calculated effect of fractionation. Fractionation was calculated for isotope equilibrium between mantle and hydrothermal pyrite and fluid, and recrystallized pentlandite and fluid ($\Delta_{pyrite\text{-}H_2S}$ and $\Delta_{pentlandite\text{-}H_2S}$,

respectively) in closed and open (Rayleigh) systems. The starting composition of 0‰ was chosen for mantle pyrite (Sakai et al., 1984; Shanks et al., 1995; Alt et al., 1998) and 8‰ for hydrothermal pyrite, the average of pyrite isotopic analyses here. The value of 6.7‰ for the recrystallised pentlandite was taken from the average analyses of the pentlandite grains in the Serra di Pigno samples. There are currently no fluid-mineral isotope fractionation factors available for pentlandite, so it is assumed that fractionation factors would be similar to either violarite ($Fe^{2+}Ni_2S_4$; Li and Liu, 2006) or pyrrhotite (Ohmoto and Rye, 1979), or somewhere in between these two end members. Fractionation at 250 ºC is minor for both violarite (-1.2‰, Li and Liu, 2006) and pyrrhotite (0.1‰, Ohmoto and Rye, 1979). Therefore, $\Delta_{pentlandite\text{-}H_2S}$ would be minimal at temperatures of 250ºC and above, in both the closed and open system calculations (Fig. 6.10a, b). Likewise, $\Delta_{pyrite\text{-}H_2S}$ would also be minor at 250ºC, at 1.5‰ (Ohmoto and Rye, 1979). Therefore, fractionation between reduced sulphide species in solution and sulphide minerals would not be a first order control on the sulphur isotope signatures.

6.6.1.2 The effect of fluid buffering on sulphur isotope fractionation

In contrast to the Serra di Pigno samples, the Capu Corvoli samples, CO14-03 and the late assemblage in CO14-04 have high variance mineral assemblages with silicates + magnetite + pyrite, and are therefore inferred to be fluid buffered, where magnetite + pyrite record an increased aS_2 and possibly aO_2, reflecting increasingly oxidising conditions. $\Delta_{pyrite\text{-}SO_2}$ fractionation was calculated for the open and closed system models (Fig. 6.10c, d) using fractionation values from Ohmoto and Rye (1979). SO_2 was chosen as the species in the fluid phase the calculations because dissolution of anhydrite is likely to produce H_2S and SO_2-bearing fluids (Newton and Manning, 2005) and because SO_2-bearing fluids have been proposed to be the likely transport vector for redox sensitive elements from the slab to the sub-arc mantle (Evans, 2012; Tomkins and Evans, 2015; Debret et al., 2016). It is evident that there is greater fractionation between pyrite and SO_2, at ~23‰ (Fig. 6.10c, d), compared to pyrite and H_2S. Given the relatively texturally late setting of pyrite grains in the hybrid samples (section 6.3.2), with the exception of the early assemblage in CO14-04 (see 6.6.1.1), it is inferred that the hybrid

samples are recording fluid buffering during exhumation and that during this time fluid:rock isotope fractionation could have been significant.

6.6.1.3 The S^{3-} ion

The S^{3-} ion, on the basis of microbeam Raman spectroscopy and thermodynamic modelling, has been proposed to account for ~10% of dissolved sulphur in fluids at temperatures of 300 to 500 ºC and at pressures of 0.5 to 1.5 GPa devolatilised from pyrite-bearing rocks (Pokrovski and Dubessy, 2015). Furthermore, at temperatures above 400 ºC in aqueous fluids of seawater salinity, this species may dominate over SO_2, and possibly SO_4^{2-}, and thus could be significant at the P-T conditions recorded by the blueschist–eclogite facies samples in this study. However, currently there is a lack of isotope fractionation data for S^{3-} and therefore this species could not be included in the models (Fig. 6.10). Δpyrite–S^{3-} or Δpentlandite-S^{3-} and Δpyrite-H_2S or Δpentlandite-H_2S would have similar fractionation factors, but Δpyrite–S^{3-} or Δpentlandite-S^{3-} would be negative, as would be expected from the –1/3 valence of S^{3-} (e.g. Evans et al., 2014). Therefore, fractionation between pentlandite and pyrite and S^{3-} would not be significantly different to that calculated for H_2S (Fig. 6.10).

6.6.1.4 Summary of fractionation effects

In summary, fractionation would be minor during metamorphism in the rock-buffered Serra di Pigno samples, whereas fluid-buffered samples, where SO_2 is inferred to be present in the fluid phase, may record greater fractionation during fluid buffering attributed to retrogression associated with exhumation. Therefore, in both the rock-buffered and fluid-buffered samples, sulphide $\delta^{34}S$ values in prograde to early retrograde sulphides reflect the fluid isotopic composition that either infiltrated the rock during seafloor serpentinisation, prograde metamorphism, or early exhumation. However, fractionation must be taken into account whne the late sulphides in the hybrid samples (CO14-03 and CO14-04) are interpreted.

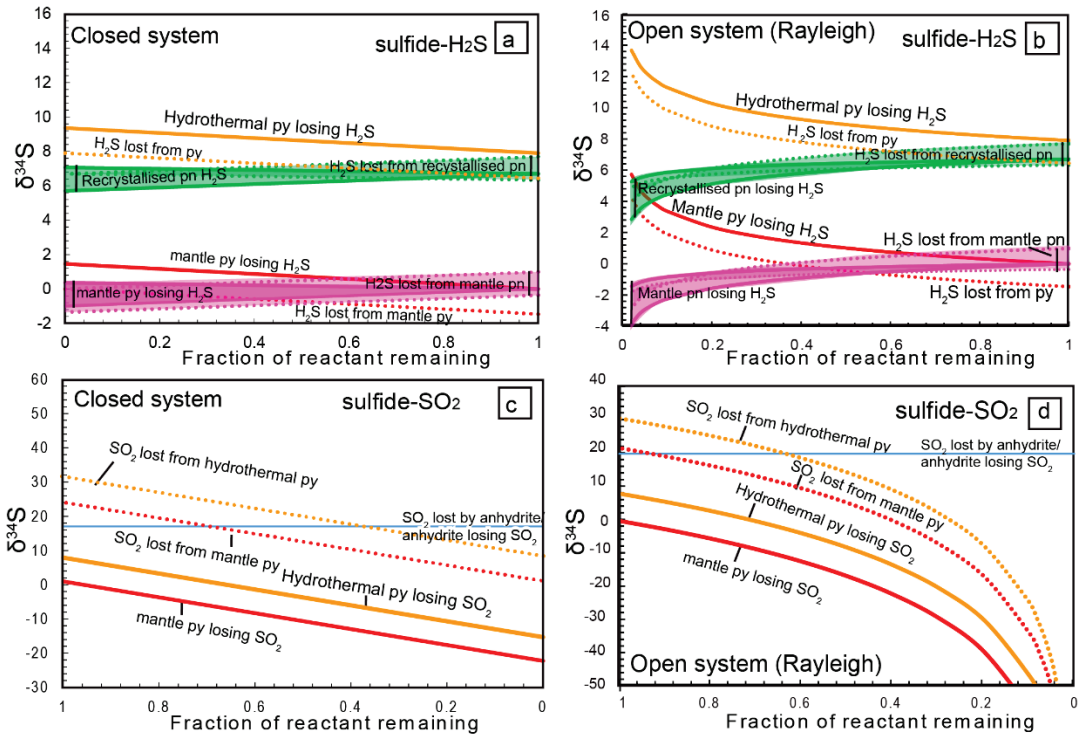

Figure 6.10: Fractionation calculation plots between $\delta^{34}S$ and the pentlandite-H_2S reaction for (a) a closed system and (b) open system (Rayleigh) fractionation, and between $\delta^{34}S$ and the pyrite-SO_2 reaction for (c) a closed system and (d) an open system (Rayleigh).

6.6.2 The effect of pH on isotope compositions

Serpentinites record significant changes in pH over the course of their evolution, pH increases with progressive serpentinisation prior to subduction, reaching values as high as 10 (e.g. Seyfried et al., 2007; Frost and Beard, 2007 and Foustoukos et al., 2008). Sulphur isotope fractionation between sulphate and sulphide is dependent on pH (Ohmoto and Lasaga, 1982; Seal et al., 2006), and controlled by the abundance of the intermediate valence thiosulphate species ($S_2O_3^{2-}$). However, because the prograde assemblages are consistent with equilibration with H_2S or HS- in solution, the effects of pH on isotopic compositions are assumed to be negligible.

6.6.3 Trace element relationships with $\delta^{34}S$

EPMA mapping reveals complexities in element zoning that may be associated with fluid infiltration. Whereas no significant correlation was observed between Co or Ni and $\delta^{34}S$ in CO14-03 (R^2 = 0.30 and 0.12, respectively) or Ni in CO14-04 (R^2=0.23), the correlation between Co and $\delta^{34}S$ in CO14-04 was found to be statistically significant at a 95% confidence level (P=0.048). Therefore, in general $\delta^{34}S$ is inferred to be decoupled from Ni and Co, with the exception of Co

in CO14-04. Generally, it seems that trace elements are not controlled by the same processes that determine the S isotopic compositions in the pyrite grains on the basis of the limited data presented here. However, due to the restrictions of the beam size for analysis, it was not possible to assess the $\delta^{34}S$ zonation on the <5 μm scale of the Co and Ni zoning, so small length scale variations in S isotope values would have been obscured by the relatively large beam size (10 μm).

Similarly it was not possible to determine relationships between trace element concentrations and sulphur isotopic compositions in pentlandite grains due to the small size of the grains analysed, so areas selected for analysis were considered to be homogeneous in Co, Ni and As. However, zonation observed by Nano-SIMS analysis provides useful insights into variations in the characteristics of fluid associated with post seafloor modification (section 6.6.5).

6.6.4 The effect of seafloor processes on sulphur geochemistry

The infiltration of sulphate-bearing seawater into mantle peridotite and consequent serpentinisation results in the addition of seawater-derived sulphur to the rock (Alt and Shanks, 1998; Delacour et al., 2008). In the case of Alpine Corsica, primary mantle rocks are thought to have been exposed and juxtaposed with the continental basement during Tethyan rifting in the Middle to Late Jurassic (Bathonian to Oxfordian) in an ultra-slow spreading centre or an ocean-continent transition setting (e.g. Vitale Brovarone et al., 2011; 2013). During this time, seawater sulphate had $\delta^{34}S$ values of ~ 17‰ (Kampschulte and Strauss, 2004), therefore any sulphides in equilibrium with the seawater would reflect this value. Hydrothermal alteration may also occur during initial subduction associated with slab bending (Ranero and Sallares, 2004).

The wide range of sulphur isotope values in both the Serra di Pigno samples (with an overall range from 3.1 to 8.9‰) and the Capu Corvoli samples (3.6 to 15.5‰) implies that seawater sulphate may have been retained in sulphides with the heaviest isotopic signatures but subsequent processes were most likely responsible for the decrease in $\delta^{34}S$ values either during seafloor alteration, subduction and/or exhumation.

Hydrogen and CH_4 released during seafloor serpentinisation, provides an energy source for sulphate reducing micro-organisms (e.g. Alt and Shanks, 1998; Kelley et al., 2005; Brazelton et al., 2006; Schwarzenbach et al., 2012). Bacterial sulphate reduction (BSR) enriches the light isotope in the mineral products, therefore if BSR occurred during serpentinisation in an open system then negative $\delta^{34}S$ are expected (e.g. Schwarzenbach et al., 2012). Such a signal is not observed in the sulphides measured here. However, in a closed system, where there is limited fluid circulation, such as in deep sections of magma poor rifted margins (i.e. an ocean-continent transition zone, the proposed pre-subduction geodynamic setting of Alpine Corsica), BSR could produce ^{34}S-enriched signatures if the conversion of sulphate to sulphide were close to completion. Nevertheless, if sulphides produced by microbial sulphate reduction were preserved, at least a few negative isotopic values would be expected as most sulphides would have grown in an open system, but this is not the case so BSR is not thought to have played a significant role in the production of the $\delta^{34}S$ signatures recorded by the samples described here.

A recent study has shown that $\Delta^{33}S$ in addition to $\delta^{34}S$ can be used to distinguish between open or closed system sulphate reduction, and hydrothermal versus bacterial sulphate reduction. $\Delta^{33}S$ signatures in the samples analysed here indicate a small but significant mass-independent fractionation (MIF) in three pentlandite grains from CO13-40, four pentlandite grains from CO13-55 and three pyrite grains in CO14-04. The data was carefully checked for any variations caused by a drop in S counts or beam centring and crystallographic orientation has been determined to have no effect on $\Delta^{33}S$ (LaFlamme et al., 2016) so the $\Delta^{33}S$ values are concluded to result from MIF i.e. variation in isotope abundance which is not dependent on mass and thus records other processes. The lack of $\Delta^{33}S$ HSR signatures in most grains is probably a matter of precision. For example, the +0.10‰ values detected in pentlandite would be at upper range of expected values e.g. +0.16‰ is the maximum recorded in Ono et al. (2012). More precise measurements of $\Delta^{33}S$ are possible using bulk powders and mineral separates (Ono et al., 2012), but not with the *in-situ* SIMS technique used in this study, required for analysis of the small grains in our samples. Useful insights are inferred from such values, but more measurements are required to test the scenarios outlined here.

Py1 grains record values of between -0.04 and +0.1‰. Positive $\delta^{34}S$ signatures in pentlandite are associated with $\Delta^{33}S$ of at least +0.10‰ (where the analytical error is taken into account). Such $\Delta^{33}S$ values for pentlandite and pyrite, coincident with their heavy $\delta^{34}S$ values, are consistent with a scenario in which sulphide minerals are derived from hydrothermal sulphate reduction (HSR, Ono et al., 2012), rather than BSR. Lower $\Delta^{33}S$ values in pyrite may be consistent with HSR in an open system, which typically produce more negative $\Delta^{33}S$ signatures.

With the exception of one grain (CO13-55 a2 s1-1), pentlandite grains with significant $\Delta^{33}S$ values are associated with prograde metamorphism and thus hydrothermal sulphate reduction occurred either during seafloor alteration or prograde metamorphism. Given that the availability of sulphate in the subduction zone was most likely low, sulphate reduction during seafloor alteration is the preferred option. In contrast, pyrite $\Delta^{33}S$ values are found in both early and late pyrite. It has been proposed that a MIF derived signal could result from the breakdown or formation of S^{3-}, which could be present in fluids at depth in subduction zones, particularly in fluids of seawater salinity, because saline supercritical fluids contain higher concentrations of S^{3-} than those of low salinity (Pokrovski and Dubessy, 2015). Pokrovski and Dubessy (2015) proposed that the S^{3-} effect on MIF could result from its radical properties and resemblance to ozone (O_3). It is possible that the MIF signal reflects either HSR or mineral S^{3-} fractionation or a combination of both. For example, hydrothermal sulphate could have been reduced on the seafloor, and S^{3-} further could contribute to the MIF signal during subduction.

At present, due to the lack of fractionation factors for the S^{3-} ion, it is not possible to assess which model is correct but in either case, the presence of saline fluids are recorded in the high-pressure samples presented here. For example, NanoSIMS mapping revealed that a pentlandite grain with the heaviest $\delta^{34}S$ value of 8.9‰ and a MIF fractionation in CO13-40 has late cobaltite and a chalcopyrite vein at grain boundaries (Fig. 6.4e, f). The solubility of Co and Cu increases with fluid salinity (e.g. Williams et al., 1995; Nadeau et al., 2010; Liu et al., 2011) thus the growth of Co, As and Cu-rich sulphides could be consistent with the infiltration of more saline fluids on at least the scale of the pentlandite grain (~50µm). Similar textures with Co-Ni rich sulphides as rims on pentlandite (siegenite) were noted in

other Corsican serpentinites from the east of Corsica, near Monte San Petrone and this texture was ascribed to the infiltration of fluids enriched in Co and Ni (El Gadarri, 1995).

6.6.5 Retention of seafloor $\delta^{34}S$ in prograde sulphides

Sulphides texturally related to prograde to peak metamorphism include pentlandite in CO13-40, pn1 in CO13-33, pn2 in CO13-55 and py1 and pyrrhotite in CO14-04. $\delta^{34}S$ values in CO13-40 and CO13-33 are similar and range from 4.3 to 10.4‰ in CO13-40 and 6.5 to 8.8‰ in CO13-33. Pn2 in CO13-55 has lower values (1.9 to 5.7‰). $\delta^{34}S$ signatures were not significantly affected by BSR on the seafloor or fluid-rock fractionation during prograde metamorphism. Prograde sulphides likely contain sulphur with isotope values set by the process of HSR during seafloor alteration.

The preservation of seafloor HSR signatures is consistent with the conclusions of Alt et al. (2012a) who compared high-pressure serpentinites from the Voltri Massif and seafloor serpentinite considered unaffected by metamorphism from Val Graveglia, and found no change in content or isotopic composition of sulphur during subduction on a sample scale. Sulphur isotope values recorded by high-pressure serpentinites from 6.0 to 14.3‰ were suggested to reflect the retention of sulphur from seafloor serpentinisation, where seafloor compositions range from –4 to 9.8‰.

However, modification of sulphides grown during prograde metamorphism is possible. In addition, the mineral assemblage consisting of magnetite and pyrite in the fluid buffered samples are consistent with more oxidised sulphur species suggestive of possible modification via infiltrating fluids during exhumation (section 6.6.6).

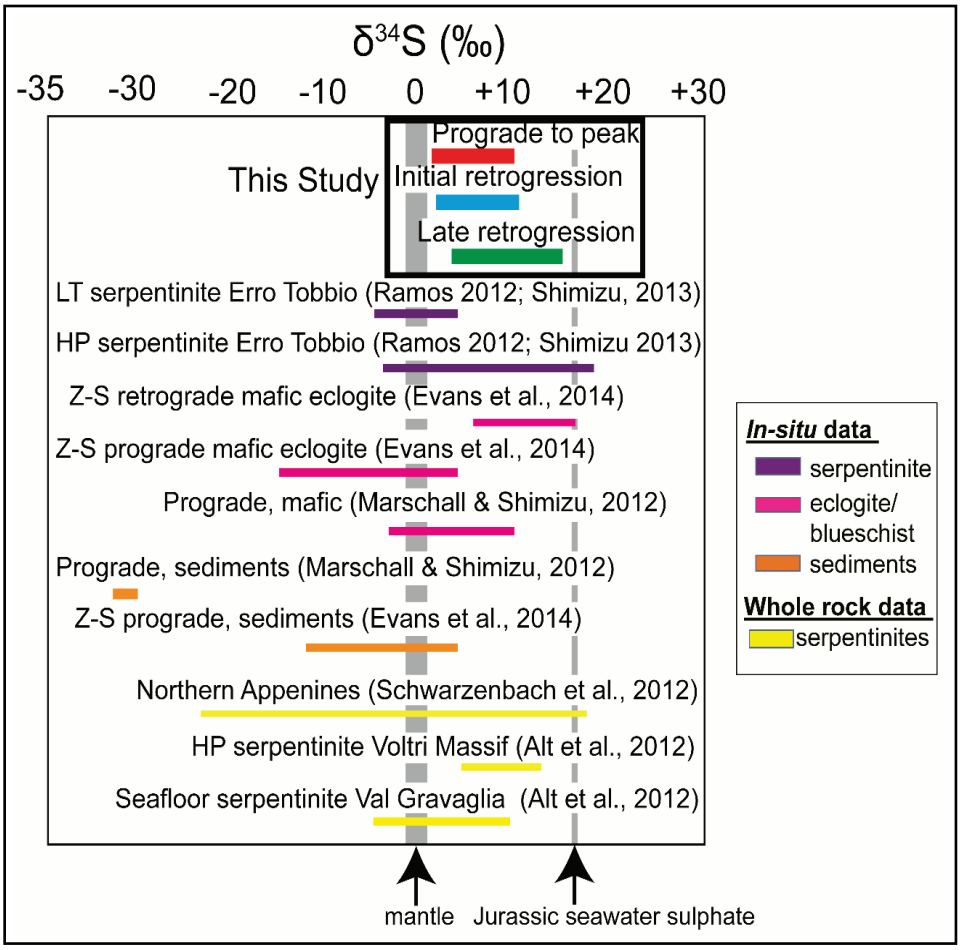

Figure 6.11: Comparison of data from this study to other whole rock and *in-situ* studies.

6.6.6 Sulphides associated with exhumation

The similarity of sulphur isotope values in both prograde and sulphides associated with the onset of exhumation in CO13-33, CO13-55 and CO14-04 is consistent with the interpretation of early HSR as the dominant control on $\delta^{34}S$ signatures. However, pn4 in CO13-55 with $\delta^{34}S$ values of up to 5.5–8.0‰ records a significant shift to heavier isotopic signatures associated with more advanced stages of exhumation. In addition, pyrites in CO14-03 with $\delta^{34}S$ values of up to 15.5‰, are consistent with the isotopic compositions of pyrites in Zermatt-Saas mafic eclogite samples associated with retrogression to blueschist facies (10–16.5‰, Evans et al., 2014, Fig. 6.11). The heterogeneity of the pyrites in CO14-03 likely reflects the mixing of fluids from different sources, as expected for a hybridised ultramafic/mafic rock. Fluid mixing is possibly facilitated during deformation via fluid migration to low pressure zones (e.g. Evans et al., 2014). Thus

the similarity of some of the pyrite S isotope signatures to those of retrogressive pyrites from mafic samples from the Zermatt-Saas implies that the source of oxidised sulphur-bearing fluids the same as those in the mafic samples. Fluid transport of sulphur on a sample scale or greater in CO14-03 is consistent with the high variance mineral assemblage, and thus high fluid:rock ratios. The shift from magnetite to pyrite growth during late retrogression associated with exhumation records an increase in sulphur activity during this stage. The increase in sulphur activity probably occurred on relatively short time scales, given the aggregate nature of the pyrites in CO14-03, where such a texture suggests rapid growth and inadequate time to form well-defined crystal faces. Rapid pyrite growth is likely consistent with a sudden influx of a sulphur-rich and, given the heavy sulphur isotope signatures, oxidised fluid. Large clusters of aggregate pyrites record the heaviest $\delta^{34}S$ values, some of which surround magnetite grains. It is therefore possible that the ferric iron in magnetite reacted with reduced sulphur fluids to produce oxidised sulphur species in solution that produced the heavier $\delta^{34}S$ signatures recorded in the pyrite grains here. H_2S production from sulphate reduction, and reaction with iron from magnetite, where ferric iron reacts much faster with H_2S than ferrous iron (Canfield et al., 1992; Ono et al., 2012), may have been responsible for the rapid growth of pyrite, and hence the observed clusters around magnetite. Alternatively, heavy oxidised sulphur may have been present in the infiltrating fluids.

CO14-04 pyrites record relatively light (4–5‰) and homogeneous $\delta^{34}S$ compositions. The transition from prograde to exhumation is associated with a small but significant shift to lighter $\delta^{34}S$ in the pyrites. The shift from low to high variance sulphide and oxide mineral assemblages associated with this transition, records a switch from a rock buffered or closed system to fluid buffered or open system. The low variance assemblage associated with prograde metamorphism would be consistent with rock buffering with H_2S or HS^- in solution. Therefore, it is possible that the infiltration of external fluids homogenised pre-existing heterogeneous $\delta^{34}S$ compositions that were associated with pre-exhumation stages of metamorphism.

6.6.7 Implications for sulphur cycling

The *in-situ* $\delta^{34}S$ data presented here is consistent with the range of whole rock $\delta^{34}S$ values presented in Alt et al. (2012) from the Voltri Massif in the Ligurian Alps, where the pre-subduction setting is similar to that of the samples studied here. Alt et al. (2012) proposed that the $\delta^{34}S$ isotopic composition of serpentinites remained unaltered during subduction. The *in-situ* technique, however, allows the evolution of $\delta^{34}S$ compositions to be assessed as a function of the stage of sulphide growth, and provides an insight into fluid:rock interaction. The observation that all sulphides record $\delta^{34}S$ compositions in between those of the mantle and Jurassic seawater-derived sulphate, suggests that sulphides could record mixing between these two end members. However, the textural preservation of sulphides that include antigorite, a high pressure serpentine polymorph, and the overprinting of late antigorite generations by retrogressive sulphides suggest that sulphur has been redistributed on at least a millimetre scale during subduction. Spatially heterogeneous $\delta^{34}S$ signatures and low variance mineral assemblages are consistent with redistribution only on a local scale, and associated with low fluid:rock ratios.

On the other hand, sulphides associated with advanced stages of exhumation in CO13-55, record a significant shift towards heavier $\delta^{34}S$ signatures, and therefore the presence of fluids with the ability to carry oxidised sulphur (SO_2 or SO_4^{2-}) at depth within subduction zones. The hybrid samples are fluid buffered on at least the scale of the pyrites (0.1 to 1cm) and therefore the homogeneity of the early and late $\delta^{34}S$ compositions of pyrite in CO14-04 suggests that fluids and therefore sulphur were sourced externally, consistent with the metasomatic alteration of this sample. Furthermore the high variance mineral assemblage of CO14-03 suggests extensive fluid infiltration, and coincides with heterogeneous $\delta^{34}S$ signatures, suggesting that sulphur was derived from both mafic and ultramafic sources, consistent with the hybrid nature of this sample.

The composition of fluids released during dehydration of serpentinites are poorly constrained, however a fluid inclusion study in high-pressure serpentinites from Cima di Gagnone, Swiss Alps, suggests the release of Cl-bearing fluids during the dehydration reactions of chrysotile, and antigorite + brucite (Scambelluri et al., 2004a; Scambelluri et al., 2004b; Kodolanyi and Pettke, 2011; Scambelluri et al.,

2015). On the basis of the presence of sulphides in the fluid inclusions, the speciation of sulphur in such fluids is proposed to be reduced (Scambelluri et al., 2015). On the other hand, low ferric iron and heavy Fe isotopic values suggest the loss of SO_2-bearing fluids from serpentinites (Debret et al., 2016). Furthermore, diamond-bearing fluid inclusions in Alpine metasediments are SO_4^{2-} bearing. It is difficult to resolve the nature of fluids derived from serpentinites, although heavy $\delta^{34}S$ recorded in the sulphides here could be consistent with the infiltration of sulphate-bearing fluids derived from serpentinites deeper in the slab during prograde metamorphism as well as during exhumation, where fluid flow may be facilitated by deformation.

6.7 Conclusions

In-situ sulphur isotope data, in combination with textural and trace element compositions provides insights into the processes, evolution of the redox state and source of sulphur in serpentinites and hybrid mafic/ultramafic rocks through the subduction cycle. Heavy $\delta^{34}S$ values were recorded in all sulphides, where the simplest explanation for this observation is the early fixation and retention of seawater sulphate in the serpentinites and hybrid samples, in general consistent with heterogeneous values, low variance mineral assemblage and hence low fluid:rock interaction. Therefore sulphur is only redistributed on a very local scale in the serpentinites during the subduction cycle, consistent with the conclusions of previous studies (e.g. Alt et al., 2012a). However, infiltration of slab derived fluids during exhumation affected the sulphur mineral assemblages and sulphur isotope compositions in hybrid samples and is possibly recorded by a shift towards heavier isotopic signatures in pentlandite grains associated with late exhumation in one serpentinite sample. The exhumation process could therefore enhance access to fluids from the downgoing slab. Furthermore, hybridisation of mafic/ultramafic rocks appears to be dominated by fluid-buffered assemblages with high sulphur activities, suggesting mobilisation of oxidised sulphur during the 'mixing' of these lithologies on a scale greater than a thin-section sized sample.

6.8 Acknowledgements

Luke Daly and Sarah Hayes are thanked for samples CO14-03 and CO14-04 and for discussions on field observations of these samples. Malcolm Roberts is thanked

for his assistance with the JEOL 8530 WDS microprobe at the Centre for Microscopy, Characterisation and Analysis (CMCA), the University of Western Australia (UWA). The authors acknowledge the facilities, and the scientific and technical assistance of the Australian Microscopy & Microanalysis Research Facility at the CMCA, UWA, a facility funded by the University, State and Commonwealth Governments. This work was supported by an Australian Research Council (ARC) Future Fellowship (FF12000579) to K.E. and a Curtin International Postgraduate Research Scholarship (CIPRS) to R.J.C.

6.9 References

Alt, J. C., Garrido, C. J., Shanks, W., Turchyn, A., Padrón-Navarta, J. A., Sánchez-Vizcaino, V. L., Pugnaire, M. T. G. & Marchesi, C. (2012b), 'Recycling of water, carbon, and sulphur during subduction of serpentinites: A stable isotope study of Cerro del Almirez, Spain', *Earth and Planetary Science Letters* **327**, 50–60.

Alt, J. C., Shanks, W., Crispini, L., Gaggero, L., Schwarzenbach, E. M., Früh-Green, G. L. & Bernasconi, S. M. (2012a), 'Uptake of carbon and sulphur during seafloor serpentinization and the effects of subduction metamorphism in Ligurian peridotites', *Chemical Geology* **322**, 268–277.

Alt, J. C. & Shanks, W. C. (2003), 'Serpentinization of abyssal peridotites from the MARK area, Mid-Atlantic Ridge: sulphur geochemistry and reaction modeling', *Geochimica et Cosmochimica Acta* **67**(4), 641–653.

Alt, J. C. & Shanks, W. C. (1998), 'Sulphur in serpentinized oceanic peridotites: Serpentinization processes and microbial sulphate reduction', *Journal of Geophysical Research: Solid Earth* **103**(B5), 9917–9929.

Alt, J. C., Shanks, W. C. & Jackson, M. C. (1993), 'Cycling of sulphur in subduction zones: The geochemistry of sulphur in the Mariana Island Arc and back-arc trough', *Earth and Planetary Science Letters* **119**(4), 477–494.

Aulbach, S., Stachel, T., Seitz, H.-M. & Brey, G. P. (2012), 'Chalcophile and siderophile elements in sulphide inclusions in eclogitic diamonds and metal cycling in a Paleoproterozoic subduction zone', *Geochimica et Cosmochimica Acta* **93**, 278–299.

Ault, W. & Jensen, M. (1963), 'Summary of sulphur isotope standards.', *In: Biogeochemistry of Sulphur Isotopes.Jensen ML (ed) Nat Sci Found, Symp Proc, Yale University*.

Barnes, S. J., Heggie, G. J. & Fiorentini, M. L. (2013), 'Spatial variation in platinum group element concentrations in ore-bearing komatiite at the Long-Victor deposit, Kambalda Dome, Western Australia: enlarging the footprint of nickel sulphide orebodies', *Economic Geology* **108**(5), 913–933.

Brazelton, W. J., Schrenk, M. O., Kelley, D. S. & Baross, J. A. (2006), 'Methane- and sulphur-metabolizing microbial communities dominate the Lost City hydrothermal field ecosystem', *Applied and Environmental Microbiology* **72**(9), 6257–6270.

Canfield D. E., Raiswell R. and Bottrell S. (1992) The reactivity of sedimentary iron minerals toward sulphide. Am. J. Sci. 292, 659-659.

Debret, B., Andreani, M., Mucoz, M., Bolfan-Casanova, N., Carlut, J., Nicollet, C., Schwartz, S. & Trcera, N. (2014), 'Evolution of Fe redox state in serpentine during subduction', *Earth and Planetary Science Letters* **400**, 206–218.

Debret, B., Millet, M.-A., Pons, M.-L., Bouilhol, P., Inglis, E. & Williams, H. (2016), 'Isotopic evidence for iron mobility during subduction', *Geology* **44**(3), 215–218.

Delacour, A., Früh-Green, G. L., Bernasconi, S. M. & Kelley, D. S. (2008), 'Sulphur in peridotites and gabbros at Lost City (30 N, MAR): Implications for hydrothermal alteration and microbial activity during serpentinization', *Geochimica et Cosmochimica Acta* **72**(20), 5090–5110.

El Gadarri, M. (1995.), 'Les mineralisations sulphurees associees aux ophiolites de Corse : un ex-emple de systeme hydrothermal de sous-plancher oceanique.', Mineralogie. Universite d'Orleans. Thesis.

Evans, K. (2012), 'The redox budget of subduction zones', *Earth-Science Reviews* **113**(1), 11–32.

Evans, K.; Reddy, S.; Tomkins, A., Crossley, R. & Frost, B. (2017), 'Effects of geodynamic setting on the redox state of fluids released by subducted mantle lithosphere', *Lithos*, 278, 26-42.

Evans, K., Tomkins, A., Cliff, J. & Fiorentini, M. (2014), 'Insights into subduction zone sulphur recycling from isotopic analysis of eclogite-hosted sulphides', *Chemical Geology* **365**, 1–19.

Farquhar, J., Bao, H. & Thiemens, M. (2000), 'Atmospheric influence of Earth's earliest sulphur cycle', *Science* **289**(5480), 756–758.

Farquhar, J., Cliff, J., Zerkle, A. L., Kamyshny, A., Poulton, S. W., Claire, M., Adams, D. & Harms, B. (2013), 'Pathways for Neoarchean pyrite formation constrained by mass-independent sulphur isotopes', *Proceedings of the National Academy of Sciences* **110**(44), 17638–17643.

Foustoukos, D. I., Savov, I. P. & Janecky, D. R. (2008), 'Chemical and isotopic constraints on water/rock interactions at the Lost City hydrothermal field, 30 N Mid-Atlantic Ridge', *Geochimica et Cosmochimica Acta* **72**(22), 5457–5474.

Frost, B. R. & Beard, J. S. (2007), 'On silica activity and serpentinization', *Journal of Petrology* **48**(7), 1351–1368.

Giacometti, F., Evans, K. A., Rebay, G., Cliff, J., Tomkins, A. G., Rossetti, P., Vaggelli, G. & Adams, D. T. (2014), 'Sulphur isotope evolution in sulphide ores from Western Alps: Assessing the influence of subduction-related metamorphism', *Geochemistry, Geophysics, Geosystems* **15**(10), 3808–3829.

Grinenko, V., Dmitriev, L., Migdisov, A. & Sharaskin, A. Y. (1975), 'Sulphur contents and isotope compositions for igneous and metamorphic rocks from mid-ocean ridges', *Geochem Int* **12**(1), 132.

Ishihara, S. & Sasaki, A. (1989), 'Sulphur isotopic ratios of the magnetite-series and ilmenite-series granitoids of the Sierra Nevada batholith—a reconnaissance study', *Geology* **17**(9), 788–791.

Jégo, S. & Dasgupta, R. (2013), 'Fluid-present melting of sulphide-bearing ocean-crust: Experimental constraints on the transport of sulphur from subducting slab to mantle wedge', *Geochimica et Cosmochimica Acta* **110**, 106–134.

Kampschulte, A. & Strauss, H. (2004), 'The sulphur isotopic evolution of Phanerozoic seawater based on the analysis of structurally substituted sulphate in carbonates', *Chemical Geology* **204**(3), 255–286.

Kelley, D. S., Karson, J. A., Früh-Green, G. L., Yoerger, D. R., Shank, T. M., Butterfield, D. A., Hayes, J. M., Schrenk, M. O., Olson, E. J., Proskurowski, G. & others (2005), 'A serpentinite-hosted ecosystem: the Lost City hydrothermal field', *Science* **307**(5714), 1428–1434.

Kodolányi, J. & Pettke, T. (2011), 'Loss of trace elements from serpentinites during fluid-assisted transformation of chrysotile to antigorite—An example from Guatemala', *Chemical Geology* **284**(3), 351–362.

LaFlamme, C., Martin, L., Jeon, H., Reddy, Steven, M., Selvaraja, V., Caruso, S., Bui, Hao, T., Roberts, M. P., Voute, F., Hagemann, S., Wacey, D., Wing, B., Fiorentini, M. & Kilburn, M. R. (in revision), 'In situ multiple sulphur isotope analysis by SIMS of pyrrhotite, pentlandite and chalcopyrite to refine magmatic ore genetic models', *Chemical Geology* **444**, 1–15.

Lahondère, D. & Guerrot, C. (1997), 'Datation Nd-Sm du métamorphisme éclogitique en Corse alpine: un argument pour l'existence, au Crétacé supérieur, d'une zone de subduction active localisée le long du block corse-sarde.', *Géologie de la France* **3**, 3-11.

Li, Y. & Liu, J. (2006), 'Calculation of sulphur isotope fractionation in sulphides', *Geochimica et Cosmochimica Acta* **70**(7), 1789–1795.

Liu, W., Borg, S. J., Testemale, D., Etschmann, B., Hazemann, J.-L. & Brugger, J. (2011), 'Speciation and thermodynamic properties for cobalt chloride complexes in hydrothermal fluids at 35–440 C and 600bar: an in-situ XAS study', *Geochimica et Cosmochimica Acta* **75**(5), 1227–1248.

Marini, L., Moretti, R. & Accornero, M. (2011), 'Sulphur isotopes in magmatic-hydrothermal systems, melts, and magmas', *Reviews in Mineralogy and Geochemistry* **73**(1), 423–492.

Marschall, H. R. & Shimizu, N. (2012), 'Sulphur Isotopes in High-Pressure Rocks', *Mineralogical Magazine* **76(6)**, 2070.

Nadeau, O., Stix, J. & Williams-Jones, A. E. (2013), 'The behavior of Cu, Zn and Pb during magmatic–hydrothermal activity at Merapi volcano, Indonesia', *Chemical Geology* **342**, 167–179.

Newton, R. C. & Manning, C. E. (2005), 'Solubility of anhydrite, CaSO4, in NaCl–H2O solutions at high pressures and temperatures: applications to fluid–rock interaction', *Journal of Petrology* **46**(4), 701–716.

Ohmoto, H. & Lasaga, A. C. (1982), 'Kinetics of reactions between aqueous sulphates and sulphides in hydrothermal systems', *Geochimica et Cosmochimica Acta* **46**(10), 1727–1745.

Ohmoto, H. & Rye, R. (1979), 'Isotopes of sulphur and carbon. Geochemistry of Hydrothermal Ore Deposits (Barnes, HL, ed.), 509-567', John Wiley & Sons Inc., New York.

Ono, S., Keller, N. S., Rouxel, O. & Alt, J. C. (2012), 'Sulphur-33 constraints on the origin of secondary pyrite in altered oceanic basement', *Geochimica et Cosmochimica Acta* **87**, 323–340.

Peretti, A., Dubessy, J., Mullis, J., Frost, B. R. & Trommsdorff, V. (1992), 'Highly reducing conditions during Alpine metamorphism of the Malenco peridotite (Sondrio, northern Italy) indicated by mineral paragenesis and H2 in fluid inclusions', *Contributions to Mineralogy and Petrology* **112**(2-3), 329–340.

Pokrovski, G. S. & Dubessy, J. (2015), 'Stability and abundance of the trisulphur radical ion in hydrothermal fluids', *Earth and Planetary Science Letters* **411**, 298–309.

Ranero, C. & Sallares, V. (2004), 'Geophysical evidence for hydration of the crust and mantle of the Nazca plate during bending at the north Chile trench', *Geology* **32**(7), 549–552.

Ravna, E., Andersen, T. B., Jolivet, L. & De Capitani, C. (2010), 'Cold subduction and the formation of lawsonite eclogite–constraints from prograde evolution of eclogitized pillow lava from Corsica', *Journal of Metamorphic Geology* **28**(4), 381–395.

Rees, C., Jenkins, W. & Monster, J. (1978), 'The sulphur isotopic composition of ocean water sulphate', *Geochimica et Cosmochimica Acta* **42**(4), 377–381.

Sakai, H., Des Marais, D., Ueda, A. & Moore, J. (1984), 'Concentrations and isotope ratios of carbon, nitrogen and sulphur in ocean-floor basalts', *Geochimica et Cosmochimica Acta* **48**(12), 2433–2441.

Santiago Ramos, D., Shimizu, N. & Scambelluri, M. (2012), Sulphur isotopic variations during subduction of hydrated lithosphere: the Erro Tobbio case, *in* 'AGU Fall Meeting Abstracts', pp. 04.

Scambelluri, M., Fiebig, J., Malaspina, N., Müntener, O. & Pettke, T. (2004b), 'Serpentinite subduction: implications for fluid processes and trace-element recycling', *International Geology Review* **46**(7), 595–613.

Scambelluri, M., Müntener, O., Ottolini, L., Pettke, T. T. & Vannucci, R. (2004a),

'The fate of B, Cl and Li in the subducted oceanic mantle and in the antigorite breakdown fluids', *Earth and Planetary Science Letters* **222**(1), 217–234.

Scambelluri, M., Pettke, T. & Cannaт, E. (2015), 'Fluid-related inclusions in Alpine high-pressure peridotite reveal trace element recycling during subduction-zone dehydration of serpentinized mantle (Cima di Gagnone, Swiss Alps)', *Earth and Planetary Science Letters* **429**, 45–59.

Schwarzenbach, E. M., Früh-Green, G. L., Bernasconi, S. M., Alt, J. C. & Plas, A. (2013), 'Serpentinization and carbon sequestration: A study of two ancient peridotite-hosted hydrothermal systems', *Chemical Geology* **351**, 115–133.

Seal, R. R. (2006), 'Sulphur isotope geochemistry of sulphide minerals', *Reviews in mineralogy and geochemistry* **61**(1), 633–677.

Seyfried, W., Foustoukos, D. & Fu, Q. (2007), 'Redox evolution and mass transfer during serpentinization: An experimental and theoretical study at 200° C, 500bar with implications for ultramafic-hosted hydrothermal systems at Mid-Ocean Ridges', *Geochimica et Cosmochimica Acta* **71**(15), 3872–3886.

Shanks, W., Bцhlke, J. & Seal, R. (1995), 'Stable Isotopes in Mid-Ocean Ridge Hydrothermal Systems: Interactions Between Fluids, Minerals, and Organisms', *Seafloor Hydrothermal Systems: Physical, Chemical, Biological, and Geological Interactions*, 194–221.

Shanks, W., Bischoff, J. L. & Rosenbauer, R. J. (1981), 'Seawater sulphate reduction and sulphur isotope fractionation in basaltic systems: interaction of seawater with fayalite and magnetite at 200–350 C', *Geochimica et Cosmochimica Acta* **45**(11), 1977–1995.

Shimizu N, Scambelluri M, S. R. D. &. T. S. (2013), 'Boron and Sulphur Isotopic Variations during Subduction of Hydrated Lithosphere: The Erro Tobbio Case', *Mineralogical Magazine* **77(5)**, 2201.

Spandler, C., Hermann, J., Faure, K., Mavrogenes, J. A. & Arculus, R. J. (2008), 'The importance of talc and chlorite "hybrid" rocks for volatile recycling through subduction zones, evidence from the high-pressure subduction mélange of New Caledonia', *Contributions to Mineralogy and Petrology* **155**(2), 181–198.

Tostevin, R., Turchyn, A. V., Farquhar, J., Johnston, D. T., Eldridge, D. L., Bishop, J. K. & McIlvin, M. (2014), 'Multiple sulphur isotope constraints on the modern sulphur cycle', *Earth and planetary science letters* **396**, 14–21.

Ueda, A. & Sakai, H. (1984), 'Sulphur isotope study of Quaternary volcanic rocks from the Japanese Islands Arc', *Geochimica et Cosmochimica Acta* **48**(9), 1837–1848.

Vitale Brovarone, A., Beltrando, M., Malavieille, J., Giuntoli, F., Tondella, E., Groppo, C., Beyssac, O. & Compagnoni, R. (2011), 'Inherited ocean–continent transition zones in deeply subducted terranes: insights from Alpine Corsica', *Lithos* **124**(3), 273–290.

Vitale Brovarone, A., Beyssac, O., Malavieille, J., Molli, G., Beltrando, M. & Compagnoni, R. (2013), 'Stacking and metamorphism of continuous segments of subducted lithosphere in a high-pressure wedge: the example of Alpine Corsica (France)', *Earth-Science Reviews* **116**, 35–56.

Vitale Brovarone, A. & Herwartz, D. (2013), 'Timing of HP metamorphism in the Schistes Lustrés of Alpine Corsica: New Lu–Hf garnet and lawsonite ages', *Lithos* **172**, 175–191.

Wacey, D., Kilburn, M. R., Saunders, M., Cliff, J. & Brasier, M. D. (2011), 'Microfossils of sulphur-metabolizing cells in 3.4-billion-year-old rocks of Western Australia', *Nature Geoscience* **4**(10), 698–702.

Wagner, T. & Boyce, A. J. (2006), 'Pyrite metamorphism in the Devonian Hunsrück Slate of Germany: Insights from laser microprobe sulphur isotope analysis and thermodynamic modeling', *American Journal of Science* **306**(7), 525–552.

Wallace, P. J. & Edmonds, M. (2011), 'The sulphur budget in magmas: evidence from melt inclusions, submarine glasses, and volcanic gas emissions', *Reviews in Mineralogy and Geochemistry* **73**(1), 215–246.

Williams, T. J., Candela, P. A. & Piccoli, P. M. (1995), 'The partitioning of copper between silicate melts and two-phase aqueous fluids: an experimental investigation at 1 kbar, 800 C and 0.5 kbar, 850 C', *Contributions to Mineralogy and Petrology* **121**(4), 388–399.

Woodhead, J. D., Harmon, R. S. & Fraser, D. G. (1987), 'O, S, Sr, and Pb isotope variations in volcanic rocks from the Northern Mariana Islands: implications for crustal recycling in intra-oceanic arcs', *Earth and Planetary Science Letters* **83**(1), 39–52.

CHAPTER 7

CONCLUSIONS, SYNTHESIS AND FURTHER RESEARCH

7.1 Introduction

This study has investigated the distribution of iron, sulphur and highly siderophile elements within subducted serpentinites and hybrid rocks. Most previous studies have focused on the whole rock scale distribution of these elements in high-pressure serpentinites (e.g. Debret et al., 2014; 2016; Alt et al., 2012a, Blanco-Quintero et al., 2011), which provide substantial insights into the proportions of these elements during subduction, however the effects of exhumation are not assessed. Here it is shown that useful insights into the distribution of these elements and processes that control their distribution can additionally be obtained through investigation of changes to mineral hosts of S, Fe and HSE and trace element geochemistry of mineral hosts from seafloor alteration to exhumation. Prior to this work, and to the author's best knowledge, this study presents the first *in-situ* highly siderophile element analyses of sulphides and oxides within high-pressure serpentinites and hybrid ultramafic/mafic rocks. In addition, there are currently no published articles on isotopic analyses of sulphides in high-pressure serpentinites and hybrid rocks. Here, the findings are summarised and synthesised to address the objectives outlined in Chapter 1, and suggestions are made for further research.

7.2 Changes in iron and sulphur bearing phases through the subduction cycle

Pre-subduction sulphur and iron contents and oxidation state on a whole rock scale are variable and therefore it is difficult to assess the changes to iron and sulphur bearing phases during the prograde and/or retrograde metamorphic evolution on the whole rock scale using whole rock geochemistry alone. However, an assessment of changes to minerals that host sulphur and iron provide through careful mineral textural analysis, parageneses and mineral compositional data, provide evidence for changes to the distribution of iron and sulphur from seafloor alteration to retrogression associated with exhumation.

At the seafloor alteration stage, iron is mainly hosted in primary Cr-Al or Cr-rich spinel with increasing ferric iron towards the rim. The prograde evolution

is characterised by development of porous textures infilled with antigorite as observed in the Corsican samples, and magnetite rims. The porous texture is attributed to the reaction of antigorite with primary Cr-Al cores in the presence of fluids (Chapter 5). In two 'hybrid' samples with an ultramafic/mafic origin, one from Pfulwe, and one from Capu Corvoli from Alpine Corsica, large late magnetite grains are observed cross-cutting the dominant foliation, surrounded by talc, a phase related to decompression associated with advanced exhumation (Evans and Powell, 2015), and hence magnetite is attributed to the onset of exhumation (Chapters 3 and 5). Therefore, there is evidence for oxidation of existing iron and/or addition of ferric iron at the onset of fluid infiltration.

Whole rock sulphur concentrations are highly variable, with no systematic trends associated with proximity to other lithologies, consistent with highly variable seafloor sulphur geochemistry (Alt et al., 2012a). Sulphides record changes in texture throughout the subduction cycle (Chapters 4 and 6). Primary sulphides were not identified in the samples. Pentlandite and heazlewoodite record alteration of seafloor precursors during subduction, with the timing indicated by the presence of antigorite inclusions and with late antigorite associated with exhumation overprinting such grains. Prograde pyrite grains contain inclusions of non-porous Al-poor, Cr-rich spinel, an alteration product of primary spinel. Late pentlandite grains overprint antigorite veins, spinel and magnetite grains, providing evidence for sulphur mobilisation on the mineral scale. Late pyrite is observed on the rim of late magnetite grains in one hybrid sample, and therefore records late exhumation.

7.3 Tracing the distribution of HSE through the subduction cycle

In the work presented in Chapter 4, HSE concentrations in sulphides are shown to be depleted but net changes in HSE concentrations are not observed for the serpentinites compared to pre-subduction analogues, with the exception of moderate Au enrichment in one sample. The redistribution of HSE from sulphides to alloys are proposed to explain the depletion as a result of more reducing conditions or mobilisation on a micron to millimetre scale. However, reducing conditions are not consistent with heavy sulphur isotope signatures recorded in the pentlandites (Chapter 6), most likely because the isotopic signatures are set relatively early during hydrothermal sulphate reduction on the seafloor. PGE and Re are proposed to be mobilised in oxidised, Cl-rich fluids (e.g. Xiong and Wood,

2000; 2002; Hanley et al., 2005). At present, the conditions of HSE alloy formation (e.g. Os-Ir and Pt alloys) are not well constrained and alloys are difficult to detect, especially pure and hence high density HSE alloys, which require the analysis of several thin sections before trace amounts are detected. In contrast, the hybrid samples show evidence for the fractionation of Re, Ru, Ir and Au during subduction on a whole rock scale as a result of interaction with proximal metagabbro and depletion in all HSE except for Re in sulphides. Sulphur addition during exhumation is inferred to explain the highly depleted HSE concentrations in pyrites within hybrid samples, with the exception of rhenium. The differences in the extent of mobilisation of HSE in serpentinites and hybrid rocks are attributed to rock buffered versus fluid buffered systems, where fluid buffering is associated with hybrid samples.

7.4 The source and redox state of iron and sulphur

Insights from oxide and sulphide mineral parageneses allows the assessment of rock buffered versus fluid buffered conditions, with a higher variance mineral assemblage associated with fluid buffering i.e. two or less mineral phases in equilibrium, to assess the effect of external fluids on changes to iron and sulphur bearing phases. Serpentinites are dominantly rock buffered, whereas the hybrid rocks are fluid buffered (Chapter 4).

The presence of late magnetite in hybrid samples without an obvious iron source within the rock indicate that the source of iron may be external, and that exhumation may enhance the infiltration of external fluids. On the basis of an increase in the mode of magnetite at the onset of exhumation, the infiltration of oxidised fluids or fluids with the ability to carry Fe^{3+} are required. One potential source of oxidised fluids is serpentinites from the downgoing slab, which have been proposed to release oxidising fluids on the basis of decreasing redox budgets of serpentinites with increasing metamorphic grade observed by Debret et al. (2014; 2016). The solubility of Fe^{3+} is considered to be limited at present, although the possibility of the introduction of titanium in PF-001 before peak metamorphism, a seemingly immobile element, that cannot be entirely accounted for by physical mixing with metagabbro, may suggest fluid mediated mechanisms for Ti, and therefore mobilisation of Fe^{3+} is possible (Chapter 3). In addition, complex spinel zonation patterns with Fe-rich cores in one sample, and 'veins' of magnetite cross

cutting Cr-spinel cores suggest that such textures are not dominantly a function of pressure, but is most likely controlled by dissolution-precipitation reactions on a local scale (Chapter 5). Primary Cr-Al spinels are altered to Fe^{3+}-enriched compositions during prograde metamorphism in serpentinites suggesting mobilisation or oxidation of Fe^{3+} on at least a mineral scale via reaction of antigorite and primary spinel in the presence of Fe^{3+}-bearing or oxidised fluids, or via electron acceptors such as SO_4^{2-} and SO_2.

Sulphur isotope signatures suggest that serpentinites retained hydrothermal sulphate reduction signatures from seafloor alteration, consistent with low fluid:rock ratios during metamorphism, in agreement with the conclusions of Alt et al. (2012a). On the other hand, the shift towards heavier S isotope values in one serpentinite sample proximal could suggest the infiltration of sulphate during exhumation. Additionally, one hybridised mafic/ultramafic sample reflects a mixed sulphur source with values of up to 15.5‰ (Chapter 6). The dehydration and infiltration of fluids derived from sulphate-bearing lithologies from the downgoing slab could account for heavy sulphur isotope signatures, where access to such fluids is enhanced during exhumation.

7.5 Further research

7.5.1 Experimental studies on the solubility of Ti and Fe^{3+}

The Zermatt-Saas samples show evidence for the late addition of ferric iron but it was not possible to determine whether this was a result of oxidation or mobilisation of ferric iron at the onset of exhumation. The enrichment of Ti within the Pfulwe serpentinite, an 'immobile' element, could imply the addition of Ti prior to peak metamorphism, therefore if Ti is mobilised, Fe^{3+}, also generally considered immobile, may have also been mobilised. The same fluids responsible for Ti-enrichment could have the ability to carry ferric iron. There is currently a lack of data on fluid chemistry and the solubilities of Ti and Fe^{3+} at pressures associated with subduction and therefore this could be a focus for future work.

7.5.2 An assessment of the sensitivity of HSE distribution to sulphidation and/or oxidation

Further work is required to fully constrain the controls on the solubility or precipitation of HSE (e.g. Foustoukos et al., 2015), particularly at high pressure. An assessment of the sensitivity of HSE distribution to sulphidation and/or

oxidation could utilise bulk and mineral separate stable isotope compositions e.g. copper, iron and zinc. Systematic changes in stable isotope signatures of zinc and iron of Alpine serpentinites during prograde metamorphism have been inferred which suggest the release of sulphate-bearing fluids (Pons et al., 2016; Debret et al., 2016). Stable isotope systems could act as sensitive tracers of the redox state of sulphur throughout the subduction cycle and provide insights into the slab derived fluids with analyses of hybrid samples and serpentinites recording exhumation. However, it would not be possible to distinguish between prograde and retrograde oxidation using bulk stable isotopes, and many sulphide grains are too small for mineral separate analysis in the samples studied.

Additional constraints could be provided with the use of transmission electron microscopy techniques in combination with electron energy loss spectroscopy (EELS) to allow quantification of $Fe^{3+}/\Sigma Fe$ in retrogressive antigorite at the scale of the veins observed in the samples. Retrogressive antigorite would record the onset of fluid infiltration derived from greater depths in the slab, from other lithologies or during exhumation, and therefore would provide complementary information to the stable isotope techniques described above on the oxidation state of fluids infiltrating serpentinites during subduction.

A recent study (Evans et al., in revision) has proposed that samples from New Caledonia from a pre-subduction supra-subduction environment are less oxidised than samples from the Western Alps upon subduction, where Western Alps samples were likely in an ocean-continent transition zone setting pre-subduction (e.g. Vitale Brovarone et al., 2014; Beltrando et al., 2014). The comparison between these two localities would allow the robustness of HSE as sensitive tracers of redox conditions at a scale greater than a subduction zone system.

7.5.3 Seafloor processes: open versus closed system and bacterial versus hydrothermal sulphate reduction

Chapter six identified that more precise measurements of $\Delta^{33}S$ would be required to fully assess open versus closed system sulphate reduction, and hydrothermal (HSR) versus bacterial sulphate reduction (BSR), and the retention of these signatures in subduction zones. This is not currently possible using the *in-situ* SIMS technique as for this study, and the technique outlined in Ono et al. (2006

and 2012) would require sulphide mineral separates analysis where larger sulphides would be required, and using bulk powders would mean that the detailed stages of the subduction cycle signatures would be lost. However, this technique could be applied to samples which record only one generation of sulphide is recorded e.g. CO13-40, and to the hybrid samples which record large pyrites.

Furthermore, the establishment of fractionation factors for S^{3-} ions via experimental work provides scope for future work. This would allow the distinction between seafloor BSR and HSR processes and subduction derived non-zero $\Delta^{33}S$ signatures.

7.6 Outlook

The inaccessibility of a complete record of changes from seafloor through subduction and exhumation demonstrates the importance of continued mineral-scale investigations in deciphering changes to the distribution of redox sensitive elements throughout the subduction cycle. In addition, hybrid rocks appear to record substantial changes to iron, sulphur and highly siderophile elements compared to their ultramafic and/or mafic precursors. Therefore, the continued study of such lithologies is considered essential to understand the mobilisation of redox sensitive elements in subduction zones and their capacity to oxidise the sub-arc mantle. In particular, their close proximity to the slab/mantle interface suggests hybrid lithologies are likely to record fluids and redox sensitive elements ultimately transferred to the sub-arc mantle.

BIBLIOGRAPHY
A

Agard, P. & Vitale-Brovarone, A. (2013), 'Thermal regime of continental subduction: the record from exhumed HP–LT terranes (New Caledonia, Oman, Corsica)', *Tectonophysics* **601**, 206–215.

Ague, J. J. (2007), 'Models of permeability contrasts in subduction zone mélange: implications for gradients in fluid fluxes, Syros and Tinos Islands, Greece', *Chemical Geology* **239**(3), 217–227.

Alard, O.; Luguet, A.; Pearson, N. J.; Griffin, W. L.; Lorand, J.-P.; Gannoun, A.; Burton, K. W. & O'Reilly, S. Y. (2005), 'In situ Os isotopes in abyssal peridotites bridge the isotopic gap between MORBs and their source mantle', *Nature* **436**(7053), 1005–1008.

Allen, D. E. & Seyfried, W. (2003), 'Compositional controls on vent fluids from ultramafic-hosted hydrothermal systems at mid-ocean ridges: An experimental study at 400 C, 500 bars', *Geochimica et Cosmochimica Acta* **67**(8), 1531–1542.

Alt, J. C.; Garrido, C. J.; Shanks, W.; Turchyn, A.; Padrón-Navarta, J. A.; Sánchez-Vizcaino, V. L.; Pugnaire, M. T. G. & Marchesi, C. (2012b), 'Recycling of water, carbon, and sulfur during subduction of serpentinites: A stable isotope study of Cerro del Almirez, Spain', *Earth and Planetary Science Letters* **327**, 50–60.

Alt, J. C.; Shanks, W.; Crispini, L.; Gaggero, L.; Schwarzenbach, E. M.; Früh-Green, G. L. & Bernasconi, S. M. (2012a), 'Uptake of carbon and sulfur during seafloor serpentinization and the effects of subduction metamorphism in Ligurian peridotites', *Chemical Geology* **322**, 268–277.

Alt, J. C. & Shanks, W. C. (2003), 'Serpentinization of abyssal peridotites from the MARK area, Mid-Atlantic Ridge: sulfur geochemistry and reaction modeling', *Geochimica et Cosmochimica Acta* **67**(4), 641–653.

Alt, J. C. & Shanks, W. C. (1998), 'Sulfur in serpentinized oceanic peridotites: Serpentinization processes and microbial sulfate reduction', *Journal of Geophysical Research: Solid Earth* **103**(B5), 9917–9929.

Alt, J. C.; Shanks, W. C. & Jackson, M. C. (1993), 'Cycling of sulfur in subduction zones: The geochemistry of sulfur in the Mariana Island Arc and back-arc trough', *Earth and Planetary Science Letters* **119**(4), 477–494.

Andreani, M.; Mével, C.; Boullier, A.-M. & Escartin, J. (2007), 'Dynamic control on serpentine crystallization in veins: Constraints on hydration processes in oceanic peridotites', *Geochemistry, Geophysics, Geosystems* **8**(2).

Andreani, M.; Munoz, M.; Marcaillou, C. & Delacour, A. (2013), 'XANES study of iron redox state in serpentine during oceanic serpentinization', *Lithos* **178**, 70–83.

Angiboust, S. & Agard, P. (2010), 'Initial water budget: The key to detaching large volumes of eclogitized oceanic crust along the subduction channel?', *Lithos* **120**(3), 453–474.

Angiboust, S.; Agard, P.; Jolivet, L. & Beyssac, O. (2009), 'The Zermatt-Saas ophiolite: the largest (60-km wide) and deepest (c. 70–80 km) continuous slice of oceanic lithosphere detached from a subduction zone?', *Terra Nova* **21**(3), 171–180.

Arai, S. (1992), 'Chemistry of chromian spinel in volcanic rocks as a potential guide to magma chemistry', *Mineralogical Magazine* **56**(383), 173–184.

Aulbach, S.; Stachel, T.; Seitz, H.-M. & Brey, G. P. (2012), 'Chalcophile and siderophile elements in sulphide inclusions in eclogitic diamonds and metal cycling in a Paleoproterozoic subduction zone', *Geochimica et Cosmochimica Acta* **93**, 278–299.

Ault, W. & Jensen, M. (1963), 'Summary of sulfur isotope standards.', *In: Biogeochemistry of Sulfur Isotopes.Jensen ML (ed) Nat Sci Found, Symp Proc, Yale University*.

B

Bach, W.; Garrido, C. J.; Paulick, H.; Harvey, J. & Rosner, M. (2004), 'Seawater-peridotite interactions: First insights from ODP Leg 209, MAR 15 N', *Geochemistry, Geophysics, Geosystems* **5**(9).

Baird, A. & Dewey, J. (1986), 'Structural evolution in thrust belts and relative plate motion: The Upper Pennine Piemont Zone of the internal Alps, southwest Switzerland and northwest Italy', *Tectonics* **5**(3), 375–387.

Ballèvre, M.; Kienast, J.-R. & Vuichard, J.-P. (1986), 'La nappe de la Dent-Blanche(Alpes occidentales): deux unités austroAlpines indépendantes', *Eclogae Geologicae Helvetiae* **79**(1), 57–74.

Ballhaus, C.; Berry, R. & Green, D. (1991), 'High pressure experimental calibration of the olivine-orthopyroxene-spinel oxygen geobarometer: implications for the oxidation state of the upper mantle', *Contributions to Mineralogy and Petrology* **107**(1), 27–40.

Barnes, J. D.; Beltrando, M.; Lee, C.-T. A.; Cisneros, M.; Loewy, S. & Chin, E. (2014), 'Geochemistry of Alpine serpentinites from rifting to subduction: A view across paleogeographic domains and metamorphic grade', *Chemical Geology* **389**, 29–47.

Barnes, S. J. (2000), 'Chromite in komatiites, II. Modification during greenschist to mid-amphibolite facies metamorphism', *Journal of Petrology* **41**(3), 387–409.

Barnes, S. J.; Heggie, G. J. & Fiorentini, M. L. (2013), 'Spatial variation in platinum group element concentrations in ore-bearing komatiite at the Long-Victor deposit, Kambalda Dome, Western Australia: enlarging the footprint of nickel sulfide orebodies', *Economic Geology* **108**(5), 913–933.

Barnes, S. J.; Mungall, J. E. & Maier, W. D. (2015), 'Platinum group elements in mantle melts and mantle samples', Lithos 232, 395–417.

Barnes, S. J. & Roeder, P. L. (2001), 'The range of spinel compositions in terrestrial mafic and ultramafic rocks', *Journal of Petrology* **42**(12), 2279–2302.

Barnicoat, A. & Cartwright, I. (1995), 'Focused fluid flow during subduction: oxygen isotope data from high-pressure ophiolites of the western Alps', *Earth and Planetary Science Letters* **132**(1), 53–61.

Barnicoat, A.; Cliff, R.; Inger, S. & Rex, D. (1993), 'Assesing the age of high-pressure metamorphism in the western Alps using Sm-Nd and 40Ar/39Ar', *Terra Nova* **5**, 380.

Barnicoat, A. & Fry, N. (1986), 'High-pressure metamorphism of the Zermatt-Saas ophiolite zone, Switzerland', *Journal of the Geological Society* **143**(4), 607–618.

Barra F, Gervilla F, Hernández E, Reich M, Padrón-Navarta JA (2014) 'Altered chromian spinels from La Cabaña peridotite, south central Chile: considerations on the formation of ferritchromite.', *Miner Petrol.* **10**, 819–836.

Bearth, P. (1981), 'The post-Triassic sediments of the ophiolite zone Zermatt-Saas Fee and the associated manganese mineralizations', *Eclogae Geologicae Helvetiae* **74 (2)**, 189-205.

Beccaluva, L.; Dalpiaz, G. & Macciotta, G. (1984), 'Transitional to normal MORB affinities in ophiolitic metabasites from the Zermatt-Saas, Combin and Antrona units, Western Alps-implications for the paleogeographic evolution of the Western Tethyan basin', *Geologie en Mijnbouw* **63**(2), 165–177.

Becker, H. (2000), 'Re–Os fractionation in eclogites and blueschists and the implications for recycling of oceanic crust into the mantle', *Earth and Planetary Science Letters* **177**(3), 287–300.

Becker, H.; Horan, M.; Walker, R.; Gao, S.; Lorand, J.-P. & Rudnick, R. (2006), 'Highly siderophile element composition of the Earth's primitive upper mantle: constraints from new data on peridotite massifs and xenoliths', *Geochimica et Cosmochimica Acta* **70**(17), 4528–4550.

Beltrando, M.; Compagnoni, R. & Lombardo, B. (2010), '(Ultra-) High-pressure metamorphism and orogenesis: An Alpine perspective', *Gondwana Research* **18**(1), 147–166.

Beltrando, M.; Manatschal, G.; Mohn, G.; Dal Piaz, G. V.; Brovarone, A. V. & Masini, E. (2014), 'Recognizing remnants of magma-poor rifted margins in high-pressure orogenic belts: The Alpine case study', *Earth-Science Reviews* **131**, 88–115.

Beltrando, M.; Rubatto, D. & Manatschal, G. (2010), 'From passive margins to orogens: The link between ocean-continent transition zones and (ultra) high-pressure metamorphism', *Geology* **38**(6), 559–562.

Blanco-Quintero, I.; Fernández, J. A. P.; Casco, A. G.; Tauler, E. & others (2011), 'Serpentinites and serpentinites within a fossil subduction channel: La Corea mélange, eastern Cuba', *Geologica Acta* **9**(3).

Bliss, N. & MacLean, W. (1975), 'The paragenesis of zoned chromite from central Manitoba', *Geochimica et Cosmochimica Acta* **39**(6), 973–990.

Bouilhol, P.; Magni, V.; van Hunen, J. & Kaislaniemi, L. (2015), 'A numerical approach to melting in warm subduction zones', *Earth and Planetary Science Letters* **411**, 37–44.

Bowtell, S.; Cliff, R. & Barnicoat, A. (1994), 'Sm-Nd isotopic evidence on the age of eclogitization in the Zermatt-Saas ophiolite', *Journal of Metamorphic Geology* **12**(2), 187–196.

Bragagni, A.; Fonseca, R.; van Acken, D.; Speelmanns, I.; Heuser, A. & A., L. (2015), 'Highly Siderophile Elements and 187Os/188Os in Individual Sulfides by Isotope Dilution', *Goldschmidt Abstracts* **374**.

Bragg, W. H. (1915), 'XXX. The structure of the spinel group of crystals', *The London, Edinburgh, and Dublin Philosophical Magazine and Journal of Science* **30**(176), 305–315.

Brandon, A. D.; Creaser, R. A.; Shirey, S. B. & Carlson, R. W. (1996), 'Osmium recycling in subduction zones', Science 272(5263), 861–863.

Brandon, A. D. & Draper, D. S. (1996), 'Constraints on the origin of the oxidation state of mantle overlying subduction zones: an example from Simcoe, Washington, USA', *Geochimica et Cosmochimica Acta* **60**(10), 1739–1749.

Brandon, A. D.; Snow, J. E.; Walker, R. J.; Morgan, J. W. & Mock, T. D. (2000), '^{190}Pt–^{186}Os and ^{187}Re–^{187}Os systematics of abyssal peridotites', *Earth and Planetary Science Letters* **177**(3), 319–335.

Brazelton, W. J.; Schrenk, M. O.; Kelley, D. S. & Baross, J. A. (2006), 'Methane- and sulfur-metabolizing microbial communities dominate the Lost City hydrothermal field ecosystem', *Applied and Environmental Microbiology* **72**(9), 6257–6270.

Brenan, J. M. & Andrews, D. (2001), 'High-temperature stability of laurite and Ru–Os–Ir alloy and their role in PGE fractionation in mafic magmas', The Canadian Mineralogist 39(2), 341–360.

Brenan, J. M.; Finnigan, C. F.; McDonough, W. F. & Homolova, V. (2012), 'Experimental constraints on the partitioning of Ru, Rh, Ir, Pt and Pd between chromite and silicate melt: the importance of ferric iron', *Chemical Geology* **302**, 16–32.

Bromiley, G. D. & Pawley, A. R. (2003), 'The stability of antigorite in the systems MgO-SiO2-H2O (MSH) and MgO-Al2O3-SiO2-H2O (MASH): The effects of Al3+ substitution on high-pressure stability', *American Mineralogist* **88**(1), 99–108.

Bucher, K.; Fazis, Y.; Capitani, C. D. & Grapes, R. (2005), 'Blueschists, eclogites, and decompression assemblages of the Zermatt-Saas ophiolite: High-pressure metamorphism of subducted Tethys lithosphere', *American Mineralogist* **90**(5-6), 821–835.

Bucher, K. & Grapes, R. (2009), 'The eclogite-facies Allalin Gabbro of the Zermatt–Saas ophiolite, Western Alps: a record of subduction zone hydration', *Journal of Petrology*, egp035.

Buddington, A. & Lindsley, D. (1964), 'Iron-titanium oxide minerals and synthetic equivalents', *Journal of petrology* **5**(2), 310–357.

Burkhard, D. J. (1993), 'Accessory chromium spinels: their coexistence and alteration in serpentinites', *Geochimica et Cosmochimica Acta* **57**(6), 1297–1306.

C

Canfield D. E., Raiswell R. and Bottrell S. (1992) The reactivity of sedimentary iron minerals toward sulfide. Am. J. Sci. 292, 659-659.

Cannao, E.; Agostini, S.; Scambelluri, M.; Tonarini, S. & Godard, M. (2015), 'B, Sr and Pb isotope geochemistry of high-pressure Alpine metaperidotites monitors fluid-mediated element recycling during serpentinite dehydration in subduction mélange (Cima di Gagnone, Swiss Central Alps)', *Geochimica et Cosmochimica Acta* **163**, 80–100.

Caruso, L. J., & Chernosky, J. V. (1979). The stability of lizardite. *The Canadian Mineralogist*, **17**(4), 757-769.

Caron, J. & Delcey, R. (1979), 'Lithostratigraphie des schistes lustrés corses: diversité des series post-ophiolitiques', *Compte Rendu Académies des Sci, Paris* **208**, 1525–1528.

Cartwright, I. & Barnicoat, A. (2002), 'Petrology, geochronology, and tectonics of shear zones in the Zermatt–Saas and Combin zones of the Western Alps', *Journal of Metamorphic Geology* **20**(2), 263–281.

Cartwright, I. & Buick, I. (2000), 'Fluid generation, vein formation and the degree of fluid–rock interaction during decompression of high-pressure terranes: the Schistes Lustrés, Alpine Corsica, France', *Journal of Metamorphic Geology* **18**(6), 607–624.

Chan, T. & Finch, I. (2001), Determination of platinum-group elements and gold by inductively coupled plasma mass spectrometry, *in* 'Australian Platinum Conference, Perth, Western Australia', pp. 1–9.

Chopin, C.; Beyssac, O.; Bernard, S. & Malavieille, J. (2008), 'Aragonite–grossular intergrowths in eclogite-facies marble, Alpine Corsica', *european Journal of Mineralogy* **20**(5), 857–865.

Colás, V.; González-Jiménez, J. M.; Griffin, W. L.; Fanlo, I.; Gervilla, F.; O'Reilly, S. Y.; Pearson, N. J.; Kerestedjian, T. & Proenza, J. A. (2014), 'Fingerprints of metamorphism in chromite: New insights from minor and trace elements', *Chemical Geology* **389**, 137–152.

Colás, V.; Padrón-Navarta, J. A.; González-Jiménez, J. M.; Griffin, W. L.; Fanlo, I.; O'reilly, S. Y.; Gervilla, F.; Proenza, J. A.; Pearson, N. J. & Escayola, M. P. (2016), 'Compositional effects on the solubility of minor and trace elements in oxide spinel minerals: Insights from crystal-crystal partition coefficients in chromite exsolution', *American Mineralogist* **101**(6), 1360–1372.

Compagnoni, R.; Dal Piaz, G.; Hunziker, J.; Gosso, G.; Lombardo, B. & Williams, P. (1977), 'The Sesia-Lanzo Zone, a slice of continental crust with Alpine high pressure-low temperature assemblages in the Western Italian Alps', *Rend. Soc. Ital. Mineral. Petrol* **33**(1), 281–334.

Compagnoni, R.; Giovanni, F. & Flora, L. (1983), 'Balangeroite, a new fibrous silicate related to gageite from Balangero, Italy', *Am. Mineral*, 214–19.

Compagnoni, R., R. F. &. T. E. (2000), 'UHP Terranes in the Western Alps "31st International Geological Congress, Rio de Janeiro, Brazil, 6–17 August, 4 p. (Extended Abstract), CD geobr2000, ISBN 85-901482-5-4.'.

Coward, M. & Dietrich, D. (1989), 'Alpine tectonics—an overview', *Geological Society, London, Special Publications* **45**(1), 1–29.

Cressey, G.; Cressey, B. & Wicks, F. (2008), 'The significance of the aluminium content of a lizardite at the nanoscale: the role of clinochlore as an aluminium sink', *Mineralogical Magazine* **72**(3), 817–825.

Cruz, M. R.; Puga, E. & Nieto, J. (1999), 'Silicate and oxide exsolution in pseudo-spinifex olivine from metaultramafic rocks of the Betic Ophiolitic Association: A TEM study', *Am. Miner* **84**(11-12), 1915–1924.

D

Dal Piaz, G. (1999), 'The Austroalpine-Piedmont nappe stack and the puzzle of Alpine Tethys', *Memorie di Scienze Geologiche* **51**(1), 155–176.

Dal Piaz, G.; Cortiana, G.; Del Moro, A.; Martin, S.; Pennacchioni, G. & Tartarotti, P. (2001), 'Tertiary age and paleostructural inferences of the eclogitic imprint in the Austroalpine outliers and Zermatt–Saas ophiolite, western Alps', *International Journal of Earth Sciences* **90**(3), 668–684.

Dal Piaz, G.V. (2004) From the European continental margin to the Mesozoic Thetyan Ocean: A geological map of the upper Ayas Valley (Western Alps). In: Pasquaré, G., Venturini C., (Eds), Groppelli G., (Ass.t Ed.), Mapping Geology in Italy. APAT - Agenzia per la Protenzione dell'Ambiente e per i Servizi Tecnici, Dipartimento Difesa del Suolo - Servizio Geologico d'Italia, S.EL.CA., Firenze, 267-272

Dale, C.; Burton, K.; Pearson, D.; Gannoun, A.; Alard, O.; Argles, T. & Parkinson, I. (2009), 'Highly siderophile element behaviour accompanying subduction of oceanic crust: whole rock and mineral-scale insights from a high-pressure terrain', *Geochimica et Cosmochimica Acta* **73**(5), 1394–1416.

Dale, C.; Gannoun, A.; Burton, K.; Argles, T. & Parkinson, I. (2007), 'Rhenium–osmium isotope and elemental behaviour during subduction of oceanic crust and the implications for mantle recycling', *Earth and Planetary Science Letters* **253**(1), 211–225.

Dale, C. W.; Macpherson, C. G.; Pearson, D. G.; Hammond, S. J. & Arculus, R. J. (2012), 'Inter-element fractionation of highly siderophile elements in the Tonga Arc due to flux melting of a depleted source', *Geochimica et Cosmochimica Acta* **89**, 202–225.

Danyushevsky, L.; Robinson, P.; Gilbert, S.; Norman, M.; Large, R.; McGoldrick, P. & Shelley, M. (2011), 'Routine quantitative multi-element analysis of sulphide minerals by laser ablation ICP-MS: Standard development and consideration of matrix effects', *Geochemistry: Exploration, Environment, Analysis* **11**(1), 51–60.

Dare, S. A.; Barnes, S.-J. & Beaudoin, G. (2012), 'Variation in trace element content of magnetite crystallized from a fractionating sulfide liquid, Sudbury, Canada: implications for provenance discrimination', *Geochimica et Cosmochimica Acta* **88**, 27–50.

Dauphas, N.; Craddock, P. R.; Asimow, P. D.; Bennett, V. C.; Nutman, A. P. & Ohnenstetter, D. (2009), 'Iron isotopes may reveal the redox conditions of mantle melting from Archean to Present', *Earth and Planetary Science Letters* **288**(1), 255–267.

De Hoog, J. C.; Hattori, K. & Jung, H. (2014), 'Titanium-and water-rich metamorphic olivine in high-pressure serpentinites from the Voltri Massif (Ligurian Alps, Italy): evidence for deep subduction of high-field strength and fluid-mobile elements', *Contributions to Mineralogy and Petrology* **167**(3), 1–15.

Debret, B.; Andreani, M.; Mucoz, M.; Bolfan-Casanova, N.; Carlut, J.; Nicollet, C.; Schwartz, S. & Trcera, N. (2014), 'Evolution of Fe redox state in serpentine during subduction', *Earth and Planetary Science Letters* **400**, 206–218.

Debret, B.; Bolfan-Casanova, N.; Padrón-Navarta, J. A.; Martin-Hernandez, F.; Andreani, M.; Garrido, C. J.; Sánchez-Vizcaino, V. L.; Gómez-Pugnaire, M. T.; Mucoz, M. & Trcera, N. (2015), 'Redox state of iron during high-pressure serpentinite dehydration', *Contributions to Mineralogy and Petrology* **169**(4), 1–18.

Debret, B.; Koga, K. T.; Nicollet, C.; Andreani, M. & Schwartz, S. (2014), 'F, Cl and S input via serpentinite in subduction zones: implications for the nature of the fluid released at depth', *Terra Nova* 26(2), 96–101.

Debret, B.; Millet, M.-A.; Pons, M.-L.; Bouilhol, P.; Inglis, E. & Williams, H. (2016), 'Isotopic evidence for iron mobility during subduction', *Geology* **44**(3), 215–218.

Debret, B. & Sverjensky, D. (2017), 'Highly oxidising fluids generated during serpentinite breakdown in subduction zones', *Scientific reports* 7.

Deer, W. A.; Howie, R. A.; Zussman, J. & others (1992), *An introduction to the rock-forming minerals*, Vol. 696, Longman London.

Deer, W.; Howie, R. & Zussman, J. (1963), 'Rock forming minerals, Sheet Silicates, v. 3', London, Longman Green and Co., 270p.

Delacour, A.; Früh-Green, G. L.; Bernasconi, S. M. & Kelley, D. S. (2008), 'Sulfur in peridotites and gabbros at Lost City (30 N, MAR): Implications for hydrothermal alteration and microbial activity during serpentinization', *Geochimica et Cosmochimica Acta* **72**(20), 5090–5110.

Deschamps, F.; Godard, M.; Guillot, S. & Hattori, K. (2013), 'Geochemistry of subduction zone serpentinites: A review', *Lithos* **178**, 96–127.

Deschamps, F.; Guillot, S.; Godard, M.; Andreani, M. & Hattori, K. (2011), 'Serpentinites act as sponges for fluid-mobile elements in abyssal and subduction zone environments', *Terra Nova* **23**(3), 171–178.

Dewey, J. F.; Pitman, W. C.; Ryan, W. B. & Bonnin, J. (1973), 'Plate tectonics and the evolution of the Alpine system', *Geological society of America bulletin* **84**(10), 3137–3180.

Dick, H. J. & Bullen, T. (1984), 'Chromian spinel as a petrogenetic indicator in abyssal and alpine-type peridotites and spatially associated lavas', *Contributions to mineralogy and petrology* **86**(1), 54–76.

Donovan, J.; Kremser, D. & Fournelle, J. (2012), 'Probe for EPMA: acquisition, automation and analysis', *Probe Software, Inc., Eugene, Oregon*.

Draper, D. S. & Green, T. H. (1997), 'P–T phase relations of silicic, alkaline, aluminous mantle-xenolith glasses under anhydrous and C–O–H fluid-saturated conditions', *Journal of Petrology* **38**(9), 1187–1224.

E

El Gadarri, M. (1995.), 'Les mineralisations sulfurees associees aux ophiolites de Corse : un ex-emple de systeme hydrothermal de sous-plancher oceanique.', *Mineralogie. Universite d'Orleans*.

Ernst, W. & Dal Piaz, G. (1978), 'Mineral parageneses of eclogitic rocks and related mafic schists of the Piemonte ophiolite nappe, Breuil-St. Jacques area, Italian Western Alps', *American Mineralogist* **63**(7-8), 621–640.

Escher, A. & Beaumont, C. (1997), 'Formation, burial and exhumation of basement nappes at crustal scale: a geometric model based on the Western Swiss-Italian Alps', *Journal of Structural Geology* **19**(7), 955–974.

Evans, B. W. (2008), 'Control of the products of serpentinization by the Fe2+ Mg-1 exchange potential of olivine and orthopyroxene', *Journal of Petrology* **49**(10), 1873–1887.

Evans, B. W. (2004), 'The serpentinite multisystem revisited: chrysotile is metastable', *International Geology Review* **46**(6), 479–506.

Evans, B. W.; Darby Dyar, M. & Kuehner, S. M. (2012), 'Implications of ferrous and ferric iron in antigorite', *American Mineralogist* **97**(1), 184–196.

Evans, B. W. & Frost, B. R. (1975), 'Chrome-spinel in progressive metamorphism—a preliminary analysis', *Geochimica et Cosmochimica Acta* **39**(6-7), 959–972.

Evans, B. W. & Kuehner, S. M. (2011), 'A nickel-iron analogue of balangeroite and gageite (Sasaguri, Kyushu, Japan)', *European Journal of Mineralogy* **23**(5), 717–720.

Evans, K. (2012), 'The redox budget of subduction zones', *Earth-Science Reviews* **113**(1), 11–32.

Evans, K. (2006), 'Redox decoupling and redox budgets: Conceptual tools for the study of earth systems', *Geology* **34**(6), 489–492.

Evans, K.; Elburg, M. & Kamenetsky, V. (2012), 'Oxidation state of subarc mantle', *Geology* **40**(9), 783–786.

Evans, K. & Powell, R. (2015), 'The effect of subduction on the sulphur, carbon and redox budget of lithospheric mantle', *Journal of Metamorphic Geology* **33**(6), 649–670.

Evans, K.; Reddy, S.; Tomkins, A., Crossley, R. & Frost, B. (2017), 'Effects of geodynamic setting on the redox state of fluids released by subducted mantle lithosphere', *Lithos*, 278, 26-42.

Evans, K.; Tomkins, A.; Cliff, J. & Fiorentini, M. (2014), 'Insights into subduction zone sulfur recycling from isotopic analysis of eclogite-hosted sulfides', *Chemical Geology* **365**, 1–19.

Evans, K. & Powell, R. (2015), 'The effect of subduction on sulfur, carbon, and redox budget contents of lithospheric mantle.', *Journal of Metamorphic Geology*.

F

Fanlo, I.; Gervilla, F.; Colás, V. & Subias, I. (2015), 'Zn-, Mn-and Co-rich chromian spinels from the Bou-Azzer mining district (Morocco): Constraints on their relationship with the mineralizing process', *Ore Geology Reviews* **71**, 82–98.

Farquhar, J.; Bao, H. & Thiemens, M. (2000), 'Atmospheric influence of Earth's earliest sulfur cycle', *Science* **289**(5480), 756–758.

Farquhar, J.; Cliff, J.; Zerkle, A. L.; Kamyshny, A.; Poulton, S. W.; Claire, M.; Adams, D. & Harms, B. (2013), 'Pathways for Neoarchean pyrite formation constrained by mass-independent sulfur isotopes', *Proceedings of the National Academy of Sciences* **110**(44), 17638–17643.

Faure, M. & Malavieille, J. (1981), 'Etude structurale d'un cisallement ductile: le charriage ophiolitique Corse dans la région de Bastia.', *Bulletin de la Societe Geologique de France, 23*.

Ferrando, S.; Frezzotti, M.; Dallai, L. & Compagnoni, R. (2005), 'Multiphase solid inclusions in UHP rocks (Su-Lu, China): remnants of supercritical silicate-rich aqueous fluids released during continental subduction', *Chemical Geology* **223**(1), 68–81.

Ferrando, S.; Frezzotti, M. L.; Orione, P.; Conte, R. C. & Compagnoni, R. (2010), 'Late-Alpine rodingitization in the Bellecombe meta-ophiolites (Aosta Valley, Italian Western Alps): evidence from mineral assemblages and serpentinization-derived H2-bearing brine', *International Geology Review* **52**(10-12), 1220–1243.

Fischer- Gödde, M.; Becker, H. & Wombacher, F. (2010), 'Rhodium, gold and other highly siderophile element abundances in chondritic meteorites', *Geochimica et Cosmochimica Acta* **74**(1), 356–379.

Fitzherbert, J.; Clarke, G.; Marmo, B. & Powell, R. (2004), 'The origin and P–T evolution of peridotites and serpentinites of NE New Caledonia: prograde interaction between continental margin and the mantle wedge', *Journal of Metamorphic Geology* **22**(4), 327–344.

Fleet, M. (1981), 'The structure of magnetite', *Acta Crystallographica Section B: Structural Crystallography and Crystal Chemistry* **37**(4), 917–920.

Fleet, M.; Crocket, J.; Liu, M. & Stone, W. (1999), 'Laboratory partitioning of platinum-group elements (PGE) and gold with application to magmatic sulfide–PGE deposits', *Lithos* **47**(1), 127–142.

Fonseca, R. O.; Campbell, I. H.; O'Neill, H. S. C. & Allen, C. M. (2009), 'Solubility of Pt in sulphide mattes: implications for the genesis of PGE-rich horizons in layered intrusions', *Geochimica et Cosmochimica Acta* **73**(19), 5764–5777.

Fonseca, R. O.; Laurenz, V.; Mallmann, G.; Luguet, A.; Hoehne, N. & Jochum, K. P. (2012), 'New constraints on the genesis and long-term stability of Os-rich alloys in the Earth's mantle', *Geochimica et Cosmochimica Acta* **87**, 227–242.

Fonseca, R. O.; Mallmann, G.; O'Neill, H. S. C. & Campbell, I. H. (2007), 'How chalcophile is rhenium? An experimental study of the solubility of Re in sulphide mattes', *Earth and Planetary Science Letters* **260**(3), 537–548.

Forster, M.; Lister, G.; Compagnoni, R.; Giles, D.; Hills, Q.; Betts, P.; Beltrando, M. & Tamagno, E. (2004), 'Mapping of oceanic crust with HP to UHP metamorphism: the Lago di Cignana Unit (Western Alps)', *Mapping geology in Italy*, 279–286.

Fournier, M.; Jolivet, L.; Goffé, B. & Dubois, R. (1991), 'Alpine Corsica metamorphic core complex', *Tectonics* **10**(6), 1173–1186.

Foustoukos, D. I.; Bizimis, M.; Frisby, C. & Shirey, S. B. (2015), 'Redox controls on Ni–Fe–PGE mineralization and Re/Os fractionation during serpentinization of abyssal peridotite', *Geochimica et Cosmochimica Acta* **150**, 11–25.

Foustoukos, D. I.; Savov, I. P. & Janecky, D. R. (2008), 'Chemical and isotopic constraints on water/rock interactions at the Lost City hydrothermal field, 30 N Mid-Atlantic Ridge', *Geochimica et Cosmochimica Acta* **72**(22), 5457–5474.

Frezzotti, M.; Selverstone, J.; Sharp, Z. & Compagnoni, R. (2011), 'Carbonate dissolution during subduction revealed by diamond-bearing rocks from the Alps', *Nature Geoscience* **4**(10), 703–706.

Frost, B. R. (1991), 'Stability of oxide minerals in metamorphic rocks', *Reviews in Mineralogy and Geochemistry* **25**(1), 469–488.

Frost, B. R. (1985), 'On the stability of sulfides, oxides, and native metals in serpentinite', *Journal of Petrology* **26**(1), 31–63.

Frost, B. R. & Ballhaus, C. (1998), 'Comment on" Constraints on the origin of the oxidation state of mantle overlying subduction zones: an example from Simcoe, Washington, USA" by AD Brandon and DS Draper', *Geochimica et Cosmochimica Acta* **62**, 329–332.

Frost, B. R. & Beard, J. S. (2007), 'On silica activity and serpentinization', *Journal of Petrology* **48**(7), 1351–1368.

Frost, B. R.; Evans, K. A.; Swapp, S. M.; Beard, J. S. & Mothersole, F. E. (2013), 'The process of serpentinization in dunite from New Caledonia', *Lithos* **178**, 24–39.

G

Gahlan, H. A. & Arai, S. (2007), 'Genesis of peculiarly zoned Co, Zn and Mn-rich chromian spinel in serpentinite of Bou-Azzer ophiolite, Anti-Atlas, Morocco', *Journal of Mineralogical and Petrological Sciences* **102**(2), 69–85.

Galvez, M. E.; Martinez, I.; Beyssac, O.; Benzerara, K.; Agrinier, P. & Assayag, N. (2013), 'Metasomatism and graphite formation at a lithological interface in Malaspina (Alpine Corsica, France)', *Contributions to Mineralogy and Petrology* **166**(6), 1687–1708.

Gannoun, A.; Burton, K. W.; Day, J. M.; Harvey, J.; Schiano, P. & Parkinson, I. (2016), 'Highly siderophile element and Os isotope systematics of volcanic rocks at divergent and convergent plate boundaries and in intraplate settings', *Reviews in Mineralogy and Geochemistry* **81**(1), 651–724.

Gargiulo, M.; Bjerg, E. & Mogessie, A. (2013), 'Spinel group minerals in metamorphosed ultramafic rocks from Rio de Las Tunas belt, Central Andes, Argentina', *Geologica Acta* **11**(2), 133–148.

Gao, J., John, T., Klemd, R., & Xiong, X. (2007). Mobilization of Ti–Nb–Ta during subduction: Evidence from rutile-bearing dehydration segregations and veins hosted in eclogite, Tianshan, NW China. *Geochimica et Cosmochimica Acta*, 71(20), 4974–4996.

Gasco, I., Gattiglio, M., & Borghi, A. (2013). Review of metamorphic and kinematic data from Internal Crystalline Massifs (Western Alps): PTt paths and exhumation history. Journal of Geodynamics, 63, 1-19.

Gervilla, F.; Padrón-Navarta, J.; Kerestedjian, T.; Sergeeva, I.; González-Jiménez, J. & Fanlo, I. (2012), 'Formation of ferrian chromite in podiform chromitites from the Golyamo Kamenyane serpentinite, Eastern Rhodopes, SE Bulgaria: a two-stage process', *Contributions to Mineralogy and Petrology* **164**(4), 643–657.

Gervilla, F.; Proenza, J.; Frei, R.; González-Jiménez, J.; Garrido, C.; Melgarejo, J.; Meibom, A.; Diaz-Martinez, R. & Lavaut, W. (2005), 'Distribution of platinum-group elements and Os isotopes in chromite ores from Mayari-Baracoa Ophiolitic Belt (eastern Cuba)', *Contributions to Mineralogy and Petrology* **150**(6), 589–607.

Giacometti, F.; Evans, K. A.; Rebay, G.; Cliff, J.; Tomkins, A. G.; Rossetti, P.; Vaggelli, G. & Adams, D. T. (2014), 'Sulfur isotope evolution in sulfide ores from Western Alps: Assessing the influence of subduction-related metamorphism', *Geochemistry, Geophysics, Geosystems* **15**(10), 3808–3829.

Gieré, R. (1993). Transport and deposition of REE in H2S-rich fluids: Evidence from accessory mineral assemblages. Chemical Geology, 717, 110(1–3), 251–268.

Gill, R. (2010), *Igneous rocks and processes: a practical guide*, John Wiley & Sons.

González-Jiménez, J. M.; Griffin, W. L.; Gervilla, F.; Kerestedjian, T. N.; O'Reilly, S. Y.; Proenza, J. A.; Pearson, N. J. & Sergeeva, I. (2012), 'Metamorphism disturbs the Re-Os signatures of platinum-group minerals in ophiolite chromitites', *Geology* **40**(7), 659–662.

Goodge, J. W. & Holdaway, M. J. (1995), 'Rock-buffered fluid evolution of metapelites and quartzites in the Picuris Range, northern New Mexico', *Journal of Petrology* **36**(5), 1229–1250.

Gouzu, C.; Itaya, T.; Hyodo, H. & Matsuda, T. (2006), 'Excess 40 Ar-free phengite in ultrahigh-pressure metamorphic rocks from the Lago di Cignana area, Western Alps', *Lithos* **92**(3), 418–430.

Grieco, G. & Merlini, A. (2012), 'Chromite alteration processes within Vourinos ophiolite', *International Journal of Earth Sciences* **101**(6), 1523–1533.

Grinenko, V.; Dmitriev, L.; Migdisov, A. & Sharaskin, A. Y. (1975), 'Sulfur contents and isotope compositions for igneous and metamorphic rocks from mid-ocean ridges', *Geochem Int* **12**(1), 132.

Groppo, C.; Beltrando, M. & Compagnoni, R. (2009), 'The P–T path of the ultra-high pressure Lago Di Cignana and adjoining high-pressure meta-ophiolitic units: insights into the evolution of the subducting Tethyan slab', *Journal of Metamorphic Geology* **27**(3), 207–231.

Groppo, C. & Compagnoni, R. (2007), 'Metamorphic veins from the serpentinites of the Piemonte Zone, western Alps, Italy: a review', *Periodico di Mineralogia* **76**, 127–153.

Guillot, S.; Hattori, K. H. & de Sigoyer, J. (2000), 'Mantle wedge serpentinization and exhumation of eclogites: insights from eastern Ladakh, northwest Himalaya', *Geology* **28**(3), 199–202.

H

Hack, A. C. & Thompson, A. B. (2010), 'Density and viscosity of hydrous magmas and related fluids and their role in subduction zone processes', *Journal of Petrology*, egq048.

Hanley, J. J.; Pettke, T.; Mungall, J. E. & Spooner, E. T. (2005), 'The solubility of platinum and gold in NaCl brines at 1.5 kbar, 600 to 800 C: a laser ablation ICP-MS pilot study of synthetic fluid inclusions', *Geochimica et Cosmochimica Acta* **69**(10), 2593–2611.

Harris, L. (1985), 'Progressive and polyphase deformation of the schistes lustrés in Cap Corse, Alpine Corsica', *Journal of Structural Geology* **7**(6), 637–650.
Hart, S. R. & Ravizza, G. E. (1996), 'Os partitioning between phases in lherzolite and basalt', *Earth Processes: Reading the Isotopic Code*, 123–134.

Hart, S. R. & Ravizza, G. E. (1996), 'Os partitioning between phases in lherzolite and basalt', Earth Processes: Reading the Isotopic Code, 123–134.

Hattori, K. H. & Guillot, S. (2007), 'Geochemical character of serpentinites associated with high-to ultrahigh-pressure metamorphic rocks in the Alps, Cuba, and the Himalayas: Recycling of elements in subduction zones', *Geochemistry, Geophysics, Geosystems* **8**(9).

Herwartz, D.; Münker, C.; Scherer, E. E.; Nagel, T. J.; Pleuger, J. & Froitzheim, N. (2008), Lu-Hf garnet geochronology of eclogites from the Balma Unit (Pennine Alps): implications for Alpine paleotectonic reconstructions'Orogenic Processes in the Alpine Collision Zone', Springer, , pp. S173–S189.

I

Irvine, T. (1965), 'Chromian spinel as a petrogenetic indicator: Part 1. Theory', *Canadian Journal of Earth Sciences* **2**(6), 648–672.

Irvine, T. (1967), 'Chromian spinel as a petrogenetic indicator: Part 2. Petrologic applications', *Canadian Journal of Earth Sciences* **4**(1), 71–103.

Ishihara, S. & Sasaki, A. (1989), 'Sulfur isotopic ratios of the magnetite-series and ilmenite-series granitoids of the Sierra Nevada batholith—a reconnaissance study', *Geology* **17**(9), 788–791.

J

Jégo, S. & Dasgupta, R. (2013), 'Fluid-present melting of sulfide-bearing ocean-crust: Experimental constraints on the transport of sulfur from subducting slab to mantle wedge', *Geochimica et Cosmochimica Acta* **110**, 106–134.

John, T.; Gussone, N.; Podladchikov, Y. Y.; Bebout, G. E.; Dohmen, R.; Halama, R.; Klemd, R.; Magna, T. & Seitz, H.-M. (2012), 'Volcanic arcs fed by rapid pulsed fluid flow through subducting slabs', *Nature Geoscience* **5**(7), 489–492.

Jolivet, L.; Daniel, J.-M. & Fournier, M. (1991), 'Geometry and kinematics of extension in Alpine Corsica', *Earth and Planetary Science Letters* **104**(2), 278–291.

Jolivet, L.; Dubois, R.; Fournier, M.; Goffé, B.; Michard, A. & Jourdan, C. (1990), 'Ductile extension in alpine Corsica', *Geology* **18**(10), 1007–1010.

Jolivet, L.; Faccenna, C.; Goffé, B.; Mattei, M.; Rossetti, F.; Brunet, C.; Storti, F.; Funiciello, R.; Cadet, J. P.; d'Agostino, N. & others (1998), 'Midcrustal shear zones in postorogenic extension: example from the northern Tyrrhenian Sea', *Journal of Geophysical Research: Solid Earth* **103**(B6), 12123–12160.

K

Kamenetsky, V. S.; Crawford, A. J. & Meffre, S. (2001), 'Factors controlling chemistry of magmatic spinel: an empirical study of associated olivine, Cr-spinel and melt inclusions from primitive rocks', *Journal of Petrology* **42**(4), 655–671.

Kampschulte, A. & Strauss, H. (2004), 'The sulfur isotopic evolution of Phanerozoic seawater based on the analysis of structurally substituted sulfate in carbonates', *Chemical Geology* **204**(3), 255–286.

Kelley, D. S.; Karson, J. A.; Früh-Green, G. L.; Yoerger, D. R.; Shank, T. M.; Butterfield, D. A.; Hayes, J. M.; Schrenk, M. O.; Olson, E. J.; Proskurowski, G. & others (2005), 'A serpentinite-hosted ecosystem: the Lost City hydrothermal field', *Science* **307**(5714), 1428–1434.

Kelley, K. A. & Cottrell, E. (2009), 'Water and the oxidation state of subduction zone magmas', *Science* **325**(5940), 605–607.

Kerrick, D. (2002), 'Serpentinite seduction', *Science* **298**(5597), 1344–1345.

Kerrick, D. & Connolly, J. (1998), 'Subduction of ophicarbonates and recycling of CO2 and H2O', *Geology* **26**(4), 375–378.

Khalil, K.I. & El-Makky, A.M., (2009), Alteration mechanisms of chromian-spinel during serpentinization at Wadi Sifein area, Eastern Desert, Egypt, *Resource Geology,* **59**(2), 194–211.

Kimball, K. L. (1990), 'Effects of hydrothermal alteration on the compositions of chromian spinels', *Contributions to Mineralogy and Petrology* **105**(3), 337–346.

Kodolányi, J. & Pettke, T. (2011), 'Loss of trace elements from serpentinites during fluid-assisted transformation of chrysotile to antigorite—An example from Guatemala', *Chemical Geology* **284**(3), 351–362.

Kushiro, I. (1972), 'Effect of water on the composition of magmas formed at high pressures', *Journal of Petrology* **13**(2), 311–334.

L

Lacombe, O. & Jolivet, L. (2005), 'Structural and kinematic relationships between Corsica and the Pyrenees-Provence domain at the time of the Pyrenean orogeny', *Tectonics* **24**(1).

Lafay, R.; Deschamps, F.; Schwartz, S.; Guillot, S.; Godard, M.; Debret, B. & Nicollet, C. (2013), 'High-pressure serpentinites, a trap-and-release system controlled by metamorphic conditions: Example from the Piedmont zone of the western Alps', *Chemical Geology* **343**, 38–54.

LaFlamme, C.; Martin, L.; Jeon, H.; Reddy, Steven, M.; Selvaraja, V.; Caruso, S.; Bui; Hao, T.; Roberts, M. P.; Voute, F.; Hagemann, S.; Wacey, D.; Wing, B.;

Fiorentini, M. & Kilburn, M. R. (2016), 'In situ multiple sulfur isotope analysis by SIMS of pyrrhotite, pentlandite and chalcopyrite to refine magmatic ore genetic models', *Chemical Geology* **444**, 1-15.

Lahondère, D. (1996, p. 294), 'Les schistes bleus et les éclogites a lawsonite des unités continentales et océaniques de la Corse alpine: nouvelles données pétrologiques et structurales', PhD thesis, Documents du BRGM 240, Orléans.

Lahondère, J.; Conchon, O.; Lahondıre, D.; Dominici, R. & Vautrelle, C. (1983), 'Carte géol', *France (1/50000), feuille Bastia (1104). Orléans: BRGM*.

Lahondère, J.; Lahondıre, D.; Lluch, D.; Ohnenstetter, M.; Dominici, R. & Vautralle, C. (1992), 'Carte géologique de la France a 1/50000', *Luri, BRGM*.

Lahondère, D. & Guerrot, C. (1997), 'Datation Nd-Sm du métamorphisme éclogitique en Corse alpine: un argument pour l'existence, au Crétacé supérieur, d'une zone de subduction active localisée le long du block corse-sarde.', *Géologie de la France* **3**, 3-11.

Lahondère, J.; Conchon, O.; Lahondère, D.; Dominici, R. & Vautrelle, C. (1994, 67 pp.), 'Carte géol.France (1/50000), feuille Vescovato (1107).', *Orléans: BRGM.*.

Lapen, T. J.; Johnson, C. M.; Baumgartner, L. P.; Mahlen, N. J.; Beard, B. L. & Amato, J. M. (2003), 'Burial rates during prograde metamorphism of an ultra-high-pressure terrane: an example from Lago di Cignana, western Alps, Italy', *Earth and Planetary Science Letters* **215**(1), 57–72.

Lécuyer, C. & Ricard, Y. (1999), 'Long-term fluxes and budget of ferric iron: implication for the redox states of the Earth's mantle and atmosphere', *Earth and Planetary Science Letters* **165**(2), 197–211.

Lee, C.-t. A.; Leeman, W. P.; Canil, D. & Li, Z.-X. A. (2005), 'Similar V/Sc systematics in MORB and arc basalts: implications for the oxygen fugacities of their mantle source regions', *Journal of Petrology* **46**(11), 2313–2336.

Lee, C.-T. A.; Luffi, P.; Le Roux, V.; Dasgupta, R.; Albaréde, F. & Leeman, W. P. (2010), 'The redox state of arc mantle using Zn/Fe systematics', *Nature* **468**(7324), 681–685.

Li, X.-P.; Rahn, M. & Bucher, K. (2004), 'Serpentinites of the Zermatt-Saas ophiolite complex and their texture evolution', *Journal of Metamorphic Geology* **22**(3), 159–177.

Li, Y. & Liu, J. (2006), 'Calculation of sulfur isotope fractionation in sulfides', *Geochimica et Cosmochimica Acta* **70**(7), 1789–1795.

Lindsley, D. H. & Banerjee, S. (1991), 'Oxide minerals: petrologic and magnetic significance', 509.

Liu, W.; Borg, S. J.; Testemale, D.; Etschmann, B.; Hazemann, J.-L. & Brugger, J. (2011), 'Speciation and thermodynamic properties for cobalt chloride complexes in hydrothermal fluids at 35–440 C and 600bar: an in-situ XAS study', *Geochimica et Cosmochimica Acta* **75**(5), 1227–1248.

Lorand, J.-P.; Alard, O. & Luguet, A. (2010), 'Platinum-group element micronuggets and refertilization process in Lherz orogenic peridotite (northeastern Pyrenees, France)', *Earth and Planetary Science Letters* **289**(1), 298–310.

Lorand, J.-P.; Luguet, A.; Alard, O.; Bezos, A. & Meisel, T. (2008), 'Abundance and distribution of platinum-group elements in orogenic lherzolites; a case study in a Fontete Rouge lherzolite (French Pyrénées)', *Chemical Geology* **248**(3), 174–194.

López Sánchez-Vizcaino, V.; Gómez-Pugnaire, M. T.; Garrido, C. J.; Padrón-Navarta, J. A. & Mellini, M. (2009), 'Breakdown mechanisms of titanclinohumite in antigorite serpentinite (Cerro del Almirez massif, S. Spain): a petrological and TEM study', *Lithos* **107**(3), 216–226.

López Sánchez-Vizcaino, V.; Trommsdorff, V.; Gómez-Pugnaire, M.; Garrido, C.; Müntener, O. & Connolly, J. (2005), 'Petrology of titanian clinohumite and olivine at the high-pressure breakdown of antigorite serpentinite to chlorite harzburgite (Almirez Massif, S. Spain)', *Contributions to Mineralogy and Petrology* **149**(6), 627–646.

Loucks, R. R. & Mavrogenes, J. A. (1999), 'Gold solubility in supercritical hydrothermal brines measured in synthetic fluid inclusions', *Science* **284**(5423), 2159–2163.

Luguet, A.; Lorand, J.-P. & Seyler, M. (2003), 'Sulfide petrology and highly siderophile element geochemistry of abyssal peridotites: A coupled study of samples from the Kane Fracture Zone (45 W 23 20N, MARK area, Atlantic Ocean)', Geochimica et Cosmochimica Acta 67(8), 1553–1570.

Luguet, A.; Lorand, J.-P.; Alard, O. & Cottin, J.-Y. (2004), 'A multi-technique study of platinum group element systematic in some Ligurian ophiolitic peridotites, Italy', *Chemical Geology* **208**(1), 175–194.

M

MacNamara, J. & Thode, H. (1950), 'Comparison of the isotopic constitution of terrestrial and meteoritic sulfur', *Physical Review* **78**(3), 307.

Magott, R.; Fabbri, O. & Fournier, M. (2016), 'Subduction zone intermediate-depth seismicity: Insights from the structural analysis of Alpine high-pressure ophiolite-hosted pseudotachylyte (Corsica, France)', *Journal of Structural Geology* **87**, 95–114.

Mallmann, G. & O'Neill, H. S. C. (2009), 'The crystal/melt partitioning of V during mantle melting as a function of oxygen fugacity compared with some other elements (Al, P, Ca, Sc, Ti, Cr, Fe, Ga, Y, Zr and Nb)', *Journal of Petrology* **50**(9), 1765–1794.

Mallmann, G. & O'Neill, H. S. C. (2007), 'The effect of oxygen fugacity on the partitioning of Re between crystals and silicate melt during mantle melting', *Geochimica et Cosmochimica Acta* **71**(11), 2837–2857.

Malvoisin, B.; Chopin, C.; Brunet, F. & Galvez, M. E. (2012), 'Low-temperature wollastonite formed by carbonate reduction: a marker of serpentinite redox conditions', *Journal of Petrology* **53**(1), 159–176.

Manatschal, G. & Müntener, O. (2009), 'A type sequence across an ancient magma-poor ocean–continent transition: the example of the western Alpine Tethys ophiolites', *Tectonophysics* **473**(1), 4–19.

Manning, C. E. (2004), 'The chemistry of subduction-zone fluids', *Earth and Planetary Science Letters* **223**(1), 1–16.

Marini, L.; Moretti, R. & Accornero, M. (2011), 'Sulfur isotopes in magmatic-hydrothermal systems, melts, and magmas', *Reviews in Mineralogy and Geochemistry* **73**(1), 423–492.

Marschall, H. R. & Shimizu, N. (2012), 'Sulfur Isotopes in High-Pressure Rocks', *Mineralogical Magazine* **76(6)**(6), 2070.

Marschall, H. R. & Schumacher, J. C. (2012), 'Arc magmas sourced from mélange diapirs in subduction zones', *Nature Geoscience* **5**(12), 862–867.

Martin, S.; Rebay, G.; Kienast, J.-R. & Mével, C. (2008), 'An eclogitised oceanic palaeo-hydrothermal field from the St. Marcel Valley (Italian Western Alps)', *Ofioliti* **33**(1), 49–63.

Mattauer, M.; Faure, M. & Malavieille, J. (1981), 'Transverse lineation and large-scale structures related to Alpine obduction in Corsica', *Journal of Structural Geology* **3**(4), 401–409.

Mattauer, M.; Proust, F. & Etchecopar, A. (1977), 'Lineation" a" et mecanisme de cisaillement simple lie au chevauchement de la nappe des schistes lustres en Corse', *Bulletin de la Société Géologique de France* **7**(4), 841–847.

Mayer, A.; Abouchami, W. & Dal Piaz, G. (1999), 'Eocene Sm-Nd age for the eclogitic metamorphism of the Zermatt-Saas ophiolite in Ayas Valley, western Alps', *Eur Union Geosci* **10**, 809.

McClure, D. S. (1957), 'The distribution of transition metal cations in spinels', *Journal of Physics and Chemistry of Solids* **3**(3-4), 311–317.

McCollom, T. M. & Bach, W. (2009), 'Thermodynamic constraints on hydrogen generation during serpentinization of ultramafic rocks', *Geochimica et Cosmochimica Acta* **73**(3), 856–875.

McDonough, W. F., & Sun, S. S. (1995). The composition of the Earth. *Chemical Geology*, 120(3-4), 223-253.

McInnes, B. I.; McBride, J. S.; Evans, N. J.; Lambert, D. D. & Andrew, A. S. (1999), 'Osmium isotope constraints on ore metal recycling in subduction zones', *Science* **286**(5439), 512–516.

Mellini, M.; Rumori, C. & Viti, C. (2005), 'Hydrothermally reset magmatic spinels in retrograde serpentinites: formation of "ferritchromit" rims and chlorite aureoles', *Contributions to Mineralogy and Petrology* **149**(3), 266–275.

Meresse, F.; Lagabrielle, Y.; Malavieille, J. & Ildefonse, B. (2012), 'A fossil Ocean–Continent Transition of the Mesozoic Tethys preserved in the Schistes Lustrés nappe of northern Corsica', *Tectonophysics* **579**, 4–16.

Merlini, A.; Grieco, G. & Diella, V. (2009), 'Ferritchromite and chromian-chlorite formation in mélange-hosted Kalkan chromitite (Southern Urals, Russia)', *American Mineralogist* **94**(10), 1459–1467.

Mével, C. (2003), 'Serpentinization of abyssal peridotites at mid-ocean ridges', *Comptes Rendus Geoscience* **335**(10), 825–852.

Miller, D. P.; Marschall, H. R. & Schumacher, J. C. (2009), 'Metasomatic formation and petrology of blueschist-facies hybrid rocks from Syros (Greece): implications for reactions at the slab–mantle interface', *Lithos* **107**(1), 53–67.

Mitchell, R. H. & Keays, R. R. (1981), 'Abundance and distribution of gold, palladium and iridium in some spinel and garnet lherzolites: implications for the nature and origin of precious metal-rich intergranular components in the upper mantle', *Geochimica et Cosmochimica Acta* **45**(12), 2425–2442.

Molli, G. (2008), 'Northern Apennine–Corsica orogenic system: an updated overview', *Geological Society, London, Special Publications* **298**(1), 413–442.

Molli, G. & Malavieille, J. (2011), 'Orogenic processes and the Corsica/Apennines geodynamic evolution: insights from Taiwan', *International Journal of Earth Sciences* **100**(5), 1207–1224.

Molli, G.; Tribuzio, R. & Marquer, D. (2006), 'Deformation and metamorphism at the eastern border of the Tenda Massif (NE Corsica): a record of subduction and exhumation of continental crust', *Journal of Structural Geology* **28**(10), 1748–1766.

Mukherjee, R.; Mondal, S. K.; Rosing, M. T. & Frei, R. (2010), 'Compositional variations in the Mesoarchean chromites of the Nuggihalli schist belt, Western Dharwar Craton (India): potential parental melts and implications for tectonic setting', *Contributions to Mineralogy and Petrology* **160**(6), 865–885.

Mungall, J. E. (2002), 'Roasting the mantle: slab melting and the genesis of major Au and Au-rich Cu deposits', *Geology* **30**(10), 915–918.

Mungall, J. E. & Brenan, J. M. (2014), 'Partitioning of platinum-group elements and Au between sulfide liquid and basalt and the origins of mantle-crust fractionation of the chalcophile elements', Geochimica et Cosmochimica Acta 125, 265–289.

Müntener, O. & Hermann, J. (1994), 'Titanian andradite in a metapyroxenite layer from the Malenco ultramafics (Italy): implications for Ti-mobility and low oxygen fugacity', *Contributions to Mineralogy and Petrology* **116**(1-2), 156–168.

Müntener, O.; Manatschal, G.; Desmurs, L. & Pettke, T. (2009), 'Plagioclase peridotites in ocean–continent transitions: refertilized mantle domains generated by melt stagnation in the shallow mantle lithosphere', *Journal of Petrology*, egp087.

Mysen, B. O.; Virgo, D.; Neumann, E.-R. & Seifert, F. A. (1985), 'Redox equilibria and the structural states of ferric and ferrous iron in melts in the system CaO-MgO-Al 2 O 3-SiO 2-Fe-O; relationships between redox equilibria, melt structure and liquidus phase equilibria', *American Mineralogist* **70**(3-4), 317–331.

N

Nadeau, O.; Stix, J. & Williams-Jones, A. E. (2013), 'The behavior of Cu, Zn and Pb during magmatic–hydrothermal activity at Merapi volcano, Indonesia', *Chemical Geology* **342**, 167–179.

Nadoll, P.; Angerer, T.; Mauk, J. L.; French, D. & Walshe, J. (2014), 'The chemistry of hydrothermal magnetite: a review', *Ore Geology Reviews* **61**, 1–32.

Nadoll, P. & Koenig, A. E. (2011), 'LA-ICP-MS of magnetite: methods and reference materials', *Journal of Analytical Atomic Spectrometry* **26**(9), 1872–1877.

Nebel, O.; Arculus, R.; Sossi, P.; Jenner, F. & Whan, T. (2013), 'Iron isotopic evidence for convective resurfacing of recycled arc-front mantle beneath back-arc basins', *Geophysical Research Letters* **40**(22), 5849–5853.

Nebel, O.; Sossi, P.; Bénard, A.; Wille, M.; Vroon, P. & Arculus, R. (2015), 'Redox-variability and controls in subduction zones from an iron-isotope perspective', *Earth and Planetary Science Letters* **432**, 142–151.

Nell J. & Wood, B. J. (1991), 'High-temperature electrical measurements and thermodynamic properties of Fe_3O_4-$FeCr_2O_4$-$MgCr_2O_4$-$FeAl_2O_4$ spinels', *American Mineralogist* **76**, 405–426.

Newton, R. C. & Manning, C. E. (2005), 'Solubility of anhydrite, CaSO4, in NaCl–H2O solutions at high pressures and temperatures: applications to fluid–rock interaction', *Journal of Petrology* **46**(4), 701–716.

Niu, Y. (2004), 'Bulk-rock major and trace element compositions of abyssal peridotites: implications for mantle melting, melt extraction and post-melting processes beneath mid-ocean ridges', *Journal of Petrology* **45**(12), 2423–2458.

O

Oberhänsli, R. (1980), 'PT Bestimmungen anhand von Mineralanalysen in Eklogiten und Glaukophaniten der Ophiolite von Zermatt', *Schweizerische Mineralogische und PetrographischeMitteilungen*, 60, 215-235.

Ohmoto, H. & Lasaga, A. C. (1982), 'Kinetics of reactions between aqueous sulfates and sulfides in hydrothermal systems', *Geochimica et Cosmochimica Acta* **46**(10), 1727–1745.

Ohmoto, H. & Rye, R. (1979), 'Isotopes of sulfur and carbon. Geochemistry of Hydrothermal Ore Deposits (Barnes, HL, ed.), 509-567', John Wiley & Sons Inc., New York.

Ohnenstetter, M. (1992), 'Platinum group element enrichment in the upper mantle peridotites of the Monte Maggiore ophiolitic massif (Corsica, France): mineralogical evidence for ore-fluid metasomatism', *Mineralogy and Petrology* **46**(1), 85–107.

Ono, S.; Keller, N. S.; Rouxel, O. & Alt, J. C. (2012), 'Sulfur-33 constraints on the origin of secondary pyrite in altered oceanic basement', *Geochimica et Cosmochimica Acta* **87**, 323–340.

P

Padrón-Navarta, J.; Sánchez-Vizcaino, V. L.; Garrido, C.; Gómez-Pugnaire, M.; Jabaloy, A.; Capitani, G. & Mellini, M. (2008), 'Highly ordered antigorite from Cerro del Almirez HP–HT serpentinites, SE Spain', *Contributions to Mineralogy and Petrology* **156**(5), 679–688.

Padrón-Navarta, J. A., Sánchez-Vizcaíno, V. L., Hermann, J., Connolly, J. A., Garrido, C. J., Gómez-Pugnaire, M. T., & Marchesi, C. (2013). Tschermak's substitution in antigorite and consequences for phase relations and water liberation in high-grade serpentinites. *Lithos*, **178**, 186-196.

Pagé, P. & Barnes, S.-J. (2009), 'Using trace elements in chromites to constrain the origin of podiform chromitites in the Thetford Mines ophiolite, Québec, Canada', *Economic Geology* **104**(7), 997–1018.

Parkinson, I. J. & Arculus, R. J. (1999), 'The redox state of subduction zones: insights from arc-peridotites', *Chemical Geology* **160**(4), 409–423.

Pagé, P. & Barnes, S.-J. (2009), 'Using trace elements in chromites to constrain the origin of podiform chromitites in the Thetford Mines ophiolite, Québec, Canada', *Economic Geology* **104**(7), 997–1018.

Pagé, P. & Barnes, S.-J. (2016), 'The influence of chromite on osmium, iridium, ruthenium and rhodium distribution during early magmatic processes', Chemical Geology 420, 51–68.

Pagé, P.; Barnes, S.-J.; Bédard, J. H. & Zientek, M. L. (2012), 'In situ determination of Os, Ir, and Ru in chromites formed from komatiite, tholeiite and boninite magmas: implications for chromite control of Os, Ir and Ru during partial melting and crystal fractionation', Chemical Geology 302, 3–15.

Paton, C.; Hellstrom, J.; Paul, B.; Woodhead, J. & Hergt, J. (2011), 'Iolite: Freeware for the visualisation and processing of mass spectrometric data', *Journal of Analytical Atomic Spectrometry* **26**(12), 2508–2518.

Pearson, D.; Irvine, G.; Ionov, D.; Boyd, F. & Dreibus, G. (2004), 'Re–Os isotope systematics and platinum group element fractionation during mantle melt extraction: a study of massif and xenolith peridotite suites', *Chemical Geology* **208**(1), 29–59.

Penniston-Dorland, S. C.; Gorman, J. K.; Bebout, G. E.; Piccoli, P. M. & Walker, R. J. (2014), 'Reaction rind formation in the Catalina Schist: Deciphering a history of mechanical mixing and metasomatic alteration', *Chemical Geology* **384**, 47–61.

Penniston-Dorland, S. C.; Walker, R. J.; Pitcher, L. & Sorensen, S. S. (2012), 'Mantle–crust interactions in a paleosubduction zone: Evidence from highly siderophile element systematics of eclogite and related rocks', *Earth and Planetary Science Letters* **319**, 295–306.

Peregoedova, A.; Barnes, S.-J. & Baker, D. R. (2004), 'The formation of Pt–Ir alloys and Cu–Pd-rich sulfide melts by partial desulfurization of Fe–Ni–Cu sulfides: results of experiments and implications for natural systems', Chemical Geology 208(1), 247–264.

Peretti, A.; Dubessy, J.; Mullis, J.; Frost, B. R. & Trommsdorff, V. (1992), 'Highly reducing conditions during Alpine metamorphism of the Malenco peridotite (Sondrio, northern Italy) indicated by mineral paragenesis and H2 in fluid inclusions', *Contributions to Mineralogy and Petrology* **112**(2-3), 329–340.

Philippot, P. & Selverstone, J. (1991), 'Trace-element-rich brines in eclogitic veins: implications for fluid composition and transport during subduction', *Contributions to Mineralogy and Petrology* **106**(4), 417–430.

Pleuger, J.; Roller, S.; Walter, J. M.; Jansen, E. & Froitzheim, N. (2007), 'Structural evolution of the contact between two Penninic nappes (Zermatt-Saas zone and Combin zone, Western Alps) and implications for the exhumation mechanism and palaeogeography', *International Journal of Earth Sciences* **96**(2), 229–252.

Plümper, O.; Beinlich, A.; Bach, W.; Janots, E. & Austrheim, H. (2014), 'Garnets within geode-like serpentinite veins: Implications for element transport, hydrogen production and life-supporting environment formation', *Geochimica et Cosmochimica Acta* **141**, 454–471.

Pognante, U. (1989), 'Lawsonite, blueschist and eclogite formation in the southern Sesia zone (western Alps, Italy)', *European Journal of Mineralogy*, 89–104.

Pokrovski, G. S. & Dubessy, J. (2015), 'Stability and abundance of the trisulfur radical ion in hydrothermal fluids', *Earth and Planetary Science Letters* **411**, 298–309.

Polino, R. & Lemoine, M. (1984), 'Détritisme mixte d'origine continentale et océanique dans les sédiments jurassico-crétacés supra-ophiolitiques de la Téthys ligure: la série du Lago Nero (Alpes Occidentales franco-italiennes)', *Comptes-rendus des séances de l'Académie des sciences. Série 2, Mécanique-physique, chimie, sciences de l'univers, sciences de la terre* **298**(8), 359–364.

Pons, M. L., Debret, B., Bouilhol, P., Delacour, A., & Williams, H. (2016). Zinc isotope evidence for sulfate-rich fluid transfer across subduction zones. *Nature communications*, *7*, 13794.

Prabhakar, N. & Bhattacharya, A. (2013), 'Origin of zoned spinel by coupled dissolution–precipitation and inter-crystalline diffusion: evidence from serpentinized wehrlite, Bangriposi, Eastern India', *Contributions to Mineralogy and Petrology* **166**(4), 1047–1066.

Puchtel, I. S. & Humayun, M. (2001), 'Platinum group element fractionation in a komatiitic basalt lava lake', *Geochimica et Cosmochimica Acta* **65**(17), 2979–2993.

Puchtel, I. S.; Humayun, M.; Campbell, A. J.; Sproule, R. A. & Lesher, C. M. (2004), 'Platinum group element geochemistry of komatiites from the Alexo and Pyke Hill areas, Ontario, Canada', *Geochimica et Cosmochimica Acta* **68**(6), 1361–1383.

Putnis, A. & Austrheim, H. (2010), 'Fluid-induced processes: metasomatism and metamorphism', *Geofluids* **10**(1-2), 254–269.

R

Rahn, M. & Rahn, K. (1998), 'Titanian clinohumite formation in the Zermatt-Saas ophiolites, central Alps', *Mineralogy and Petrology* **64**(1-4), 1–13.

Ranero, C. & Sallares, V. (2004), 'Geophysical evidence for hydration of the crust and mantle of the Nazca plate during bending at the north Chile trench', *Geology* **32**(7), 549–552.

Ravna, E.; Andersen, T. B.; Jolivet, L. & De Capitani, C. (2010), 'Cold subduction and the formation of lawsonite eclogite–constraints from prograde evolution of eclogitized pillow lava from Corsica', *Journal of Metamorphic Geology* **28**(4), 381–395.

Rebay, G.; Spalla, M. & Zanoni, D. (2012), 'Interaction of deformation and metamorphism during subduction and exhumation of hydrated oceanic mantle: Insights from the Western Alps', *Journal of Metamorphic Geology* **30**(7), 687–702.

Reddy, S.; Wheeler, J.; Butler, R.; Cliff, R.; Freeman, S.; Inger, S.; Pickles, C. & Kelley, S. (2003), 'Kinematic reworking and exhumation within the convergent Alpine Orogen', *Tectonophysics* **365**(1), 77–102.

Reddy, S.; Wheeler, J. & Cliff, R. (1999), 'The geometry and timing of orogenic extension: an example from the Western Italian Alps', *Journal of Metamorphic Geology* **17**, 573–590.

Rees, C.; Jenkins, W. & Monster, J. (1978), 'The sulphur isotopic composition of ocean water sulphate', *Geochimica et Cosmochimica Acta* **42**(4), 377–381.

Rehkämper, M.; Halliday, A.; Fitton, J.; Lee, D.-C.; Wieneke, M. & Arndt, N. (1999), 'Ir, Ru, Pt, and Pd in basalts and komatiites: new constraints for the geochemical behavior of the platinum-group elements in the mantle', *Geochimica et Cosmochimica Acta* **63**(22), 3915–3934.

Reinecke, T. (1998), 'Prograde high-to ultrahigh-pressure metamorphism and exhumation of oceanic sediments at Lago di Cignana, Zermatt-Saas Zone, western Alps', *Lithos* **42**(3), 147–189.

Reinecke, T. (1991), 'Very-high-pressure metamorphism and uplift of coesite-bearing metasediments from the Zermatt-Saas zone, Western Alps', *European Journal of Mineralogy*, 7–18.

Richards, J. P. (2009), 'Postsubduction porphyry Cu-Au and epithermal Au deposits: Products of remelting of subduction-modified lithosphere', *Geology,* 37(3), 247–250.

Richards, J. P. (2015), 'The oxidation state, and sulfur and Cu contents of arc magmas: implications for metallogeny', *Lithos* **233**, 27–45.

Richards, J. P. (2011), 'Magmatic to hydrothermal metal fluxes in convergent and collided margins', *Ore Geology Reviews* **40**(1), 1–26.

Ringwood, A. (1958), 'The constitution of the mantle—I: Thermodynamics of the olivine-spinel transition', *Geochimica et Cosmochimica Acta* **13**(4), 303–321.

Rosenbaum, G. & Lister, G. S. (2005), 'The Western Alps from the Jurassic to Oligocene: spatio-temporal constraints and evolutionary reconstructions', *Earth-Science Reviews* **69**(3), 281–306.

Rubatto, D.; Gebauer, D. & Fanning, M. (1998), 'Jurassic formation and Eocene subduction of the Zermatt–Saas-Fee ophiolites: implications for the geodynamic evolution of the Central and Western Alps', *Contributions to Mineralogy and Petrology* **132**(3), 269–287.

S

Sakai, H.; Des Marais, D.; Ueda, A. & Moore, J. (1984), 'Concentrations and isotope ratios of carbon, nitrogen and sulfur in ocean-floor basalts', *Geochimica et Cosmochimica Acta* **48**(12), 2433–2441.

Salters, V. J. & Stracke, A. (2004), 'Composition of the depleted mantle', *Geochemistry, Geophysics, Geosystems* **5**(5).

Santiago Ramos, D.; Shimizu, N. & Scambelluri, M. (2012), Sulfur isotopic variations during subduction of hydrated lithosphere: the Erro Tobbio case, *in* 'AGU Fall Meeting Abstracts', pp. 04.

Savard, D.; Barnes, S.-J. & Meisel, T. (2010), 'Comparison between Nickel-Sulfur Fire Assay Te Co-precipitation and Isotope Dilution with High-Pressure Asher Acid Digestion for the Determination of Platinum-Group Elements, Rhenium and Gold', *Geostandards and Geoanalytical Research* **34**(3), 281–291.

Scambelluri, M.; Fiebig, J.; Malaspina, N.; Müntener, O. & Pettke, T. (2004b), 'Serpentinite subduction: implications for fluid processes and trace-element recycling', *International Geology Review* **46**(7), 595–613.

Scambelluri, M.; Müntener, O.; Ottolini, L.; Pettke, T. T. & Vannucci, R. (2004a), 'The fate of B, Cl and Li in the subducted oceanic mantle and in the antigorite breakdown fluids', *Earth and Planetary Science Letters* **222**(1), 217–234.

Scambelluri, M.; Pettke, T. & Cannaт, E. (2015), 'Fluid-related inclusions in Alpine high-pressure peridotite reveal trace element recycling during subduction-zone dehydration of serpentinized mantle (Cima di Gagnone, Swiss Alps)', *Earth and Planetary Science Letters* **429**, 45–59.

Scambelluri, M.; Pettke, T.; Rampone, E.; Godard, M. & Reusser, E. (2014), 'Petrology and trace element budgets of high-pressure peridotites indicate subduction dehydration of serpentinized mantle (Cima di Gagnone, Central Alps, Switzerland)', *Journal of Petrology*, egt068.

Scambelluri, M. & Rampone, E. (1999), 'Mg-metasomatism of oceanic gabbros and its control on Ti-clinohumite formation during eclogitization', *Contributions to Mineralogy and Petrology* **135**(1), 1–17.

Scambelluri, M. & Tonarini, S. (2012), 'Boron isotope evidence for shallow fluid transfer across subduction zones by serpentinized mantle', *Geology* 40(10), 907–910.

Schauble, E. A. (2004), 'Applying stable isotope fractionation theory to new systems', *Reviews in Mineralogy and Geochemistry* **55**(1), 65–111.

Schneider, M. E. & Eggler, D. H. (1986), 'Fluids in equilibrium with peridotite minerals: implications for mantle metasomatism', *Geochimica et Cosmochimica Acta* **50**(5), 711–724.

Schwarzenbach, E. M.; Früh-Green, G. L.; Bernasconi, S. M.; Alt, J. C. & Plas, A. (2013), 'Serpentinization and carbon sequestration: A study of two ancient peridotite-hosted hydrothermal systems', *Chemical Geology* **351**, 115–133.

Schwarzenbach, E. M.; Früh-Green, G. L.; Bernasconi, S. M.; Alt, J. C.; Shanks III, W. C.; Gaggero, L. & Crispini, L. (2012), 'Sulfur geochemistry of peridotite-hosted hydrothermal systems: comparing the Ligurian ophiolites with oceanic serpentinites', *Geochimica et Cosmochimica Acta* **91**, 283–305.

Schwarzenbach, E. M.; Gazel, E. & Caddick, M. J. (2014), 'Hydrothermal processes in partially serpentinized peridotites from Costa Rica: evidence from native copper and complex sulfide assemblages', *Contributions to Mineralogy and Petrology* **168**(5), 1–21.

Schwarzenbach, E. M.; Gill, B. C.; Gazel, E. & Madrigal, P. (2016), 'Sulfur and carbon geochemistry of the Santa Elena peridotites: Comparing oceanic and continental processes during peridotite alteration', *Lithos* **252**, 92–108.

Seal, R. R. (2006), 'Sulfur isotope geochemistry of sulfide minerals', *Reviews in mineralogy and geochemistry* **61**(1), 633–677.

Seyfried, W.; Foustoukos, D. & Fu, Q. (2007), 'Redox evolution and mass transfer during serpentinization: An experimental and theoretical study at 200° C, 500bar with implications for ultramafic-hosted hydrothermal systems at Mid-Ocean Ridges', *Geochimica et Cosmochimica Acta* **71**(15), 3872–3886.

Shanks, W.; Bohlke, J. & Seal, R. (1995), 'Stable Isotopes in Mid-Ocean Ridge Hydrothermal Systems: Interactions Between Fluids, Minerals, and Organisms', *Seafloor Hydrothermal Systems: Physical, Chemical, Biological, and Geological Interactions*, 194–221.

Shanks, W.; Bischoff, J. L. & Rosenbauer, R. J. (1981), 'Seawater sulfate reduction and sulfur isotope fractionation in basaltic systems: interaction of seawater with fayalite and magnetite at 200–350 C', *Geochimica et Cosmochimica Acta* **45**(11), 1977–1995.

Shen, A. H.; Keppler, H. & others (1997), 'Direct observation of complete miscibility the albite-H2O system', *Nature* **385**(6618), 710–712.

Shimazaki, H. (1998), 'On the occurrence of silician magnetites', *Resource Geology* **48**(1), 23–29.

Shimizu N, Scambelluri M, S. R. D. &. T. S. (2013), 'Boron and Sulfur Isotopic Variations during Subduction of Hydrated Lithosphere: The Erro Tobbio Case', *Mineralogical Magazine* **77(5)**, 2201.

Singh, A. K. & Singh, R. B. (2013), 'Genetic implications of Zn-and Mn-rich Cr-spinels in serpentinites of the Tidding Suture Zone, eastern Himalaya, NE India', *Geological Journal* **48**(1), 22–38.

Snow, J. E. & Dick, H. J. (1995), 'Pervasive magnesium loss by marine weathering of peridotite', *Geochimica et Cosmochimica Acta* **59**(20), 4219–4235.

Spandler, C.; Hermann, J.; Faure, K.; Mavrogenes, J. A. & Arculus, R. J. (2008), 'The importance of talc and chlorite "hybrid" rocks for volatile recycling through subduction zones; evidence from the high-pressure subduction mélange of New Caledonia', *Contributions to Mineralogy and Petrology* **155**(2), 181–198.

Spandler, C.; Pettke, T. & Hermann, J. (2014), 'Experimental study of trace element release during ultrahigh-pressure serpentinite dehydration', *Earth and Planetary Science Letters* **391**, 296–306.

Spandler, C.; Pettke, T. & Rubatto, D. (2011), 'Internal and external fluid sources for eclogite-facies veins in the Monviso meta-ophiolite, Western Alps: implications for fluid flow in subduction zones', *Journal of Petrology* **52**(6), 1207–1236.

Spandler, C. & Pirard, C. (2013), 'Element recycling from subducting slabs to arc crust: A review', *Lithos* **170**, 208–223.

Stampfli, G. M. & Borel, G. (2001), *Geology of the Western Swiss Alps: A Guide-book*, Section des Sciences de la terre de l'université.

Sturani, C. & Nazionale delle Ricerche (Italia), C. (1975), *Explanatory notes on the Western Alps (from the Sestri-Voltaggio Line to the Val d'Ossola)*, Vol. 90, pp. 149-174.

T

Tomkins, A. G. & Evans, K. A. (2015), 'Separate zones of sulfate and sulfide release from subducted mafic oceanic crust', *Earth and Planetary Science Letters* **428**, 73–83.

Tostevin, R.; Turchyn, A. V.; Farquhar, J.; Johnston, D. T.; Eldridge, D. L.; Bishop, J. K. & McIlvin, M. (2014), 'Multiple sulfur isotope constraints on the modern sulfur cycle', *Earth and planetary science letters* **396**, 14–21.

Tribuzio, R. & Giacomini, F. (2002), 'Blueschist facies metamorphism of peralkaline rhyolites from the Tenda crystalline massif (northern Corsica): evidence for involvement in the Alpine subduction event?', *Journal of Metamorphic Geology* **20**(5), 513–526.

Trommsdorff, V. & Evans, B. W. (1980), 'Titanian hydroxyl-clinohumite: formation and breakdown in antigorite rocks (Malenco, Italy)', *Contributions to Mineralogy and Petrology* **72**(3), 229–242.

Trommsdorff, V.; Sánchez-Vizcaino, V. L.; Gomez-Pugnaire, M. & Müntener, O. (1998), 'High pressure breakdown of antigorite to spinifex-textured olivine and orthopyroxene, SE Spain', *Contributions to Mineralogy and Petrology* **132**(2), 139–148.

Tropper, P. & Manning, C. E. (2005), 'Letter: Very low solubility of rutile in H2O at high pressure and temperature, and its implications for Ti mobility in subduction zones', *American Mineralogist* **90**(2-3), 502–505.

U

Ueda, A. & Sakai, H. (1984), 'Sulfur isotope study of Quaternary volcanic rocks from the Japanese Islands Arc', *Geochimica et Cosmochimica Acta* **48**(9), 1837–1848.

Ulmer, P.; Trommsdorff, V. & others (1999), 'Phase relations of hydrous mantle subducting to 300 km', *Mantle petrology: field observations and high pressure experimentation: a tribute to Francis R.(Joe) Boyd* **6**, 259–281.

V

Vitale Brovarone, A.; Beltrando, M.; Malavieille, J.; Giuntoli, F.; Tondella, E.; Groppo, C.; Beyssac, O. & Compagnoni, R. (2011), 'Inherited ocean–continent transition zones in deeply subducted terranes: insights from Alpine Corsica', *Lithos* **124**(3), 273–290.

Vitale Brovarone, A.; Beyssac, O.; Malavieille, J.; Molli, G.; Beltrando, M. & Compagnoni, R. (2013), 'Stacking and metamorphism of continuous segments of subducted lithosphere in a high-pressure wedge: the example of Alpine Corsica (France)', *Earth-Science Reviews* **116**, 35–56.

Vitale Brovarone, A. & Herwartz, D. (2013), 'Timing of HP metamorphism in the Schistes Lustrés of Alpine Corsica: New Lu–Hf garnet and lawsonite ages', *Lithos* **172**, 175–191.

W

Wacey, D.; Kilburn, M. R.; Saunders, M.; Cliff, J. & Brasier, M. D. (2011), 'Microfossils of sulphur-metabolizing cells in 3.4-billion-year-old rocks of Western Australia', *Nature Geoscience* **4**(10), 698–702.

Wagner, T. & Boyce, A. J. (2006), 'Pyrite metamorphism in the Devonian Hunsrück Slate of Germany: Insights from laser microprobe sulfur isotope analysis and thermodynamic modeling', *American Journal of Science* **306**(7), 525–552.

Walker, R.; Brandon, A.; Bird, J.; Piccoli, P.; McDonough, W. & Ash, R. (2005), '187 Os–186 Os systematics of Os–Ir–Ru alloy grains from southwestern Oregon', *Earth and Planetary Science Letters* **230**(1), 211–226.

Wallace, P. J. & Edmonds, M. (2011), 'The sulfur budget in magmas: evidence from melt inclusions, submarine glasses, and volcanic gas emissions', *Reviews in Mineralogy and Geochemistry* **73**(1), 215–246.

Warburton, J. (1986), 'The ophiolite-bearing Schistes Lustrés nappe in Alpine Corsica: a model for the emplacement of ophiolites that have suffered HP/LT metamorphism', *Geological Society of America Memoirs* **164**, 313–332.

Wechsler, B. A.; Lindsley, D. H. & Prewitt, C. T. (1984), 'Crystal structure and cation distribution in titanomagnetites (Fe (sub 3-x) Ti x O 4)', *American Mineralogist* **69**(7-8), 754–770.

Wicks, F. J. (1984), 'Deformation histories as recorded by serpentinites; II, deformation during and after serpentinization', *The Canadian Mineralogist* **22**(1), 197–203.

Williams, T. J.; Candela, P. A. & Piccoli, P. M. (1995), 'The partitioning of copper between silicate melts and two-phase aqueous fluids: an experimental investigation at 1 kbar, 800 C and 0.5 kbar, 850 C', *Contributions to Mineralogy and Petrology* **121**(4), 388–399.

Williams-Jones, A. E.; Bowell, R. J. & Migdisov, A. A. (2009), 'Gold in solution', *Elements* **5**(5), 281–287.

Woodhead, J. D.; Harmon, R. S. & Fraser, D. G. (1987), 'O, S, Sr, and Pb isotope variations in volcanic rocks from the Northern Mariana Islands: implications for crustal recycling in intra-oceanic arcs', *Earth and Planetary Science Letters* **83**(1), 39–52.

Woodland, S.; Pearson, D. & Thirlwall, M. (2002), 'A platinum group element and Re–Os isotope investigation of siderophile element recycling in subduction zones: comparison of Grenada, Lesser Antilles Arc, and the Izu–Bonin Arc', *Journal of Petrology* **43**(1), 171–198.

Wunder, B.; Wirth, R. & Gottschalk, M. (2001), 'Antigorite: Pressure and temperature dependence of polysomatism and water content', *European Journal of Mineralogy* **13**(3), 485–495.

Wylie, A. G.; Candela, P. A. & Burke, T. M. (1987), 'Compositional zoning in unusual Zn-rich chromite from the Sykesville District of Maryland and its bearing on the origin of" ferritchromit"', *American Mineralogist* **72**(3-4), 413–422.

X

Xiong, Y. & Wood, S. (2000), 'Experimental quantification of hydrothermal solubility of platinum-group elements with special reference to porphyry copper environments', *Mineralogy and Petrology* **68**(1-3), 1–28.

Xiong, Y. & Wood, S. A. (2002), 'Experimental determination of the hydrothermal solubility of ReS2 and the Re-ReO2 buffer assemblage and transport of rhenium under supercritical conditions', *Geochem. Trans* **3**(1), 1–10.

Y

Yang, J.-J. & Powell, R. (2006), 'Calculated phase relations in the system Na2O–CaO–K2O–FeO–MgO–Al2O3–SiO2–H2O with applications to UHP eclogites and whiteschists', *Journal of Petrology* **47**(10), 2047–2071.

Yokoyama, T.; Nakazato, T. & Tarutani, T. (1980), 'Polymerization of silicic acid adsorbed on iron (III) hydroxide', *Bulletin of the Chemical Society of Japan* **53**(4), 850–853.

Z

Zack, T. & John, T. (2007), 'An evaluation of reactive fluid flow and trace element mobility in subducting slabs', *Chemical Geology* **239**(3), 199–216.

Zotov, N. & Keppler, H. (1998), 'The influence of water on the structure of hydrous sodium tetrasilicate glasses', *American Mineralogist* **83**(7-8), 823–834.

Zotov, N.; Keppler, H.; Hannon, A. & Soper, A. (1996), 'The effect of water on the structure of silicate glasses—A neutron diffraction study', *Journal of Non-Crystalline Solids* **202**(1), 153–163.

APPENDIX A
SUPPLEMENTARY PETROGRAPHY AND WHOLE ROCK DATA

A1: SUPPLEMENTARY PETROGRAPHY

Here petrographic descriptions are provided for samples in close contact with serpentinites and hybrid samples.

Alpine Corsica

CO13-20: psammite

Feldspar is of two types, large laths ~up to 1.5 cm, and smaller laths <20µm but both appear to be synchronous. Feldspar is low relief with low birefringence from brown-grey and is twinned.

Mica is interstitial to quartz and feldspar. Pale green-white colour in PPL. 'mottled' appearance in XPL. Defines the main foliation.

Euhedral titanite (up to 500µm) associated with mica (interstitial) and quartz. Both mica and titanite are overprinted by actinolite.

Actinolite: 120 degree cleavage, up to 500 µm across. Birefringence from grey-black-brown. Contains small inclusions of quartz. Cuts the mica-defined foliation.

Small pyrite grains (< 10 microns) are included in mica.

Modal %

Quartz – 25%

Feldspar – 25%

Mica -20%

Actinolite -15%

Titanite – 1%

Pyrite – trace

CO13-22: Mafic blueschist (no quartz veins)

Fine grained matrix, well-defined foliation.

Plagioclase has low relief, orange-grey birefringence, reacting out in contact with epidote. Actinolite/glaucophane replaces plagioclase.

Layer of large grains of actinolite with 120 cleavage, green/blue birefringence in XPL, and green-brown pleochroism in PPL. Glaucophane rims are present on actinolite which is defined by its pink pleochroism colours and distinct blue in PPL.

Epidote occurs as fine/small euhedral crystals with high birefringence. In association with chlorite, epidote defines a significant proportion of the matrix.

Epidote and chlorite forms in veins which overprint plagioclase.

Chlorite rims on actinolite, glaucophane and epidote have anomalous birefringence from brown-cream-grey, pleochroic brown-green and epidote.

Calcite patches with twinning and high birefringence in matrix, which overprint plagioclase. Calcite is associated with chlorite and epidote.

Small magnetite in veins of chlorite/epidote. Lighter mt along vein of chlorite next to glaucophane and epidote.

Modal %

Chlorite – 30%

Plag – 20%

Talc – 20%

Epidote – 15%

Actinolite – 10%

Trace – Calcite, glaucophane.

CO13-28: Calc schist

Hand sample

Alternating carbonaceous brown layers and mica rich blue layers ~0.1cm wide. Fine layers of quartz occur heterogeneously.

Thin section

Calcite defines the matrix with minor quartz. In places, iron-rich or siderite nodules (up to 50 μm in diameter) overprint the matrix.

Late calcite grains

Quartz and calcite layers overprint pyrite.

In this thin section, mica-rich layers form 2% of the overall section, although more layers are observed in the hand specimen.

One large pyrite grain (~100 μm) is associated with calcite and smaller pyrites (<10 μm) are overprinted by calcite and quartz.

Modal %:

Calcite – 80%

Quartz – 10%

Talc - 2%

Siderite – 8%

CO13-29: Metaquartzite next to serpentinite breccia

Hand sample

Crenulated and finely layered.

Quartz clasts ~0.5cm.

Small brown minerals (barely visible ~0.1–0.2 cm) within dark thin (~0.3cm wide) veins of graphite.

Thin section

Foliation - two orientations.

Quartz and albite (where albite is defined by polysynthetic twinning, low relief and low birefringence) are overprinted by chlorite.

Patchy chlorite occurs as veins (anomalous brown/green birefringence and pleochroic) and is overprinted by mica

Chlorite veins contain titanite.

Mica (high birefringence) occurs as veins interstitially to quartz. Small titanite grains occur within mica.

Modal %:

Quartz: 50%

Mica: 20%

Chlorite = 15%

albite – 10%

titanite – 5%

CO13-30: Serpentinite breccia

Hand Sample

Not magnetic – no visible magnetite.

Green sheared veins of serpentine

Thin section

20 μm pyrites and small cpy ~0.4mm, and follow foliation defined by calcite (the dominant mineral)/serpentine matrix.

Titanite replaces pyrite and occurs within the calcite matrix. Titanite also contains inclusions of trace magnetite grains (<2 microns)

Albite is twinned with low birefringence with a maximum order of orange birefringence. Albite and chlorite both replace pyrite.

'Swirly' carbonate overprints titanite.

Very fine calcite occurs within 200-500 μm in diameter veins. Serpentine is interlayered with calcite in these veins, and occurs as fine needles (typically <2 μm) and the veins also contain clasts of actinolite.

serpentine – 10%

calcite – 40%

titanite – 15%

actinolite – 20%

Carbonate – 10%

Cpy - 1%

Py = 3%

Mt = <1%

CO13-32: Metagabbro with calcite

Hand Sample

Pale green veins associated with white veins of calcite with pale feldspars. White euhedral grains look sheared like porphyroclasts.

Small ~1mm long clasts.

Holes where weathered, 'careous', suggests carbonaceous material present.

Largely retrogressed.

Thin section

Fine grained matrix consisting quartz and clinopyroxene with kink bands

Blue laths of glaucophane. There is also a pleochroic blue-light brown/pink mineral which surrounds this but doesn't look quite as purple/blue as glaucophane, which suggests transition to actinolite.

Glaucophane also occurs as subhedral-euhedral cores (up to 300 μm in diameter) to actinolite (pleochroic green-brown, good 120 cleavage).

White, low birefringence feldspar, surrounded by laths of epidote (high relief, high birefringence w blue, purple, yellow and pink colours).

Na and Ca-rich plagioclase compositions are present, with the Ca-rich form (individual laths are ~30–60 μm in diameter) replacing the Na-rich form (>100 μm), where Ca-rich composition is associated with titanite grains up to 50 μm in length (appear to be synchronous).

Large titanite grains (individual grains are ~100 μm) are aligned with crenulated foliation. Titanite is anisotropic from brown-bluish grey in RL in reflected light. Small blebs of rutile (1–3 μm and light grey in RL) and pyrite (~10 μm in size). These veins are associated with actinolite (found proximal to veins and appears synchronous to the

veins) but are overprinted by veins of mica (indistinguishable individual grains, high birefringence, pink, blue, purple, mottled appearance)

Subhedral to euhedral titanite grains ~2–5 μm in diameter are included in sodic plagioclase but appear to be connected with surrounding large >20 μm titanite grains.

Veins of chlorite and actinolite with low birefringence (grey/white, orange for actinolite), replace glaucophance and cut dominant foliation at ~90 degree angles.

SEM work revealed the presence of small Cu-Zn alloy within Ca-rich plagioclase, although possible contaminant given its presence near a fracture.

Modal %:

Mica = 30%

Actinolite = 10%

Glaucophane = 25%

Titanite = 5%

Chlorite = 10%

Epidote/zoisite = 10%

Pyrite = 1%

CO13-34: Metagabbro, veined with quartz.

Hand sample

Very quartz rich, folds.

Several fold generations with a thin layer of epidote or light green layer in places. Thin veins of quartz in dark matrix.

Refolded folds.

Thin section

Section is comprised of an antiform fold. Quartz grains (40–100μm) comprise most of the matrix, with 1.5–2cm layers/bands of epidote grains.

Glaucophane defines the core of the antiform with anhedral grains (up to 100 μm) of epidote. Epidote is defined by its light yellow-green colour and high relief, optic angle and high birefringence. Glaucophane laths are ~20–100 μm wide, lengths are variable from <100 to >500 μm and are variably overprinted by actinolite grains (~150–250 μm). Mica (muscovite) is interstitial between glaucophane grains and is also replaced by actinolite.

Thin laths of magnetite (~10–50 μm wide and up to 100 μm in length) are indispersed in epidote/glauc layer – interstitial mica associated with magnetite. Magnetite occurs dominantly in the layer at the core of the antiform.

Quartz – 55%

Epidote – 15%

Mica – 10%

Glaucophane – 15%

Magnetite – 5%

CO13-35a: Metagabbro near calc schist

Hand sample

Layer of green epidote.

Folded veins with a large quartz vein ~0.4cm wide folded and wrapped around a layer of retrogressed metagabbro with a dark green minerals of chlorite and amphibole.

Feldspathic layer in between 2 layers of thin epidote veins ~0.2mm wide surround pink feldspar crystals with amphibole rims

Thin section

Entire layers of glaucophane.

Veins of epidote + mica come into glauc + plag layers + chl. After quartz.

Rutile with ilmenite rim in blueschist layers – HP to LP mineral.

In places partially retrogressed with actinolite replacing glaucophane.

Actinolite rims on plag in layers of quartz.

Rutile – occurs along quartz veins and glaucophane – so HP veins.

Tiny mt ~epidote

Modal %

Glaucophane – 25%

Actinolite – 5% (overprinted by glauc?)

Epidote – 20%

Quartz – 35%

Rutile – 5%

Mt- trace ~ px reacting out in quartz vein.

Cpx – 5% (unstable in qtz vein).

Talc – 10% ~ epidote layer occurs interstitially.

CO13-35b: Metagabbro

Thin section

More retrogressed and finer grained than CO13-35.

This section contains a higher mode of actinolite than CO13-35a, where individual grains are ~50–200 µm, within which quartz and glaucophane are included (up to ~250 µm laths) than CO13-35 and glaucophane occurs in layers, replacing quartz and epidote grains.

Quartz veins are dispersed through the section.

Glaucophane also occurs in quartz veins which indicates that these veins were formed at high pressure.

Titanite is observed associated with actinolite surrounding the quartz veins, and is orientated with the dominant foliation.

Modal %:

Epidote ~20%

Glaucophane ~15%

Quartz ~30%

Actinolite ~10%

Titanite ~2%

Mica ~5%

CO13-36: Calc schist

Hand sample

0.7cm wide brown carbonaceous bands with a pink/whitish reaction rim.

~0.3cm wide blue micaceous layer.

Thin section

Matrix mostly comprised of carbonate with minor quartz grains ~100 µm in diameter and interstitial mica and chlorite.

One pyrite grain observed which is ~50 µm in diameter within carbonate matrix, aligned and therefore likely associated with mica and chlorite minor interstitial veins. Small grains <50 µm. Has grey rims – likely an oxidation/weathering feature?

Modal %:

Mica ~5%

Carbonate ~75%

Chlorite ~5%

Quartz ~15%

Trace: pyrite.

CO13-41: Calc schist

Thin section

Matrix dominantly carbonate with albite laths along calcite boundaries (~50-120 µm), and interstitial mica and chlorite veins.

Trace pyrite (two large grains ~50 to 100 µm, smaller grains <5 µm within calcite), occurring as subhedral to euhedral grains along mica vein.

Late chlorite occurs as green/brown veins with low birefringence (1st order greys) which cross cut calcite and contain titanite grains that are ~20–50 µm.

Modal %:

Carbonate ~70%

Chlorite ~5%

Mica ~5%

Quartz ~5%

Pyrite ~2%

Albite - ~13%

Titanite – trace

CO13-42 – Fine grained metaquartzite

Thin section

Folded layers of mica (light green- pale brown in PPL, high birefringence with blue, pink and green colours with a mottled appearance in XPL) within a matrix of quartz clasts.

The quartz clasts show a preferred orientation, and are slightly elongated in the direction of preferred orientation (typically ~60–100 µm wide and 100–250 µm in length). In some areas mica intergrows with chlorite, observed as brown/grey 1st order colours in XPL.

Ilmenite is associated with mica, and follows mica-defined foliation and consists of thin needles to laths up to 20 microns in diameter. Mica also contains small grains of euhedral epidote in between layers of angular quartz.

Modal %:

15% mica

5% chlorite

3% epidote

10% ilmenite

67% quartz

CO13-49: Breccia proximal to serpentinite

Thin section

Clinopyroxene consists of large grains >5 mm across which are variably broken down into smaller clasts within a foliated chlorite matrix and later veins ~50–200 μm across, comprised of chlorite (30%, comprises the matrix) and clinopyroxene, along which chalcopyrite grain was observed ~300 μm in diameter.

Actinolite with 120 degree cleavage overprints chlorite matrix with individual grains up to 130 μm.

Modal %

Chlorite – 30%

Cpx (porphyroclasts) – 50%

Actinolite – 20%

Ilm - <1%

Py - <1%

CO13-50: Metagabbro

Thin section

Crenulated matrix comprised of fine serpentine/chlorite + talc + altered/sheared pyroxene.

serpentine/chlorite ~30 % of the section.

Subhedral chalcopyrite grains ~5 μm are observed parallel to cleavage within large >500 μm porphyroclasts of cpx (augite).

Elongated and orientated parallel to foliation are ~1–5 across by 5 μm to ~20 μm in length titanite grains within plagioclase.

cpx folded with serpentine +/- talc (very high birefringence, low relief). Talc veins cut through cpx.

Modal %

Cpx ~40%

Serp/chlorite matrix ~35%

Talc 25%

Titanite 1%

CO13-56a: Serpentinite Breccia

Thin section

Epidote + zoisite overprint magnetite. ilmenite and py grains. Ilmenite smaller than in b ~2%.

CO13-56b: Serpentinite Breccia

Thin section

The overall texture appears to record brittle deformation, with regions of shearing associated with matrix areas of finer-grained zoisite. Compared to CO13-56a, CO13-56b has less epidote, and more actinolite + zoisite.

Actinolite is present as ~20–160 μm grains.

Titanite grains ~50–200 μm in diameter and are observed on rims of actinolite, and within actinolite although these appear to be connected to the matrix.

Titanite grains are overprinted by zoisite laths, which comprise the majority of the matrix. In addition zoisite laths overprint areas of brown patchy calcite + actinolite. Parts of the matrix are comprised of actinolite reacting out in contact with zoisite.

Ilmenite + titanite grains are the dominant oxides and outline the psuedomorphs of what appears to have been large euhedral magnetite grains which would have cross cut pre-existing foliation, similar to magnetite textures observed in samples from elsewhere (e.g. PF-001 and CO14-04).

A second generation of actinolite occurs as veins up to ~35 μm in diameter, cross-cutting zoisite in addition to laths, (up to ~300 μm x 100 μm), where zoning is apparent from Fe-rich cores to Fe-poorer rims (revealed by SEM analyses).

Modal %

~45% zoisite

~20% matrix/early actinolite

~20% coarse actinolite

~7% titanite

~5% epidote

~3% ilm

CO13-57: Metagabbro

Near contact between brown carbonaceous metasediment and blueschist.

Hand sample

Sample is very foliated.

Large ~1cm quartz crystals at the base of blueschist layer.

Epidote vein along boundary between blueschist and carbonaceous layers

?sulphides along veins and contact with carbonaceous layer – euhedral grains.

Thin section

Chlorite overprints primary plagioclase, and is in turn overprinted by a second generation of zoisite grains.

Patchy quartz is overprinted by carbonate, which is in turn overprinted by actinolite. Fluid inclusions are observed in carbonate and cross cut cleavage.

Actinolite consists of grains >100 μm on average, which appears to have 'reacted out' within with regions of chlorite/actinolite lamellae and were once much larger grains, as observed elsewhere in the section with grains >1 mm in size. Within actinolite are lenses of augite ~20–50 μm.

Lawsonite is defined by its polysynthetic twinning, colourless appearance, good cleavage, platy appearance and moderate birefringence. It occurs as very fine grains (individual grains are indistinguishable) intergrown with zoisite and wrap around actinolite lenses (actinolite is ~500 μm across). The foliation is defined by lawsonite+zoisite.

Titanite grains are aligned with lawsonite/zoisite foliation and are up to 200 μm in diameter but are typically much smaller (<50 μm).

Modal %:

Plagioclase: 5 %

Chlorite: 30%

Quartz: 5%

Carbonate: 10%

Actinolite: 20%

Lawsonite: 17%

Augite: 2%

Zoisite: 10%

Titanite: 1%

CO13-59: contact between calcschist and blueschist

Thin section

Tiny magnetite grains associate with talc and sulphide and carbonate.

Talc and serpentine veins.

Talc cuts through carbonate layer.

Carbonate layer has quartz randomly distributed throughout.

Mica overprints chlorite.

Carbonate rims quartz, chlorite rims carbonate.

Modal %:

Carbonate – 50%

Quartz – 20%

Mica – 15%

Chlorite – 15%

Trace – magnetite and pyrite

CO13-60b: Retrogressed blueschist

Hand sample

Green veins of epidote 0.1cm wide cut glaucophane/actinolite.

Small sulphides (dark brown) in actinolitic parts.

Quartz veins ~0.2cm cut through everything.

Glaucophane rich

Non magnetic

CO13-60b-1: Retrogressed blueschist

Thin section

Magnetite is replaced by plagioclase, quartz and chlorite. Magnetite occurs as inclusions (2.5 μm) within cpx. This generation of magnetite is replaced by fsp, quartz and chlorite. A second generation of magnetite occurs as 0.2–1 mm laths. The large magnetite laths are ~synchronous with chlorite.

Modal% :

Chlorite = 40%

Plagioclase: 25%

Actinolite: 15%

Magnetite = 15%

Epidote = 5%

Quartz = 10%

CO13-61: Metagabbro

Thin Section

Chlorite, epidote and talc occur within veins that overprint earlier actinolite and zoisite grains (typically up to 100 μm in length).

Very small ~1 μm magnetite and pyrite grains occur within a chlorite + talc + epidote vein.

Ilmenite and larger grains of magnetite (~100 μm) are cut by talc veins. Ilmenite (~50–70 μm) is also replaced by chlorite.

Modal %

Qtz – 30%

Talc – 20%

Chlorite – 15%

Amphibole – 15%

Plag – 12%

Ilmenite – 5%

Pyrite – 3%

CO14-05: Metagabbro

Thin section

The sample is overall very fine grained, with foliation defined by layers of chlorite. Chlorite replaces patchy layers of plagioclase (individual grains are ~10–50 μm in diameter). Chlorite consists of thin brown veins of chlorite (<30 μm across), which cross-cuts green chlorite; these have blue and green/brown birefringence respectively.

Epidote consists of high-relief brown grains ~30–65 μm across, and replace chlorite.

Epidote and both generations of chlorite are overprinted by a second generation of cross-cutting calcite veins ~250–500μm in diameter.

Pyrite consists of subhedral to euhedral grains ~50–250 μm in diameter. Pyrite is found overprinting veins of first generation patchy calcite, aligned with the dominant foliation defined by chlorite. Pyrite contains inclusions of calcite (~10 μm in diameter).

Rutile grains are defined by a dark-brown colour in PPL and light grey colour in rfl. Rutile is preserved as cores to Titanite, consisting of grains up to 100 μm in size. Titanite is brecciated, and individual grains are 10–70 μm, though they appear to have once been part of a larger grain. Chlorite wraps around Titanite rims.

Modal %

Chlorite – 40%

Plagioclase -18%

Epidote – 15%

Calcite 1 – 5%

Calcite 2 – 15%

Pyrite – 5%

Rutile – 2%

A2: Whole Rock Data

Elements	Al2O3	Ba	Ba	C	CaO	Co	Cr	Cs	FeO	Fe2O3 (total)	Ga	K2O
Units	%	ppm	ppm	%	%	ppm	ppm	ppm	%	%	ppm	%
Detection	0.01	50.00	0.50	0.01	0.01	0.10	20.00	0.10	0.05	0.01	0.10	0.01
Method	FB6/OE	FB6/OE	FB6/MS	/CSA	FB6/OE	4A/MS	FB6/OE	FB6/MS	AD71/VOL	FB6/OE	FB6/MS	FB6/OE
Corsica												
CO13-20	13.4	154	150.70	0.03	0.08	2.26	0.00	1.80	0.67	1.33	15.9	4.46
CO13-21	2.01	X	0.70	0.02	0.06	112.87	2468	0.00	2.03	7.07	2.90	0.01
CO13-22	14.9	X	23.5	0.10	8.36	51.9	105	0.30	5.28	9.51	16.8	0.17
CO13-27	5.70	X	2.00	0.03	0.07	81.2	388	0.10	10.2	16.1	7.90	0.00
CO13-28-1	0.91	X	39.2	10.4	43.9	12.1	0.00	0.40	X	0.45	1.70	0.19
CO13-28-2	4.13	137	134	9.04	41.4	41.3	29.0	1.40	0.27	1.49	6.00	0.84
CO13-29	8.33	143	145	0.02	0.54	27.0	49.0	4.90	0.86	3.56	11.9	2.29
CO13-30	15.7	X	27.9	0.02	11.3	31.1	0.00	0.70	4.09	6.43	20.1	0.52
CO13-31	1.19	X	0.50	0.02	0.03	103	2245	X	2.56	6.54	1.80	0.01
CO13-32	15.6	X	30.4	0.04	8.23	28.4	748.00	0.60	4.37	7.18	17.1	0.52
CO13-33	1.88	X	3.70	0.03	0.04	114	2411	0.00	2.90	8.98	2.10	X
CO13-34	1.82	X	35.1	X	0.47	2.03	0.00	0.80	0.92	2.60	3.20	0.44
CO13-35	7.97	71.0	71.0	0.05	3.73	22.1	58.0	2.00	2.81	8.79	12.0	1.17
CO13-36	1.83	55.0	53.0	9.76	47.2	9.07	0.00	0.70	0.66	1.01	2.90	0.41
CO13-40	1.52	X	0.70	0.02	0.16	130.1	2750	0.00	4.15	9.09	2.60	0.00
CO13-41	7.69	X	32.9	4.88	23.5	21.9	128	0.60	2.60	3.52	8.20	0.37
CO13-41-2	7.28	X	42.7	5.05	24.7	19.4	130	0.80	2.18	3.05	7.60	0.50
CO13-49	12.5	X	12.3	0.02	14.3	27.9	111	1.00	3.41	5.52	11.1	0.04
CO13-50	16.0	134	134	0.02	10.7	35.5	208	1.70	3.25	5.53	12.2	1.65
CO13-55	1.69	X	4.50	0.02	2.04	99.2	1812	X	3.26	6.42	2.70	0.00
CO13-56a	16.1	X	9.50	1.48	21.8	29.4	246	X	5.60	7.67	22.0	0.00
CO13-56b-1	17.8	X	2.10	0.45	22.5	106.8	60.0	X	5.60	6.81	23.9	0.00
CO13-56b-2	15.7	X	2.70	0.63	22.5	31.4	53.0	X	6.15	7.41	21.3	0.00
CO13-57	12.5	X	6.00	2.46	16.6	29.9	697	0.20	3.61	4.63	11.8	0.10
CO13-58	0.52	X	19.3	10.4	48.7	9.99	0.00	0.20	X	0.41	1.40	0.08
CO13-59-1	9.33	251	260	2.07	9.11	32.3	58.0	3.50	6.12	4.26	13.6	1.85
CO13-59-2	1.08	X	24.8	8.93	43.0	7.16	0.00	0.30	0.63	0.97	2.00	0.15
CO13-59-3	6.76	172	168	4.54	21.0	23.8	44.0	2.20	2.24	3.08	8.70	1.25
CO13-60a	13.7	X	3.10	0.68	4.25	40.9	170	0.20	8.71	10.3	17.5	X
CO13-60b-1	16.8	X	3.60	0.07	2.90	61.7	186	0.10	6.18	14.9	21.2	X
CO13-60b-2	16.4	X	4.20	0.06	2.83	63.0	183	0.00	6.15	14.5	20.2	X
CO13-61-1	9.76	193	192	0.04	1.69	31.7	55.0	5.90	1.73	4.74	13.8	2.72
CO13-61-2	8.34	167	170	0.04	1.17	31.1	49.0	5.00	1.69	3.82	11.5	2.33
CO14-03	10.8	X	2.70	0.02	4.97	123	621	X	12.3	20.4	19.9	X
CO14-04	1.82	X	1.10	0.03	0.03	85.2	2061	X	5.65	8.48	3.7	0.01
CO14-05	13.7	X	14.7	0.57	9.94	45.5	186.00	0.20	7.94	12.3	17.4	0.01

Elements	Al2O3	Ba	Ba	C	CaO	Co	Cr	Cs	FeO	Fe2O3 (total)	Ga	K2O
Units	%	ppm	ppm	%	%	ppm	ppm	ppm	%	%	ppm	%
Detection	0.01	50.00	0.50	0.01	0.01	0.10	20.00	0.10	0.05	0.01	0.10	0.01
Method	FB6/OE	FB6/OE	FB6/MS	/CSA	FB6/OE	4A/MS	FB6/OE	FB6/MS	AD71/VOL	FB6/OE	FB6/MS	FB6/OE
Zermatt-Saas												
S09-VSZ02	13.34	X	5.70	0.05	25.1	40.0	25.0	0.60	3.33	6.47	5.90	X
S09-VSZ03	2.14	X	1.00	0.04	2.33	85.4	2747	0.20	3.91	9.12	2.50	X
S09-VSZ05	1.29	X	6.70	0.03	0.36	114	2876	0.20	3.38	8.53	2.10	X
S09-GSZ11	1.26	X	X	0.05	1.10	119	1978	X	4.05	8.39	1.30	X
S09-AZS09	3.64	X	2.30	X	1.17	81.6	2079	X	2.52	7.86	3.10	X
PF001	7.23	0.00	0.90	0.05	0.67	97.3	118	0.30	6.19	11.2	7.30	0.00
LC015	2.03	0.00	1.90	0.04	0.04	111	2734	0.10	3.62	11.5	2.60	0.01
CHECKS												
CO13-20	13.1	155	158	0.04	0.07	56.20	0.00	1.90		1.32	15.6	4.45
CO13-55	1.67	0.00	5.10	0.03	1.86	102	1778	0.10	3.23	6.72	2.70	0.01
STANDARDS												
FER-3									13.6			
GBW07103												
GBW07103	13.7	334	331		1.65		0.00	36.0		2.21	19.9	5.10
OREAS 45e				0.54								
GBW07105												
GBW07105	13.92	535	552		8.63		140	0.40		13.0	25.2	2.32
MA-1b				2.41								
SY-4									2.86			
FER-3									13.6			
GBW07107												
GBW07107	18.4	439	427		0.60		107	13.4		7.26	26.1	4.55
GGC-05				9.34								
OREAS 24b												
OREAS 24b	14.7	738	748		1.48		144	10.6		6.10	20.5	3.66
OREAS 25a												
OREAS 25a	17.4	146	156		0.44		130	6.30		9.20	27.6	0.64
MPL-5												
BLANKS												
Control Blank	0.00	0.00	0.00	0.00	0.01		0.00	0.00		0.00	0.20	0.01
Control Blank												
Control Blank	0.00	0.00	0.70		0.02		0.00	0.00		0.00	0.00	0.01
Acid Blank												
Acid Blank	0.00	0.00	0.00		0.00		0.00	0.00		0.00	0.00	0.00

Elements	MgO	MnO	Mo	Na2O	Ni	P2O5	Rb	S	S	Sc	SiO2	Sn
Units	%	%	ppm	%	ppm	%	ppm	%	%	ppm	%	ppm
Detection	0.01	0.01	0.10	0.01	0.50	0.01	0.10	0.01	0.01	10.0	0.0	1.00
Method	FB6/OE	FB6/OE	4A/MS	FB6/OE	4A/MS	FB6/OE	FB6/MS	/CSA	FB6/OE	FB6/OE	FB6/OE	FB6/MS
Corsica												
CO13-20	1.01	0.04	0.20	3.29	2.40	0.02	195.10	X	0.01	X	74.7	3.00
CO13-21	38.7	0.11	X	0.13	2166	0.00	0.40	0.07	0.10	X	38.5	X
CO13-22	10.63	0.13	X	3.40	152	0.15	5.50	X	X	41.0	47.9	2.00
CO13-27	27.9	0.98	X	0.11	1528	0.02	0.30	0.00	X	27.0	29.1	X
CO13-28-1	0.34	0.46	X	0.18	18.7	0.03	6.70	0.02	0.04	X	9.2	X
CO13-28-2	1.22	0.54	0.40	0.26	52.6	0.06	34.20	0.02	X	X	14.9	X
CO13-29	1.64	0.10	X	1.03	61.3	0.11	81.60	X	X	10.0	78.8	2.00
CO13-30	7.15	0.18	X	3.92	35.6	0.01	17.10	0.02	X	34.0	52.6	X
CO13-31	39.0	0.13	X	0.13	2028	0.00	0.30	0.03	0.05	X	40.5	X
CO13-32	9.58	0.19	X	3.72	133	0.13	9.30	X	0.02	35.0	50.4	1.00
CO13-33	38.4	0.09	X	0.14	2254	0.00	0.30	0.11	0.11	10.0	39.2	X
CO13-34	0.61	0.02	X	0.86	12.80	0.20	15.80	X	0.00	X	93.2	X
CO13-35	3.41	0.13	X	2.63	60.1	0.19	40.70	X	0.00	11.0	69.4	2.00
CO13-36	0.54	0.09	X	0.17	20.2	0.07	17.40	0.02	0.02	X	13.0	X
CO13-40	36.4	0.10	X	0.11	2287	0.00	0.20	0.03	0.04	X	42.2	X
CO13-41	3.78	0.17	X	2.16	81.6	0.06	13.60	0.02	X	13.0	37.7	1.00
CO13-41-2	3.50	0.17	X	1.92	80.1	0.06	18.60	0.02	0.02	11.0	39.0	X
CO13-49	9.65	0.12	X	4.76	91.0	0.02	1.50	X	0.03	37.0	51.1	3.00
CO13-50	9.63	0.11	X	3.69	136	0.02	53.90	X	0.03	32.0	51.2	X
CO13-55	37.7	0.11	X	0.09	2047	0.02	0.40	0.02	0.03	X	42.6	X
CO13-56a	4.84	0.21	0.10	0.42	215	0.13	0.50	0.02	0.02	22.0	41.6	3.00
CO13-56b-1	4.93	0.19	0.10	0.41	154	0.14	0.30	X	0.02	13.0	42.3	2.00
CO13-56b-2	5.70	0.20	X	0.41	157	0.11	0.30	X	0.01	13.0	43.6	2.00
CO13-57	8.39	0.12	X	2.43	129	0.04	2.40	0.02	X	34.0	42.5	X
CO13-58	0.32	0.43	0.40	0.12	12.40	0.04	3.40	0.02	0.03	X	10.7	X
CO13-59-1	1.71	0.10	X	0.46	82.3	0.09	75.90	0.02	0.01	11.0	62.4	2.00
CO13-59-2	0.53	0.16	0.20	0.14	11.6	0.05	6.00	0.02	0.02	X	22.2	X
CO13-59-3	1.32	0.12	X	0.40	51.6	0.07	48.70	0.0	0.03	X	49.4	1.00
CO13-60a	8.95	0.24	X	2.41	87.8	0.22	0.70	X	0.03	32.0	52.5	1.00
CO13-60b-1	7.98	0.27	X	4.82	98.0	0.22	0.40	0.02	0.01	45.0	46.7	2.00
CO13-60b-2	7.67	0.26	X	4.79	101	0.20	0.40	X	0.02	43.0	46.5	1.00
CO13-61-1	1.96	0.11	X	0.18	83.4	0.11	97.90	X	0.01	12.0	75.6	2.00
CO13-61-2	1.83	0.10	X	0.14	72.5	0.08	84.30	X	X	10.0	79.5	1.00
CO14-03	17.89	0.18	0.10	X	613	0.09	0.1	0.43	0.54	40	31.4	2.00
CO14-04	24.78	0.06	X	X	1579	0.01	0.2	0.94	0.96	X	58.7	X
CO14-05	7.45	0.19	X	1.76	89.60	0.11	0.70	0.67	-	40.0	46.5	3.00

Elements	MgO	MnO	Mo	Na2O	Ni	P2O5	Rb	S	S	Sc	SiO2	Sn
Units	%	%	ppm	%	ppm	%	ppm	%	%	ppm	%	ppm
Detection	0.01	0.01	0.10	0.01	0.50	0.01	0.10	0.01	0.01	10.0	0.0	1.00
Method	FB6/OE	FB6/OE	4A/MS	FB6/OE	4A/MS	FB6/OE	FB6/MS	/CSA	FB6/OE	FB6/OE	FB6/OE	FB6/MS
Zermatt-Saas												
S09-VSZ02	10.5	0.23	X	0.07	152	0.02	0.80	X	-	48.0	42.3	3.00
S09-VSZ03	35.5	0.09	0.10	0.05	1747	X	0.60	0.01	-	14.0	40.6	3.00
S09-VSZ05	39.3	0.12	X	0.01	2093	X	0.40	0.02	-	X	40.4	2.00
S09-GSZ11	40.9	0.16	X	0.05	1990	X	0.30	X	-	X	40.8	2.00
S09-AZS09	37.4	0.21	X	0.05	1498	0.08	0.40	X	-	12.0	38.8	2.00
PF001	33.5	0.11	0.00	0.07	1449	0.02	0.30	0.00	0.00	13.0	37.4	0.00
LC015	36.4	0.14	0.00	0.09	1929	0.00	0.70	0.02	0.04	13.0	37.7	0.00
CHECKS												
CO13-20	1.00	0.04	0.30	3.20	3.60	0.02	196.80	0.02	0.01	0.0	74.5	4.00
CO13-55	37.72	0.11	0.00	0.07	2002	0.00	0.30	0.02	0.03	0.0	42.5	0.00
STANDARDS												
FER-3												
GBW07103			3.40		1.50							
GBW07103	0.41	0.06		3.14		0.09	473.10		0.04	0.0	74.0	14.00
OREAS 45e								0.05				
GBW07105			2.80		148							
GBW07105	7.47	0.17		3.31		0.96	38.10		0.02	14.0	44.0	2.00
MA-1b								1.19				
SY-4												
FER-3												
GBW07107			0.40		45.8							
GBW07107	1.85	0.02		0.37		0.16	203		0.04	18.0	57.0	2.00
GGC-05								0.06				
OREAS 24b			3.80		59.7							
OREAS 24b	2.56	0.06		1.13		0.16	169		0.22	14.0	63.6	4.00
OREAS 25a			2.30		44.6							
OREAS 25a	0.52	0.07		0.23		0.11	61.10		0.07	13.0	52.2	5.00
MPL-5												
BLANKS												
Control Blank	0.01	0.00	0.00	0.00	0.00	0.00	0.00	0.00	0.00	0.0	0.0	0.00
Control Blank			0.00		0.00							
Control Blank	0.00	0.00		0.07		0.00	0.30		0.04	0.0	0.0	0.00
Acid Blank			0.00		0.00							
Acid Blank	0.00	0.00		0.00		0.00	0.00		0.00	0.0	0.0	0.00

Elements	Sr	TiO2	U	V	V	W	Zn	LOI-1000
Units	ppm	%	ppm	ppm	ppm	ppm	ppm	%
Detection	0.20	0.01	0.10	10.00	5.00	1.00	1.00	0.01
Method	FB6/MS	FB6/OE	FB6/MS	FB6/OE	FB6/MS	FB6/MS	4A/MS	/TGA
Corsica								
CO13-20	7.90	0.12	4.70	0.00	18.00	534.00	22.00	1.20
CO13-21	0.50	0.03	X	49.00	15.00	26.00	37.00	12.08
CO13-22	333.20	1.55	0.20	286.00	288.00	166.00	25.00	3.56
CO13-27	1.00	7.27	0.00	563.00	536.00	43.00	64.00	8.93
CO13-28-1	362.20	0.04	0.40	X	16.00	177.00	12.00	39.26
CO13-28-2	388.40	0.20	0.70	34.00	43.00	94.00	38.00	34.50
CO13-29	25.40	0.33	1.00	71.00	87.00	374.00	58.00	1.62
CO13-30	86.70	0.45	X	166.00	167.00	100.00	39.00	3.22
CO13-31	X	0.03	X	50.00	25.00	49.00	39.00	11.68
CO13-32	124.30	0.36	0.20	114.00	118.00	116.00	76.00	4.08
CO13-33	1.70	0.05	X	48.00	23.00	36.00	40.00	11.59
CO13-34	10.60	0.07	0.70	41.00	58.00	471.00	18.00	0.34
CO13-35	377.00	0.35	1.50	161.00	176.00	378.00	45.00	1.28
CO13-36	341.70	0.08	0.30	12.00	27.00	109.00	19.00	37.19
CO13-40	0.30	0.04	0.00	47.00	14.00	80.00	63.00	11.23
CO13-41	221.30	0.39	0.50	73.00	79.00	147.00	39.00	19.64
CO13-41-2	217.60	0.26	0.50	58.00	72.00	206.00	35.00	20.30
CO13-49	36.80	0.34	X	161.00	173.00	154.00	27.00	2.03
CO13-50	53.00	0.27	X	120.00	138.00	190.00	33.00	3.19
CO13-55	1.30	0.02	X	41.00	25.00	48.00	32.00	10.66
CO13-56a	27.50	0.80	2.20	129.00	141.00	166.00	133.00	5.36
CO13-56b-1	25.00	0.44	1.20	95.00	110.00	484.00	97.00	4.63
CO13-56b-2	23.20	0.39	1.00	88.00	96.00	278.00	99.00	4.30
CO13-57	141.40	0.28	X	97.00	96.00	196.00	31.00	12.50
CO13-58	481.10	0.02	0.20	X	14.00	88.00	10.00	38.89
CO13-59-1	64.90	0.36	1.00	60.00	76.00	209.00	86.00	9.27
CO13-59-2	250.70	0.05	0.20	X	19.00	282.00	23.00	33.64
CO13-59-3	138.70	0.27	0.70	43.00	59.00	282.00	62.00	17.93
CO13-60a	46.10	1.57	0.30	216.00	228.00	136.00	74.00	6.61
CO13-60b-1	93.10	1.85	0.30	407.00	395.00	89.00	192.00	3.91
CO13-60b-2	92.50	1.86	0.30	387.00	396.00	85.00	195.00	3.79
CO13-61-1	342.20	0.40	1.30	91.00	105.00	305.00	62.00	1.89
CO13-61-2	234.30	0.32	1.00	77.00	88.00	785.00	60.00	1.89
CO14-03	9.7	5.24	0.1	470	473	22	92	7.24
CO14-04	1.7	0.04	X	33	28	7	56	5.45
CO14-05	150.00	2.78	X	446.00	-	45.00	3.40	5.13

Elements	Sr	TiO2	U	V	V	W	Zn	LOI-1000
Units	ppm	%	ppm	ppm	ppm	ppm	ppm	%
Detection	0.20	0.01	0.10	10.00	5.00	1.00	1.00	0.01
Method	FB6/MS	FB6/OE	FB6/MS	FB6/OE	FB6/MS	FB6/MS	4A/MS	/TGA
Zermatt-Saas								
S09-VSZ02	34.10	0.45	X	213.00	-	80.00	16.00	2.15
S09-VSZ03	1.90	0.06	X	74.00	-	24.00	49.00	9.78
S09-VSZ05	2.10	0.08	X	34.00	-	20.00	56.00	9.16
S09-GSZ11	1.00	0.01	X	21.00	-	19.00	45.00	7.36
S09-AZS09	2.60	0.63	X	53.00	-	18.00	91.00	2.00
PF001	2.50	0.89	0.00	119.00	136.00	39.00	53.00	10.31
LC015	2.30	0.09	0.00	82.00	63.00	68.00	55.00	10.72
CHECKS								
CO13-20	7.20	0.12	5.20	0.00	23.00	543.00	24.00	1.25
CO13-55	1.40	0.02	0.00	41.00	23.00	32.00	34.00	10.78
STANDARDS								
FER-3								
GBW07103							25.00	
GBW07103	109.70	0.29	19.90	24.00	33.00	10.00		
OREAS 45e								
GBW07105							155.00	
GBW07105	1177.40	2.29	1.40	175.00	183.00	3.00		
MA-1b								
SY-4								
FER-3								
GBW07107							57.00	
GBW07107	89.60	0.65	1.60	91.00	96.00	4.00		
GGC-05								
OREAS 24b							106.00	
OREAS 24b	123.90	0.79	3.30	118.00	127.00	7.00		
OREAS 25a							47.00	
OREAS 25a	47.90	1.89	3.40	183.00	178.00	4.00		
MPL-5								
BLANKS								
Control Blank	1.90	0.00	0.00	0.00	0.00	0.00	0.00	
Control Blank							1.00	
Control Blank	0.00	0.00	0.00	0.00	10.00	2.00		
Acid Blank							0.00	
Acid Blank	0.00	0.00	0.00	0.00	9.00	0.00		

X = less than detection limit. Method descriptions: FB6/MS = Lithium borate fusion + ICP-MS, FB6/OE = Li borate fusion + ICP-OES, 4A/MS = 4-acid digest ICP-MS, TGA = Thermo Gravimetric analysis, single point LOI at 1000ºC, AD71/VOL = Acid digestion (ceric sulfate) and titration, CSA = Total Carbon and sulfur by Induction Furnace and Infrared Spectrometry (CS analyser).

Sample preparation was carried out by Rosalind Crossley. All bulk analyses were performed by Intertek Genalysis at Maddington, Western Australia.

APPENDIX B

SUPPLEMENTARY DATA FOR THE ZERMATT-SAAS SAMPLES (CHAPTER 3)

The full analytical results of the compositions of minerals from the Zermatt-Saas samples are provided here. The data was collected using electron microprobe analysis (EMPA), using the technique as outlined in section 3.3.1. The mineral formulae calculation methods are provided in section 3.3.2. Each table includes the name given to the point of analysis, a description, average and standard deviation for each wt% oxide. The percent relative analytical uncertainty (2σ) is $\leq \pm$ 2% for silicates and oxides present at concentrations >5 wt%. Also included are preliminary mass balance calculations, and a summary of the method used.

B1: Silicate mineral chemistry

Serpentine and chlorite data

The Mg/(Mg+Fe) ratio $(X_{Mg})_{srp}$ ranges from 0.95–0.97 for LC-015, GSZ-11, VSZ-03 and VSZ-05, 0.90–0.91 for PF-001, and 0.91–0.99 for ASZ-09. The difference in (X_{Mg}) between chlorite and antigorite is statistically indistinguishable at 0.90–0.91 and 0.94–0.95 for both chlorite and antigorite in PF-001 and ASZ-09, respectively. The wide range of Mg numbers for ASZ-09 reflects a significant difference (P=0.01 for X_{Mg}) in composition between inclusions of antigorite in Ti-clinohumite (atg1) and veins and laths (atg2), with higher X_{Mg} values in atg1. Notably, there are significant differences in Al_2O_3 ($P=5x10^{-8}$), and MgO (P=0.001). Some antigorite inclusions in Ti-clinohumite were also found to contain up to 5.8 wt % TiO_2, but it is possible that a Ti-rich phase such as ilmenite was incorporated into the analysis volume.

There are significant differences in Cr, Al and Mg content between the minerals identified as antigorite in all samples, which reflects bulk compositional variation. Ni contents are similarly low in most samples, with contents of 0.1–0.3 wt % NiO (Table S3). However, some anomalous Ni concentrations of up to 0.64wt % in ASZ-09, 0.9 wt % in VSZ-03, and 2.3 wt % in VSZ-05 possibly reflect the inclusion of micron-size Ni-rich phases, e.g., pentlandite or a discrete Ni-rich serpentine vein (S4, S12).

An SiO_2 content of < 35 wt % and 10.8–13.4 wt % Al_2O_3 in chlorite is consistent with a penninite composition for chlorite in samples PF-001 and ASZ-09 which is defined as ~6.4–7 Si and a Fe/Fe+Mg ratio (XFe) of up to 0.1. In comparison, chlinochlore is present in VSZ-02, with 5.6–5.7 Si c.p.f.u and XFe of 0.15–0.17. An intermediate phase between chlorite and antigorite in PF-001 and ASZ-09 is comprised of 35.5–37.9 wt % SiO_2, 8.3–10.5 wt % Al_2O_3 and 33.8–35.3 wt % MgO (Fig. 4b, Table 2), with SiO_2 contents statistically distinguishable from serpentine (P value=1.22×10^{-4}) and from chlorite (P =5.85×10^{-4}). It is possible that the intermediate composition is produced by analysis of fine interlayers of antigorite and penninite (c.f. Cressey et al. 2008, Table S4, S13).

Tremolite and talc

Tremolite and talc were analysed in PF-001. The maximum Al_2O_3 contents in talc and tremolite in PF-001 are 1.2 wt % and 2.1 wt %, respectively with average values of 0.5 and 0.2 wt % Al_2O_3 in tremolite and talc, correspondingly. Tremolite FeO content varies from 2.5 to 3.4 wt % FeO and shows a slight decrease in Fe in the vicinity of magnetite. Talc FeO contents are slightly lower than tremolite at 2.1–2.3 wt % FeO (Table S4, S14).

Clinopyroxene

Clinopyroxene is classified as diopside in composition in VSZ-02, VSZ-03 and ASZ-09, however the Al, Fe, Ti and Cr content varies within samples and between samples. Diopside grains in VSZ-03 have the highest Al_2O_3 contents with up to 2.3 wt %, with up to 1.1 wt % in VSZ-02, and negligible amount of Al_2O_3 in ASZ-09 diopsides. Al_2O_3 decreases with increasing FeO (R^2 = 0.7–0.8, Fig. 5c) and Fe and Ti decrease with increasing Si and Mg (R^2=0.7–0.8). Iron and Ti are highest in the diopside which records exsolution lamellae in VSZ-02, followed by diopside with magnetite replacement along cleavage in VSZ-03, and the lowest in sheared diopside in VSZ-03 and ASZ-09 (Fig. 5d). Corresponding to elevated Al_2O_3 contents, the highest Cr_2O_3 concentrations are recorded in VSZ-03 with up to 1.4 wt %, with no detectable Cr_2O_3 in ASZ-09 or VSZ-02 (Table S4, S15).

Olivine

Olivine is present in VSZ-03, VSZ-05 and GSZ-11 and is forsteritic with 1.7–1.8 Mg cations per formula unit in samples VSZ-03 and VSZ-05, and a homogeneous composition in GSZ-11 (~1.8 cations of Mg, Table S4, S16).

B2 Garnet analyses. Formulae were calculated on the basis of 8 cations.

EDS

Analysis	vsz-02_GRT1 2	vsz-02_GRT1 5	vsz-02_GRT1 6	vsz-02_GRT1 8	vsz-02_A3_GRT2 7	vsz-02_A3_GRT2 8	vsz-02_A3_GRT2 9	vsz-02_A3_GRT2 1	VSZ-02_GRT3 6	VSZ-02_GRT3 8	VSZ-02_GRT3 1
Description	Grt1	Grt1	Grt1	Grt1	Grt1	Grt1	Grt1	Grt1			
wt%											
SiO_2	39.74	39.40	39.38	39.50	39.57	39.31	39.31	40.10	38.48	38.43	38.91
TiO_2	0.42	0.47	0.60	0.57	0.47	0.68	0.47	0.50	1.25	1.03	1.00
Al_2O_3	20.60	20.61	20.52	20.82	21.14	20.22	20.82	20.82	19.95	19.78	20.86
Cr_2O_3	b.d.l	b.d.l	b.d.l	b.d.l	b.d.l	b.d.l	b.d.l	b.d.l	b.d.l	b.d.l	b.d.l
V_2O_3	b.d.l	b.d.l	b.d.l	b.d.l	b.d.l	b.d.l	b.d.l	b.d.l	b.d.l	b.d.l	b.d.l
FeO*	8.34	6.61	5.70	7.23	7.71	8.44	7.68	6.23	7.06	8.29	6.01
MnO	0.59	0.46	0.00	0.39	0.28	0.68	0.00	0.45	0.52	0.37	0.53
MgO	0.51	0.48	0.00	0.41	0.00	0.51	0.46	0.46	0.00	0.56	0.27
NiO	0.85	0.00	0.00	0.00	0.00	0.00	0.00	0.00	0.00	0.00	0.00
CaO	33.28	33.89	35.36	34.30	33.46	32.87	33.32	34.96	33.40	32.26	33.66
Na2O											
Total	104.33	101.93	101.56	103.23	102.63	102.72	102.07	103.53	100.67	100.73	101.22
Si	2.92	2.95	2.95	2.92	2.95	2.93	2.94	2.95	2.93	2.92	2.93
Ti	0.02	0.03	0.03	0.03	0.03	0.04	0.03	0.03	0.07	0.06	0.06
Al	1.78	1.82	1.81	1.81	1.86	1.78	1.83	1.81	1.79	1.77	1.85
Cr	-	-	-	-	-	-	-	-	-	-	-
V	-	-	-	-	-	-	-	-	-	-	-
Fe^{3+}	0.22	0.18	0.19	0.19	0.14	0.22	0.17	0.19	0.21	0.23	0.15
Fe^{2+}	0.30	0.23	0.17	0.26	0.34	0.30	0.31	0.19	0.24	0.30	0.23
Mn	0.04	0.03	0.00	0.02	0.02	0.04	0.00	0.03	0.03	0.02	0.03
Mg	0.06	0.05	0.00	0.05	0.00	0.06	0.05	0.05	0.00	0.06	0.03
Ni	0.05	0.00	0.00	0.00	0.00	0.00	0.00	0.00	0.00	0.00	0.00
Ca	2.62	2.71	2.84	2.72	2.67	2.63	2.67	2.75	2.72	2.63	2.72
Na	0.00	0.00	0.00	0.00	0.00	0.00	0.00	0.00	0.00	0.00	0.00

***Total Fe**

WDS

Analysis	S-09-VSZ02-area3_grt1_zoning	S-09-VSZ02-area3_grt1_zoning	S-09-VSZ02-area3_grt1_zoning	S-09-VSZ02-area3_grt1_zoning	S-09-VSZ02-area4_nr_px	S-09-VSZ02-area4_ttn_nr_px	S-09-VSZ02-area4 _inpx	S-09-VSZ02-area4_grt2	S-09-VSZ02-area4_grt2	Average	St Dev
Description	Grt2	Grt2	Grt2	Grt2	Grt2	Grt2	Grt2	Grt2	Grt2	Grt2	Grt2
wt%											
SiO_2	39.38	39.07	38.41	38.67	37.34	36.28	39.52	38.94	39.05	38.94	0.87
TiO_2	0.71	0.54	0.69	0.89	1.29	1.29	0.64	0.93	0.56	0.75	0.29
Al_2O_3	20.49	20.39	19.65	18.99	16.68	16.34	18.61	20.24	20.38	19.90	1.32
Cr_2O_3	b.d.l	b.d.l	b.d.l	b.d.l	b.d.l	b.d.l	b.d.l	b.d.l	b.d.l	b.d.l	b.d.l
V_2O_3	b.d.l	b.d.l	b.d.l	b.d.l	b.d.l	b.d.l	b.d.l	b.d.l	b.d.l	b.d.l	b.d.l
FeO*	5.97	7.34	8.77	9.60	9.65	10.38	8.37	7.36	7.19	7.70	1.29
MnO	0.59	0.46	0.37	0.69	0.56	0.42	0.68	0.22	0.27	0.43	0.20
MgO	0.28	0.32	0.44	0.67	2.26	5.03	1.07	0.40	0.40	0.73	1.12
NiO	0.02	0.00	0.00	0.00	0.00	0.00	0.01	0.00	0.02	0.05	0.19
CaO	34.44	33.01	31.77	31.44	31.16	28.33	32.10	33.29	33.28	32.98	1.55
Na2O	0.13	0.11	0.14	0.13	0.08	0.09	0.12	0.11	0.13	0.12	0.02
Total	102.06	101.27	100.23	101.10	99.11	98.26	101.18	101.54	101.30	101.53	1.42
Si	2.94	2.95	2.94	2.94	2.89	2.80	2.99	2.93	2.94	2.93	0.04
Ti	0.04	0.03	0.04	0.05	0.08	0.07	0.04	0.05	0.03	0.04	0.02
Al	1.80	1.81	1.77	1.70	1.52	1.49	1.66	1.79	1.81	1.76	0.10
Cr	-	-	-	-	-	-	-	-	-	-	-
V	-	-	-	-	-	-	-	-	-	-	-
Fe^{3+}	0.20	0.19	0.23	0.30	0.48	0.51	0.34	0.21	0.19	0.24	0.10
Fe^{2+}	0.19	0.29	0.35	0.33	0.16	0.17	0.21	0.27	0.28	0.26	0.06
Mn	0.04	0.03	0.02	0.04	0.04	0.03	0.04	0.01	0.02	0.03	0.01
Mg	0.03	0.04	0.05	0.08	0.26	0.58	0.12	0.04	0.05	0.08	0.13
Ni	0.00	0.00	0.00	0.00	0.00	0.00	0.00	0.00	0.00	0.00	0.01
Ca	2.76	2.67	2.60	2.56	2.58	2.34	2.60	2.68	2.68	2.66	0.10
Na	0.02	0.02	0.02	0.02	0.01	0.01	0.02	0.02	0.02	0.01	0.01

	EDS					WDS				
Analysis	VSZ-02_GRT3 2	VSZ-02_GRT3 3	VSZ-02_GRT3 4	VSZ-02_GRT3 5	VSZ-02_GRT3 7	S-09-VSZ02-area3_grt1_zoning	S-09-VSZ02-area3_grt1_zoning	S-09-VSZ02-area3_grt1	S-09-VSZ02-area3_grt1	S-09-VSZ02-area4_grt1
Description	Gr1	Grt1	Grt1	Grt1	Gr1	Grt1	Grt1	Grt1	Grt1	Grt1
wt%										
SiO_2	39.12	39.12	39.10	39.12	39.03	39.78	39.76	38.77	39.35	39.91
TiO_2	1.60	1.90	1.65	1.98	1.53	0.60	1.04	0.76	0.98	0.84
Al_2O_3	22.35	22.64	22.47	22.35	21.77	22.30	22.59	20.78	20.98	22.18
Cr_2O_3	b.d.l	b.d.l	b.d.l	b.d.l	b.d.l	b.d.l	b.d.l	b.d.l	b.d.l	b.d.l
V_2O_3	b.d.l	b.d.l	b.d.l	b.d.l	b.d.l	b.d.l	b.d.l	b.d.l	b.d.l	b.d.l
FeO*	0.58	0.45	0.93	0.76	2.77	2.60	0.99	4.11	4.35	1.10
MnO	0.00	0.00	0.00	0.22	0.00	0.16	0.10	0.42	0.34	0.06
MgO	0.00	0.00	0.00	0.00	0.00	0.09	0.01	0.17	0.24	0.40
NiO	0.00	0.00	0.00	0.00	0.00	0.00	0.00	0.00	0.01	0.00
CaO	38.58	38.95	38.09	38.30	36.36	36.55	37.60	35.16	35.46	37.03
Na2O						0.12	0.14	0.12	0.12	0.12
Total	102.24	103.06	102.24	102.74	101.46	102.22	102.26	100.30	101.83	101.65
Si	2.89	2.86	2.89	2.88	2.92	2.94	2.93	2.93	2.93	2.95
Ti	0.09	0.10	0.09	0.11	0.09	0.03	0.06	0.04	0.06	0.05
Al	1.94	1.95	1.96	1.94	1.92	1.94	1.96	1.85	1.84	1.93
Cr	-	-	-	-	-	-	-	-	-	-
V	-	-	-	-	-	-	-	-	-	-
Fe^{3+}	0.04	0.03	0.04	0.04	0.08	0.06	0.04	0.15	0.16	0.07
Fe^{2+}	0.00	0.00	0.01	0.00	0.09	0.12	0.04	0.13	0.13	0.01
Mn	0.00	0.00	0.00	0.01	0.00	0.01	0.01	0.03	0.02	0.00
Mg	0.00	0.00	0.00	0.00	0.00	0.01	0.00	0.02	0.03	0.04
Ni	0.00	0.00	0.00	0.00	0.00	0.00	0.00	0.00	0.00	0.00
Ca	3.05	3.05	3.01	3.02	2.91	2.89	2.97	2.85	2.83	2.94
Na	0.00	0.00	0.00	0.00	0.00	0.02	0.02	0.02	0.02	0.02

EDS

Analysis	S-09-VSZ02-area4_grt1	S-09-VSZ02-area4_grt2	Average	St Dev
Description	Grt1	Grt1		
wt%				
SiO_2	39.62	39.94	39.39	0.40
TiO_2	0.64	0.50	1.17	0.53
Al_2O_3	22.40	22.74	22.13	0.63
Cr_2O_3	b.d.l	b.d.l		
V_2O_3	b.d.l	b.d.l		
FeO*	1.87	1.29	1.82	1.35
MnO	0.18	0.06	0.13	0.14
MgO	0.05	0.03	0.08	0.13
NiO	0.00	0.00	0.00	0.00
CaO	37.03	37.60	37.23	1.19
Na2O	0.12	0.11	0.12	0.01
Total	101.92	102.28	102.01	0.70
Si	2.93	2.94	2.92	0.03
Ti	0.04	0.03	0.07	0.03
Al	1.95	1.97	1.93	0.04
Cr	-	-		
V	-	-		
Fe^{3+}	0.05	0.03	0.06	0.04
Fe^{2+}	0.08	0.06	0.06	0.05
Mn	0.01	0.00	0.01	0.01
Mg	0.00	0.00	0.01	0.01
Ni	0.00	0.00	0.00	0.00
Ca	2.94	2.97	2.95	0.07
Na	0.02	0.02	0.01	0.01

***Total Fe**

B3. Ti-clinohumite analyses. Formulae were calculated on the basis of 13 cations.

ASZ-09A	EDS				WDS					WDS			
Analysis Description	ASZ-09-A3_A4_TI_CHU 1	ASZ-09-A_A4_TICHU_2 1 2	ASZ-09-A_A4_TICHU_2 1 5	ASZ-09-A_A4_TICHU_2 1 6	ASZ-09a a1_ticln1	ASZ-09a a1_ticln1	ASZ-09a a1_ticln1	AV	St Dev	ASZ-09a a3_ti_cln	ASZ-09a a3_ti_cln	ASZ-09a a3_ti_cln	ASZ-09a a4_ticln
	Tichu2					Tichu2				Tichu3			
wt%													
SiO_2	36.72	36.47	35.06	36.60	36.91	36.96	36.98	36.53	0.68	36.91	37.03	37.11	38.32
TiO_2	4.88	5.14	4.90	4.92	4.94	4.54	4.36	4.81	0.27	4.30	4.40	4.70	3.29
Al_2O_3	0.00	0.00	0.00	0.00	0.00	0.00	0.00	0.00	0.00	0.00	0.00	0.00	1.37
Fe_2O_3	6.06	6.03	5.89	6.02	5.99	6.42	6.05	6.07	0.17	6.57	6.37	6.05	5.04
FeO	0.96	0.87	0.81	0.98	0.64	0.65	0.84	0.82	0.14	0.63	0.67	0.63	0.62
MnO													
MgO	51.10	49.79	48.59	50.90	49.19	49.08	49.26	49.70	0.95	49.20	49.11	49.13	45.37
ZnO	0.00	0.00	0.00	0.00	0.17	0.17	0.10	0.06	0.08	0.19	0.20	0.15	0.11
NiO	0.00	0.00	0.00	0.00	0.00	0.00	0.02	0.00	0.01	0.00	0.00	0.00	0.00
CaO	99.72	98.29	95.25	99.41	98.04	98.05	97.79	98.08	1.45	98.03	97.99	97.96	94.39
Total													
Si	3.90	3.94	3.90	3.90	4.01	4.02	4.02	3.96	0.06	4.01	4.02	4.03	4.34
Ti	0.39	0.42	0.41	0.39	0.40	0.37	0.36	0.39	0.02	0.35	0.36	0.38	0.28
Al	0.00	0.00	0.00	0.00	0.00	0.00	0.00	0.00	0.00	0.00	0.00	0.00	0.18
Fe^{2+}	0.54	0.55	0.55	0.54	0.54	0.58	0.55	0.55	0.02	0.60	0.58	0.55	0.48
Mn	0.09	0.08	0.08	0.09	0.06	0.06	0.08	0.08	0.01	0.06	0.06	0.06	0.06
Mg	8.09	8.02	8.06	8.08	7.97	7.95	7.98	8.02	0.06	7.97	7.96	7.96	7.65
Zn													
Ni	0.00	0.00	0.00	0.00	0.01	0.01	0.01	0.01	0.01	0.02	0.02	0.01	0.01
Ca	0.00	0.00	0.00	0.00	0.00	0.00	0.00	0.00	0.00	0.00	0.00	0.00	0.00
XMg	0.94	0.94	0.94	0.94	0.94	0.93	0.94	0.94	0.00	0.93	0.93	0.94	0.94

ASZ-09A								**ASZ-09B EDS**				
Analysis	ASZ-09a a4_ticln	ASZ-09a a4_ticln	ASZ-09a a4_ticln	ASZ-09a a4_ticln	ASZ-09a a4_ticln	Av	Std Dev	ASZ_09_b_Ti_cln_a 3_1 2	ASZ_09_b_Ti_cln_a 3_1 3	ASZ_09_b_Ti_cln_a 3_1 1	ASZ_09_area3_ticl n_2 2	ASZ_09_area3_ticl n_2 3
Description	Tichu3							Tichu2				
wt%												
SiO_2	37.14	37.27	36.99	37.02	37.04	37.20	0.43	36.62	36.34	36.68	36.53	36.12
TiO_2	4.38	4.55	4.14	4.07	4.16	4.22	0.40	5.13	4.82	4.66	4.28	4.32
Al_2O_3	0.00	0.00	0.00	0.00	0.00	0.15	0.46	0.00	0.00	0.00	0.00	0.00
Fe_2O_3	6.17	6.30	6.23	6.27	6.20	6.13	0.43	6.33	6.14	6.63	6.18	6.01
FeO	0.66	0.63	0.70	0.77	0.81	0.68	0.07	0.92	0.79	0.92	0.81	0.66
MnO												
MgO	49.24	49.55	49.13	49.09	49.03	48.76	1.28	49.94	49.75	49.47	49.90	49.87
ZnO	0.12	0.15	0.17	0.17	0.19	0.16	0.03	0.00	0.27	0.00	0.00	0.00
NiO	0.00	0.00	0.00	0.00	0.00	0.00	0.00	0.00	0.00	0.00	0.00	0.00
CaO	97.89	98.65	97.65	97.60	97.65	97.53	1.22	98.92	98.10	98.36	97.70	96.98
Total												
Si	4.04	4.02	4.03	4.03	4.04	4.06	0.10	3.93	3.93	3.97	3.96	3.94
Ti	0.36	0.37	0.34	0.33	0.34	0.35	0.03	0.41	0.39	0.38	0.35	0.35
Al	0.00	0.00	0.00	0.00	0.00	0.02	0.06	0.00	0.00	0.00	0.00	0.00
Fe^{2+}	0.56	0.57	0.57	0.57	0.57	0.56	0.03	0.57	0.56	0.60	0.56	0.55
Mn	0.06	0.06	0.06	0.07	0.08	0.06	0.01	0.08	0.07	0.08	0.07	0.06
Mg	7.98	7.97	7.98	7.97	7.97	7.93	0.11	8.00	8.03	7.97	8.06	8.10
Zn												
Ni	0.01	0.01	0.02	0.01	0.02	0.01	0.00	0.00	0.02	0.00	0.00	0.00
Ca	0.00	0.00	0.00	0.00	0.00	0.00	0.00	0.00	0.00	0.00	0.00	0.00
XMg	0.93	0.93	0.93	0.93	0.93	0.93	0.00	0.93	0.94	0.93	0.94	0.94

ASZ-09A

Analysis	ASZ_09_area3_ticln_2 1	ASZ-09-B-A1_TICLN12	ASZ-09-B-A1_TICLN13	ASZ-09-B-A1_TICLN14	ASZ-09-B-A1_TICLN11	Av	St Dev	ASZ-09-B-AREA4_TICLN_1 1	ASZ-09-B-AREA4_TICLN_1 2	ASZ-09-B-AREA4_TICLN_1 3	ASZ-09-B-A5_TICLN_12	ASZ-09-B-A5_TICLN_13
Description	Tichu2							Tichu3				
wt%												
SiO_2	36.45	35.83	36.10	35.98	36.36	36.30	0.28	35.53	36.40	36.77	36.17	35.40
TiO_2	4.32	4.64	4.71	4.90	4.79	4.66	0.28	4.52	4.63	4.45	5.04	4.88
Al_2O_3	0.00	0.00	0.00	0.00	0.00	0.00	0.00	0.00	0.00	0.00	0.00	0.00
Fe_2O_3	6.10	7.04	7.13	7.09	7.00	6.56	0.46	5.80	5.97	6.03	6.14	6.15
FeO	0.71	0.80	0.88	0.80	0.92	0.82	0.09	0.74	0.71	1.01	0.81	0.87
MnO												
MgO	49.99	49.34	49.04	49.74	50.33	49.74	0.37	49.16	48.99	50.50	49.22	48.66
ZnO	0.00	0.00	0.00	0.00	0.00	0.03	0.08	0.27	0.00	0.00	0.29	0.00
NiO	0.00	0.00	0.00	0.00	0.00	0.00	0.00	0.00	0.00	0.00	0.00	0.00
CaO	97.56	97.65	97.86	98.50	99.40	98.10	0.71	96.00	96.70	98.76	97.68	95.96
Total												
Si	3.95	3.90	3.93	3.88	3.89	3.93	0.03	3.92	3.99	3.94	3.94	3.92
Ti	0.35	0.38	0.39	0.40	0.39	0.38	0.02	0.37	0.38	0.36	0.41	0.41
Al	0.00	0.00	0.00	0.00	0.00	0.00	0.00	0.00	0.00	0.00	0.00	0.00
Fe^{2+}	0.55	0.64	0.65	0.64	0.63	0.59	0.04	0.53	0.55	0.54	0.56	0.57
Mn	0.07	0.07	0.08	0.07	0.08	0.08	0.01	0.07	0.07	0.09	0.08	0.08
Mg	8.08	8.01	7.96	8.01	8.02	8.02	0.05	8.08	8.01	8.07	7.99	8.03
Zn												
Ni	0.00	0.00	0.00	0.00	0.00	0.00	0.01	0.02	0.00	0.00	0.03	0.00
Ca	0.00	0.00	0.00	0.00	0.00	0.00	0.00	0.00	0.00	0.00	0.00	0.00
XMg	0.94	0.93	0.92	0.93	0.93	0.93	0.00	0.94	0.94	0.94	0.93	0.93

ASZ-09A									**VSZ-03**				
Analysis Description	ASZ-09-B-A5_TICLN_1 1 Tichu3	ASZ-09-B-A5_TICLN_1 2	ASZ-09-B-A5-TICLN-2 2	ASZ-09-B-A5-TICLN-2 3	ASZ-09-B-A5-TICLN-2 5	ASZ-09-B-A5-TICLN-2 1	Av	Std Dev	VSZ-03-A1_TICLN Tichu1	VSZ-03_A1_TICLN_2 2	VSZ-03_A1_TICLN_2 5	VSZ-03_A1_TICLN_2 1	VSZ-03_A2_TICHU_1 2
wt%													
SiO_2	35.50	35.89	36.79	36.21	36.06	35.57	36.03	0.50	37.02	36.75	35.95	35.74	37.13
TiO_2	5.03	4.52	4.69	4.74	4.50	4.69	4.70	0.21	3.36	3.75	3.99	3.92	3.83
Al_2O_3	0.00	0.00	0.00	0.00	0.00	0.00	0.00	0.00	0.00	0.00	0.00	0.00	0.00
Fe_2O_3	6.21	6.11	6.11	6.06	5.96	5.97	6.05	0.12	10.59	10.25	9.85	9.80	10.14
FeO	0.99	0.93	0.84	0.83	0.87	0.83	0.86	0.09	0.56	0.63	0.52	0.52	0.58
MnO													
MgO	48.59	48.59	49.77	49.59	48.26	48.68	49.09	0.65	49.72	47.51	47.38	46.60	49.40
ZnO	0.00	0.00	0.00	0.00	0.00	0.00	0.05	0.11	0.32	0.00	0.33	0.00	0.25
NiO	0.00	0.00	0.00	0.00	0.00	0.17	0.02	0.05	0.00	0.00	0.00	0.00	0.00
CaO	96.33	96.04	98.20	97.42	95.64	95.90	96.79	1.06	101.57	98.89	98.03	96.59	101.34
Total													
Si	3.92	3.97	3.97	3.94	4.00	3.93	3.95	0.03	3.90	4.00	3.94	3.98	3.93
Ti	0.42	0.38	0.38	0.39	0.38	0.39	0.39	0.02	0.27	0.31	0.33	0.33	0.30
Al	0.00	0.00	0.00	0.00	0.00	0.00	0.00	0.00	0.00	0.00	0.00	0.00	0.00
Fe^{2+}	0.57	0.56	0.55	0.55	0.55	0.55	0.55	0.01	0.93	0.93	0.90	0.91	0.90
Mn	0.09	0.09	0.08	0.08	0.08	0.08	0.08	0.01	0.05	0.06	0.05	0.05	0.05
Mg	8.00	8.01	8.02	8.04	7.99	8.03	8.02	0.03	7.82	7.71	7.75	7.73	7.79
Zn													
Ni	0.00	0.00	0.00	0.00	0.00	0.00	0.00	0.01	0.03	0.00	0.03	0.00	0.02
Ca	0.00	0.00	0.00	0.00	0.00	0.02	0.00	0.01	0.00	0.00	0.00	0.00	0.00
XMg	0.93	0.93	0.94	0.94	0.94	0.94	0.94	0.00	0.89	0.89	0.90	0.89	0.90

ASZ-09A									VSZ-05				
Analysis	VSZ-03_A2_TICHU_1 3	VSZ-03_A2_TICHU_1 1	VSZ-03_A3_TI_CHU 2	VSZ-03_a4_tichu 1 1	VSZ-03_a4_tichu 1 2	VSZ-03_A4_TICHU_2	Average	Std Dev	VSZ05-area1_ticln 2	VSZ05-area1_ticln 2	VSZ05-area1_ticln 2	VSZ05-area1_ticln 3	VSZ05-area1_ticln 3
Description	Tichu1								Tichu4				
wt%													
SiO_2	37.41	37.15	34.31	36.57	36.45	35.85	36.29	0.39	36.77	36.82	36.71	36.62	38.56
TiO_2	3.54	3.52	4.20	4.24	4.08	3.97	4.10	0.14	3.67	3.53	4.05	3.93	2.43
Al_2O_3	0.00	0.00	0.00	0.00	0.00	0.00	0.00	0.00	0.00	0.00	0.02	0.00	0.68
Fe_2O_3	10.03	9.94	10.67	10.02	10.21	10.16	10.13	0.10	8.47	8.47	8.86	8.04	6.19
FeO	0.48	0.59	0.37	0.49	0.43	0.52	0.48	0.05	0.33	0.29	0.44	0.39	0.27
MnO													
MgO	49.50	49.37	45.44	49.01	48.48	47.81	48.43	0.60	47.83	47.89	46.85	48.10	44.21
ZnO	0.37	0.36	0.32	0.31	0.00	0.32	0.21	0.18	0.24	0.29	0.35	0.26	0.19
NiO	0.00	0.00	0.00	0.00	0.00	0.00	0.00	0.00	0.00	0.00	0.02	0.00	0.00
CaO	101.33	100.94	95.30	100.64	99.65	98.63	99.64	1.01	97.50	97.45	97.53	97.57	92.84
Total													
Si	3.95	3.94	3.89	3.90	3.93	3.91	3.91	0.01	4.04	4.04	4.05	4.02	4.45
Ti	0.28	0.28	0.36	0.34	0.33	0.33	0.33	0.01	0.30	0.29	0.34	0.32	0.21
Al	0.00	0.00	0.00	0.00	0.00	0.00	0.00	0.00	0.00	0.00	0.00	0.00	0.09
Fe^{2+}	0.89	0.88	1.01	0.89	0.92	0.93	0.91	0.02	0.78	0.78	0.82	0.74	0.60
Mn	0.04	0.05	0.04	0.04	0.04	0.05	0.04	0.00	0.03	0.03	0.04	0.04	0.03
Mg	7.80	7.81	7.68	7.79	7.78	7.77	7.78	0.01	7.83	7.84	7.71	7.86	7.61
Zn													
Ni	0.03	0.03	0.03	0.03	0.00	0.03	0.02	0.02	0.02	0.03	0.03	0.02	0.02
Ca	0.00	0.00	0.00	0.00	0.00	0.00	0.00	0.00	0.00	0.00	0.00	0.00	0.00
XMg	0.90	0.90	0.88	0.90	0.89	0.89	0.89	0.00	0.91	0.91	0.90	0.91	0.93

ASZ-09A

Analysis	VSZ05-area2_ticln	VSZ05-area2_ticln	VSZ05-area2_ticln	Average	Std Dev
Description	Tichu4				
wt%					
SiO_2	36.82	39.17	37.30	37.26	0.94
TiO_2	4.32	1.86	3.50	3.42	0.79
Al_2O_3	0.00	0.00	0.00	0.08	0.23
Fe_2O_3	8.03	7.90	8.17	8.03	0.75
FeO	0.44	0.37	0.43	0.38	0.07
MnO					
MgO	48.21	49.45	48.60	47.71	1.48
ZnO	0.23	0.31	0.24	0.26	0.05
NiO	0.00	0.00	0.00	0.00	0.01
CaO	98.21	99.28	98.45	97.35	1.81
Total					
Si	4.02	4.19	4.05	4.10	0.14
Ti	0.35	0.15	0.29	0.28	0.06
Al	0.00	0.00	0.00	0.01	0.03
Fe^{2+}	0.73	0.71	0.74	0.74	0.06
Mn	0.04	0.03	0.04	0.04	0.01
Mg	7.84	7.89	7.86	7.81	0.09
Zn					
Ni	0.02	0.03	0.02	0.02	0.00
Ca	0.00	0.00	0.00	0.00	0.00
XMg	0.91	0.92	0.91	0.91	0.01

B4. Titanite analyses. Formulae were calculated on the basis of 3 cations.

	WDS											
Analysis	S-09-VSZ02-area3_ttn	S-09-VSZ02-area3_ttn	S-09-VSZ02-area3_ttn	S-09-VSZ02-area4_ttn1	S-09-VSZ02-area4_ttn1	S-09-VSZ02-area4_ttn1	S-09-VSZ02-area4_ttn3	S-09-VSZ02-area4_ttn3	S-09-VSZ02-area2_ttn1	S-09-VSZ02-area2_ttn1	S-09-VSZ02-area2_ttn	S-09-VSZ02-area2_ttn2
Description												
wt%												
SiO_2	31.20	31.07	32.09	30.86	30.92	31.06	30.80	30.80	30.84	30.84	30.79	30.79
TiO_2	37.83	37.35	33.94	37.55	38.25	37.17	38.75	38.75	37.87	37.37	38.72	38.72
Al_2O_3	1.67	2.04	3.78	1.53	1.22	2.02	1.20	1.20	1.33	1.79	0.94	0.94
Cr_2O_3	0.00	0.00	0.00	0.00	0.00	0.00	0.00	0.00	0.00	0.00	0.00	0.00
V_2O_3	0.00	0.00	0.00	0.06	0.08	0.06	0.07	0.07	0.01	0.00	0.05	0.05
FeO	0.43	0.45	0.70	0.49	0.40	0.43	0.36	0.36	0.73	0.67	0.47	0.47
MnO	0.00	0.00	0.00	0.00	0.00	0.00	0.00	0.00	0.00	0.00	0.00	0.00
MgO	0.00	0.00	0.02	0.00	0.01	0.00	0.00	0.00	0.01	0.00	0.09	0.09
ZnO	0.00	0.02	0.01	0.00	0.00	0.00	0.00	0.00	0.00	0.00	0.03	0.03
NiO	0.00	0.00	0.01	0.00	0.00	0.00	0.01	0.01	0.01	0.00	0.00	0.00
CaO	28.91	28.90	29.51	28.75	28.61	29.01	28.67	28.67	28.63	28.93	28.54	28.54
	0.09	0.09	0.12	0.07	0.11	0.09	0.11	0.11	0.09	0.09	0.07	0.07
Total	100.14	99.92	100.18	99.32	99.63	99.85	99.97	99.97	99.53	99.72	99.71	99.71
Si	1.01	1.00	1.02	1.00	1.00	1.00	1.00	1.00	1.00	1.00	1.00	1.00
Ti	0.92	0.91	0.81	0.92	0.93	0.90	0.94	0.94	0.93	0.91	0.95	0.95
Al	0.06	0.08	0.14	0.06	0.05	0.08	0.05	0.05	0.05	0.07	0.04	0.04
Cr	0.00	0.00	0.00	0.00	0.00	0.00	0.00	0.00	0.00	0.00	0.00	0.00
V												
Fe^{3+}	0.01	0.01	0.02	0.01	0.01	0.01	0.01	0.01	0.02	0.02	0.01	0.01
Fe^{2+}	0.00	0.00	0.00	0.00	0.00	0.00	0.00	0.00	0.00	0.00	0.00	0.00
Mn	0.00	0.00	0.00	0.00	0.00	0.00	0.00	0.00	0.00	0.00	0.00	0.00
Mg												
Zn	0.00	0.00	0.00	0.00	0.00	0.00	0.00	0.00	0.00	0.00	0.00	0.00
Ni	0.00	0.00	0.00	0.00	0.00	0.00	0.00	0.00	0.00	0.00	0.00	0.00
Ca	1.00	1.00	1.00	1.00	1.00	1.00	1.00	1.00	1.00	1.00	0.99	0.99

Analysis	S-09-VSZ02-area2_ilm	S-09-VSZ02-area2_ilm	S-09-VSZ02-area2_ilm	average	St Dev
Description					
wt%					
SiO_2	31.15	31.15	31.19	31.04	0.33
TiO_2	38.33	38.33	37.85	37.78	1.19
Al_2O_3	1.52	1.52	1.95	1.65	0.69
Cr_2O_3	0.00	0.00	0.00	0.00	0.00
V_2O_3	0.00	0.00	0.00	0.03	0.03
FeO	0.33	0.33	0.32	0.46	0.13
MnO	0.00	0.00	0.00	0.000	0.00
MgO	0.00	0.00	0.02	0.02	0.03
ZnO	0.00	0.00	0.00	0.01	0.01
NiO	0.00	0.00	0.00	0.00	0.00
CaO	28.79	28.79	28.75	28.80	0.24
	0.08	0.08	0.08	0.09	0.01
Total	100.21	100.21	100.16	99.88	0.27
Si	1.00	1.00	1.00	1.00	0.00
Ti	0.93	0.93	0.92	0.92	0.03
Al	0.06	0.06	0.07	0.06	0.03
Cr	0.00	0.00	0.00	0.00	0.00
V					
Fe^{3+}	0.01	0.01	0.01	0.01	0.00
Fe^{2+}	0.00	0.00	0.00	0.00	0.00
Mn	0.00	0.00	0.00	0.00	0.00
Mg					
Zn	0.00	0.00	0.00	0.00	0.00
Ni	0.00	0.00	0.00	0.00	0.00
Ca	0.99	0.99	0.99	1.00	0.00

B5. Magnetite analyses including Cr-rich cores and Ti-magnetite. Formulae were calculated on the basis of 3 cations.

Analysis	LC015_5_10	LC015_1_6	LC015_1_10	LC015_1_12	LC015_1_13	LC015_3_17	LC015_3_23	LC015_4_14	LC015_5_4	average	St Dev
WDS	core	core	rim	core	core	rim	repl by srp2	core	core		
wt%											
SiO_2	b.d.l	b.d.l	0.03	b.d.l	b.d.l	0.06	0.06	0.05	0.04	0.03	0.02
TiO_2	0.84	0.14	0.11	0.31	0.32	0.09	b.d.l	0.10	0.22	0.24	0.23
Al_2O_3	0.08	b.d.l	b.d.l	b.d.l	b.d.l	b.d.l	b.d.l	b.d.l	b.d.l	b.d.l	
Cr_2O_3	31.86	5.07	3.36	8.47	9.23	4.29	2.47	5.19	7.66	8.62	8.50
V_2O_3	0.11	0.09	0.05	0.07	0.11	0.07	0.03	0.05	0.09	0.07	0.03
FeO*	55.80	93.93	97.55	88.60	87.25	94.59	97.77	93.66	89.24	88.71	12.90
MnO	5.29	0.89	0.55	1.59	1.76	0.81	0.45	0.99	1.58	1.54	1.40
MgO	2.27	1.04	0.85	1.36	1.38	0.97	0.67	0.89	1.36	1.20	0.45
ZnO	1.08	0.00	0.00	0.00	0.16	0.06	0.00	0.07	0.17	0.17	0.33
NiO	0.51	0.96	0.82	0.89	0.85	0.95	0.92	0.99	0.95	0.87	0.14
CaO	b.d.l	b.d.l	b.d.l	b.d.l	b.d.l	b.d.l	b.d.l	b.d.l	b.d.l	b.d.l	
Total	97.14	100.15	101.90	98.28	97.81	100.15	101.25	100.02	98.41	99.46	1.53
Si	-	-	0.00	-	-	0.00	0.00	0.00	0.00	0.00	0.00
Ti	0.02	0.00	0.00	0.01	0.01	0.00	-	0.00	0.01	0.01	0.01
Al	0.00	-	-	-	-	-	-	-	-	-	
Cr	0.93	0.15	0.10	0.25	0.27	0.13	0.07	0.15	0.23	0.25	0.26
V	0.00	0.00	0.00	0.00	0.00	0.00	0.00	0.00	0.00	0.00	0.00
Fe^{3+}	0.09	1.85	1.90	1.74	1.72	1.87	1.93	1.84	1.77	1.63	0.58
Fe^{2+}	0.66	0.89	0.91	0.85	0.84	0.89	0.92	0.89	0.84	0.85	0.08
Mn	0.03	0.03	0.02	0.05	0.06	0.03	0.01	0.03	0.05	0.03	0.01
Mg	0.06	0.06	0.05	0.08	0.08	0.05	0.04	0.05	0.08	0.06	0.01
Zn	0.00	0.00	0.00	0.00	0.00	0.00	0.00	0.00	0.00	0.00	0.00
Ni	0.03	0.03	0.02	0.03	0.03	0.03	0.03	0.03	0.03	0.03	0.00
Ca	-	-	-	-	-	-	-	-	-	-	-

***Total Fe**

Analysis	LC015_1_9	LC015_1_14	LC015_1_15	LC015_1_18	LC015_1_19	LC015_2_6	LC015_2_9	LC015_3_21	LC015_4_11	LC015_4_12	LC015_4_13	LC015_4_15	LC015_4_16
WDS	rim	rim	rim repl by srp2	rim repl by srp2	rim	rim repl by srp2	mt	mt nr serp	matrix	matrix	matrix	rim	rim
wt%													
SiO_2	b.d.l	0.22	b.d.l	0.08	b.d.l	0.04	b.d.l	0.04	0.10	0.61	0.10	b.d.l	b.d.l
TiO_2	0.07	b.d.l	b.d.l	b.d.l	0.06	0.07	b.d.l	b.d.l	b.d.l	0.06	b.d.l	0.06	b.d.l
Al_2O_3	b.d.l	b.d.l	b.d.l	b.d.l	b.d.l	b.d.l	b.d.l	b.d.l	b.d.l	b.d.l	b.d.l	b.d.l	b.d.l
Cr_2O_3	0.89	1.39	1.51	1.54	1.85	0.53	1.69	1.28	1.26	1.32	1.26	1.38	0.79
V_2O_3	0.10	0.08	b.d.l	0.06	0.05	0.05	b.d.l	0.07	0.07	0.06	0.05	0.07	0.06
FeO*	99.78	98.31	98.78	98.67	98.76	100.31	98.44	99.80	98.33	95.97	97.98	98.50	100.56
MnO	0.32	0.35	0.40	0.45	0.45	0.35	0.46	0.33	0.39	0.40	0.37	0.45	0.38
MgO	0.72	0.67	0.61	0.74	0.68	0.80	0.88	0.55	0.55	0.62	0.55	0.72	0.58
ZnO	b.d.l	b.d.l	0.09	b.d.l	b.d.l	b.d.l	b.d.l	b.d.l	b.d.l	b.d.l	b.d.l	b.d.l	b.d.l
NiO	0.77	0.84	0.79	0.90	0.90	0.89	0.90	0.79	0.77	0.70	0.96	0.85	0.86
CaO	b.d.l	0.04	b.d.l	b.d.l	b.d.l	b.d.l	b.d.l	b.d.l	b.d.l	0.11	b.d.l	b.d.l	b.d.l
Total	101.89	100.99	101.40	101.48	101.76	102.27	101.43	102.10	100.67	98.78	100.44	101.1	102.6
Si	-	0.00	-	0.00	-	0.00	-	0.00	0.00	0.02	0.00	-	-
Ti	-	-	-	-	-	-	-	-	-	-	-	0.00	-
Al	-	-	-	-	-	-	-	-	-	-	-	-	-
Cr	0.04	0.04	0.05	0.05	0.02	0.05	0.15	0.04	0.04	0.04	0.04	0.04	0.02
V	0.00	0.00	-	0.00	0.00	0.00	-	0.00	0.00	0.00	0.00	0.00	0.00
Fe^{3+}	1.97	1.96	1.95	1.95	1.94	1.98	1.95	1.96	1.96	1.95	1.96	1.96	1.98
Fe^{2+}	0.93	0.93	0.93	0.92	0.92	0.92	0.91	0.94	0.93	0.93	0.93	0.92	0.93
Mn	0.01	0.01	0.01	0.01	0.01	0.01	0.03	0.01	0.01	0.01	0.01	0.01	0.01
Mg	0.04	0.03	0.04	0.04	0.04	0.05	0.05	0.03	0.03	0.04	0.03	0.04	0.03
Zn	-	-	0.00	-	-	-	-	-	-	-	-	-	-
Ni	0.03	0.02	0.03	0.03	0.03	0.03	0.03	0.02	0.02	0.02	0.03	0.03	0.03
Ca	-	-	-	-	-	-	-	-	-	-	-	-	-

***Total Fe**

Analysis	LC015_4_20	LC015_4_21	LC015_4_22	LC015_4_25	LC015_5_1	LC015_5_2	LC015_5_6	LC015_5_7	LC015_5_8	LC015_5_9	LC015_6_1	LC015_6_2	LC015_6_3
WDS	matrix	matrix	matrix	matrix	matrix	matrix	rim	rim	mt nr serp	rim	lamellae	lamellae	lamellae
wt%													
SiO_2	0.06	b.d.l	b.d.l	0.09	0.07	0.04	b.d.l	0.07	b.d.l	0.07	0.11	0.04	0.06
TiO_2	0.05	b.d.l	b.d.l	0.06	b.d.l	0.06	b.d.l	0.06	0.05	0.04	0.05	0.06	0.04
Al_2O_3	b.d.l	b.d.l	b.d.l	b.d.l	b.d.l	b.d.l	b.d.l	b.d.l	b.d.l	b.d.l	b.d.l	b.d.l	b.d.l
Cr_2O_3	1.40	1.91	1.86	1.46	1.36	1.20	1.80	1.66	1.68	0.96	1.42	1.57	1.60
V_2O_3	0.07	0.13	0.06	0.04	0.04	0.08	0.05	0.09	0.06	0.04	0.05	0.07	0.06
FeO*	98.99	99.11	99.33	100.28	100.29	99.19	97.66	98.50	98.78	99.02	98.09	96.95	98.63
MnO	0.34	0.40	0.41	0.37	0.46	0.47	0.43	0.47	0.48	0.38	0.44	0.49	0.48
MgO	0.63	0.61	0.64	0.58	0.70	0.84	0.82	0.94	0.93	0.77	0.86	0.75	0.82
ZnO	b.d.l	b.d.l	b.d.l	b.d.l	b.d.l	b.d.l	b.d.l	b.d.l	b.d.l	b.d.l	b.d.l	b.d.l	b.d.l
NiO	0.71	0.83	0.79	0.61	0.70	0.89	0.94	0.85	0.88	0.81	0.87	0.93	0.94
CaO	b.d.l	b.d.l	b.d.l	b.d.l	b.d.l	b.d.l	b.d.l	b.d.l	b.d.l	b.d.l	b.d.l	b.d.l	b.d.l
Total	101.4	102.1	102.2	102.7	102.8	101.9	100.7	101.5	101.8	101.3	100.9	99.9	101.6
Si	0.00	-	-	0.00	0.00	0.00	-	0.00	-	0.00	0.00	0.00	0.00
Ti	0.00	-	-	0.00	-	0.00	-	0.00	0.00	0.00	0.00	0.00	0.00
Al	-	-	-	-	-	-	-	-	-	-	-	-	-
Cr	0.04	0.06	0.05	0.04	0.04	0.04	0.05	0.05	0.05	0.03	0.04	0.05	0.05
V	0.00	0.01	0.00	0.00	0.00	0.00	0.00	0.00	0.00	0.00	0.00	0.00	0.00
Fe^{3+}	1.96	1.94	1.94	1.95	1.96	1.96	1.95	1.95	1.95	1.97	1.96	1.95	1.95
Fe^{2+}	0.93	0.93	0.93	0.94	0.93	0.91	0.91	0.91	0.91	0.92	0.91	0.91	0.91
Mn	0.01	0.01	0.01	0.01	0.01	0.01	0.01	0.01	0.01	0.01	0.01	0.02	0.02
Mg	0.04	0.03	0.04	0.03	0.04	0.05	0.05	0.05	0.05	0.04	0.05	0.04	0.05
Zn	–	–	–	–	–	–	–	–	–	–	–	–	–
Ni	0.02	0.02	0.02	0.02	0.02	0.03	0.03	0.03	0.03	0.02	0.03	0.03	0.03
Ca	–	–	–	–	–	–	–	–	–	–	–	–	–

***Total Fe**

Analysis	LC015_6_4	LC015_6_8	LC015_6_9	LC015_6_11	LC015_6_13	LC015_6_15	av	st dev	GSZ11a_MT 4 1	GSZ11a_MT 4 2	GSZ11a_MT 4 3	GSZ11a_MT 4 4	GSZ11a_MT 4 5
WDS	lamellae	lamellae	lamellae	lamellae	lamellae	rim			core	core	core	core	core
wt%													
SiO_2	0.06	0.13	0.08	0.22	0.18	0.04	0.09	0.11	0.24	0.00	0.00	0.00	0.00
TiO_2	b.d.l	b.d.l	0.06	0.04	b.d.l	b.d.l	0.03	0.03	0.34	0.29	0.29	0.29	0.35
Al_2O_3	b.d.l	b.d.l	b.d.l	b.d.l	b.d.l	b.d.l	b.d.l		0.00	0.00	0.00	0.00	0.00
Cr_2O_3	1.47	1.28	1.44	1.31	1.50	1.61	1.41	0.31	6.43	5.36	7.10	5.57	5.71
V_2O_3	0.09	0.04	0.05	0.07	0.06	0.06	0.06	0.02					
FeO*	99.39	97.25	97.79	95.53	96.38	97.84	98.54	1.22	94.18	94.90	94.03	95.56	96.31
MnO	0.44	0.47	0.50	0.49	0.42	0.45	0.42	0.05	0.00	0.00	0.00	0.00	0.26
MgO	0.77	0.67	0.75	0.83	0.82	0.72	0.72	0.11	1.16	0.00	1.19	1.00	1.11
ZnO	b.d.l	b.d.l	b.d.l	b.d.l	b.d.l	b.d.l	b.d.l						
NiO	0.89	0.91	0.95	0.96	0.87	0.89	0.85	0.09	0.69	0.60	0.65	0.64	0.67
CaO	b.d.l	b.d.l	b.d.l	b.d.l	b.d.l	b.d.l	b.d.l						
Total	102.2	99.9	100.7	98.4	99.2	100.6	101.2	1.08	103.03	101.15	103.26	103.04	104.43
Si	0.00	0.01	0.00	0.01	0.01	0.00	0.00	0.01	0.01	0.00	0.00	0.00	0.00
Ti	-	-	0.00	0.00	-	-	0.00	0.00	0.01	0.01	0.01	0.01	0.01
Al	-	-	-	-	-	-	-	-	0.00	0.00	0.00	0.00	0.00
Cr	0.04	0.04	0.04	0.04	0.05	0.04	0.05	0.02	0.19	0.16	0.21	0.16	0.16
V	0.00	0.00	0.00	0.00	0.00	0.00	0.00	0.00	0.00	0.00	0.00	0.00	0.00
Fe^{3+}	1.95	1.96	1.95	1.96	1.95	1.96	1.96	0.01	1.80	1.83	1.79	1.83	1.83
Fe^{2+}	0.92	0.95	0.95	0.94	0.95	0.95	0.93	0.01	0.85	0.98	0.85	0.87	0.85
Mn	0.01	0.01	0.01	0.01	0.01	0.00	0.01	0.00	0.00	0.00	0.00	0.00	0.01
Mg	0.04	0.02	0.02	0.02	0.02	0.00	0.04	0.01	0.06	0.00	0.07	0.05	0.06
Zn	-	-	-	-	-	-	-	-	0.00	0.00	0.00	0.00	0.00
Ni	0.03	0.00	0.00	0.00	0.00	0.00	0.02	0.01	0.02	0.02	0.02	0.02	0.02
Ca	-	-	-	-	-	-	-	-	-	-	-	-	-

Analysis	GSZ11A MT3 5	GSZ11A MT3 1	GSZ11A MT3 2	GSZ11A MT3 3	GSZ11A MT3 4	GSZ11A MT1 5	GSZ11A MT1 1	GSZ11A MT1 2	GSZ11A MT1 3	GSZ11A MT1 4	Av	std dev
WDS	matrix	matrix	matrix	matrix	matrix	matrix	matrix	matrix	matrix	matrix		
wt%												
SiO_2	0.00	0.00	0.00	0.00	0.00	0.00	0.00	0.00	0.00	0.00	0.02	0.06
TiO_2	0.00	0.00	0.00	0.00	0.00	0.00	0.00	0.00	0.00	0.00	0.10	0.15
Al_2O_3	0.00	0.00	0.00	0.00	0.00	0.00	0.00	0.00	0.00	0.00	0.00	0.00
Cr_2O_3	0.00	0.00	0.00	0.00	0.00	0.00	0.00	0.00	0.00	0.00	2.01	2.97
V_2O_3												
FeO*	100.55	101.62	101.49	101.48	99.82	102.25	101.26	102.33	101.90	101.10	99.25	3.22
MnO	0.41	0.34	0.39	0.26	0.28	0.41	0.34	0.37	0.00	0.40	0.23	0.18
MgO	0.00	0.00	0.00	0.00	0.00	0.00	0.00	0.00	0.00	0.00	0.30	0.51
ZnO												
NiO	0.59	0.47	0.20	0.25	0.24	0.23	0.45	0.37	0.32	0.38	0.45	0.18
CaO												
Total	101.54	102.42	102.08	101.99	100.34	102.89	102.04	103.08	102.22	101.89	102.36	0.98
Si	0.00	0.00	0.00	0.00	0.00	0.00	0.00	0.00	0.00	0.00	0.00	0.00
Ti	0.00	0.00	0.00	0.00	0.00	0.00	0.00	0.00	0.00	0.00	0.00	0.00
Al	0.00	0.00	0.00	0.00	0.00	0.00	0.00	0.00	0.00	0.00	0.00	0.00
Cr	0.00	0.00	0.00	0.00	0.00	0.00	0.00	0.00	0.00	0.00	0.06	0.09
V	0.00	0.00	0.00	0.00	0.00	0.00	0.00	0.00	0.00	0.00	0.00	0.00
Fe^{3+}	2.00	2.00	2.00	2.00	2.00	2.00	2.00	2.00	2.00	2.00	1.94	0.09
Fe^{2+}	0.97	0.98	0.98	0.98	0.98	0.98	0.98	0.98	0.99	0.98	0.95	0.06
Mn	0.01	0.01	0.01	0.01	0.01	0.01	0.01	0.01	0.00	0.01	0.01	0.01
Mg	0.00	0.00	0.00	0.00	0.00	0.00	0.00	0.00	0.00	0.00	0.02	0.03
Zn	0.00	0.00	0.00	0.00	0.00	0.00	0.00	0.00	0.00	0.00	0.00	0.00
Ni	0.02	0.01	0.01	0.01	0.01	0.01	0.01	0.01	0.01	0.01	0.01	0.01
Ca	-	-	-	-	-	-	-	-	-	-	-	-

***Total Fe**

Analysis	PF-001_1_9	PF-001_1_14	PF-001_1_15	PF-001_1_18	PF-001_1_19	PF-001_2_6	PF-001_2_9	PF-001_3_21	Average	St Dev.
WDS	large mt rim	large mt rim	large mt core	large mt rim	large mt core	large mt rim	large mt core	large mt core		
wt%										
SiO_2	b.d.l	0.07	0.04	b.d.l	b.d.l	b.d.l	0.03	b.d.l	b.d.l	
TiO_2	0.08	0.07	0.14	b.d.l	0.08	0.03	b.d.l	0.03	0.05	0.04
Al_2O_3	b.d.l	b.d.l	b.d.l	b.d.l	b.d.l	b.d.l	b.d.l	b.d.l	b.d.l	
Cr_2O_3	0.06	b.d.l	b.d.l	0.03	0.04	b.d.l	0.04	0.03	0.03	0.02
V_2O_3	0.10	0.10	0.11	0.07	0.10	0.09	0.10	0.10	0.10	0.01
FeO*	102.01	101.49	102.01	101.83	102.11	101.82	101.97	101.81	101.88	0.19
MnO	0.05	0.04	0.09	b.d.l	0.05	b.d.l	b.d.l	b.d.l	0.04	0.03
MgO	0.197	0.092	0.231	0.084	0.217	0.098	0.046	0.106	0.134	0.070
ZnO	b.d.l	b.d.l	b.d.l	b.d.l	b.d.l	b.d.l	b.d.l	b.d.l	b.d.l	
NiO	0.27	0.23	0.41	0.25	0.25	0.31	0.29	0.25	0.28	0.06
CaO	b.d.l	b.d.l	b.d.l	b.d.l	b.d.l	b.d.l	b.d.l	0.40	0.05	0.14
Total	102.55	101.90	102.77	102.18	102.63	102.26	102.36	102.49	102.39	0.28
Si	-	0.00	0.00	-	-	-	0.00	-	-	-
Ti	0.00	0.00	0.00	0.00	0.00	0.00	0.00	0.00	0.00	0.00
Al	-	-	-	-	-	-	-	-	-	-
Cr	0.00	-	-	0.00	0.00	-	0.00	0.00	0.00	0.00
V	0.00	0.00	0.00	0.00	0.00	0.00	0.00	0.00	0.00	0.00
Fe^{3+}	1.99	2.00	1.99	2.00	1.99	2.00	2.00	2.00	1.99	0.00
Fe^{2+}	0.98	0.99	0.97	0.99	0.98	0.98	0.99	0.99	0.98	0.01
Mn	0.00	0.00	0.00	-	0.00	-	-	-	0.00	0.00
Mg	0.01	0.01	0.01	-	0.01	-	-	-	0.01	0.00
Zn	-	-	-	-	-	-	-	-	-	-
Ni	0.01	0.01	0.01	0.01	0.01	0.01	0.01	0.01	0.01	0.00
Ca	-	-	-	-	-	-	-	-	-	-

***Total Fe**

Ti-magnetite

Analysis	PF001_1_16	PF001_1_18	PF001_1_22	PF001_2_1	PF001_3_10	Average	St Dev
WDS	core to ilm	core to ilm	core to ilm	core to ilm	core to ilm		
wt%							
SiO_2	0.04	0.03	0.03	0.08	0.71	0.18	0.44
TiO_2	40.53	33.70	32.55	19.89	14.40	28.21	3.88
Al_2O_3	b.d.l	b.d.l	b.d.l	b.d.l	b.d.l	b.d.l	
Cr_2O_3	0.03	b.d.l	b.d.l	b.d.l	0.06	b.d.l	0.03
V_2O_3	0.34	0.33	0.29	0.25	0.22	0.29	0.02
FeO*	57.04	63.68	64.71	76.47	81.80	68.74	10.11
MnO	1.38	1.12	1.08	0.60	0.29	0.89	0.22
MgO	0.29	0.25	0.26	0.20	0.52	0.31	0.22
ZnO	b.d.l	b.d.l	b.d.l	b.d.l	b.d.l	b.d.l	
NiO	b.d.l	b.d.l	b.d.l	b.d.l	b.d.l	b.d.l	
CaO	b.d.l	b.d.l	b.d.l	b.d.l	0.22	0.06	0.14
Total	99.66	99.12	98.93	97.50	98.23	98.50	0.13
Si	0.00	0.00	0.00	0.00	0.03	0.01	0.21
Ti	1.04	0.86	0.83	0.51	0.36	0.72	0.10
Al	-	-	-	-	-	-	-
Cr	0.00	-	-	-	0.00	-	-
V	0.01	0.01	0.01	0.01	0.01	0.01	0.00
Fe^{3+}	0.52	0.75	0.79	1.21	1.40	0.93	0.36
Fe^{2+}	0.95	1.13	1.16	1.48	1.63	1.27	0.00
Mn	0.05	0.04	0.04	0.02	0.01	0.03	0.01
Mg	0.02	0.02	0.02	0.01	0.02	0.02	0.00
Zn	-	-	-	-	-	-	-
Ni	-	-	-	-	-	-	
Ca	-	-	-	-	0.01	0.00	0.01

Analysis	VSZ-03_A1_MT1 1	VSZ-03_A1_MT1 2	VSZ-03_A1_MT1 3	VSZ-03_A1_MT2 2	VSZ-03_A1_MT2 3	VSZ-03_A1_MT2 4	VSZ-03_A1_MT2 5	VSZ-03_A1_MT2 1	VSZ-03_A2_MT1 2	VSZ-03_A2_MT1 1	VSZ-03_A2_MT1 2
EDS	mt1	mt1	mt1	mt1	mt1	mt1	mt1	mt1	mt1	mt1	mt1
wt%											
SiO_2	0.00	0.00	0.00	0.00	0.00	0.00	0.00	0.00	0.00	0.00	0.00
TiO_2	0.40	0.51	0.51	0.56	0.54	0.48	0.62	0.61	0.53	0.51	0.53
Al_2O_3											
Cr_2O_3	2.13	2.62	3.30	2.47	2.25	1.86	3.41	3.55	1.48	2.15	1.84
V_2O_3											
FeO*	97.69	99.62	93.60	96.44	97.50	95.79	97.99	97.84	96.33	98.43	98.16
MnO	0.32	0.37	0.00	0.00	0.00	0.00	0.34	0.00	0.00	0.37	0.00
MgO	0.75	0.85	0.00	0.91	0.00	0.00	1.00	0.00	0.00	0.83	0.00
ZnO											
NiO	0.00	0.00	0.00	0.00	0.51	0.00	0.00	0.60	0.61	0.00	0.00
CaO											
Total	101.29	103.97	97.41	100.39	100.81	98.12	103.35	102.60	98.94	102.29	100.53
Si	0.00	0.00	0.00	0.00	0.00	0.00	0.00	0.00	0.00	0.00	0.00
Ti	0.01	0.01	0.02	0.02	0.02	0.01	0.02	0.02	0.02	0.01	0.02
Al	0.00	0.00	0.00	0.00	0.00	0.00	0.00	0.00	0.00	0.00	0.00
Cr	0.06	0.08	0.10	0.07	0.07	0.06	0.10	0.11	0.05	0.06	0.06
V	0.00	0.00	0.00	0.00	0.00	0.00	0.00	0.00	0.00	0.00	0.00
Fe^{3+}	1.93	1.91	1.88	1.91	1.92	1.93	1.88	1.88	1.94	1.92	1.93
Fe^{2+}	0.91	0.90	1.00	0.90	0.98	1.00	0.88	0.98	0.98	0.90	1.00
Mn	0.01	0.01	0.00	0.00	0.00	0.00	0.01	0.00	0.00	0.01	0.00
Mg	0.04	0.05	0.00	0.05	0.00	0.00	0.05	0.00	0.00	0.05	0.00
Zn	0.00	0.00	0.00	0.00	0.00	0.00	0.00	0.00	0.00	0.00	0.00
Ni	0.00	0.00	0.00	0.00	0.02	0.00	0.00	0.02	0.02	0.00	0.00
Ca	-	-	-	-	-	-	-	-	-	-	-

***Total Fe**

Analysis	VSZ-03_A2_MT1 3	VSZ-03_A2_MT3_ 2	VSZ-03_A2_MT3_ 3	VSZ-03_A2_MT3_ 1	VSZ-03_A2_MT4 1	VSZ-03_A2_MT4 2	VSZ-03_A2_MT4 3	VSZ-03_A2_MT4 4	VSZ-03_A2_MT4 5		
EDS	mt1	mt1	mt1	mt1	mt1	mt1	mt1	mt1	mt1	Average	St Dev
wt%											
SiO_2	0.00	0.00	0.00	0.00	0.00	0.00	0.00	0.00	0.00	0.00	0.00
TiO_2	0.48	0.53	0.61	0.51	0.61	0.48	0.53	0.72	0.54	0.54	0.07
Al_2O_3											
Cr_2O_3	0.22	2.73	2.60	2.70	1.75	1.43	1.08	1.53	2.44	2.18	0.82
V_2O_3											
FeO*	98.70	93.78	93.33	93.63	96.33	95.06	95.03	96.53	95.39	96.36	1.88
MnO	0.00	0.00	0.00	0.00	0.00	0.00	0.00	0.00	0.00	0.07	0.14
MgO	0.00	0.00	0.00	0.00	0.00	0.00	0.00	0.00	0.66	0.25	0.40
ZnO											
NiO	0.00	0.66	0.00	0.57	0.57	0.00	0.57	0.00	0.00	0.20	0.29
CaO											
Total	99.40	97.71	96.54	97.42	99.26	96.97	97.21	98.78	99.03	99.60	2.23
Si	0.00	0.00	0.00	0.00	0.00	0.00	0.00	0.00	0.00	0.00	0.00
Ti	0.01	0.02	0.02	0.02	0.02	0.01	0.02	0.02	0.02	0.02	0.00
Al	0.00	0.00	0.00	0.00	0.00	0.00	0.00	0.00	0.00	0.00	0.00
Cr	0.01	0.08	0.08	0.08	0.05	0.04	0.03	0.05	0.07	0.07	0.02
V	0.00	0.00	0.00	0.00	0.00	0.00	0.00	0.00	0.00	0.00	0.00
Fe^{3+}	1.98	1.90	1.90	1.90	1.93	1.94	1.95	1.93	1.91	1.92	0.02
Fe^{2+}	1.00	0.98	1.00	0.98	0.98	1.00	0.98	1.00	0.92	0.96	0.04
Mn	0.00	0.00	0.00	0.00	0.00	0.00	0.00	0.00	0.00	0.00	0.00
Mg	0.00	0.00	0.00	0.00	0.00	0.00	0.00	0.00	0.04	0.01	0.02
Zn	0.00	0.00	0.00	0.00	0.00	0.00	0.00	0.00	0.00	0.00	0.00
Ni	0.00	0.02	0.00	0.02	0.02	0.00	0.02	0.00	0.00	0.01	0.01
Ca	-	-	-	-	-	-	-	-	-	-	-

Analysis	VSZ-03_A3_MT2 2	VSZ-03_A3_MT2 3	VSZ-03_A3_MT2 1	VSZ_03_A4_MT1 2			VSZ05-a1	VSZ05-a1	VSZ05-a2_largemt	VSZ05-a2_largemt	VSZ05-a2_largemt	VSZ05-a4_mt1
WDS	mt3	mt3	mt3	mt3	Av	St Dev	mt4	mt4	mt4	mt4	mt4	mt4
wt%												
SiO_2	0.00	0.30	0.00	0.00	0.07	0.15	0.02	0.08	0.00	0.00	0.00	0.00
TiO_2	0.54	0.59	0.38	0.00	0.38	0.27	0.31	0.33	0.28	0.38	0.83	0.37
Al_2O_3							0.00	0.00	0.00	0.00	0.03	0.00
Cr_2O_3	3.52	4.02	3.62	0.00	2.79	1.87	1.04	1.47	2.34	5.99	11.07	1.21
V_2O_3							0.00	0.00	0.00	0.00	0.00	0.00
FeO*	96.89	90.01	99.63	99.04	96.39	4.42	97.95	97.47	97.62	93.43	85.52	98.54
MnO	0.00	0.00	0.32	0.00	0.08	0.16	0.15	0.13	0.11	0.28	0.64	0.10
MgO	0.90	0.95	0.00	0.00	0.46	0.53	0.68	0.77	0.89	1.11	1.46	0.66
ZnO							0.00	0.02	0.02	0.00	0.15	0.00
NiO	0.00	0.59	0.59	0.00	0.29	0.34	0.57	0.56	0.57	0.53	0.57	0.55
CaO							0.00	0.05	0.00	0.00	0.00	0.00
Total	101.85	98.45	102.55	99.04	100.47	2.03	100.72	100.89	101.83	101.72	100.28	101.43
Si	0.00	0.01	0.00	0.00	0.00	0.01	0.00	0.00	0.00	0.00	0.00	0.00
Ti	0.02	0.02	0.01	0.00	0.01	0.01	0.01	0.01	0.01	0.01	0.02	0.01
Al	0.00	0.00	0.00	0.00	0.00	0.00	0.00	0.00	0.00	0.00	0.00	0.00
Cr	0.10	0.13	0.11	0.00	0.08	0.06	0.03	0.04	0.07	0.18	0.33	0.04
V	0.00	0.00	0.00	0.00	0.00	0.00	0.00	0.00	0.00	0.00	0.00	0.00
Fe^{3+}	1.88	1.86	1.88	2.00	1.91	0.06	1.96	1.95	1.92	1.81	1.64	1.95
Fe^{2+}	0.90	0.87	0.97	1.00	0.94	0.06	0.90	0.89	0.88	0.85	0.80	0.91
Mn	0.00	0.00	0.01	0.00	0.00	0.01	0.00	0.00	0.00	0.01	0.02	0.00
Mg	0.05	0.06	0.00	0.00	0.03	0.03	0.04	0.04	0.05	0.06	0.08	0.04
Zn	0.00	0.00	0.00	0.00	0.00	0.00	0.00	0.00	0.00	0.00	0.00	0.00
Ni	0.00	0.02	0.02	0.00	0.01	0.01	0.02	0.02	0.02	0.02	0.02	0.02
Ca	-	-	-	-	-	-	-	-	-	-	-	-

***Total Fe**

Analysis	VSZ05-a4_mt1	VSZ05-a4_mt1			ASZ-09-B-A1-MT1 1	ASZ-09-B-A1-MT1 2	ASZ-09-B-A1-MT1 3	ASZ-09-B-A1-MT1 4	ASZ-09-B_A1_MT2 2	ASZ-09-B_A1_MT2 3	ASZ-09-B_A1_MT2 4	ASZ-09-B_A1_MT2 5	ASZ-09-B_A1_MT2 1
EDS	mt4	mt4	Av	St Dev	mt2	mt2	mt2	mt2	mt2	mt2	mt2	mt2	mt2
wt%					in Tichu	in Tichu	in Tichu	in Tichu	in Tichu	in Tichu	in Tichu	in Tichu	in Tichu
SiO_2	0.00	0.00	0.01	0.03	0.00	0.00	0.00	0.00	0.00	0.28	0.30	0.00	0.00
TiO_2	0.36	0.41	0.41	0.17	0.40	0.38	0.38	0.38	0.30	0.00	0.30	0.24	0.24
Al_2O_3	0.00	0.00	0.00	0.01									
Cr_2O_3	1.55	1.24	3.24	3.56	0.00	0.00	0.00	0.26	0.00	0.67	1.04	0.77	0.91
V_2O_3	0.00	0.00	0.00	0.00									
FeO*	98.55	98.21	95.91	4.52	98.10	98.64	98.00	99.00	97.49	96.96	97.04	97.76	97.42
MnO	0.16	0.09	0.21	0.18	0.48	0.39	0.56	0.53	0.44	0.67	0.61	0.43	0.50
MgO	0.66	0.63	0.86	0.29	1.28	1.28	1.14	0.00	1.19	1.34	1.24	0.00	1.38
ZnO	0.00	0.00	0.02	0.05									
NiO	0.50	0.52	0.55	0.03	0.00	0.00	0.50	0.00	0.00	0.00	0.00	0.48	0.00
CaO	0.01	0.01	0.01	0.02									
Total	101.80	101.11	101.22	0.57	100.26	100.69	100.58	100.18	99.42	99.92	100.54	99.68	100.44
Si	0.00	0.00	0.00	0.00	0.00	0.00	0.00	0.00	0.00	0.01	0.01	0.00	0.00
Ti	0.01	0.01	0.01	0.00	0.01	0.01	0.01	0.01	0.01	0.00	0.01	0.01	0.01
Al	0.00	0.00	0.00	0.00	0.00	0.00	0.00	0.00	0.00	0.00	0.00	0.00	0.00
Cr	0.05	0.04	0.10	0.11	0.00	0.00	0.00	0.01	0.00	0.02	0.03	0.02	0.03
V	0.00	0.00	0.00	0.00	0.00	0.00	0.00	0.00	0.00	0.00	0.00	0.00	0.00
Fe^{3+}	1.94	1.95	1.89	0.11	1.99	1.99	1.99	1.98	1.99	1.98	1.96	1.97	1.97
Fe^{2+}	0.91	0.91	0.88	0.04	0.84	0.84	0.84	0.98	0.85	0.83	0.84	0.97	0.83
Mn	0.00	0.00	0.01	0.01	0.02	0.01	0.02	0.02	0.01	0.02	0.02	0.01	0.02
Mg	0.04	0.04	0.05	0.02	0.07	0.07	0.06	0.00	0.07	0.08	0.07	0.00	0.08
Zn	0.00	0.00	0.00	0.00	0.00	0.00	0.00	0.00	0.00	0.00	0.00	0.00	0.00
Ni	0.02	0.02	0.02	0.00	0.00	0.00	0.02	0.00	0.00	0.00	0.00	0.01	0.00
Ca	-	-	-	-									

***Total Fe**

***Total Fe** Analysis	ASZ-09-B-A1_MT2_REPEAT 2	ASZ-09-B-A1_MT2_REPEAT 3	ASZ-09-B-A1_MT2_REPEAT 1	ASZ-09a a1_mt1	ASZ-09-B_A4_MT1 1	ASZ-09-B_A4_MT1 2	ASZ-09-B_A4_MT1 3	ASZ-09-B-A4_MT2 1	ASZ-09-B-A4_MT2 2	ASZ-09-B-A4_MT2 3	ASZ-09-A_A4_MT1 4 2	ASZ-09-A_A4_MT1 4 3
WDS	mt2	mt2	mt2	mt2	mt2	mt2	mt2	mt2	mt2	mt2	mt2	mt2
wt%	in Tichu	in Tichu	in Tichu	megacryst	megacryst	megacryst	megacryst	megacryst	megacryst	megacryst	megacryst	megacryst
SiO_2	0.00	0.00	0.00	0.44	0.49	0.00	0.00	0.32	0.28	0.36	0.00	0.00
TiO_2	0.27	0.29	0.42	0.60	0.42	0.43	0.37	0.42	0.48	0.45	0.42	0.37
Al_2O_3				0.00								
Cr_2O_3	1.01	0.91	0.85	0.05	0.42	0.50	0.51	0.00	0.48	0.22	0.00	0.00
V_2O_3				0.00								
FeO*	98.82	98.64	98.36	96.14	98.63	99.83	99.65	98.99	99.23	99.46	102.15	99.67
MnO	0.54	0.57	0.52	0.33	0.50	0.44	0.00	0.00	0.53	0.45	0.00	0.50
MgO	1.44	1.41	0.00	3.51	1.14	1.18	0.00	1.00	1.08	1.06	0.00	1.18
ZnO				0.03								
NiO	0.00	0.41	0.00	0.21	0.00	0.00	0.00	0.00	0.00	0.00	0.00	0.00
CaO				0.02								
Total	102.08	102.22	100.14	102.33	101.61	102.38	100.53	100.72	102.08	102.00	102.56	101.72
Si	0.00	0.00	0.00	0.05	0.02	0.00	0.00	0.01	0.01	0.01	0.00	0.00
Ti	0.01	0.01	0.01	0.02	0.01	0.01	0.01	0.01	0.01	0.01	0.01	0.01
Al	0.00	0.00	0.00	0.00	0.00	0.00	0.00	0.00	0.00	0.00	0.00	0.00
Cr	0.03	0.03	0.03	0.00	0.01	0.01	0.02	0.00	0.01	0.01	0.00	0.00
V	0.00	0.00	0.00	0.00	0.00	0.00	0.00	0.00	0.00	0.00	0.00	0.00
Fe^{3+}	1.96	1.97	1.96	2.00	1.98	1.97	1.97	1.99	1.97	1.98	1.99	1.99
Fe^{2+}	0.82	0.81	0.98	1.00	0.86	0.86	1.00	0.89	0.86	0.87	1.00	0.85
Mn	0.02	0.02	0.02	0.01	0.02	0.01	0.00	0.00	0.02	0.01	0.00	0.02
Mg	0.08	0.08	0.00	0.19	0.06	0.07	0.00	0.06	0.06	0.06	0.00	0.07
Zn	0.00	0.00	0.00	0.00	0.00	0.00	0.00	0.00	0.00	0.00	0.00	0.00
Ni	0.00	0.01	0.00	0.01	0.00	0.00	0.00	0.00	0.00	0.00	0.00	0.00
Ca												

Analysis	ASZ-09-A_A4_MT1 4 1	ASZ-09-A_A3_MT1 2	ASZ-09-A_A3_MT1 3	ASZ-09-A_A3_MT1 1	ASZ-09-A_A3_MT_1 2	ASZ-09-A_A3_MT_1 5	ASZ-09-A_A3_MT_1 6	ASZ-09-A_A4_MT3 3	ASZ-09-A_A4_MT3 6	ASZ-09-A_A4_MT3 7	ASZ-09-A_A4_MT3 10
EDS	mt2	mt2	mt2	mt2	mt2	mt2	mt2	mt2	mt2	mt2	mt2
wt%	megacryst	megacryst	megacryst	megacryst	megacryst	megacryst	megacryst	megacryst	megacryst	megacryst	megacryst
SiO_2	0.00	0.00	0.00	0.00	0.00	0.00	0.00	0.00	0.00	0.00	0.00
TiO_2	0.50	0.69	0.56	0.26	0.51	0.43	0.40	0.45	0.45	0.40	0.48
Al_2O_3											
Cr_2O_3	0.00	0.00	0.00	0.00	0.96	0.73	1.05	0.61	0.47	0.58	0.38
V_2O_3											
FeO*	101.59	100.62	102.40	102.10	96.44	100.15	100.10	97.27	100.27	97.34	99.30
MnO	0.54	0.36	0.41	0.39	0.52	0.50	0.61	0.44	0.49	0.50	0.52
MgO	0.00	1.06	0.00	0.81	0.85	0.00	1.41	1.39	1.26	1.31	1.29
ZnO											
NiO	0.00	0.00	0.00	0.00	0.60	0.00	0.00	0.00	0.00	0.00	0.00
CaO											
Total	102.63	102.73	103.38	103.56	99.88	101.81	103.57	100.17	102.94	100.14	101.97
Si	0.00	0.00	0.00	0.00	0.00	0.00	0.00	0.00	0.00	0.00	0.00
Ti	0.01	0.02	0.02	0.01	0.01	0.01	0.01	0.01	0.01	0.01	0.01
Al	0.00	0.00	0.00	0.00	0.00	0.00	0.00	0.00	0.00	0.00	0.00
Cr	0.00	0.00	0.00	0.00	0.03	0.02	0.03	0.02	0.01	0.02	0.01
V	0.00	0.00	0.00	0.00	0.00	0.00	0.00	0.00	0.00	0.00	0.00
Fe^{3+}	1.99	1.98	1.98	1.99	1.96	1.97	1.96	1.97	1.97	1.97	1.98
Fe^{2+}	0.98	0.87	0.99	0.90	0.87	0.98	0.83	0.83	0.85	0.84	0.84
Mn	0.02	0.01	0.01	0.01	0.02	0.02	0.02	0.01	0.02	0.02	0.02
Mg	0.00	0.06	0.00	0.04	0.05	0.00	0.08	0.08	0.07	0.07	0.07
Zn	0.00	0.00	0.00	0.00	0.00	0.00	0.00	0.00	0.00	0.00	0.00
Ni	0.00	0.00	0.00	0.00	0.02	0.00	0.00	0.00	0.00	0.00	0.00
Ca											

***Total Fe**

Analysis	ASZ-09a a3_mt1	ASZ-09a a3_mt1	ASZ-09a a3_mt1	ASZ-09a a3_mt2	ASZ-09a a3_mt2	ASZ-09a a4_mt1	ASZ-09a a4_mt1	Analysis	ASZ-09-B-a3_mt1 1	ASZ-09-B-a3_mt1 2	ASZ-09-B-a3_mt1 3	ASZ-09-a3_porous_mt		
WDS	mt3	mt3	mt3	mt3	mt3	mt3	mt3	EDS	mt3	mt3	mt3	mt3	Average	St Dev
wt%														
SiO_2	0.00	0.00	0.00	0.01	0.04	0.00	0.00		0.00	0.00	0.00	0.00	0.04	0.11
TiO_2	0.43	0.33	0.41	0.38	0.24	0.38	0.45		0.48	0.46	0.35	0.00	0.43	0.09
Al_2O_3	0.00	0.00	0.00	0.00	0.00	0.00	0.00						0.00	0.00
Cr_2O_3	0.50	0.43	0.08	0.02	0.02	0.02	0.20		0.50	0.45	0.25	0.00	0.29	0.33
V_2O_3	0.00	0.00	0.00	0.00	0.00	0.00	0.00						0.00	0.00
FeO*	98.86	99.08	99.37	100.33	100.70	100.20	99.92		99.42	99.73	99.86	101.26	99.81	1.50
MnO	0.41	0.42	0.42	0.32	0.25	0.42	0.43		0.44	0.45	0.48	0.37	0.41	0.15
MgO	0.80	0.85	0.81	0.59	0.59	0.94	0.95		1.19	1.44	1.33	0.95	0.84	0.45
ZnO	0.03	0.00	0.00	0.00	0.00	0.02	0.00						0.01	0.01
NiO	0.30	0.32	0.29	0.14	0.10	0.34	0.40		0.42	0.00	0.00	0.00	0.11	0.17
CaO	0.11	0.04	0.10	0.02	0.02	0.00	0.00						0.04	0.05
Total	101.46	101.48	101.47	101.80	102.03	102.31	102.35		102.45	102.54	102.27	102.58		
Si	0.00	0.00	0.00	0.00	0.00	0.00	0.00		0.00	0.00	0.00	0.00	0.00	0.00
Ti	0.01	0.01	0.01	0.01	0.01	0.01	0.01		0.01	0.01	0.01	0.00	0.01	0.00
Al	0.00	0.00	0.00	0.00	0.00	0.00	0.00		0.00	0.00	0.00	0.00	0.00	0.00
Cr	0.01	0.01	0.00	0.00	0.00	0.00	0.01		0.01	0.01	0.01	0.00	0.01	0.01
V	0.00	0.00	0.00	0.00	0.00	0.00	0.00		0.00	0.00	0.00	0.00	0.00	0.00
Fe^{3+}	2.00	2.00	2.00	2.00	2.00	2.00	2.00		1.97	1.97	1.98	2.00	1.98	0.01
Fe^{2+}	1.00	1.00	1.00	1.00	1.00	1.00	1.00		0.84	0.83	0.84	0.88	0.92	0.07
Mn	0.01	0.01	0.01	0.01	0.01	0.01	0.01		0.01	0.01	0.02	0.01	0.01	0.00
Mg	0.05	0.05	0.05	0.03	0.03	0.05	0.05		0.07	0.08	0.07	0.05	0.05	0.03
Zn	0.00	0.00	0.00	0.00	0.00	0.00	0.00		0.00	0.00	0.00	0.00	0.00	0.00
Ni	0.01	0.01	0.01	0.00	0.00	0.01	0.01		0.01	0.00	0.00	0.00	0.00	0.01
Ca														

***Total Fe**

B6. Ilmenite analyses. Formulae were calculated on the basis of 2 cations.

Analysis	LC015_2_1	LC015_2_2	LC015_3_1	LC015_3_2	LC015_3_3	LC015_3_4	LC015_3_5	LC015_3_6	LC015_3_7	LC015_3_8	LC015_3_9
WDS	ilm core	ilm rim	small ilm	ilm rim	small ilm	small ilm	small ilm	ilm rim	ilm core	ilm core	small ilm
wt%											
SiO_2	b.d.l	b.d.l	b.d.l	0.04	b.d.l	0.07	0.09	0.08	0.04	0.04	0.04
TiO_2	55.12	54.84	54.21	53.76	54.66	53.32	53.87	54.22	55.37	54.36	53.70
Al_2O_3	b.d.l	b.d.l	b.d.l	b.d.l	b.d.l	b.d.l	b.d.l	b.d.l	b.d.l	b.d.l	b.d.l
Cr_2O_3	0.13	0.05	0.04	0.09	0.04	0.06	b.d.l	b.d.l	0.04	0.03	0.06
V_2O_3	0.38	0.36	0.35	0.37	0.37	0.38	0.37	0.37	0.38	0.39	0.35
Fe_2O_3	0.20	0.25	0.23	0.36	0.23	0.48	0.39	0.23	0.18	0.42	0.24
FeO	23.93	20.49	26.21	23.35	25.94	24.19	21.72	25.06	26.76	26.78	27.30
MnO	13.63	16.69	15.58	18.24	15.35	16.18	19.34	16.38	13.90	14.27	14.28
MgO	7.48	7.54	4.71	4.28	4.72	4.42	4.21	4.15	5.04	4.59	4.59
ZnO	13.63	16.69	15.58	18.24	15.35	16.18	19.34	16.38	13.90	14.27	14.28
NiO	0.11	0.14	0.11	0.13	0.13	0.15	0.14	0.06	0.08	0.20	0.11
CaO	b.d.l	b.d.l	b.d.l	b.d.l	b.d.l	b.d.l	b.d.l	b.d.l	b.d.l	b.d.l	b.d.l
Total	101.01	100.38	101.48	100.68	101.46	99.33	100.14	100.57	101.79	101.09	100.67
Si	-	-	-	0.00	-	0.00	0.00	0.00	0.00	0.00	0.00
Ti	1.09	1.09	1.07	1.07	1.08	1.07	1.08	1.08	1.09	1.08	1.07
Al	-	-	-	-	-	-	-	-	-	-	-
Cr	0.01	0.00	0.00	0.00	0.00	0.00	-	-	0.00	0.00	0.00
V	0.01	0.01	0.01	0.01	0.01	0.01	0.01	0.01	0.01	0.01	0.01
Fe^{3+}	0.00	0.00	0.00	0.00	0.00	0.01	0.00	0.00	0.00	0.01	0.00
Fe^{2+}	0.48	0.41	0.52	0.47	0.52	0.50	0.44	0.50	0.53	0.54	0.55
Mn	0.00	0.00	0.00	0.00	0.00	0.00	0.00	0.00	0.00	0.00	0.00
Mg	-	-	-	-	-	-	-	-	-	-	-
Zn	0.27	0.33	0.31	0.36	0.30	0.33	0.39	0.33	0.27	0.28	0.28
Ni	0.15	0.15	0.09	0.09	0.09	0.09	0.08	0.08	0.10	0.09	0.09
Ca	-	-	-	-	-	-	-	-	-	-	-

Analysis	LC015_3_10	LC015_4_1	LC015_4_2	LC015_4_4	LC015_4_5	av	st dev	PF001_1_14	PF001_1_15	PF001_1_16	PF001_1_19	PF001_1_25	PF001_2_8
WDS	small ilm	ilm rim	ilm rim	ilm core	ilm rim			matrix	matrix	rim to ti-mt	rim to ti-mt	matrix	matrix
wt%													
SiO_2	b.d.l	0.03	0.05	0.03	0.05	0.04	0.02	0.22	0.06	b.d.l	0.32	b.d.l	0.06
TiO_2	55.00	54.72	54.14	54.15	54.25	54.36	0.56	50.14	50.59	40.53	50.41	50.45	50.28
Al_2O_3	b.d.l	b.d.l	b.d.l	b.d.l	b.d.l	b.d.l	b.d.l	b.d.l	b.d.l	b.d.l	0.07	b.d.l	b.d.l
Cr_2O_3	0.03	b.d.l	0.05	b.d.l	b.d.l	0.04	0.03	b.d.l	b.d.l	b.d.l	b.d.l	b.d.l	b.d.l
V_2O_3	0.38	0.41	0.39	0.39	0.35	0.37	0.02	0.40	0.39	0.34	0.39	0.36	0.35
Fe_2O_3	0.33	0.20	0.30	0.17	0.35	0.29	0.09	0.52	0.07	0.04	0.33	0.17	0.06
FeO	26.86	21.75	20.62	20.61	20.07	23.85	2.65	46.98	46.78	55.64	46.45	47.77	47.75
MnO	13.76	18.64	20.37	20.17	20.77	16.72	2.53	1.80	1.88	1.38	1.85	2.20	2.21
MgO	5.10	5.53	5.02	4.90	4.70	5.06	1.02	0.54	0.30	0.29	0.70	0.38	0.51
ZnO	13.76	18.64	20.37	20.17	20.77	16.72	2.53	b.d.l	b.d.l	b.d.l	b.d.l	b.d.l	b.d.l
NiO	0.15	0.09	0.12	0.08	0.07	0.12	0.04	0.05	0.06	b.d.l	0.07	0.08	b.d.l
CaO	b.d.l	b.d.l	b.d.l	b.d.l	b.d.l	b.d.l		b.d.l	b.d.l	b.d.l	b.d.l	b.d.l	b.d.l
Total	101.67	101.39	101.07	100.49	100.70	100.87	0.64	100.72	100.13	98.31	100.64	101.48	101.25
Si	-	0.00	0.00	0.00	0.00	0.00	0.00	0.00	0.00	-	0.00	-	0.00
Ti	1.08	1.08	1.07	1.08	1.08	1.08	0.01	0.99	1.01	0.82	1.00	0.99	0.99
Al	-	-	-	-	-	-	-	-	-	-	-	-	-
Cr	0.00	-	0.00	-	-	0.00	0.00	-	-	-	-	-	-
V	0.01	0.01	0.01	0.01	0.01	0.01	0.00	0.01	0.01	0.01	0.01	0.01	0.01
Fe^{3+}	0.00	0.00	0.00	0.00	0.00	0.00	0.00	0.01	0.00	0.00	0.01	0.00	0.00
Fe^{2+}	0.53	0.43	0.41	0.41	0.41	0.48	0.05	0.94	0.94	1.13	0.93	0.94	0.94
Mn	0.00	0.00	0.00	0.00	0.00	0.00	0.00	0.04	0.04	0.03	0.04	0.04	0.04
Mg	-	-	-	-	-	-	-	0.01	0.01	0.01	0.02	0.01	0.01
Zn	0.27	0.37	0.40	0.40	0.41	0.33	0.05	-	-	-	-	-	-
Ni	0.10	0.11	0.10	0.10	0.09	0.10	0.02	0.00	0.00	-	0.00	0.00	-
Ca	-	-	-	-	-	-	-	-	-	-	-	-	-

Analysis	PF001_2_12	PF001_2_33	PF001_3_9	PF001_3_11	PF001_3_19	PF001_3_20	PF001_3_32	PF001_3_37	PF001_3_40	PF001_5_1	PF001_5_2	PF001_5_3	Average	St Dev.
WDS	matrix	matrix	rim to ti-mt	rim to ti-mt	matrix	matrix	matrix	rim to ti-mt	nr trem	matrix	matrix	matrix		
wt%														
SiO_2	b.d.l	b.d.l	0.11	b.d.l	0.07	0.08	0.39	b.d.l	0.13	0.11	0.08	b.d.l	0.10	0.10
TiO_2	51.81	50.88	50.20	50.28	49.98	49.97	51.42	51.64	50.76	49.78	50.68	51.05	50.05	2.44
Al_2O_3	b.d.l	b.d.l	b.d.l	b.d.l	b.d.l	b.d.l	b.d.l	b.d.l	0.14	b.d.l	b.d.l	b.d.l	b.d.l	
Cr_2O_3	b.d.l	b.d.l	b.d.l	b.d.l	b.d.l	b.d.l	b.d.l	b.d.l	b.d.l	b.d.l	b.d.l	b.d.l	b.d.l	
V_2O_3	0.35	0.39	0.37	0.35	0.37	0.39	0.38	0.37	0.34	0.39	0.39	0.36	0.37	0.02
Fe_2O_3	0.09	0.09	0.34	0.32	0.37	0.60	0.16	0.13	0.55	0.23	0.11	0.14	0.24	0.18
FeO	46.36	46.38	46.34	45.92	45.38	45.87	45.20	45.72	45.46	46.79	46.09	46.91	46.88	2.30
MnO	2.35	2.28	2.20	2.40	2.32	2.26	2.51	2.43	2.51	1.92	1.92	1.98	2.13	0.30
MgO	0.34	0.47	0.52	0.48	0.45	0.54	1.02	0.53	0.51	0.30	0.31	0.34	0.47	0.18
ZnO	b.d.l	b.d.l	b.d.l	b.d.l	b.d.l	0.07	b.d.l	b.d.l	b.d.l	b.d.l	b.d.l	0.05	b.d.l	
NiO	0.08	b.d.l	b.d.l	b.d.l	b.d.l	0.04	b.d.l	0.07	b.d.l	b.d.l	0.04	0.04	0.04	0.03
CaO	b.d.l	b.d.l	0.16	0.16	0.18	0.23	b.d.l	b.d.l	b.d.l	b.d.l	b.d.l	b.d.l	0.05	0.07
Total	101.45	100.60	100.25	99.97	99.14	100.05	101.16	100.97	100.45	99.63	99.65	100.91	100.38	0.84
Si	-	-	0.00	-	0.00	0.00	0.00	-	0.00	0.00	0.00	-	0.00	0.00
Ti	1.02	1.01	1.00	1.00	1.01	1.00	1.02	1.02	1.01	1.00	1.02	1.01	1.00	0.04
Al	-	-	-	-	-	-	-	-	-	-	-	-	-	-
Cr	-	-	-	-	-	-	-	-	-	-	-	-	-	-
V	0.01	0.01	0.01	0.01	0.01	0.01	0.01	0.01	0.01	0.01	0.01	0.01	0.01	0.00
Fe^{3+}	0.00	0.00	0.01	0.01	0.01	0.01	0.00	0.00	0.01	0.00	0.00	0.00	0.00	0.00
Fe^{2+}	0.92	0.92	0.93	0.92	0.92	0.93	0.90	0.91	0.91	0.94	0.93	0.93	0.94	0.05
Mn	0.05	0.04	0.04	0.05	0.05	0.04	0.05	0.05	0.05	0.04	0.04	0.04	0.04	0.01
Mg	0.01	0.01	0.01	0.01	0.01	0.01	0.02	0.01	0.01	0.01	0.01	0.01	0.01	0.00
Zn	-	-	-	-	-	-	-	-	-	-	-	-	-	-
Ni	0.00	-	0.00	0.00	0.00	0.00	-	0.00	-	0.00	0.00	0.00	0.00	0.00
Ca	-	-	-	-	-	-	-	-	-	-	-	-	-	-

Analysis	S-09-ASZ-09a a3_ti_mt_matrix_sulf	S-09-ASZ-09a a3_ti_mt_matrix_sulf	S-09-VSZ02-area2_ilm
WDS			
wt%			
SiO_2	0.04	0.25	2.05
TiO_2	54.71	54.65	51.29
Al_2O_3	0.00	0.00	0.05
Cr_2O_3	0.00	0.00	0.00
V_2O_3	0.00	0.00	0.00
Fe_2O_3	24.89	23.10	40.43
FeO			
MnO	13.61	14.94	2.13
MgO	5.93	5.77	0.92
ZnO	0.03	0.02	0.01
NiO	0.00	0.00	0.00
CaO	0.49	2.02	2.43
Total	99.75	100.77	99.30
Si			
Ti	1.09	1.06	1.03
Al	0.00	0.00	0.00
Cr	0.00	0.00	0.00
V	0.00	0.00	0.00
Fe^{3+}	0.49	0.45	0.81
Fe^{2+}	0.27	0.28	0.04
Mn	0.13	0.13	0.02
Mg	0.00	0.00	0.00
Zn	0.00	0.00	0.00
Ni	0.02	0.08	0.10
Ca	-	-	-

B7. Sulfide analyses. Mole %.

Pentlandite		Analysis	S	Fe	Co	Ni	Total	XS	Xfe	Xco	Xni
VSZ-05											
WDS	pn1	VSZ05_area2_s3_2	33.54	29.29	6.00	29.53	98.47	0.48	0.24	0.05	0.23
	pn1	VSZ05_area2_s3_3	33.70	29.71	5.97	29.73	99.23	0.48	0.24	0.05	0.23
	pn1	VSZ05_area2_s3_4	33.60	29.51	6.11	29.89	99.26	0.48	0.24	0.05	0.23
	pn1	VSZ05_area1_s1_1	33.02	31.21	4.14	28.91	97.39	0.48	0.26	0.03	0.23
	pn1	VSZ05_area1_s1_1	33.66	31.22	4.17	29.49	98.63	0.48	0.26	0.03	0.23
	pn1	VSZ05_area3_s3	33.82	29.75	5.51	30.39	99.62	0.48	0.24	0.04	0.24
	pn2	VSZ05_area2_s3_1	33.94	29.35	5.91	29.47	98.78	0.48	0.24	0.05	0.23
	pn2	VSZ05_area3_s3	33.57	29.39	5.49	29.95	98.55	0.48	0.24	0.04	0.23
	pn2	VSZ05_area4_s1	32.96	28.78	7.07	30.88	99.82	0.47	0.24	0.05	0.24
	pn2	VSZ05_area4_s1	32.46	29.30	7.03	31.03	99.88	0.46	0.24	0.05	0.24
	pn2	VSZ05_area4_s2	33.61	28.99	7.24	29.79	99.77	0.48	0.24	0.06	0.23
		Average	33.45	29.68	5.88	29.91	99.04	0.48	0.24	0.05	0.23
		St Dev	0.44	0.81	1.04	0.63	0.76	0.01	0.01	0.01	0.00
ASZ-09											
EDS	pn3	ASZ-09-B-A2_SULF1 1	32.71	29.19	2.35	33.55	97.80	0.47	0.24	0.02	0.27
	pn3	ASZ-09-B-A2_SULF1 5	32.67	29.28	2.30	33.56	97.81	0.47	0.24	0.02	0.27
	pn3	ASZ-09-B-A2_SULF1 4	32.83	28.62	3.09	32.75	97.29	0.48	0.24	0.02	0.26
	pn3	ASZ-09-B-A2_SULF1 3	32.48	29.13	2.41	33.98	98.00	0.47	0.24	0.02	0.27
	pn3	ASZ-09-B-A2_SULF1 2	32.52	29.17	2.21	33.47	97.37	0.47	0.24	0.02	0.27
WDS	pn3	ASZ-S09-b area3_s1	33.12	28.93	2.19	34.34	98.71	0.48	0.24	0.02	0.27
	pn3	ASZ-S09-b area3_s1	32.86	29.24	2.11	33.98	98.33	0.47	0.24	0.02	0.27
	pn3	ASZ-S09-b area3_s1	32.77	29.38	2.11	33.76	98.16	0.47	0.24	0.02	0.27
EDS	pn2	ASZ-09-B-A5 SULF1 5	33.35	29.09	3.09	33.40	99.14	0.48	0.24	0.02	0.26
	pn2	ASZ-09-B-A5 SULF1 4	32.58	29.27	1.85	33.47	97.17	0.47	0.24	0.01	0.27
	pn2	ASZ-09-B-A5 SULF1 3	33.48	28.94	2.65	33.24	98.31	0.48	0.24	0.01	0.26
	pn2	ASZ-09-B-A5 SULF1 2	33.56	29.19	2.69	33.05	98.50	0.48	0.24	0.01	0.26
	pn2	ASZ-09-B-A5 SULF1 1	32.77	29.32	2.01	33.21	97.31	0.48	0.24	0.02	0.26
WDS	pn2	ASZ-S09-b area5_s1	33.94	29.15	2.18	33.93	99.40	0.48	0.24	0.02	0.26
	pn2	ASZ-S09-b area5_s1_2	33.90	28.87	2.16	34.22	99.29	0.48	0.24	0.02	0.27
	pn2	ASZ-S09-b area5_s1_2	33.80	28.02	2.28	34.54	98.78	0.48	0.23	0.02	0.27
	pn2	ASZ-S09-b area5_s2	33.76	27.52	2.11	35.53	99.11	0.48	0.23	0.02	0.28
	pn2	ASZ-S09-b area5_s2	33.65	27.46	2.15	35.45	99.01	0.48	0.23	0.02	0.28
	pn2	ASZ-S09-b area5_s2	33.72	26.98	2.04	35.21	98.13	0.48	0.22	0.02	0.28
	pn2	ASZ-S09-b area5_s3	33.76	26.90	2.07	34.79	97.64	0.49	0.22	0.02	0.27
	pn2	ASZ-S09-b area5_s4	33.35	28.72	1.91	33.59	97.76	0.48	0.24	0.02	0.27
	pn2	ASZ-S09-b area5_s5	33.91	28.93	1.97	33.97	99.02	0.48	0.24	0.02	0.26
	pn1	ASZ-S09-b area1_s1	33.69	27.75	2.05	34.62	98.31	0.48	0.23	0.02	0.27
	pn1	ASZ-S09-b area1_s2	33.52	28.43	2.24	34.18	98.53	0.48	0.23	0.02	0.27
	pn1	ASZ-S09-b area1_s2	33.48	29.16	2.27	34.33	99.49	0.48	0.24	0.02	0.27
	pn1	ASZ-S09-b area1_s2	33.67	29.28	2.32	34.44	99.89	0.48	0.24	0.02	0.27

Pentlandite											
		Analysis	**S**	**Fe**	**Co**	**Ni**	**Total**	**XS**	**Xfe**	**Xco**	**Xni**
WDS	pn1	ASZ-S09-b area1_s2	33.25	28.80	2.25	34.38	98.86	0.48	0.24	0.02	0.27
	pn1	ASZ-S09-b area1_s2	33.65	29.12	2.26	34.43	99.68	0.48	0.24	0.02	0.27
	pn1	ASZ-S09-b area1_s3	33.74	29.02	2.21	34.46	99.60	0.48	0.24	0.02	0.27
	pn1	ASZ-S09-b area1_s4	33.65	29.29	2.27	34.51	99.94	0.48	0.24	0.02	0.27
	pn1	ASZ-S09-b area1_s4	33.48	28.91	2.26	34.62	99.45	0.48	0.24	0.02	0.27
	pn1	ASZ-S09-b area1_s4	33.61	28.74	2.30	34.64	99.53	0.48	0.23	0.02	0.27
	pn1	ASZ-S09-b area4_s1	32.83	27.00	2.30	35.22	97.59	0.48	0.23	0.02	0.28
	pn1	ASZ-S09-b area4_s2	32.78	28.37	2.32	34.18	97.80	0.47	0.24	0.02	0.27
	pn1	ASZ-S09-b area4_s2	32.67	27.68	2.31	34.42	97.24	0.48	0.23	0.02	0.27
	pn1	ASZ-S09-b area4_s3	32.75	27.73	2.18	35.38	98.11	0.47	0.23	0.02	0.28
	pn1	ASZ-S09-b area4_s3	32.72	27.58	2.26	35.59	98.28	0.47	0.23	0.02	0.28
	pn1	ASZ-S09-b area4_s3	32.90	26.80	2.45	35.37	97.65	0.48	0.22	0.02	0.28
		Average	33.26	28.55	2.27	34.26	98.47	0.48	0.24	0.02	0.27
		St Dev	0.47	0.81	0.26	0.74	0.82	0.00	0.01	0.00	0.01

Heazlewoodite		**Analysis**	**S**	**Fe**	**Co**	**Ni**	**Total**	**XS**	**Xfe**	**Xco**	**Xni**
VSZ-03											
EDS	hz1	VSZ-03_A1_SULF1_2	28.19			71.66	99.85	0.42	0.00	0.00	0.58
	hz1	VSZ-03_A1_SULF1_3	28.21			71.47	99.68	0.42	0.00	0.00	0.58
	hz1	VSZ-03_A1_SULF1_4	27.83	0.41		71.43	99.67	0.41	0.00	0.00	0.58
	hz1	VSZ-03_A1_SULF1_1	27.33	1.12		70.12	98.57	0.41	0.01	0.00	0.58
	hz2	VSZ_03_A4_SULF_1 2	27.36	3.81		68.71	99.88	0.41	0.03	0.00	0.56
		Av	27.78	1.78	#DIV/0!	70.68	99.53	0.41	0.01	0.00	0.58
		St Dev	0.43	1.79	#DIV/0!	1.26	0.55	0.00	0.01	0.00	0.01
VSZ-05											
WDS	hz1	VSZ05_area3_s1	27.12	1.70	0.00	72.29	101.19	0.40	0.01	0.00	0.58
	hz1	VSZ05_area3_s1	27.14	1.49	0.00	72.63	101.41	0.40	0.01	0.00	0.59
	hz1	VSZ05_area3_s1	27.32	0.72	0.00	73.16	101.33	0.40	0.01	0.00	0.59
	hz1	VSZ05_area3_s1	27.24	0.97	0.34	72.22	101.01	0.40	0.01	0.00	0.59
	hz1	VSZ05_area3_s1	27.27	0.77	0.00	72.86	101.00	0.40	0.01	0.00	0.59
	hz1	VSZ05_area3_s1	27.19	3.81	0.00	71.83	102.98	0.40	0.03	0.00	0.57
	hz1	VSZ05_area3_s4	27.39	0.65	0.00	71.67	99.85	0.41	0.01	0.00	0.59
	hz1	VSZ05_area3_s4	27.39	0.65	0.00	71.67	99.85	0.41	0.01	0.00	0.59
	hz1	VSZ05_area4_s2	30.57	1.01	0.05	67.85	99.68	0.45	0.01	0.00	0.54
	hz1	VSZ05_area4_s2	27.34	0.49	0.01	73.07	101.00	0.40	0.00	0.00	0.59
	hz1	VSZ05_area4_s2	27.25	0.27	0.00	72.74	100.39	0.41	0.00	0.00	0.59
	hz1	VSZ05_area4_s2	27.31	0.12	0.00	73.33	100.87	0.40	0.00	0.00	0.59
	hz1	VSZ05_area4_s2	27.34	0.21	0.00	73.21	100.86	0.41	0.00	0.00	0.59
	hz1	VSZ05_area4_s2	27.20	0.11	0.00	72.92	100.39	0.41	0.00	0.00	0.59
	hz1	VSZ05_area4_s2	29.22	0.21	0.00	71.09	100.68	0.43	0.00	0.00	0.57
	hz2	VSZ05_area3_s3	27.81	0.71	0.02	73.04	101.66	0.41	0.01	0.00	0.59

Heazlewoodite											
		Analysis	**S**	**Fe**	**Co**	**Ni**	**Total**	**XS**	**Xfe**	**Xco**	**Xni**
VSZ-05	hz2	VSZ05_area3_s3	27.86	0.41	0.00	73.05	101.49	0.41	0.00	0.00	0.59
	hz2	VSZ05_area3_s6	28.55	0.35	0.00	71.83	100.88	0.42	0.00	0.00	0.58
	hz2	VSZ05_area3_s6	29.23	0.33	0.00	70.82	100.54	0.43	0.00	0.00	0.57
	hz2	VSZ05_area3_s6	28.55	0.35	0.00	71.83	100.88	0.42	0.00	0.00	0.58
	hz2	VSZ05_area3_s6	29.23	0.33	0.00	70.82	100.54	0.43	0.00	0.00	0.57
		Av	27.88	0.75	0.02	72.09	100.88	0.41	0.01	0.00	0.58
		St dev	0.96	0.82	0.07	1.25	0.72	0.01	0.01	0.00	0.01
GSZ-11											
WDS	hz	GSZ11-area1_s1	29.62	0.39	0.00	67.58	97.72	0.44	0.00	0.00	0.55
		GSZ11-area2_s2	27.06	0.49	0.00	71.72	99.39	0.41	0.00	0.00	0.59
		GSZ11-area4_s1	27.54	0.83	0.00	72.32	100.86	0.41	0.01	0.00	0.59
		GSZ11-area4_s1	27.14	0.80	0.00	71.89	99.96	0.41	0.01	0.00	0.59
		GSZ11-area4_s2	27.23	2.62	0.00	72.59	102.58	0.40	0.02	0.00	0.58
		GSZ11-area4_s2	27.66	2.09	0.00	72.81	102.77	0.40	0.02	0.00	0.58
		GSZ11-area4_s2	27.03	3.13	0.00	72.45	102.75	0.39	0.03	0.00	0.58
		GSZ11-area4_s2	26.88	3.30	0.00	72.24	102.58	0.39	0.03	0.00	0.58
		GSZ11-area4_s3	30.15	2.36	0.00	67.86	100.56	0.44	0.02	0.00	0.54
		GSZ11-area4_s3	27.07	2.61	0.00	72.34	102.15	0.40	0.02	0.00	0.58
	hz	GSZ-11a-sulf-1	27.13	2.83		72.25	102.22	0.40	0.02	0.00	0.58
		GSZ-11a-sulf-1	26.50	2.73		72.60	101.83	0.39	0.02	0.00	0.59
		GSZ-11a-sulf-1	29.84	2.66		67.85	100.35	0.44	0.02	0.00	0.54
		GSZ-11a-sulf-1	27.16	2.56		72.11	101.82	0.40	0.02	0.00	0.58
		GSZ-11a-sulf-1	26.74	2.60		72.34	101.69	0.39	0.02	0.00	0.58
		GSZ-11a-sulf-3	25.54	1.50		74.54	101.57	0.38	0.01	0.00	0.61
		GSZ-11a-sulf-3	25.79	1.55		76.01	103.35	0.38	0.01	0.00	0.61
		GSZ-11a-sulf-4	25.93	2.52		74.95	103.41	0.38	0.02	0.00	0.60
		GSZ-11a-sulf-4	25.84	2.52		74.63	102.99	0.38	0.02	0.00	0.60
		GSZ-11a-sulf-4	25.93	2.70		75.01	103.65	0.38	0.02	0.00	0.60
		GSZ-11a-sulf-4	29.70	2.66		70.27	102.62	0.43	0.02	0.00	0.55
		GSZ-11a-sulf-4	25.89	3.06		75.17	104.12	0.38	0.03	0.00	0.60
		GSZ-11a-sulf-4	25.40	5.09		74.40	104.89	0.37	0.04	0.00	0.59
		GSZ-11a-sulf-4	25.41	5.40		74.98	105.78	0.37	0.04	0.00	0.59
		GSZ-11a-sulf-4	24.36	9.45		70.24	104.06	0.36	0.08	0.00	0.56
		GSZ-11a-sulf-4	25.68	6.12		74.30	106.09	0.37	0.05	0.00	0.58
		GSZ-11a-sulf-5	27.25	1.57		73.83	102.66	0.40	0.01	0.00	0.59
		GSZ-11a-sulf-5	27.48	1.55		73.81	102.84	0.40	0.01	0.00	0.59
		GSZ-11a-sulf-5	27.67	1.64		73.68	102.99	0.40	0.01	0.00	0.58
		GSZ-11a-sulf-5	30.95	1.79		68.34	101.07	0.45	0.01	0.00	0.54
		GSZ-11a-sulf-6	27.37	3.95		74.21	105.52	0.39	0.03	0.00	0.58
		GSZ-11a-sulf-7	27.13	2.83		72.25	102.39	0.40	0.02	0.00	0.58

Heazlewoodite										
	Analysis	**S**	**Fe**	**Co**	**Ni**	**Total**	**XS**	**Xfe**	**Xco**	**Xni**
WDS	GSZ-11a-sulf-8	26.50	2.73		72.60	101.95	0.39	0.02	0.00	0.59
	GSZ-11a-sulf-9	29.84	2.66		67.85	100.44	0.44	0.02	0.00	0.54
	GSZ-11a-sulf-10	27.16	2.56		72.11	101.98	0.40	0.02	0.00	0.58
	GSZ-11a-sulf-11	26.74	2.60		72.34	101.81	0.40	0.02	0.00	0.58
EDS	GSZ11A-HZ4 1	26.94	1.68		70.81	99.43	0.41	0.01	0.00	0.58
	GSZ11A-HZ4 2	26.82	1.61		71.05	99.48	0.40	0.01	0.00	0.58
	GSZ11A-HZ4 3	26.83	1.53		71.06	99.42	0.40	0.01	0.00	0.58
	GSZ11A-HZ4 4	27.76	1.57		71.18	100.51	0.41	0.01	0.00	0.58
	GSZ11A-HZ5 1	27.20	1.44		70.85	99.49	0.41	0.01	0.00	0.58
	GSZ11A-HZ5 2	27.42	1.35		71.24	100.01	0.41	0.01	0.00	0.58
	GSZ11A-HZ5 3	27.47	1.33		71.27	100.07	0.41	0.01	0.00	0.58
	GSZ11A-HZ5 4	27.33	1.38		71.49	100.20	0.41	0.01	0.00	0.58
	GSZ11A-HZ2 1	27.53	1.77		71.84	101.14	0.41	0.01	0.00	0.58
	GSZ11A-HZ2 2	27.40	1.50		71.80	100.70	0.41	0.01	0.00	0.58
	GSZ11A-HZ2 3	27.23	1.54		71.65	100.42	0.41	0.01	0.00	0.58
	GSZ11A-HZ2 4	27.83	1.64		71.57	101.04	0.41	0.01	0.00	0.58
	GSZ11A-HZ2 5	27.54	3.05		70.73	101.32	0.41	0.03	0.00	0.57
	GSZ11A-HZ2 6	27.08	3.15		70.67	100.90	0.40	0.03	0.00	0.57
	Av	27.21	2.46	0.00	72.07	101.79	0.40	0.02	0.00	0.58
	St Dev	1.28	1.51	0.00	1.99	1.78	0.02	0.01	0.00	0.02

Millerite	Analysis	S	Fe	Co	Ni	Total	XS	Xfe	Xco	Xni
VSZ-05										
WDS	VSZ05_area3_s3	31.42	0.67	0.02	65.96	99.50	0.46	0.01	0.00	0.53
	VSZ05_area3_s5	32.58	0.33	0.00	65.49	98.55	0.48	0.00	0.00	0.52
	VSZ05_area4_s1	33.08	0.23	0.00	63.68	97.05	0.49	0.00	0.00	0.51
	Av	32.36	0.41	0.01	65.04	98.37	0.47	0.00	0.00	0.52
	St Dev	0.85	0.23	0.01	1.21	1.23	0.01	0.00	0.00	0.01
GSZ-11	GSZ11-area1_s1	34.81	0.53	0.00	63.07	98.53	0.50	0.00	0.00	0.50
WDS	GSZ-11a-sulf-2	32.48	2.54		65.86	100.88	0.46	0.02	0.00	0.51
	GSZ-11a-sulf-2	32.33	2.50		65.75	100.57	0.46	0.02	0.00	0.52
	GSZ-11a-sulf-2	32.85	2.53		64.97	100.35	0.47	0.02	0.00	0.51
	GSZ-11a-sulf-2	32.77	2.57		65.58	100.92	0.47	0.02	0.00	0.51
	GSZ-11a-sulf-2	30.97	2.39		67.13	100.50	0.45	0.02	0.00	0.53
EDS	GSZ11A-MILL3 4	35.74	1.62		63.20	100.56	0.50	0.01	0.00	0.48
	GSZ11A-MILL2 2	35.79	1.95		64.12	101.86	0.50	0.02	0.00	0.49
	GSZ11A-MILL2 3	35.91	1.55		63.46	100.92	0.50	0.01	0.00	0.48
	GSZ11A-MILL2 4	35.68	1.59		64.11	101.38	0.50	0.01	0.00	0.49
	GSZ11A-MILL2 5	32.98	1.43		65.97	100.38	0.47	0.01	0.00	0.52
	GSZ11A-MILL2 1	33.07	1.29		65.98	100.34	0.47	0.01	0.00	0.52
	GSZ11A-MILL3 1	35.69	1.59		64.01	101.29	0.50	0.01	0.00	0.49
	GSZ11A-MILL3 2	35.16	1.42		63.57	100.15	0.50	0.01	0.00	0.49
	GSZ11A-MILL3 3	35.20	1.57		64.03	100.80	0.50	0.01	0.00	0.49
	GSZ11A-MILL1 6	35.55	2.40		64.16	102.11	0.49	0.02	0.00	0.49
	GSZ11A-MILL1 1	34.79	1.97		63.11	99.87	0.49	0.02	0.00	0.49
	GSZ11A-MILL1 2	36.17	2.05		63.05	101.27	0.50	0.02	0.00	0.48
	GSZ11A-MILL1 3	34.17	3.07		64.35	101.59	0.48	0.02	0.00	0.49
	GSZ11A-MILL1 4	36.12	3.06		62.94	102.12	0.50	0.02	0.00	0.48
	GSZ11A-MILL1 5	32.68	2.39		65.08	100.15	0.47	0.02	0.00	0.51
	Av	34.33	2.00		64.45	100.79	0.49	0.02	0.00	0.50
	St Dev	1.58	0.64		1.21	0.83	0.02	0.01	0.00	0.02

B8. Serpentine analyses. Formulae were calculated on the basis of 20 cations.

Analysis	LC015_1_1	LC015_1_3	LC015_1_4	LC015_1_5	LC015_1_16	LC015_1_17	LC015_2_3	LC015_2_7	LC015_3_11	LC015_3_12	LC015_3_14	LC015_4_3	LC015_4_6	LC015_4_10	LC015_4_19
WDS	nr Cr-mt	nr Cr-mt	nr Cr-mt	nr Cr-mt	matrix	nr Cr-mt	nr ilm	nr Cr-mt	nr ilm	matrix	matrix	nr ilm	matrix	nr ilm	matrix
wt%															
SiO_2	40.7	42.1	42.0	42.4	41.5	43.2	42.3	41.1	42.0	42.9	43.1	43.5	43.0	42.9	43.3
TiO_2	b.d.l	b.d.l	b.d.l	b.d.l	b.d.l	b.d.l	0.05	b.d.l	0.12	0.05	0.09	0.04	0.17	b.d.l	b.d.l
Al_2O_3	2.22	1.88	1.93	2.23	2.44	1.96	2.11	2.41	2.37	1.90	2.10	1.95	2.09	2.20	1.88
Cr_2O_3	0.52	0.30	0.30	0.46	0.63	0.38	0.30	0.11	0.36	0.30	0.40	0.24	0.32	0.28	0.33
V_2O_3	b.d.l	0.03	b.d.l	b.d.l	b.d.l	0.03	b.d.l	b.d.l	b.d.l	b.d.l	b.d.l	b.d.l	b.d.l	b.d.l	b.d.l
FeO	3.46	3.38	3.62	3.35	3.12	3.37	2.52	3.60	2.93	2.42	2.56	2.47	2.64	3.47	3.29
MnO	0.07	0.10	0.11	0.13	0.11	0.08	0.16	0.08	0.18	0.14	0.13	0.10	0.16	0.09	0.12
MgO	39.1	39.9	39.4	39.9	39.9	40.8	40.2	39.6	40.1	40.5	40.9	41.0	41.1	41.1	41.4
ZnO	b.d.l	b.d.l	b.d.l	b.d.l	b.d.l	b.d.l	b.d.l	b.d.l	b.d.l	b.d.l	b.d.l	b.d.l	0.03	b.d.l	0.04
NiO	0.15	0.22	0.19	0.30	0.14	0.12	0.15	0.22	0.15	0.18	0.19	0.17	0.18	0.16	0.15
CaO	0.01	0.01	0.02	0.01	0.00	0.01	0.01	0.02	0.00	0.01	0.00	0.00	0.00	0.00	0.02
Total	86.2	86.2	86.2	86.3	86.2	86.3	86.2	86.2	86.2	86.2	86.2	86.2	86.2	86.3	86.3
Si	7.74	7.86	7.88	7.85	7.74	7.88	7.88	7.73	7.80	7.94	7.89	7.95	7.85	7.88	7.84
Ti	-	-	-	-	-	-	-	-	-	-	-	-	0.01	-	-
Al	0.50	0.41	0.43	0.49	0.54	0.42	0.46	0.53	0.52	0.41	0.45	0.42	0.45	0.47	0.40
Cr	0.08	0.04	0.04	0.07	0.09	0.05	0.04	0.02	0.05	0.04	0.06	0.03	0.05	0.04	0.05
V	-	-	-	-	-	-	-	-	-	-	-	-	-	-	-
Fe^{2+}	0.55	0.53	0.57	0.52	0.49	0.51	0.39	0.57	0.45	0.37	0.39	0.38	0.40	0.53	0.50
Mn	0.00	0.00	0.00	0.00	0.00	0.00	0.01	0.00	0.01	0.01	0.01	0.00	0.01	0.00	0.00
Mg	11.09	11.09	11.03	11.01	11.10	11.09	11.17	11.10	11.10	11.17	11.15	11.17	11.17	11.13	11.16
Zn	-	-	-	-	-	-	-	-	-	-	-	-	-	-	-
Ni	0.02	0.03	0.03	0.04	0.02	0.02	0.02	0.03	0.02	0.03	0.03	0.02	0.03	0.02	0.02
Ca	-	-	-	-	-	-	-	-	-	-	-	-	-	-	-
X(Mg)	0.95	0.95	0.95	0.96	0.96	0.96	0.97	0.95	0.96	0.97	0.97	0.97	0.97	0.95	0.96

Analysis	LC015_4_23	LC015_4_24	LC015_5_3	LC015_5_8	Av	St. Dev	LC015_2_4	LC015_2_10	LC015_3_15	LC015_3_18	LC015_3_19	LC015_3_20	LC015_3_22	LC015_4_8	LC015_4_9
WDS wt%	nr small Cr-mt	nr small Cr-mt	nr Cr-mt	nr Cr-mt			nr ilm	nr Cr-mt	nr Cr-mt	nr Cr-mt	nr Cr-mt	nr Cr-mt	nr Cr-mt	nr Cr-mt	nr ilm
SiO_2	42.5	43.0	43.1	42.8	42.5	0.77	42.32	42.96	43.25	42.99	43.04	43.01	42.55	41.98	42.69
TiO_2	b.d.l	b.d.l	b.d.l	b.d.l	b.d.l		0.11	0.00	0.01	0.00	0.01	0.00	0.00	0.00	0.25
Al_2O_3	2.39	1.93	1.86	2.10	2.10	0.20	2.14	2.27	1.91	2.09	1.88	2.12	2.47	2.27	2.03
Cr_2O_3	0.33	0.28	0.33	0.33	0.34	0.11	0.41	0.32	0.27	0.30	0.37	0.31	0.37	0.48	0.37
V_2O_3	b.d.l	b.d.l	b.d.l	b.d.l	b.d.l	0.00	b.d.l	b.d.l	b.d.l	b.d.l	b.d.l	b.d.l	b.d.l	0.03	b.d.l
FeO	3.37	3.20	3.67	3.54	3.16	0.43	2.62	3.39	3.11	3.25	3.58	3.86	3.66	3.30	2.55
MnO	0.07	0.11	0.10	0.09	0.11	0.03	0.18	0.13	0.07	0.10	0.09	0.14	0.09	0.09	0.21
MgO	40.7	41.3	41.7	41.0	40.5	0.73	40.33	40.71	40.98	40.64	40.62	41.30	40.76	40.19	40.74
ZnO	0.03	b.d.l	b.d.l	b.d.l	b.d.l		b.d.l	b.d.l	b.d.l	b.d.l	b.d.l	b.d.l	b.d.l	b.d.l	b.d.l
NiO	0.17	0.12	0.21	0.16	0.17	0.04	0.18	0.17	0.19	0.16	0.16	0.16	0.20	0.23	0.22
CaO	0.01	0.01	0.00	0.00	0.01	0.01	b.d.l	b.d.l	b.d.l	b.d.l	b.d.l	b.d.l	b.d.l	b.d.l	b.d.l
Total	86.3	86.3	86.3	86.3	86.2	0.03	88.31	89.98	89.80	89.55	89.77	90.91	90.10	88.59	89.07
Si	7.78	7.82	7.77	7.79	7.83	0.06	1.89	1.89	1.90	1.90	1.90	1.87	1.87	1.87	1.89
Ti	-	-	-	-	0.00	0.00	0.00	0.00	0.00	0.00	0.00	0.00	0.00	0.00	0.01
Al	0.52	0.41	0.40	0.45	0.46	0.05	0.11	0.12	0.10	0.11	0.10	0.11	0.13	0.12	0.11
Cr	0.05	0.04	0.05	0.05	0.05	0.02	0.01	0.01	0.01	0.01	0.01	0.01	0.01	0.02	0.01
V	-	-	-	-	0.00	0.00	0.00	0.00	0.00	0.00	0.00	0.00	0.00	0.00	0.00
Fe^{2+}	0.52	0.49	0.55	0.54	0.49	0.07	0.10	0.12	0.11	0.12	0.13	0.14	0.13	0.12	0.09
Mn	0.00	0.00	0.00	0.00	0.00	0.00	0.01	0.00	0.00	0.00	0.00	0.01	0.00	0.00	0.01
Mg	11.10	11.20	11.19	11.13	11.12	0.05	2.69	2.67	2.69	2.68	2.67	2.68	2.67	2.68	2.69
Zn	-	-	-	-	-	-	0.00	0.00	0.00	0.00	0.00	0.00	0.00	0.00	0.00
Ni	0.02	0.02	0.03	0.02	0.03	0.01	0.01	0.01	0.01	0.01	0.01	0.01	0.01	0.01	0.01
Ca	-	-	-	-	-	-	-	-	-	-	-	-	-	-	-
X(Mg)	0.96	0.96	0.95	0.95	0.96	0.01	0.96	0.96	0.96	0.96	0.95	0.95	0.95	0.96	0.97

Analysis	LC015_4_17	LC015_4_18	LC015_5_11	LC015_6_5	LC015_6_6	LC015_6_7	LC015_6_10	LC015_6_12	LC015_6_14	LC015_2_8	LC015_3_24	Av	St. Dev
WDS wt%	nr Cr-mt	nr Cr-mt	in Cr-mt	matrix	matrix	matrix	matrix	matrix	nr Cr-mt	nr Cr-mt	nr Cr-mt		
SiO_2	42.34	42.66	43.00	42.37	43.10	42.58	42.30	43.20	42.19	41.08	43.03	42.63	0.52
TiO_2	0.00	0.00	0.00	0.00	0.00	0.00	0.03	0.00	0.00	0.00	0.07	0.02	0.06
Al_2O_3	2.14	2.17	1.99	2.35	2.02	2.11	2.31	2.15	2.64	2.45	2.05	2.18	0.19
Cr_2O_3	0.42	0.41	0.30	0.50	0.40	0.48	0.31	0.29	1.21	0.24	0.24	0.40	0.20
V_2O_3	b.d.l	b.d.l	b.d.l	b.d.l	b.d.l	b.d.l	0.03	b.d.l	b.d.l	b.d.l	b.d.l	b.d.l	
FeO	3.58	2.61	3.55	2.97	2.86	2.60	3.12	3.32	3.34	2.93	2.44	3.13	0.42
MnO	0.10	0.13	0.09	0.09	0.10	0.11	0.10	0.09	0.13	0.06	0.13	0.11	0.03
MgO	40.75	40.48	41.19	40.49	40.91	40.92	40.73	41.34	40.52	39.61	40.72	40.70	0.39
ZnO	b.d.l	b.d.l	0.06	b.d.l	b.d.l	0.04	b.d.l	b.d.l	b.d.l	b.d.l	b.d.l	b.d.l	
NiO	0.20	0.20	0.16	0.19	0.16	0.17	0.18	0.10	0.10	0.18	0.16	0.17	0.03
CaO	b.d.l	b.d.l	b.d.l	b.d.l	b.d.l	b.d.l	b.d.l	b.d.l	b.d.l	b.d.l	b.d.l	b.d.l	b.d.l
Total	89.55	88.68	90.34	88.96	89.57	89.01	89.12	90.49	90.12	86.59	88.82	89.37	0.89
Si	1.87	1.90	1.88	1.88	1.90	1.89	1.87	1.89	1.86	1.87	1.91	1.89	0.01
Ti	0.00	0.00	0.00	0.00	0.00	0.00	0.00	0.00	0.00	0.00	0.00	0.00	0.00
Al	0.11	0.11	0.10	0.12	0.11	0.11	0.12	0.11	0.14	0.13	0.11	0.11	0.01
Cr	0.01	0.01	0.01	0.02	0.01	0.02	0.01	0.01	0.04	0.01	0.01	0.01	0.01
V	0.00	0.00	0.00	0.00	0.00	0.00	0.00	0.00	0.00	0.00	0.00	0.00	0.00
Fe^{2+}	0.13	0.10	0.13	0.11	0.11	0.10	0.12	0.12	0.12	0.11	0.09	0.12	0.01
Mn	0.00	0.01	0.00	0.00	0.00	0.00	0.00	0.00	0.00	0.00	0.00	0.00	0.00
Mg	2.68	2.69	2.69	2.68	2.69	2.70	2.69	2.69	2.66	2.69	2.69	2.68	0.01
Zn	0.00	0.00	0.00	0.00	0.00	0.00	0.00	0.00	0.00	0.00	0.00	0.00	0.00
Ni	0.01	0.01	0.01	0.01	0.01	0.01	0.01	0.00	0.00	0.01	0.01	0.01	0.00
Ca	-	-	-	-	-	-	-	-	-	-	-	-	-
X(Mg)	0.95	0.97	0.95	0.96	0.96	0.97	0.96	0.96	0.96	0.96	0.97	0.96	0.01

Analysis	ASZ-09-A_A3_SERP_12	ASZ-09-A_A3_SERP_13	ASZ-09-A_A3_SERP_14	ASZ-09-A_A3_SERP_11	ASZ-09a a1_atg_in_ticln2	ASZ-09a a1_atg_in_ticln2	ASZ-09a a1_atg_in_ticln2	ASZ-09-B-A3-SERP1 2	ASZ-09-B-A3-SERP1 3	ASZ-09-B-A3-SERP1 1	Av	St dev
EDS	atg1	atg1	atg1	atg1	atg1	atg1	atg1	atg1	atg1	atg1		
wt%												
SiO_2	43.67	42.17	38.11	40.35	43.49	42.75	41.85	42.58	44.03	44.25	42.32	1.88
TiO_2	0.00	0.22	5.77	2.24	0.14	0.65	1.83	0.22	0.00	0.00	1.11	1.82
Al_2O_3	1.42	0.51	0.53	0.68	0.52	0.50	0.40	0.91	0.00	0.00	0.55	0.41
Cr_2O_3	0.00	0.00	0.00	0.00	0.28	0.26	0.22	0.00	0.00	0.00	0.08	0.12
V_2O_3	n.d.	n.d.	n.d.	n.d.	n.d.	n.d.	n.d.	n.d.	n.d.	n.d.	n.d.	n.d.
FeO	1.85	1.74	5.13	2.69	1.64	2.16	2.86	2.84	1.93	2.24	2.51	1.03
MnO	0.00	0.00	1.65	0.59	0.07	0.13	0.38	0.00	0.00	0.00	0.28	0.52
MgO	41.76	41.59	38.79	39.87	39.46	40.47	42.26	40.07	40.68	40.86	40.58	1.08
ZnO	n.d.	n.d.	n.d.	n.d.	n.d.	n.d.	n.d.	n.d.	n.d.	n.d.	n.d.	n.d.
NiO	0.00	0.00	0.00	0.34	0.02	0.03	0.08	0.00	0.00	0.00	0.05	0.11
CaO	n.d.	n.d.	n.d.	n.d.	n.d.	n.d.	n.d.	n.d.	n.d.	n.d.	n.d.	n.d.
Total	88.70	86.23	89.98	86.76	85.69	86.97	89.96	86.61	86.64	87.35	87.49	1.53
Si	8.00	7.93	7.27	7.71	8.32	8.08	7.73	8.04	8.29	8.27	7.96	0.32
Ti	0.00	0.02	0.50	0.19	0.00	0.00	0.00	0.02	0.00	0.00	0.07	0.16
Al	0.31	0.11	0.12	0.15	0.12	0.11	0.09	0.20	0.00	0.00	0.12	0.09
Cr	0.00	0.00	0.00	0.00	0.04	0.04	0.03	0.00	0.00	0.00	0.01	0.02
V	-	-	-	-	-	-	-	-	-	-	-	-
Fe^{2+}	0.28	0.27	0.82	0.43	0.26	0.34	0.44	0.45	0.30	0.35	0.40	0.16
Mn	0.00	0.00	0.27	0.10	0.01	0.02	0.06	0.00	0.00	0.00	0.05	0.08
Mg	11.41	11.66	11.03	11.36	11.25	11.40	11.64	11.29	11.41	11.38	11.38	0.18
Zn	-	-	-	-	-	-	-	-	-	-	-	-
Ni	0.00	0.00	0.00	0.05	0.00	0.00	0.01	0.00	0.00	0.00	0.01	0.02
Ca	-	-	-	-	-	-	-	-	-	-	-	-
X(Mg)	0.98	0.98	0.93	0.96	0.98	0.97	0.96	0.96	0.97	0.97	0.97	0.01

Analysis EDS wt%	ASZ-09-B-AREA4-SRP1 3 atg2	ASZ-09-B-AREA4-SRP1 4 atg2	ASZ-09-B-AREA4-SRP1 5 atg2	ASZ-09-B-AREA4-SRP1 1 atg2	ASZ-09-B-A2_SERP atg2	ASZ-09-B-A2-SERP2 2 atg2	ASZ-09-B-A2-SERP2 3 atg2	ASZ-09-A_A4_SERP 1 3 1 atg2	ASZ-09-A SERP 2 1 2 atg2	ASZ-09-A_A4_SERP 3 2 1 atg2	ASZ-09-A_A4_SERP 3 2 2 atg2	ASZ-09-A_A4_SERP 3 2 3 atg2	ASZ-09-A_A4_SERP 3 2 4 atg2	ASZ-09a a1_atg_light 2 atg2	ASZ-09a a1_atg_light 2 atg2
SiO_2	42.69	42.32	41.21	42.56	41.47	39.78	40.27	38.21	45.00	42.30	40.84	44.31	42.24	41.79	42.02
TiO_2	0.00	0.00	0.00	0.00	0.00	0.00	0.00	0.00	0.00	0.00	0.00	0.00	0.00	0.01	0.03
Al_2O_3	3.42	3.04	2.80	3.31	2.44	3.99	3.68	0.00	1.10	2.49	5.74	2.68	2.80	2.58	2.64
Cr_2O_3	0.00	0.00	0.00	0.00	0.00	0.00	0.00	0.00	0.00	0.00	0.00	0.00	0.00	0.34	0.34
V_2O_3	n.d.	n.d.	n.d.	n.d.	n.d.	n.d.	n.d.	n.d.	n.d.	n.d.	n.d.	n.d.	n.d.	n.d.	n.d.
FeO	3.13	2.87	2.62	3.13	2.65	2.88	3.19	5.45	2.23	2.41	3.02	2.70	2.55	2.52	2.54
MnO	0.00	0.00	0.00	0.00	0.00	0.00	0.00	0.54	0.00	0.00	0.00	0.00	0.19	0.09	0.05
MgO	39.40	38.76	38.31	39.40	37.63	37.41	37.76	39.57	41.76	39.95	39.32	41.89	39.97	37.68	38.12
ZnO	n.d.	n.d.	n.d.	n.d.	n.d.	n.d.	n.d.	n.d.	n.d.	n.d.	n.d.	n.d.	n.d.	n.d.	n.d.
NiO	0.00	0.00	0.00	0.00	0.00	0.00	0.00	0.64	0.00	0.00	0.00	0.00	0.00	0.09	0.08
CaO	n.d.	n.d.	n.d.	n.d.	n.d.	n.d.	n.d.	n.d.	n.d.	n.d.	n.d.	n.d.	n.d.	n.d.	n.d.
Total	88.64	86.99	84.94	88.39	84.18	84.06	84.90	84.42	90.08	87.15	88.93	91.59	87.74	85.19	85.91
Si	7.90	7.98	7.93	7.88	8.08	7.75	7.78	7.43	8.15	7.92	7.51	7.90	7.86	8.07	8.04
Ti	0.00	0.00	0.00	0.00	0.00	0.00	0.00	0.00	0.00	0.00	0.00	0.00	0.00	0.00	0.00
Al	0.75	0.68	0.63	0.72	0.56	0.92	0.84	0.00	0.23	0.55	1.24	0.56	0.61	0.59	0.60
Cr	0.00	0.00	0.00	0.00	0.00	0.00	0.00	0.00	0.00	0.00	0.00	0.00	0.00	0.05	0.05
V	-	-	-	-	-	-	-	-	-	-	-	-	-	-	-
Fe^{2+}	0.48	0.45	0.42	0.48	0.43	0.47	0.52	0.89	0.34	0.38	0.46	0.40	0.40	0.41	0.41
Mn	0.00	0.00	0.00	0.00	0.00	0.00	0.00	0.09	0.00	0.00	0.00	0.00	0.03	0.02	0.01
Mg	10.87	10.89	10.99	10.88	10.93	10.87	10.87	11.47	11.28	11.15	10.78	11.13	11.09	10.85	10.88
Zn	-	-	-	-	-	-	-	-	-	-	-	-	-	-	-
Ni	0.00	0.00	0.00	0.00	0.00	0.00	0.00	0.10	0.00	0.00	0.00	0.00	0.00	0.01	0.01
Ca	-	-	-	-	-	-	-	-	-	-	-	-	-	-	-
X(Mg)	0.96	0.96	0.96	0.96	0.96	0.96	0.95	0.93	0.97	0.97	0.96	0.97	0.97	0.96	0.96

WDS							**EDS**							
Analysis Description	ASZ-09a a1_atg_light 2	ASZ-09a a4_srp2	ASZ-09a a4_srp2	ASZ-09a a4_srp2	Average	St Dev	VSZ-03_SERP_1 4	VSZ-03_A1_SERP 2 3	VSZ-03_A1_SERP 2 4	VSZ-03_A1_SERP 2 4	VSZ-03_A1_SERP 2 1	VSZ-03_A1_SERP 2 2	VSZ-03_A2_SERP 1 2	VSZ-03_A2_SERP 1 4
wt%	atg3	atg3	atg3	atg3			atg1	atg1	atg1	atg1	atg1	atg1	atg1	atg1
SiO_2	41.31	42.14	41.62	41.89	41.79	1.49	40.91	41.51	41.36	41.14	41.42	40.82	42.73	41.51
TiO_2	0.01	0.01	0.00	0.01	0.00	0.01	0.00	0.00	0.00	0.00	0.00	0.00	0.00	0.00
Al_2O_3	2.72	2.13	2.74	2.57	2.78	1.13	3.06	2.23	2.21	2.38	2.12	2.29	2.44	2.32
Cr_2O_3	0.37	0.28	0.31	0.29	0.10	0.15	0.66	0.29	0.31	0.23	0.29	0.00	0.28	0.39
V_2O_3	n.d.	n.d.	n.d.	n.d.	n.d.	n.d.	n.d.	n.d.	n.d.	n.d.	n.d.	n.d.	n.d.	n.d.
FeO	2.49	2.59	2.94	2.82	2.88	0.68	3.69	3.27	3.33	3.22	3.34	3.22	3.04	3.47
MnO	0.08	0.05	0.06	0.06	0.06	0.13	0.00	0.00	0.00	0.00	0.00	0.00	0.00	0.00
MgO	37.47	38.08	37.80	37.92	38.85	1.35	36.77	37.20	37.78	37.96	37.73	37.27	39.70	38.13
ZnO	n.d.	n.d.	n.d.	n.d.	n.d.	n.d.	n.d.	n.d.	n.d.	n.d.	n.d.	n.d.	n.d.	n.d.
NiO	0.09	0.07	0.07	0.08	0.06	0.14	0.00	0.00	0.00	0.59	0.90	0.48	0.00	0.00
CaO	n.d.	n.d.	n.d.	n.d.	n.d.	n.d.	n.d.	n.d.	n.d.	n.d.	n.d.	n.d.	n.d.	n.d.
Total	84.66	85.36	85.59	85.68	86.55	2.16	85.09	84.50	84.99	85.52	85.81	84.07	88.18	85.83
Si	8.03	8.11	8.00	8.04	7.91	0.19	0.68	0.69	0.69	0.68	0.69	0.68	0.71	0.69
Ti	0.00	0.00	0.00	0.00	0.00	0.00	0.00	0.00	0.00	0.00	0.00	0.00	0.00	0.00
Al	0.62	0.48	0.62	0.58	0.62	0.25	0.06	0.04	0.04	0.05	0.04	0.04	0.05	0.05
Cr	0.06	0.04	0.05	0.04	0.02	0.02	0.01	0.00	0.00	0.00	0.00	0.00	0.00	0.01
V	-	-	-	-	-	-	-	-	-	-	-	-	-	-
Fe^{2+}	0.40	0.42	0.47	0.45	0.46	0.11	0.05	0.05	0.05	0.04	0.05	0.04	0.04	0.05
Mn	0.01	0.01	0.01	0.01	0.01	0.02	0.00	0.00	0.00	0.00	0.00	0.00	0.00	0.00
Mg	10.86	10.93	10.84	10.86	10.97	0.18	0.91	0.92	0.94	0.94	0.94	0.92	0.99	0.95
Zn	-	-	-	-	-	-	-	-	-	-	-	-	-	-
Ni	0.01	0.01	0.01	0.01	0.01	0.02	0.00	0.00	0.00	0.01	0.01	0.01	0.00	0.00
Ca	-	-	-	-	-	-	-	-	-	-	-	-	-	-
X(Mg)	0.96	0.96	0.96	0.96	0.96	0.01	0.95	0.95	0.95	0.95	0.95	0.95	0.96	0.95

Analysis	VSZ-03_A2_SERP15	VSZ-03_A2_SERP11	VSZ-03_A2_SERP16	VSZ-03_A2_SERP22	VSZ-03_A2_SERP21	VSZ-03_A2_SERP_32	VSZ-03_A2_SERP_33	VSZ-03_A2_SERP_31	Average	St dev
WDS	atg1	atg1	atg1	atg1	atg1	atg1	atg1	atg1		
wt%										
SiO_2	40.95	45.85	41.68	40.89	40.72	41.91	41.34	41.19	41.62	1.23
TiO_2	0.00	0.00	0.00	0.00	0.00	0.00	0.00	0.00	0.00	0.00
Al_2O_3	2.34	1.85	2.46	2.46	2.15	1.98	2.42	2.49	2.33	0.27
Cr_2O_3	0.41	0.34	0.63	0.45	0.38	0.26	0.37	0.45	0.36	0.15
V_2O_3	n.d.	n.d.	n.d.	n.d.	n.d.	n.d.	n.d.	n.d.	n.d.	n.d.
FeO	3.09	2.82	3.24	3.20	2.98	3.22	3.09	3.60	3.24	0.22
MnO	0.00	0.00	0.00	0.00	0.00	0.00	0.00	0.00	0.00	0.00
MgO	38.29	37.03	38.91	38.23	37.71	38.94	38.39	38.43	38.03	0.77
ZnO	n.d.	n.d.	n.d.	n.d.	n.d.	n.d.	n.d.	n.d.	n.d.	n.d.
NiO	0.00	0.00	0.00	0.23	0.00	0.00	0.00	0.00	0.14	0.28
CaO	n.d.	n.d.	n.d.	n.d.	n.d.	n.d.	n.d.	n.d.	n.d.	n.d.
Total	85.08	87.89	86.91	85.46	83.95	86.32	85.60	86.16	85.71	1.20
Si	0.68	0.76	0.69	0.68	0.68	0.70	0.69	0.69	0.69	0.02
Ti	0.00	0.00	0.00	0.00	0.00	0.00	0.00	0.00	0.00	0.00
Al	0.05	0.04	0.05	0.05	0.04	0.04	0.05	0.05	0.05	0.01
Cr	0.01	0.00	0.01	0.01	0.01	0.00	0.00	0.01	0.00	0.00
V	-	-	-	-	-	-	-	-	-	-
Fe^{2+}	0.04	0.04	0.05	0.04	0.04	0.04	0.04	0.05	0.05	0.00
Mn	0.00	0.00	0.00	0.00	0.00	0.00	0.00	0.00	0.00	0.00
Mg	0.95	0.92	0.97	0.95	0.94	0.97	0.95	0.95	0.94	0.02
Zn	-	-	-	-	-	-	-	-	-	-
Ni	0.00	0.00	0.00	0.00	0.00	0.00	0.00	0.00	0.00	0.00
Ca	-	-	-	-	-	-	-	-	-	-
X(Mg)	0.96	0.96	0.96	0.96	0.96	0.96	0.96	0.95	0.95	0.00

Analysis	VSZ-03_A4_SERP1 1	VSZ-03_A4_SERP1 2	VSZ-03_A4_SERP1 3	VSZ-03_A4_SERP1 4	VSZ-03_A4_SERP1 1	VSZ-03_A4_SERP1 2	VSZ-03_A4_SERP1 3	VSZ-03_A4_SERP1 4	Average	St Dev
WDS	atg2	atg2	atg2	atg2	atg2	atg2	atg2	atg2		
wt%										
SiO_2	41.32	42.11	41.25	41.04	41.85	41.08	42.06	42.15	41.61	0.48
TiO_2	0.00	0.00	0.00	0.00	0.00	0.00	0.00	0.00	0.00	0.00
Al_2O_3	2.66	2.19	2.57	2.31	2.23	2.04	2.19	2.38	2.32	0.21
Cr_2O_3	0.25	0.00	0.00	0.38	0.29	0.00	0.34	0.35	0.20	0.17
V_2O_3	n.d.	n.d.	n.d.	n.d.	n.d.	n.d.	n.d.	n.d.	n.d.	n.d.
FeO	3.60	4.21	3.60	3.90	3.34	3.32	3.06	3.43	3.56	0.36
MnO	0.00	0.00	0.00	0.00	0.00	0.00	0.00	0.00	0.00	0.00
MgO	38.08	38.58	38.36	37.91	38.36	37.53	39.40	38.08	38.29	0.55
ZnO	n.d.	n.d.	n.d.	n.d.	n.d.	n.d.	n.d.	n.d.	n.d.	n.d.
NiO	0.00	0.00	0.00	0.24	0.00	0.00	0.00	0.00	0.03	0.09
CaO	n.d.	n.d.	n.d.	n.d.	n.d.	n.d.	n.d.	n.d.	n.d.	n.d.
Total	85.91	87.08	85.78	85.77	86.08	83.97	87.06	86.39	86.01	0.98
Si	0.69	0.70	0.69	0.68	0.70	0.68	0.70	0.70	0.69	0.01
Ti	0.00	0.00	0.00	0.00	0.00	0.00	0.00	0.00	0.00	0.00
Al	0.05	0.04	0.05	0.05	0.04	0.04	0.04	0.05	0.05	0.00
Cr	0.00	0.00	0.00	0.01	0.00	0.00	0.00	0.00	0.00	0.00
V	-	-	-	-	-	-	-	-	-	-
Fe^{2+}	0.05	0.06	0.05	0.05	0.05	0.05	0.04	0.05	0.05	0.01
Mn	0.00	0.00	0.00	0.00	0.00	0.00	0.00	0.00	0.00	0.00
Mg	0.94	0.96	0.95	0.94	0.95	0.93	0.98	0.94	0.95	0.01
Zn	-	-	-	-	-	-	-	-	-	-
Ni	0.00	0.00	0.00	0.00	0.00	0.00	0.00	0.00	0.00	0.00
Ca	-	-	-	-	-	-	-	-	-	-
X(Mg)	0.95	0.94	0.95	0.95	0.95	0.95	0.96	0.95	0.95	0.00

Analysis	VSZ05-area1_atg1_fine	VSZ05-area1_atg1_fine	VSZ05-area1_atg1_fine	VSZ05-area4_atg1	VSZ05-area4_atg1	VSZ05-area4_atg1	VSZ05-area4_atglaths1	VSZ05-area4_atglaths1	VSZ05-area4_atglaths1	Average	St Dev
WDS wt%	atg1	atg1	atg1	atg1	atg1	atg1	atg1	atg1	atg1	atg1	
SiO_2	42.25	42.37	42.76	42.55	42.52	42.39	42.30	41.97	41.78	42.32	0.30
TiO_2	0.01	0.00	0.00	0.01	0.01	0.02	0.01	0.00	0.00	0.01	0.01
Al_2O_3	1.92	1.65	1.59	1.70	1.88	1.77	1.89	1.86	1.19	1.72	0.23
Cr_2O_3	0.73	0.59	0.55	0.53	0.52	0.55	0.67	0.56	0.52	0.58	0.07
V_2O_3	n.d.	n.d.	n.d.	0.01	0.00	0.00	0.01	0.00	0.01	0.01	0.01
FeO	2.72	2.75	2.68	3.68	3.77	2.93	2.68	2.87	3.92	3.11	0.52
MnO	0.04	0.02	0.02	0.02	0.04	0.06	0.04	0.04	0.03	0.03	0.01
MgO	38.05	38.10	38.19	38.26	38.27	38.14	38.07	37.72	41.04	38.43	0.99
ZnO	n.d.	n.d.	n.d.	n.d.	n.d.	n.d.	n.d.	n.d.	n.d.	n.d.	n.d.
NiO	0.14	0.14	0.13	0.14	0.11	0.20	0.15	0.18	0.18	0.15	0.03
CaO	n.d.	n.d.	n.d.	0.01	0.00	0.00	0.01	0.00	0.00	0.00	0.01
Total	85.92	85.62	85.94	86.92	87.15	86.11	85.89	85.24	88.70	86.39	1.05
Si	0.70	0.71	0.71	0.71	0.71	0.71	0.70	0.70	0.70	0.70	0.00
Ti	0.00	0.00	0.00	0.00	0.00	0.00	0.00	0.00	0.00	0.00	0.00
Al	0.04	0.03	0.03	0.03	0.04	0.03	0.04	0.04	0.02	0.03	0.00
Cr	0.01	0.01	0.01	0.01	0.01	0.01	0.01	0.01	0.01	0.01	0.00
V	-	-	-	-	-	-	-	-	-	-	-
Fe^{2+}	0.04	0.04	0.04	0.05	0.05	0.04	0.04	0.04	0.05	0.04	0.01
Mn	0.00	0.00	0.00	0.00	0.00	0.00	0.00	0.00	0.00	0.00	0.00
Mg	0.94	0.95	0.95	0.95	0.95	0.95	0.94	0.94	1.02	0.95	0.02
Zn	-	-	-	-	-	-	-	-	-	-	-
Ni	0.00	0.00	0.00	0.00	0.00	0.00	0.00	0.00	0.00	0.00	0.00
Ca	-	-	-	-	-	-	-	-	-	-	-
X(Mg)	0.96	0.96	0.96	0.95	0.95	0.96	0.96	0.96	0.95	0.96	0.01

Analysis	VSZ05-area1_atg1_coarse	VSZ05-area1_atg1_coarse	VSZ05-area1_atg1_coarse	VSZ05-area1_atg1_coarse2	VSZ05-area1_atg1_coarse2	VSZ05-area1_atg1_coarse2	VSZ05-area2_atgvein	VSZ05-area2_atgvein	VSZ05-area2_atgvein
WDS	atg2	atg2	atg2	atg2	atg2	atg2	atg2	atg2	atg2
wt%									
SiO_2	41.91	41.91	41.88	42.12	41.99	41.78	42.81	41.71	42.85
TiO_2	0.00	0.00	0.00	0.00	0.01	0.03	0.02	0.00	0.02
Al_2O_3	1.77	2.00	1.99	1.79	1.90	2.07	1.53	1.45	1.71
Cr_2O_3	1.17	0.84	0.67	0.89	0.89	1.12	0.45	0.37	0.37
V_2O_3	0.00	0.02	0.00	0.01	0.01	0.01	0.00	0.00	0.02
FeO	2.71	2.59	2.74	2.62	2.68	2.56	2.69	2.71	2.66
MnO	0.00	0.01	0.01	0.05	0.04	0.01	0.01	0.05	0.00
MgO	37.53	37.54	37.65	37.73	37.73	37.55	38.43	37.85	38.50
ZnO	n.d.	n.d.	n.d.	n.d.	n.d.	n.d.	n.d.	n.d.	n.d.
NiO	0.13	0.13	0.13	0.13	0.11	0.15	0.14	2.28	0.25
CaO	0.00	0.00	0.00	0.00	0.01	0.00	0.00	0.01	0.00
Total	85.27	85.08	85.14	85.38	85.38	85.29	86.17	86.47	86.37
Si	0.70	0.70	0.70	0.70	0.70	0.70	0.71	0.69	0.71
Ti	0.00	0.00	0.00	0.00	0.00	0.00	0.00	0.00	0.00
Al	0.03	0.04	0.04	0.04	0.04	0.04	0.03	0.03	0.03
Cr	0.02	0.01	0.01	0.01	0.01	0.01	0.01	0.00	0.00
V	-	-	-	-	-	-	-	-	-
Fe^{2+}	0.04	0.04	0.04	0.04	0.04	0.04	0.04	0.04	0.04
Mn	0.00	0.00	0.00	0.00	0.00	0.00	0.00	0.00	0.00
Mg	0.93	0.93	0.93	0.94	0.94	0.93	0.95	0.94	0.96
Zn	-	-	-	-	-	-	-	-	-
Ni	0.00	0.00	0.00	0.00	0.00	0.00	0.00	0.03	0.00
Ca	-	-	-	-	-	-	-	-	-
X(Mg)	0.96	0.96	0.96	0.96	0.96	0.96	0.96	0.96	0.96

Analysis	VSZ05-area2_atg_aroundmt	VSZ05-area2_atg_aroundmt	Av	St Dev	PF001_3_34 rims ilm w ti-mt core	PF001_3_8	PF001_3_38	PF001_1_27	PF001_6_8	Av	St Dev
WDS wt%	atg2	atg2				matrix	matrix	matrix	matrix		
SiO_2	42.14	42.79	42.46	0.51	41.45	42.59	41.29	42.79	40.11	36.54	1.06
TiO_2	0.00	0.00	0.01	0.01	0.48	0.17	0.03	0.04	0.00	b.d.l	
Al_2O_3	1.89	1.43	1.60	0.20	3.57	3.51	4.31	7.69	7.09	9.14	1.16
Cr_2O_3	0.68	0.52	0.48	0.13	0.03	0.03	0.01	0.06	0.01	b.d.l	b.d.l
V_2O_3	0.00	0.00	0.01	0.01	0.03	b.d.l	0.03	b.d.l	b.d.l	0.01	0.01
FeO	3.02	3.47	2.91	0.34	6.19	5.96	5.99	6.29	6.25	6.12	0.14
MnO	0.06	0.01	0.03	0.03	0.06	0.06	0.06	0.05	0.08	0.06	0.01
MgO	37.84	38.53	38.23	0.35	34.5	34.4	33.9	35.3	35.1	34.5	0.60
ZnO	n.d.	n.d.	n.d.	n.d.	b.d.l	b.d.l	b.d.l	b.d.l	b.d.l	b.d.l	-
NiO	0.15	0.11	0.59	0.95	0.21	0.18	0.23	0.18	0.20	0.19	0.03
CaO	0.01	0.02	0.01	0.01	0.03	b.d.l	0.15	0.05	0.10	0.06	0.05
Total	85.82	86.87	86.34	0.39	87.1	86.6	86.7	87.8	87.7	87.2	0.57
Si	0.70	0.71	0.71	0.01	6.78	6.93	6.92	7.18	7.20	7.00	0.18
Ti	0.00	0.00	0.00	0.00	-	-	-	0.01	0.01	-	-
Al	0.04	0.03	0.03	0.00	2.36	2.23	2.30	1.78	1.80	2.10	0.28
Cr	0.01	0.01	0.01	0.00	-	-	0.01	-	-	b.d.l	b.d.l
V	-	-	-	-	-	-	-	-	-	-	-
Fe^{2+}	0.04	0.05	0.04	0.00	0.99	0.96	0.96	1.00	0.99	0.98	0.02
Mn	0.00	0.00	0.00	0.00	0.01	0.01	0.01	0.01	0.01	0.01	0.00
Mg	0.94	0.96	0.95	0.01	9.82	9.84	9.72	9.98	9.93	9.86	0.10
Zn	-	-	-	-	-	-	-	-	-	-	-
Ni	0.00	0.00	0.01	0.01	0.03	0.03	0.04	0.03	0.03	0.03	0.00
Ca	-	-	-	-	0.01	-	0.03	0.01	0.02	0.01	0.01
X(Mg)	0.96	0.95	0.96	0.00	0.909	0.909	0.911	0.910	0.909	0.909	0.001

Analysis EDS wt%	GSZ-11	GSZ-11	GSZ-11	GSZ-11	GSZ-11	GSZ-11	GSZ-11	GSZ-11	GSZ-11	GSZ-11	Average	St Dev
SiO_2	42.33	42.01	41.58	41.79	42.22	41.90	41.92	42.48	41.77	41.60	41.96	0.30
TiO_2	0.00	0.00	0.00	0.00	0.00	0.00	0.00	0.00	0.00	0.00	0.00	0.00
Al_2O_3	2.08	2.17	2.40	2.34	2.25	2.17	2.25	2.31	2.42	2.42	2.28	0.12
Cr_2O_3	0.00	0.00	0.00	0.00	0.00	0.00	0.00	0.00	0.00	0.00	0.00	0.00
V_2O_3	n.d.	n.d.	n.d.	n.d.	n.d.	n.d.	n.d.	n.d.	n.d.	n.d.	n.d.	n.d.
FeO	3.31	3.14	3.98	3.49	3.41	3.55	3.36	3.46	3.32	3.33	3.43	0.22
MnO	0.00	0.00	0.00	0.00	0.00	0.00	0.00	0.00	0.00	0.00	0.00	0.00
MgO	38.64	38.06	38.21	38.56	38.19	38.29	38.16	38.82	37.66	37.80	38.24	0.36
ZnO	n.d.	n.d.	n.d.	n.d.	n.d.	n.d.	n.d.	n.d.	n.d.	n.d.	n.d.	n.d.
NiO	0.20	0.19	0.00	0.19	0.00	0.19	0.00	0.24	0.00	0.24	0.13	0.11
CaO	n.d.	n.d.	n.d.	n.d.	n.d.	n.d.	n.d.	n.d.	n.d.	n.d.		
Total	86.56	85.57	86.16	86.37	86.07	86.11	85.69	87.31	85.17	85.39	86.04	0.63
Si	0.70	0.70	0.69	0.70	0.70	0.70	0.70	0.71	0.70	0.69	0.70	0.01
Ti	-	-	-	-	-	-	-	-	-	-	-	-
Al	0.04	0.04	0.05	0.05	0.04	0.04	0.04	0.05	0.05	0.05	0.04	0.00
Cr	-	-	-	-	-	-	-	-	-	-	-	-
V	-	-	-	-	-	-	-	-	-	-	-	-
Fe^{2+}	0.05	0.04	0.06	0.05	0.05	0.05	0.05	0.05	0.05	0.05	0.05	0.00
Mn	0.00	0.00	0.00	0.00	0.00	0.00	0.00	0.00	0.00	0.00	0.00	0.00
Mg	0.96	0.94	0.95	0.96	0.95	0.95	0.95	0.96	0.93	0.94	0.95	0.01
Zn	-	-	-	-	-	-	-	-	-	-	-	-
Ni	0.00	0.00	0.00	0.00	0.00	0.00	0.00	0.00	0.00	0.00	0.00	0.00
Ca	-	-	-	-	-	-	-	-	-	-	-	-
X(Mg)	0.95	0.96	0.94	0.95	0.95	0.95	0.95	0.95	0.95	0.95	0.95	0.00

B9. Analyses of chlorite and intermediate compositions between chlorite and serpentine. Formulae were calculated on the basis of 20 cations.

Chlorite

Analysis WDS	PF001_1_ 20	PF001_1_ 28	PF001_2_ 13	PF001_2_ 17	PF001_2_ 18	PF001_2_ 19	PF001_2_ 22	PF001_2_ 28	PF001_3_ 12	PF001_3_ 13	PF001_3_ 26	PF001_3_ 37	PF001_4_ 4	Av	St. Dev
wt%															
SiO_2	34.48	34.80	33.20	33.16	32.97	32.96	33.24	34.09	34.26	33.97	34.02	34.19	33.62	33.77	0.61
TiO_2	0.37	0.30	b.d.l	b.d.l	b.d.l	b.d.l	0.15	0.26	0.16	b.d.l	b.d.l	0.20	b.d.l	0.11	0.13
Al_2O_3	11.58	10.78	13.11	13.22	12.99	13.30	13.22	12.65	12.40	13.02	12.77	12.94	13.40	12.72	0.76
Cr_2O_3	b.d.l	0.04	b.d.l	0.05	0.10	0.05	0.08	0.04	b.d.l	b.d.l	0.05	0.03	b.d.l	0.05	0.02
V_2O_3	b.d.l	b.d.l	b.d.l	b.d.l	b.d.l	b.d.l	b.d.l	b.d.l	0.05	0.04	b.d.l	0.03	0.03	b.d.l	-
FeO	6.24	6.37	5.98	5.97	5.92	5.88	6.17	6.38	6.06	5.81	5.64	6.10	6.01	6.04	0.21
MnO	0.03	0.05	0.05	0.10	0.08	0.05	0.06	0.05	0.10	0.06	0.03	0.06	0.07	0.06	0.02
MgO	33.51	34.00	33.13	33.22	33.44	33.18	33.19	33.82	33.51	33.76	34.16	34.04	33.95	33.61	0.37
ZnO	b.d.l	b.d.l	b.d.l	0.09	b.d.l	b.d.l	b.d.l	b.d.l	b.d.l	b.d.l	b.d.l	b.d.l	b.d.l	b.d.l	-
NiO	0.22	0.18	0.20	0.18	0.22	0.23	0.28	0.14	0.18	0.00	0.26	0.23	0.17	0.19	0.07
CaO	0.03	0.03	b.d.l	0.03	0.03	0.03	b.d.l	0.05	0.11	0.09	b.d.l	0.03	b.d.l	0.05	0.03
Total	86.47	86.49	86.45	86.47	86.47	86.46	86.49	86.50	86.47	86.44	86.45	86.49	86.48	86.47	0.02
Si	6.64	6.69	6.43	6.40	6.37	6.38	6.40	6.48	6.56	6.49	6.48	6.46	6.39	6.48	0.10
Ti	0.05	0.04	-	-	-	-	0.02	0.04	0.02	-	-	0.03	-	0.02	0.02
Al	5.27	4.90	5.98	6.02	5.92	6.07	6.00	5.68	5.61	5.87	5.73	5.78	6.00	5.76	0.34
Cr	-	0.01	-	0.01	0.01	0.01	0.01	0.01	-	-	0.01	-	-	-	-
V	-	-	-	-	-	-	-	-	0.01	0.01	-	-	-	-	-
Fe^{2+}	1.00	1.02	0.97	0.96	0.96	0.95	0.99	1.01	0.97	0.93	0.90	0.96	0.95	0.97	0.03
Mn	-	0.01	0.01	0.01	0.01	0.01	0.01	0.01	0.01	0.01	-	0.01	0.01	0.01	0.00
Mg	9.62	9.75	9.57	9.56	9.64	9.57	9.52	9.58	9.57	9.61	9.70	9.60	9.61	9.61	0.06
Zn	-	-	-	0.01	-	-	-	-	-	-	-	-	-	-	-
Ni	0.03	0.03	0.03	0.03	0.03	0.04	0.04	0.02	0.03	-	0.04	0.03	0.03	0.03	0.01
Ca	0.01	0.01	0.00	0.01	0.01	0.01	-	0.01	0.02	0.02	-	0.01	-	0.01	0.01
X(Mg)	0.91	0.90	0.91	0.91	0.91	0.91	0.91	0.90	0.91	0.91	0.92	0.91	0.91	0.91	0.00

Intermediate chlorite–serpentine analyses

Analysis WDS	PF001_4_7	PF001_1_7	PF001_2_16	PF001_3_1	PF001_3_30	PF001_3_39	Av	St. Dev
wt%								
SiO_2	35.54	35.79	36.11	36.03	37.89	37.89	36.54	1.06
TiO_2	0.00	0.00	0.00	0.00	0.09	0.04	0.02	0.04
Al_2O_3	10.51	8.26	9.86	10.17	7.97	8.06	9.14	1.16
Cr_2O_3	b.d.l	b.d.l	b.d.l	b.d.l	b.d.l	b.d.l		
V_2O_3	0.01	0.06	0.02	0.08	0.01	0.01	0.03	0.03
FeO	6.19	6.03	5.96	5.99	6.29	6.25	6.12	0.14
MnO	0.06	0.04	0.06	0.06	0.05	0.08	0.06	0.01
MgO	34.51	33.80	34.42	33.94	35.31	35.07	34.51	0.60
ZnO	b.d.l	b.d.l	b.d.l	b.d.l	b.d.l	b.d.l		
NiO	0.21	0.15	0.18	0.23	0.18	0.20	0.19	0.03
CaO								
Total	87.09	84.21	86.64	86.68	87.84	87.71	86.69	1.32
Si	6.78	7.07	6.93	6.93	7.19	7.21	7.02	0.17
Ti	-	-	-	-	-	-		
Al	4.73	3.85	4.46	4.61	3.56	3.61	4.14	0.52
Cr	0.00	0.02	0.01	0.02	0.00	0.00	0.01	0.01
V	0.00	0.00	0.00	0.00	0.00	0.00	0.00	0.00
Fe^{2+}	0.99	1.00	0.96	0.96	1.00	0.99	0.98	0.02
Mn	0.01	0.01	0.01	0.01	0.01	0.01	0.01	0.00
Mg	9.82	9.96	9.85	9.74	9.99	9.95	9.88	0.10
Zn	-	-	-	-	-	-		
Ni	0.03	0.02	0.03	0.04	0.03	0.03	0.03	0.00
Ca	-	-	-	-	-	-		
X(Mg)	0.91	0.91	0.91	0.91	0.91	0.91	0.91	0.00

Chlorite

Analysis WDS	VSZ02-area3_chl1	VSZ02-area3_chl1	VSZ02-area3_chl1	VSZ02-area4_matrix	VSZ02-area4_matrix	VSZ02-area4_matrix	VSZ02-area4_chl1	VSZ02-area4_chl1	VSZ02-area2_chl	VSZ02-area2_chl	VSZ02-area2_chl	VSZ02-area2_coarsechl	VSZ02-area2_coarsechl	Av.	St Dev
wt%															
SiO_2	28.91	28.75	28.62	28.39	28.52	28.71	28.65	29.04	28.40	28.93	28.69	28.91	28.50	28.69	0.21
TiO_2	0.00	0.01	0.00	0.03	0.00	0.00	0.03	0.04	0.00	b.d.l2807	0.06	0.01	0.00	0.02	0.02
Al_2O_3	20.34	20.86	20.58	21.24	21.07	21.00	20.82	20.69	21.42	20.95	21.12	20.73	20.87	20.90	0.28
Cr_2O_3	0.08	0.07	0.07	0.07	0.08	0.08	0.16	0.12	0.07	0.07	0.08	0.10	0.10	0.09	0.03
V_2O_3	b.d.l	b.d.l	b.d.l	b.d.l	b.d.l	b.d.l	b.d.l	b.d.l	b.d.l	b.d.l	b.d.l	b.d.l	b.d.l		
FeO	9.30	9.66	9.53	9.93	9.72	9.40	9.16	9.09	9.17	9.05	9.12	9.28	9.21	9.36	0.28
MnO	0.02	0.08	0.04	0.10	0.13	0.09	0.05	0.04	0.12	0.08	0.09	0.04	0.06	0.07	0.03
MgO	26.97	26.71	26.59	26.26	26.63	26.29	26.76	26.85	26.67	26.95	26.76	27.24	27.10	26.75	0.28
ZnO	b.d.l	b.d.l	b.d.l	b.d.l	b.d.l	b.d.l	b.d.l	b.d.l	b.d.l	b.d.l	b.d.l	b.d.l	b.d.l	b.d.l	-
NiO	0.03	0.03	0.05	0.07	0.08	0.07	0.08	0.10	0.09	0.10	0.12	0.10	0.09	0.08	0.03
CaO	b.d.l	b.d.l	b.d.l	b.d.l	b.d.l	b.d.l	b.d.l	b.d.l	b.d.l	b.d.l	b.d.l	b.d.l	b.d.l	b.d.l	-
Total	85.72	86.25	85.55	86.18	86.30	85.72	85.80	86.07	86.00	86.22	86.13	86.50	86.03	86.04	0.27
Si	5.73	5.67	5.69	5.62	5.62	5.70	5.67	5.74	5.61	5.70	5.66	5.67	5.62	5.67	0.04
Ti	0.00	0.00	0.00	0.00	0.00	0.00	0.00	0.00	0.00	0.00	0.00	0.00	0.00	0.00	-
Al	9.50	9.70	9.64	9.91	9.79	9.83	9.72	9.63	9.97	9.72	9.82	9.59	9.70	9.73	0.13
Cr	-	-	-	-	-	-	-	-	-	-	-	-	-	-	-
V	-	-	-	-	-	-	-	-	-	-	-	-	-	-	-
Fe^{2+}	1.54	1.59	1.58	1.64	1.60	1.56	1.52	1.50	1.51	1.49	1.51	1.52	1.52	1.55	0.05
Mn	0.00	0.01	0.01	0.02	0.02	0.01	0.01	0.01	0.02	0.01	0.02	0.01	0.01	0.01	0.01
Mg	7.96	7.86	7.88	7.75	7.83	7.78	7.90	7.91	7.85	7.91	7.87	7.97	7.97	7.88	0.07
Zn	-	-	-	-	-	-	-	-	-	-	-	-	-	-	-
Ni	0.00	0.01	0.01	0.01	0.01	0.01	0.01	0.02	0.01	0.02	0.02	0.02	0.01	0.01	0.00
Ca	-	-	-	-	-	-	-	-	-	-	-	-	-	-	-
X(Mg)	0.84	0.83	0.83	0.82	0.83	0.83	0.84	0.84	0.84	0.84	0.84	0.84	0.84	0.84	0.01

Chlorite

	EDS												
Analysis	ASZ-09-B-A4-CHL1 1	ASZ-09-B-A4-CHL1 2	ASZ-09-B-A4-CHL1 3	ASZ-09-B-A1_CHL1 5	ASZ-09-B_A2_SRP1 1	ASZ-09-B_A2_SRP1 4	ASZ-09-B_A2_CHL1 1	ASZ-09-A_A3_CHL 2	ASZ-09-A_A3_CHL 3	ASZ-09-A_A3_CHL 5	ASZ-09-A_A3_CHL 1	Av	St. Dev
wt%													
SiO_2	35.35	33.74	34.30	34.92	33.72	33.57	33.25	33.55	37.12	35.50	34.04	34.46	1.16
TiO_2	0.00	0.00	0.00	0.00	0.00	0.00	0.00	0.00	0.00	0.00	0.00	0.00	0.00
Al_2O_3	11.41	12.22	12.90	11.02	11.24	10.75	11.68	12.77	9.96	10.03	13.07	11.55	1.10
Cr_2O_3	0.45	0.32	0.79	0.00	0.00	0.00	0.00	0.28	0.00	0.00	0.66	0.23	0.30
V_2O_3	b.d.l	b.d.l	b.d.l	b.d.l	b.d.l	b.d.l	b.d.l	b.d.l	b.d.l	b.d.l	b.d.l	b.d.l	
FeO	3.99	4.14	3.77	4.12	4.17	3.69	3.41	3.81	3.63	4.35	3.67	3.89	0.29
MnO	b.d.l	b.d.l	b.d.l	b.d.l	b.d.l	b.d.l	b.d.l	b.d.l	b.d.l	b.d.l	b.d.l	b.d.l	
MgO	36.10	34.51	35.26	35.95	35.08	34.36	34.30	35.87	38.14	36.59	36.04	35.65	1.13
ZnO	b.d.l	b.d.l	b.d.l	b.d.l	b.d.l	b.d.l	b.d.l	b.d.l	b.d.l	b.d.l	b.d.l	b.d.l	
NiO	b.d.l	b.d.l	b.d.l	b.d.l	0.51	b.d.l	b.d.l	b.d.l	b.d.l	b.d.l	b.d.l	0.05	0.15
CaO	b.d.l	b.d.l	b.d.l	b.d.l	b.d.l	b.d.l	b.d.l	b.d.l	b.d.l	b.d.l	b.d.l		
Total	87.30	84.94	87.02	86.01	84.72	82.38	82.63	86.28	88.85	86.46	87.48	85.82	2.01
Si	0.59	0.56	0.57	0.58	0.56	0.56	0.55	0.56	0.62	0.59	0.57	0.57	0.02
Ti	-	-	-	-	-	-	-	-	-	-	-	-	-
Al	0.22	0.24	0.25	0.22	0.22	0.21	0.23	0.25	0.20	0.20	0.26	0.23	0.02
Cr	-	-	-	-	-	-	-	-	-	-	-	-	-
V	-	-	-	-	-	-	-	-	-	-	-	-	-
Fe^{2+}	0.06	0.06	0.05	0.06	0.06	0.05	0.05	0.05	0.05	0.06	0.05	0.05	0.00
Mn	-	-	-	-	-	-	-	-	-	-	-	-	-
Mg	0.90	0.86	0.87	0.89	0.87	0.85	0.85	0.89	0.95	0.91	0.89	0.88	0.03
Zn	-	-	-	-	-	-	-	-	-	-	-	-	-
Ni	-	-	-	-	0.00	-	-	-	-	-	-	-	-
Ca	-	-	-	-	-	-	-	-	-	-	-	-	-
X(Mg)	0.94	0.94	0.94	0.94	0.94	0.94	0.95	0.94	0.95	0.94	0.95	0.94	0.00

B10. Tremolite analyses. Formulae were calculated on the basis of 14 cations.

	Tremolite													
Description	matrix	nr mt	matrix	matrix	matrix	nr ilm	nr ilm	nr mt	nr mt	matrix	matrix	matrix	Av	St. Dev
Analysis	PF001_3_2	PF001_3_4	PF001_3_5	PF001_3_6	PF001_3_7	PF001_3_16	PF001_3_17	PF001_3_23	PF001_3_24	PF001_3_25	PF001_3_31	PF001_6_5		
wt%														
SiO_2	59.62	58.72	56.35	55.10	59.04	59.08	59.33	59.67	59.89	58.44	57.81	57.85	58.41	1.44
TiO_2	0.10	0.03	0.08	b.d.l	b.d.l	0.09	0.13	b.d.l	0.05	b.d.l	b.d.l	b.d.l	0.04	0.05
Al_2O_3	0.07	0.23	1.12	2.07	0.22	0.28	0.22	0.12	0.13	0.27	0.50	0.19	0.45	0.58
Cr_2O_3	0.04	b.d.l	b.d.l	b.d.l	b.d.l	0.04	0.03	0.04	b.d.l	b.d.l	0.04	0.04	b.d.l	
V_2O_3	b.d.l	b.d.l	b.d.l	b.d.l	b.d.l	b.d.l	b.d.l	b.d.l	0.04	b.d.l	b.d.l	b.d.l	b.d.l	
FeO	2.53	2.64	3.31	3.11	2.72	2.91	2.99	2.49	2.52	2.91	2.88	2.83	2.82	0.25
MnO	0.15	0.20	0.18	0.16	0.21	0.25	0.21	0.20	0.17	0.17	0.20	0.18	0.19	0.03
MgO	23.59	23.49	25.21	25.12	23.82	23.45	23.84	23.76	23.47	24.15	24.39	23.50	23.98	0.63
ZnO	b.d.l	b.d.l	b.d.l	b.d.l	b.d.l	b.d.l	b.d.l	b.d.l	b.d.l	b.d.l	b.d.l	b.d.l	b.d.l	
NiO	0.08	0.06	0.09	0.09	0.05	0.09	0.09	0.13	0.05	0.07	0.05	0.09	0.08	0.02
CaO	13.24	12.49	10.88	10.77	12.63	12.41	12.33	12.92	12.82	12.25	12.20	12.39	12.28	0.74
Total	99.70	98.11	97.50	96.65	98.96	98.99	97.26	99.65	99.53	98.56	98.37	97.34	98.38	1.03
Si	7.47	7.46	7.10	7.01	7.43	7.44	7.43	7.46	7.50	7.36	7.27	7.42	7.36	0.16
Ti	0.01	0.00	0.01	-	-	0.01	0.01	-	0.00	-	-	-	0.00	0.00
Al	0.01	0.02	0.11	0.21	0.02	0.03	0.02	0.01	0.01	0.03	0.05	0.01	0.04	0.06
Cr	0.01	-	-	-	0.01	0.01	0.01	0.01	-	-	0.01	0.01	0.01	0.00
V	-	-	-	-	-	-	-	-	-	-	-	-	-	-
Fe^{2+}	0.26	0.27	0.34	0.32	0.28	0.30	0.30	0.25	0.25	0.29	0.29	0.29	0.29	0.03
Mn	0.01	0.02	0.02	0.01	0.02	0.02	0.02	0.02	0.02	0.02	0.02	0.02	0.02	0.00
Mg	5.73	5.79	6.16	6.20	5.81	5.72	5.79	5.76	5.70	5.90	5.95	5.85	5.86	0.16
Zn	-	-	-	-	-	-	-	-	-	-	-	-	-	-
Ni	0.01	0.01	0.01	0.01	0.01	0.01	0.01	0.01	0.00	0.01	0.01	0.01	0.01	0.00
Ca	1.41	1.34	1.16	1.16	1.35	1.32	1.31	1.37	1.36	1.31	1.30	1.35	1.31	0.08
X(Mg)	0.957	0.955	0.948	0.951	0.955	0.951	0.950	0.958	0.957	0.952	0.953	0.952	0.954	0.003

B11. Talc analyses. Formulae were calculated on the basis of 14 cations.

	Talc											
Description	matrix	nr mt	matrix	matrix	matrix	nr ilm	nr ilm	nr mt	nr mt	matrix	Av	St. Dev
Analysis	PF001_3_2	PF001_3_4	PF001_3_5	PF001_3_6	PF001_3_7	PF001_3_16	PF001_3_17	PF001_3_23	PF001_3_24	PF001_3_25		
wt%												
SiO_2	62.97	62.63	61.37	60.19	63.61	60.61	62.39	62.54	63.79	63.72	62.38	1.28
TiO_2	0.17	0.03	0.17	0.20	0.23	0.53	0.14	0.08	0.11	0.16	0.18	0.13
Al_2O_3	0.05	0.05	0.12	1.19	0.11	0.10	0.10	0.42	0.07	0.03	0.22	0.36
Cr_2O_3	b.d.l	b.d.l	b.d.l	b.d.l	b.d.l	b.d.l	b.d.l	b.d.l	b.d.l	b.d.l	b.d.l	
V_2O_3	b.d.l	b.d.l	b.d.l	b.d.l	b.d.l	b.d.l	b.d.l	b.d.l	b.d.l	b.d.l	b.d.l	
FeO	2.21	2.16	2.05	2.34	2.27	2.35	2.12	2.10	2.19	2.06	2.18	0.11
MnO	b.d.l	b.d.l	0.05	0.04	0.06	0.05	0.04	b.d.l	0.05	0.03	0.04	0.01
MgO	29.66	29.35	28.89	29.59	29.94	28.45	29.96	30.07	30.09	29.99	29.60	0.55
ZnO	b.d.l	b.d.l	b.d.l	b.d.l	0.04	b.d.l	b.d.l	b.d.l	b.d.l	b.d.l	b.d.l	
NiO	0.26	0.22	0.29	0.20	0.23	0.19	0.25	0.20	0.16	0.22	0.22	0.04
CaO	b.d.l	0.06	0.04	0.03	b.d.l	0.10	0.04	b.d.l	b.d.l	b.d.l	0.03	0.03
Total	95.39	94.54	93.03	93.81	96.55	92.38	95.07	95.45	96.48	96.24	94.89	1.44
Si	8.04	8.00	7.84	7.69	8.12	7.74	7.97	7.99	8.15	8.14	7.97	0.16
Ti	0.02	0.00	0.02	0.02	0.02	0.05	0.01	0.01	0.01	0.02	0.02	0.00
Al	0.02	0.01	0.04	0.36	0.03	0.03	0.03	0.12	0.02	0.01	0.07	0.00
Cr	-	-	-	-	-	-	-	-	-	-	-	-
V	-	-	-	-	-	-	-	-	-	-	-	-
Fe^{2+}	0.24	0.23	0.22	0.25	0.24	0.26	0.23	0.22	0.23	0.22	0.23	0.28
Mn	-	-	0.00	0.00	0.01	0.01	0.00	-	0.01	0.00	0.00	0.02
Mg	5.65	5.59	5.50	5.63	5.70	5.42	5.70	5.72	5.73	5.71	5.63	0.11
Zn	-	-	-	-	-	-	-	-	-	-	-	-
Ni	0.03	0.02	0.03	0.02	0.02	0.02	0.03	0.02	0.02	0.02	0.02	0.01
Ca	-	0.01	0.01	0.00	-	0.01	0.01	-	-	-	0.00	0.00
X(Mg)	0.960	0.960	0.961	0.958	0.960	0.954	0.962	0.963	0.961	0.963	0.960	0.003

B12. Clinopyroxene analyses. Formulae were calculated on the basis of 4 cations.

WDS											
Analysis	VSZ02-area3_	VSZ02-area3_	VSZ02-area3_	VSZ02-area4_px1	VSZ02-area4_px1	VSZ02-area4_px1	VSZ02-area2_px	VSZ02-area2_px	VSZ02-area2_px	Average	St Dev
wt%											
SiO_2	55.43	55.38	55.38	54.96	54.75	54.13	55.25	54.52	54.57	54.93	0.46
TiO_2	0.02	0.02	0.03	0.11	0.13	0.11	0.03	0.12	0.06	0.07	0.05
Al_2O_3	0.14	0.11	0.16	0.62	0.59	1.08	0.09	0.25	0.39	0.38	0.33
Cr_2O_3	0.00	0.00	0.00	0.00	0.00	0.00	0.00	0.00	0.00	0.00	0.00
V_2O_3											
FeO	3.24	3.01	3.24	4.48	4.74	5.13	3.71	4.42	4.30	4.03	0.75
MnO	0.01	0.01	0.02	0.11	0.16	0.14	0.00	0.15	0.20	0.09	0.08
MgO	16.39	16.61	16.34	15.75	15.63	15.98	16.15	15.91	16.04	16.09	0.32
ZnO											
NiO	0.02	0.03	0.02	0.00	0.01	0.00	0.02	0.01	0.00	0.01	0.01
CaO	26.03	26.18	25.94	25.02	24.70	23.86	25.68	24.87	25.22	25.28	0.75
Na2O	0.19	0.17	0.17	0.26	0.32	0.31	0.18	0.25	0.26	0.23	0.06
Total	101.48	101.56	101.32	101.38	101.04	100.73	101.14	100.48	101.07	101.13	0.35
Si	1.99	1.99	2.00	1.98	1.98	1.96	2.00	1.99	1.98	1.99	0.01
Ti	0.00	0.00	0.00	0.00	0.00	0.00	0.00	0.00	0.00	0.00	0.00
Al	0.01	0.00	0.01	0.03	0.03	0.05	0.00	0.01	0.02	0.02	0.01
Cr	0.00	0.00	0.00	0.00	0.00	0.00	0.00	0.00	0.00	0.00	0.00
V											
Fe^{2+}	0.10	0.09	0.10	0.14	0.14	0.15	0.11	0.13	0.13	0.12	0.02
Mn	0.00	0.00	0.00	0.02	0.02	0.03	0.00	0.01	0.01	0.01	0.01
Mg	0.88	0.89	0.88	0.85	0.84	0.86	0.87	0.86	0.87	0.87	0.01
Zn											
Ni	0.00	0.00	0.00	0.00	0.00	0.00	0.00	0.00	0.00	0.00	0.00
Ca	1.00	1.01	1.00	0.97	0.96	0.92	1.00	0.97	0.98	0.98	0.03
Na	0.01	0.01	0.01	0.02	0.02	0.02	0.01	0.02	0.02	0.02	0.00
X(Mg)	0.90	0.91	0.90	0.86	0.85	0.85	0.89	0.87	0.87	0.88	0.02

WDS													
Analysis	VSZ-03_DI_22	VSZ-03_DI_23	VSZ-03_DI_24	VSZ-03_DI_25	VSZ-03_DI_21	VSZ-03_A2_DI_12	VSZ-03_A2_DI_13	VSZ-03_A2_DI_33	VSZ-03_A2_DI_41	VSZ-03_A2_DI_43	VSZ-03_A2_DI_42	Average	St Dev
wt%	di1	di1	di1	di1	di1	di1	di1	di1	di1	di1	di1		
SiO_2	51.14	50.58	50.33	51.08	52.51	53.45	51.50	53.30	53.36	54.09	55.40	52.43	1.63
TiO_2	0.00	0.00	0.23	0.00	0.33	0.00	0.40	0.00	0.00	0.35	0.00	0.12	0.17
Al_2O_3	1.55	0.57	1.45	1.17	2.36	0.66	2.31	1.42	1.89	2.02	0.51	1.45	0.67
Cr_2O_3	0.86	0.44	0.75	0.67	1.17	0.25	1.37	1.07	0.83	1.05	0.00	0.77	0.41
V_2O_3													
FeO	1.99	1.62	2.29	1.97	2.48	1.33	4.31	2.38	2.79	2.66	1.62	2.31	0.81
MnO													
MgO	17.40	16.35	17.55	16.65	16.63	17.68	17.21	17.68	17.86	17.38	18.52	17.36	0.63
ZnO													
NiO	0.00	0.00	0.00	0.00	0.00	0.00	0.00	0.00	0.00	0.00	0.00	0.00	0.00
CaO	23.25	24.12	22.02	23.86	23.98	25.55	23.34	24.40	24.04	24.67	26.04	24.12	1.09
Na2O	0.27	0.00	0.20	0.00	0.40	0.00	0.36	0.39	0.35	0.32	0.00	0.21	0.18
Total	96.46	93.68	94.82	95.39	99.88	98.91	100.81	100.63	101.13	102.55	102.09	98.76	3.13
Si	1.92	1.96	1.92	1.95	1.91	1.96	1.86	1.92	1.91	1.92	1.96	1.93	0.03
Ti	0.00	0.00	0.01	0.00	0.01	0.00	0.01	0.00	0.00	0.01	0.00	0.00	0.00
Al	0.07	0.03	0.07	0.05	0.10	0.03	0.10	0.06	0.08	0.08	0.02	0.06	0.03
Cr	0.03	0.01	0.02	0.02	0.03	0.01	0.04	0.03	0.02	0.03	0.00	0.02	0.01
V													
Fe^{2+}	0.06	0.05	0.07	0.06	0.08	0.04	0.13	0.07	0.08	0.08	0.05	0.07	0.02
Mn													
Mg	0.97	0.95	1.00	0.95	0.90	0.96	0.93	0.95	0.95	0.92	0.98	0.95	0.03
Zn													
Ni	0.00	0.00	0.00	0.00	0.00	0.00	0.00	0.00	0.00	0.00	0.00	0.00	0.00
Ca	0.93	1.00	0.90	0.97	0.94	1.00	0.90	0.94	0.92	0.94	0.99	0.95	0.04
Na	0.02	0.00	0.01	0.00	0.03	0.00	0.03	0.03	0.02	0.02	0.00	0.01	0.01
X(Mg)	0.94	0.95	0.93	0.94	0.92	0.96	0.88	0.93	0.92	0.92	0.95	0.93	0.02

EDS															
Analysis	VSZ-03_A1_DI 1	VSZ-03_DI_ 3 2	VSZ-03_DI_ 3 3	VSZ-03_DI_ 3 1	VSZ-03_A1_DI_ 3 1	VSZ-03_A1_DI_ 3 2	VSZ-03_A2_DI_ 1 1	VSZ-03_A2_DI_ 3 1	VSZ-03_A2_DI_ 3 2	VSZ-03_A3_DI 1	Spectrum 94	VSZ-03_A1_TICLN_ 2 4	VSZ-03_A3_TI_CHU 1	Av	St Dev
wt%	di2	di2	di2	di2	di2	di2	di2	di2	di2	di2	di2	di2	di2		
SiO_2	54.99	53.83	53.36	54.63	55.18	54.86	55.87	55.46	55.57	54.41	56.10	54.41	53.75	54.80	0.84
TiO_2	0.00	0.00	0.00	0.00	0.00	0.00	0.00	0.00	0.00	0.00	0.00	0.00	0.00	0.00	0.00
Al_2O_3	0.00	0.00	0.00	0.00	0.00	0.00	0.00	0.00	0.00	0.00	0.00	0.00	0.00	0.00	0.00
Cr_2O_3	0.00	0.00	0.00	0.00	0.00	0.00	0.00	0.00	0.00	0.00	0.00	0.00	0.00	0.00	0.00
V_2O_3															
FeO	1.33	1.21	1.04	1.16	1.17	1.14	1.17	1.51	1.29	1.57	1.00	1.29	1.36	1.25	0.16
MnO															
MgO	18.54	17.74	17.50	18.03	18.06	18.06	18.82	18.47	18.69	18.52	18.79	18.46	20.40	18.47	0.71
ZnO															
NiO	0.00	0.00	0.00	0.00	0.67	0.80	0.00	0.00	0.00	0.00	0.00	0.00	0.00	0.11	0.28
CaO	26.11	25.76	25.42	25.69	25.83	25.76	26.68	25.98	26.40	25.90	26.74	25.45	24.39	25.86	0.61
Na2O	0.00	0.00	0.00	0.00	0.00	0.00	0.00	0.00	0.00	0.00	0.00	0.00	0.00	0.00	0.00
Total	100.96	98.55	97.33	99.50	100.92	100.63	102.54	101.42	101.95	100.41	102.63	99.61	99.90	100.49	1.53
Si	1.97	1.98	1.98	1.99	1.98	1.98	1.97	1.98	1.97	1.96	1.98	1.97	1.93	1.97	0.01
Ti	0.00	0.00	0.00	0.00	0.00	0.00	0.00	0.00	0.00	0.00	0.00	0.00	0.00	0.00	0.00
Al	0.00	0.00	0.00	0.00	0.00	0.00	0.00	0.00	0.00	0.00	0.00	0.00	0.00	0.00	0.00
Cr	0.00	0.00	0.00	0.00	0.00	0.00	0.00	0.00	0.00	0.00	0.00	0.00	0.00	0.00	0.00
V															
Fe^{2+}	0.04	0.04	0.03	0.04	0.04	0.03	0.03	0.04	0.04	0.05	0.03	0.04	0.04	0.04	0.00
Mn															
Mg	0.99	0.97	0.97	0.98	0.97	0.97	0.99	0.98	0.99	0.99	0.99	1.00	1.09	0.99	0.03
Zn															
Ni	0.00	0.00	0.00	0.00	0.02	0.02	0.00	0.00	0.00	0.00	0.00	0.00	0.00	0.00	0.01
Ca	1.00	1.01	1.01	1.00	0.99	0.99	1.01	0.99	1.00	1.00	1.01	0.99	0.94	1.00	0.02
Na	0.00	0.00	0.00	0.00	0.00	0.00	0.00	0.00	0.00	0.00	0.00	0.00	0.00	0.00	0.00
X(Mg)	0.96	0.96	0.97	0.97	0.96	0.97	0.97	0.96	0.96	0.95	0.97	0.96	0.96	0.96	0.00

B13. Olivine analyses. Formulae were calculated on the basis of 3 cations.

EDS													
Analysis wt%	ASZ--09-B-AREA4-DI_1 1	ASZ--09-B-AREA4-DI_1 2	ASZ--09-B-AREA4-DI_1 3	AZB-A4-DI_2 1	AZB-A4-DI_2 2	AZB-A4-DI_2 3	ASZ-09-A5_DI1 1	ASZ-09-A5_DI1 2	ASZ-09-A5_DI1 3	DI1 4	ASZ-09-B-A5-DI_1	Average	St Dev
SiO_2	54.93	55.22	55.27	55.67	55.05	55.37	54.99	55.63	55.72	54.28	54.35	55.14	0.49
TiO_2	0.00	0.00	0.00	0.00	0.00	0.00	0.00	0.00	0.00	0.00	0.00	0.00	0.00
Al_2O_3	0.00	0.00	0.00	0.00	0.00	0.00	0.00	0.00	0.00	0.00	0.00	0.00	0.00
Cr_2O_3	0.00	0.00	0.00	0.00	0.00	0.00	0.00	0.00	0.00	0.00	0.00	0.00	0.00
V_2O_3													
FeO	0.51	0.59	0.55	1.17	0.78	1.21	0.93	0.72	0.71	0.60	0.63	0.76	0.24
MnO												#DIV/0!	#DIV/0!
MgO	18.57	18.29	18.21	18.52	18.42	18.64	18.23	18.41	18.08	18.14	18.03	18.32	0.21
ZnO													
NiO	0.00	0.00	0.00	0.00	0.00	0.00	0.43	0.37	0.00	0.00	0.00	0.07	0.16
CaO	26.05	26.00	26.32	26.01	26.03	26.36	26.07	26.45	26.12	25.90	25.82	26.10	0.20
Na2O	0.00	0.00	0.00	0.00	0.00	0.00	0.00	0.00	0.00	0.00	0.00	0.00	0.00
Total	100.07	100.11	100.35	101.38	100.29	101.59	100.64	101.57	100.62	98.93	98.82	100.40	0.93
Si	1.98	1.99	1.99	1.99	1.98	1.97	1.98	1.98	2.00	1.98	1.99	1.98	0.01
Ti	0.00	0.00	0.00	0.00	0.00	0.00	0.00	0.00	0.00	0.00	0.00	0.00	0.00
Al	0.00	0.00	0.00	0.00	0.00	0.00	0.00	0.00	0.00	0.00	0.00	0.00	0.00
Cr	0.00	0.00	0.00	0.00	0.00	0.00	0.00	0.00	0.00	0.00	0.00	0.00	0.00
V													
Fe^{2+}	0.02	0.02	0.02	0.03	0.02	0.04	0.03	0.02	0.02	0.02	0.02	0.02	0.01
Mn													
Mg	1.00	0.98	0.98	0.99	0.99	0.99	0.98	0.98	0.97	0.99	0.98	0.98	0.01
Zn													
Ni	0.00	0.00	0.00	0.00	0.00	0.00	0.01	0.01	0.00	0.00	0.00	0.00	0.00
Ca	1.01	1.01	1.02	0.99	1.00	1.00	1.00	1.01	1.01	1.01	1.01	1.01	0.01
Na	0.00	0.00	0.00	0.00	0.00	0.00	0.00	0.00	0.00	0.00	0.00	0.00	0.00
X(Mg)	0.98	0.98	0.98	0.97	0.98	0.96	0.97	0.98	0.98	0.98	0.98	0.98	0.01

EDS	**ol1**									**WDS**	**ol2**									
Analysis	VSZ-03_A1_OL1	VSZ-03_A1_OL2	VSZ-03_A3_OL1	VSZ-03_A3_OL2	VSZ_03_A3_OL3	S-09-VSZ05-area2_ol1	S-09-VSZ05-area2_ol1	Av	St Dev		VSZ-03_A4_OL1 2	VSZ-03_A4_OL1 1	S-09-VSZ05-area1_ol	S-09-VSZ05-area1_ol	S-09-VSZ05-area4_ol	S-09-VSZ05-area4_ol	S-09-VSZ05-area4_ol	S-09-VSZ05-area2_ol1	Av	St Dev
wt%																				
SiO_2	38.80	39.10	39.74	39.27	37.94	40.59	40.72	38.97	0.67		39.74	40.21	40.81	41.11	41.23	41.05	41.36	40.91	41.08	0.20
TiO_2	0.00	0.00	0.00	0.00	0.00	0.01	0.01	0.00	0.00		0.00	0.00	0.00	0.00	0.02	0.00	0.00	0.00	0.00	0.01
Al_2O_3																				
Cr_2O_3						0.07	0.08						0.11	0.11	0.14	0.09	0.14	0.10	0.11	0.02
V_2O_3																				
FeO	12.30	12.68	12.84	11.68	11.30	11.65	11.00	12.16	0.66		9.97	10.51	9.91	9.56	8.58	10.13	8.60	10.14	9.49	0.72
MnO	0.34	0.34	0.35	0.27	0.36	0.25	0.24	0.33	0.03		0.61	0.45	0.34	0.28	0.33	0.32	0.34	0.32	0.32	0.02
MgO	45.70	45.95	47.93	48.09	46.75	47.32	48.00	46.89	1.10		49.24	50.05	48.79	48.96	49.86	48.52	49.86	48.76	49.12	0.59
ZnO																				
NiO	0.38	0.37	0.00	0.41	0.25	0.32	0.30	0.28	0.17		0.36	0.33	0.38	0.37	0.34	0.37	0.33	0.30	0.35	0.03
CaO																				
Na2O						0.08	0.10	####	####				0.05	0.07	0.06	0.08	0.07	0.09	0.07	0.01
Total	97.52	98.44	100.85	99.72	96.60	100.21	100.36	98.63	1.70		99.91	101.55	100.32	100.41	100.50	100.48	100.64	100.52	100.48	0.11
Si	0.99	0.99	0.98	0.97	0.97	1.00	1.00	0.98	0.01		0.97	0.97	1.00	1.00	1.00	1.00	1.00	1.00	1.00	0.00
Ti	0.00	0.00	0.00	0.00	0.00	0.00	0.00	0.00	0.00		0.00	0.00	0.00	0.00	0.00	0.00	0.00	0.00	0.00	0.00
Al																				
Cr	0.00	0.00	0.00	0.00	0.00	0.00	0.00	0.00	0.00		0.00	0.00	0.00	0.00	0.00	0.00	0.00	0.00	0.00	0.00
V																				
Fe^{2+}	0.26	0.27	0.26	0.24	0.24	0.24	0.23	0.26	0.01		0.20	0.21	0.20	0.20	0.17	0.21	0.17	0.21	0.19	0.02
Mn	0.01	0.01	0.01	0.01	0.01	0.01	0.01	0.01	0.00		0.01	0.01	0.01	0.01	0.01	0.01	0.01	0.01	0.01	0.00
Mg	1.74	1.73	1.75	1.77	1.78	1.74	1.76	1.75	0.02		1.80	1.80	1.78	1.78	1.81	1.77	1.80	1.78	1.79	0.01
Zn																				
Ni	0.01	0.01	0.00	0.01	0.01	0.01	0.01	0.01	0.00		0.01	0.01	0.01	0.01	0.01	0.01	0.01	0.01	0.01	0.00
Ca																				
Na	0.00	0.00	0.00	0.00	0.00	0.00	0.00	0.00	0.00		0.00	0.00	0.00	0.00	0.00	0.00	0.00	0.00	0.00	0.00
X(Mg)	0.87	0.87	0.87	0.88	0.88	0.88	0.89	0.87	0.01		0.90	0.89	0.90	0.90	0.91	0.90	0.91	0.90	0.90	0.01

WDS																			
Analysis	GSZ-11a-ol-1	GSZ-11a-ol-1	GSZ-11a-ol-1	GSZ-11a-ol-1	GSZ-11a-ol-1	GSZ-11a-ol-1	GSZ-11a-ol-1	GSZ-11a-ol-2	GSZ-11a-ol-2	GSZ-11a-ol-2	GSZ-11a-ol-2	GSZ-11a-ol-2	GSZ-11a-ol-3	GSZ-11a-ol-3	GSZ-11a-ol-3	GSZ-11a-ol-3	GSZ-11a-ol-3	Average	St Dev
wt%																			
SiO_2	39.74	39.53	39.69	39.39	39.49	39.56	39.30	39.12	39.64	39.18	39.16	38.57	39.71	39.48	39.72	39.54	40.08	39.46	0.33
TiO_2	0.01	0.00	0.01	0.00	0.00	0.00	0.01	0.01	0.00	0.03	0.00	0.01	0.00	0.00	0.01	0.00	0.01	0.01	0.01
Al_2O_3																			
Cr_2O_3	0.00	0.00	0.00	0.00	0.00	0.00	0.00	0.00	0.00	0.00	0.00	0.00	0.00	0.00	0.00	0.00	0.00	0.00	0.00
V_2O_3																			
FeO	9.63	9.47	9.47	9.64	9.49	9.32	9.66	9.38	9.39	9.58	9.46	9.72	9.27	9.41	9.31	9.60	9.58	9.49	0.13
MnO	0.23	0.23	0.23	0.22	0.23	0.23	0.23	0.22	0.23	0.23	0.23	0.22	0.25	0.23	0.24	0.20	0.23	0.23	0.01
MgO	48.59	48.64	48.63	48.80	48.63	48.40	48.78	47.89	47.33	47.88	48.48	47.77	48.04	48.05	48.43	47.96	48.58	48.29	0.42
ZnO																			
NiO	0.39	0.39	0.40	0.41	0.40	0.41	0.39	0.39	0.41	0.39	0.39	0.38	0.36	0.36	0.43	0.37	0.37	0.39	0.02
CaO																			
Na2O	0.00	0.00	0.00	0.00	0.01	0.00	0.00	0.00	0.00	0.00	0.00	0.00	0.00	0.00	0.00	0.00	0.04	0.00	0.01
Total	98.59	98.26	98.43	98.46	98.24	97.92	98.37	97.00	97.00	97.29	97.72	96.67	97.62	97.53	98.14	97.67	98.85	97.87	0.63
Si	0.99	0.98	0.99	0.98	0.98	0.99	0.98	0.99	1.00	0.99	0.98	0.98	1.00	0.99	0.99	0.99	0.99	0.99	0.01
Ti	0.00	0.00	0.00	0.00	0.00	0.00	0.00	0.00	0.00	0.00	0.00	0.00	0.00	0.00	0.00	0.00	0.00	0.00	0.00
Al																			
Cr	0.00	0.00	0.00	0.00	0.00	0.00	0.00	0.00	0.00	0.00	0.00	0.00	0.00	0.00	0.00	0.00	0.00	0.00	0.00
V																			
Fe^{2+}	0.20	0.20	0.20	0.20	0.20	0.19	0.20	0.20	0.20	0.20	0.20	0.21	0.19	0.20	0.19	0.20	0.20	0.20	0.00
Mn	0.00	0.00	0.00	0.00	0.00	0.00	0.00	0.00	0.00	0.00	0.00	0.00	0.01	0.00	0.01	0.00	0.00	0.00	0.00
Mg	1.80	1.81	1.80	1.81	1.81	1.80	1.81	1.80	1.79	1.80	1.81	1.80	1.80	1.80	1.80	1.79	1.79	1.80	0.01
Zn																			
Ni	0.01	0.01	0.01	0.01	0.01	0.01	0.01	0.01	0.01	0.01	0.01	0.01	0.01	0.01	0.01	0.01	0.01	0.01	0.00
Ca																			
Na	0.00	0.00	0.00	0.00	0.00	0.00	0.00	0.00	0.00	0.00	0.00	0.00	0.00	0.00	0.00	0.00	0.00	0.00	0.00
X(Mg)	0.90	0.90	0.90	0.90	0.90	0.90	0.90	0.90	0.90	0.90	0.90	0.90	0.90	0.90	0.90	0.90	0.90	0.90	0.00

B14. Preliminary mass balance calculations
Example: Fe

Lizardite

To determine if lizardite contributed Fe^{3+} to form magnetite, mass balance calculations were carried out with the following assumptions:

1. To establish the maximum ferric iron contribution from lizardite, the Fe_2O_3 concentration of lizardite was assumed to be 1 wt % (as quantified by Beard and Frost, 2017 for a wide range of samples).
2. Lizardite is not observed in any of the samples but the mode is assumed to be the same as antigorite and chlorite (i.e., all lizardite was converted to antigorite, and chlorite thereafter where observed e.g., PF001).
3. The formula of lizardite was calculated to 5 cations.
4. The Fe content of lizardite was similar to the measured ∑FeO content in antigorite, although it is likely lizardite contains higher ∑FeO. However, maximum concentrations of ∑FeO were used for the calculations.

For example, in PF-001 mole% of ∑Fe, Fe^{2+} and Fe^{3+} hosted in lizardite per 100g of rock were calculated using the equation:

g of ∑Fe or Fe^{3+} or Fe^{2+} hosted in lizardite per 100g of rock/ g of ∑Fe or Fe^{3+} or Fe^{2+} hosted in 100g of rock, where:

1) g of ∑Fe hosted in lizardite per 100g of rock = $(100/n \sum_{Fe} * M \sum_{Fe}) * M_{liz} * v * \rho_{liz} / v * \rho_{rock}$

2) g of Fe^{3+} hosted in lizardite per 100g of rock = $(100/n * M_{Fe^{3+}}) * M_{liz} * v * \rho_{liz} / v * \rho_{rock}$

- assuming the mass of Fe_2O_3 was 1 wt% (0.6994 wt% Fe^{3+})

3) g of Fe^{2+} hosted in lizardite per 100g of rock = $(100/n * M_{Fe^{2+}}) * M_{liz} * v * \rho_{liz} / v * \rho_{rock}$

- In the case of lizardite only, $n\ Fe^{2+} = n \sum Fe - n\ Fe^{3+}$, for all other minerals calculated Fe^{3+} (see supplementary S2) or measured concentrations were available from EPMA analyses (see supplementary S6–S16).

m = mass, v = mode by volume (cm^3), ρ = density (g/cm^3), *n* = measured number of moles of Fe per mole of lizardite, $M_{\sum Fe}$ = molar mass of Fe and M_{liz} = molar mass of lizardite.
* = multiplication symbol.

Steps 1–3 were carried out for each Fe-bearing mineral in each sample.

Note: For garnet, the composition is widely variable, so the calculations used the average composition of each the core, and the rim.

Example: Ti

Additionally, to determine if Ti addition occurred, or if Ti redistribution occurred from a possible precursor phase of e.g. ülvospinel, mass balance calculations assumed that ülvospinel was of the mode as Ti-magnetite in PF-001.
For example, in PF-001 mole% of Ti hosted in ülvospinel per 100g of rock was calculated using the equation:

g of Ti hosted in l ülvospinel per 100g of rock/ g of Ti hosted in 100g of rock, where,
g of Ti hosted in ülvospinel per 100g of rock = $(100/n_{Ti} * M_{Ti}) * M_{ulv} * v * \rho_{ulv} / v * \rho_{rock}$

- Assuming 1 mole of Ti per 1 mole of ülvospinel

where m = mass, v = mode by volume (cm^3), ρ = density (g/cm^3), *n* = measured number of moles of Ti per mole of ülvospinel, M_{Ti} = molar mass of Ti and M_{ulv} = molar mass of ülvospinel.

This method was carried out for each Ti-bearing mineral in each sample.

PF-001 Fe and Ti mass balance calculations

PF-001	liz	ülvo spinel	mt	trem	talc	ilm	Ti-mt	ap	Total
mode by vol (cc)	0.65	0.01	0.12	0.07	0.10	0.03	0.01	0.02	1.01
density (g/cm3)	2.63	4.66	5.15	2.96	2.78	4.72	5.15	3.17	
mass (g)	1.71	0.05	0.62	0.21	0.28	0.14	0.05	0.06	3.01
g of mineral per 100g rock	0.57	0.02	0.21	0.07	0.09	0.05	0.02	0.02	
moles of Fe per mole mineral	0.19	1.00	3.00	0.29	0.23	0.94	2.21		
g of Fe per mole mineral	10.61	55.85	167.54	16.20	12.84	52.49	123.42		
molar mass	277.1 1	223.57	231.54	812.3 7	379.2 7	151.7 3	224.76		
g of Fe per 100g mineral	3.83	24.98	72.36	1.99	3.39	34.60	54.91		
g of ∑Fe hosted in mineral per 100g rock	2.18	0.39	14.88	0.14	0.31	1.63	0.94		20.46
moles of Fe2+ per mole mineral	0.10	1.00	1.00	0.29	0.23	0.94	0.93		
g of Fe2+ permole mineral	5.61	55.85	55.85	16.20	12.84	52.49	51.94		
g of Fe2+ per 100g mineral	2.02	24.98	24.12	1.99	3.39	34.60	23.11		
g of Fe2+ hosted in mineral per 100g rock	1.15	0.39	4.96	0.14	0.31	1.63	0.40		8.97
mole% Fe2+	12.83	4.32	55.26	1.53	3.49	18.16	4.41		
moles of Fe3+ per mole mineral	0.09	0.00	2.00	0.00	0.00	0.00	1.27		
g of Fe3+ per mole mineral	5.00	0.00	111.69	0.00	0.00	0.00	70.92		
g of Fe3+ per 100g mineral	1.80	0.00	48.24	0.00	0.00	0.00	31.56		
g of Fe3+ hosted in mineral per 100g rock	1.03	0.00	9.92	0.00	0.00	0.00	0.54		11.48
mol% Fe3+	8.94	0.00	86.36	0.00	0.00	0.00	4.71		
moles of Ti per mole mineral	0.00	1.00	0.00	0.00	0.03	1.00	0.72		
g of Ti per mole mineral	0.00	47.87	0.00	0.00	1.55	47.87	34.47		
g of Ti per 100g mineral	0.00	21.41	0.00	0.00	0.41	31.55	15.34		
g of Ti hosted in mineral per 100g rock	0.00	0.33	0.00	0.00	0.04	1.49	0.26		2.12
mol% Ti	0.00	15.67	0.00	0.00	1.79	70.15	12.40		

LC-015 Fe and Ti mass balance calculations

LC-015	lizardite	magnetite	chromite	ilmenite	Talc	Total
mode by vol (cc)	0.82	0.11	0.02	0.02	0.03	1.00
density (g/cm3)	2.52	5.15	5.12	4.72	2.78	
mass (g)	2.07	0.57	0.10	0.09	0.08	2.91
g of mineral per 100g rock	0.71	0.19	0.04	0.03	0.03	1.00
moles of Fe per mole mineral	0.20	2.89	1.00	0.94	0.23	
g of Fe per mole mineral	11.17	161.39	55.85	52.49	12.84	
molar mass	277.11	231.19	226.92	151.73	379.27	
g of Fe per 100g mineral	4.03	69.81	24.61	34.60	3.39	
g of ∑Fe hosted in mineral per 100g rock	2.86	13.58	0.87	1.12	0.10	
moles of Fe2+ per mole mineral	0.11	0.93	1.00	1.00	0.23	
g of Fe2+ permole mineral	6.17	51.94	55.85	55.85	12.84	
g of Fe2+ per 100g mineral	2.23	22.46	24.61	36.81	3.39	
g of Fe2+ hosted in mineral per 100g rock	1.58	4.37	0.87	1.19	0.10	8.10
mole% Fe2+	19.49	53.92	10.68	14.72	1.20	
moles of Fe3+ per mole mineral	0.09	1.96	0.00	0.00	0.00	
g of Fe3+ per mole mineral	5.00	109.46	0.00	0.00	0.00	
g of Fe3+ per 100g mineral	1.80	47.34	0.00	0.00	0.00	
g of Fe3+ hosted in mineral per 100g rock	1.28	9.21	0.00	0.00	0.00	9.21
mol% Fe3+	13.90	100.00	0.00	0.00	0.00	
moles of Ti per mole mineral	0.00	0.01	0.00	1.00	0.00	
g of Ti per mole mineral	0.00	0.48	0.00	47.87	0.00	
g of Ti per 100g mineral	0.00	0.21	0.00	31.55	0.00	
g of Ti hosted in mineral per 100g rock	0.00	0.04	0.00	1.02	0.00	1.06
mol% Ti	0.00	3.79	0.00	96.21	0.00	

GSZ-11 Fe and Ti mass balance calculations

GSZ-11	mill	hz	**liz**	**mt**	chromite	olivine	Di	Total
mode by vol (cc)	0.01	0.01	0.80	0.05	0.03	0.07	0.03	1.00
density (g/cm3)	5.37	5.82	2.58	5.15	5.12	3.32		
mass (g)	0.05	0.06	2.06	0.26	0.15	0.23		2.82
g of mineral per 100g rock	0.02	0.02	0.73	0.09	0.05	0.08		1.00
moles of Fe per mole mineral	0.00	0.02	0.14	2.89	1.00	0.26	0.03	
g of Fe per mole mineral	0.00	1.12	7.82	161.39	55.85	14.52	1.68	
molar mass	90.76	240.20	277.11	231.54	231.19	153.31	153.31	
g of Fe per 100g mineral	0.00	0.46	2.82	69.70	24.16	9.47	1.09	
g of ∑Fe hosted in mineral per 100g rock	0.00	0.01	2.07	6.37	1.32	0.78	0.00	
moles of Fe2+ per mole mineral	0.00	0.01	0.05	0.98	1.00	0.26	0.03	
g of Fe2+ permole mineral	0.00	0.56	2.79	54.73	55.85	14.52	1.68	
g of Fe2+ per 100g mineral	0.00	0.23	1.01	23.64	24.16	9.47	1.09	
g of Fe2+ hosted in mineral per 100g rock	0.00	0.00	0.74	2.16	1.32	0.78	0.00	5.00
mole% Fe2+	0.00	0.10	14.76	43.19	26.33	15.62	0.00	
moles of Fe3+ per mole mineral	0.00	0.00	0.09	2.00	0.00	0.00	0.00	
g of Fe3+ per mole mineral	0.00	0.00	5.03	111.69	0.00	0.00	0.00	
g of Fe3+ per 100g mineral	0.00	0.00	1.81	48.24	0.00	0.00	0.00	
g of Fe3+ hosted in mineral per 100g rock	0.00	0.00	1.33	4.41	0.00	0.00	0.00	5.73
mol% Fe3+	0.00	0.00	23.16	76.84	0.00	0.00	0.00	
moles of Ti per mole mineral	0.00	0.00	0.00	0.00	0.00	0.00	0.00	
g of Ti per mole mineral	0.00	0.00	0.00	0.00	0.00	0.00	0.00	
g of Ti per 100g mineral	0.00	0.00	0.00	0.00	0.00	0.00	0.00	
g of Ti hosted in mineral per 100g rock	0.00	0.00	0.00	0.00	0.00	0.00	0.00	
mol% Ti	0.00	0.00	0.00	0.00	0.00	0.00	0.00	

VSZ-03 Fe and Ti mass balance calculations

VSZ-03	Di1	ol1	Tichu1	**liz**	Mt1	ol2	Hz1	Pn3	Tichu4	Mt3	
mode by vol (cc)	0.10	0.02	0.01	0.75	0.01	0.03	0.01	0.01	0.03	0.01	0.98
density (g/cm3)	2.58	3.32	3.44	2.58	5.15	3.32	5.82	4.87	3.44	5.15	
mass (g)	0.26	0.07	0.03	1.94	0.05	0.10	0.06	0.05	0.10	0.05	2.71
g of mineral per 100g rock	0.10	0.02	0.01	0.71	0.02	0.04	0.02	0.02	0.04	0.02	
moles of Fe per mole mineral	0.04	0.26	0.59	0.14	2.88	0.19	0.01	0.24	0.74	2.85	
g of Fe per mole mineral	2.23	14.5	32.9	7.82	160.8	10.61	0.56	13.40	41.33	159.16	
molar mass	217	153	643	277	232	231	240	772	637	232	
g of Fe per 100g mineral	1.03	9.47	5.13	2.82	69.46	4.59	0.23	1.74	6.48	68.74	
g of ∑Fe hosted in mineral per 100g rock	0.10	0.23	0.07	2.02	1.32	0.17	0.00	0.03	0.25	1.31	
moles of Fe2+ per mole mineral	0.00	0.01	0.59	0.05	1.00	0.19	0.01	0.02	0.03	0.94	
g of Fe2+ permole mineral	0.00	0.56	32.95	2.79	55.85	10.61	0.56	1.12	1.68	52.5	
g of Fe2+ per 100g mineral	0.00	0.36	5.13	1.01	24.12	4.59	0.23	0.14	0.26	22.7	
g of Fe2+ hosted in mineral per 100g rock	0.00	0.01	0.07	0.72	0.46	0.17	0.00	1.43	0.01	0.43	3.30
mole% Fe2+	0.00	0.27	1.98	21.9	13.9	5.12	0.15	43.3	0.30	13.09	
moles of Fe3+ per mole mineral	0.00	0.00	0.00	0.09	1.92	0.00	0.00	0.00	0.00	1.91	
g of Fe3+ per mole mineral	0.00	0.00	0.00	5.03	107.2	0.00	0.00	0.00	0.00	107	
g of Fe3+ per 100g mineral	0.00	0.00	0.00	1.81	46.31	0.00	0.00	0.00	0.00	46.1	
g of Fe3+ hosted in mineral per 100g rock	0.00	0.00	0.00	1.30	0.88	0.00	0.00	0.00	0.00	0.88	3.05
mol% Fe3+	0.00	0.00	0.00	42.5	28.8	0.00	0.00	0.00	0.00	28.70	
moles of Ti per mole mineral	0.00	0.00	0.33	0.00	0.02	0.00	0.00	0.00	0.28	0.01	
g of Ti per mole mineral	0.00	0.00	15.80	0.00	0.96	0.00	0.00	0.00	13.40	0.48	
g of Ti per 100g mineral	0.00	0.00	2.46	0.00	0.41	0.00	0.00	0.00	2.10	0.21	
g of Ti hosted in mineral per 100g rock	0.00	0.00	0.38	0.00	0.18	0.00	0.00	0.00	0.33	0.09	0.98
mol% Ti	0.00	0.00	39.03	0.00	18.2	0.00	0.00	0.00	33.65	9.11	

VSZ-05 Fe and Ti mass balance calculations

ASZ-09 Fe and Ti mass balance calculations

VSZ-05	**lizardite**	ol2	Hz1	Pn3	Tichu4	Mt3	Mt4	di2	Total
mode by vol (cc)	0.80	0.03	0.01	0.01	0.05	0.01	0.02	0.07	1.00
density (g/cm3)	2.58	3.32	5.82	4.87	3.44	5.15	5.15	3.40	
mass (g)	2.06	0.10	0.06	0.05	0.17	0.05	0.10	0.24	2.84
g of mineral per 100g rock	0.73	0.04	0.02	0.02	0.06	0.02	0.04	0.08	
moles of Fe per mole mineral	0.12	0.19	0.05	2.16	0.74	2.85	2.77	0.00	
g of Fe per mole mineral	6.70	10.61	2.79	120.63	41.33	159.16	154.69	0.00	
molar mass	277.11	231.19	240.20	771.94	637.40	231.54	231.54	216.55	
g of Fe per 100g mineral	2.42	4.59	1.16	15.63	6.48	68.74	66.81	0.00	
g of ∑Fe hosted in mineral per 100g rock	1.76	0.16	0.02	0.27	0.39	1.25	2.43	0.00	
moles of Fe2+ per mole mineral	0.00	0.01	0.05	2.16	1.00	2.85	2.77	0.02	
g of Fe2+ permole mineral	0.00	0.56	2.79	120.63	55.85	159.16	154.69	1.12	
g of Fe2+ per 100g mineral	0.00	0.24	1.16	15.63	8.76	68.74	66.81	0.52	
g of Fe2+ hosted in mineral per 100g rock	0.00	0.01	0.02	0.27	0.53	1.25	2.43	0.04	4.55
mole% Fe2+	0.00	0.19	0.52	5.90	11.68	27.43	53.33	0.95	
moles of Fe3+ per mole mineral	0.09	0.00	0.00	0.00	0.00	1.91	1.89	0.00	
g of Fe3+ per mole mineral	5.03	0.00	0.00	0.00	0.00	106.66	105.55	0.00	
g of Fe3+ per 100g mineral	1.81	0.00	0.00	0.00	0.00	46.07	45.58	0.00	
g of Fe3+ hosted in mineral per 100g rock	1.32	0.00	0.00	0.00	0.00	0.84	1.66	0.00	3.81
mol% Fe3+	34.63	0.00	0.00	0.00	0.00	21.94	43.43	0.00	
moles of Ti per mole mineral	0.00	0.00	0.00	0.00	0.28	0.01	0.01	-	
g of Ti per mole mineral	0.00	0.00	0.00	0.00	13.40	0.48	0.48		
g of Ti per 100g mineral	0.00	0.00	0.00	0.00	2.10	0.21	0.21		
g of Ti hosted in mineral per 100g rock	0.00	0.00	0.00	0.00	0.33	0.09	0.09	0.51	
mol% Ti	0.00	0.00	0.00	0.00	64.88	17.56	17.56	-	

ASZ-09	perov	ilm	Ti-chu2	liz	di	Tichu 3	pn2	Ttn	mt2	mt3	Total
mode by vol (cc)	trace	trace	0.30	0.45	0.07	0.10	0.02	0.03	0.01	0.02	1.00
density (g/cm3)			3.44	2.58	3.40	3.44	4.87	3.47	5.15	5.15	
mass (g)			1.03	1.16	0.24	0.34	0.10	0.10	0.05	0.10	3.13
g of mineral per 100g rock			0.33	0.37	0.08	0.11	0.03	0.03	0.02	0.03	
moles of Fe per mole mineral			0.38	0.12	0.02	0.58	2.16	0.01	2.90	2.88	
g of Fe per mole mineral			21.22	6.70	1.12	32.39	120.6 3	0.56	161.9 5	160.8 3	
molar mass			629.1 8	277.1 1	216.5 5	632.7 3	771.9 4	197.7 6	231.5 4	231.5 4	
g of Fe per 100g mineral			3.37	2.42	0.52	5.12	15.63	0.28	69.94	69.46	
g of ∑Fe hosted in mineral per 100g rock			1.11	0.90	0.04	0.56	0.49	0.01	1.15	2.29	
moles of Fe2+ per mole mineral			0.00	0.01	0.02	0.58	1.00	0.00	2.90	0.02	
g of Fe2+ permole mineral			0.00	0.56	1.12	32.39	55.85	0.00	161.9 5	1.12	
g of Fe2+ per 100g mineral			0.00	0.20	0.52	5.12	7.23	0.00	69.94	0.48	
g of Fe2+ hosted in mineral per 100g rock			0.00	0.07	0.04	0.56	0.23	0.00	1.15	0.02	2.07
mol% Fe2+			0.00	3.61	1.90	27.20	10.88	0.00	55.64	0.77	
moles of Fe3+ per mole mineral			0.00	0.09	0.00	0.00	0.00	0.01	1.98	1.98	
g of Fe3+ per mole mineral			0.00	5.03	0.00	0.00	0.00	0.56	110.5 7	110.5 7	
g of Fe3+ per 100g mineral			0.00	1.81	0.00	0.00	0.00	0.28	47.76	47.76	
g of Fe3+ hosted in mineral per 100g rock			0.00	0.67	0.00	0.00	0.00	0.01	0.79	1.57	3.04
mol% Fe3+			0.00	22.13	0.00	0.00	0.00	0.31	25.85	51.70	
moles of Ti per mole mineral			0.38	0.00	0.00	0.39	0.00	0.92	0.01	0.01	
g of Ti per mole mineral			18.19	0.00	0.00	18.67	0.00	44.04	0.48	0.48	
g of Ti per 100g mineral			2.89	0.00	0.00	2.95	0.00	22.27	0.21	0.21	
g of Ti hosted in mineral per 100g rock			0.46	0.00	0.00	0.47	0.00	11.26	0.09	0.09	12.3 7
mol% Ti			3.72	0.00	0.00	3.77	0.00	91.07	0.72	0.72	

VSZ-02 Fe and Ti mass balance calculations

VSZ-02	chl	grt core	grtt rim	ilm	di	caclite	ttn	ap	Total
mode by vol (cc)	0.40	0.13	0.17	0.01	0.20	0.05	0.04	trace	1.00
density (g/cm3)	2.65	3.53	3.55	4.72	3.40	2.71	3.47		
mass (g)	1.06	0.46	0.60	0.05	0.68	0.14	0.14		
g of mineral per 100g rock	0.39	0.17	0.22	0.02	0.25	0.05	0.05		
moles of Fe per mole mineral	0.13	0.12	0.50	0.94	0.07	0.00	0.01		
g of Fe per mole mineral	7.26	6.70	27.92	52.49	3.91	0.00	0.56		
molar mass	595	461	520	152	217	101	198		
g of Fe per 100g mineral	1.22	1.45	5.37	34.60	1.81	0.00	0.28		
g of ∑Fe hosted in mineral per 100g rock	0.48	0.25	1.20	0.58	0.45	0.00	0.01		
moles of Fe2+ per mole mineral	0.00	0.01	0.24	0.94	0.00	0.00	0.00		
g of Fe2+ permole mineral	0.00	0.56	13.40	52.49	0.00	0.00	0.00		
g of Fe2+ per 100g mineral	0.00	0.12	2.58	34.60	0.00	0.00	0.00		
g of Fe2+ hosted in mineral per 100g rock	0.00	0.02	0.57	0.58	0.00	0.00	0.00		1.17
mole% Fe2+	0.00	1.75	48.92	49.33	0.00	0.00	0.00		
moles of Fe3+ per mole mineral	0.00	0.06	0.26	0.94	0.07	0.00	0.01		
g of Fe3+ per mole mineral	0.00	3.35	14.52	52.49	3.91	0.00	0.56		
g of Fe3+ per 100g mineral	0.00	0.73	2.79	34.60	1.81	0.00	0.28		
g of Fe3+ hosted in mineral per 100g rock	0.00	0.12	0.62	0.58	0.45	0.00	0.01		1.79
mol% Fe3+	0.00	6.88	34.71	32.31	25.30	0.00	0.81		
moles of Ti per mole mineral	0.00	0.07	0.04	1.00	0.00	0.00	0.92		
g of Ti per mole mineral	0.00	3.35	1.91	47.87	0.00	0.00	44.04		
g of Ti per 100g mineral	0.00	0.73	0.37	31.55	0.00	0.00	22.27		
g of Ti hosted in mineral per 100g rock	0.00	0.16	0.07	20.79	0.00	0.00	11.26		32.28
mol% Ti	0.00	0.49	0.22	64.41	0.00	0.00	34.88		

APPENDIX C

SUPPLEMENTARY DATA:

TRACING HSE THROUGH

SUBDUCTION (CHAPTER 4)

C1: Whole rock HSE uncertainties

Measured HSE concentrations for whole rock samples and standards. Uncertainties are reported in brackets (2 sigma). Certified and provisional values for the standard AMIS078 (African Mineral Standards, 2011) are available at: http://www.amis.co.za/certificates-depleted-stock?limit=100&limitstart=100.
Certified , provisional and in-house values for AMIS078 were measured using Ni fire assay. Average reference values for MORE-L were derived from average measured values from sodium peroxide fusion or 4 acid digest. b.d.l = below detection limit.

Uncertainties were calculated using the equation (Eurachem CITAC, 2000, p108)

$u(x) = \sqrt{S_0^2 + (x \,.\, S_1)^2}$

where $u(x)$ is the combined standard uncertainty in the result x (uncertainty expressed as a standard deviation), s_0 represents a constant contribution to the overall uncertainty, $s1$ is a proportionality constant.

Samples

ppb	Os	Ir	Ru	Rh	Pd	Pt	Au	Re	Re (Check)
CO13-31-1	4.0(4)	4.0(3)	6.0(5)	1.0(2)	11.0(9)	9(2)	4(1)	b.d.l	
CO13-31-2	3.0(3)	3.0(3)	6.0(5)	1.0(2)	7.0(9)	8(2)	3(1)	b.d.l	
CO13-33-1	3.0(3)	3.0(3)	6.0(5)	1.0(2)	6.0(8)	7(2)	2(1)	b.d.l	
CO13-55-1	2.0(3)	3.0(3)	6.0(5)	1.0(2)	6.0(8)	7(2)	2(1)	b.d.l	
CO13-55-2	2.0(3)	3.0(3)	6.0(5)	1.0(2)	6.0(8)	6(2)	2(1)	b.d.l	
CO14-03	b.d.l	b.d.l	2.0(5)	b.d.l	8.0(9)	3(2)	5(1)	2(2)	
CO14-04	3.0(3)	4.0(3)	5.0(5)	2.0(2)	8.0(9)	8(2)	4(1)	6(2)	5(2)

Detection Limits

ppb	Os	Ir	Ru	Rh	Pd	Pt	Au	Re	Re (Check)
	1	1	1	1	1	1	2	2	2

Blanks

ppb	Os	Ir	Ru	Rh	Pd	Pt	Au	Re
Blank 1	b.d.l	b.d.l	b.d.l	1	b.d.l	2	b.d.l	b.d.l
Blank 2	b.d.l	b.d.l	b.d.l	b.d.l	b.d.l	b.d.l	b.d.l	b.d.l

Measured Standards

ppb	Os	Ir	Ru	Rh	Pd	Pt	Au	Re
AMIS0278	17(1)	36(2)	147	150(9)	2040(10)	1690(80)	26(2)	
	26(2)	36(2)	17(1)	2040(10)	1690(80)		150(9)	
MORE-L								13600(500)
MPL-5								1500(50)

In House Reference Values*

Standard	**Element**	**Mean**	**SD**	**# analyses**	**Units**
MORE-L	Re	14520	431	38	ppb
MPL-5	Re	1537	65	2411	ppb
AMIS0278	Os	17.7	4.64	509	ppb
Provisional Reference Values (5-15% RSD)					
AMIS0278	Au	26	3	72	ppb
AMIS0278	Ir	36	6	64	ppb
AMIS0278	Rh	150	20	80	ppb
AMIS0278	Ru	150	40	72	ppb
Certified Reference Values (5% RSD)					
AMIS0278	Pt	1690	160	72	ppb
AMIS0278	Pd	2100	20	80	ppb

C2: BonnSulfVI standard calibration against Laflamme Po726

Against Laflamme Po726

Bonn SulfVI	Analysis	S_Bonn_1	S_Bonn_2	S_Bonn_3	S_Bonn_4	S_Bonn_1	S_Bonn_2	S_Bonn_3	S_Bonn_1	S_Bonn_2	S_Bonn_1	S_Bonn_2	S_Bonn_3
ppm	Os	26.2	26.7	27.9	25.9	26.22	26.38	24.77	22.4	26.8	27.35	26.13	24.91
	Ir	21.3	20.9	21.5	20.1	20.97	21.02	19.98	18.5	22.1	22.1	21.36	20.35
	Ru	23.04	22.17	23.23	21.23	22.07	21.99	20.89	18.87	22.46	22.93	22.87	21.38
	Rh	18.6	18.28	19.17	17.99	18.7	18.07	18.15	16.58	19.53	19.44	18.93	19.72
	Pd	15.7	14.83	15.99	14.99	14.3	14.13	14.49	13.46	15.46	15.57	15.72	16.23
	Pt	13.85	14.22	14.44	14.02	13.81	13.65	13.54	12.48	14.55	14.67	15.14	14.76
	Au	10.71	11.31	11.47	11.81	11	10.57	11.02	11.25	12.28	11.96	12.36	12.52

Bonn SulfVI	**Analysis**	S_Bonn_1	S_Bonn_2	S_Bonn_1	S_Bonn_2	ST DEV
ppm	Os	24.44	24.93	23.95	26.3	1.39
	Ir	19.52	20.1	19.38	20.36	0.99
	Ru	20.21	21.73	19.48	20.67	1.29
	Rh	17.49	18.63	17.69	17.97	0.83
	Pd	13.59	14.19	14.77	14.24	0.85
	Pt	13.17	13.83	13.7	14.55	0.67
	Au	11.25	11.22	11.85	11.58	0.58

Against Laflamme Po726	Ru101	Rh103	Pd105	Os190	Ir193	Pt195	Au197	Re
reference value [1]	19.4	20.5	16.3	23	20.8	17.6	11.3	3.9
Av. Bonn SulfVI (n=16)	21.57625	18.43375	14.85375	25.705	20.59625	14.02375	11.51	
%diff	10.08632	-11.2091	-9.7366	10.52324	-0.98926	-25.5014	1.8245	

[1] Bragagni et al., 2015, *Goldschmidt Abstracts* 374.
%diff=percentage difference to reference values

C3: Time resolved spectrum of ^{66}Cu (blue), ^{103}Rh (green) and ^{105}Pd (orange) in sulphide grains. Integration areas are shown with rectangles.

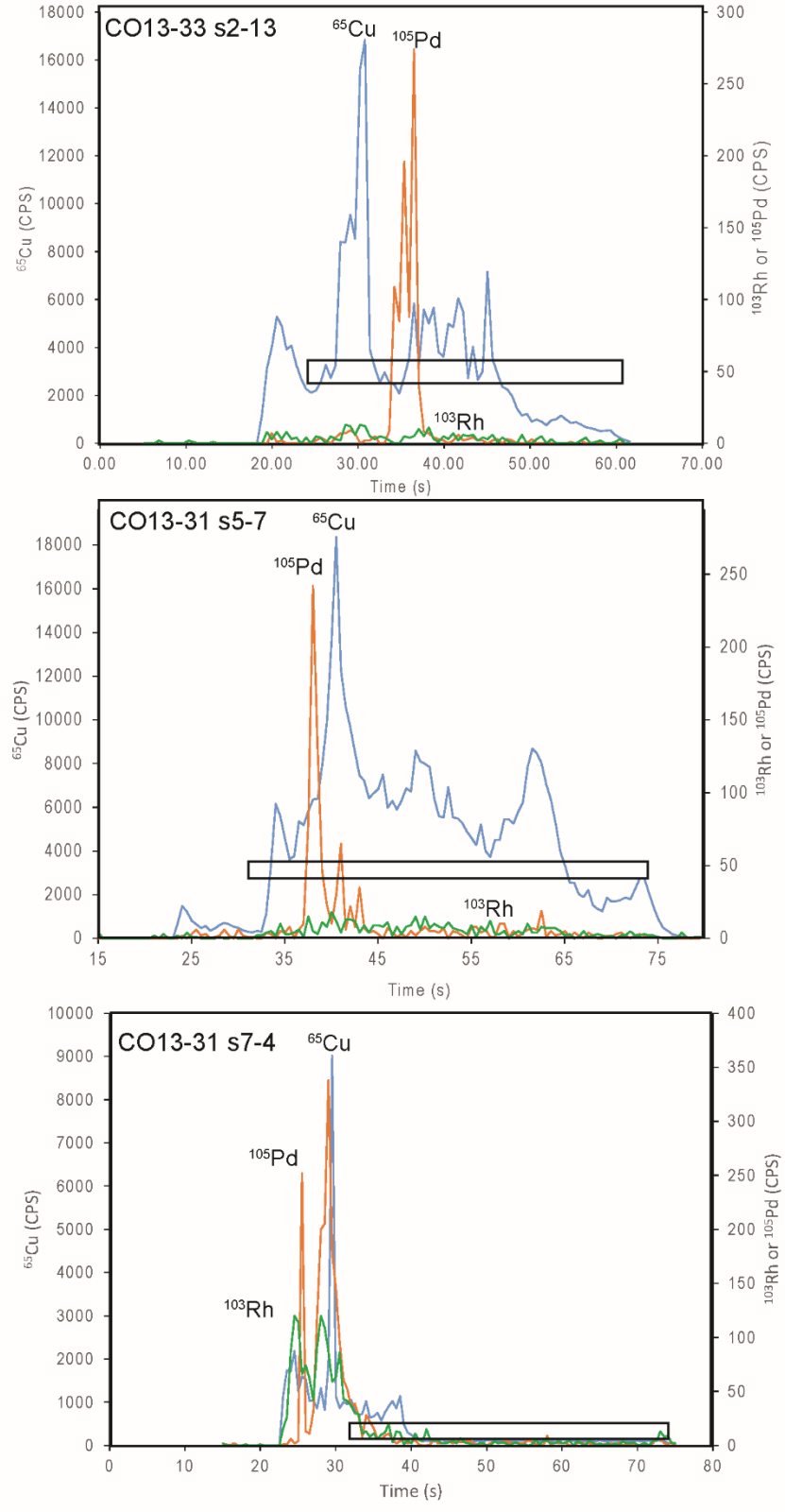

C4: EPMA analyses of matrix antigorite

Analysis (wt%)	CO13-33 a3_3	CO13-33_a3_s1	CO13-33 a3 s2	CO13-33 a2 s1_2	CO13-33 a2 s1_1	CO13-33 a2 s1_3	CO13-33 a2 s1_4	CO13-33 a2 s2	CO13-33 a2 s2_2	CO13-33 a2 s2_3	CO13-33 a5 s1	CO13-33 a5 s2
SiO_2	42.74	44.59	44.79	45.59	43.36	45.41	44.49	46.02	45.83	46.28	42.99	42.91
TiO_2	b.d.l	b.d.l	b.d.l	b.d.l	b.d.l	b.d.l	b.d.l	b.d.l	b.d.l	b.d.l	b.d.l	b.d.l
V_2O_3	b.d.l	b.d.l	b.d.l	b.d.l	b.d.l	b.d.l	b.d.l	b.d.l	b.d.l	b.d.l	b.d.l	b.d.l
Al_2O_3	2.42	1.82	0.96	0.46	1.84	0.88	1.19	0.97	0.00	0.07	2.54	2.61
Cr_2O_3	1.52	0.92	0.06	0.05	0.79	0.21	0.51	0.05	b.d.l	b.d.l	0.87	0.83
FeO	3.37	2.79	2.49	2.23	3.22	2.15	2.25	1.85	1.80	1.82	2.62	2.74
NiO	0.27	0.17	0.21	0.12	0.33	0.19	0.20	0.16	0.15	0.22	0.40	0.62
MnO	0.10	0.07	0.08	0.10	0.05	0.06	0.10	0.08	0.09	0.10	0.07	0.06
MgO	38.28	40.15	40.63	40.73	40.24	41.08	40.62	41.74	40.75	40.92	38.62	38.91
CaO	0.01	0.01	0.00	0.00	0.00	0.00	0.00	0.00	0.00	0.00	0.03	0.04
Na_2O	b.d.l	b.d.l	b.d.l	b.d.l	b.d.l	b.d.l	b.d.l	b.d.l	b.d.l	b.d.l	b.d.l	b.d.l
Total	88.73	90.56	89.22	89.27	89.84	90.00	89.35	90.88	88.63	89.42	88.16	88.76
Si	7.99	8.12	8.23	8.37	7.95	8.27	8.17	8.28	8.46	8.48	8.05	7.98
Ti	0.00	0.00	0.00	0.00	0.00	0.00	0.00	0.00	0.00	0.00	0.00	0.00
V	0.00	0.00	0.00	0.00	0.00	0.00	0.00	0.00	0.00	0.00	0.00	0.00
Al	0.53	0.39	0.21	0.10	0.40	0.19	0.26	0.20	0.00	0.02	0.56	0.57
Cr	0.22	0.13	0.01	0.01	0.11	0.03	0.07	0.01	0.00	0.00	0.13	0.12
Fe	0.53	0.42	0.38	0.34	0.49	0.33	0.35	0.28	0.28	0.28	0.41	0.43
Ni	0.04	0.03	0.03	0.02	0.05	0.03	0.03	0.02	0.02	0.03	0.06	0.09
Mn	0.01	0.01	0.01	0.01	0.01	0.01	0.01	0.01	0.01	0.01	0.01	0.01
Mg	10.67	10.90	11.13	11.15	10.99	11.15	11.12	11.20	11.22	11.18	10.78	10.79
Ca	0.00	0.00	0.00	0.00	0.00	0.00	0.00	0.00	0.00	0.00	0.01	0.01
X(Mg)	0.95	0.96	0.97	0.97	0.96	0.97	0.97	0.98	0.98	0.98	0.96	0.96

Analysis (wt%)	CO13-33 a5_m2	CO13-33 a5 m2	CO13-33 a4 s1_1	CO13-33 a5 s1_1	CO13-33 a5 s1_2	CO13-33 a5 s1_3	CO13-33 a5 m1	CO13-33 a5 m1	CO13-33 a5 m1	CO13-33 a5 m1	CO13-33 a5 m1	CO13-33 a6 s1
SiO_2	42.96	43.79	43.70	43.63	43.19	41.76	45.94	45.71	44.33	46.44	45.14	42.94
TiO_2	b.d.l	b.d.l	b.d.l	b.d.l	b.d.l	b.d.l	b.d.l	b.d.l	b.d.l	b.d.l	b.d.l	b.d.l
V_2O_3	b.d.l	b.d.l	b.d.l	b.d.l	b.d.l	b.d.l	b.d.l	b.d.l	b.d.l	b.d.l	b.d.l	b.d.l
Al_2O_3	2.91	2.45	2.61	2.16	2.76	3.29	0.45	0.94	1.70	0.97	1.28	2.63
Cr_2O_3	0.84	0.84	0.77	0.84	0.58	0.55	0.03	0.17	0.31	0.07	0.29	0.90
FeO	2.91	2.73	2.67	2.38	2.62	2.42	2.00	2.15	2.78	2.46	2.87	2.49
NiO	0.19	0.20	0.28	0.35	0.28	0.57	0.17	0.18	0.17	0.14	0.17	0.24
MnO	0.06	0.13	0.06	0.11	0.08	0.06	0.09	0.09	0.13	0.10	0.07	0.04
MgO	38.89	39.57	39.79	39.47	40.15	38.52	41.12	40.89	40.22	41.17	40.86	39.57
CaO	0.03	0.04	0.03	0.02	0.00	0.01	0.02	0.01	0.01	0.02	0.00	0.01
Na_2O	b.d.l	b.d.l	b.d.l	b.d.l	b.d.l	b.d.l	b.d.l	b.d.l	b.d.l	b.d.l	b.d.l	b.d.l
Total	88.86	89.92	89.92	88.95	89.66	87.19	89.84	90.16	89.66	91.39	90.70	88.87
Si	7.98	8.04	8.00	8.08	7.91	7.88	8.38	8.32	8.13	8.35	8.18	7.95
Ti	0.00	0.00	0.00	0.00	0.00	0.00	0.00	0.00	0.00	0.00	0.00	0.00
V	0.00	0.00	0.00	0.00	0.00	0.00	0.00	0.00	0.00	0.00	0.00	0.00
Al	0.64	0.53	0.56	0.47	0.60	0.73	0.10	0.20	0.37	0.21	0.27	0.57
Cr	0.12	0.12	0.11	0.12	0.08	0.08	0.00	0.03	0.04	0.01	0.04	0.13
Fe	0.45	0.42	0.41	0.37	0.40	0.38	0.30	0.33	0.43	0.37	0.44	0.39
Ni	0.03	0.03	0.04	0.05	0.04	0.09	0.02	0.03	0.02	0.02	0.02	0.04
Mn	0.01	0.02	0.01	0.01	0.01	0.01	0.01	0.01	0.02	0.01	0.01	0.00
Mg	10.77	10.83	10.86	10.89	10.96	10.83	11.18	11.09	10.99	11.03	11.04	10.92
Ca	0.01	0.01	0.01	0.00	0.00	0.00	0.00	0.00	0.00	0.00	0.00	0.00
X(Mg)	0.96	0.96	0.96	0.97	0.96	0.97	0.97	0.97	0.96	0.97	0.96	0.97

Analysis (wt%)	CO13-33 a6 s2	CO13-33 a6 s3	Average	STD	CO13-55 a6s1_1	CO13-55 a6s1_2	CO13-55a6 s1_3	CO13-55a6 s2_1	CO13-55a6 s2_2	CO13-55a6 s2_3	CO13-55a6 s3_1	CO13-55a6 s3_2
SiO_2	43.92	42.59	44.27	1.34	45.06	44.74	45.06	44.92	45.63	44.93	44.61	43.99
TiO_2	b.d.l	b.d.l	b.d.l	-	b.d.l	b.d.l	b.d.l	b.d.l	b.d.l	b.d.l	b.d.l	b.d.l
V_2O_3	b.d.l	b.d.l	b.d.l	-	b.d.l	b.d.l	b.d.l	b.d.l	b.d.l	b.d.l	b.d.l	b.d.l
Al_2O_3	1.91	2.12	1.69	0.93	1.68	2.55	1.07	1.43	1.18	1.61	1.57	2.35
Cr_2O_3	0.47	0.69	0.55	0.38	0.58	0.65	0.23	0.64	0.67	0.61	0.79	0.66
FeO	2.64	2.78	2.51	0.40	3.53	3.33	3.51	3.21	4.64	3.35	3.54	4.07
NiO	0.29	0.40	0.26	0.13	0.23	0.33	0.25	0.24	0.19	0.24	0.29	0.22
MnO	0.09	0.03	0.08	0.02	0.10	0.06	0.08	0.05	0.12	0.10	0.09	0.07
MgO	40.53	39.51	40.11	0.93	39.70	38.99	38.82	38.74	40.00	39.09	38.61	38.81
CaO	0.01	0.02	0.01	0.01	0.04	0.04	0.02	0.01	0.02	0.02	0.03	0.02
Na_2O	b.d.l	b.d.l	b.d.l	-	b.d.l	b.d.l	b.d.l	b.d.l	b.d.l	b.d.l	b.d.l	b.d.l
Total	89.85	88.17	89.46	0.93	90.93	90.68	89.07	89.25	92.44	89.94	89.53	90.19
Si	8.02	7.94	8.13	0.18	8.20	8.17	8.37	8.33	8.20	8.27	8.27	8.09
Ti	0.00	0.00	0.00	0.00	0.00	0.00	0.00	0.00	0.00	0.00	0.00	0.00
V	0.00	0.00	0.00	0.00	0.00	0.00	0.00	0.00	0.00	0.00	0.00	0.00
Al	0.41	0.47	0.37	0.21	0.36	0.55	0.23	0.31	0.25	0.35	0.34	0.51
Cr	0.07	0.10	0.07	0.06	0.08	0.09	0.03	0.09	0.10	0.09	0.12	0.10
Fe	0.40	0.43	0.39	0.06	0.54	0.51	0.55	0.50	0.70	0.52	0.55	0.63
Ni	0.04	0.06	0.04	0.02	0.03	0.05	0.04	0.04	0.03	0.04	0.04	0.03
Mn	0.01	0.00	0.01	0.00	0.01	0.01	0.01	0.01	0.01	0.01	0.01	0.01
Mg	11.04	10.99	10.99	0.15	10.77	10.61	10.76	10.72	10.71	10.73	10.67	10.64
Ca	0.00	0.00	0.00	0.00	0.01	0.01	0.00	0.00	0.00	0.00	0.01	0.00
X(Mg)	0.96	0.96	0.96	0.96	0.95	0.95	0.95	0.96	0.94	0.95	0.95	0.94

Analysis	CO13-55a6	CO13-55a7	CO13-55a7	CO13-55_a7	CO13-55_a7	CO13-55_a8	CO13-55_a8	CO13-55_a8	CO13-55_a8	CO13-55_a8	CO13-55	CO13-55
SiO_2	45.28	41.11	43.85	43.84	44.28	44.39	45.70	45.33	44.20	44.57	42.83	44.08
TiO_2	b.d.l	b.d.l	b.d.l	b.d.l	b.d.l	b.d.l	b.d.l	b.d.l	b.d.l	b.d.l	b.d.l	b.d.l
V2O3	b.d.l	b.d.l	b.d.l	b.d.l	b.d.l	b.d.l	b.d.l	b.d.l	b.d.l	b.d.l	b.d.l	b.d.l
Al2O3	1.12	4.75	2.25	2.21	2.15	2.23	0.31	0.69	1.44	1.24	4.12	2.75
Cr2O3	0.58	3.01	1.62	0.70	0.48	0.23	b.d.l	0.05	0.28	0.28	0.31	0.44
FeO	3.49	4.41	4.10	3.95	3.34	4.83	4.47	8.15	4.44	4.07	3.99	4.26
NiO	0.25	0.18	0.24	0.17	0.34	0.61	0.78	4.38	1.97	0.17	0.81	0.59
MnO	0.11	0.11	0.12	0.09	0.11	0.08	0.14	0.08	0.13	0.11	0.05	0.06
MgO	39.00	37.83	38.71	38.48	38.65	37.61	36.60	33.55	37.31	39.43	38.80	37.66
CaO	0.01	0.04	0.08	0.00	0.02	0.02	0.56	0.24	0.03	0.00	0.06	0.07
Na2O	b.d.l	b.d.l	b.d.l	b.d.l	b.d.l	b.d.l	b.d.l	b.d.l	b.d.l	b.d.l	b.d.l	b.d.l
Total	89.85	91.45	90.96	89.44	89.37	90.02	88.57	92.50	89.80	89.87	90.97	89.91
Si	8.35	7.51	8.03	8.13	8.20	8.23	8.65	8.48	8.25	8.20	7.80	8.17
Ti	0.00	0.00	0.00	0.00	0.00	0.00	0.00	0.00	0.00	0.00	0.00	0.00
V	0.00	0.00	0.00	0.00	0.00	0.00	0.00	0.00	0.00	0.00	0.00	0.00
Al	0.24	1.02	0.49	0.48	0.47	0.49	0.07	0.15	0.32	0.27	0.88	0.60
Cr	0.09	0.43	0.24	0.10	0.07	0.03	0.00	0.01	0.04	0.04	0.05	0.06
Fe	0.54	0.67	0.63	0.61	0.52	0.75	0.71	1.28	0.69	0.63	0.61	0.66
Ni	0.04	0.03	0.04	0.03	0.05	0.09	0.12	0.66	0.30	0.03	0.12	0.09
Mn	0.01	0.01	0.01	0.01	0.01	0.01	0.02	0.01	0.02	0.01	0.01	0.01
Mg	10.73	10.31	10.56	10.64	10.67	10.40	10.33	9.36	10.38	10.82	10.53	10.40
Ca	0.00	0.01	0.01	0.00	0.00	0.00	0.11	0.05	0.01	0.00	0.01	0.01
X(Mg)	0.95	0.94	0.94	0.95	0.95	0.93	0.94	0.88	0.94	0.95	0.95	0.94

Analysis (wt%)	CO13-55 a2	CO13-55 a2 s1	CO13-55 a2 s2	CO13-55 a2 s3	CO13-55 a2 s3	CO13-55 a2 s3	CO13-55 a2 s3	CO13-55 a2 s4	CO13-55 a2 s5	Average	STD
SiO_2	43.97	45.22	47.37	44.44	44.69	43.66	42.94	43.54	44.69	44.44	1.10
TiO_2	b.d.l	b.d.l	b.d.l	b.d.l	b.d.l	b.d.l	b.d.l	b.d.l	b.d.l	b.d.l	-
V2O3	b.d.l	b.d.l	b.d.l	b.d.l	b.d.l	b.d.l	b.d.l	b.d.l	b.d.l	b.d.l	-
Al2O3	3.09	0.87	0.95	1.51	0.62	2.19	2.11	3.85	1.59	1.91	1.05
Cr2O3	0.20	0.25	0.28	b.d.l	b.d.l	b.d.l	b.d.l	0.15	0.23	0.58	0.61
FeO	3.34	3.73	3.64	3.66	6.81	4.09	6.61	3.62	3.15	4.18	1.15
NiO	0.41	0.15	0.15	0.38	0.09	0.12	0.08	0.61	0.40	0.51	0.83
MnO	0.04	0.07	0.08	0.12	0.11	0.07	0.14	0.06	0.08	0.09	0.03
MgO	39.49	39.18	41.11	38.45	37.00	38.54	37.43	38.92	38.84	38.46	1.32
CaO	0.04	0.02	0.00	0.02	0.00	0.01	0.00	0.04	0.05	0.05	0.11
Na2O	b.d.l	b.d.l	b.d.l	b.d.l	b.d.l	b.d.l	b.d.l	b.d.l	b.d.l	b.d.l	-
Total	90.61	89.47	93.59	88.58	89.32	88.69	89.31	90.80	89.01	90.14	1.21
Si	8.01	8.36	8.37	8.31	8.40	8.14	8.03	7.93	8.30	8.20	0.22
Ti	0.00	0.00	0.00	0.00	0.00	0.00	0.00	0.00	0.00	0.00	0.00
V	0.00	0.00	0.00	0.00	0.00	0.00	0.00	0.00	0.00	0.00	0.00
Al	0.66	0.19	0.20	0.33	0.14	0.48	0.47	0.83	0.35	0.41	0.23
Cr	0.03	0.04	0.04	0.00	0.00	0.00	0.00	0.02	0.03	0.07	0.09
Fe	0.51	0.58	0.54	0.57	1.07	0.64	1.03	0.55	0.49	0.65	0.18
Ni	0.06	0.02	0.02	0.06	0.01	0.02	0.01	0.09	0.06	0.08	0.12
Mn	0.00	0.01	0.01	0.02	0.01	0.01	0.02	0.01	0.01	0.01	0.00
Mg	10.72	10.80	10.83	10.71	10.37	10.71	10.44	10.57	10.75	10.57	0.28
Ca	0.01	0.00	0.00	0.00	0.00	0.00	0.00	0.01	0.01	0.01	0.02
X(Mg)	0.95	0.95	0.95	0.95	0.91	0.94	0.91	0.95	0.96	0.94	0.02

C5: LA-ICP-MS derived HSE concentrations of matrix antigorite

Matrix PGE concentrations < indicates the concentration is below the detection limit. Standards used were Nist612 for Ni, Pd, Re, Pt and Au and Po726 and Bonn for all other PGE. Concentrations were derived using Fe as the internal isotope standard when using Bonn Sulf VI and Laflamme po726 and Si as the internal standard (Fe and Si concentrations provided in EA-4). For Os, Ir, Ru and Rh maximum and minimum values are reported, taking into consideration the range of Fe concentrations in antigorite.

	Nist 612				
Analysis	Ni	Pd	Re	Pt	Au
ppm					
CO13-33-m1 - 7	7450	<0.023	<0.010	<0.006	<0.013
CO13-33-m1 - 14	3694	<0.017	<0.010	<0.011	<0.016
CO13-33-m2 - 1	1611	<0.016	<0.007	<0.011	<0.019
CO13-33-m2 - 4	1836	<0.012	<0.007	<0.014	<0.013
CO13-33-m2 - 5	1940	<0.018	<0.007	<0.017	<0.019
CO13-33-m2 - 6	1855	<0.019	<0.021	<0.015	<0.02
CO13-33-m2 - 11	1772	<0.013	<0.015	<0.013	<0.016
CO13-33-s2 - 1	3980	<0.017	<0.010	<0.014	<0.017
CO13-33-s2 - 2	8500	<0.021	<0.010	<0.022	<0.018
CO13-33-s2 - 6	1927	<0.013	<0.024	<0.017	<0.025
CO13-33-s2 - 7	1908	<0.013	<0.010	<0.008	<0.014
CO13-33-s2 - 11	1695	<0.016	<0.010	<0.011	<0.016
CO13-33-s2 - 12	1606	<0.019	<0.010	<0.012	<0.012
CO13-33-s2 - 14	1806	<0.011	<0.010	<0.0097	<0.018
CO13-33-s2 - 24	2258	<0.023	<0.009	<0.022	<0.013
CO13-33-s2 - 25	1820	<0.013	<0.014	<0.0061	<0.014
CO13-33-s2 - 26	2362	<0.013	<0.019	<0.021	<0.012
CO13-33-s2 - 27	2064	<0.011	<0.009	<0.02	<0.007
CO13-33-s2 - 31	1879	<0.017	<0.015	<0.012	<0.015
CO13-33-s2 - 32	1717	<0.033	<0.007	<0.014	<0.014
CO13-33-s2 - 33	4057	<0.012	<0.010	<0.014	<0.012
CO13-33-s4 - 9	5800	<0.02	<0.015	<0.013	<0.018
CO13-33-s4 - 10	2086	<0.012	<0.010	<0.013	<0.0099
CO13-33-s1 - 3	2026	<0.021	<0.010	<0.012	<0.007
CO13-55-s3 - 1	1057	<0.004	<0.003	<0.007	<0.0043
CO13-55-s3 - 2	1116	<0.006	<0.010	<0.011	<0.011
CO13-55-s3 - 4	1794	<0.013	<0.006	<0.0055	<0.0031
CO13-55-s3 - 5	1381	<0.009	<0.010	<0.0072	<0.0034
CO13-55-s2 - 1	1122	<0.007	<0.003	<0.0081	<0.0043
CO13-55-s2 - 2	1251	<0.006	<0.010	<0.0055	<0.0033
CO13-55-s2 - 4	1367	<0.003	<0.006	<0.0096	<0.0048
CO13-55-s2 - 5	1488	<0.003	<0.010	<0.005	<0.004
CO13-55-s1 - 1	2019	<0.007	<0.010	<0.011	<0.011
CO13-55-s1 - 2	1340	<0.009	<0.006	<0.0081	<0.0061
CO13-55-s1 - 4	1223	<0.006	<0.003	<0.0073	<0.0045
CO13-55-s1 - 5	1853	<0.003	<0.006	<0.0094	<0.0049
CO13-55s4 - 1	3166	<0.017	<0.010	<0.0051	<0.0033
CO13-55s4 - 4	4965	<0.013	<0.006	<0.0024	<0.004
CO13-55s4 - 5	1841	<0.013	<0.008	<0.0086	<0.0052

	Bonn (maximum)				Bonn (minimum)			
Analysis	Os	Ir	Ru	Rh	Os	Ir	Ru	Rh
ppm								
CO13-33-m1 - 7	<0.026	<0.006	<0.020	<0.010	<0.012	<0.003	<0.010	<0.005
CO13-33-m1 - 14	<0.020	<0.019	<0.020	<0.006	<0.010	<0.009	<0.010	<0.003
CO13-33-m2 - 1	<0.030	<0.005	<0.030	<0.006	<0.015	<0.003	<0.014	<0.003
CO13-33-m2 - 4	<0.022	<0.003	<0.017	<0.004	<0.011	<0.001	<0.008	<0.002
CO13-33-m2 - 5	<0.027	<0.004	<0.020	<0.006	<0.013	<0.002	<0.010	<0.003
CO13-33-m2 - 6	<0.009	<0.005	<0.029	<0.005	<0.004	<0.002	<0.014	<0.002
CO13-33-m2 - 11	<0.023	<0.002	<0.020	<0.005	<0.011	<0.001	<0.010	<0.003
CO13-33-s2 - 1	<0.022	<0.008	<0.019	<0.007	<0.011	<0.004	<0.009	<0.003
CO13-33-s2 - 2	<0.025	<0.005	<0.020	<0.004	<0.012	<0.002	<0.010	<0.002
CO13-33-s2 - 6	<0.010	<0.005	<0.016	<0.007	<0.005	<0.003	<0.008	<0.004
CO13-33-s2 - 7	<0.025	<0.005	<0.020	<0.009	<0.012	<0.002	<0.010	<0.004
CO13-33-s2 - 11	<0.058	<0.007	<0.016	<0.008	<0.028	<0.003	<0.008	<0.004
CO13-33-s2 - 12	<0.026	<0.010	<0.020	<0.007	<0.012	<0.005	<0.010	<0.003
CO13-33-s2 - 14	<0.025	<0.007	<0.009	<0.011	<0.012	<0.003	<0.004	<0.005
CO13-33-s2 - 24	<0.037	<0.009	<0.012	<0.006	<0.018	<0.004	<0.006	<0.003
CO13-33-s2 - 25	<0.033	<0.006	<0.020	<0.003	<0.016	<0.003	<0.010	<0.001
CO13-33-s2 - 26	<0.011	<0.006	<0.018	<0.009	<0.005	<0.003	<0.009	<0.004
CO13-33-s2 - 27	<0.012	<0.003	<0.019	<0.005	<0.006	<0.001	<0.009	<0.002
CO13-33-s2 - 31	<0.026	<0.009	<0.027	<0.006	<0.012	<0.004	<0.013	<0.003
CO13-33-s2 - 32	<0.019	<0.007	<0.020	<0.008	<0.009	<0.003	<0.010	<0.004
CO13-33-s2 - 33	<0.028	<0.004	<0.030	<0.008	<0.014	<0.002	<0.014	<0.004
CO13-33-s4 - 9	<0.034	<0.006	<0.020	<0.009	<0.016	<0.003	<0.010	<0.004
CO13-33-s4 - 10	<0.031	<0.006	<0.023	<0.006	<0.015	<0.003	<0.011	<0.003
CO13-33-s1 - 3	<0.022	<0.003	<0.020	<0.005	<0.010	<0.001	<0.010	<0.003
CO13-55-s3 - 1	<0.038	<0.003	<0.013	<0.003	<0.015	<0.001	<0.005	<0.001
CO13-55-s3 - 2	<0.025	<0.008	<0.013	<0.006	<0.010	<0.003	<0.005	<0.002
CO13-55-s3 - 4	<0.038	<0.006	0.028	<0.007	<0.015	<0.002	0.011	<0.003
CO13-55-s3 - 5	<0.010	<0.003	<0.013	<0.007	<0.004	<0.001	<0.005	<0.003
CO13-55-s2 - 1	<0.030	<0.002	<0.013	<0.006	<0.011	<0.001	<0.005	<0.002
CO13-55-s2 - 2	<0.020	<0.002	<0.007	<0.007	<0.008	<0.001	<0.003	<0.003
CO13-55-s2 - 4	<0.020	<0.005	<0.013	<0.007	<0.008	<0.002	<0.005	<0.003
CO13-55-s2 - 5	<0.010	<0.005	<0.015	<0.006	<0.004	<0.002	<0.006	<0.002
CO13-55-s1 - 1	<0.013	<0.007	<0.008	<0.008	<0.005	<0.003	<0.003	<0.003
CO13-55-s1 - 2	<0.023	<0.007	<0.013	<0.008	<0.009	<0.003	<0.005	<0.003
CO13-55-s1 - 4	<0.023	<0.003	<0.011	<0.004	<0.009	<0.001	<0.004	<0.002
CO13-55-s1 - 5	<0.040	<0.006	<0.013	<0.007	<0.016	<0.002	<0.005	<0.003
CO13-55s4 - 1	<0.015	<0.006	0.036	<0.007	<0.006	<0.002	0.014	<0.003
CO13-55s4 - 4	<0.017	<0.017	0.057	<0.008	<0.007	<0.007	0.022	<0.003
CO13-55s4 - 5	<0.025	<0.009	<0.030	<0.008	<0.010	<0.004	<0.012	<0.003

	Po726 (maximum)				Po726 (minimum)			
Analysis	Os	Ir	Ru	Rh	Os	Ir	Ru	Rh
ppm								
CO13-33-m1 - 7	<0.027	<0.006	<0.021	<0.009	<0.016	<0.003	<0.011	<0.005
CO13-33-m1 - 14	<0.022	<0.018	<0.021	<0.005	<0.013	<0.011	<0.011	<0.003
CO13-33-m2 - 1	<0.032	<0.005	<0.032	<0.005	<0.019	<0.003	<0.019	<0.003
CO13-33-m2 - 4	<0.024	<0.003	<0.019	<0.004	<0.010	<0.003	<0.003	<0.002
CO13-33-m2 - 5	<0.029	<0.004	<0.021	<0.005	<0.006	<0.003	<0.019	<0.002
CO13-33-m2 - 6	<0.010	<0.005	<0.032	<0.004	<0.0005	<0.0002	<0.0007	<0.0002
CO13-33-m2 - 11	<0.025	<0.002	<0.021	<0.005	<0.015	<0.001	<0.011	<0.003
CO13-33-s2 - 1	<0.024	<0.008	<0.021	<0.006	<0.014	<0.005	<0.012	<0.004
CO13-33-s2 - 2	<0.026	<0.005	<0.021	<0.003	<0.014	<0.003	<0.011	<0.002
CO13-33-s2 - 6	<0.011	<0.005	<0.018	<0.006	<0.007	<0.003	<0.011	<0.004
CO13-33-s2 - 7	<0.026	<0.005	<0.021	<0.007	<0.014	<0.003	<0.011	<0.004
CO13-33-s2 - 11	<0.062	<0.007	<0.017	<0.007	<0.037	<0.004	<0.010	<0.004
CO13-33-s2 - 12	<0.027	<0.009	<0.022	<0.006	<0.016	<0.006	<0.013	<0.004
CO13-33-s2 - 14	<0.026	<0.007	<0.010	<0.009	<0.014	<0.004	<0.006	<0.005
CO13-33-s2 - 24	<0.038	<0.008	<0.013	<0.006	<0.022	<0.005	<0.007	<0.003
CO13-33-s2 - 25	<0.034	<0.006	<0.021	<0.003	<0.020	<0.003	<0.011	<0.002
CO13-33-s2 - 26	<0.011	<0.006	<0.018	<0.008	<0.007	<0.003	<0.011	<0.005
CO13-33-s2 - 27	<0.012	<0.003	<0.019	<0.004	<0.007	<0.002	<0.011	<0.003
CO13-33-s2 - 31	<0.025	<0.008	<0.027	<0.006	<0.015	<0.005	<0.016	<0.003
CO13-33-s2 - 32	<0.018	<0.006	<0.021	<0.007	<0.011	<0.004	<0.011	<0.004
CO13-33-s2 - 33	<0.027	<0.004	<0.029	<0.007	<0.016	<0.002	<0.017	<0.004
CO13-33-s4 - 9	<0.031	<0.005	<0.021	<0.008	<0.018	<0.003	<0.011	<0.005
CO13-33-s4 - 10	<0.028	<0.005	<0.022	<0.005	<0.017	<0.003	<0.013	<0.003
CO13-33-s1 - 3	<0.019	<0.002	<0.021	<0.005	<0.011	<0.001	<0.011	<0.003
CO13-55-s3 - 1	<0.043	<0.003	<0.015	<0.003	<0.014	<0.001	<0.005	<0.001
CO13-55-s3 - 2	<0.027	<0.008	<0.015	<0.005	<0.009	<0.002	<0.005	<0.002
CO13-55-s3 - 4	<0.042	<0.006	0.033	<0.006	<0.014	<0.002	0.011	<0.002
CO13-55-s3 - 5	<0.011	<0.002	<0.017	<0.007	<0.003	<0.0008	<0.005	<0.002
CO13-55-s2 - 1	<0.033	<0.002	<0.015	<0.006	<0.011	<0.0007	<0.005	<0.002
CO13-55-s2 - 2	<0.022	<0.002	<0.007	<0.006	<0.007	<0.0007	<0.002	<0.002
CO13-55-s2 - 4	<0.022	<0.005	<0.015	<0.007	<0.007	<0.002	<0.005	<0.002
CO13-55-s2 - 5	<0.011	<0.005	<0.017	<0.005	<0.003	<0.002	<0.005	<0.002
CO13-55-s1 - 1	<0.015	<0.007	<0.009	<0.008	<0.005	<0.002	<0.003	<0.002
CO13-55-s1 - 2	<0.026	<0.007	<0.015	<0.007	<0.008	<0.002	<0.005	<0.002
CO13-55-s1 - 4	<0.027	<0.004	<0.012	<0.004	<0.009	<0.001	<0.004	<0.001
CO13-55-s1 - 5	<0.047	<0.006	<0.015	<0.006	<0.015	<0.002	<0.005	<0.002
CO13-55s4 - 1	<0.018	<0.006	0.039	<0.006	<0.006	<0.002	0.012	<0.002
CO13-55s4 - 4	<0.021	<0.017	0.06	<0.007	<0.007	<0.006	0.019	<0.002
CO13-55s4 - 5	<0.03	<0.01	<0.034	<0.007	<0.009	<0.003	<0.011	<0.002

C6: EPMA data for sulphides

Serra di Pigno serpentinites

Wt%	Co13-21 area1-s2	CO13-21 area2-s1	Co13-21 area 3-s1_1	Co13-21 area 3-s1_2	CO13-21 area 5 s1	Co13-21 area6 s1_1	Co13-21 area6 s1_2	Co13-21 area6 s1_3
Si	0.04	0.91	0.11	0.05	0.12	0.16	0.03	0.02
Mg	0.05	1.29	0.25	0.07	0.17	0.31	0.02	0.02
Ni	35.54	34.87	35.76	35.75	35.72	36.16	36.46	36.16
Fe	26.46	26.07	26.76	26.77	26.11	26.10	26.43	26.38
Co	2.97	1.91	2.05	2.06	2.10	1.97	2.05	1.96
S	33.19	32.31	33.24	33.12	33.22	32.97	33.14	33.24
Pb	0.03	0.03	0.03	0.03	0.02	0.03	0.02	0.02
Zn	0.00	0.00	0.01	0.00	0.00	0.00	0.01	0.01
Cu	0.02	0.02	0.02	0.02	0.02	0.02	0.02	0.02
Mn	0.01	0.01	0.01	0.01	0.01	0.00	0.00	0.01
Cr	0.04	0.07	0.03	0.04	0.04	0.04	0.03	0.03
As	0.00	0.03	0.00	0.00	0.00	0.00	0.00	0.00
Sb	0.00	0.01	0.02	0.03	0.02	0.01	0.00	0.01
Total	98.36	97.51	98.29	97.95	97.56	97.76	98.21	97.87
mol%								
Ni	0.28	0.28	0.28	0.28	0.28	0.29	0.29	0.29
Fe	0.22	0.22	0.22	0.22	0.22	0.22	0.22	0.22
Co	0.02	0.02	0.02	0.02	0.02	0.02	0.02	0.02
S	0.48	0.48	0.48	0.48	0.48	0.48	0.48	0.48
	pn	pn	pn	pn	pn	pn	pn	pn
S/Ni+Fe+Co	0.92	0.92	0.92	0.92	0.93	0.92	0.92	0.92

wt%	Co13-21 area6 s1_4	CO13-21 area7 s1_1	CO13-21 area7 s1_2	CO13-21 area 8 s1_1	CO13-21 area 8 s1_2	CO13-21 area 8 s1_3	CO13-21 area9 s1_1	CO13-21 area9 s1_2
Si	0.24	0.04	0.05	0.03	0.05	0.05	0.05	0.02
Mg	0.32	0.05	0.07	0.04	0.07	0.06	0.07	0.03
Ni	35.63	36.05	36.14	63.48	64.44	63.55	36.21	36.35
Fe	26.51	26.25	26.46	1.48	1.15	1.45	26.50	26.92
Co	1.94	2.01	2.00	0.00	0.00	0.00	2.15	2.15
S	33.12	33.15	33.14	32.78	32.94	33.65	32.88	33.00
Pb	0.03	0.03	0.02	0.20	0.20	0.20	0.01	0.02
Zn	0.00	0.00	0.00	0.00	0.00	0.00	0.00	0.00
Cu	0.02	0.02	0.02	0.06	0.05	0.05	0.01	0.02
Mn	0.01	0.00	0.00	0.00	0.01	0.01	0.00	0.00
Cr	0.04	0.02	0.02	0.05	0.04	0.04	0.03	0.02
As	0.01	0.00	0.00	0.00	0.00	0.00	0.01	0.01
Sb	0.00	0.03	0.00	0.04	0.01	0.06	0.02	0.02
Total	97.86	97.66	97.93	98.16	98.97	99.11	97.94	98.56
mol%								
Ni	0.28	0.29	0.29	0.51	0.51	0.50	0.29	0.29
Fe	0.22	0.22	0.22	0.01	0.01	0.01	0.22	0.22
Co	0.02	0.02	0.02	0.00	0.00	0.00	0.02	0.02
S	0.48	0.48	0.48	0.48	0.48	0.49	0.48	0.47

wt%	CO13-21 area9 s1_3	CO13-21 area11 s1	Average pn	Std Dev
Si	0.03	0.10	0.13	0.22
Mg	0.03	0.20	0.20	0.32
Ni	36.51	36.31	35.97	0.43
Fe	26.90	26.12	26.45	0.29
Co	2.12	2.09	2.10	0.25
S	32.90	33.11	33.05	0.23
Pb	0.01	0.03	0.02	0.01
Zn	0.01	0.00	0.00	0.00
Cu	0.02	0.02	0.02	0.00
Mn	0.00	0.01	0.01	0.00
Cr	0.02	0.01	0.03	0.01
As	0.01	0.00	0.01	0.01
Sb	0.03	0.02	0.01	0.01
Total	98.59	98.01	98.00	0.33
mol%				
Ni	0.29	0.29	0.28	0.00
Fe	0.22	0.22	0.22	0.00
Co	0.02	0.02	0.02	0.00
S	0.47	0.48	0.48	0.00

wt%	CO13-40 area1_s1	CO13-40 area2_s1_1	CO13-40 area2_s1_2	CO13-40 area2_s2	CO13-40 area2_s3_1	CO13-40 area2_s3_2	CO13-40 area2_s4
S	33.18	33.78	33.89	33.51	33.68	33.81	37.16
As	0.01	0.00	0.00	0.00	0.01	0.00	0.00
Co	1.57	1.61	1.64	1.56	1.64	1.64	2.09
Fe	28.53	28.84	28.94	28.81	28.88	28.94	27.10
Ni	34.54	35.14	35.28	34.87	35.20	35.08	32.07
Total	97.83	99.37	99.75	98.76	99.41	99.47	98.43
mol%							
Ni	0.27	0.27	0.27	0.27	0.27	0.27	0.25
Fe	0.24	0.24	0.24	0.24	0.24	0.24	0.22
Co	0.01	0.01	0.01	0.01	0.01	0.01	0.02
S	0.48	0.48	0.48	0.48	0.48	0.48	0.52

wt%	CO13-40 area4_s2	CO13-40 area4_s3	CO13-40 area4_s4	Average	St Dev
S	37.77	34.56	35.64	34.70	1.61
As	0.00	0.00	0.00	0.00	0.00
Co	2.14	1.68	1.88	1.75	0.21
Fe	28.00	27.54	28.32	28.39	0.65
Ni	31.52	34.67	32.17	34.05	1.50
Total	99.42	98.45	98.00	98.89	0.68
mol%					
Ni	0.24	0.27	0.25	0.26	0.01
Fe	0.22	0.23	0.23	0.23	0.01
Co	0.02	0.01	0.01	0.01	0.00
S	0.52	0.49	0.51	0.49	0.02

Analysis wt%	CO13-55 area1_s2	CO13-55 area4_s2	CO13-55 area5_s1	CO13-55 area5_s2	CO13-55 area6_s1	CO13-55 area7_s1	CO13-55 area8_s1	CO13-55 area8_s1
Si	0.03	0.14	0.03	0.05	0.07	0.03	0.04	0.03
Mg	0.06	0.14	0.04	0.06	0.10	0.05	0.04	0.04
Ni	35.42	35.12	37.64	38.48	35.63	38.27	37.44	37.37
Fe	27.40	27.25	24.85	23.28	26.67	24.34	25.08	25.38
Co	2.19	2.03	2.48	2.31	2.37	2.69	2.40	2.27
S	33.27	32.90	33.41	33.26	33.21	33.23	33.42	33.58
Pb	0.01	0.01	0.03	0.03	0.03	0.02	0.03	0.05
Zn	0.00	0.00	0.00	0.00	0.00	0.00	0.00	0.01
Cu	0.01	0.00	0.01	0.02	0.01	0.01	0.01	0.01
Mn	0.01	0.01	0.01	0.01	0.01	0.01	0.01	0.01
Cr	0.03	0.02	0.01	0.02	0.01	0.01	0.01	0.01
Se	0.16	0.16	0.15	0.17	0.13	0.16	0.17	0.16
Ag	0.00	0.00	0.00	0.00	0.00	0.00	0.01	0.00
Bi	0.14	0.12	0.13	0.12	0.12	0.14	0.12	0.12
As	0.26	0.26	0.26	0.25	0.24	0.27	0.28	0.26
Sb	0.02	0.00	0.00	0.03	0.02	0.01	0.01	0.04
TOTAL	99.01	98.17	99.05	98.09	98.63	99.24	99.06	99.31
mol%	pn	pn	pn	pn	pn	pn	pn	pn
Ni	0.28	0.28	0.29	0.30	0.28	0.30	0.29	0.29
Fe	0.23	0.23	0.20	0.19	0.22	0.20	0.21	0.21
Co	0.02	0.02	0.02	0.02	0.02	0.02	0.02	0.02
S	0.48	0.47	0.48	0.48	0.48	0.48	0.48	0.48

Analysis wt%	CO13-55 area8_s1	CO13-55 area8_s1	CO13-55 area8_s1	CO13-55 area8_s1	CO13-55 area8_s1	CO13-55 area10_s1	CO13-55 area10_s1	CO13-55 area10_s1
Si	0.03	0.14	0.04	0.04	0.05	0.04	0.03	0.03
Mg	0.04	0.25	0.06	0.06	0.06	0.05	0.05	0.04
Ni	37.28	37.33	37.66	36.25	37.31	34.57	34.57	34.67
Fe	25.96	23.87	25.28	27.03	25.62	28.11	27.99	28.45
Co	2.24	2.39	2.41	1.97	2.35	1.94	2.02	1.94
S	33.36	33.13	33.56	33.64	33.46	33.41	33.50	33.53
Pb	0.04	0.01	0.00	0.00	0.01	0.01	0.01	0.00
Zn	0.00	0.01	0.00	0.00	0.00	0.00	0.00	0.00
Cu	0.01	0.02	0.01	0.00	0.01	0.00	0.01	0.01
Mn	0.00	0.01	0.01	0.01	0.00	0.01	0.01	0.00
Cr	0.01	0.02	0.01	0.01	0.01	0.02	0.02	0.01
Se	0.17	0.17	0.15	0.17	0.16	0.14	0.14	0.15
Ag	0.00	0.01	0.00	0.00	0.00	0.01	0.00	0.00
Bi	0.13	0.14	0.13	0.13	0.13	0.12	0.13	0.13
As	0.27	0.36	0.26	0.25	0.26	0.24	0.26	0.25
Sb	0.03	0.01	0.00	0.02	0.01	0.00	0.01	0.01
TOTAL	99.58	97.86	99.59	99.57	99.44	98.68	98.75	99.21
mol%	pn	pn	pn	pn	pn	pn	pn	pn
Ni	0.29	0.29	0.29	0.28	0.29	0.27	0.27	0.27
Fe	0.21	0.20	0.21	0.22	0.21	0.23	0.23	0.23
Co	0.02	0.02	0.02	0.02	0.02	0.02	0.02	0.02
S	0.48	0.48	0.48	0.48	0.48	0.48	0.48	0.48

Analysis wt%	CO13-55 area11_s1	CO13-55 area11_s1	CO13-55 area12_s1	CO13-55 area12_s1	CO13-55 area12_s1	CO13-55 area12_s1	CO13-55 area13_s1	CO13-55 area13_s1
Si	0.05	0.06	0.05	0.04	0.04	0.03	0.03	0.45
Mg	0.05	0.05	0.06	0.05	0.05	0.05	0.04	0.08
Ni	34.68	34.31	37.34	39.14	37.29	38.19	37.98	35.76
Fe	27.47	27.80	25.35	24.58	26.08	25.29	24.87	26.18
Co	2.04	1.97	2.38	2.44	2.04	2.35	2.45	2.19
S	33.39	33.33	33.33	33.27	33.51	33.44	33.49	32.18
Pb	0.01	0.00	0.04	0.02	0.06	0.02	0.04	0.01
Zn	0.01	0.01	0.00	0.00	0.00	0.00	0.00	0.00
Cu	0.01	0.01	0.01	0.01	0.01	0.01	0.01	0.01
Mn	0.01	0.01	0.01	0.00	0.01	0.00	0.01	0.01
Cr	0.03	0.02	0.01	0.00	0.01	0.00	0.00	0.02
Se	0.16	0.14	0.15	0.18	0.16	0.17	0.16	0.17
Ag	0.00	0.00	0.00	0.00	0.00	0.00	0.01	0.00
Bi	0.12	0.12	0.13	0.12	0.13	0.14	0.12	0.13
As	0.26	0.26	0.24	0.29	0.25	0.26	0.27	0.30
Sb	0.01	0.04	0.05	0.02	0.03	0.02	0.04	0.03
TOTAL	98.29	98.14	99.15	100.18	99.66	99.98	99.52	97.52
mol%	pn	pn	pn	pn	pn	pn	pn	pn
Ni	0.27	0.27	0.29	0.30	0.29	0.30	0.30	0.28
Fe	0.23	0.23	0.21	0.20	0.21	0.21	0.20	0.22
Co	0.02	0.02	0.02	0.02	0.02	0.02	0.02	0.02
S	0.48	0.48	0.48	0.47	0.48	0.47	0.48	0.47

Analysis wt%	CO13-55 area13_s1	CO13-55 area13_s	CO13-55 area13_s	CO13-55 area13_s	CO13-55 area13_s	CO13-55 area13_s	AV	St DEV
Si	0.05	0.03	0.01	0.09	0.03	0.17	0.06	0.08
Mg	0.05	0.05	0.02	0.07	0.05	0.14	0.07	0.04
Ni	37.31	37.75	37.46	35.99	36.09	36.92	36.71	1.34
Fe	25.50	25.05	25.04	26.40	26.22	24.48	25.90	1.33
Co	2.38	2.39	2.38	1.96	2.16	2.50	2.25	0.20
S	33.42	33.23	32.85	33.27	33.26	32.98	33.29	0.28
Pb	0.03	0.03	0.00	0.02	0.01	0.00	0.02	0.02
Zn	0.00	0.00	0.00	0.01	0.00	0.00	0.00	0.00
Cu	0.01	0.01	0.01	0.01	0.01	0.00	0.01	0.00
Mn	0.01	0.01	0.01	0.01	0.01	0.01	0.01	0.00
Cr	0.01	0.00	0.00	0.01	0.01	0.01	0.01	0.01
Se	0.17	0.15	0.12	0.14	0.14	0.09	0.15	0.02
Ag	0.01	0.00	0.02	0.00	0.00	0.00	0.00	0.00
Bi	0.13	0.14	0.16	0.13	0.14	0.13	0.13	0.01
As	0.27	0.26	0.19	0.25	0.24	0.19	0.26	0.03
Sb	0.02	0.02	0.03	0.02	0.01	0.02	0.02	0.01
TOTAL	99.37	99.12	98.31	98.39	98.37	97.63	98.90	0.70
mol%	pn	pn	pn	pn	pn	pn		
Ni	0.29	0.30	0.30	0.28	0.28	0.29	0.29	1.01
Fe	0.21	0.21	0.21	0.22	0.22	0.20	0.21	1.09
Co	0.02	0.02	0.02	0.02	0.02	0.02	1.76	0.16
S	0.48	0.48	0.47	0.48	0.48	0.48	0.48	0.25

Analysis wt%	CO13-31 area2_s1	CO13-31 area3_s 1	CO13-31 area3_s2	CO13-31 area4_s1	CO13-31 area4_s2	CO13-31 area5_s1	CO13-31 area5_s2	CO13-31 area5_s1_2
Si	0.04	0.03	0.03	0.03	0.03	0.02	0.02	0.02
Mg	0.09	0.09	0.08	0.09	0.08	0.07	0.09	0.08
Ni	73.43	73.17	72.97	73.58	73.13	74.05	73.28	73.78
Fe	0.67	0.20	0.41	0.16	0.25	0.02	0.12	0.04
Co	0.01	0.01	0.01	0.01	0.00	0.01	0.02	0.01
S	27.00	27.05	27.02	26.96	27.15	27.01	26.92	27.05
Pb	0.09	0.06	0.08	0.08	0.06	0.07	0.05	0.09
Zn	0.00	0.00	0.00	0.00	0.00	0.00	0.00	0.00
Cu	0.06	0.05	0.06	0.06	0.06	0.05	0.06	0.06
Mn	0.01	0.01	0.01	0.00	0.00	0.00	0.01	0.01
Cr	0.02	0.02	0.02	0.00	0.01	0.00	0.02	0.01
Se	0.31	0.31	0.28	0.33	0.30	0.28	0.31	0.29
Ag	0.00	0.01	0.01	0.00	0.01	0.01	0.00	0.00
Bi	0.10	0.11	0.13	0.11	0.13	0.11	0.11	0.13
As	0.34	0.33	0.31	0.34	0.35	0.33	0.33	0.33
Sb	0.03	0.02	0.03	0.02	0.01	0.03	0.03	0.04
TOTAL	102.22	101.47	101.45	101.77	101.57	102.07	101.37	101.93
mol%	hz	hz	hz	hz	hz	hz	hz	hz
Ni	0.59	0.59	0.59	0.59	0.59	0.60	0.59	0.59
Fe	0.01	0.00	0.00	0.00	0.00	0.00	0.00	0.00
Co	0.00	0.00	0.00	0.00	0.00	0.00	0.00	0.00
S	0.40	0.40	0.40	0.40	0.40	0.40	0.40	0.40

Analysis wt%	CO13-31 area5_s1_ 3	CO13-31 area6_s 1	CO13-31 area7_s1	CO13-31 area7_s1	CO13-31 area7_s1	CO13-31 area7_s1	CO13-31 area7_s1	CO13-31 area7_s1
Si	0.03	0.03	0.03	0.03	0.03	0.03	0.03	0.19
Mg	0.07	0.08	0.07	0.07	0.08	0.09	0.08	0.26
Ni	73.69	73.29	73.11	73.32	72.79	72.63	72.95	71.49
Fe	0.02	0.14	0.33	0.32	0.47	0.30	0.26	0.42
Co	0.01	0.00	0.00	0.01	0.01	0.01	0.01	0.01
S	27.28	26.99	27.04	27.10	27.03	27.03	26.99	26.57
Pb	0.08	0.08	0.06	0.08	0.07	0.08	0.10	0.06
Zn	0.00	0.00	0.00	0.00	0.00	0.00	0.00	0.00
Cu	0.06	0.05	0.06	0.06	0.06	0.06	0.06	0.06
Mn	0.00	0.00	0.01	0.00	0.01	0.01	0.00	0.01
Cr	0.00	0.02	0.01	0.01	0.03	0.01	0.01	0.03
Se	0.28	0.28	0.30	0.31	0.29	0.31	0.28	0.28
Ag	0.01	0.01	0.01	0.01	0.01	0.00	0.00	0.00
Bi	0.10	0.11	0.11	0.12	0.11	0.12	0.12	0.12
As	0.33	0.30	0.34	0.31	0.33	0.33	0.33	0.31
Sb	0.02	0.01	0.02	0.02	0.02	0.03	0.02	0.01
TOTAL	101.98	101.40	101.51	101.76	101.31	101.05	101.24	99.83
mol%	hz	hz	hz	hz	hz	hz	hz	hz
Ni	0.59	0.59	0.59	0.59	0.59	0.59	0.59	0.59
Fe	0.00	0.00	0.00	0.00	0.00	0.00	0.00	0.00
Co	0.00	0.00	0.00	0.00	0.00	0.00	0.00	0.00
S	0.40	0.40	0.40	0.40	0.40	0.40	0.40	0.40

Analysis wt%	CO13-31 area8_s1	CO13-31 area8_s1	CO13-31 area8_s1	CO13-31 area8_s1	CO13-31 area8_s1	CO13-31 area8_s1	CO13-31 area8_s1	CO13-31 area9_s1
Si	0.04	0.03	0.03	0.04	0.06	0.05	0.04	0.03
Mg	0.09	0.06	0.06	0.07	0.12	0.08	0.09	0.09
Ni	73.51	66.66	67.23	74.15	72.82	73.00	73.18	72.93
Fe	0.14	0.11	0.11	0.05	0.08	0.18	0.19	0.16
Co	0.04	0.02	0.02	0.03	0.00	0.04	0.01	0.01
S	27.00	33.11	33.19	27.01	26.89	27.00	27.00	26.98
Pb	0.07	0.11	0.12	0.06	0.13	0.08	0.09	0.07
Zn	0.00	0.00	0.00	0.00	0.00	0.00	0.00	0.00
Cu	0.06	0.05	0.06	0.06	0.05	0.06	0.06	0.06
Mn	0.00	0.01	0.00	0.00	0.00	0.00	0.01	0.01
Cr	0.01	0.01	0.01	0.01	0.01	0.02	0.02	0.00
Se	0.32	0.24	0.23	0.30	0.37	0.31	0.31	0.32
Ag	0.01	0.00	0.01	0.00	0.00	0.00	0.02	0.01
Bi	0.10	0.14	0.12	0.14	0.11	0.13	0.12	0.10
As	0.31	0.27	0.27	0.34	0.38	0.36	0.34	0.31
Sb	0.02	0.04	0.01	0.03	0.01	0.03	0.02	0.03
TOTAL	101.74	100.86	101.48	102.29	101.04	101.34	101.51	101.11
Total	2.11	2.18	2.19	2.12	2.10	2.10	2.11	2.10
mol%	hz	ml	ml	hz	hz	hz	hz	hz
Ni	0.59	0.52	0.52	0.60	0.59	0.59	0.59	0.59
Fe	0.00	0.00	0.00	0.00	0.00	0.00	0.00	0.00
Co	0.00	0.00	0.00	0.00	0.00	0.00	0.00	0.00
S	0.40	0.47	0.47	0.40	0.40	0.40	0.40	0.40

Analysis wt%	CO13-31 area9_s1	CO13-31 area9_s1	AV	ST DEV	CO13-33 area6_s1	CO13-33 area6_s2	CO13-33 area5_s1_1	CO13-33 area5_s1_2
Si	0.03	0.05	0.04	0.03	0.03	0.03	0.02	0.02
Mg	0.09	0.10	0.09	0.04	0.05	0.05	0.04	0.04
Ni	73.06	72.59	72.68	1.77	37.63	37.42	37.60	37.25
Fe	0.16	0.21	0.21	0.15	25.43	25.87	25.94	25.87
Co	0.00	0.00	0.01	0.01	2.43	2.43	2.45	2.40
S	27.08	27.09	27.48	1.67	33.38	33.32	33.30	33.32
Pb	0.08	0.08	0.08	0.02	0.05	0.00	0.00	0.04
Zn	0.00	0.00	0.00	0.00	0.00	0.00	0.00	0.01
Cu	0.06	0.06	0.06	0.00	0.01	0.01	0.02	0.01
Mn	0.01	0.01	0.01	0.00	0.01	0.01	0.00	0.00
Cr	0.00	0.00	0.01	0.01	0.02	0.01	0.01	0.02
Se	0.32	0.32	0.30	0.03	0.19	0.14	0.14	0.14
Ag	0.01	0.00	0.01	0.00	0.00	0.00	0.00	0.00
Bi	0.12	0.12	0.12	0.01	0.11	0.13	0.14	0.12
As	0.31	0.35	0.33	0.02	0.24	0.23	0.24	0.23
Sb	0.02	0.04	0.02	0.01	0.03	0.03	0.01	0.00
TOTAL	101.35	101.03	101.45	0.50	99.61	99.67	99.92	99.48
mol%	hz	hz			pn	pn	pn	pn
Ni	0.59	0.59	59.15	0.00	0.29	0.29	0.29	0.29
Fe	0.00	0.00	0.19	0.00	0.21	0.21	0.21	0.21
Co	0.00	0.00	0.01	0.00	0.02	0.02	0.02	0.02
S	0.40	0.40	39.97	0.00	0.48	0.47	0.47	0.48

Analysis wt%	CO13-33 area4_s1	CO13-33 area3_s1	CO13-33 area3_s2	CO13-33 area3_s3	CO13-33 area2_s1_1	CO13-33 area2_s1_2	CO13-33 area2_s1_3	CO13-33 area1_s2
Si		0.04	0.03	0.04	0.01	0.01	0.02	0.03
Mg	0.17	0.05	0.04	0.04	0.02	0.03	0.03	0.05
Ni	37.23	36.00	37.21	36.90	37.44	37.70	37.07	37.38
Fe	25.60	27.24	26.24	26.59	25.85	25.77	26.19	25.72
Co	2.37	2.23	2.33	2.29	2.40	2.48	2.27	2.51
S	33.28	32.19	33.55	33.16	33.30	33.36	33.42	33.24
Pb	0.02	0.00	0.01	0.00	0.00	0.02	0.02	0.01
Zn	0.00	0.01	0.01	0.02	0.01	0.00	0.00	0.00
Cu	0.01	0.00	0.01	0.01	0.02	0.01	0.01	0.01
Mn	0.01	0.06	0.03	0.08	0.01	0.00	0.01	0.01
Cr	0.02	0.45	0.28	0.72	0.00	0.00	0.02	0.02
Se	0.14	0.14	0.14	0.17	0.10	0.15	0.14	0.16
Ag	0.00	0.01	0.00	0.00	0.00	0.00	0.00	0.00
Bi	0.13	0.12	0.14	0.13	0.12	0.14	0.13	0.13
As	0.23	0.22	0.23	0.26	0.22	0.23	0.25	0.24
Sb	0.01	0.03	0.01	0.00	0.00	0.01	0.02	0.01
TOTAL	99.35	98.78	100.26	100.41	99.49	99.92	99.58	99.51
mol%	pn	pn	pn	pn	pn	pn	pn	pn
Ni	0.29	0.28	0.29	0.29	0.29	0.29	0.29	0.29
Fe	0.21	0.23	0.21	0.22	0.21	0.21	0.21	0.21
Co	0.02	0.02	0.02	0.02	0.02	0.02	0.02	0.02
S	0.48	0.46	0.47	0.47	0.48	0.47	0.48	0.47

Analysis wt%	CO13-33 area7_s1	CO13-33 area7_s1	CO13-33 area7_s1	CO13-33 area7_s1	CO13-33 area8_s1	CO13-33 area8_s1	CO13-33 area8_s1	CO13-33 area9_s1
Si	0.05	0.03	0.03	0.07	0.00		0.04	0.03
Mg	0.06	0.05	0.06	0.10	0.03	0.31	0.05	0.05
Ni	37.53	37.50	37.46	37.12	37.13	37.04	37.31	36.68
Fe	25.11	25.17	25.45	25.42	25.97	25.91	25.96	25.52
Co	2.27	2.31	2.32	2.31	2.40	2.36	2.37	2.26
S	33.44	33.30	33.58	33.31	33.01	33.11	34.39	33.28
Pb	0.03	0.02	0.02	0.03	0.02	0.02	0.10	0.00
Zn	0.00	0.01	0.00	0.00	0.00	0.00	0.00	0.01
Cu	0.01	0.01	0.02	0.01	0.01	0.02	0.01	0.01
Mn	0.01	0.01	0.01	0.01	0.00	0.01	0.00	0.03
Cr	0.01	0.02	0.02	0.03	0.01	0.02	0.01	0.24
Se	0.14	0.12	0.14	0.17	0.05	0.17	0.16	0.14
Ag	0.00	0.01	0.00	0.00	0.00	0.00	0.00	0.01
Bi	0.13	0.12	0.13	0.13	0.14	0.13	0.12	0.14
As	0.25	0.22	0.23	0.24	0.17	0.22	0.24	0.21
Sb	0.02	0.02	0.01	0.03	0.00	0.02	0.00	0.01
TOTAL	99.05	98.90	99.47	98.98	98.94	99.52	100.76	98.61
mol%	pn	pn	pn	pn	pn	pn	pn	pn
Ni	0.29	0.29	0.29	0.29	0.29	0.29	0.29	0.29
Fe	0.21	0.21	0.21	0.21	0.21	0.21	0.21	0.21
Co	0.02	0.02	0.02	0.02	0.02	0.02	0.02	0.02
S	0.48	0.48	0.48	0.48	0.47	0.47	0.48	0.48

Analysis wt%	CO13-33 area9_s1	CO13-33 area9_s1	CO13-33 area9_s1	CO13-33 area10_s1	CO13-33 area10_s1	CO13-33 area10_s1	CO13-33 area11_s1	CO13-33 area11_s1
Si	0.07	0.03	0.03	0.03	0.01	0.02		0.04
Mg	0.13	0.04	0.05	0.05	0.04	0.04	0.27	0.06
Ni	36.98	36.77	36.54	37.23	37.39	37.39	36.35	37.20
Fe	25.71	25.66	25.97	25.01	25.30	25.20	24.84	25.82
Co	2.36	2.26	2.20	2.41	2.38	2.37	2.37	2.33
S	33.30	33.09	33.43	33.25	33.52	33.44	32.09	33.13
Pb	0.02	0.03	0.04	0.00	0.03	0.03	0.00	0.00
Zn	0.01	0.01	0.00	0.01	0.00	0.00	0.00	0.01
Cu	0.02	0.01	0.67	0.02	0.01	0.02	0.01	0.01
Mn	0.02	0.03	0.02	0.01	0.00	0.00	0.01	0.01
Cr	0.25	0.32	0.17	0.01	0.01	0.01	0.02	0.01
Se	0.15	0.13	0.15	0.15	0.14	0.14	0.14	0.16
Ag	0.01	0.00	0.01	0.01	0.00	0.00	0.00	0.00
Bi	0.13	0.13	0.13	0.13	0.12	0.13	0.12	0.11
As	0.26	0.23	0.24	0.24	0.22	0.23	0.24	0.25
Sb	0.02	0.01	0.01	0.04	0.01	0.03	0.02	0.03
TOTAL	99.43	98.74	99.66	98.60	99.21	99.06	96.83	99.16
mol%	pn	pn	pn	pn	pn	pn	pn	pn
Ni	0.29	0.29	0.29	0.29	0.29	0.29	0.29	0.29
Fe	0.21	0.21	0.21	0.21	0.21	0.21	0.21	0.21
Co	0.02	0.02	0.02	0.02	0.02	0.02	0.02	0.02
S	0.47	0.48	0.48	0.48	0.48	0.48	0.47	0.47

Analysis wt%	CO13-33 area12_s1	CO13-33 area12_s1	CO13-33 area12_s1	CO13-33 area12_s1	AV	ST DEV
Si		0.08	0.07	0.06	0.03	0.02
Mg	0.28	0.16	0.09	0.05	0.08	0.08
Ni	37.04	36.83	36.97	37.12	37.14	0.38
Fe	25.76	25.54	25.73	25.48	25.71	0.47
Co	2.35	2.35	2.35	2.34	2.35	0.07
S	33.19	33.07	33.18	33.22	33.25	0.38
Pb	0.00	0.01	0.02	0.00	0.02	0.02
Zn	0.00	0.00	0.00	0.00	0.00	0.00
Cu	0.01	0.01	0.02	0.01	0.03	0.12
Mn	0.01	0.03	0.02	0.01	0.01	0.02
Cr	0.14	0.17	0.15	0.15	0.10	0.16
Se	0.13	0.12	0.13	0.12	0.14	0.02
Ag	0.01	0.00	0.01	0.00	0.00	0.00
Bi	0.13	0.15	0.13	0.13	0.13	0.01
As	0.20	0.22	0.21	0.21	0.23	0.02
Sb	0.01	0.02	0.00	0.03	0.02	0.01
TOTAL	99.37	98.76	99.08	98.92	99.28	0.68
mol%	pn	pn	pn	pn		
Ni	0.29	0.29	0.29	0.29	0.29	0.00
Fe	0.21	0.21	0.21	0.21	0.21	0.00
Co	0.02	0.02	0.02	0.02	0.02	0.00
S	0.47	0.47	0.47	0.48	0.48	0.00

Capu Corvoli hybrid rocks

wt%	Co14-03 area2-1	Co14-03 area2-2	Co14-03 area2-3	Co14-03 area2-4	Co14-03 area2-5	Co14-03 area2-2-1	Co14-03 area2-2-2	Co14-03 area2-2-3	Co14-03 area2-3-1	Co14-03 area2-3-2	Co14-03 area2-3-3	Co14-03 area2-3-4	Co14-03 area2-3-5	CO14-03 area-2-4-1	CO14-03 area-2-4-2	CO14-03 area-2-4-3
Si	0.00	0.00	0.00	0.00	0.00	0.00	0.00	0.00	0.00	0.00	0.00	0.01	0.01	0.00	0.00	0.00
Mg	0.00	0.00	0.00	0.00	0.00	0.00	0.00	0.00	0.00	0.00	0.00	0.00	0.01	0.00	0.00	0.00
Ni	0.00	0.00	0.00	0.00	0.00	0.00	0.00	0.00	0.00	0.00	0.00	0.00	0.00	0.00	0.00	0.01
Fe	31.39	45.76	45.78	45.86	46.00	45.79	46.00	46.10	46.06	45.18	46.17	45.79	45.96	44.97	45.82	46.30
Co	0.01	0.99	0.83	0.73	0.61	0.96	0.60	0.60	0.56	1.35	0.42	0.95	0.72	1.60	0.85	0.54
S	34.85	54.12	54.03	53.94	53.88	53.87	53.80	53.72	54.13	53.92	53.56	53.65	53.45	53.93	53.78	53.41
Pb	0.00	0.01	0.00	0.00	0.00	0.02	0.02	0.00	0.00	0.01	0.00	0.00	0.00	0.00	0.00	0.02
Zn	0.05	0.00	0.00	0.00	0.00	0.00	0.00	0.00	0.00	0.00	0.00	0.00	0.00	0.00	0.00	0.00
Cu	33.21	0.00	0.00	0.00	0.00	0.00	0.00	0.00	0.00	0.00	0.00	0.00	0.00	0.00	0.00	0.00
Mn	0.00	0.00	0.00	0.00	0.00	0.00	0.00	0.00	0.00	0.00	0.00	0.00	0.00	0.00	0.00	0.00
Cr	0.00	0.00	0.00	0.01	0.00	0.00	0.00	0.01	0.00	0.00	0.00	0.01	0.01	0.00	0.00	0.01
As	0.00	0.00	0.00	0.00	0.00	0.00	0.00	0.00	0.00	0.00	0.00	0.00	0.01	0.00	0.00	0.00
Sb	0.03	0.01	0.03	0.03	0.02	0.01	0.02	0.03	0.01	0.00	0.03	0.02	0.04	0.00	0.03	0.01
Total	99.55	100.90	100.68	100.56	100.52	100.64	100.44	100.46	100.76	100.47	100.19	100.42	100.20	100.50	100.47	100.29
mol%	Cpy (trace)	py	py	py	py	py	py	py	py	py	py	py	py	py	py	py
Fe	0.26	0.33	0.33	0.33	0.33	0.33	0.33	0.33	0.33	0.32	0.33	0.33	0.33	0.32	0.33	0.33
S	0.50	0.67	0.67	0.67	0.67	0.67	0.67	0.67	0.67	0.68	0.67	0.67	0.67	0.68	0.67	0.67
Cu	0.24	0.00	0.00	0.00	0.00	0.00	0.00	0.00	0.00	0.00	0.00	0.00	0.00	0.00	0.00	0.00

wt%	CO14-03 area-2-4-4	CO14-03 area-2-4-5	CO14-03 area-2-4-6	CO14-03 area7_1	CO14-03 area7_1	CO14-03 area7_1_1	CO14-03 area7_1_2	CO14-03 area7_1_3	CO14-03 area7_1_4	CO14-03 area7_1_5	Co14-03 area3-2	Co14-03 area3-3	Co14-03 area3-6	Co14-03 area3-7	Co14-03 area3-8	Co14-03 area3-9
Si	0.00	0.00	0.01	0.00	0.00	0.00	0.00	0.00	0.00	0.00	0.00	0.00	0.00	0.00	0.00	0.00
Mg	0.00	0.00	0.00	0.00	0.00	0.00	0.00	0.00	0.00	0.00	0.00	0.00	0.00	0.00	0.00	0.00
Ni	0.00	0.00	0.00	0.00	0.00	0.00	0.00	0.00	0.00	0.00	0.01	0.00	0.01	0.00	0.00	0.00
Fe	45.31	46.20	45.03	45.50	45.49	45.46	46.43	45.33	45.63	44.97	45.20	45.87	45.22	45.45	45.43	44.51
Co	1.45	0.49	1.68	1.03	1.00	1.07	0.03	1.11	0.99	1.72	1.52	0.95	1.11	1.07	1.09	1.95
S	54.17	53.98	53.64	54.10	53.71	53.74	53.60	53.80	53.75	53.67	53.70	53.90	53.52	53.84	53.57	53.42
Pb	0.02	0.01	0.02	0.00	0.02	0.02	0.01	0.00	0.01	0.01	0.00	0.00	0.02	0.01	0.01	0.01
Zn	0.00	0.00	0.00	0.00	0.00	0.00	0.00	0.00	0.00	0.00	0.00	0.00	0.00	0.00	0.00	0.00
Cu	0.00	0.00	0.00	0.00	0.00	0.00	0.18	0.00	0.00	0.00	0.00	0.00	0.00	0.00	0.00	0.00
Mn	0.00	0.00	0.00	0.00	0.00	0.00	0.00	0.00	0.00	0.00	0.00	0.00	0.00	0.00	0.00	0.00
Cr	0.01	0.01	0.01	0.00	0.00	0.00	0.00	0.00	0.00	0.00	0.01	0.00	0.01	0.02	0.01	0.00
As	0.00	0.00	0.00	0.00	0.00	0.00	0.00	0.00	0.00	0.00	0.00	0.00	0.00	0.00	0.00	0.00
Sb	0.02	0.01	0.02	0.01	0.01	0.02	0.00	0.01	0.01	0.00	0.02	0.02	0.03	0.02	0.02	0.01
Total	100.99	100.70	100.42	100.64	100.24	100.31	100.27	100.25	100.41	100.39	100.46	100.73	99.92	100.40	100.14	99.91
mol%	py	py	py	py	py	py	py	py	py	py	py	py	py	py	py	py
Fe	0.32	0.33	0.33	0.33	0.33	0.33	0.33	0.33	0.33	0.32	0.33	0.33	0.33	0.33	0.33	0.32
S	0.68	0.67	0.67	0.67	0.67	0.67	0.67	0.67	0.67	0.68	0.67	0.67	0.67	0.67	0.67	0.68
Cu	0.00	0.00	0.00	0.00	0.00	0.00	0.00	0.00	0.00	0.00	0.00	0.00	0.00	0.00	0.00	0.00

wt%	Co14-03 area3-10	Co14-03 area4-1	Co14-03 area4-2	Co14-03 area4-3	Co14-03 area4-4	Co14-03 area4-5	Co14-03 area4-6	Av	St Dev
Si	0.00	0.00	0.00	0.00	0.00	0.00	0.00	0.00	0.00
Mg	0.00	0.00	0.00	0.00	0.00	0.00	0.00	0.00	0.00
Ni	0.01	0.01	0.00	0.00	0.00	0.00	0.00	0.00	0.00
Fe	44.63	45.54	46.04	46.30	45.18	45.54	45.87	45.26	0.46
Co	1.88	0.95	0.58	0.36	1.48	1.00	0.55	0.96	0.44
S	53.64	53.65	53.80	53.83	53.61	53.63	53.56	53.28	0.20
Pb	0.01	0.01	0.02	0.01	0.02	0.00	0.00	0.01	0.01
Zn	0.00	0.00	0.00	0.00	0.00	0.00	0.00	0.00	0.00
Cu	0.00	0.00	0.00	0.00	0.00	0.00	0.00	0.86	0.03
Mn	0.00	0.00	0.00	0.00	0.00	0.00	0.00	0.00	0.00
Cr	0.01	0.01	0.01	0.01	0.00	0.01	0.00	0.00	0.00
As	0.00	0.00	0.00	0.00	0.01	0.00	0.00	0.00	0.00
Sb	0.00	0.01	0.02	0.01	0.03	0.02	0.01	0.02	0.01
Total	100.18	100.18	100.46	100.53	100.33	100.20	99.99	100.39	0.25
mol%	py	py	py	py	py	py	py	py	py
Fe	0.32	0.33	0.33	0.33	0.33	0.33	0.33	0.33	0.00
S	0.68	0.67	0.67	0.67	0.67	0.67	0.67	0.67	0.00
Cu	0.00	0.00	0.00	0.00	0.00	0.00	0.00	0.01	0.00

wt%	CO13-04 area1_1	CO13-04 area1_2	Co13-04 area 1_3	CO13-04 area 1_4	CO13-04 area1_5	CO13-04 area1_6	CO13-04 area1_7_1	CO13-04 area1_7_2	CO13-04 area1_7_3	CO13-04 area1_7_4	CO13-04 area1_7_5	CO13-04 area1_7_6
Si	0.00	0.00	0.00	0.00	0.00	0.00	0.02	0.02	0.01	0.01	0.02	0.00
Mg	0.00	0.00	0.00	0.00	0.00	0.00	0.01	0.01	0.01	0.00	0.01	0.00
Ni	0.18	0.07	0.12	0.13	0.11	0.04	0.32	0.02	0.32	0.32	0.32	0.31
Fe	46.98	46.86	46.85	46.89	46.93	46.84	60.23	46.33	46.79	46.72	46.92	46.71
Co	0.02	0.00	0.02	0.02	0.00	0.00	0.03	1.17	0.00	0.00	0.00	0.03
S	53.88	54.11	54.05	54.13	54.34	54.43	39.04	53.76	53.92	53.97	53.14	53.96
Pb	0.01	0.00	0.00	0.00	0.00	0.01	0.00	0.01	0.01	0.00	0.00	0.00
Zn	0.00	0.00	0.00	0.00	0.00	0.00	0.00	0.00	0.00	0.00	0.00	0.00
Cu	0.00	0.00	0.00	0.00	0.00	0.00	0.00	0.00	0.00	0.00	0.00	0.00
Mn	0.00	0.00	0.00	0.00	0.00	0.00	0.00	0.00	0.00	0.00	0.00	0.00
Cr	0.00	0.00	0.00	0.00	0.01	0.00	0.00	0.00	0.01	0.00	0.00	0.00
As	0.00	0.00	0.00	0.00	0.00	0.00	0.02	0.20	0.00	0.00	0.00	0.00
Sb	0.04	0.03	0.01	0.01	0.02	0.02	0.00	0.03	0.02	0.02	0.01	0.01
Total	101.10	101.09	101.04	101.17	101.40	101.34	99.68	101.55	101.08	101.05	100.42	101.03
mol%	py1	py1	py1	py1	py1	py1	po	py1	py1	py1	py1	py1
Fe	0.33	0.33	0.33	0.33	0.33	0.33	0.47	0.33	0.33	0.33	0.34	0.33
S	0.67	0.67	0.67	0.67	0.67	0.67	0.53	0.66	0.67	0.67	0.66	0.67

wt%	CO13-04 area1_7_7	CO13-04 area2_1_1	CO13-04 area2_1_2	CO13-04 area2_1_3	CO13-04 area2_1_4	CO14-04 area 2_2_1	CO14-04 area 2_2_2	CO14-04 area 2_2_3	CO14-04 area 2_2_4	CO14-04 area 2_2_5	CO14-04 area 2_2_6	CO14-04 area 2_3_1	CO14-04 area 2_3_2
Si	0.00	0.01	0.01	0.00	0.01	0.00	0.00	0.00	0.00	0.00	0.00	0.01	0.00
Mg	0.00	0.00	0.00	0.00	0.00	0.00	0.00	0.00	0.00	0.00	0.00	0.01	0.01
Ni	0.15	0.53	0.18	0.07	0.09	0.00	0.04	0.02	0.00	0.00	0.00	0.60	0.38
Fe	46.88	46.74	47.01	46.96	47.03	47.07	47.33	47.07	47.21	47.20	47.09	46.39	46.61
Co	0.00	0.02	0.00	0.00	0.00	0.00	0.01	0.00	0.00	0.00	0.00	0.08	0.00
S	53.94	53.96	54.04	54.06	53.87	54.23	53.60	54.02	53.62	54.10	54.20	53.54	53.68
Pb	0.01	0.00	0.00	0.00	0.00	0.00	0.00	0.01	0.00	0.01	0.01	0.01	0.00
Zn	0.01	0.00	0.00	0.00	0.01	0.00	0.00	0.00	0.00	0.00	0.00	0.00	0.00
Cu	0.00	0.00	0.00	0.00	0.00	0.00	0.00	0.00	0.00	0.00	0.00	0.00	0.00
Mn	0.00	0.00	0.00	0.00	0.00	0.00	0.00	0.00	0.00	0.00	0.00	0.00	0.00
Cr	0.00	0.00	0.00	0.00	0.00	0.00	0.03	0.00	0.00	0.00	0.01	0.01	0.00
As	0.00	0.00	0.00	0.00	0.00	0.00	0.00	0.00	0.00	0.00	0.00	0.00	0.00
Sb	0.02	0.01	0.02	0.02	0.02	0.03	0.02	0.02	0.00	0.03	0.01	0.00	0.02
Total	101.01	101.27	101.26	101.12	101.02	101.34	101.02	101.14	100.83	101.34	101.32	100.65	100.70
mol%	py1	py1	py1	py1	py1	py2	py2	py2	py2	py2	py2	py2	py2
Fe	0.33	0.33	0.33	0.33	0.33	0.33	0.34	0.33	0.34	0.33	0.33	0.33	0.33
S	0.67	0.67	0.67	0.67	0.67	0.67	0.66	0.67	0.66	0.67	0.67	0.66	0.67

wt%	CO14-04 area 2_3_3	CO14-04 area 2_3_4	CO14-04 area 2_3_5	CO14-04 area 2_3_6	CO14-04 area 2_3_7	CO14-04 area 2_3_8	CO14-04 area 2_4_1	CO14-04 area 2_4_2	CO14-04 area 2_4_3	CO14-04 area 2_4_4	CO14-04 area 2_4_5	CO14-04 area 2_4_6	CO14-04 area 2_4_7	CO14-04 area 2_4_8
Si	0.00	0.00	0.01	0.00	0.00	0.00	0.00	0.00	0.00	0.00	0.00	0.00	0.00	0.01
Mg	0.00	0.00	0.00	0.00	0.00	0.01	0.00	0.00	0.00	0.00	0.00	0.00	0.00	0.00
Ni	0.41	0.34	0.25	0.23	0.10	0.17	0.04	0.19	0.12	0.23	0.36	0.07	0.02	0.12
Fe	46.41	46.64	47.06	46.72	46.83	46.89	47.19	47.13	46.99	46.78	46.59	46.98	46.95	47.14
Co	0.02	0.00	0.00	0.00	0.01	0.00	0.00	0.00	0.02	0.02	0.11	0.01	0.00	0.00
S	53.76	53.76	53.34	53.73	53.82	53.75	54.24	53.80	54.01	54.08	54.18	54.08	54.22	53.82
Pb	0.00	0.00	0.00	0.00	0.00	0.00	0.00	0.00	0.00	0.01	0.01	0.00	0.00	0.00
Zn	0.01	0.00	0.00	0.00	0.00	0.00	0.00	0.01	0.00	0.00	0.00	0.00	0.00	0.00
Cu	0.00	0.00	0.00	0.00	0.00	0.00	0.00	0.00	0.00	0.00	0.00	0.00	0.00	0.00
Mn	0.00	0.00	0.00	0.00	0.00	0.00	0.00	0.00	0.00	0.00	0.00	0.00	0.00	0.00
Cr	0.01	0.01	0.00	0.00	0.00	0.01	0.01	0.01	0.01	0.00	0.00	0.00	0.00	0.00
As	0.00	0.00	0.01	0.00	0.00	0.00	0.00	0.00	0.00	0.00	0.00	0.00	0.00	0.00
Sb	0.03	0.01	0.00	0.00	0.02	0.00	0.01	0.01	0.01	0.03	0.00	0.02	0.00	0.02
Total	100.66	100.76	100.68	100.68	100.79	100.83	101.49	101.14	101.16	101.14	101.25	101.17	101.19	101.10
mol%	py2	py2	py2	py2	py2	py2	py2	py2	py2	py2	py2	py2	py2	py2
Fe	0.33	0.33	0.34	0.33	0.33	0.33	0.33	0.33	0.33	0.33	0.33	0.33	0.33	0.33
S	0.67	0.67	0.66	0.67	0.67	0.67	0.67	0.66	0.67	0.67	0.67	0.67	0.67	0.66

wt%	CO14-04 area 2_4_9	CO14-04 area3_1_1	CO14-04 area3_1_2	CO14-04 area3_1_3	Co14-04 area 3-2_1	Co14-04 area 3-2_2	Co14-04 area 3-2_3	CO14-04 area4_1	CO14-04 area4_2	CO14-04 area4_3	CO14-04 area4_4	CO14-04 area4_6	CO14-04 area5_1_1	CO14-04 area5_1_2
Si	0.00	0.01	0.01	0.00	0.01	0.00	0.02	0.00	0.00	0.01	0.00	0.01	0.01	0.01
Mg	0.00	0.01	0.01	0.00	0.01	0.00	0.01	0.01	0.00	0.01	0.00	0.00	0.01	0.01
Ni	0.01	0.49	0.50	0.28	0.11	0.35	0.21	0.01	0.00	0.65	0.00	0.19	0.33	0.01
Fe	47.07	46.60	46.38	46.67	47.10	46.59	46.73	46.12	45.64	46.21	46.41	46.92	60.11	46.87
Co	0.00	0.04	0.01	0.05	0.00	0.07	0.09	1.04	1.30	0.41	1.06	0.03	0.01	0.37
S	54.09	53.23	53.70	53.95	54.36	54.11	53.13	54.14	54.38	53.78	54.19	53.97	39.38	53.97
Pb	0.00	0.00	0.00	0.00	0.00	0.02	0.00	0.02	0.02	0.02	0.00	0.00	0.00	0.00
Zn	0.01	0.00	0.00	0.00	0.01	0.00	0.00	0.00	0.00	0.01	0.00	0.00	0.01	0.00
Cu	0.00	0.00	0.00	0.00	0.00	0.00	0.00	0.00	0.00	0.00	0.00	0.00	0.00	0.00
Mn	0.00	0.00	0.00	0.00	0.00	0.00	0.00	0.00	0.00	0.00	0.00	0.00	0.00	0.00
Cr	0.00	0.01	0.00	0.00	0.00	0.00	0.01	0.05	0.03	0.00	0.03	0.01	0.01	0.01
As	0.00	0.00	0.00	0.00	0.00	0.00	0.03	0.15	0.13	0.00	0.10	0.00	0.02	0.02
Sb	0.02	0.05	0.02	0.01	0.04	0.01	0.04	0.00	0.00	0.02	0.00	0.03	0.01	0.02
Total	101.19	100.43	100.63	100.98	101.64	101.13	100.28	101.53	101.49	101.09	101.79	101.15	99.90	101.28
mol%	py2	py1	py1	py1	py2	py2	py2	py2	py2	py2	py2	py2	po	py1
Fe	0.33	0.33	0.33	0.33	0.33	0.33	0.33	0.33	0.32	0.33	0.33	0.33	0.47	0.33
S	0.67	0.66	0.67	0.67	0.67	0.67	0.66	0.67	0.67	0.66	0.67	0.67	0.53	0.67

wt%	CO14-04 area5_1_3	CO14-04 area5_1_4	CO14-04 area5_1_5	CO14-04 area5_1_6	CO14-04 area5_1_7	CO14-04 area5_1_8	CO14-04 area5_1_9	CO14-04 area5_1_10	Average py1	St Dev	Average py2	St Dev
Si	0.01	0.01	0.01	0.00	0.01	0.01	0.00	0.00	0.01	0.00	0.00	0.00
Mg	0.01	0.00	0.00	0.00	0.00	0.01	0.00	0.00	0.00	0.00	0.00	0.00
Ni	0.00	0.00	0.18	0.26	0.02	0.00	0.06	0.15	0.18	0.16	0.17	0.18
Fe	46.21	46.24	46.69	46.82	46.44	45.97	47.02	47.01	47.19	2.52	46.81	0.38
Co	1.15	0.86	0.31	0.03	0.75	1.16	0.00	0.03	0.21	0.39	0.14	0.34
S	53.86	54.12	54.07	54.10	53.67	53.34	53.83	54.37	53.41	2.78	53.93	0.30
Pb	0.01	0.02	0.00	0.00	0.00	0.00	0.00	0.00	0.00	0.00	0.00	0.01
Zn	0.00	0.00	0.00	0.00	0.00	0.00	0.00	0.00	0.00	0.00	0.00	0.00
Cu	0.00	0.00	0.00	0.00	0.00	0.00	0.00	0.00	0.00	0.00	0.00	0.00
Mn	0.00	0.00	0.00	0.00	0.00	0.00	0.00	0.00	0.00	0.00	0.00	0.00
Cr	0.01	0.00	0.01	0.00	0.01	0.01	0.00	0.00	0.00	0.00	0.01	0.01
As	0.09	0.08	0.01	0.00	0.02	0.21	0.00	0.01	0.02	0.06	0.01	0.04
Sb	0.01	0.01	0.01	0.01	0.02	0.01	0.04	0.01	0.02	0.01	0.01	0.01
Total	101.35	101.35	101.29	101.23	100.93	100.71	100.95	101.58	101.05	0.39	101.08	0.34
mol%	py1	py1	py1	py1	py1	py1	py1	py1	py1		py2	
Fe	0.33	0.33	0.33	0.33	0.33	0.33	0.33	0.33	0.34	0.03	0.33	0.00
S	0.66	0.67	0.67	0.67	0.66	0.66	0.67	0.67	0.66	0.03	0.67	0.00

C7: Traverse EPMA data for spinels

Analysis	wt%	CO13-33 area3 sp2	CO13-33 area3 sp2	CO13-33 area3 sp2	CO13-33 area3 sp2	CO13-33 area3 sp2	CO13-33 area3 sp2	CO13-33 area3 sp2	CO13-33 area3 sp2	CO13-33 area3 sp2	CO13-33 area3 sp2
	Desc	Mt rim	PFR	PFR	PFR	PFR	PC	PFR	PFR	PFR	PFR
	SiO_2	0.08	0.23	0.28	1.08	1.46	1.48	3.01	0.65	0.74	2.05
	TiO_2	0.11	0.13	0.11	0.14	0.13	0.28	0.11	0.15	0.04	0.13
	Al_2O_3	0.00	0.55	0.36	0.45	0.59	1.11	0.78	0.33	0.35	0.74
	Cr_2O_3	2.60	7.97	7.72	7.39	8.58	15.14	8.24	7.69	5.34	6.92
	V_2O_3	0.03	0.04	0.02	0.04	0.02	0.06	0.05	0.03	0.03	0.04
	Fe_3O_4	96.73	88.49	90.49	89.86	86.37	76.93	84.60	90.04	92.63	86.33
	MnO	0.18	1.05	0.83	0.91	1.07	1.81	0.81	0.79	0.51	0.58
	MgO	0.21	0.53	0.38	1.14	1.22	1.74	3.56	0.86	0.90	1.91
	ZnO	0.00	0.32	0.16	0.14	0.15	0.75	0.28	0.26	0.08	0.23
	NiO	0.27	0.17	0.19	0.21	0.21	0.14	0.22	0.26	0.23	0.19
	CaO	0.01	0.00	0.01	0.00	0.00	0.01	0.00	0.02	0.00	0.02
	Na_2O	0.12	0.03	0.00	0.00	0.05	0.00	0.01	0.00	0.05	0.03
	K_2O	0.00	0.00	0.00	0.00	0.00	0.00	0.00	0.00	0.00	0.00
	TOTAL	100.33	99.51	100.55	101.37	99.85	99.46	101.67	101.06	100.89	99.17
Cations per 3 cations											
Sites for 3+	Al	0.00	0.02	0.02	0.02	0.03	0.05	0.03	0.01	0.02	0.03
	Cr	0.08	0.24	0.23	0.22	0.25	0.44	0.23	0.23	0.16	0.20
	V	0.00	0.00	0.00	0.00	0.00	0.00	0.00	0.00	0.00	0.00
	Ti	0.00	0.00	0.00	0.00	0.00	0.01	0.00	0.00	0.00	0.00
	Fe	1.80	1.61	1.62	1.58	1.50	1.29	1.43	1.60	1.66	1.50
Sites for 2+	Fe	0.97	0.93	0.95	0.90	0.89	0.84	0.78	0.92	0.93	0.87
	Ni	0.01	0.01	0.01	0.01	0.01	0.00	0.01	0.01	0.01	0.01
	Mn	0.01	0.03	0.03	0.03	0.03	0.06	0.02	0.02	0.02	0.02
	Mg	0.01	0.03	0.02	0.06	0.07	0.10	0.19	0.05	0.05	0.10
mol	Fe3+	0.63	0.61	0.61	0.61	0.60	0.58	0.62	0.61	0.62	0.61
	Fe2+	0.34	0.35	0.35	0.35	0.36	0.38	0.34	0.35	0.34	0.35
wt%	Fe_2O_3	60.48	53.88	54.93	54.92	52.08	44.57	52.52	54.96	57.25	52.54
	FeO	36.25	34.61	35.55	34.94	34.29	32.36	32.08	35.07	35.38	33.79

Analysis	wt% Desc	CO13-33 area3 sp2 PFR	CO13-33 area3 sp2 PC	max Fe	min Fe
	SiO_2	3.65	0.98	0.08	0.98
	TiO_2	0.14	0.26	0.11	0.26
	Al_2O_3	1.27	1.43	0.00	1.43
	Cr_2O_3	6.23	16.75	2.60	16.75
	V_2O_3	0.05	0.07	0.03	0.07
	Fe_3O_4	80.15	76.78	96.73	76.78
	MnO	0.50	1.83	0.18	1.83
	MgO	5.31	1.46	0.21	1.46
	ZnO	0.14	0.53	0.00	0.53
	NiO	0.19	0.20	0.27	0.20
	CaO	0.01	0.01	0.01	0.01
	Na_2O	0.02	0.00	0.12	0.00
	K_2O	0.00	0.04	0.00	0.04
	Total	97.67	100.33	100.33	100.33
Cations per 3 cations					
Sites for 3+	Al	0.05	0.06	0.00	0.06
	Cr	0.17	0.49	0.08	0.49
	V	0.00	0.00	0.00	0.00
	Ti	0.00	0.01	0.00	0.01
	Fe	1.42	1.27	1.80	1.27
Sites for 2+	Fe	0.70	0.86	0.97	0.86
	Ni	0.01	0.01	0.01	0.01
	Mn	0.02	0.06	0.01	0.06
	Mg	0.28	0.08	0.01	0.08
mol	Fe3+	0.65	0.57	0.63	0.57
	Fe2+	0.32	0.39	0.34	0.39
wt%	Fe_2O_3	51.73	43.85	60.48	43.85
	FeO	28.42	32.93	36.25	32.93

Analysis	wt%	CO13-33 area3-sp2	CO13-33 area3-sp2	CO13-33 area3-sp2	CO13-33 area3-sp2	CO13-33 area3-sp2	CO13-33 area3-sp2	CO13-33 area3-sp2	CO13-33 area3-sp2	max	min
	Desc	PC	PC	PC	PC	PC	PC	PC	PC	Fe	Fe
	SiO_2	1.85	1.08	0.62	0.81	0.58	1.45	0.97	1.11	1.08	3.04
	TiO_2	0.21	0.20	0.27	0.25	0.37	0.19	0.20	0.33	0.20	0.38
	Al_2O_3	0.19	0.12	0.19	0.18	0.13	0.21	0.15	0.24	0.12	0.62
	Cr_2O_3	10.96	10.80	17.82	19.42	17.86	11.10	13.51	17.77	10.80	20.66
	V_2O_3	0.04	0.04	0.04	0.06	0.05	0.05	0.04	0.05	0.04	0.09
	Fe_3O_4	82.58	85.89	76.30	74.04	75.38	83.07	80.20	75.78	85.89	66.59
	MnO	1.33	1.38	2.34	2.79	2.73	1.52	1.85	2.37	1.38	3.20
	MgO	2.04	1.22	1.02	1.21	0.91	2.07	1.23	1.56	1.22	4.46
	ZnO	0.38	0.35	0.57	0.80	0.66	0.32	0.44	0.55	0.35	0.62
	NiO	0.12	0.22	0.24	0.18	0.21	0.19	0.15	0.25	0.22	0.14
	CaO	0.03	0.03	0.05	0.03	0.12	0.02	0.03	0.03	0.03	0.02
	Na_2O	0.00	0.00	0.01	0.00	0.00	0.00	0.00	0.03	0.00	0.00
	K_2O	0.00	0.00	0.00	0.02	0.02	0.00	0.02	0.00	0.00	0.01
	TOTAL	99.73	101.32	99.47	99.79	99.01	100.19	98.80	100.05	101.32	99.81
Cations per 3 cations											
Sites for 3+	Al	0.01	0.01	0.01	0.01	0.01	0.01	0.01	0.01	0.01	0.03
	Cr	0.32	0.32	0.53	0.58	0.54	0.32	0.41	0.52	0.32	0.58
	V	0.00	0.00	0.00	0.00	0.00	0.00	0.00	0.00	0.00	0.00
	Ti	0.00	0.00	0.01	0.01	0.01	0.00	0.00	0.01	0.00	0.01
	Fe	1.43	1.49	1.30	1.25	1.30	1.45	1.41	1.28	1.49	1.09
Sites for 2+	Fe	0.84	0.88	0.86	0.84	0.85	0.83	0.87	0.83	0.88	0.67
	Ni	0.00	0.01	0.01	0.01	0.01	0.01	0.00	0.01	0.01	0.00
	Mn	0.04	0.04	0.08	0.09	0.09	0.05	0.06	0.07	0.04	0.10
	Mg	0.11	0.07	0.06	0.07	0.05	0.11	0.07	0.09	0.07	0.23
mol	Fe3+	0.60	0.60	0.58	0.57	0.58	0.61	0.59	0.58	0.60	0.59
	Fe2+	0.36	0.36	0.38	0.38	0.38	0.35	0.37	0.38	0.36	0.37
wt%	Fe_2O_3	49.87	51.80	44.02	42.41	43.56	50.77	47.62	43.96	51.80	39.60
	FeO	32.71	34.09	32.28	31.63	31.82	32.30	32.58	31.82	34.09	26.99

Analysis	wt%	CO13-33 area 2 sp1 PFR	CO13-33 area 2 sp1 PFR	CO13-33 area 2 sp1 PFR	CO13-33 area 2 sp1 PFR	CO13-33 area 2 sp1 PFR	CO13-33 area 2 sp1 PC	CO13-33 area 2 sp1 PC	CO13-33 area 2 sp1 PC	CO13-33 area 2 sp1 PFR	CO13-33 area 2 sp1 PC
	SiO_2	0.85	0.01	0.03	0.22	0.01	6.86	7.39	1.75	0.01	6.86
	TiO_2	0.08	0.03	0.03	0.07	0.08	0.74	0.68	0.39	0.08	0.74
	Al_2O_3	0.12	0.00	0.00	0.00	0.00	1.49	1.46	0.44	0.00	1.49
	Cr_2O_3	4.01	2.91	2.62	2.83	4.60	27.45	25.85	21.76	4.60	27.45
	V_2O_3	0.02	0.02	0.02	0.02	0.05	0.08	0.06	0.05	0.05	0.08
	Fe_3O_4	93.61	95.70	96.90	96.14	95.72	48.54	50.54	71.47	95.72	48.54
	MnO	0.42	0.25	0.08	0.30	0.12	3.58	3.16	2.76	0.12	3.58
	MgO	1.23	0.25	0.18	0.35	0.26	7.69	8.09	2.56	0.26	7.69
	ZnO	0.02	0.00	0.00	0.00	0.00	0.88	0.71	0.71	0.00	0.88
	NiO	0.27	0.19	0.25	0.18	0.29	0.17	0.15	0.17	0.29	0.17
	CaO	0.01	0.00	0.00	0.00	0.01	0.02	0.04	0.03	0.01	0.02
	Na_2O	0.04	0.01	0.04	0.05	0.00	0.04	0.00	0.02	0.00	0.04
	K_2O	0.01	0.00	0.00	0.02	0.02	0.00	0.00	0.01	0.02	0.00
	TOTAL	100.68	99.37	100.15	100.18	101.16	97.52	98.13	102.11	101.16	97.52
Cations per 3 cations											
Sites for 3+	Al	0.01	0.00	0.00	0.00	0.00	0.06	0.06	0.02	0.00	0.06
	Cr	0.12	0.09	0.08	0.09	0.14	0.71	0.66	0.62	0.14	0.71
	V	0.00	0.00	0.00	0.00	0.00	0.00	0.00	0.00	0.00	0.00
	Ti	0.00	0.00	0.00	0.00	0.00	0.02	0.01	0.01	0.00	0.02
	Fe	1.71	1.80	1.81	1.79	1.75	0.67	0.70	1.13	1.75	0.67
Sites for 2+	Fe	0.91	0.97	0.98	0.96	0.97	0.52	0.52	0.77	0.97	0.52
	Ni	0.01	0.01	0.01	0.01	0.01	0.00	0.00	0.00	0.01	0.00
	Mn	0.01	0.01	0.00	0.01	0.00	0.10	0.09	0.08	0.00	0.10
	Mg	0.07	0.01	0.01	0.02	0.01	0.38	0.39	0.14	0.01	0.38
mol	Fe3+	0.63	0.63	0.62	0.63	0.62	0.54	0.55	0.57	0.62	0.54
	Fe2+	0.34	0.34	0.34	0.34	0.34	0.42	0.41	0.39	0.34	0.42
wt%	Fe_2O_3	58.77	59.88	60.53	60.12	59.20	26.09	27.65	40.63	59.20	26.09
	FeO	34.84	35.83	36.37	36.02	36.52	22.46	22.89	30.84	36.52	22.46

Analysis Desc	wt%	CO13-33 area 2 sp2 PC	CO13-33 area 2 sp2 PC	CO13-33 area 2 sp2 PC	CO13-33 area 2 sp2 PC	CO13-33 area 2 sp2 PC	CO13-33 area 2 sp2 PC	CO13-33 area 2 sp2 PC	CO13-33 area 2 sp2 PC	CO13-33 area 2 sp2 PFR	max Fe	min Fe
	SiO_2	6.46	0.03	3.35	3.74	8.24	9.49	8.84	7.95	0.10	0.03	9.49
	TiO_2	0.72	0.06	0.48	0.57	0.64	0.61	0.66	0.65	0.12	0.06	0.61
	Al_2O_3	1.40	0.00	0.88	0.94	2.08	2.32	2.11	1.93	0.00	0.00	2.32
	Cr_2O_3	28.07	5.87	21.96	25.81	27.34	26.08	26.06	25.92	6.66	5.87	26.08
	V_2O_3	0.06	0.04	0.06	0.04	0.05	0.05	0.06	0.07	0.03	0.04	0.05
	Fe_3O_4	49.67	94.45	64.17	58.22	44.78	41.00	43.65	47.36	93.42	94.45	41.00
	MnO	3.78	0.42	3.13	3.64	3.40	3.81	3.49	3.20	0.58	0.42	3.81
	MgO	7.85	0.21	5.01	3.70	9.59	10.70	9.74	8.98	0.23	0.21	10.70
	ZnO	0.91	0.03	0.62	0.81	0.91	0.86	0.84	0.91	0.05	0.03	0.86
	NiO	0.14	0.25	0.20	0.13	0.15	0.15	0.10	0.15	0.24	0.25	0.15
	CaO	0.04	0.02	0.03	0.02	0.03	0.01	0.04	0.03	0.01	0.02	0.01
	Na_2O	0.00	0.00	0.00	0.00	0.00	0.00	0.00	0.00	0.00	0.00	0.00
	K_2O	0.00	0.02	0.00	0.00	0.00	0.02	0.01	0.00	0.02	0.02	0.02
	TOTAL	99.09	101.40	99.87	97.61	97.20	95.08	95.59	97.14	101.46	101.40	95.08
Cations per 3 cations Sites for												
3+	Al	0.05	0.00	0.04	0.04	0.08	0.09	0.08	0.07	0.00	0.00	0.09
	Cr	0.72	0.18	0.60	0.73	0.69	0.65	0.66	0.66	0.20	0.18	0.65
	V	0.00	0.00	0.00	0.00	0.00	0.00	0.00	0.00	0.00	0.00	0.00
	Ti	0.02	0.00	0.01	0.01	0.01	0.01	0.01	0.01	0.00	0.00	0.01
	Fe	0.70	1.71	1.03	0.85	0.61	0.57	0.60	0.65	1.68	1.71	0.57
Sites for												
2+	Fe	0.51	0.97	0.64	0.69	0.45	0.39	0.44	0.48	0.96	0.97	0.39
	Ni	0.00	0.01	0.01	0.00	0.00	0.00	0.00	0.00	0.01	0.01	0.00
	Mn	0.10	0.01	0.09	0.11	0.09	0.10	0.09	0.09	0.02	0.01	0.10
	Mg	0.38	0.01	0.26	0.20	0.45	0.50	0.46	0.43	0.01	0.01	0.50
mol	Fe3+	0.55	0.61	0.59	0.53	0.55	0.57	0.55	0.55	0.61	0.61	0.57
	Fe2+	0.40	0.35	0.37	0.43	0.41	0.39	0.41	0.40	0.35	0.35	0.39
wt%	Fe_2O_3	27.39	58.04	37.85	30.70	24.60	23.20	23.97	26.10	57.18	58.04	23.20
	FeO	22.28	36.41	26.32	27.51	20.18	17.80	19.69	21.26	36.25	36.41	17.80

Analysis	wt%	CO13-31 sp5 PC	CO13-31 sp5 Core	CO13-31 sp5 Core	CO13-31 sp5 Core	CO13-31 sp5 Core	CO13-31 sp5 PFR	max Fe	min Fe
	SiO_2	0.39	0.02	0.02	1.34	0.00	1.11	1.11	0.02
	TiO_2	0.58	0.26	0.26	0.31	0.28	0.12	0.12	0.26
	Al_2O_3	6.41	29.90	29.66	25.35	29.42	0.38	0.38	29.90
	Cr_2O_3	25.56	35.02	35.22	33.37	34.87	2.37	2.37	35.02
	V_2O_3	0.12	0.24	0.24	0.23	0.25	0.04	0.04	0.24
	Fe_3O_4	58.78	23.24	24.06	26.96	24.32	94.11	94.11	23.24
	MnO	4.00	0.30	0.41	1.70	0.43	0.31	0.31	0.30
	MgO	2.34	12.40	12.31	10.66	11.94	1.20	1.20	12.40
	ZnO	0.79	0.32	0.33	0.69	0.28	0.04	0.04	0.32
	NiO	0.37	0.20	0.14	0.17	0.21	0.49	0.49	0.20
	CaO	0.00	0.00	0.01	0.01	0.00	0.02	0.02	0.00
	Na_2O	0.00	0.00	0.00	0.00	0.00	0.04	0.04	0.00
	K_2O	0.00	0.00	0.01	0.03	0.01	0.01	0.01	0.00
	TOTAL	99.33	101.90	102.67	100.82	102.00	100.24	100.24	101.90
Cations per 3 cations									
Sites for 3+	Al	0.28	1.05	1.04	0.91	1.04	0.02	0.02	1.05
	Cr	0.74	0.83	0.83	0.81	0.83	0.07	0.07	0.83
	V	0.00	0.01	0.01	0.01	0.01	0.00	0.00	0.01
	Ti	0.01	0.00	0.01	0.01	0.01	0.00	0.00	0.00
	Fe	0.86	0.06	0.07	0.13	0.07	1.72	1.72	0.06
Sites for 2+	Fe	0.74	0.43	0.44	0.46	0.45	0.91	0.91	0.43
	Ni	0.01	0.00	0.00	0.00	0.01	0.01	0.01	0.00
	Mn	0.12	0.01	0.01	0.04	0.01	0.01	0.01	0.01
	Mg	0.13	0.55	0.55	0.49	0.53	0.07	0.07	0.55
mol	Fe3+	0.51	0.11	0.12	0.20	0.12	0.63	0.63	0.11
	Fe2+	0.44	0.80	0.79	0.72	0.79	0.33	0.33	0.80
wt%	Fe_2O_3	30.04	2.52	2.99	5.31	2.99	59.31	59.31	2.52
	FeO	28.74	20.73	21.07	21.65	21.33	34.80	34.80	20.73

Analysis	wt%	CO13-31 sp5 PFR	CO13-31 sp5 Core	CO13-31 sp5 Core	CO13-31 sp5 Core	CO13-31 sp5 PC	CO13-31 sp5 Core	CO13-31 sp5 Core	CO13-31 sp5 Core	CO13-31 sp5 Core	CO13-31 sp5 Core	CO13-31 sp5 Core
	SiO_2	0.40	0.00	0.04	0.05	4.60	0.00	0.44	0.00	0.07	0.05	0.13
	TiO_2	0.22	0.26	0.32	0.28	0.31	0.26	0.28	0.28	0.23	0.38	0.20
	Al_2O_3	1.15	29.37	27.09	29.63	1.30	29.09	26.70	29.22	28.59	23.20	30.02
	Cr_2O_3	6.62	34.58	34.40	34.95	13.02	34.97	33.35	34.94	34.85	33.69	33.37
	V_2O_3	0.09	0.27	0.24	0.26	0.05	0.30	0.22	0.23	0.24	0.22	0.21
	Fe_3O_4	89.63	24.56	25.74	24.25	70.91	24.08	26.84	23.61	24.04	29.66	24.89
	MnO	0.96	0.34	0.62	0.30	1.85	0.31	1.25	0.23	0.35	1.91	1.79
	MgO	1.13	12.01	10.86	12.28	5.56	12.12	10.50	12.40	11.77	8.93	10.51
	ZnO	0.10	0.37	0.37	0.26	0.21	0.25	0.61	0.22	0.31	0.50	0.73
	NiO	0.52	0.20	0.17	0.13	0.58	0.16	0.12	0.16	0.14	0.20	0.13
	CaO	0.00	0.00	0.02	0.01	0.02	0.00	0.01	0.01	0.00	0.00	0.05
	Na_2O	0.00	0.00	0.00	0.00	0.00	0.00	0.00	0.00	0.04	0.00	0.00
	K_2O	0.01	0.00	0.00	0.00	0.01	0.02	0.00	0.00	0.00	0.00	0.00
	TOTAL	100.84	101.96	99.85	102.39	98.43	101.55	100.32	101.32	100.62	98.75	102.02
Cations per 3 cations												
Sites for 3+	Al	0.05	1.04	0.99	1.04	0.05	1.03	0.97	1.04	1.03	0.88	1.07
	Cr	0.20	0.82	0.85	0.82	0.35	0.83	0.82	0.83	0.84	0.86	0.80
	V	0.00	0.01	0.01	0.01	0.00	0.01	0.01	0.01	0.01	0.01	0.00
	Ti	0.01	0.00	0.01	0.01	0.01	0.00	0.01	0.01	0.00	0.01	0.00
	Fe	1.62	0.08	0.09	0.07	1.18	0.07	0.12	0.07	0.07	0.18	0.06
Sites for 2+	Fe	0.89	0.45	0.48	0.44	0.65	0.44	0.48	0.43	0.45	0.51	0.48
	Ni	0.02	0.00	0.00	0.00	0.02	0.00	0.00	0.00	0.00	0.01	0.00
	Mn	0.03	0.01	0.02	0.01	0.05	0.01	0.03	0.01	0.01	0.05	0.05
	Mg	0.06	0.54	0.50	0.55	0.28	0.54	0.48	0.56	0.53	0.43	0.47
mol	Fe3+	0.62	0.13	0.15	0.13	0.62	0.13	0.18	0.13	0.12	0.24	0.10
	Fe2+	0.34	0.78	0.76	0.79	0.34	0.79	0.74	0.78	0.79	0.68	0.81
wt%	Fe_2O_3	55.61	3.30	3.89	3.05	44.06	3.10	4.77	3.08	2.87	7.13	2.45
	FeO	34.03	21.26	21.84	21.21	26.85	20.98	22.07	20.53	21.17	22.53	22.44

Analysis	wt%	CO13-31 sp5 Core	CO13-31 sp5 Core	CO13-31 sp5 Core	max Fe	min Fe
	SiO_2	0.00	0.73	2.69	0.40	0.00
	TiO_2	0.26	0.75	0.77	0.22	0.28
	Al_2O_3	30.57	1.50	3.58	1.15	29.22
	Cr_2O_3	34.01	25.88	30.54	6.62	34.94
	V_2O_3	0.26	0.17	0.17	0.09	0.23
	Fe_3O_4	23.89	63.68	51.55	89.63	23.61
	MnO	0.23	4.45	5.64	0.96	0.23
	MgO	12.27	1.75	4.05	1.13	12.40
	ZnO	0.32	0.61	0.88	0.10	0.22
	NiO	0.11	0.40	0.32	0.52	0.16
	CaO	0.00	0.00	0.01	0.00	0.01
	Na_2O	0.00	0.01	0.00	0.00	0.00
	K_2O	0.02	0.02	0.01	0.01	0.00
	TOTAL	101.92	99.94	100.22	100.84	101.32
Cations per 3 cations						
Sites for 3+	Al	1.08	0.07	0.15	0.05	1.04
	Cr	0.80	0.76	0.84	0.20	0.83
	V	0.01	0.00	0.00	0.00	0.01
	Ti	0.00	0.02	0.02	0.01	0.01
	Fe	0.06	1.01	0.72	1.62	0.07
Sites for 2+	Fe	0.45	0.75	0.61	0.89	0.43
	Ni	0.00	0.01	0.01	0.02	0.00
	Mn	0.01	0.14	0.17	0.03	0.01
	Mg	0.55	0.10	0.21	0.06	0.56
mol	Fe3+	0.11	0.55	0.51	0.62	0.13
	Fe2+	0.80	0.41	0.44	0.34	0.78
wt%	Fe_2O_3	2.62	34.89	26.48	55.61	3.08
	FeO	21.26	28.79	25.07	34.03	20.53

Analysis	wt%	CO13-31 sp1 Mt rim	CO13-31 sp1 Mt rim	CO13-31 sp1 Mt rim	CO13-31 sp1 Mt rim	CO13-31 sp1 Core	CO13-31 sp1 Core	CO13-31 sp1 Mt rim	CO13-31 sp1 Core	max Fe	min Fe
	SiO_2	0.01	0.02	0.04	0.00	0.08	0.05	1.39	0.14	1.39	0.08
	TiO_2	0.22	0.09	0.14	0.20	0.38	0.23	0.11	0.30	0.11	0.38
	Al_2O_3	0.00	0.00	0.00	0.00	28.29	29.31	0.10	25.83	0.10	28.29
	Cr_2O_3	0.01	0.02	0.00	0.01	35.54	34.86	1.17	33.45	1.17	35.54
	V_2O_3	0.02	0.03	0.02	0.01	0.27	0.25	0.04	0.22	0.04	0.27
	Fe_3O_4	98.90	98.95	98.65	99.01	24.57	24.79	95.58	28.39	95.58	24.57
	MnO	0.27	0.27	0.32	0.31	0.39	0.59	0.29	1.01	0.29	0.39
	MgO	0.36	0.34	0.31	0.35	11.68	11.72	1.35	10.19	1.35	11.68
	ZnO	0.00	0.00	0.00	0.05	0.21	0.20	0.01	0.51	0.01	0.21
	NiO	0.51	0.50	0.49	0.55	0.11	0.11	0.49	0.17	0.49	0.11
	CaO	0.01	0.00	0.00	0.00	0.00	0.01	0.01	0.01	0.01	0.00
	Na_2O	0.00	0.00	0.03	0.03	0.00	0.00	0.00	0.00	0.00	0.00
	K_2O	0.00	0.00	0.01	0.00	0.04	0.00	0.00	0.02	0.00	0.04
	Total	100.3	100.2	100.0	100.5	101.6	102.1	100.5	100.2	100.5	101.6
Cations per 3 cations											
Sites for											
3+	Al	0.00	0.00	0.00	0.00	1.01	1.04	0.00	0.95	0.00	1.01
	Cr	0.00	0.00	0.00	0.00	0.85	0.83	0.03	0.83	0.03	0.85
	V	0.00	0.00	0.00	0.00	0.01	0.01	0.00	0.01	0.00	0.01
	Ti	0.01	0.00	0.00	0.00	0.01	0.00	0.00	0.01	0.00	0.01
	Fe	1.89	1.89	1.89	1.89	0.07	0.07	1.75	0.14	1.75	0.07
Sites for											
2+	Fe	0.95	0.96	0.96	0.95	0.46	0.46	0.90	0.49	0.90	0.46
	Ni	0.02	0.02	0.02	0.02	0.00	0.00	0.01	0.00	0.01	0.00
	Mn	0.01	0.01	0.01	0.01	0.01	0.01	0.01	0.03	0.01	0.01
	Mg	0.02	0.02	0.02	0.02	0.53	0.52	0.07	0.48	0.07	0.53
mol	Fe3+	0.64	0.64	0.64	0.64	0.12	0.12	0.64	0.21	0.64	0.12
	Fe2+	0.32	0.32	0.32	0.32	0.79	0.79	0.33	0.71	0.33	0.79
wt%	Fe_2O_3	63.34	63.35	63.12	63.48	2.93	3.06	60.77	5.91	60.77	2.93
	FeO	35.56	35.60	35.53	35.53	21.64	21.73	34.81	22.48	34.81	21.64

Analysis	wt%	CO13-31 sp1 PCR	CO13-31 sp1 PCR	CO13-31 sp1 PCR	CO13-31 sp1 PCR
cores	SiO_2	0.02	1.02	7.36	0.02
	TiO_2	0.62	0.92	0.50	0.74
	Al_2O_3	0.54	0.74	3.82	0.60
	Cr_2O_3	26.97	30.01	24.17	26.68
	V_2O_3	0.15	0.12	0.09	0.16
	Fe_3O_4	64.51	58.78	46.90	64.96
	MnO	5.03	5.75	3.80	4.63
	MgO	0.85	1.55	10.52	0.85
	ZnO	0.61	0.80	0.63	0.68
	NiO	0.34	0.31	0.24	0.39
	CaO	0.00	0.01	0.02	0.01
	Na_2O	0.00	0.00	0.00	0.00
	K_2O	0.00	0.00	0.00	0.01
	TOTAL	99.64	100.00	98.04	99.72
Cations per 3 cations					
Sites for 3+	Al	0.02	0.03	0.14	0.03
	Cr	0.81	0.88	0.60	0.81
	V	0.00	0.00	0.00	0.00
	Ti	0.02	0.02	0.01	0.02
	Fe	1.05	0.90	0.71	1.06
Sites for 2+	Fe	0.78	0.72	0.40	0.79
	Ni	0.01	0.01	0.01	0.01
	Mn	0.16	0.18	0.10	0.15
	Mg	0.05	0.09	0.49	0.05
mol	Fe3+	0.55	0.53	0.61	0.55
	Fe2+	0.41	0.43	0.35	0.41
wt%	Fe_2O_3	35.46	31.04	28.80	35.48
	FeO	29.05	27.74	18.10	29.48

Analysis	wt%	CO13-40 area2_1 Mt rim	CO13-40 area2_1 Mt rim	CO13-40 area2_1 Mt rim	CO13-40 area2_1 Mt rim	CO13-40 area2_1 Mt rim	CO13-40 area2_2 PC	CO13-40 area2_2 Core	CO13-40 area2_2 Core	CO13-40 area2_2 PFR	CO13-40 area2_2 PC
	SiO_2	0.01	0.00	0.05	2.53	0.03	2.16	0.04	0.02	0.00	2.89
	TiO_2	0.11	0.18	0.13	0.11	0.08	0.56	0.18	0.19	0.18	0.62
	Al_2O_3	0.00	0.00	0.00	0.00	0.00	1.40	28.75	28.35	0.04	2.19
	Cr_2O_3	1.90	1.88	1.62	0.99	1.86	33.17	37.47	37.86	3.19	31.21
	V_2O_3	0.01	0.02	0.00	0.02	0.02	0.07	0.23	0.24	0.04	0.07
	Fe_3O_4	96.32	96.81	97.90	90.93	97.59	54.59	19.14	19.48	98.56	53.93
	MnO	0.21	0.10	0.14	0.06	0.08	2.54	0.21	0.16	0.30	2.32
	MgO	0.21	0.20	0.19	0.36	0.21	3.07	13.52	13.05	0.17	3.95
	ZnO	0.00	0.04	0.00	0.00	0.00	1.18	0.20	0.19	0.05	1.06
	NiO	0.07	0.05	0.08	2.68	0.08	0.00	0.07	0.04	0.07	0.06
	CaO	0.00	0.01	0.00	0.00	0.00	0.01	0.00	0.00	0.00	0.02
	Na_2O	0.03	0.00	0.00	0.00	0.00	0.00	0.00	0.02	0.00	0.00
	K_2O	0.00	0.00	0.01	0.01	0.01	0.00	0.00	0.00	0.00	0.00
	Total	98.87	99.28	100.1	97.67	99.96	98.74	99.80	99.61	102.6	98.31
Cations per 3 cations											
Sites for 3+	Al	0.00	0.00	0.00	0.00	0.00	0.06	1.03	1.02	0.00	0.09
	Cr	0.06	0.06	0.05	0.03	0.06	0.96	0.90	0.91	0.09	0.88
	V	0.00	0.00	0.00	0.00	0.00	0.00	0.01	0.01	0.00	0.00
	Ti	0.00	0.00	0.00	0.00	0.00	0.01	0.00	0.00	0.00	0.01
	Fe	1.83	1.83	1.84	1.67	1.83	0.71	0.03	0.02	1.79	0.71
Sites for 2+	Fe	0.98	0.98	0.98	0.90	0.98	0.75	0.38	0.40	0.98	0.72
	Ni	0.00	0.00	0.00	0.08	0.00	0.00	0.00	0.00	0.00	0.00
	Mn	0.01	0.00	0.00	0.00	0.00	0.08	0.01	0.00	0.01	0.07
	Mg	0.01	0.01	0.01	0.02	0.01	0.17	0.61	0.59	0.01	0.21
mol	Fe3+	0.63	0.63	0.63	0.63	0.63	0.46	0.06	0.03	0.62	0.47
	Fe2+	0.34	0.34	0.34	0.34	0.34	0.49	0.85	0.87	0.34	0.48
wt%	Fe_2O_3	60.42	60.60	61.42	56.91	61.15	25.14	1.08	0.65	61.33	25.36
	FeO	35.89	36.21	36.48	34.02	36.44	29.45	18.06	18.83	37.22	28.57

Analysis	wt%	CO13-40 a2_2 Mt rim	CO13-40 a2_2 PC	CO13-40 a2_3 Mt rim	CO13-40 a2_3 Mt rim	CO13-40 a2_3 Mt rim	CO13-40 a3_1 PFR	CO13-40 a3_1 PC	CO13-40 a3_1 PC	CO13-40 a3_1 PC	CO13-40 a3_1 PC
	SiO_2	0.05	0.14	0.05	0.00	1.09	0.18	9.65	6.29	1.71	1.77
	TiO_2	0.10	0.48	0.16	0.08	0.17	0.18	0.40	0.41	0.44	0.36
	Al_2O_3	0.00	0.58	0.00	0.00	0.01	0.00	1.71	1.62	0.32	0.32
	Cr_2O_3	2.02	23.67	0.13	0.58	0.55	6.30	17.62	16.96	16.17	13.76
	V_2O_3	0.01	0.06	0.02	0.02	0.02	0.03	0.03	0.01	0.03	0.01
	Fe_3O_4	98.54	72.08	99.09	98.60	96.26	92.49	55.90	65.06	77.48	79.04
	MnO	0.20	1.58	0.13	0.04	0.06	0.35	1.25	1.49	1.10	1.11
	MgO	0.15	0.55	0.17	0.18	1.52	0.35	11.24	9.54	2.40	2.75
	ZnO	0.02	0.64	0.01	0.00	0.00	0.03	0.38	0.28	0.41	0.25
	NiO	0.08	0.07	0.05	0.05	0.07	0.08	0.00	0.05	0.02	0.05
	CaO	0.00	0.01	0.01	0.00	0.00	0.01	0.10	0.09	0.06	0.07
	Na_2O	0.04	0.01	0.00	0.00	0.00	0.02	0.00	0.07	0.00	0.00
	K_2O	0.00	0.03	0.00	0.00	0.01	0.00	0.01	0.00	0.01	0.00
	Total	101.2	99.90	99.83	99.54	99.77	100.0	98.27	101.9	100.2	99.47
Cations per 3 cations											
Sites for 3+	Al	0.00	0.03	0.00	0.00	0.00	0.00	0.06	0.06	0.01	0.01
	Cr	0.06	0.72	0.00	0.02	0.02	0.19	0.42	0.42	0.47	0.40
	V	0.00	0.00	0.00	0.00	0.00	0.00	0.00	0.00	0.00	0.00
	Ti	0.00	0.01	0.00	0.00	0.00	0.00	0.01	0.01	0.01	0.01
	Fe	1.82	1.13	1.88	1.87	1.79	1.68	0.82	1.03	1.28	1.35
Sites for 2+	Fe	0.98	0.92	0.98	0.99	0.91	0.97	0.46	0.51	0.83	0.81
	Ni	0.00	0.00	0.00	0.00	0.00	0.00	0.00	0.00	0.00	0.00
	Mn	0.01	0.05	0.00	0.00	0.00	0.01	0.03	0.04	0.03	0.03
	Mg	0.01	0.03	0.01	0.01	0.08	0.02	0.51	0.45	0.13	0.15
mol	Fe3+	0.63	0.53	0.63	0.63	0.64	0.61	0.62	0.64	0.58	0.60
	Fe2+	0.34	0.43	0.33	0.33	0.33	0.35	0.34	0.32	0.38	0.36
wt%	Fe_2O_3	61.68	37.98	62.65	62.19	61.52	56.49	34.56	41.87	44.93	47.31
	FeO	36.86	34.10	36.45	36.41	34.74	36.00	21.34	23.18	32.55	31.73

Analysis	wt%	CO13-40 a3_1 PC	CO13-40 a3_1 PC	CO13-40 a3_1 PC	CO13-40 a3_1 PC	CO13-40 a3_1 PC	CO13-40 a3_1 PC	CO13-40 a3_1 PC	CO13-40 a3_1 Mt rim	CO13-40 a3_1_2 Mt rim	CO13-40 a3_2 Mt rim
	SiO_2	0.98	0.57	3.41	0.61	10.93	10.16	2.30	0.05	0.00	0.57
	TiO_2	0.35	0.35	0.29	0.25	0.41	0.67	0.32	0.11	0.16	0.09
	Al_2O_3	0.14	0.06	0.62	0.06	2.40	2.25	0.55	0.00	0.00	0.01
	Cr_2O_3	12.96	16.83	15.38	13.72	19.92	27.21	14.70	2.86	1.57	0.45
	V_2O_3	0.05	0.05	0.03	0.04	0.04	0.04	0.03	0.00	0.01	0.03
	Fe_3O_4	83.31	79.40	75.47	84.47	54.80	48.83	78.19	95.17	99.73	97.60
	MnO	0.90	1.20	1.13	0.79	1.43	2.17	0.97	0.11	0.03	0.03
	MgO	0.93	0.60	4.41	0.64	12.14	9.84	3.27	0.13	0.13	0.60
	ZnO	0.19	0.43	0.37	0.18	0.52	1.03	0.34	0.00	0.06	0.00
	NiO	0.05	0.07	0.07	0.07	0.02	0.00	0.03	0.00	0.06	0.04
	CaO	0.05	0.04	0.07	0.03	0.07	0.28	0.04	0.01	0.01	0.00
	Na_2O	0.00	0.00	0.00	0.06	0.01	0.00	0.01	0.00	0.01	0.01
	K_2O	0.00	0.00	0.03	0.01	0.00	0.01	0.00	0.00	0.00	0.02
	Total	99.89	99.60	101.27	100.94	102.68	102.49	100.72	98.45	101.77	99.44
Cations per 3 cations											
Sites for 3+	Al	0.01	0.00	0.03	0.00	0.08	0.08	0.02	0.00	0.00	0.00
	Cr	0.38	0.51	0.42	0.41	0.45	0.64	0.41	0.09	0.05	0.01
	V	0.00	0.00	0.00	0.00	0.00	0.00	0.00	0.00	0.00	0.00
	Ti	0.01	0.01	0.01	0.01	0.01	0.01	0.01	0.00	0.00	0.00
	Fe	1.42	1.33	1.21	1.43	0.73	0.56	1.29	1.79	1.84	1.83
Sites for 2+	Fe	0.92	0.92	0.74	0.94	0.44	0.51	0.80	0.99	0.99	0.96
	Ni	0.00	0.00	0.00	0.00	0.00	0.00	0.00	0.00	0.00	0.00
	Mn	0.03	0.04	0.03	0.03	0.03	0.05	0.03	0.00	0.00	0.00
	Mg	0.05	0.03	0.23	0.04	0.52	0.43	0.17	0.01	0.01	0.03
mol	Fe3+	0.58	0.56	0.60	0.58	0.60	0.50	0.59	0.62	0.63	0.63
	Fe2+	0.38	0.39	0.36	0.38	0.36	0.45	0.37	0.34	0.34	0.33
wt%	Fe_2O_3	48.46	44.80	45.02	48.89	32.75	24.21	46.39	59.05	62.43	61.60
	FeO	34.84	34.60	30.45	35.58	22.05	24.62	31.80	36.12	37.29	36.00

Analysis	wt%	CO13-40 area3_2 Mt rim	CO13-40 area3_2 Mt rim	CO13-40 area3_2 Mt rim
	SiO_2	0.06	0.74	0.15
	TiO_2	0.11	0.07	0.09
	Al_2O_3	0.00	0.00	0.00
	Cr_2O_3	0.33	0.36	0.38
	V_2O_3	0.02	0.02	0.00
	Fe_3O_4	97.71	97.48	98.96
	MnO	0.03	0.04	0.03
	MgO	0.27	0.83	0.21
	ZnO	0.00	0.00	0.00
	NiO	0.07	0.04	0.06
	CaO	0.01	0.01	0.00
	Na_2O	0.01	0.00	0.00
	K_2O	0.00	0.00	0.00
	TOTAL	98.60	99.59	99.88
Cations per 3 cations				
Sites for 3+	Al	0.00	0.00	0.00
	Cr	0.01	0.01	0.01
	V	0.00	0.00	0.00
	Ti	0.00	0.00	0.00
	Fe	1.87	1.82	1.87
Sites for 2+	Fe	0.98	0.95	0.99
	Ni	0.00	0.00	0.00
	Mn	0.00	0.00	0.00
	Mg	0.02	0.05	0.01
mol	Fe3+	0.63	0.63	0.63
	Fe2+	0.33	0.33	0.33
wt%	Fe_2O_3	61.77	61.73	62.38
	FeO	35.94	35.75	36.57

Analysis	wt%	CO13-55 sp2 PC Nr grt	CO13-55 sp2 PC Nr grt	CO13-55 sp2_2 Mt rim Nr grt	CO13-55 sp2_2 Mt rim Nr grt	CO13-55 sp1 Mt rim Nr grt	CO13-55 3_sp1 PC Nr grt
	SiO_2	0.05	0.01	0.04	0.14	0.03	2.46
	TiO_2	0.21	0.70	0.20	0.14	0.13	0.60
	Al_2O_3	0.03	0.03	0.00	0.00	0.00	0.14
	Cr_2O_3	19.98	20.10	1.84	1.40	1.67	27.63
	V_2O_3	0.08	0.12	0.03	0.03	0.01	0.11
	Fe_3O_4	78.47	73.62	98.33	98.45	98.34	63.44
	MnO	2.14	2.17	0.26	0.13	0.11	2.91
	MgO	0.56	0.62	0.26	0.45	0.23	1.11
	ZnO	0.50	0.46	0.00	0.00	0.00	0.66
	NiO	0.21	0.13	0.13	0.08	0.12	0.12
	CaO	0.28	0.50	0.06	0.01	0.13	1.96
	Na_2O	0.00	0.05	0.01	0.05	0.00	0.00
	K_2O	0.00	0.00	0.00	0.01	0.01	0.03
	Total	102.51	98.51	101.14	100.90	100.78	101.16
Cations per 3 cations							
	Ti	0.00	0.02	0.00	0.00	0.00	0.01
	Al	0.00	0.00	0.00	0.00	0.00	0.01
	V	0.00	0.00	0.00	0.00	0.00	0.00
	Cr	0.59	0.62	0.06	0.04	0.05	0.78
	Fe	2.28	2.22	2.91	2.91	2.92	1.76
	Ni	0.01	0.00	0.00	0.00	0.00	0.00
	Mn	0.07	0.07	0.01	0.00	0.00	0.09
	Mg	0.03	0.04	0.01	0.03	0.01	0.06
Sites for 3+							
	Al	0.00	0.00	0.00	0.00	0.00	0.01
	Cr	0.59	0.62	0.06	0.04	0.05	0.78
	V	0.00	0.00	0.00	0.00	0.00	0.00
	Ti	0.00	0.02	0.00	0.00	0.00	0.01
	Fe	1.28	1.23	1.83	1.83	1.83	0.81
Sites for 2+							
	Fe	0.90	0.89	0.97	0.97	0.98	0.85
	Ni	0.01	0.00	0.00	0.00	0.00	0.00
	Mn	0.07	0.07	0.01	0.00	0.00	0.09
	Mg	0.03	0.04	0.01	0.03	0.01	0.06
mol	Fe3+	0.56	0.56	0.63	0.63	0.63	0.46
	Fe2+	0.39	0.40	0.33	0.33	0.34	0.48
wt%	Fe_2O_3	44.24	40.91	61.78	62.09	61.65	29.39
	FeO	34.23	32.71	36.55	36.36	36.68	34.05

Notes

Cores = primary cores to spinel

PC = porous chromite

PFR = porous Fe-rich rim

Mt rim = magnetite rim to spinel grain

Nr grt = near to andradite garnet

C8: EPMA analyses for magnetite grains.

Analysis	wt%	CO13-31 area3 mt6	CO13-31 area3 mt7	CO13-31 area2 mt1_1	CO13-31 area2 mt1_2	CO13-31 area2 mt1_3	CO13-31 area2 mt inc_2	CO13-31 area5 mt1	CO13-31 area5 mt1_2	CO13-31 area5 mt1_3	CO13-31 area5 mt2
	SiO_2	0.08	0.05	0.04	0.05	0.06	0.06	0.16	0.09	0.22	0.50
	TiO_2	0.17	0.17	0.17	0.15	0.16	0.17	0.18	0.18	0.18	0.76
	Al_2O_3	0.01	0.01	0.00	0.02	0.00	0.00	0.01	0.00	0.00	0.01
	Cr_2O_3	2.11	0.80	0.36	0.44	0.15	3.66	1.57	0.26	0.35	2.14
	V_2O_3	0.04	0.03	0.02	0.03	0.02	0.04	0.05	0.04	0.03	0.05
	Fe_3O_4	98.19	99.95	99.60	99.09	100.3	93.97	98.41	99.43	99.37	95.77
	MnO	0.31	0.28	0.23	0.18	0.24	0.46	0.25	0.19	0.18	0.40
	MgO	0.40	0.32	0.34	0.39	0.41	0.46	0.47	0.39	0.46	1.03
	ZnO	n.d.	n.d.	n.d.	n.d.	n.d.	n.d.	n.d.	n.d.	n.d.	n.d.
	NiO	0.52	0.43	0.85	0.52	0.47	1.62	0.51	0.39	0.43	0.52
	CaO	0.00	0.00	0.00	0.00	0.00	0.00	0.00	0.02	0.00	0.00
	Na_2O	n.d.	n.d.	n.d.	n.d.	n.d.	n.d.	n.d.	n.d.	n.d.	n.d.
	K_2O	n.d.	n.d.	n.d.	n.d.	n.d.	n.d.	n.d.	n.d.	n.d.	n.d.
	Total	100.7	101.4	101.0	100.3	101.4	98.53	100.6	100.5	100.6	99.29
Cations per 3 cations											
Sites 3+	Al	0.00	0.00	0.00	0.00	0.00	0.00	0.00	0.00	0.00	0.00
	Cr	0.06	0.02	0.01	0.01	0.00	0.11	0.05	0.01	0.01	0.06
	V	0.00	0.00	0.00	0.00	0.00	0.00	0.00	0.00	0.00	0.00
	Ti	0.00	0.00	0.00	0.00	0.00	0.00	0.00	0.00	0.00	0.02
	Fe	1.82	1.86	1.88	1.87	1.88	1.78	1.83	1.87	1.86	1.78
Sites 2+	Fe	0.95	0.96	0.95	0.96	0.96	0.91	0.95	0.96	0.96	0.91
	Ni	0.02	0.01	0.03	0.02	0.01	0.05	0.02	0.01	0.01	0.02
	Mn	0.01	0.01	0.01	0.01	0.01	0.01	0.01	0.01	0.01	0.01
	Mg	0.02	0.02	0.02	0.02	0.02	0.03	0.03	0.02	0.03	0.06
mol	Fe3+	0.63	0.64	0.64	0.64	0.64	0.64	0.63	0.64	0.64	0.64
	Fe2+	0.33	0.33	0.32	0.33	0.32	0.33	0.33	0.33	0.33	0.33
wt%	Fe_2O_3	62.11	63.56	63.83	63.24	64.14	59.96	62.42	63.36	63.31	60.94
	FeO	36.07	36.39	35.77	35.85	36.15	34.01	36.00	36.07	36.06	34.83

Analysis	wt%	CO13-31 area5 mt2	CO13-31 area5 mt2	CO13-31 area4 mt1_1	CO13-31 area4 mt1_2	CO13-31 area4 mt1_3	CO13-31 area5 mt1	CO13-31 area5 mt1	CO13-31 area5 mt1	CO13-31 area6 mt1_1	CO13-31 area6 mt1_2
	SiO_2	0.02	0.03	0.08	0.03	0.10	0.08	0.06	0.11	0.04	0.11
	TiO_2	1.87	1.68	0.15	0.19	0.22	0.11	0.10	0.08	0.29	0.30
	Al_2O_3	0.00	0.00	0.00	0.00	0.00	0.03	0.00	0.00	0.00	0.00
	Cr_2O_3	2.86	1.67	2.11	1.52	1.00	0.04	0.04	0.06	1.38	1.70
	V_2O_3	0.02	0.04	0.04	0.04	0.06	0.02	0.04	0.06	0.02	0.02
	Fe_3O_4	94.43	96.38	96.38	97.63	100.01	99.49	99.02	98.47	98.06	97.98
	MnO	0.74	0.67	0.34	0.29	0.28	0.23	0.22	0.22	0.28	0.30
	MgO	0.38	0.37	0.42	0.39	0.39	0.35	0.33	0.36	0.41	0.44
	ZnO	n.d.	n.d.	n.d.	n.d.	n.d.	n.d.	n.d.	n.d.	n.d.	n.d.
	NiO	0.65	0.62	1.62	0.72	0.35	0.59	0.47	0.51	0.31	0.43
	CaO	0.01	0.00	0.00	0.00	0.00	0.00	0.01	0.01	0.00	0.00
	Na_2O	n.d.	n.d.	n.d.	n.d.	n.d.	n.d.	n.d.	n.d.	n.d.	n.d.
	K_2O	n.d.	n.d.	n.d.	n.d.	n.d.	n.d.	n.d.	n.d.	n.d.	n.d.
	Total	98.86	99.80	99.76	99.85	101.65	100.53	99.93	99.43	99.91	100.22
Cations per 3 cations											
Sites 3+	Al	0.00	0.00	0.00	0.00	0.00	0.00	0.00	0.00	0.00	0.00
	Cr	0.09	0.05	0.06	0.05	0.03	0.00	0.00	0.00	0.04	0.05
	V	0.00	0.00	0.00	0.00	0.00	0.00	0.00	0.00	0.00	0.00
	Ti	0.05	0.04	0.00	0.00	0.01	0.00	0.00	0.00	0.01	0.01
	Fe	1.76	1.80	1.82	1.84	1.85	1.88	1.88	1.88	1.84	1.83
Sites 2+	Fe	0.93	0.94	0.92	0.95	0.96	0.95	0.96	0.96	0.96	0.95
	Ni	0.02	0.02	0.05	0.02	0.01	0.02	0.01	0.02	0.01	0.01
	Mn	0.02	0.02	0.01	0.01	0.01	0.01	0.01	0.01	0.01	0.01
	Mg	0.02	0.02	0.02	0.02	0.02	0.02	0.02	0.02	0.02	0.02
mol	Fe3+	0.63	0.63	0.64	0.64	0.63	0.64	0.64	0.64	0.63	0.63
	Fe2+	0.33	0.33	0.32	0.33	0.33	0.32	0.33	0.33	0.33	0.33
wt%	Fe_2O_3	59.45	61.08	61.89	62.16	63.48	63.67	63.27	62.92	62.15	62.07
	FeO	34.98	35.30	34.49	35.47	36.53	35.83	35.75	35.55	35.90	35.91

Analysis	wt%	CO13-31 a5	CO13-31 a5	CO13-31 a5	Average	Std dev
	SiO_2	0.07	0.04	0.08	0.09	0.10
	TiO_2	1.16	2.05	6.13	0.72	1.30
	Al_2O_3	0.01	0.00	0.00	0.00	0.01
	Cr_2O_3	3.00	2.18	2.04	1.37	1.03
	V_2O_3	0.04	0.04	0.04	0.04	0.01
	Fe_3O_4	95.01	96.30	92.68	97.65	2.10
	MnO	0.60	0.71	1.97	0.42	0.37
	MgO	0.44	0.35	0.55	0.43	0.14
	ZnO	n.d.	n.d.	n.d.	n.d.	n.d.
	NiO	0.48	0.54	0.46	0.61	0.33
	CaO	0.03	0.03	0.03	0.01	0.01
	Na_2O	n.d.	n.d.	n.d.	n.d.	n.d.
	K_2O	n.d.	n.d.	n.d.	n.d.	n.d.
	Total	98.94	100.28	100.07	100.15	0.79
Cations per 3 actions						
Sites 3+	Al	0.00	0.00	0.00	0.00	0.00
	Cr	0.09	0.06	0.06	0.04	0.03
	V	0.00	0.00	0.00	0.00	0.00
	Ti	0.03	0.05	0.15	0.02	0.03
	Fe	1.77	1.78	1.69	1.83	0.05
Sites 2+	Fe	0.94	0.94	0.89	0.94	0.02
	Ni	0.01	0.02	0.01	0.02	0.01
	Mn	0.02	0.02	0.06	0.01	0.01
	Mg	0.03	0.02	0.03	0.02	0.01
mol	Fe3+	0.63	0.63	0.63	0.64	0.00
	Fe2+	0.33	0.33	0.33	0.33	0.00
wt%	Fe_2O_3	59.74	60.63	58.36	62.08	1.56
	FeO	35.27	35.66	34.32	35.57	0.64

	Analysis Wt%	CO13-55 a6 mt1_1	CO13-55 a6 mt1_2	CO13-55 a6 mt1_3	CO13-55 a7 mt1	CO13-55 a7 mt1	CO13-55 a7 mt2	CO13-55 a8 mt1	CO13-55 a2 mt1_2
	SiO_2	0.04	0.05	0.06	0.04	0.07	0.01	0.07	0.01
	TiO_2	0.09	0.14	0.14	0.07	0.09	0.13	0.12	0.13
	V_2O_3	0.03	0.03	0.04	0.03	0.01	0.03	0.01	0.01
	Al_2O_3	0.00	0.00	0.00	0.00	0.01	0.00	0.01	0.00
	Cr_2O_3	0.48	0.52	1.84	1.98	2.39	0.55	0.16	0.79
	Fe_3O_4 (tot)	100.5	101.4	98.41	98.25	98.37	100.2	99.75	98.98
	NiO	0.14	0.13	0.20	0.21	0.22	0.09	0.18	0.24
	MnO	0.15	0.19	0.22	0.15	0.19	0.13	0.14	0.16
	MgO	0.28	0.28	0.31	0.27	0.19	0.31	0.28	0.29
	CaO	0.04	0.02	0.00	0.07	0.18	0.00	0.25	0.01
	Total	101.32	102.30	100.31	100.17	100.68	101.03	100.57	100.09
Cations per 3 cations Sites for									
3+	Al	0.00	0.00	0.00	0.00	0.00	0.00	0.00	0.00
	Cr	0.01	0.01	0.05	0.06	0.07	0.02	0.00	0.02
	V	0.00	0.00	0.00	0.00	0.00	0.00	0.00	0.00
	Ti	0.00	0.00	0.00	0.00	0.00	0.00	0.00	0.00
	Fe	1.98	1.98	1.94	1.94	1.93	1.98	1.99	1.97
Sites for									
2+	Fe	0.98	0.98	0.97	0.97	0.97	0.98	0.96	0.97
	Mg	0.01	0.01	0.02	0.01	0.01	0.02	0.01	0.02
	Ni	0.00	0.00	0.01	0.01	0.01	0.00	0.01	0.01
	Mn	0.00	0.01	0.01	0.00	0.01	0.00	0.00	0.00
	Mg	0.01	0.01	0.02	0.01	0.01	0.02	0.01	0.02
mass	Fe_2O_3	67.36	67.95	65.62	65.48	65.51	67.10	67.25	66.31
	FeO	33.11	33.44	32.78	32.76	32.85	33.11	32.50	32.66

Analysis Wt%	CO13-55 a2 mt1_3	CO13-55 a2 mt2_1	CO13-55 a2 mt3	CO13-55 a2 mt4	AV	ST DEV
SiO_2	0.07	0.19	0.05	0.06	0.06	0.05
TiO_2	0.09	0.12	0.11	0.12	0.11	0.02
V_2O_3	0.03	0.04	0.03	0.05	0.03	0.01
Al_2O_3	0.00	0.00	0.00	0.01	0.00	0.00
Cr_2O_3	0.54	0.23	0.11	0.11	0.81	0.80
Fe_3O_4 (tot)	99.66	100.41	101.04	101.03	99.83	1.12
NiO	0.14	0.03	0.03	0.05	0.14	0.07
MnO	0.15	0.16	0.13	0.16	0.16	0.03
MgO	0.28	0.38	0.25	0.28	0.28	0.04
CaO	0.01	0.03	0.01	0.03	0.05	0.08
Total	100.56	101.15	101.51	101.61	100.94	0.67
Cations per 3 cations						
Sites for 3+						
Al	0.00	0.00	0.00	0.00	0.00	0.00
Cr	0.02	0.01	0.00	0.00	0.02	0.02
V	0.00	0.00	0.00	0.00	0.00	0.00
Ti	0.00	0.00	0.00	0.00	0.00	0.00
Fe	1.98	1.99	1.99	1.99	1.97	0.02
Sites for 2+						
Fe	0.98	0.97	0.98	0.98	0.97	0.00
Mg	0.01	0.02	0.01	0.01	0.01	0.00
Ni	0.00	0.00	0.00	0.00	0.00	0.00
Mn	0.00	0.00	0.00	0.00	0.00	0.00
Mg	0.01	0.02	0.01	0.01	0.01	0.00
Fe_2O_3	66.78	67.44	67.70	67.79	66.86	0.91
FeO	32.89	32.97	33.34	33.24	32.97	0.28

	Analysis Wt%	CO13-33 a6 mt1	CO13-33 a6 mt2	CO13-33 a6 mt3	CO13-33 a5 mt1_1	CO13-33 a5 mt1_2	CO13-33 a5 mt2_2	CO13-33 a5 mt2_3	CO13-33 a3 mt1	CO13-33 a3 mt1
	SiO_2	0.98	0.08	0.08	0.26	0.11	0.89	0.20	0.06	0.07
	TiO_2	0.07	0.10	0.10	0.12	0.11	0.06	0.07	0.11	0.17
	V_2O_3	0.04	0.04	0.03	0.03	0.04	0.01	0.02	0.04	0.03
	Al_2O_3	0.04	0.01	0.00	0.00	0.02	0.00	0.02	0.13	0.62
	Cr_2O_3	0.90	0.46	1.17	0.79	1.10	0.96	0.75	2.11	3.78
	Fe_3O_4 (tot)	97.31	99.08	96.70	98.20	98.28	96.83	98.76	99.30	96.44
	NiO	0.43	0.24	0.26	0.22	0.22	0.23	0.24	0.19	0.21
	MnO	0.16	0.09	0.20	0.11	0.15	0.17	0.13	0.24	0.59
	MgO	1.27	0.26	0.26	0.30	0.26	1.21	0.27	0.19	0.29
	CaO	0.00	0.00	0.00	0.00	0.00	0.00	0.00	0.01	0.01
	Total	99.70	99.96	98.13	99.40	99.63	98.99	99.88	101.39	100.31
Cations per 3 cations										
Sites for 3+	Al	0.00	0.00	0.00	0.00	0.00	0.00	0.00	0.01	0.03
	Cr	0.03	0.01	0.03	0.02	0.03	0.03	0.02	0.06	0.10
	V	0.00	0.00	0.00	0.00	0.00	0.00	0.00	0.00	0.00
	Ti	0.00	0.00	0.00	0.00	0.00	0.00	0.00	0.00	0.00
	Fe	1.97	1.98	1.96	1.97	1.96	1.97	1.98	1.93	1.87
Sites for 2+	Fe	0.92	0.98	0.97	0.97	0.97	0.92	0.98	0.98	0.96
	Mg	0.07	0.01	0.01	0.02	0.01	0.06	0.01	0.01	0.02
	Ni	0.01	0.01	0.01	0.01	0.01	0.01	0.01	0.01	0.01
	Mn	0.00	0.00	0.01	0.00	0.00	0.01	0.00	0.01	0.02
	Mg	0.07	0.01	0.01	0.02	0.01	0.06	0.01	0.01	0.02
mass	Fe_2O_3	66.43	66.39	64.68	65.75	65.68	65.94	66.13	65.94	63.66
	FeO	30.88	32.68	32.02	32.45	32.60	30.89	32.63	33.35	32.78

Analysis	CO13-33 a3 mt2	CO13-33 a2 mt1	CO13-33 a2 mt1_2	CO13-33 a12 mt1_1	CO13-33 a12 mt1_2	CO13-33 a12 mt1_3	CO13-33 a3_1 mt2_3	CO13-33 a6 mt3	CO13-33 a5 mt1_2	Av	St Dev
Wt%											
SiO_2	0.17	0.09	0.59	0.06	0.07	0.03	0.05	0.08	0.11	0.24	0.30
TiO_2	0.10	0.12	0.06	0.13	0.09	0.08	0.10	0.10	0.11	0.10	0.03
V_2O_3	0.02	0.03	0.01	0.03	0.03	0.03	0.04	0.03	0.04	0.03	0.01
Al_2O_3	0.00	0.00	0.00	0.00	0.00	0.00	0.00	0.00	0.02	0.05	0.15
Cr_2O_3	3.94	0.97	0.77	0.22	2.20	1.23	2.69	1.17	1.10	1.50	1.13
Fe_3O_4 (tot)	95.4	98.3	98.3	100.8	98.2	99.1	97.8	96.7	98.3	98.0	1.30
NiO	0.38	0.28	0.23	0.22	0.26	0.31	0.28	0.26	0.22	0.26	0.06
MnO	0.28	0.21	0.15	0.11	0.22	0.17	0.25	0.20	0.15	0.20	0.12
MgO	0.31	0.23	0.80	0.24	0.32	0.22	0.25	0.26	0.26	0.42	0.35
CaO	0.01	0.00	0.02	0.00	0.00	0.00	0.01	0.00	0.00	0.00	0.01
Total	99.0	99.6	99.9	101.5	100.4	100.5	100.3	98.1	99.6	99.9	0.85
cations Sites for 3+											
Al	0.00	0.00	0.00	0.00	0.00	0.00	0.00	0.00	0.00	0.00	0.01
Cr	0.11	0.03	0.02	0.01	0.06	0.03	0.08	0.03	0.03	0.04	0.03
V	0.00	0.00	0.00	0.00	0.00	0.00	0.00	0.00	0.00	0.00	0.00
Ti	0.00	0.00	0.00	0.00	0.00	0.00	0.00	0.00	0.00	0.00	0.00
Fe	1.89	1.97	1.98	1.99	1.94	1.96	1.92	1.96	1.96	1.95	0.04
Sites for 2+											
Fe	0.96	0.97	0.95	0.98	0.97	0.97	0.97	0.97	0.98	0.96	0.02
Mg	0.02	0.01	0.04	0.01	0.02	0.01	0.01	0.01	0.01	0.02	0.02
Ni	0.01	0.01	0.01	0.01	0.01	0.01	0.01	0.01	0.01	0.01	0.00
Mn	0.01	0.01	0.00	0.00	0.01	0.01	0.01	0.01	0.00	0.01	0.00
Mg	0.02	0.01	0.04	0.01	0.02	0.01	0.01	0.01	0.01	0.02	0.02
Fe3+	63.1	65.8	66.5	67.6	65.5	66.25	65.0	64.7	65.7	65.6	1.09
Fe2+	32.3	32.51	31.8	33.2	32.8	32.9	32.8	32.0	32.6	32.4	0.71

Analysis	CO13-33 a3 mt2	CO13-33 a2 mt1	CO13-33 a2 mt1_2	CO13-33 a12 mt1_1	CO13-33 a12 mt1_2	CO13-33 a12 mt1_3	CO13-33 a3_1 mt2_3	CO13-33 a6 mt3	CO13-33 a5 mt1_2	Av	St Dev
wt%											
SiO_2	0.17	0.09	0.59	0.06	0.07	0.03	0.05	0.08	0.11	0.24	0.30
TiO_2	0.10	0.12	0.06	0.13	0.09	0.08	0.10	0.10	0.11	0.10	0.03
V_2O_3	0.02	0.03	0.01	0.03	0.03	0.03	0.04	0.03	0.04	0.03	0.01
Al_2O_3	0.00	0.00	0.00	0.00	0.00	0.00	0.00	0.00	0.02	0.05	0.15
Cr_2O_3	3.94	0.97	0.77	0.22	2.20	1.23	2.69	1.17	1.10	1.50	1.13
Fe_3O_4 (tot)	95.40	98.27	98.25	100.76	98.23	99.06	97.79	96.70	98.28	98.04	1.30
NiO	0.38	0.28	0.23	0.22	0.26	0.31	0.28	0.26	0.22	0.26	0.06
MnO	0.28	0.21	0.15	0.11	0.22	0.17	0.25	0.20	0.15	0.20	0.12
MgO	0.31	0.23	0.80	0.24	0.32	0.22	0.25	0.26	0.26	0.42	0.35
CaO	0.01	0.00	0.02	0.00	0.00	0.00	0.01	0.00	0.00	0.00	0.01
Total	98.96	99.60	99.89	101.46	100.40	100.50	100.31	98.13	99.63	99.91	0.85
Cations per 3 cations											
Ti	0.00	0.00	0.00	0.00	0.00	0.00	0.00	0.00	0.00	0.00	0.00
V	0.00	0.00	0.00	0.00	0.00	0.00	0.00	0.00	0.00	0.00	0.00
Al	0.00	0.00	0.00	0.00	0.00	0.00	0.00	0.00	0.00	0.00	0.01
Cr	0.11	0.03	0.02	0.01	0.06	0.03	0.08	0.03	0.03	0.04	0.03
Fe	2.85	2.94	2.92	2.97	2.90	2.94	2.89	2.94	2.94	2.92	0.04
Ni	0.01	0.01	0.01	0.01	0.01	0.01	0.01	0.01	0.01	0.01	0.00
Mn	0.01	0.01	0.00	0.00	0.01	0.01	0.01	0.01	0.00	0.01	0.00
Mg	0.02	0.01	0.04	0.01	0.02	0.01	0.01	0.01	0.01	0.02	0.02
Site Occupancies											
Sites for 3+											
Al	0.00	0.00	0.00	0.00	0.00	0.00	0.00	0.00	0.00	0.00	0.01
Cr	0.11	0.03	0.02	0.01	0.06	0.03	0.08	0.03	0.03	0.04	0.03
V	0.00	0.00	0.00	0.00	0.00	0.00	0.00	0.00	0.00	0.00	0.00
Ti	0.00	0.00	0.00	0.00	0.00	0.00	0.00	0.00	0.00	0.00	0.00
Fe	1.89	1.97	1.98	1.99	1.94	1.96	1.92	1.96	1.96	1.95	0.04
Sites for 2+											
Fe	0.96	0.97	0.95	0.98	0.97	0.97	0.97	0.97	0.98	0.96	0.02
Mg	0.02	0.01	0.04	0.01	0.02	0.01	0.01	0.01	0.01	0.02	0.02
Ni	0.01	0.01	0.01	0.01	0.01	0.01	0.01	0.01	0.01	0.01	0.00
Mn	0.01	0.01	0.00	0.00	0.01	0.01	0.01	0.01	0.00	0.01	0.00
Mg	0.02	0.01	0.04	0.01	0.02	0.01	0.01	0.01	0.01	0.02	0.02
Fe_2O_3	63.14	65.76	66.46	67.57	65.45	66.20	64.97	64.68	65.68	65.63	1.09
FeO	32.27	32.51	31.79	33.20	32.77	32.86	32.82	32.02	32.60	32.41	0.71

Analysis wt%	CO13-40 a1_1	CO13-40 a1_1	CO13-40 a1_5	CO13-40 a1_5	CO13-40 a1_5	Av	St Dev
SiO_2	0.01	0.04	1.97	0.12	0.05	0.44	0.86
TiO_2	0.15	0.07	0.11	0.06	0.05	0.09	0.04
V_2O_3	0.01	0.02	0.02	0.00	0.02	0.01	0.01
Al_2O_3	0.00	0.00	0.01	0.00	0.00	0.00	0.01
Cr_2O_3	2.11	3.01	0.52	0.48	0.32	1.29	1.20
Fe_3O_4 (tot)	98.23	97.66	95.32	99.12	99.22	97.91	1.58
NiO	0.08	0.02	0.04	0.05	0.02	0.04	0.02
MnO	0.15	0.14	0.09	0.09	0.04	0.10	0.05
MgO	0.18	0.16	2.06	0.14	0.14	0.54	0.85
CaO	0.01	0.04	0.00	0.02	0.00	0.02	0.02
Total	100.94	101.15	100.16	100.14	99.87	100.45	0.56
Cations per 3 cations							
Ti	0.00	0.00	0.00	0.00	0.00	0.00	0.00
V	0.00	0.00	0.00	0.00	0.00	0.00	0.00
Al	0.00	0.00	0.00	0.00	0.00	0.00	0.00
Cr	0.06	0.08	0.01	0.01	0.01	0.04	0.03
Fe	2.92	2.90	2.87	2.97	2.98	2.93	0.05
Ni	0.00	0.00	0.00	0.00	0.00	0.00	0.00
Mn	0.00	0.00	0.00	0.00	0.00	0.00	0.00
Mg	0.01	0.01	0.11	0.01	0.01	0.03	0.05
Site Occupancies							
Sites for 3+							
Al	0.00	0.00	0.00	0.00	0.00	0.00	0.00
Cr	0.06	0.08	0.01	0.01	0.01	0.04	0.03
V	0.00	0.00	0.00	0.00	0.00	0.00	0.00
Ti	0.00	0.00	0.00	0.00	0.00	0.00	0.00
Fe	1.94	1.91	1.98	1.99	1.99	1.96	0.03
Sites for 2+							
Fe	0.98	0.99	0.89	0.99	0.99	0.97	0.05
Mg	0.01	0.01	0.11	0.01	0.01	0.03	0.05
Ni	0.00	0.00	0.00	0.00	0.00	0.00	0.00
Mn	0.00	0.00	0.00	0.00	0.00	0.00	0.00
Mg	0.01	0.01	0.11	0.01	0.01	0.03	0.05
Fe_2O_3	65.15	64.42	65.89	66.17	66.23	65.57	0.77
FeO	33.08	33.23	29.44	32.95	32.98	32.34	1.62

Analysis wt%	CO13-21_a1_2	CO13-21_a1_2	CO13-21_a1_3	CO13-21_a3_1	CO13-21_a3_3	CO13-21_a4_1	CO13-21_a5_1	CO13-21_a6_1	CO13-21_a6_1
SiO_2	0.01	0.05	0.06	0.10	0.08	0.03	0.06	0.13	4.20
TiO_2	0.03	0.06	0.06	0.09	0.10	0.08	0.15	0.04	0.04
V_2O_3	0.03	0.01	0.01	0.03	0.02	0.01	0.04	0.01	0.03
Al_2O_3	0.00	0.00	0.00	0.00	0.00	0.00	0.00	0.00	0.05
Cr_2O_3	0.38	0.55	0.81	1.55	1.52	0.89	3.13	0.37	0.59
Fe_3O_4 (tot)	99.86	100.99	98.45	98.37	97.64	99.30	96.85	99.02	90.23
NiO	0.09	0.07	0.12	0.09	0.08	0.10	0.10	0.08	0.13
MnO	0.31	0.20	0.26	0.32	0.25	0.22	0.36	0.26	0.20
MgO	0.30	0.26	0.33	0.35	0.32	0.32	0.29	0.34	6.06
CaO	0.02	0.06	0.07	0.01	0.00	0.00	0.19	0.00	0.01
Total	101.10	102.26	100.17	100.95	100.14	100.97	101.22	100.27	101.59
Cations per 3 cations									
Ti	0.00	0.00	0.00	0.00	0.00	0.00	0.00	0.00	0.00
V	0.00	0.00	0.00	0.00	0.00	0.00	0.00	0.00	0.00
Al	0.00	0.00	0.00	0.00	0.00	0.00	0.00	0.00	0.00
Cr	0.01	0.02	0.02	0.04	0.04	0.02	0.09	0.01	0.02
Fe	2.96	2.96	2.95	2.92	2.93	2.95	2.88	2.96	2.65
Ni	0.00	0.00	0.00	0.00	0.00	0.00	0.00	0.00	0.00
Mn	0.01	0.01	0.01	0.01	0.01	0.01	0.01	0.01	0.01
Mg	0.02	0.01	0.02	0.02	0.02	0.02	0.02	0.02	0.32
Site Occupancies									
Sites for 3+									
Al	0.00	0.00	0.00	0.00	0.00	0.00	0.00	0.00	0.00
Cr	0.01	0.02	0.02	0.04	0.04	0.02	0.09	0.01	0.02
V	0.00	0.00	0.00	0.00	0.00	0.00	0.00	0.00	0.00
Ti	0.00	0.00	0.00	0.00	0.00	0.00	0.00	0.00	0.00
Fe	1.99	1.98	1.98	1.95	1.95	1.97	1.91	1.99	1.98
Sites for 2+									
Fe	0.97	0.98	0.97	0.97	0.97	0.97	0.97	0.97	0.67
Mg	0.02	0.01	0.02	0.02	0.02	0.02	0.02	0.02	0.32
Ni	0.00	0.00	0.00	0.00	0.00	0.00	0.00	0.00	0.00
Mn	0.01	0.01	0.01	0.01	0.01	0.01	0.01	0.01	0.01
Mg	0.02	0.01	0.02	0.02	0.02	0.02	0.02	0.02	0.32
Fe_2O_3	67.05	67.63	66.00	65.75	65.18	66.49	64.18	66.52	67.34
FeO	32.81	33.36	32.45	32.62	32.46	32.82	32.66	32.50	22.89

Analysis wt%	CO13-21_a6_2	CO13-21_a6_2	CO13-21_a6_2	Av	St Dev
SiO_2	0.33	0.08	0.27	1.00	1.79
TiO_2	0.06	0.18	0.04	0.07	0.06
V_2O_3	0.01	0.03	0.03	0.02	0.01
Al_2O_3	0.00	0.00	0.00	0.01	0.02
Cr_2O_3	0.36	0.54	0.42	0.45	0.10
Fe_3O_4 (tot)	98.51	98.65	100.06	97.29	4.00
NiO	0.09	0.08	0.09	0.09	0.02
MnO	0.17	0.30	0.22	0.23	0.05
MgO	0.62	0.34	0.52	1.58	2.51
CaO	0.03	0.00	0.00	0.01	0.01
Total	100.24	100.25	101.75	100.82	0.78
Cations per 3 cations					
Ti	0.00	0.00	0.00	0.00	0.00
V	0.00	0.00	0.00	0.00	0.00
Al	0.00	0.00	0.00	0.00	0.00
Cr	0.01	0.02	0.01	0.01	0.00
Fe	2.95	2.95	2.95	2.89	0.13
Ni	0.00	0.00	0.00	0.00	0.00
Mn	0.01	0.01	0.01	0.01	0.00
Mg	0.03	0.02	0.03	0.08	0.13
Site Occupancies					
Sites for 3+					
Al	0.00	0.00	0.00	0.00	0.00
Cr	0.01	0.02	0.01	0.01	0.00
V	0.00	0.00	0.00	0.00	0.00
Ti	0.00	0.00	0.00	0.00	0.00
Fe	1.99	1.98	1.99	1.98	0.00
Sites for 2+					
Fe	0.96	0.97	0.96	0.91	0.13
Mg	0.03	0.02	0.03	0.08	0.13
Ni	0.00	0.00	0.00	0.00	0.00
Mn	0.01	0.01	0.01	0.01	0.00
Mg	0.03	0.02	0.03	0.08	0.13
Fe_2O_3	66.46	66.20	67.38	66.78	0.54
FeO	32.06	32.45	32.68	30.52	4.27

wt%	Co14-03 area1_mt1_2_nrchl	Co14-03 area1_mt1_2_nrchl	Co14-03 area1_mt1_2_nrchl	Co14-03 area1_mt1_2_nrchl	Co14-03 area1_mt1 rim	Co14-03 area1_mt1 rim	Co14-03 area1_mt1 rim	CO14-03 core	CO14-03 core
SiO_2	0.12	0.12	0.12	0.10	0.02	0.01	0.03	0.13	0.12
TiO_2	0.13	0.11	0.13	0.23	0.13	0.10	0.24	0.00	0.04
Al_2O_3	0.00	0.00	0.00	0.00	0.00	0.00	0.00	0.00	0.00
Cr_2O_3	0.00	0.02	0.01	0.00	0.01	0.00	0.00	0.00	0.00
V_2O_3	0.25	0.26	0.28	0.27	0.12	0.12	0.14	0.24	0.21
Fe_3O_4	100.50	101.25	101.36	101.06	102.35	101.20	101.28	101.34	102.26
MnO	0.10	0.08	0.04	0.04	0.02	0.01	0.03	0.07	0.04
MgO	0.06	0.07	0.04	0.04	0.02	0.03	0.05	0.05	0.04
NiO	0.00	0.01	0.00	0.00	0.02	0.02	0.02	0.03	0.00
CaO	0.04	0.03	0.02	0.08	0.04	0.01	0.09	0.00	0.00
Na_2O	0.01	0.02	0.00	0.00	0.00	0.00	0.00	0.00	0.00
K_2O	0.00	0.00	0.00	0.00	0.00	0.00	0.00	0.00	0.00
Total	100.95	101.69	101.75	101.52	102.59	101.38	101.7	101.7	102.5
Cations per 3 cations									
Sites for 3+									
Al	0.00	0.00	0.00	0.00	0.00	0.00	0.00	0.00	0.00
Cr	0.00	0.00	0.00	0.00	0.00	0.00	0.00	0.00	0.00
V	0.01	0.01	0.01	0.01	0.00	0.00	0.00	0.01	0.01
Ti	0.00	0.00	0.00	0.01	0.00	0.00	0.01	0.00	0.00
Fe	1.87	1.87	1.87	1.86	1.88	1.88	1.87	1.87	1.87
Sites for 2+									
Fe	0.99	0.99	1.00	1.00	1.00	1.00	1.00	0.99	1.00
Ni	0.00	0.00	0.00	0.00	0.00	0.00	0.00	0.00	0.00
Mn	0.00	0.00	0.00	0.00	0.00	0.00	0.00	0.00	0.00
Mg	0.01	0.00	0.00	0.00	0.00	0.00	0.00	0.00	0.00
Fe3+	0.63	0.63	0.63	0.63	0.63	0.63	0.63	0.63	0.63
Fe2+	0.33	0.33	0.34	0.34	0.33	0.33	0.33	0.33	0.33
Fe_2O_3	63.25	63.69	63.66	63.42	64.41	63.69	63.68	63.8	64.3
FeO	37.24	37.56	37.70	37.64	37.94	37.51	37.60	37.5	38.0

wt%	CO14-03 core	CO14-03 core	CO14-03 core	CO14-03 core	CO14-03 core	CO14-03 core	CO14-03 core	CO14-03 core	CO14-03 core	CO14-03 core	CO14-03 core
SiO_2	0.03	0.05	0.02	0.00	0.01	0.10	0.07	0.10	0.02	0.03	0.06
TiO_2	0.04	0.03	0.03	0.03	0.01	0.04	0.01	0.03	0.01	0.04	0.07
Al_2O_3	0.00	0.00	0.00	0.00	0.00	0.00	0.00	0.00	0.00	0.00	0.00
Cr_2O_3	0.04	0.03	0.01	0.01	0.00	0.01	0.01	0.00	0.01	0.00	0.01
V_2O_3	0.25	0.25	0.25	0.12	0.30	0.18	0.20	0.18	0.13	0.13	0.20
Fe_3O_4	102.0	101.6	101.3	101.5	101.7	101.5	101.3	102.1	102.3	101.7	101.6
MnO	0.01	0.05	0.09	0.05	0.10	0.09	0.05	0.07	0.03	0.01	0.05
MgO	0.05	0.06	0.06	0.03	0.05	0.06	0.04	0.05	0.03	0.05	0.05
NiO	0.01	0.00	0.00	0.08	0.00	0.00	0.03	0.01	0.00	0.00	0.01
CaO	0.01	0.01	0.00	0.01	0.01	0.01	0.00	0.00	0.00	0.01	0.02
Na_2O	0.00	0.01	0.00	0.00	0.00	0.00	0.00	0.01	0.00	0.03	0.00
K_2O	0.00	0.00	0.00	0.00	0.00	0.00	0.00	0.00	0.00	0.00	0.00
Total	102.31	101.89	101.55	101.77	102.05	101.79	101.60	102.35	102.45	101.90	101.86
Cations per 3 cations											
Sites for 3+											
Al	0.00	0.00	0.00	0.00	0.00	0.00	0.00	0.00	0.00	0.00	0.00
Cr	0.00	0.00	0.00	0.00	0.00	0.00	0.00	0.00	0.00	0.00	0.00
V	0.01	0.01	0.01	0.00	0.01	0.01	0.01	0.01	0.00	0.00	0.01
Ti	0.00	0.00	0.00	0.00	0.00	0.00	0.00	0.00	0.00	0.00	0.00
Fe	1.88	1.88	1.88	1.89	1.88	1.88	1.88	1.88	1.88	1.88	1.88
Sites for 2+											
Fe	1.00	1.00	0.99	0.99	0.99	0.99	0.99	0.99	1.00	1.00	1.00
Ni	0.00	0.00	0.00	0.00	0.00	0.00	0.00	0.00	0.00	0.00	0.00
Mn	0.00	0.00	0.00	0.00	0.00	0.00	0.00	0.00	0.00	0.00	0.00
Mg	0.00	0.00	0.00	0.00	0.01	0.01	0.00	0.00	0.00	0.00	0.00
Fe3+	0.63	0.63	0.63	0.63	0.63	0.63	0.63	0.63	0.63	0.63	0.63
Fe2+	0.33	0.33	0.33	0.33	0.33	0.33	0.33	0.33	0.33	0.33	0.33
Fe_2O_3	64.15	63.94	63.86	64.08	64.17	63.95	63.84	64.30	64.45	63.99	63.93
FeO	37.88	37.64	37.40	37.46	37.55	37.53	37.51	37.78	37.85	37.71	37.63

The data was collected using electron microprobe analysis (EMPA). The percent relative analytical uncertainty (2σ) is $\leq \pm 2\%$ for elements in silicates, sulfides and oxides present at concentrations >5 wt%.

C9: Highly siderophile element data for spinels

Analysis (ppm)	Os max	Os min	Ir max	Ir min	Ru max	Ru min	Rh max	Rh min	Pt max	Pt min	Pd max	Pd min	Au max	Au min	Re max	Re min
CO13-31 mt5-1	<0.033	<0.021	<0.0065	<0.0054	<0.027	<0.0074	<0.019	<0.0052	<0.016	<0.0044	<0.022	<0.012	<0.028	<0.0078	<0.029	<0.005
CO13-31 mt5-2	<0.033	<0.021	<0.013	<0.0041	<0.020	<0.0063	<0.021	<0.0066	<0.033	<0.010	<0.013	<0.0042	<0.017	<0.0053	<0.023	<0.0070
CO13-31 mt5-3	<0.033	<0.032	<0.0066	<0.0064	<0.0095	<0.0092	<0.0089	<0.0086	<0.017	<0.017	<0.022	<0.012	<0.016	<0.015	<0.029	<0.005
CO13-31 mt5-4	<0.013	<0.0054	<0.0030	<0.0012	<0.028	<0.012	<0.0043	<0.0018	<0.022	<0.0092	<0.022	<0.012	<0.0053	<0.0022	<0.011	<0.0053
CO13-31 mt5-5	<0.033	<0.021	<0.0058	<0.0054	<0.020	<0.018	<0.0064	<0.0060	<0.013	<0.012	<0.015	<0.014	<0.019	<0.015	<0.029	<0.005
CO13-31 mt5-6	<0.033	<0.0210.	<0.028	<0.0077	<0.080	<0.022	<0.025	<0.0068	<0.048	<0.013	<0.053	<0.015	<0.044	<0.012	<0.029	<0.005
CO13-31 mt2-1	<0.012	<0.0038	<0.0065	<0.0054	<0.019	<0.018	<0.0077	<0.0070	<0.014	<0.012	<0.013	<0.012	<0.011	<0.010	<0.029	<0.005
CO13-31 mt2-5	<0.025	<0.023	<0.0058	<0.0054	<0.052	<0.041	<0.0070	<0.0065	<0.0053	<0.0050	<0.0060	<0.0056	<0.012	<0.011	<0.0185	
CO13-31 mt2-7	<0.012	<0.011	<0.0084	<0.0078	<0.0091	<0.0085	<0.0062	<0.0058	<0.015	<0.014	<0.020	<0.019	<0.0035	<0.0032	<0.029	<0.005
CO13-31 mt2-8	<0.037	-	<0.0055	-	<0.028	<0.028	<0.060	-	<0.016	-	<0.017	-	<0.015	-	<0.029	-
CO13-31 mt3-1	<0.026	-	<0.0045	-	0.022	-	<0.0049	-	<0.019	-	<0.0062	-	<0.0058	-	<0.029	-
CO13-31 mt3-2	<0.024	<0.022	<0.0061	<0.0056	<0.019	<0.016	<0.010	<0.0094	<0.012	<0.011	<0.0063	<0.0058	<0.015	<0.014	<0.029	<0.005
CO13-31 mt4-2	<0.027	<0.025	<0.0079	<0.0073	<0.0089	<0.0082	<0.0070	<0.0064	<0.016	<0.015	<0.0059	<0.0055	<0.0067	<0.0062	<0.0096	
CO13-31 mt4-3	<0.025	-	<0.0050	-	<0.020	-	<0.0087	-	<0.011	-	<0.019	-	<0.0074	-	<0.020	-
CO13-31 mt4-4	<0.044	<0.0411	<0.0030	<0.0028	<0.010	<0.095	<0.0066	<0.0061	<0.0060	<0.0057	<0.0067	<0.0063	<0.0053	<0.050	<0.011	
CO13-31 mt1-1	<0.11	<0.031	<0.021	<0.0060	<0.11	<0.031	<0.034	<0.0098	<0.054	<0.015	<0.057	<0.016	<0.041	<0.012	<0.085	<0.0024
CO13-31 mt1-2	0.72285	0.1725	0.5214	0.11	1.19	0.29	0.14	0.03335	0.062	0.015	0.24885	0.05865	<0.0083	<0.033	<0.091	<0.025
CO13-31 mt2-1-1	<0.043	-	<0.0079	-	<0.46	-	<0.0061	-	<0.0096	-	<0.018	-	<0.014	-	<0.029	-
CO13-31 mt2-1-2	<0.030	-	<0.0048	-	0.009	-	<0.0085	-	<0.0059	-	<0.0066	-	<0.0062	-	<0.024	-
CO13-33-m1 - 1	<0.033	<0.033	<0.0076	<0.0036	0.0059	<0.017	0.0094	0.004	<0.028	<0.013	0.025	0.0077	<0.020	<0.0010	<0.029	<0.024
CO13-33-m1 - 2	<0.049	<0.023	<0.0061	<0.0029	0.0037	<0.010	<0.011	<0.0051	<0.022	<0.011	<0.014	<0.0067	<0.016	<0.0075	<0.018	<0.009
CO13-33-m1 - 3	<0.021	<0.010	<0.010	<0.0050	0.0069	0.0027	<0.0069	<0.0033	<0.019	<0.011	<0.020	<0.0095	<0.036	<0.017	<0.012	<0.006
CO13-33-m1 - 4	<0.033	<0.021	<0.009	<0.0043	0.0095	0.0045	0.0490	0.0204	<0.0067	<0.0032	<0.065	<0.031	<0.025	<0.012	<0.029	<0.024
CO13-33-m1 - 5	<0.033	<0.021	<0.011	<0.0055	<0.262	<0.125	<0.0088	<0.0042	<0.036	<0.017	<0.038	<0.018	<0.088	<0.042	<0.029	<0.024

Analysis (ppm)	Os max	Os min	Ir max	Ir min	Ru max	Ru min	Rh max	Rh min	Pt max	Pt min	Pd max	Pd min	Au max	Au min	Re max	Re min
CO13-33-m1 - 8	<0.143	<0.068	<0.023	<0.011	<0.0331	<0.016	<0.016	<0.0076	<0.062	<0.030	<0.036	<0.0174	<0.063	<0.030	<0.067	<0.032
CO13-33-m1 - 9	<0.082	<0.039	<0.013	<0.0064	<0.0181	<0.0087	0.0172	0.0082	<0.013	<0.0063	<0.0351	0.0168	<0.039	<0.019	<0.029	<0.024
CO13-33-m1 - 10	<0.060	<0.029	<0.019	<0.0092	<0.091	<0.071	<0.0133	<0.0063	<0.040	<0.019	<0.047	<0.023	<0.047	<0.022	<0.029	<0.024
CO13-33-m1 - 11	<0.203	<0.176	<0.0063	<0.0030	<0.0377	<0.018	<0.0157	<0.0075	<0.041	<0.020	<0.044	<0.021	<0.035	<0.017	<0.016	<0.097
CO13-33-m1 - 12	<0.043	<0.021	<0.039	<0.029	0.476	0.227	<0.022	<0.011	<0.042	<0.020	<0.079	<0.038	<0.095	<0.045	<0.029	<0.024
CO13-33-s2 - 4	<0.714	<0.567	<0.177	<0.141	<0.533	<0.423	<0.106	<0.084	<0.393	<0.312	<0.234	<0.186	<0.353	<0.280	<0.016	<0.007
CO13-33-s2 - 5	<0.876	<0.696	<0.114	<0.090	<0.071	<0.071	<0.157	<0.124	<0.380	<0.302	<0.284	<0.226	<0.394	<0.313	<0.024	<0.011
CO13-33-m2 - 7	<0.023	<0.019	<0.008	<0.006	<0.029	<0.023	<0.009	<0.0157	<0.009	<0.007	<0.009	<0.007	<0.056	<0.044	<0.024	<0.012
CO13-33-m2 - 9	<0.032	<0.026	<0.0149	<0.0059	<0.026	<0.021	<0.015	<0.012	<0.019	<0.015	<0.017	<0.014	<0.030	<0.024	<0.035	<0.017
CO13-33-s2 - 28	<0.095	<0.075	<0.015	<0.012	<0.059	<0.047	<0.011	<0.0089	<0.017	<0.013	<0.058	<0.046	<0.027	<0.021	<0.043	<0.021
CO13-33-s2 - 29	<0.131	<0.104	<0.028	<0.022	0.0049	0.0033	<0.019	<0.015	<0.066	<0.052	<0.075	<0.059	<0.047	<0.038	<0.029	<0.024
CO13-33-s2 - 34	<0.035	<0.034	<0.014	<0.014	<0.071	<0.071	<0.015	<0.015	<0.033	<0.032	<0.023	<0.023	<0.014	<0.013	<0.029	<0.0240.

The < symbol indicates the concentration is below the detection limit, where the number following the < symbol is the detection limit. (-) indicates where there is no minimum value, i.e. the spinel has homogenous Fe, so the value provided in 'maximum' is the true value.

The analytical error on all HSE analyses where the element >1 ppm ranges from 10–25% relative analytical uncertainty (2σ), with larger errors reported for Pt.

C10: Complete petrographic descriptions of Sierra di Pigno serpentinites and Capu Corvoli hybrid mafic/ultramafic rocks.

Sample distal to contacts: CO13-31

CO13-31 contains lizardite (15%), 67% antigorite (57% atg1 and 10% atg2), chlorite (5%), chromite (2%), magnetite (7%), minor silicate veins (1%) including compositionally variable Mg-Mn-Fe hydrous silicates (balangeroite, $(Mg, Fe^{2+}, Fe^{3+}, Mn^{2+})_{42}Si_{16}O_{54}(OH)_{40}$) that range from the Mn-rich to the Fe-rich endmember, heazlewoodite (2%), pentlandite (1%), and trace Pt-alloys.

Lizardite (15%) is comprised of radiating and coarse laths (~0.1–0.3 mm by 0.05–0.2mm), consistent with bastite textures previously described in the replacement of pyroxene by lizardite (e.g. Schwarzenbach et al., 2012), which, due to the Al-poor composition of the sample, was probably orthopyroxene. The cleavage of bastite is outlined by fine (1 µm in diameter) balangeroite and early magnetite (mt1) veins (see below). The early generation of antigorite (atg1, 57%) defines the foliation and comprises fine grained, orientated matrix platy and needle antigorite grains, (<3 µm in diameter) and overprints lizardite. Atg2 (10%) is present as a network of ~10 µm or less antigorite veins cross-cutting atg1. Balangeroite veins (1–2 µm in diameter, analysed by EDS) form along the margins of atg2 veins. Two types of chlorite occur in this sample; one with blue anomalous birefringence and another with brown anomalous birefringence, but the two types occur in identical textural settings and thus are not distinguished in the mineral paragenesis (Electronic Appendix 9). Both types of chlorite occur as a rim on magnetite (mt1), and overprint both atg1 and some chlorite overprints atg2 and balangeroite veins.

Cr-Al spinel can be seen in reflected light as darker grey cores in grey-white magnetite (mt1, 4%). Mt1 grains also occur as rims on bastite grains, contains inclusions of atg1, and are partially replaced by chlorite. A later generation of magnetite, mt2, (3%) is associated with, or occurs as inclusions in, atg2 veins, and some (<1%) are aligned along balangeroite veins.

Heazlewoodite and pentlandite co-exist with, or contain inclusions of, euhedral mt1. Heazlewoodite is ~50–100 µm in diameter and is associated with or overprinted by atg2 and, in places, balangeroite veins (Fig. 4.2d). A small proportion (less than

10%) of heazlewoodite grains include ~30 µm grains of millerite (Fig 4.2e). Pentlandite occurs on the edges of heazlewoodite grains, overprints atg2 and contains inclusions of mt2 and atg1. Feature mapping revealed 2–5 µm Pt-rich metal alloys on the rim of two heazlewoodite grains, (Fig. 4.2n), and Co-rich pentlandite (>10 wt% Co) along a atg2 vein.

Sample distal to contacts: CO13-40

CO13-40 is from a serpentinite ridge ~0.5 km south of Serra di Pigno and consists of chrysotile (5%), lizardite (15%), omphacite grains (trace), andradite (2%), fine antigorite laths (45%), chlorite (3%), coarse antigorite laths (10%), Fe-rich to Ni-rich serpentine veins (<1%), Mg-Fe-Ni balangeroite veins (<1%). Oxide phases include Cr-spinel (5%), magnetite (10%), and ilmenite (~3%). Sulphide phases consist of pentlandite (2%), chalcopyrite (trace) and Cu-rich alloys (trace).

Large chrysotile laths (200–500 µm), are overprinted by lizardite pseudomorphs of primary orthopyroxene or 'bastite' and trace omphacite grains associated with lizardite (~5–15 µm). Andradite (200–500 µm) occurs as rims on lizardite pseudomorphs and trace omphacite grains. A fine orientated antigorite matrix (atg1) defines the predominant foliation and consists of <1 to ~5 µm laths which overprint chrysotile and lizardite, and is overprinted by coarse antigorite laths (up to 30 µm across), which have a weak preferred orientation, in addition to Fe-rich to Ni-rich serpentine and Mg-Fe-Ni rich balangeroite veins (both of which are <5 µm). In this sample, balangeroite is not associated with antigorite veins, and coarse antigorite is texturally later, thus it is named atg3 (instead of atg2, which is associated with balangeroite). Fine chlorite needles (~2–3 µm) occur within outer rims of eccentrically zoned Cr-spinel-magnetite grains and larger laths (>10 µm) overprint mt1 rims.

Opaque phases consist of 1–2.5 mm magnetite grains (mt1) with Cr-Al rich spinel cores. In these grains, magnetite also cuts through Cr-Al rich cores in the form of ~5 µm veins. Cr-rich spinel also occurs as porous grains infilled with antigorite. Some of the porous spinel grains are concentrically zoned and comprise alternating Fe and Cr-rich bands, with Fe-rich cores. Mt1 also occurs as skeletal magnetite (~10 µm, trace). Mt1 and ilmenite (~3%) are both present within the antigorite matrix. Texturally later magnetite grains (~20 µm, mt2) are found within coarse antigorite laths, but these

appear to be connected to the matrix, and are thus proposed to be synchronous with or grew after atg3.

Minor sulphide phases include chalcopyrite (~1–5 µm) within porous Cr-spinel. The dominant sulphide phase is pentlandite, which is found as grains up to ~50 µm that contain inclusions of atg1, and are overprinted by late atg3 laths (Fig. 4.2f). Some pentlandite rims also are more enriched in Co and As, and thus appear darker in reflected light (Fig. 4.2f).

Sample proximal to psammite and calcareous schist: CO13-21

Sample CO13-21 is a sheared ultramafic sample proximal to calcareous schist consisting of lizardite (20%), fine antigorite (50%) and coarse antigorite laths (10%), andradite garnet (1%). Cr-spinel (3%) and magnetite (7%), diopside (7%) and pentlandite (2%).

Lizardite is of two textural types. One type has a mesh structure (lz1, 12%) which is consistent with textures described to occur from lizardite pseudomorphs of olivine (e.g. Wicks and Whittaker, 1977). The other type consists of fine grained, randomly orientated laths (lz2, 8%) which overprints lz1. Andradite garnet is found as rims on mt1, and are ~50–300 µm in size. Fine, interlocking light green-brown antigorite (atg1) comprises the matrix and defines the foliation, which is overprinted by coarse, cross-cutting antigorite laths (atg3, as for CO13-40) with a kink-banded texture. Diopside is comprised of grains up to ~200 µm in diameter, and is overprinted by atg3 and a later generation of magnetite, mt2, (described below), where its cleavage it is outlined by mt2 grains.

Spinel is comprised of two dominant types; variably altered porous Cr-rich porous cores with pure magnetite rims (mt1), up to ~250 µm in diameter, and 'network' magnetite comprised of orientated clasts of magnetite associated with atg2, from ~1 µm to >75 µm (mt2). Mt2 contains inclusions of or is overprinted by atg3, which also overprints earlier generations of lizardite and atg1.

An early generation of pentlandite (pn1) is aligned and included in atg1, and consists of small, euhedral grains ~1–5 µm in size (pn1). Larger grains of pentlandite (~10–50 µm in diameter, pn2) are associated with or are overprinted by mt2 grains,

and contain inclusions of atg3, though these appear to be connected to the matrix via fractures (Fig. 4.2g), and millerite.

Sample proximal to metagabbro and metaquartzite: CO13-33

CO13-33 is proximal to metagabbro and metaquartzite and contains fine antigorite (atg1, 20%), chlorite (13%), coarse antigorite veins (atg2, 30%), fine antigorite veins (atg4, 10%), magnetite (10%), pentlandite (5%), chromite (2%), trace heazlewoodite, trace 1 µm veins of Fe-Ni to Fe rich serpentine, trace Mg-Fe-Mn-Ni to Mg-Fe balangeroite, trace kamacite (Fe-rich end member of Fe-Ni alloys) and trace chalcopyrite.

Fine grained foliated antigorite (atg1, <1–6 µm) comprises most of the matrix and pseudomorphs pyroxene, where given the low Al bulk composition and 90º cleavage, the pyroxene is most likely to have been orthopyroxene. Chlorite is pleochroic brown-green in ppl, with brown anomalous birefringence in xpl and replaces mt1 and chromite. Coarse antigorite veins, atg2, are ~95 µm across, within which are fine (1–2 µm across) Mg-Ni-rich silicate veins with brighter (in terms of BSE signal) ~5 µm kamacite grains. Fe-rich serpentine and Mg-Fe-Ni-Mn balangeroite veins are found outlining cleavage planes in orthopyroxene pseudomorphs, and are hosted in atg2 veins, where both balangeroite and atg2 cross-cut the atg1 defined foliation. A late generation of antigorite, atg4, occur as fine veins (<0.5 µm across) that cut atg1 and atg2 at angles of ~75°.

Oxide phases consist of Cr-Al spinel cores, porous spinel and magnetite. Cr-rich porous spinel (2%) occurs as cores to porous Fe-rich spinel and mt1 grains and as mt1-chromite lamellae. Magnetite is of two distinct types; one that forms rims and cuts chromite in the form of 'veins' within large magnetite boudins (mt1, 2%), which are overprinted by chlorite, and the other (mt2) replaces a second generation of pentlandite, pn2 at the rim.

Sulphides are present as trace chalcopyrite, pentlandite (which consists of three generations from pn1–3) and trace heazlewoodite. Trace chalcopyrite (<1 µm) is included in Cr-rich spinel. Trace heazlewoodite (1–2 µm in diameter) is associated with balangeroite veins included in atg2. Pn1 (1%) are elongate grains (~5 µm, Fig. 4.2h), associated with atg2. Pn2 (2%) are ~30-50 µm in size, and replace chromite,

mt1 and chlorite (Fig. 4.2i). Pn3 are euhedral grains in the matrix, ~35 µm and overprint atg2 and atg4 veins (Fig. 4.2j).

Sample proximal to calcschist, breccia and metagabbro: CO13-55

CO13-55 is proximal to calcschist and metagabbro and contains ~20% fine antigorite, atg1, 30% atg3 and 10% atg5), 13% diopside, 10% magnetite, 7% chlorite, 6% chromite, 2% pentlandite, 2% andradite garnet and <1% ilmenite, pyrite and chalcopyrite.

Andradite garnet is dark brown in ppl and appears as aggregates, which comprise grains of up to 100 µm in diameter. An early generation of andradite occurs as rims on mt1 on Cr-rich spinel porous grains (grt1). Atg1 (20%) is fine grained matrix antigorite, and probable olivine pseudomorphs are observed Atg3 (30%) occurs as coarse laths associated with diopside, although some is overprints diopside and cuts chlorite. Atg5 (10%) consists of coarse veins cross cutting atg1 and atg3 with grey anomalous birefringence, and is found adjacent to diopside and magnetite veins (mt2). Chlorite is of two dominant types. Chl1 (2%) has blue birefringence and occurs as small interlocking needles/laths (individual grains indistinguishable to 2–3 µm) within small lenses in veins of atg3. Chl2 (5%) has brown birefringence and occurs as laths up to 500 µm in diameter associated with atg3 in addition to finer grains (~10 µm) where chl2 overprints mt1 and atg1. Diopside occurs as randomly orientated idioblastic prisms (~50–250 µm across), as needles (<10 µm across), and as veins, where both forms overprint or cut atg1. Garnet is dark brown in colour and appears as aggregates, which comprise grains of up to 100 µm in diameter. A late generation of andradite garnet is associated with ilmenite and atg5 veins (grt2).

Porous Cr-rich spinel occurs as cores to mt1, is ~20–50 µm in diameter, and Cr-spinel and mt1 contain atg1 inclusions. Ilmenite and a late generation of magnetite, mt2, are associated with or overprinted by the late generation of antigorite, atg5.

Sulphides include pentlandite (pn1–4), pyrite and chlacopyrite. Pn1 (<1%) consist of euhedral grains ~5 µm in diameter which are included in mt1 on rims of Cr-rich spinel. Pyrite grains (<5 µm, <1%) occur as rims on, and are in textural equilibrium with, mt1 grains (Fig. 4.2a) and are also included in atg3 and diopside with chalcopyrite. Pn2 is comprised of larger grains 10–30 µm in diameter, contain

small chromite grains (2–3 µm) and overprints or is in equilibrium with mt1 but is itself cut by atg2. Pn3 is associated with or overprinted by magnetite (mt2), atg3 and diopside 'veins' through atg1 (1%, 10–30 µm, Fig. 4.2k). Pn4 occurs as euhedral grains ~50 µm in diameter which overprint atg3 and overprints or is synchronous with atg5 veins (1%, Fig. 4.2l).

Petrographic analysis of Capu Corvoli hybrid mafic/ultramafic samples

Sample below contact with metagabbro: CO14-03

CO14-03 is a retrogressed 'hybrid' ultramafic/mafic rock proximal to metagabbro and calcareous schist. The sample consists of chlorite (~45%, ~40% chl1 and 5% chl2), antigorite (5%), magnetite (15%), talc (10%), actinolite (7%), pyrite (5%) and titanate (3%).

Chl1 has blue anomalous birefringence, and defines a planar fabric consisting of preferentially orientated laths ~50–500 µm in length, ~25–50 µm across, which comprise most of the matrix. Small veins of antigorite that occur as fine layers (<10 µm in diameter) dispersed in chlorite. Actinolite consists of elongated grains ~25–50 µm in diameter, and are aligned with chl2. Chl2 is comprised of local veins up to ~60 µm in diameter that cross-cut magnetite grains. Talc occurs as rims on magnetite and as veins which also cut magnetite (~30 µm in diameter).

Magnetite consists of large 1–5mm euhedral grains which cut the chlorite-defined fabric but magnetite has undergone brittle deformation during a later event. Titanite occurs as ~2–5 µm inclusions in magnetite and throughout the matrix (up to ~30 µm) (Fig. 4.2c).

Pyrite exists as euhedral aggregates (~50–100 µm) on the rims of large magnetite grains (~3%, Fig. 4.2m) and within magnetite (<1%), although these are associated with fractures in magnetite. Matrix pyrites (30–1000 µm, ~2%) are relatively euhedral and either occur as single grains or as aggregates. Most pyrite grains have an iron hydroxide rim (Fig. 4.2c).

Sample above contact with metagabbro: CO14-04

CO14-04 is a metasomatised ultramafic proximal to metagabbro and calcareous schist comprised of talc (60%), Cr-spinel (2%), magnetite (3%), chlorite (15%), spinel (5%), pyrite (15%), and trace pyrrhotite.

Fine grained talc (talc1) is the dominant matrix mineral, where individual talc grains are indistinguishable (50%). Chlorite (~50–700 µm in diameter) is dispersed irregularly in the matrix, and cuts and overprints chromite grains with a Fe-rich rim (15%, 50–100 µm, Fig. 4.2m). Coarse talc (~100 µm, talc2) pseudomorphs a pre-existing euhedral magnetite phase and cross-cuts talc1 (10%).

Spinel grains are ~40–100 µm, and contain Cr-Al rich spinel cores (2%) and pure magnetite rims (3%). There are two texturally distinct forms of pyrite (py1 and py2). Py1 grains (5%) are ~70–100 µm in size, contain inclusions of Cr-rich spinel (~5 µm) pyrrhotite (po1, ~1-2 µm, Fig. 4.2m), and near the py1 rim, a Pt-bearing alloy (Fig. 4.2n). Py1 grains have an iron hydroxide rim with ~5–10 µm inclusions of pyrrhotite (po2, Fig. 4.2b). Py2 (10%) occurs as large euhedral grains, (50–300 µm) which cuts the chlorite-talc1 matrix and appear to have undergone brittle deformation. Py2 has a talc rim (Fig. 4.2m) and contains inclusions of talc that are up to 50 µm in diameter, though these are connected to the matrix.

C11: Mineral Parageneses

CO13-31

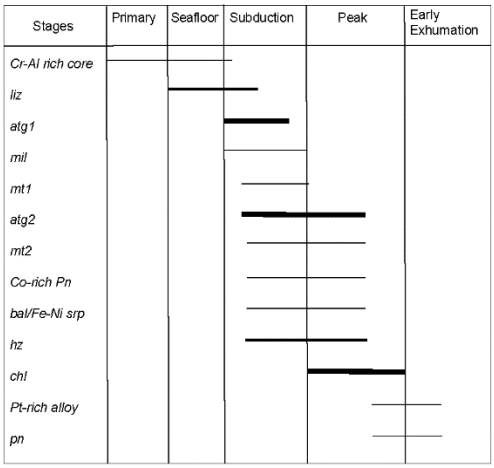

CO13-40

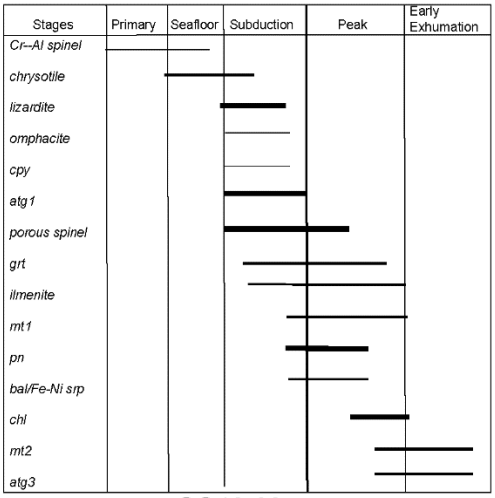

CO13-21

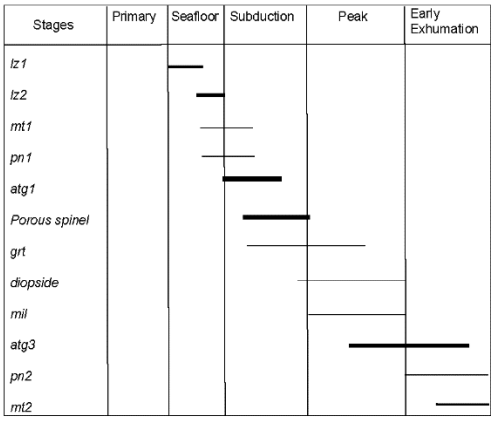

CO13-33

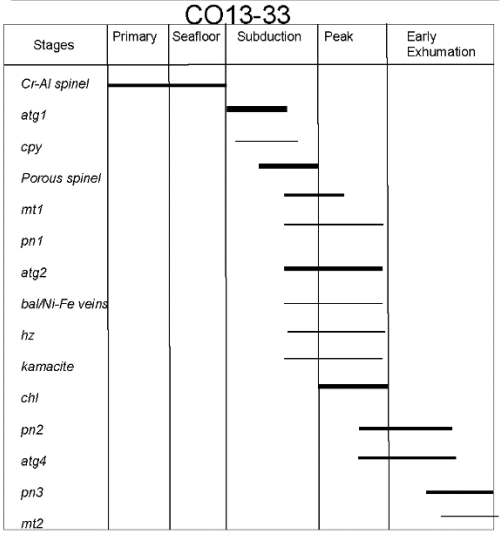

CO13-55

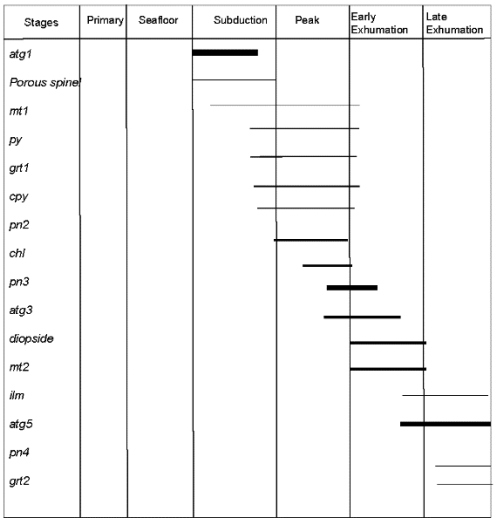

CO14-03

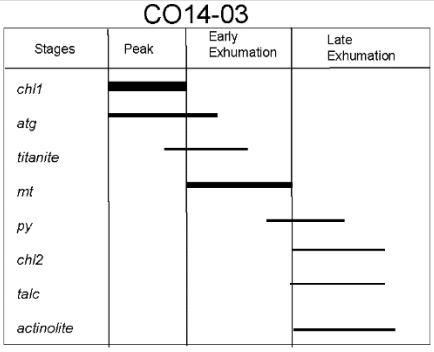

CO14-04

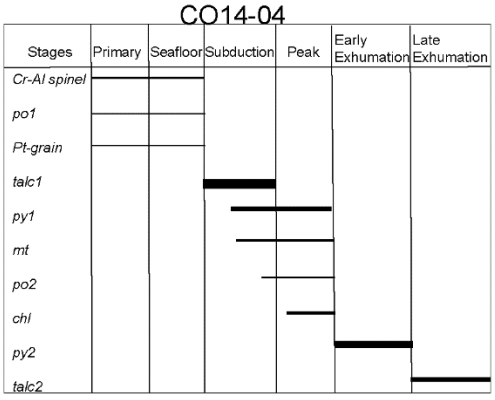

C12: Limits of detection for LA-ICP-MS: Data and Methods

Limits of Detection Method

The limits of detection (LOD) were calculated in Iolite using the Iolite 3.4 Trace Elements DRS, which uses the method described in Longerich et al. 1996, summarised below.

$$\text{LOD is defined as } [\ 3 \times 1\sigma(\text{background}) \times \sqrt{(1/nb + 1/na)}\ ] / S$$

Here, 1σ(background) is 1 standard deviation of the background measurement for this element (noise), nb is the number of measurements in the background integration, na is the number of measurements in the sample integration, and, S is sensitivity, which is defined below.

$$S = (R\_ancal/C\_ancal) * (R\_ISsam/R\_IScal \times C\_IScal/C\_ISsam)$$

The two terms, R_ancal and C_ancal define the amount of each element in the standard and the sensitivity of the machine to the element, and combined to give units of cps/ppm. Thus, if it is known that there is a high concentration of an element in the standard but the count rates are low then the sensitivity is low. R_ancal is the count rate of the analyte (e.g. ^{105}Pd) in the calibration standard (e.g. Laflamme po726). The units are cps. C_ancal is the concentration of the analyte in the calibration standard (in ppm in the case of the data presented in this thesis).
R_ISsam is the count rate of the internal standard (IS) isotope (i.e. ^{56}Fe for spinel and most sulphides) in the sample. R_IScal is the count rate of the internal standard (IS) isotope (^{56}Fe) in the calibration standard. C_IScal is the concentration of the IS isotope in the calibration standard, and C_ISsam is the concentration of the (IS) isotope in the sample, and is derived from the Internal Standard Wave. This second half of the equation could be rearranged to:

$$(R\_ISsam/C\_ISsam \div R\_IScal/C\_IScal)$$

R_ancal and C_ancal count rates are derived from the splines of the standard. R_ancal is derived from the current element spline over the sample integration period (e.g., ^{105}Pd). R_IScal is derived from the internal standard element over the sample integration period (i.e. ^{56}Fe). The average counts for the internal standard give R_ISsam.

REFERENCE

Longerich, H. P., S. E. Jackson, et al. (1996). "Laser Ablation Inductively Coupled Plasma Mass Spectrometric Transient Signal Data Acquisition and Analyte Concentration Calculation." *Journal of Analytical Atomic Spectrometry* **11** (9) pp. 899 - 904.

Detection Limits for sulphide LA-ICP-MS analyses

po726

ppm	Os	Ir	Ru	Rh	Pt	Pd	Au
CO13-31							
CO13-31-s1 - 1	0.043	0.014	0.014	0.015	0.022	0.027	0.018
CO13-31-s2 - 2	0.003	0.002	0.006	0.002	0.005	0.005	0.002
CO13-31-s3 - 2	0.012	0.009	0.033	0.011	0.014	0.017	0.013
CO13-31-s4 - 4	0.017	0.005	0.013	0.004	0.005	0.006	0.062
CO13-s5 - 5.d	0.009	0.004	0.004	0.004	0.009	0.006	0.006
CO13-s5 - 6.d	0.004	0.003	0.010	0.004	0.005	0.012	0.004
CO13-31-s6 - 4	0.025	0.003	0.013	0.005	0.014	0.010	0.009
CO13-31-s7 - 4	0.038	0.003	0.012	0.003	0.008	0.007	0.004
CO13-31-s7 - 6	0.004	0.003	0.005	0.004	0.005	0.018	0.003
CO13-33							
CO13-33-s1 - 2.d	0.032	0.008	0.025	0.012	0.017	0.016	0.013
CO13-33-s2 - 13	0.024	0.006	0.043	0.005	0.017	0.006	0.017
CO13-33-s2 - 18	0.013	0.004	0.015	0.009	0.009	0.016	0.009
CO13-33-s2 - 23	0.037	0.007	0.026	0.008	0.025	0.017	0.028
CO13-33-s3 - 2.d	0.036	0.004	0.025	0.006	0.009	0.016	0.017
CO13-33-s4 - 3.d	0.016	0.009	0.025	0.007	0.018	0.016	0.008
CO13-33-s4 - 8.d	0.058	0.004	0.016	0.014	0.020	0.023	0.024
CO13-55							
CO13-55-s3 - 3.d	0.011	0.005	0.017	0.003	0.009	0.012	0.005
CO13-55-s2 - 3.d	0.041	0.018	0.011	0.004	0.007	0.007	0.014
CO13-55-s1 - 3.d	0.007	0.004	0.006	0.005	0.014	0.003	0.006
CO13-55s4 - 2.d	0.036	0.007	0.041	0.015	0.028	0.028	0.007
CO13-55s4 - 3.d	0.013	0.002	0.011	0.003	0.007	0.008	0.004

Detection Limits for sulphide LA-ICP-MS analyses

po726

ppm	Os	Ir	Ru	Rh	Pt	Pd	Au
CO14-03							
s-CO14-03-1 - 1.d	0.004	0.001	0.003	0.001	0.002	0.003	0.002
s-CO14-03-1 - 2.d	0.004	0.001	0.001	0.001	0.002	0.002	0.003
s-CO14-03-1 - 3.d	0.003	0.001	0.003	0.001	0.002	0.002	0.001
s-CO14-03-1 - 4.d	0.004	0.001	0.003	0.001	0.002	0.002	0.001
s-CO14-03-1 - 5.d	0.008	0.001	0.003	0.001	0.002	0.002	0.002
s-CO14-03-1 - 6.d	0.008	0.001	0.002	0.001	0.002	0.002	0.001
s-CO14-03-2 - 1.d	0.003	0.001	0.002	0.002	0.003	0.002	0.001
s-CO14-03-2 - 2.d	0.004	0.001	0.003	0.002	0.001	0.002	0.001
s-CO14-03-2 - 3.d	0.004	0.001	0.005	0.001	0.004	0.003	0.002
s-CO14-03-2 - 4.d	0.004	0.001	0.004	0.002	0.001	0.002	0.002
s-CO14-03-2 - 5.d	0.004	0.001	0.003	0.001	0.002	0.002	0.001
s-CO14-03-2 - 6.d	0.004	0.001	0.003	0.001	0.004	0.002	0.002
s-CO14-03-2 - 7.d	0.004	0.001	0.006	0.001	0.003	0.002	0.001
s-CO14-03-3 - 1.d	0.010	0.001	0.004	0.001	0.002	0.002	0.001
s-CO14-03-3 - 2.d	0.013	0.001	0.003	0.001	0.004	0.002	0.003
s-CO14-03-3 - 3.d	0.008	0.002	0.004	0.001	0.003	0.002	0.001
s-CO14-03-3 - 4.d	0.004	0.001	0.003	0.001	0.001	0.002	0.003
s-CO14-03-3 - 5.d	0.004	0.001	0.003	0.001	0.002	0.002	0.002
CO14-04							
CO14-04-s1 - 1.d	0.003	0.002	0.002	0.001	0.004	0.005	0.001
CO14-04-s1 - 2.d	0.006	0.002	0.003	0.001	0.003	0.005	0.003
CO14-04-s1 - 3.d	0.006	0.001	0.002	0.001	0.001	0.003	0.002
CO14-04-s2 - 1.d	0.003	0.001	0.005	0.001	0.003	0.002	0.003
CO14-04-s2 - 2.d	0.005	0.002	0.004	0.001	0.004	0.004	0.002
CO14-04-s2 - 3.d	0.002	0.002	0.005	0.001	0.004	0.005	0.003
CO14-04-s3-1 - 1.d	0.009	0.002	0.004	0.003	0.004	0.009	0.007
CO14-04-s3-1 - 2.d	0.006	0.002	0.004	0.005	0.006	0.005	0.007
CO14-04-s3-1 - 3.d	0.004	0.003	0.011	0.001	0.003	0.013	0.008
CO14-04-s4 - 1.d	0.009	0.002	0.004	0.002	0.006	0.005	0.008
CO14-04-s4 - 2.d	0.008	0.002	0.004	0.002	0.009	0.005	0.009

Detection Limits for sulphide LA-ICP-MS analyses

Bonn

ppm	Os	Ir	Ru	Rh	Pt	Pd	Ag	Au	Re
CO13-31									
CO13-31-s1	0.040	0.014	0.013	0.019	0.032	0.034	0.024	0.018	0.007
CO13-s2 - 2	0.004	0.002	0.007	0.003	0.008	0.006	0.010	0.022	0.007
CO13-s3 - 2	0.013	0.010	0.034	0.015	0.021	0.021	0.015	0.016	0.007
CO13-s4 - 4	0.017	0.005	0.013	0.005	0.008	0.008	0.013	0.011	0.007
CO13-s5 - 5	0.009	0.004	0.004	0.005	0.014	0.007	0.009	0.007	0.010
CO13-s5 - 6	0.004	0.003	0.011	0.006	0.008	0.014	0.006	0.005	0.004
CO13-s6 - 4	0.027	0.004	0.015	0.007	0.023	0.013	0.006	0.012	0.009
CO13-s7 - 4	0.017	0.003	0.012	0.004	0.013	0.009	0.010	0.005	0.005
CO13-s7 - 6	0.004	0.004	0.006	0.005	0.008	0.014	0.015	0.004	0.007
CO13-33									
CO13-33-s1 - 2	0.033	0.008	0.022	0.012	0.019	0.016	0.021	0.011	0.027
CO13-33-s2 - 13	0.022	0.006	0.037	0.005	0.021	0.007	0.024	0.016	0.008
CO13-33-s2 - 18	0.012	0.004	0.013	0.009	0.011	0.017	0.014	0.009	0.009
CO13-33-s2 - 23	0.034	0.007	0.023	0.008	0.031	0.017	0.022	0.026	0.026
CO13-33-s3 - 2	0.036	0.004	0.022	0.006	0.011	0.016	0.019	0.014	0.018
CO13-33-s4 - 3	0.015	0.009	0.022	0.007	0.021	0.016	0.007	0.007	0.026
CO13-33-s4 - 8	0.058	0.005	0.015	0.015	0.023	0.023	0.024	0.020	0.052
CO13-55									
CO13-55-s3 - 3	0.009	0.005	0.015	0.003	0.011	0.013	0.013	0.005	0.008
CO13-55-s2 - 3	0.037	0.018	0.010	0.005	0.009	0.008	0.016	0.015	0.010
CO13-55-s1 - 3	0.006	0.003	0.005	0.006	0.018	0.004	0.005	0.006	0.007
CO13-55s4 - 2	0.030	0.007	0.036	0.017	0.036	0.032	0.030	0.007	0.007
CO13-55s4 - 3	0.012	0.002	0.009	0.003	0.009	0.010	0.004	0.004	0.004
CO14-03									
s-CO14-03-1 - 1	0.004	0.001	0.003	0.001	0.003	0.003	0.002	0.001	0.003
s-CO14-03-1 - 2	0.004	0.001	0.001	0.001	0.002	0.002	0.002	0.002	0.003
s-CO14-03-1 - 3	0.003	0.001	0.003	0.001	0.003	0.002	0.002	0.001	0.003
s-CO14-03-1 - 4	0.004	0.001	0.003	0.001	0.003	0.002	0.002	0.001	0.001
s-CO14-03-1 - 5	0.008	0.001	0.003	0.002	0.003	0.002	0.004	0.002	0.003
s-CO14-03-1 - 6	0.005	0.001	0.002	0.001	0.003	0.002	0.003	0.001	0.003
s-CO14-03-2 - 1	0.003	0.001	0.002	0.002	0.004	0.002	0.004	0.001	0.003
s-CO14-03-2 - 2	0.004	0.001	0.003	0.002	0.001	0.002	0.003	0.001	0.004
s-CO14-03-2 - 3	0.003	0.001	0.005	0.001	0.005	0.004	0.003	0.001	0.003
s-CO14-03-2 - 4	0.004	0.001	0.003	0.002	0.002	0.002	0.003	0.001	0.001
s-CO14-03-2 - 5	0.004	0.001	0.003	0.001	0.002	0.002	0.003	0.001	0.004
s-CO14-03-2 - 6	0.004	0.001	0.003	0.001	0.005	0.002	0.002	0.001	0.001
s-CO14-03-2 - 7	0.004	0.002	0.006	0.001	0.004	0.002	0.004	0.001	0.003
s-CO14-03-3 - 1	0.002	0.001	0.003	0.001	0.003	0.003	0.004	0.001	0.004

Detection Limits for sulphide LA-ICP-MS analyses

Bonn

ppm	Os	Ir	Ru	Rh	Pt	Pd	Ag	Au	Re
CO14-03									
s-CO14-03-3 - 2	0.004	0.002	0.003	0.001	0.006	0.002	0.004	0.003	0.002
s-CO14-03-3 - 3	0.007	0.002	0.004	0.001	0.004	0.002	0.004	0.001	0.003
s-CO14-03-3 - 4	0.004	0.001	0.003	0.001	0.002	0.002	0.006	0.003	0.002
s-CO14-03-3 - 5	0.003	0.001	0.003	0.001	0.002	0.002	0.002	0.001	0.003
CO14-04									
CO14-04-s1 - 1	0.004	0.002	0.003	0.002	0.004	0.004	0.006	0.002	0.004
CO14-04-s1 - 2	0.005	0.002	0.003	0.001	0.004	0.004	0.003	0.003	0.005
CO14-04-s1 - 3	0.005	0.001	0.005	0.001	0.002	0.004	0.005	0.003	0.005
CO14-04-s2 - 1	0.003	0.001	0.005	0.001	0.005	0.002	0.005	0.004	0.004
CO14-04-s2 - 2	0.007	0.003	0.005	0.002	0.006	0.004	0.008	0.002	0.004
CO14-04-s2 - 3	0.003	0.002	0.005	0.001	0.004	0.004	0.004	0.003	0.004
CO14-04-s3-1 - 1	0.006	0.002	0.005	0.002	0.004	0.004	0.005	0.002	0.002
CO14-04-s3-1 - 2	0.005	0.002	0.005	0.002	0.004	0.004	0.006	0.002	0.004
CO14-04-s3-1 - 3	0.003	0.002	0.007	0.000	0.002	0.005	0.004	0.002	0.004
CO14-04-s4 - 1	0.006	0.002	0.005	0.001	0.004	0.004	0.004	0.003	0.004
CO14-04-s4 - 2	0.006	0.002	0.005	0.001	0.006	0.004	0.005	0.002	0.004

APPENDIX D
SUPPLEMENTARY DATA:
SUBDUCTED SPINELS
(CHAPTER 5)

Appendix D1: GSD standard calibration against NIST 610 and 612

Against NIST 610		**CO13-31 run**				**CO13-33 run**				**CO14-03 run**			
	Analysis	gsd - 1.d	gsd - 2.d	gsd - 3.d	gsd - 4.d	gsd - 2.d	gsd - 3.d	gsd - 4.d	gsd - 5.d	gsd - 1.d	gsd - 2.d	gsd - 3.d	ST DEV
GSD													
1g_A	Ga	57.1	54.8	53.6	51.1	53.4	51.68	53.3	53.7	53.39	51.96	52.39	1.64
ppm	Ti	6615	7060	6690	6710	6750	6780	6720	6790	6450	6530	6590	161
	Ni	59.0	58.5	56.2	54.5	55.6	57.8	55.4	57.5	53.1	51.8	54.5	2.27
	Cu	42.4	42.1	38.3	40.3	40.4	40.1	38.9	40.2	39.1	38.1	39.2	1.40
	Zn	55.3	53.3	48.5	47.6	52.3	49.9	49.1	50.4	50.3	49.0	47.7	2.42
	Co	39.8	38.9	37.1	37.1	36.6	36.6	36.5	38.0	35.4	35.1	36.6	1.39
	Mn	231	231	220	218	215	216	217	226	207	204	214	8.60
	V	39.3	42.5	49.8	42.0	40.9	40.9	40.3	40.3	38.5	39.5	40.8	3.03
	Sc	45.3	48.9	45.8	44.9	45.4	45.4	44.9	46.5	44.5	45.3	46.5	1.22

Against NIST 610	Ga	Ti	Ni	Cu	Zn	Co	Mn	V	Sc
reference value (ppm)	54(7)	7432(360)	58(4)	42(2)	54(2)	40(2)	220(20)	44(2)	52(2)
	54	7432	58	42	54	40	220	44	52
Av. GSD 1g_A	53.3	6699	55.8	39.9	50.3	37.1	218	41.3	45.8
%diff	1.28	9.87	3.78	4.96	6.83	7.35	0.89	6.05	12.0
%ref uncertainty	12.96	4.84	6.90	4.76	3.70	5.00	9.09	4.55	3.85

Against NIST612		CO13-31 run				CO13-33 run				CO14-03 run			
	Analysis	gsd - 1.d	gsd - 2.d	gsd - 3.d	gsd - 4.d	gsd - 2.d	gsd - 3.d	gsd - 4.d	gsd - 5.d	gsd - 1.d	gsd - 2.d	gsd - 3.d	ST DEV
GSD 1g_A	Ga	53.70	52.10	49.80	50.50	52.60	50.81	52.20	52.30	54.49	49.52	56.15	2.03
ppm	Ti	7600	7840	7390	7760	7800	7890	7900	8070	8120	7390	9380	539
	Ni	56.7	59.2	55.0	53.3	55.0	58.9	55.2	56.9	53.1	53.5	58.0	2.20
	Cu	44.2	41.5	37.3	42.2	40.8	40.6	39.6	41.1	39.3	37.2	43.0	2.18
	Zn	53.3	52.6	48.7	48.5	53.4	52.3	49.1	52.7	53.3	47.8	52.1	2.22
	Co	39.8	39.8	36.5	37.8	38.3	38.6	38.3	39.5	38.1	35.8	38.8	1.25
	Mn	203	207	196	214	182	217	190	219	197	190	205	12.0
	V	44.5	42.1	41.1	42.0	45.5	46.4	46.7	47.9	34.7	47.6	59.8	6.13
	Sc	48.1	50.2	46.5	47.1	49.4	49.6	49.3	51.4	49.7	48.2	53.8	2.03

Notes: The GSD standard was measured as an unknown calibrated against both NIST 610 and 612. The relative difference of the average measured GSD-1g compared to the GEOREM reference values (available at http://georem.mpch-mainz.gwdg.de) is shown as %diff. The number in brackets is the GEOREM reference standard uncertainty (ppm).

Against NIST 612	Ga	Ti	Ni	Cu	Zn	Co	Mn	V	Sc
reference value (ppm)	54(7)	7432(360)	58(4)	42(2)	54(2)	40(2)	220(20)	44(2)	52(2)
	54.0	7432	58.0	42.0	54.0	40.0	220	44.0	52.0
Av. GSD 1g_A	52.2	7922	55.9	40.6	51.3	38.3	202	45.3	49.4
%diff	3.34	-6.59	3.63	3.29	5.08	4.25	8.31	-2.95	5.02
%ref uncertainty	12.96	4.84	6.90	4.76	3.70	5.00	9.09	4.55	3.85

Appendix D2: Fine antigorite Trace Element Compositions

ppm	Mg	Al	Cr	Ga	Ti	Ni	Cu	Zn	Co	Mn	V	Sc
M -CO13-31-5 - 1	2.61E+05	3593	496	0.776	67.2	1428	1.76	25.3	86.6	824	3.39	9.53
M -CO13-31-5 - 2	2.62E+05	1620	157	0.464	39.9	1436	1.43	25.2	85.9	796	1.22	5.86
M -CO13-31-5 - 3	2.65E+05	1581	199	0.62	36.5	1423	2.36	31.8	82.8	785	1.46	5.04
M -CO13-31-2 - 1	2.78E+05	1596	71.1	0.532	50.3	1615	1.62	24.35	94.1	881	0.508	7.67
M -CO13-31-2 - 2	2.80E+05	14140	5760	3.15	222	2018	0.62	30.8	132.5	1554	27.54	22.05
M-CO13-31-3 - 1	2.77E+05	17770	5729	2.92	245.6	1589	1.29	23.3	88.5	721	27.31	25.14
M-CO13-31-3 - 2	2.64E+05	2750	191.8	0.76	40.8	1426	1.42	22	85.2	811	0.99	6.84
M-CO13-31-3 - 3	2.61E+05	1061	117.2	0.397	24.8	1389	1.8	23.6	85.6	926	0.593	5.42
M-CO13-31-4 - 5 - 1	2.84E+05	8920	138.3	1.72	129	1723	2.02	29.1	106	931	1.37	16.25
M-CO13-31-4 - 5 - 2	2.86E+05	8940	135	1.67	139.9	1775	1.17	27.7	111.3	938	1.29	16.17
M-CO13-31-4 - 5 - 3	2.80E+05	9340	191.4	1.55	129.8	1569	0.49	24.5	95.4	849	1.54	16.04
M-CO13-31-1 - 1	2.65E+05	5390	371	1.07	66	1502	1.22	23.7	92.5	894	1.97	9.98
M-CO13-31-1 - 2	2.74E+05	2047	247	0.502	36.3	1552	1.49	29.2	91.9	872	0.97	6.84
M-CO13-31-1 - 3	2.78E+05	4490	452	0.798	66.7	1521	3.9	26.1	94.5	873	2.43	9.23
M-CO13-31-1 - 4	2.85E+05	10160	1688	1.78	135.5	1879	1.13	27.4	104.6	887	8.44	19.25
M-CO13-31-1 - 5	2.74E+05	4760	423	0.91	66.2	1533	0.61	25.4	94.1	943	2.21	10.6

ppm	Mg	Al	Cr	Ga	Ti	Ni	Cu	Zn	Co	Mn	V	Sc
CO13-33-m1 - 7	2.59E+05	9920	2081	2.14	169.7	3541	7.79	31.4	147.8	650.8	10.02	13.24
CO13-33-m1 - 13	2.64E+05	12380	3189	2.52	248.3	3130	33.5	38.2	173	792	15.31	14.02
CO13-33-m1 - 14	2.69E+05	12080	2310	2.58	230.1	1863	9.05	29.7	48.9	684	11.29	14.69
CO13-33-m2 - 1	2.65E+05	12090	2799	2.44	207.4	812	1.44	29.5	19.83	783	13.15	13.72
CO13-33-m2 - 2	2.60E+05	11040	3069	2.47	229	914	1.45	36.7	21.74	785	14.47	12.85
CO13-33-m2 - 4	2.60E+05	20800	4020	4.09	194	918	1.61	30.7	29.5	724.4	18.4	13.63
CO13-33-m2 - 5	2.64E+05	22110	4092	4.02	230.4	964	1.31	31.6	30.98	719.1	18.9	14.77
CO13-33-m2 - 6	2.67E+05	16720	2359	3.57	335.2	920	1.76	31.4	21.88	659.5	12.02	14.34
CO13-33-s2 - 1	2.65E+05	9800	3227	2.09	205	1923	1.44	29.9	81.4	670.1	14.97	12.37
CO13-33-s2 - 2	2.66E+05	11380	2892	2.32	240.1	4130	14.83	33.8	263.2	697	13.61	13.76
CO13-33-s2 - 6	2.61E+05	10630	1823	2.59	212.6	911	1.18	28.6	19.61	1250	9.45	14.24
CO13-33-s2 - 7	2.58E+05	12330	1674	2.51	249.4	900.7	1.23	30.6	18.61	548.1	8.84	14.96
CO13-33-s2 - 27	2.59E+05	12960	2947	2.93	239.2	1008	1.36	30	22.39	743	14.35	14.11
CO13-33-s2 - 35	2.62E+05	10180	6000	1.96	177.4	1028	1.16	31.3	30.08	746	26.43	10.51
CO13-33-s2 - 36	2.63E+05	9780	1978	4.8	252.8	950	1.58	34.8	28.44	1780	9.94	13.8

Detection Limits for antigorite

ppm	Mg	Al	Sc	Ti	V	Cr	Mn	Co	Ni	Cu	Zn	Ga
M -CO13-31-5 - 1	14998	221	0.59	5.45	0.26	15.14	51.34	6.34	105.18	8.48	3.14	0.19
M -CO13-31-5 - 2	14302	199	0.67	5.98	0.26	16.87	48.67	6.77	96.87	10.93	1.51	0.15
M -CO13-31-5 - 3	14346	73	0.44	2.46	0.24	32.71	44.96	6.28	88.12	7.08	1.92	0.15
M -CO13-31-2 - 1	21913	177	0.79	5.98	0.27	4.41	64.46	7.91	146.94	5.00	3.25	0.14
M -CO13-31-2 - 2	18601	694	1.64	13.18	1.37	201.65	71.05	7.67	130.13	8.26	2.82	0.21
M-CO13-31-3 - 1	13993	961	1.56	13.37	1.64	220.29	40.01	5.94	121.38	12.93	2.89	0.20
M-CO13-31-3 - 2	14017	169	0.72	5.82	0.19	9.60	42.88	5.81	90.05	7.00	2.36	0.11
M-CO13-31-3 - 3	12772	93	0.42	1.82	0.25	6.87	39.95	5.80	88.71	7.26	2.53	0.14
M-CO13-31-4 - 5 - 1	21717	707	1.16	11.17	0.25	8.56	65.25	15.07	149.36	7.41	3.98	0.21
M-CO13-31-4 - 5 - 2	22357	677	1.43	11.33	0.25	6.39	65.83	9.06	148.52	6.82	2.55	0.21
M-CO13-31-4 - 5 - 3	20271	581	1.02	8.51	0.32	11.98	60.25	9.01	150.77	5.78	2.05	0.16
M-CO13-31-1 - 1	12540	281	0.71	4.92	0.27	13.31	41.01	6.17	104.37	3.91	2.10	0.10
M-CO13-31-1 - 2	15601	109	0.59	6.24	1.24	20.20	54.21	6.58	117.00	6.52	16.39	0.26
M-CO13-31-1 - 3	15843	250	0.64	4.18	0.37	180.24	48.59	6.00	105.42	4.64	1.64	0.12
M-CO13-31-1 - 4	17975	668	1.44	13.58	0.76	96.81	58.79	8.28	153.10	6.58	3.03	0.19
M-CO13-31-1 - 5	17192	373	0.88	5.48	0.38	23.38	55.21	6.59	116.43	5.39	2.56	0.12

ppm	Mg	Al	Sc	Ti	V	Cr	Mn	Co	Ni	Cu	Zn	Ga
CO13-33-m1 - 7	10276	328	0.76	5.05	0.50	62.15	31.73	9.38	216	5.26	3.05	0.14
CO13-33-m1 - 13	10684	494	0.72	11.27	0.62	84.54	29.86	5.74	154	3.47	3.19	0.12
CO13-33-m1 - 14	18145	699	1.33	20.38	1.05	134	51.36	4.52	186	4.66	4.67	0.16
CO13-33-m2 - 1	17058	751	0.81	9.78	0.89	120	50.96	1.33	53.99	4.14	2.26	0.19
CO13-33-m2 - 2	19883	795	0.78	15.84	1.10	187	71.49	2.45	80.97	4.74	4.87	0.19
CO13-33-m2 - 3	16339	890	0.83	14.12	0.90	138	41.36	398	6586	22.59	4.85	0.25
CO13-33-m2 - 4	7231	1445	0.71	11.88	1.17	139	18.71	2.27	66.71	3.65	2.07	0.35
CO13-33-m2 - 5	18321	1132	0.98	22.24	1.11	160	44.35	2.53	104	4.28	3.22	0.37
CO13-33-m2 - 6	18913	1062	1.03	24.40	1.07	115	61.35	1.95	79.72	3.06	2.91	0.27
CO13-33-s2 - 1	14027	609	0.83	9.06	0.99	118	39.98	6.42	125	4.66	2.90	0.16
CO13-33-s2 - 2	21521	899	1.12	18.39	1.24	164	56.55	28.90	396	4.82	3.47	0.21
CO13-33-s2 - 6	12770	598	1.01	16.50	0.85	87.51	64.96	1.10	57.83	4.84	4.57	0.25
CO13-33-s2 - 7	14160	595	0.91	15.16	0.59	59.72	35.38	1.49	60.52	3.72	2.79	0.19
CO13-33-s2 - 27	16007	747	1.08	14.34	1.17	144	48.14	1.72	71.41	4.16	3.67	0.25
CO13-33-s2 - 35	15994	603	0.99	14.70	1.58	252	45.74	2.33	82.64	3.74	3.99	0.17
CO13-33-s2 - 36	22030	710	1.31	19.84	0.88	111	61.21	2.37	80.72	5.01	6.24	0.31

Appendix D3: Spinel trace element LA-ICP-MS data

CO13-31														
grain	sp2-5 max	sp2-5 min	sp2-7 max	sp2-7 min	sp2-8 max	sp2-8 min	sp3-1 max	sp3-1 min	sp3-2 max	sp3-2 min	sp4-2 max	sp4-2 min	sp4-3 max	sp4-3 min
Description	magnetite		magnetite		magnetite		magnetite		magnetite		magnetite		magnetite	
Fe wt%	69.677	64.445	70.83	65.46	44.245	42.59	51.876	51.69	70.39	64.75	59.296	54.77	49.47	47.64
corr %	5	5	3	3	29	29	23	23	3	2	17	15	25	25
ppm														
Ga	0.132*	0.119*	0.143*	0.131*	0.328*	0.275*	0.283*	0.283*	0.046*	0.064*	0.121*	0.118*	0.22*	0.195*
Ti	868	794	751	694	646	582	537	536	683	625	1110	850	625	593
Sn	0.035	0.026	0.070*	0.065*	<0.060	<0.053	0.072*	0.072*	0.048	0.027	0.022*	0.021*	0.026*	0.023*
Ni	2035	1875	2674	2468	4020	3536	3152	3152	3621	3310	3281	2986	3644	3494
Zn	18.9	17.5	19.5	18	23.4	20.03	20.7	20.6	19.3	17.8	20.9	19.1	19.7	18.7
Cu	0	0	0	0	0	<5.09	0	0	<9.87	0	0	0	0	0
Co	372	343	363	335	349	308	351	350	378	345	362	329	335	322
Mn	1540	883	1650	1520	1610	1420	1570	1570	1640	1500	1670	1510	1530	1450
V	4.6	0.509	4.41	4.07	3.98	3.58	3.41	3.4	3.46	3.35	5.53	4.98	4.01	3.81
Sc	0.47*	0.47*	0.316*	0.275*	5.25*	4.47*	2.67*	2.66*	0.71*	0.65*	2.72*	2.51*	4.5*	4.3*

CO13-31													
grain	sp 5-1 max	sp 5-1 min	sp5-2 max	sp5-2 min	sp5-3 max	sp5-3 min	sp5-4 max	sp5-4 min	sp5-5 min	sp5-5 max	sp5-5 min	sp2-1 max	sp2-1 min
Description	Cr-Al core/porous rim		Cr-Al core/porous rim		magnetite rim		Cr-Al core/porous rim		Cr-Al core/porous rim		magnetite		
Fe wt%	65.02	18.35	57.86	17.81	66.65	61.84	38.29	16.35	60.36	64.37	17.83	68.725	63.66
corr %	8	-	10	2	9	9	10	10	10	10	10	5	5
ppm													
Ga	52.1	13.6	36.50	10.43	0.21*	0.19*	4.38	1.83	0.27*	88.4	22.5	0.115*	0.10*
Ti	2700	702	2100	609	627	576	1850	616	884	5870	1480	622	575
Sn	0.18	0.07	0.15	0.044	0.03755	<0.0647	<2.549	<1.089	0.07	0.438	0.044	0.068	0.058
Ni	3972	1068	3553	1027	4053	3752	2690	1067	3832	3808	980	2949	2628
Zn	7158	1870	7048	2012	19.4	17.8	3484	1489	25.0	23041	5864	21.8	20.0
Cu	0	0	16.0	<5.584	0	<14.3	0	0	0	<60.6	<16.8	0	0
Co	1113	293	989	283	408	378	590	247	393	2605	663	378	350
Mn	13800	3590	12300	3570	1710	1570	5380	1900	1670	48400	12200	1610	1490
V	1110	289	775	224	15.9	14.6	355	118	11.6	2370	597	3.83	3.54
Sc	0.838*	0.236*	0.73*	0.24*	1.07*	0.998*	3.96*	1.31*	0.947*	1.27*	0.391*	0.827*	0.743*

CO13-31										
grain	sp4-4 max	sp4-4 min	sp1-1 max	sp1-1 min	sp1-2 max	sp1-2 min	sp2-1-1	sp2-1-1	sp2-2-1	sp2-2-2
Description	magnetite		Cr-Al core/porous rim		Cr-Al core/porous rim		magnetite		magnetite	
Fe wt%	66.84	62.36	67.13	19.1	64.51	16.01	56.846	52.63	56.72	53.35
corr %	8	7	7	-	15	7	18.5	18.5	18.5	18.5
ppm										
Ga	0.10	0.96	0.35	0.92	0.45	1.77	0.95	0.71	0.38	0.708*
Ti	818	2900	1621	3258	1758	4960	2951	1523	784	462
Sn	0.058*	<0.071	<0.04	0.053*	0.0026*	0.0078*	0.042*	0.04068	0.0222	0.03541
Ni	4103	1257	391	1388	682	970	527	2105	1109	31652
Zn	23.3	9366	5238	9355	4706	15827	8584	3817	1955	613
Cu	0	168	93.122	176	89	44	24	652	335	64
Co	400	210	105	242	121	356	193	134	69.9	2168
Mn	1720	30830	17186	32146	16150	47460	25747	13089	6733	2811
V	5.05	808	452	872	439	1265	686	390	200	106
Sc*	1.98	4.06	1.11	3.89	1.89	3.75	2.35	2.33	1.29	1.43

CO13-33														
grain	sp1-1 max porous Cr/Fe-rich spinel	sp1-1 min	sp1-2 max porous Cr/Fe-rich spinel	sp1-2 min	sp1-3 max porous Cr/Fe-rich spinel	sp1-3 min	sp1-4 max porous Cr/Fe-rich spinel	sp 1-4 min	sp1-5 max porous Cr/Fe-rich spinel	sp1-5 min	sp1-8 max porous Cr/Fe-rich spinel	sp1-8 min	sp1-9 max porous Cr/Fe-rich spinel	sp1-9 min
Description														
Fe wt%	52.68	29.48	55.97	30.2	47.68	28.4	51.78	29.29	39.99	26.68	54.64	29.3	60.02	31.08
corr %	20	20	17	9	24	13	21	10	31	18	18.5	14	14	11
ppm														
Ga	0.96	0.35	0.92	0.45	1.77	0.95	0.71	0.38	0.708*	0.472*	1.15	0.50	0.71	0.20
Ti	2900	1621	3258	1758	4960	2951	1523	784	462	280	5510	2952	3320	1719
Sn	<0.071	<0.04	0.053*	0.0026*	0.0078*	0.042*	0.04	0.02	0.04	0.02	0.093*	0.041*	0.041*	<0.028
Ni	1257	391	1388	682	970	527	2105	1109	31652	19069	1274	499	2685	1140
Zn	9366	5238	9355	4706	15827	8584	3817	1955	613	368	14842	7656	10475	5570
Cu	168	93.1	176	88.86	43.5	23.62	652	335	63.6	38.2	22.30	11.1	459	243
Co	210	105	242	121	356	193	134	70	2168	1307	381	190	316	156
Mn	30830	17186	32146	16150	47460	25747	13089	6733	2811	1700	44637	22994	32107	17020
V	808	452	872	439	1265	686	390	200	106	66	1222	630	849	451
Sc*	4.06	1.11	3.89	1.89	3.75	2.35	2.33	1.29	1.43	0.51	3.00	1.63	7.75	3.04

CO13-33	sp1-10		sp1-11		sp1-12 max	sp1-12 min	sp2-4 max	sp2-4 min	sp2-5 max	sp2-5 min	s2-34 max	s2-34 min	sps2-28	sps2-29
Description	porous spinel	Cr/Fe-rich	porous spinel	Cr/Fe-rich	Cr-spinel core		porous spinel	Fe-rich	porous spinel	Fe-rich	porous spinel	Fe-rich	porous spinel	Fe-rich
Fe wt%	58.28	30.7	58.28	31.17	30.9	24.86	65.78	52.94	65.46	52.75	56.7	55.3	70.14	70.14
corr %	14	6	12	7	36	21	5	5	6	6	20	17	48	39
ppm														
Ga	0.88	0.46	0.72	0.33	0.436*	0.352*	0.341*	0.275*	0.34	0.24	0.57	0.56	3.11	2.57
Ti	4639	2474	4387	2256	233	178	1508	1192	1875	1506	559	535	755	1076
Sn	<0.067	0.023*	0.057*	0.046*	0.045*	0.036*	0.06	0.05	0.05	0.04	0.04	0.04	0.03	0.03
Ni	1576	815	2434	1157	46113	33247	2085	1651	2100	1680	2063	1972	1709	1401
Zn	12171	6040	12563	6172	35.41	26.80	2846	2249	3398	2734	92.60	88.60	1118	2688
Cu	14.41	7.22	14.00	6.78	105.76	85.37	4.18	3.36	17.30	13.90	0.00	0.00	0.00	0.00
Co	326	163	367	179	2852	2047	149	118	164	132	44.13	43.26	47.80	54.40
Mn	37153	18426	37532	18433	33580	17270	10078	7970	11945	9592	1682	1624	5528	8843
V	1027	509	1019	500	24.05	17.8	305	241	353	284	67*	65.7*	187	259
Sc*	2.32	1.38	1.86	0.98	0	0	0.58	0.33	0.99	0.63	6.08	6.08	0.00	0.00

CO14-03															
grain	1-1	1-2	1-3	1-4	3-1	3-2	3-3	3-4	3-5	3-6	4-1	4-3	4-4	4-5	4-6
Description															
Fe wt%	73.51	73.51	73.51	73.51	73.51	73.51	73.51	73.51	73.51	73.51	73.51	73.51	73.51	73.51	73.51
corr %	-	-	-	-	-	-	-	-	-	-	-	-	-	-	
ppm															
Ga	3.27	3.61	3.87	3.58	2.17	2.94	2.63	2.96	1.76	3.72	2.48	2.97	2.50	2.30	2.1
Ti	186	201	202	190	6300	206	9040	205	179	198	370	195	238	347	4300
Sn	0.075	0.057	0.05	0.055	0.378	0.058	0.05	0.054	0.048	0.043	0.043	0.043	0.028	0.055	0.296
Ni	63.9	64.8	67.8	63	115	108	115	110	104	117	70.8	69.1	95.5	137	224.5
Zn	23.0	22.9	20.3	23.1	21.5	22.2	22.4	22.5	23.6	22.0	25.1	24.8	25.5	23.6	23.1
Cu	0	0	0	0	0	0	<0.522	0	0	0	0	<0.4862	<1.5816	<2.5694	<1.6616
Co	55.6	46.1	31.5	50.4	47.7	45.7	49.6	48.6	52.4	35.7	46.5	43.1	44.9	48.0	54.92
Mn	504	579	621	586	422	494	1221	498	432	559	571	659	652	558	465.5
V	1.47	1.56	1.44	1.57	37.30	1.74	53.80	1.64	1.22	1.71	2.82	1.64	1.81	2.23	27.3
Sc	1.87	1.98	2.14	2.00	1.73	1.27	2.99	1.33	2.23	1.15	1.71	1.58	1.61	1.82	2.28

Notes: < symbol indicates concentrations are lower than the detection limit. GSD-1g-A was used as the standard for all data reduction, using Fe as the internal standard using the concentrations stated in the tables. Maximum and minimum values are provided where the scale of zonation was smaller than the spot size. Also indicated is the percentage of correction for silica contamination. * indicates maximum values where antigorite concentrations were higher than spinel concentrations. Antigorite spots used for correction were proximal to the spinel analysis.

Appendix D4: EPMA chlorite analyses near spinel grains

wt%	CO13-55 area6 chl1_1	CO13-55 area6 chl1_2	CO13-55 area6 chl1_3	CO13-33 area3 chl1	CO13-33 area3 chl2	CO13-33 area4 chl_	CO13-31 area3 chl_
SiO_2	33.65	33.48	33.28	35.56	34.91	38.21	36.27
TiO_2	0.02	0.00	0.00	0.00	0.00	0.00	0.07
V_2O_3	0.02	0.02	0.02	0.00	0.00	0.01	0.00
Al_2O_3	15.56	16.50	16.46	13.17	14.09	9.24	2.19
Cr_2O_3	1.54	1.83	1.81	1.49	1.25	0.94	3.88
FeO	2.61	2.65	2.38	3.56	3.72	3.29	12.39
NiO	0.15	0.22	0.15	0.08	0.03	0.35	0.63
MnO	0.00	0.03	0.00	0.05	0.04	0.04	0.34
MgO	34.46	33.92	34.06	35.14	34.80	36.93	35.45
CaO	0.01	0.02	0.02	0.01	0.00	0.01	0.09
Na_2O	0.00	0.00	0.00	0.00	0.00	0.00	0.00
K2O	0.00	0.00	0.01	0.00	0.00	0.00	0.00
Total	88.02	88.67	88.20	89.06	88.85	89.01	91.31
cations normalised to 20							
Si	6.30	6.24	6.22	6.60	6.49	7.08	6.84
Ti	0.00	0.00	0.00	0.00	0.00	0.00	0.00
V	0.00	0.00	0.00	0.00	0.00	0.00	0.00
Al	3.43	3.62	3.63	2.88	3.09	2.02	0.49
Cr	0.23	0.27	0.27	0.22	0.18	0.14	0.58
Fe	0.41	0.41	0.37	0.55	0.58	0.51	1.96
Ni	0.02	0.03	0.02	0.01	0.00	0.05	0.10
Mn	0.00	0.00	0.00	0.01	0.01	0.00	0.04
Mg	9.61	9.42	9.49	9.73	9.65	10.20	9.97
Ca	0.00	0.00	0.00	0.00	0.00	0.00	0.02
Mg/Mg+Fe (M)	0.96	0.96	0.96	0.95	0.94	0.95	0.84

APPENDIX E

SUPPLEMENTARY SULPHUR ISOTOPE METHODS AND DATA (CHAPTER 6)

E1: Sample preparation

Sample Mount Preparation for Cameca IMS 1280

The samples CO13-33, CO13-40, CO13-55, CO14-03 and CO14-04 were prepared in the Department of Applied Geology, Curtin University, for in-situ S isotope analysis on the Cameca IMS 1280 ion probe at CMCA, the University of Western Australia (UWA).

A thin slice was cut from the top of the previously polished thin section billet. Three areas of interest, 7 mm in diameter, were selected using reflected light microscopy and drilled from each sample. One mount was made for each of the five samples using a 2.5 cm diameter round mould. A square piece of double sided sticky tape was cut and placed carefully on a square glass plate. The mould was lubricated on the inside and placed in the centre of the tape. The pucks of the areas of interest were placed with the polished side down in the centre of the mould, with the standards carefully placed in between the areas. The standards included the VMSO pentlandite, nifty 'B' chalcopyrite and Sonora 3 Pyrite. The orientation of the standards and thin-section billet areas were recorded for each mount.

The Struers EpoFix resin and hardener were measured and mixed in the recommended quantities for five mounts. The epoxy was continuously stirred prior to sonication in a water bath for 5 minutes to reduce the number of air bubbles. The mould was then filled with the mixture and left to harden. The mounts were removed from the glass plate and subsequently polished (see below) and the backs of the mounts were cut with a precision saw to less than 6 mm to fit in the sample holder of the Cameca IMS 1280 instrument.

Polishing Technique for Cameca IMS 1280

The polishing of sample mounts for in-situ analysis on the Cameca IMS 1280 was carried out by hand using a continuous figure of eight motion and rotating the sample to ensure even polishing. The sample polish was checked using reflected light microscopy at each stage of the polishing to ensure the polish was sufficient prior to moving on to a finer polish. Polishing was carried out on a flat surface using wet 1200 grit paper for ~ 6 minutes, 800 grit paper for ~ 4 minutes and 400 grit paper from ~ 2 minutes. Between each stage of polishing with grit paper, the mounts were sonicated in a water bath for 5 minutes. This was followed by a finer polish to 6 µm using 6 µm Stuers DP-Suspension P, polyscrystalline diamond solution, lubricating fluid and a Stuers Largo 300 mm diameter MD-nap attached to a Struers Planopol-V polishing machine. Further polishing to 3 µm and 1 µm was carried out as above but with two different Struers Largo MD Naps; one for 3 µm polishing and one for 1 µm polishing and with 3 and 1 µm Stuers DP-Suspension P, polyscrystalline diamond solutions, respectively.

Appendix E2: Average standard compositions (LaFlamme et al., 2016)

Standard	Mineral	Formula	Fe (wt%)	Ni (wt%)	Co (wt%)	S (wt%)
Sierra	Pyrite	FeS_2	53.3(0.5)			46.7(0.4)
VMSO	Pentlandite	$Fe_{4.1}Ni_{4.8}Co_{0.1}S_8$	29.4(0.8)	35.8(0.9)	0.3(0.1)	32.9(0.4)

Average standard chemical compositions (LaFlamme et al., 2016).
Uncertainty is in brackets (2 standard deviations)

Appendix E3: The Mann-Whitney U test

To determine if there was a statistically significant difference of $\delta^{34}S$ values both between different generations of sulphides within the same sample, and between different samples, the Mann-Whitney U test was applied. This test was chosen because $\delta^{34}S$ may be non-parametric, that is, the values may not be taken from a normal distribution. It is not possible to test whether the distribution is normal or not due to the small size of the sample set, and a lack of interval or ratio scale samples, so the non-parametric test is preferred. The test is used to determine whether two independent samples are from the same population and assumes that the data are ordinal (Siddiqui and Parizek, 1972). The null hypothesis was set to 'there is no difference the $\delta^{34}S$ values between the two groups of sulphides'. $\delta^{34}S$ values were ranked all together, and where two or more values were the same (to one decimal place), the number assigned to them was the average of the ranks that would have been assigned if they had been different. The addition of ranks $(R1)$ of sulphide1, and the ranks $(R2)$ of sulphide2 gave $n1$ and $n2$, respectively. The Mann-Whitney U value is the smallest calculated value of $U1$ and $U2$. The following formula was used to calculate $U1$ and $U2$ values,

$$U1 = n1n2 + \left(\frac{n1(n1+1)}{2}\right) - R1$$

$$U2 = n1n2 + \left(\frac{n2(n2+1)}{2}\right) - R2$$

Z-test values, necessary for n >20, where U approaches a normal distribution, were calculated using the following formula,

$$Z = \frac{U - ((n_1 * n_2)/2}{Std\ dev}$$

Probability values (P) were then obtained using the following formula, where *normdist* is the normal cumulative distribution of the absolute z-test value.

$$P = (1 - normdist(abs(z)) * 2$$

P values of <0.01 were taken as significant, i.e. the null hypothesis that there was no significant difference between the two groups of sulphides was rejected.

Appendix E4: Sulphur Isotope Data

Pentlandite Analyses

Analysis name	PB (nA)	^{32}S (cps)	$\delta^{33}S_{VCDT}$ (‰)	2σ (‰)	$\delta^{34}S_{VCDT}$ (‰)	2σ (‰)	$\Delta^{33}S_{VCDT}$ (‰)	2σ (‰)
C013-40_vmso@1			1.50	0.24	2.99	0.32	-0.04	0.25
C013-40_vmso@2			1.62	0.19	3.29	0.25	-0.07	0.18
C013-40_vmso@3			1.67	0.20	3.29	0.23	-0.03	0.18
C013-40_vmso@4			1.70	0.21	3.32	0.23	-0.01	0.18
C013-40_vmso@5			1.66	0.19	3.17	0.23	0.03	0.17
C013-40_vmso@6			1.60	0.20	3.17	0.24	-0.03	0.18
C013-40_vmso@7			1.78	0.20	3.26	0.25	0.10	0.19
C013-40_vmso@8			1.74	0.21	3.29	0.26	0.05	0.20
C013-40_area2_s1@1	2.06	8.24E+08	3.61	0.22	7.57	0.31	-0.28	0.23
C013-40_area2_s2@1	2.06	4.44E+08	2.61	0.33	5.39	0.37	-0.16	0.35
C013-40_area2_s3@1	2.07	7.39E+08	2.95	0.30	6.07	0.42	-0.17	0.34
C013-40_area2_s3@2	2.07	6.81E+08	3.38	0.30	6.57	0.51	0.00	0.37
C013-40_area3_s1@1	2.08	8.54E+08	3.90	0.28	7.22	0.46	0.19	0.34
C013-40_area3_s1@2	2.08	8.93E+08	4.02	0.23	7.41	0.36	0.21	0.26
C013-40_area3_s1@3*	2.01	3.20E+08	4.06	0.38	5.52	0.26	1.22	0.37
C013-40_area3_s2@1	2.06	7.95E+08	2.91	0.26	5.23	0.41	0.22	0.30
C013-40_area3_s2@2*	2.04	5.66E+08	3.91	0.27	6.63	0.51	0.50	0.34
C013-40_area3_s3@1	2.09	9.14E+08	4.93	0.23	8.85	0.32	0.38	0.24

*indicates the presence of a small inclusion - MIF values not trusted

PB = Primary beam current (nA)
cps = counts per second
VCDT= Vienna Canyo Diablo Troilite
2σ errors are absolute

Analysis name	PB (nA)	^{32}S (cps)	$\delta^{33}S_{VCDT}$ (‰)	2σ (‰)	$\delta^{34}S_{VCDT}$ (‰)	2σ (‰)	$\Delta^{33}S_{VCDT}$ (‰)	2σ (‰)
CO13-40_vmso@10	3.47	1.31E+09	1.86	0.38	3.77	0.73	-0.08	0.36
CO13-40_vmso@11	3.51	1.36E+09	1.60	0.39	3.12	0.75	-0.01	0.38
CO13-40_vmso@12	3.49	1.33E+09	1.54	0.40	3.23	0.74	-0.12	0.40
CO13-40_vmso@13	3.45	1.32E+09	1.81	0.38	3.61	0.77	-0.05	0.39
CO13-40_vmso@14	3.42	1.33E+09	1.70	0.40	3.16	0.77	0.08	0.41
CO13-40_vmso@15	3.25	1.22E+09	1.53	0.40	2.85	0.82	0.07	0.44
CO13-40_vmso@16	3.22	1.21E+09	1.77	0.39	3.33	0.80	0.05	0.42
CO13-40_vmso@3	3.49	1.17E+09	1.69	0.45	3.23	0.86	0.02	0.50
CO13-40_vmso@4	3.50	1.23E+09	1.86	0.41	3.47	0.79	0.07	0.43
CO13-40_vmso@5	3.45	1.20E+09	1.58	0.46	3.02	0.87	0.03	0.52
CO13-40_vmso@8	3.50	1.31E+09	1.52	0.48	2.93	0.96	0.01	0.57
CO13-40_vmso@9	3.51	1.27E+09	1.46	0.44	2.94	0.85	-0.05	0.49
CO13-40_area1@s1-1	3.42	1.16E+09	4.69	0.43	8.34	0.84	0.40	0.47
CO13-40_area1@s1-2	3.57	1.29E+09	3.99	0.51	7.42	0.99	0.18	0.61
CO13-40_area1@s1-3	3.53	1.32E+09	3.45	0.55	5.93	1.12	0.40	0.70
CO13-40_area1@s2-1	3.52	1.07E+09	4.00	0.49	7.68	1.00	0.05	0.59
CO13-40_area1@s2-2	3.53	1.35E+09	5.96	0.55	10.98	1.13	0.32	0.70
CO13-40_area1@s3	3.91	1.42E+09	4.76	0.47	8.80	0.93	0.24	0.55
CO13-40_area1@s4	3.53	1.18E+09	2.45	0.57	4.27	1.10	0.26	0.70
CO13-40_area3@s10	3.53	1.09E+09	4.89	0.45	9.36	0.86	0.08	0.50
CO13-40_area3@s11	3.43	1.39E+09	3.12	0.66	5.37	1.34	0.36	0.88
CO13-40_area3@s1-1	3.25	1.12E+09	4.85	0.47	8.78	0.92	0.33	0.54
CO13-40_area3@s1-2	3.25	9.89E+08	5.06	0.34	8.83	0.69	0.52	0.30
CO13-40_area3@s12-1	3.44	1.12E+09	5.25	0.58	9.44	1.10	0.40	0.71
CO13-40_area3@s12-2	3.44	1.01E+09	4.40	0.62	8.01	1.22	0.29	0.79
CO13-40_area3@s12-3	3.45	1.32E+09	3.14	0.44	4.80	0.89	0.67	0.50
CO13-40_area3@s13	3.27	1.06E+09	4.90	0.43	8.83	0.78	0.36	0.45
CO13-40_area3@s14	3.46	1.35E+09	2.58	0.40	5.03	0.79	0.00	0.42
CO13-40_area3@s15-2	3.42	1.44E+09	2.67	0.47	4.39	0.94	0.41	0.55
CO13-40_area3@s16	3.42	1.06E+09	4.35	0.39	8.03	0.82	0.22	0.43
CO13-40_area3@s2	3.47	1.26E+09	3.00	0.58	5.80	1.17	0.01	0.74
CO13-40_area3@s4	3.30	1.28E+09	5.81	0.46	10.43	0.90	0.45	0.53
CO13-40_area3@s5	3.33	1.30E+09	3.86	0.57	6.77	1.14	0.38	0.71
CO13-40_area3@s6-1	3.46	7.52E+08	3.41	0.59	6.21	1.09	0.22	0.72
CO13-40_area3@s8-1	3.80	1.12E+09	3.37	0.52	6.25	1.06	0.16	0.65
CO13-40_area3@s8-2	3.67	9.57E+08	5.38	0.49	10.01	0.96	0.23	0.57
CO13-40_area3@s8-3	3.58	8.79E+08	5.34	0.49	9.94	0.87	0.23	0.54

Analysis name	PB (nA)	^{32}S (cps)	$\delta^{33}S_{VCDT}$ (‰)	2σ (‰)	$\delta^{34}S_{VCDT}$ (‰)	2σ (‰)	$\Delta^{33}S_{VCDT}$ (‰)	2σ (‰)
CO13-33_vmso@1	2.16	1.04E+09	1.54	0.42	3.24	0.73	-0.13	0.55
CO13-33_vmso@10	2.14	1.02E+09	1.72	0.44	3.42	0.75	-0.04	0.57
CO13-33_vmso@11	2.13	1.02E+09	1.91	0.45	3.39	0.77	0.17	0.58
CO13-33_vmso@12	2.13	1.00E+09	1.73	0.45	3.36	0.74	0.00	0.57
CO13-33_vmso@13	2.13	1.03E+09	1.67	0.42	3.34	0.75	-0.05	0.55
CO13-33_vmso@14	2.12	1.02E+09	1.71	0.44	3.45	0.77	-0.06	0.58
CO13-33_vmso@15	2.12	1.02E+09	1.46	0.45	2.84	0.80	0.00	0.59
CO13-33_vmso@16	2.12	9.99E+08	1.81	0.42	3.33	0.73	0.10	0.54
CO13-33_vmso@2	2.15	1.03E+09	1.76	0.41	3.35	0.71	0.03	0.53
CO13-33_vmso@3	2.16	1.03E+09	1.59	0.43	3.12	0.74	-0.01	0.56
CO13-33_vmso@4	2.15	1.05E+09	1.49	0.44	3.08	0.71	-0.10	0.56
CO13-33_vmso@5	2.15	1.04E+09	1.56	0.41	3.10	0.74	-0.04	0.54
CO13-33_vmso@6	2.15	1.02E+09	1.57	0.41	3.18	0.77	-0.07	0.55
CO13-33_vmso@7	2.15	1.05E+09	1.69	0.40	3.09	0.71	0.10	0.53
CO13-33_vmso@8	2.14	1.03E+09	1.64	0.44	3.14	0.76	0.02	0.57
CO13-33_vmso@9	2.14	9.96E+08	1.71	0.43	3.14	0.72	0.09	0.55
CO13-33_area2@s2	2.14	1.05E+09	2.83	0.44	5.50	0.76	0.00	0.57
CO13-33_area2@s3	2.13	1.01E+09	4.01	0.43	7.88	0.74	-0.04	0.56
CO13-33_area2@s4a	2.14	9.96E+08	5.07	0.45	9.76	0.84	0.06	0.61
CO13-33_area2@s4b	2.14	1.04E+09	4.45	0.45	8.61	0.78	0.02	0.59
CO13-33_area2@s5	2.15	1.02E+09	1.99	0.57	3.88	0.90	-0.01	0.72
CO13-33_area2@s6	2.15	9.86E+08	3.76	0.42	7.27	0.75	0.02	0.56
CO13-33_area2@s7	2.12	8.03E+08	4.33	0.43	8.42	0.72	0.01	0.55
CO13-33_area2@s8	2.13	9.88E+08	4.18	0.49	8.20	0.82	-0.04	0.63
CO13-33_area2@s9	2.13	1.01E+09	4.10	0.46	7.91	0.76	0.04	0.59
CO13-33_area2@s10	2.12	1.05E+09	2.80	0.41	5.65	0.72	-0.10	0.54
CO13-33_area3@s1a	2.15	9.49E+08	3.73	0.46	7.10	0.82	0.08	0.60
CO13-33_area3@s2	2.14	9.48E+08	4.53	0.41	8.82	0.79	0.00	0.56
CO13-33_area3@s4	2.15	9.56E+08	3.34	0.41	6.54	0.73	-0.03	0.54
CO13-33_area3@s6	2.15	9.89E+08	3.87	0.45	7.54	0.83	-0.01	0.60
CO13-33_area3@s7	2.15	9.21E+08	3.93	0.40	7.56	0.74	0.04	0.53
CO13-33_area3@s10	2.15	1.05E+09	0.79	0.45	1.75	0.74	-0.11	0.57
CO13-33_area3@s13	2.15	1.03E+09	3.31	0.47	6.53	0.74	-0.05	0.59
CO13-33_area3@s14	2.15	9.58E+08	4.28	0.45	8.40	0.75	-0.04	0.58
CO13-33_area3@s15	2.16	9.73E+08	3.96	0.41	7.78	0.76	-0.04	0.55

Analysis name	PB (nA)	^{32}S (cps)	$\delta^{33}S_{VCDT}$ (‰)	2σ (‰)	$\delta^{34}S_{VCDT}$ (‰)	2σ (‰)	$\Delta^{33}S_{VCDT}$ (‰)	2σ (‰)
C013-55_vmso@1			1.61	0.18	3.41	0.35	-0.15	0.21
C013-55_vmso@10			1.67	0.16	3.26	0.32	-0.01	0.18
C013-55_vmso@11			1.77	0.16	3.41	0.33	0.01	0.18
C013-55_vmso@12			1.61	0.18	3.29	0.33	-0.08	0.20
C013-55_vmso@2			1.69	0.17	3.27	0.35	0.01	0.20
C013-55_vmso@3			1.70	0.21	3.24	0.34	0.03	0.23
C013-55_vmso@4			1.66	0.20	3.10	0.34	0.07	0.23
C013-55_vmso@5			1.63	0.20	3.12	0.35	0.03	0.23
C013-55_vmso@6			1.51	0.20	2.85	0.39	0.04	0.24
C013-55_vmso@7			1.73	0.16	3.26	0.32	0.05	0.18
C013-55_vmso@9			1.67	0.17	3.24	0.32	0.01	0.18
C013-55_area1_s1@1	2.09	7.81E+08	2.80	0.21	5.49	0.35	-0.02	0.24
C013-55_area1_s1@2	2.09	7.98E+08	3.38	0.21	6.55	0.34	0.02	0.23
C013-55_area1_s2@1	2.09	6.65E+08	3.40	0.17	6.35	0.38	0.14	0.21
C013-55_area1_s2@2	2.09	6.88E+08	2.28	0.22	4.01	0.35	0.21	0.24
C013-55_area1_s3@1	2.09	7.45E+08	3.23	0.23	5.91	0.42	0.19	0.28
C013-55_area2_s1@1	2.38	8.27E+08	3.21	0.19	5.61	0.36	0.33	0.23
C013-55_area2_s1@2	2.37	8.16E+08	2.57	0.20	4.56	0.36	0.22	0.23
C013-55_area2_s1@3	2.37	7.57E+08	3.03	0.24	5.71	0.37	0.09	0.27
C013-55_area2_s1@4	2.37	6.35E+08	2.27	0.24	4.00	0.54	0.22	0.33
C013-55_area2_s2@1	2.36	7.21E+08	1.65	0.19	3.11	0.34	0.05	0.21
C013-55_area2_s2@2*	2.34	7.29E+08	4.63	0.25	3.40	0.41	2.89	0.29
C013-55_area2_s3@1	2.39	7.57E+08	3.10	0.22	5.32	0.44	0.37	0.28
C013-55_area2_s3@2	2.38	6.35E+08	3.36	0.19	6.49	0.35	0.03	0.22
C013-55_area3_s1@1	2.33	6.05E+08	3.60	0.22	6.92	0.38	0.04	0.26
C013-55_area3_s1@2	2.32	6.89E+08	3.98	0.17	7.96	0.34	-0.11	0.20
C013-55_area3_s2@1	2.34	6.05E+08	2.12	0.20	3.37	0.36	0.38	0.23
C013-55_area3_s2@2*	2.33	7.29E+08	1.73	0.22	3.08	0.37	0.14	0.25
C013-55_area3_s2@3	2.31	6.32E+08	0.98	0.28	1.92	0.45	-0.01	0.33
C013-55_area3_s2@4	2.31	8.29E+08	2.35	0.26	3.62	0.44	0.49	0.31

*indicates the presence of a small inclusion, Cap delta 33 ignored.

Pyrite Analyses

Analysis name	PB (nA	^{32}S (cps)	$\delta\ ^{33}S_{VCDT}$ (‰)	2σ (‰)	$\delta\ ^{34}S_{VCDT}$ (‰)	2σ (‰)	$\Delta^{33}S_{VCDT}$ (‰)	2σ (‰)
C014-03_Son-a@10	2.24	1.65E+09	1.08	0.15	2.18	0.21	-0.05	0.14
C014-03_Son-a@11	2.37	1.67E+09	1.13	0.14	2.24	0.21	-0.03	0.13
C014-03_Son-a@12	2.45	1.72E+09	1.09	0.15	2.23	0.21	-0.06	0.14
C014-03_Son-a@13	2.45	1.72E+09	1.18	0.15	2.25	0.21	0.02	0.14
C014-03_Son-a@14	2.33	1.63E+09	1.06	0.16	2.14	0.21	-0.04	0.15
C014-03_Son-a@15	2.30	1.61E+09	1.07	0.17	2.06	0.21	0.01	0.15
C014-03_Son-a@16	2.23	1.57E+09	1.09	0.14	2.12	0.21	0.00	0.13
C014-03_Son-a@17	2.22	1.56E+09	1.10	0.15	2.19	0.21	-0.02	0.14
C014-03_Son-a@18	2.16	1.51E+09	1.09	0.14	2.24	0.21	-0.07	0.13
C014-03_Son-a@19	2.14	1.49E+09	1.07	0.16	2.35	0.21	-0.14	0.14
C014-03_Son-a@20	2.03	1.42E+09	1.14	0.16	2.28	0.21	-0.03	0.14
C014-03_Son-a@21	2.02	1.41E+09	1.15	0.14	2.25	0.21	-0.01	0.12
C014-03_Son-a@22	1.91	1.33E+09	1.14	0.15	2.21	0.21	0.00	0.14
C014-03_Son-a@23	1.90	1.32E+09	1.15	0.17	2.29	0.21	-0.03	0.16
C014-03_Son-a@24	1.85	1.29E+09	1.13	0.17	2.20	0.21	0.00	0.16
C014-03_Son-a@25	1.84	1.29E+09	1.06	0.15	2.10	0.21	-0.02	0.14
C014-03_Son-a@26	1.76	1.23E+09	1.12	0.15	2.17	0.21	0.00	0.14
C014-03_Son-a@27	1.75	1.22E+09	1.06	0.16	2.23	0.21	-0.08	0.15
C014-03_Son-a@28	1.69	1.18E+09	1.11	0.16	2.28	0.21	-0.06	0.15
C014-03_Son-a@29	1.69	1.18E+09	1.17	0.16	2.23	0.22	0.03	0.15
C014-03_Son-a@30	1.69	1.18E+09	1.20	0.16	2.31	0.21	0.01	0.15
C014-03_Son-b@03	2.38	1.64E+09	1.08	0.14	2.10	0.21	0.00	0.13
C014-03_Son-b@04	2.43	1.65E+09	1.07	0.15	2.12	0.21	-0.02	0.14
C014-03_Son-b@05	2.28	1.54E+09	1.13	0.14	2.17	0.21	0.02	0.13
C014-03_Son-b@06	2.21	1.51E+09	1.09	0.14	2.12	0.21	0.00	0.13
C014-03_Son-b@07	2.13	1.45E+09	1.10	0.14	2.16	0.21	-0.01	0.13
C014-03_Son-b@08	2.01	1.36E+09	1.08	0.15	2.09	0.21	0.01	0.14
C014-03_Son-b@09	1.89	1.28E+09	0.94	0.15	2.00	0.21	-0.09	0.14
C014-03_Son-b@10	1.84	1.27E+09	0.89	0.16	2.09	0.21	-0.18	0.15
C014-03_Son-b@11	1.74	1.27E+09	1.05	0.17	1.85	0.79	0.10	0.43
C014-03_area1@1	2.24	1.30E+09	3.55	0.15	7.04	0.21	-0.06	0.14
C014-03_area1@2	2.20	1.31E+09	3.00	0.16	5.89	0.21	-0.03	0.15
C014-03_area1@3	2.36	1.50E+09	3.38	0.14	6.68	0.21	-0.05	0.13
C014-03_area1@4	2.35	1.53E+09	3.87	0.16	7.28	0.21	0.12	0.15
C014-03_area1@4-1	2.37	1.54E+09	3.39	0.15	6.58	0.21	0.01	0.14
C014-03_area1@5	2.35	1.54E+09	3.37	0.15	6.42	0.21	0.07	0.14
C014-03_area1@6	2.24	1.46E+09	3.90	0.17	7.61	0.21	-0.02	0.15
C014-03_area1@7	2.25	1.46E+09	3.93	0.14	7.59	0.21	0.03	0.13
C014-03_area1@8	2.25	1.47E+09	3.35	0.14	6.52	0.21	-0.01	0.13
C014-03_area2@1	2.08	1.38E+09	5.55	0.14	10.77	0.21	0.02	0.13
C014-03_area2@10	1.93	1.27E+09	5.60	0.16	10.92	0.21	-0.01	0.15
C014-03_area2@11	1.95	1.27E+09	3.81	0.16	7.47	0.21	-0.03	0.15
C014-03_area2@12	1.96	1.28E+09	3.09	0.17	6.17	0.21	-0.08	0.16
C014-03_area2@13	1.98	1.28E+09	3.96	0.15	7.85	0.21	-0.08	0.14
C014-03_area2@2	2.18	1.46E+09	6.20	0.15	12.10	0.21	-0.01	0.14
C014-03_area2@3	2.19	1.48E+09	6.35	0.14	12.47	0.21	-0.05	0.13
C014-03_area2@4	2.20	1.50E+09	7.88	0.16	15.48	0.21	-0.07	0.15
C014-03_area2@5	2.06	1.36E+09	7.67	0.16	15.08	0.21	-0.07	0.15
C014-03_area2@7	2.04	1.36E+09	6.81	0.15	13.08	0.21	0.10	0.13
C014-03_area2@8	2.05	1.38E+09	3.84	0.15	7.52	0.21	-0.02	0.13
C014-03_area2@9	1.87	1.24E+09	4.20	0.15	8.23	0.21	-0.03	0.14
C014-03_area3@1	1.71	1.16E+09	3.83	0.15	7.58	0.21	-0.07	0.14
C014-03_area3@10	1.70	1.14E+09	6.15	0.16	12.15	0.21	-0.09	0.15
C014-03_area3@11	1.70	1.16E+09	3.32	0.16	6.41	0.22	0.03	0.15
C014-03_area3@2	1.78	1.20E+09	4.13	0.16	7.99	0.21	0.02	0.15
C014-03_area3@3	1.79	1.21E+09	6.86	0.16	13.38	0.21	-0.01	0.15
C014-03_area3@4	1.80	1.22E+09	4.49	0.16	8.94	0.21	-0.10	0.15
C014-03_area3@5	1.86	1.26E+09	3.90	0.14	7.57	0.21	0.00	0.13
C014-03_area3@6	1.81	1.22E+09	6.82	0.15	13.51	0.21	-0.11	0.14
C014-03_area3@7	1.87	1.28E+09	3.65	0.14	7.06	0.21	0.03	0.13
C014-03_area3@8	1.86	1.28E+09	3.87	0.15	7.58	0.21	-0.03	0.14
C014-03_area3@9	1.70	1.12E+09	6.05	0.15	11.95	0.22	-0.08	0.14

Analysis name	PB (nA)	^{32}S (cps)	$\delta^{33}S_{VCDT}$ (‰)	2σ (‰)	$\delta^{34}S_{VCDT}$ (‰)	2σ (‰)	$\Delta^{33}S_{VCDT}$ (‰)	2σ (‰)
CO14-04_son@1	2.08	1.75E+09	1.12	0.12	2.25	0.15	-0.04	0.10
CO14-04_son@03	2.08	1.79E+09	1.08	0.13	2.14	0.15	-0.02	0.11
CO14-04_son@04	2.08	1.78E+09	1.04	0.12	2.10	0.16	-0.04	0.10
CO14-04_son@05	2.09	1.74E+09	1.02	0.12	1.98	0.15	0.00	0.10
CO14-04_son@06	2.09	1.81E+09	1.12	0.12	2.21	0.15	-0.02	0.10
CO14-04_son@07	2.08	1.80E+09	1.15	0.13	2.21	0.15	0.01	0.11
CO14-04_son@08	2.07	1.80E+09	1.19	0.17	2.28	0.15	0.02	0.15
CO14-04_son@09	2.06	1.80E+09	1.11	0.12	2.17	0.15	0.00	0.10
CO14-04_son@10	2.06	1.78E+09	1.14	0.13	2.22	0.16	-0.01	0.11
CO14-04_son@11	2.05	1.79E+09	1.08	0.12	2.18	0.15	-0.04	0.09
CO14-04_son@12	2.04	1.77E+09	1.05	0.12	2.25	0.15	-0.11	0.10
CO14-04_son@13	2.04	1.79E+09	1.12	0.12	2.19	0.15	-0.01	0.10
CO14-04_son@14	2.02	1.76E+09	1.07	0.13	2.20	0.15	-0.06	0.11
CO14-04_son@15	2.01	1.78E+09	1.11	0.13	2.12	0.15	0.02	0.11
CO14-04_son@16	2.01	1.77E+09	1.00	0.12	2.11	0.15	-0.08	0.10
CO14-04_area1@1	2.09	1.77E+09	1.99	0.12	3.82	0.15	0.02	0.10
CO14-04_area1@2	2.09	1.78E+09	2.12	0.12	3.92	0.15	0.11	0.10
CO14-04_area1@3	2.10	1.83E+09	2.05	0.12	3.90	0.15	0.04	0.10
CO14-04_area1@4	2.11	1.82E+09	1.98	0.13	4.04	0.15	-0.10	0.11
CO14-04_area1@5	2.12	1.82E+09	2.08	0.13	3.92	0.15	0.06	0.11
CO14-04_area1@6	2.08	1.80E+09	2.13	0.12	3.99	0.15	0.08	0.10
CO14-04_area1@7	2.07	1.79E+09	2.04	0.12	4.04	0.15	-0.04	0.10
CO14-04_area1@8	2.07	1.80E+09	2.03	0.13	3.85	0.15	0.05	0.11
CO14-04_area1@9	2.07	1.79E+09	2.01	0.13	3.90	0.15	0.00	0.11
CO14-04_area1@10	2.07	1.82E+09	1.87	0.12	3.66	0.15	-0.02	0.10
CO14-04_area1@21	2.05	1.77E+09	1.84	0.13	3.62	0.15	-0.03	0.11
CO14-04_area1@22	2.05	1.76E+09	2.00	0.14	4.02	0.15	-0.07	0.12
CO14-04_area1@23	2.05	1.75E+09	2.36	0.12	4.47	0.15	0.06	0.10
CO14-04_area1@24	2.05	1.76E+09	2.13	0.14	4.21	0.15	-0.04	0.12
CO14-04_area1@25	2.06	1.78E+09	2.16	0.12	4.21	0.15	0.00	0.10
CO14-04_area1@26	2.05	1.75E+09	2.03	0.12	3.93	0.15	0.01	0.10
CO14-04_area1@27	2.05	1.76E+09	2.04	0.12	3.91	0.15	0.02	0.10

Analysis name	PB (nA)	^{32}S (cps)	$\delta^{33}S_{VCDT}$ (‰)	2σ (‰)	$\delta^{34}S_{VCDT}$ (‰)	2σ (‰)	$\Delta^{33}S_{VCDT}$ (‰)	2σ (‰)
C014-04_son@01	2.35	1.12E+09	1.05	0.14	2.11	0.11	-0.04	0.13
C014-04_son@02	2.35	1.33E+09	0.87	0.14	2.04	0.10	-0.18	0.13
C014-04_son@03	2.45	1.40E+09	0.93	0.15	2.18	0.10	-0.19	0.14
C014-04_son@04	2.46	1.40E+09	1.02	0.15	2.27	0.10	-0.15	0.14
C014-04_son@05	2.45	1.40E+09	1.12	0.14	2.21	0.10	-0.02	0.13
C014-04_son@06	2.44	1.41E+09	1.15	0.14	2.17	0.10	0.03	0.13
C014-04_son@07	2.44	1.39E+09	1.08	0.15	2.14	0.15	-0.02	0.16
C014-04_son@08	2.44	1.42E+09	1.09	0.14	2.22	0.10	-0.05	0.13
C014-04_son@09	2.43	1.39E+09	1.21	0.13	2.21	0.10	0.07	0.12
C014-04_son@10	2.42	1.40E+09	1.04	0.14	2.15	0.10	-0.07	0.13
C014-04_son@11	2.37	1.36E+09	1.05	0.14	2.13	0.10	-0.05	0.13
C014-04_son@12	2.37	1.36E+09	1.10	0.14	2.11	0.10	0.02	0.13
C014-04_son@13	2.30	1.33E+09	1.12	0.15	2.13	0.10	0.02	0.14
C014-04_son@14	2.30	1.31E+09	1.12	0.15	2.22	0.10	-0.02	0.14
C014-04_son@15	2.25	1.34E+09	1.11	0.15	2.15	0.10	0.01	0.14
C014-04_son@16	2.25	1.34E+09	1.10	0.14	2.17	0.10	-0.02	0.13
C014-04_son@17	2.21	1.32E+09	1.18	0.15	2.14	0.11	0.07	0.14
C014-04_son@18	2.20	1.32E+09	1.13	0.14	2.24	0.10	-0.02	0.13
C014-04_son@19	2.19	1.31E+09	1.01	0.14	2.18	0.10	-0.11	0.13
C014-04_son@20	2.18	1.31E+09	1.02	0.15	2.20	0.11	-0.11	0.14
C014-04_area2@1	2.44	1.43E+09	2.33	0.13	4.58	0.10	-0.03	0.12
C014-04_area2@11	2.37	1.36E+09	2.24	0.14	4.57	0.10	-0.11	0.13
C014-04_area2@12	2.37	1.36E+09	2.15	0.14	4.37	0.10	-0.10	0.13
C014-04_area2@13	2.36	1.39E+09	2.22	0.14	4.28	0.10	0.02	0.13
C014-04_area2@14	2.35	1.39E+09	2.14	0.13	4.30	0.10	-0.07	0.12
C014-04_area2@2	2.44	1.44E+09	2.45	0.14	4.61	0.10	0.07	0.13
C014-04_area2@21	2.34	1.36E+09	2.22	0.14	4.14	0.16	0.09	0.14
C014-04_area2@22	2.32	1.37E+09	2.25	0.13	4.41	0.10	-0.02	0.12
C014-04_area2@23	2.31	1.38E+09	2.11	0.15	4.10	0.14	0.00	0.15
C014-04_area2@24	2.29	1.24E+09	2.10	0.17	4.07	0.20	0.00	0.19
C014-04_area2@25	2.29	1.30E+09	2.36	0.15	4.48	0.12	0.06	0.14
C014-04_area2@26	2.28	1.26E+09	2.47	0.15	4.92	0.11	-0.06	0.14
C014-04_area2@27	2.27	1.24E+09	2.56	0.14	5.01	0.10	-0.02	0.13
C014-04_area2@28	2.26	1.36E+09	2.32	0.15	4.66	0.10	-0.08	0.14
C014-04_area2@29	2.24	1.36E+09	2.22	0.14	4.42	0.10	-0.06	0.13
C014-04_area2@3	2.19	1.33E+09	2.24	0.13	4.50	0.10	-0.08	0.12
C014-04_area2@30	2.23	1.41E+09	2.25	0.14	4.51	0.10	-0.07	0.13
C014-04_area2@31	2.23	1.41E+09	2.23	0.15	4.40	0.10	-0.04	0.14
C014-04_area2@32	2.22	1.41E+09	2.26	0.15	4.39	0.11	0.00	0.14
C014-04_area2@4	2.44	1.47E+09	2.21	0.16	4.38	0.10	-0.04	0.15
C014-04_area2@5	2.44	1.48E+09	2.19	0.15	4.46	0.10	-0.10	0.14
C014-04_area2@6	2.44	1.41E+09	2.30	0.16	4.35	0.10	0.06	0.15
C014-04_area2@7	2.41	1.41E+09	2.28	0.15	4.59	0.10	-0.08	0.14
C014-04_area2@8	2.40	1.36E+09	2.20	0.15	4.38	0.10	-0.05	0.14
C014-04_area2@9	2.39	1.40E+09	2.11	0.13	4.41	0.10	-0.16	0.12
C014-04_area2_s3@1	2.20	1.32E+09	2.58	0.16	5.06	0.10	-0.03	0.15
C014-04_area3@1	2.20	1.32E+09	2.67	0.16	5.11	0.10	0.04	0.15
C014-04_area3@2	2.19	1.33E+09	2.21	0.16	4.64	0.10	-0.17	0.15
C014-04_area3@3	2.19	1.29E+09	2.76	0.14	5.42	0.10	-0.03	0.13
C014-04_area3@4	2.21	1.30E+09	2.53	0.14	5.02	0.10	-0.06	0.13

APPENDIX F

CONFERENCE ABSTRACTS

The results of this thesis have been presented at international and local conferences during the time of candidature, as follows:

Crossley, R., Evans, K., Evans, N. & McDonald, B. "An *in situ* investigation of chalcophile and siderophile element cycling in Subduction Zones: insights from high-pressure ultramafic rocks from Alpine Corsica", *Goldschmidt Abstracts*, 2015, 618. Oral presentation, Prague, Czech Republic, August 2015.

Crossley, R., Evans, K., Evans, N., McDonald, B., Roberts, M., Hayes, S. & Reddy, S. "Trace element zonation of sulphides and spinels in ultramafic rocks from Alpine Corsica", *2015 TIGeR Conference abstracts 'Key issues in fluid-rock interaction: from the nano to the macroscale'*, p. 54. Poster presentation, Curtin University, Perth, Western Australia, September 2015.

Crossley, R., Evans, K., Jeon, H., Kilburn, M., Roberts, M., & Reddy S., "In-situ isotopic analysis of sulfides in high-pressure serpentinites", *Goldschmidt Abstracts*, 2016, 565. Oral presentation, Yokohama, Japan, June 2016.

Crossley, R., Evans, K., Evans, N., McDonald, B. & Reddy, S. "PGE mobilisation in subduction zones and implications for ore deposit formation", 13th International Ni-Cu-PGE-Symposium, Fremantle, Australia, *WA Dept Mines and Petroleum Record 2016/13*, 39. Poster presentation, September 2016.

Crossley, R., Evans, K., Evans, N., McDonald, B. & Reddy, S. "HSE (PGE, Au & Au) mobilisation in subduction zones", *2016 TIGeR conference abstracts 'Rock alteration in the Upper Crust: Element mobility and concentration',* p12. Poster presentation, TIGeR conference, Perth, Western Australia, September 2016.

Crossley, R., Evans, K., Reddy, S. & Lester, G. "Redistribution of iron and titanium in subduction zones: insights from high-pressure serpentinites." *EGU General Assembly Conference Abstracts*, 19, 1081. Oral presentation, Vienna, Austria, April 2017.